Russian Academy of Sciences

Proceedings

St Petersburg
Russia
23–27 June 1997

DISTRIBUTION STATEMENT A
Approved for public release;
Distribution Unlimited

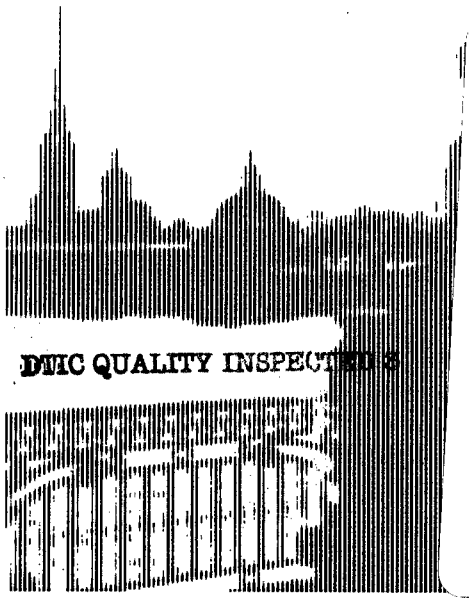

DTIC QUALITY INSPECTED 3

19970909 164

International Symposium

INDUSTRIAL FLOWS AND PROCESSES

NANOSTRUCTURES:
PHYSICS AND TECHNOLOGY

International Symposium

Co-Chairmen

Zh.Alferov
L.Esaki

PROCEEDINGS

St Petersburg, Russia, June 23–27, 1997

DTIC QUALITY INSPECTED 5

ISBN 5-86763-106-0

Published by Ioffe Physico-Technical Institute
26 Polytechnicheskaya, St Petersburg 194021, Russia
Phones: (812) 247 6805, 247 9932
Fax: (812) 247 2135

The Symposium is held under the auspices of
the Russian Academy of Sciences

Organizers

The Institutions of the Russian Academy of Sciences:
Division of General Physics and Astronomy
St Petersburg Scientific Centre
Ioffe Physico-Technical Institute
Research & Engineering Centre for Micrcelectronics at the Ioffe Institute

Location and Date

The Symposium will be held at the hotel
Dom Tvorchestva Kinematographistov
in St Petersburg's recreation area Repino
on June 23–27, 1997.

Acknowledgments

The Programme and Organizing Committees are grateful to
the following organizations for their financial support:
Russian Ministry of Science and Technologies
Russian Foundation for Basic Research
The European Research Office of the U.S. Army
Ioffe Physico Technical Institute

Programme Committee

R. Suris, Chair *(St Petersburg)*
Zh. Alferov *(St Petersburg)*
L. Asryan, Secretary *(St Petersburg)*
S. Gaponov *(Nizhnii Novgorod)*
A. Gippius *(Moscow)*
Yu. Gulyaev *(Moscow)*
S. Gurevich *(St Petersburg)*
L. Keldysh *(Moscow)*
Yu. Kopaev *(Moscow)*
P. Kop'ev *(St Petersburg)*
M. Kupriyanov *(Moscow)*
V. Mokerov *(Moscow)*
V. Panov *(Moscow)*
N. Samsonov *(Moscow)*
N. Sibel'din *(Moscow)*
V. Timofeev *(Chernogolovka)*
B. Zakharchenya *(St Petersburg)*

Organizing Committee

M. Mizerov, Chair *(Centre for Microelectronics)*
V. Grigor'yants, Secretary *(Ioffe Institute)*
L. Asryan *(Ioffe Institute)*
B. Egorov *(Ioffe Institute)*
P. Kop'ev *(Ioffe Institute)*
A. Orbeli *(Ioffe Institute)*
A. Prokhorenko *(St Petersburg Scientific Centre)*
L. Solov'eva *(Ioffe Institute)*
V. Zayats *(Division of General Physics and Astronomy)*

Contents

Electron phase sensitive phenomena

EPSP.01I ***H.Takayanagi***
Quantum transport in semiconductor-coupled superconducting junctions 1

EPSP.02I ***V.T.Petrashov***
Phase-periodic transport in non-equilibrium normal/superconducting nanostructures . . . . . *

EPSP.03p *Yu.G.Arapov, G.I.Harus, V.N.Neverov,* ***N.G.Shelushinina,*** *A.I.Ponomarev, A.N.Ignatenkov, L.D.Sabirzyanova, N.K.Lerinman, N.A.Babushkina*
Weak 2D-localization effects in multilayer heterostructures and highly anisotropic crystals 7

EPSP.04p *B.A.Aronzon, D.A.Bakaushin, N.K.Chumakov, E.Z.Meilikhov, V.V.Ryl'kov,* ***A.S.Vedeneev***
High-temperature mesoscopic and quantum quasi-1D percolation-like conductivity of strongly disordered field-effect systems 11

EPSP.05p *A.P.Dmitriev,* ***I.V.Gornyi,*** *V.Yu.Kachorovskii*
Nonbackscattering contribution to the weak localization 15

EPSP.06p ***V.A.Sablikov,*** *B.S.Shchamkhalova*
Resonant conductance of ineracting electrons in open mesoscopic structures 18

EPSP.07p ***S.Yu.Shapoval,*** *V.L.Gurtovoi, V.V.Valyev, V.V.Sirotkin*
Metal nanoprobe induced electrostatic quantization in near surface delta-doped GaAs structure at 300 K 22

EPSP.08p *I.N.Zhilyaev,* ***S.G.Boronin,*** *S.V.Dubonos, I.A.Sosnin*
Inverted magnetoresistive oscillations in mesoscopic aluminum films 24

EPSP.09p *I.N.Zhilyaev,* ***S.G.Boronin***
Magnetoresistance oscillations in ring-tunnel junction structure . . 25

EPSP.10p *I.N.Zhilyaev,* ***S.G.Boronin,*** *S.V.Dubonos*
New magnetoresistive oscillations in connecting lines of ring structures 26

Excitons in quantum well and superlattices

EQW/SL.01I ***V.B.Timofeev***
Interwell radiative recombination in n-i-n AlGaAs/GaAs double quantum wells 27

EQW/SL.02I ***A.V.Kavokin,*** *M.R.Vladimorova, L.C.Andreani, G.Panzarini*
Inhomogenious broadening effect on the exciton-light coupling in quantum wells 31

EQW/SL.03i ***Yu.E.Lozovik***
Phase diagram, superfluidity and exciton spectra in double quantum system 37

EQW/SL.04p *G.N.Aliev, N.V.Luk'yanova,* ***R.P.Seisyan***
Exciton-polariton behaviour of the absorption edge of thin GaAs crystals with the "super-quantum" thickness 38

EQW/SL.05p ***G.Astakhov,*** *V.Kochereshko, D.Yakovlev, A.Platonov, T.Wojovich, G.Karchevsky, W.Ossau, G.Landwehr*
Homogeneous broadening of neutral and negatively-charged exciton lines in modulation-doped QWs 42

EQW/SL.06p *A.Armitage, M.S.Skolnick, T.A.Fisher, D.M.Whittaker, J.S.Roberts, V.N.Astratov,* ***M.A.Kaliteevski,*** *A.V.Kavokin, M.R.Vladimirova, L.C.Andreani, G.Panzarini*
Photon-induced lifting of the degeneracy of excitonic states in coupled microcavities 43

EQW/SL.07p *P.G.Baranov,* ***N.G.Romanov,*** *A.Hofstaetter, B.K.Meyer, A.Scharmann, C.Schnorr, W. von Foerster, F.J.Ahlers, K.Pierz*
Splitting and order of exciton radiative levels in GaAs/AlAs superlattices: a link to the interface morphology 47

EQW/SL.08p ***G.F.Glinskii,*** *K.O.Kravchenko*
A new approach to the polariton problem in heterostructures. The correct boundary conditions and optical reflection at AlGaAs/GaAs-heterojunctions 51

EQW/SL.09p ***L.E.Golub,*** *S.V.Ivanov, E.L.Ivchenko, A.A.Kiselev, T.V.Shubina, A.A.Toropov, J.P.Bergman, G.R.Pozina, B.Monemar, M.Willander*
Hopping relaxation of localized excitons in quantum wells studied by time-resolved photoluminescence spectroscopy 54

EQW/SL.10p ***S.V.Goupalov,*** *E.L.Ivchenko, A.V.Kavokin*
Excited states of localized excitons in quantum well structures: long-range exchange splitting 58

EQW/SL.11p *P.Le Jeune,* ***X.Marie,*** *T.Amand, M.Paillard, F.Romstad, J.Barrau, M.Brousseau*
Coherent control of exciton spin in quantum well 62

EQW/SL.12p *A.V.Kavokin, M.R.Vladimirova,* ***M.A.Kaliteevski,*** *O.Lyngnes, J.D.Berger, H.M.Gibbs, G.Khitrova*
Resonant Faraday rotation in a semiconductor microcavity 64

EQW/SL.13p ***V.Kochereshko,*** *D.Yakoviev, W.Ossau, G.Landwehr, T.Wojtowicz, G.Karczewski, J.Kossut*
Combined exciton-electron processes in modulation doped QW structures 68

EQW/SL.14p ***S.I.Kokhanovskii,*** *K.Moumanis, M.E.Sasin, R.P.Seisyan*
Pecularities of the light hole transitions in substrate-free stressed heterosystem (In,Ga)As/GaAs with MQWs 69

EQW/SL.15p *V.V.Krivolapchuk, D.A.Mazurenko,* ***E.S.Moskalenko,*** *N.K.Poletaev, A.L.Zhmodikov, T.S.Cheng, C T.Foxon*
Anomalous effect of magnetic field on the indirect exciton in GaAs double quantum wells 73

EQW/SL.16p ***K.Litvinenko,*** *A.Gorshunov, V.I.Grinev, J.M.Hvam, V.G.Lyssenko*
The influence of real carriers on the optical Stark effect in GaAs/AlGaAs superlattice 77

EQW/SL.17p ***A.V.Platonov,*** *D.R.Yakovlev, U.Zehnder, V.Kochereshko, W.Ossau, F.Fisher, Th.Litz, A.Waag, G.Landwehr*
Excitonic states in type-I and type-II quantum well structures based on beryllium chalcogenides 81

EQW/SL.18p ***M.E.Portnoi,*** *I.Galbraith*
Screened excitons in quantum wells 83

General properties of low-dimensional structures

GP.01i ***A.Forchel***
Confined optical modes in photonic dots . . . . . *

GP.02i ***J.Kim,*** *H.Kan, Y.Yamamoto*
Single photon state generation and detection: single photon turnstile device and solid state photomultiplier 87

GP.03i *Yu.E.Lozovik, A.L.Dobryakov, V.M.Farztdinov, S.A.Kovalenko, Yu.A.Matveets,* ***E.A.Vinogradov***
Dynamics of semiconductor microcavity modes in femtosecond time scale 89

GP.04p ***V.I Belitsky,*** *M.Gardona, A.Cantarero, L.I.Korovin, I.G.Lang, S.T.Pavlov*
Triple magnetopolarons in quantum wells 95

GP.05p ***D.O.Filatov,*** *I.A.Karpovich, M.V.Stepikhova, W.Jantsch*
Effect of the near-QW band bending due to QW charging on confinement of light holes in the InGaAs/GaAs strained quantum well 99

GP.06p ***I.P.Ipatova,*** *A.Yu.Maslov, O.V.Proshina*
Pekar polaron in quantum wells, wires and dots 102

GP.07p ***V.K.Kalevich,*** *B.P.Zakharchenya, K.V.Kavokin, P.Le Jeune, X.Marie, D.Robart, T.Amand, J.Barrau, M.Brousseau*
Determination of the sign of the conduction-electron g-factor in semiconductor quantum wells by means of the Hanle effect and spin quantum beats techniques 106

GP.08p ***Yu.E.Kitaev,*** *A.G.Panfilov, P.Tronc, V.P.Smirnov*
Dependence of optical spectra of superlattices on the site symmetry of impurities and defects 110

GP.09p ***V.A.Larionova,*** *A.V.Germanenko*
Interband mixing between 2D electron and 3D heavy hole states in narrow gap semiconductor 114

GP.10p ***A.F.Polupanov***, *V.I.Galiev, A.N.Kruglov, S.G.Shekhovtsov, E.M.Goldys, T.L.Tansley*
Scattering of holes by quantum-well heterostructures 118

GP.11p ***Y.T.Rebane***, *Y.G.Shreter, M.Albrecht*
Stacking faults as quantum wells for electrons in wurtzite GaN . . 122

GP.12p ***A.A.Rogachev***
Exciton complexes in multi-valley semiconductors 126

GP.13p ***A.V.Subashiev***, *E.P.German*
Polarization anomalies in luminescence and electron emission from highly doped semiconductor structures with splitted valence band 130

GP.14p *E.E.Takhtamirov*, ***V.A.Volkov***
The effect of the heterojunction abruptness on the one-band envelope-function method 134

Intraband transitions and phenomena in infrared and microwave regions in quantum wells and superlattices

ITPIM.01i ***S.Sauvage***, *P.Boucaud, F.H.Julien, J.-M.Gérard, J.-Y.Marzin*
Infrared spectroscopy of intraband transitions in self-organized InAs/GaAs quantum dots 567

ITPIM.02i ***A.A.Andronov***
Real space transfer and population inversion in delta selectively doped MQW structures 565

ITPIM.03p *V.Ya.Aleshkin, N.A.Bekin, I.V.Erofeeva,* ***V.I.Gavrilenko***, *M.Helm, Z.F.Krasil'nik, O.A.Kuznetsov, M.D.Moldavskaya, V.Nikonorov, M.V.Yakunin*
Cyclotron resonance and intersubband absorption in p-type MQW Ge/GeSi heterostructures in quantizing magnetic fields 137

ITPIM.04p *V.Ya.Aleshkin, A.A.Andronov, D.M.Gaponova, V.I.Gavrilenko,* ***D.G.Revin***, *B.N.Zvonkov, I.G.Malkina, E.A.Uskova*
Lateral electric field effects on photoluminescence from InGaAs/GaAs MQW heterostructures 141

ITPIM.05p ***A.Balandin***, *A.Svizhenko, S.Bandyopadhyay*
Infrared second harmonic generation in a generic quantum wire biased with a magnetic field 144

ITPIM.06p *A.M.Belyantsev,* ***A.B.Kozyrev***
Generation of high-frequency oscillations in multilayer heterostructures with nanolayers 148

ITPIM.07p *O.Gauthier-Lafaye,* ***S.Sauvage***, *P.Boucaud, F.H.Julien*
Quantum Fountain intersubband stimulated emission in GaAs/AlGaAs quantum wells 569

ITPIM.08p ***M.P.Mikhailova***, *N.L.Bazhenov, V.A.Berezovets, A.V.Chernjaev, V.I.Ivanov-Omskii, K.D.Moiseev, R.V.Parfeniov, V.A.Smirnov, Yu.P.Yakovlev*
Infrared emission from the interface and magnetotransport of type II broken-gap p-GaInAsSb/p-InAs heterojunctions 152

ITPIM.09p ***V.I.Sankin***, *A.A.Lepneva*
Drift velocities, Bloch oscillations and electron impact ionization in silicon carbide superlattices 155

ITPIM.10p ***O.A.Tkachenko***, *D.G.Baksheyev, M.B.Wojtsekhowski, V.A.Tkachenko*
Simplest structures for stimulated photon emission by transitions from continuum to a quasilevel 159

ITPIM.11p ***L.E.Vorobjev***, *L.E.Golub, E.A.Zibik, I.E.Titkov, D.A.Firsov, V.A.Shalygin, E.Towe*
Absorption of infrared radiation caused by bound-to-bound and bound-to-continuum direct transitions of hot carriers in simple rectangular and asymmetrical coupled multiple quantum wells . . 161

ITPIM.12p ***L.E.Vorobjev***, *S.N.Danilov, D.V.Donetsky, Yu.V.Kochegarov, I.E.Titkov, D.A.Firsov, V.A.Shalygin, V.N.Tulupenko, G.G.Zegrya, E.Towe*
Emission and absorption of FIR radiation by hot electrons in simple recangular and asymmetric tunnel-coupled quantum wells 164

Lasers and optoelectronic devices

LOED.01p *A.D.Andreev*, ***G.G.Zegrya***
Calculation of threshold characteristics of 3-4 μm compressively strained InAlAsSb MQW lasers 168

LOED.02p ***A.D.Andreev***, *G.G.Zegrya*
Effect of strain on Auger recombination in type-II quantum wells . 172

LOED.03p ***L.V.Asryan***, *R.A.Suris*
Effect of carrier recombination in the optical confinement layer on the temperature dependence of threshold current density of a quantum dot laser 176

LOED.04p *A.G.Deryagin, V.I.Kuchinskii, D.V.Kuksenkov*, ***G.S.Sokolovskii***, *H.Temkin*
1.5 μm multiquantum well four-wavelength DFB laser array for multigigabit/s high-density WDM system applications 180

LOED.05p ***N.Yu.Gordeev***, *A.M.Georgievski, V.I.Kopchatov, S.V.Zaitsev, A.Yu.Egorov, A.R.Kovsh, V.M.Ustinov, A.E.Zhukov, P.S.Kop'ev*
Modal composition of radiation in room temperature quantum dot lasers 183

LOED.06p *N.A.Gun'ko, G.G.Zegrya, **Z.N.Sokolova**, V.B.Khalfin*
Influence of intervalence band absorption on characteristics of long wavelength lasers based on InAs 187

LOED.07p *M.A.Kaliteevski, E.L.Portnoi, **G.S.Sokolovskii**, J.S.McKillop*
Phase effects in grating coupled surface emitting laser diodes . . 191

LOED.08p *N.N.Ledentsov, V.M.Ustinov, A.Yu.Egorov, A.E.Zhukov, A.R.Kovsh, M.V.Maximov, P.S.Kop'ev, Zh.I.Alferov, J.A.Lott, D.Bimberg*
Low threshold (<200 μA, 300 K) vertical cavity lasers based on vertically coupled quantum dots emitting at ~1 μm 195

LOED.09p *E.Lugagne-Delpon, J.L.Oudar, A.Shen, **N.Stelmakh**, J.M.Lourtioz*
Ultrafast excitonic saturable absorption in ion-implanted InGaAs/InAlAs multiple quantum wells 199

LOED.10p ***M.V.Maximov**, Yu.M.Shernyakov, N.N.Ledentsov, Zhao Zhen, A.F.Tsatsul'nikov, A.V.Lunev, A.V.Sakharov, V.M.Ustinov, A.Yu.Egorov, A.E.Zhukov, A.R.Kovsh, S.V.Zaitsev, N.Yu.Gordeev, P.S.Kop'ev, Zh.I.Alferov, D.Bimberg*
High power InGaAs/AlGaAs quantum dot laser 202

LOED.11p ***S.Sorokin**, S.Ivanov, A.Toropov, T.Shubina, I.Sedova, M.Tkatchman, P.Kop'ev, Zh.Alferov*
MBE growth and characterization of (Zn,Mg)SSe/ZnCdSe SCH SQW blue-green lasers with short-period superlattice waveguide 206

LOED.12p *A.A.Toropov, S.V.Ivanov, T.V.Shubina, **A.V.Lebedev**, S.V.Sorokin, G.N.Aliev, M.G.Tkatchman, N.D.Il'inskaya, P.S.Kop'ev*
Waveguide and vertical-cavity optically pumped blue-green lasers based on ZnCdSe/ZnSSe superlattices and multiple quantum wells 210

LOED.13p ***G.G.Zegrya***
New fundamental approach to creation of mid-infrared lasers operating at high temperature 214

LOED.14p *G.G.Zegrya, **A.S.Polkovnikov***
Theoretical analysis of Auger recombination mechanisms in semiconductor quantum wells 218

Nanostructure characterisation and novel atomic-scale probing techniques

NC.01i *V.P.Evtikhiev, A.K.Kryganovskii, **A.N.Titkov**, V.E.Tokranov, A.Nakamura, M.Ichida*
Growth and evaporation of InAs quantum dot nanoislands on GaAs(100) vicinal surfaces misoriented to the [010] direction . . . 219

NC.02p ***O.A.Aktsipetrov**, G.B.Khomutov, A.A.Fedyanin, Yu.N.Moiseev, T.V.Murzina, A.M.Tishin, Th.Rasing, K.Pedersen*
Optical second harmonic studies of metal-organic Gd superlattices fabricated by Langmuir-Blodgett technique 221

NC.03p ***V.Ya.Aleshkin***, *V.M.Daniltsev, A.V.Murel, O.I.Khrykin, V.I.Shashkin*
Band tailing in Si delta-doped GaAs 224

NC.04p *M.V.Baidakova,* ***V.I.Siklitsky,*** *A.Ya.Vul'*
Small angle X-ray study of nanostructure of ultradisperse diamond 227

NC.05p ***A.P.Boltaev,*** *N.N.Loiko, M.M.Rzaev*
Characterization of Si/Ge/Si quantum wells based on negative capacitance effect 231

NC.06p ***P.N.Brounkov,*** *A.V.Chernigovsky, A.A.Suvorova, V.V.Chaldyshev, N.A.Bert, S.G.Konnikov, V.V.Preobrazhenski, M.A.Putyato, B.R.Semyagin*
Carrier accumulation in As clasters contained LT GaAs layers . . 233

NC.07p ***P.N.Brounkov,*** *A.A.Suvorova, M.V.Maximov, A.F.Tsatsul'nikov, A.E.Zhukov, A.Yu.Egorov, A.R.Kovsh, S.G.Konnikov, T.Ihn, S.T.Stoddart, L.Eaves, P.C.Main*
Freezing of electrons in InAs/GaAs ECQDs at low temperatures . 236

NC.08p ***A.A.Bukharaev,*** *N.I.Nurgazizov*
Local electronic characterization and formation of nanoscale silicon structures using scanning resistance microscope 240

NC.09p ***A.A.Bukharaev,*** *D.V.Ovchinnikov, E.F.Kukovitskii, N.I.Nurgazizov*
Scanning force microscopy and magnetic imaging of nanometer-sized ferromagnetic spherical nickel particles 242

NC.10p ***V.Yu.Davydov,*** *Yu.E.Kitaev, I.N.Goncharuk, A.O.Lebedev, A.N.Smirnov, A.M.Tsaregorodtsev, M.B.Smirnov, A.P.Mirgorodskii, O.K.Semchinova*
Raman spectra and phonon dispersion curves of wurtzite GaN and AlN 244

NC.11p ***S.V.Dubonos,*** *A.K.Geim*
Precision magnetometry on a nanometer scale 248

NC.12p ***N.N.Faleev,*** *V.V.Chaldyshev, A.E.Kunitsyn, V.V.Tret'yakov, V.V.Preobrazhenskii, M.A.Putyato, B.R.Semyagin*
High resolution X-ray diffraction study of perfect InAs-GaAs superlattice grown by molecular-beam-epitaxy at low temperature 252

NC.13p ***V.A.Fedirko,*** *M.D.Eremtchenko, O.I.Khrykin, V.I.Shashkin*
Atomic force microcopy of A3B5 heterostructure drops 256

NC.14p ***M.F.Kokorev,*** *A.Yu.Egorov, N.A.Gordina, A.G.Kuzminkov, N.A.Maleev, V.I.Presnov, M.V.Ustinov, A.E.Zhukov*
Capacitance methods for investigation and design of MBE-grown multi-layer nanometer structures and microwave devices 259

NC.15p *M.A.Melnik, A.N.Pikhtin, A.V.Solomonov,* ***V.I.Zubkov.*** *F.Bugge*
Capacitance-voltage profiling of heterostructures with quantum wells at different temperatures 263

NC.16p *A.V.Murel, V.M.Daniltsev, O.L.Khrykin, V.I.Shashkin*
Capacitance and current characterization of GaAs with InAs quantum layer/dots 267

NC.17p *O.A.Ryabushkin*
Radio-frequency modulated reflectance in semiconductor heterostructures with 2D electron gas 270

NC.18p *M.M.Sobolev, A.R.Kovsh, V.M.Ustinov, A.Yu.Egorov, A.E.Zhukov, M.V.Maximov, N.N.Ledentsov*
Deep level transient spectroscopy of the InAs/GaAs vertically coupled quantum dot lasers structures 274

NC.19p ***V.E.Tokranov**, V.P.Evtikhiev, E.Yu.Kotelnikov, I.V.Kudryashov, D.V.Prilutsky, N.N.Faleev*
Degradation of SCH QW and GRIN SCH QW with short period superlattices GaAs/AlGaAs lasers grown by MBE 278

Nanostructure technology-1

NT-1.01i *S.Oda*
Fabrication of silicon quantum dots by pulsed-gas plasma processes and their properties 281

NT-1.02i *K.Deppert, S.-B.Carlsson, T.Junno, M.H.Magnusson, J.-O.Malm, C.Svensson, L.Samuelson*
Fabrication, characterization and manipulation of aerosol clusters 282

NT-1.03i *E.Blinov, V.G.Fleisher, H.Huhtinen, **R.Laiho**, E.Lahderanta, P.Paturi, Yu.P.Stepanov, L.Vlasenko*
Preparation and investigation of one to three unit cell thick YBCO particles by AFM and magnetic measurements 287

NT-1.04p ***A.G.Banshchikov**, M.V.Baidakova, B.P.Zakharchenya, K.Saito, N.S.Sokolov, S.M.Suturin, M.Tanaka*
MBE growth and characterization of ferromagnetic MnAs layers on CaF_2/Si(111) 288

NT-1.05p ***V.V.Chaldyshev**, N.A.Bert, A.A.Suvorova, V.V.Preobrazhenskii, M.A.Putyato, B.R.Semyagin*
Efficiency of two-dimensional precipitation and evolution of As cluster systems in low-temperature grown GaAs films delta-doped with indium 292

NT-1.06p *G.E.Cirlin, **V.N.Petrov**, N.K.Polyakov, V.N.Demidov, N.P.Korneeva, A.O.Golubok, S.A.Masalov, N.P.Ponomareva, N.N.Ledentsov, D.Bimberg*
The mechanism of InAs/GaAs heteroepitaxial growth during submonolayer migration enhanced epitaxy 296

NT-1.07p ***A.Yu.Egorov**, A.R.Kovsh, V.M.Ustinov, A.E.Zhukov, P.S.Kop'ev*
A thermodynamic analysis of the growth of III-V compounds with two volatile group V elements by molecular beam epitaxy 300

NT-1.08p ***V.I.Emel'yanov**, I.M.Panin*
Formation of three-dimensional nanometer periodic and localized defect-deformational structures and amorphyzation in solids . . . 304

NT-1.09p *I.Grekhov, V.Borevich, **L.Delimova**, I.Liniichuk, A.Lyublinsky*
A new principle of ultrathin HTSC film fabrication 305

NT-1.10p *I.P.Ipatova, V.G.Malyshkin, **V.A.Shchukin**, A.A.Maradudin, R.F.Wallis*
Kinetic instability in the epitaxial grown of semiconductor alloys . 306

NT-1.11p ***N.G.Kalugin**, V.P.Kuznetsov, A.Yu.Andreev, M.V.Stepikhova, R.A.Rubtsova, Z.F.Krasil'nik*
Optical Er-doping of Si during sublimational MBE 310

NT-1.12p ***S.A.Komarov**, G.S.Solomon, J.S.Harris Jr.*
Lateral ordering of stacked self-assembled islands of InAs on GaAs 314

NT-1.13p *A.M.Mintairov, **A.S.Vlasov**, V.P.Khvostikov, P.A.Blagnov, A.A.Prokophiev, S.V.Sorokina*
Cluster effects in optical spectra of GaAsSb on GaAs grown by liquid phase epitaxy 316

NT-1.14p ***Yu.G.Musikhin**, N.A.Bert, V.V.Chaldyshev, A.O.Kosogov, P.Werner, V.V.Preobrazhenskii, M.A.Putyato, B.R.Semyagin*
Structure of InAs delta-layers in low-temperature grown GaAs . . 320

NT-1.15p ***V.A.Petrov***
On the possibility of the development of vicinal superlattices in quantum wires on semiconductor low-index surfaces 324

NT-1.16p ***A.V.Potapov**, L.K.Orlov*
Non-stationary growth kinetics in GeH_4-Si MBE: composition abruptness at $Si_{1-x}Ge_x$/Si interface 327

NT-1.17p ***A.V.Potapov***
Self-organizing during film nucleation in GSMBE from silane and germane 331

NT-1.18p ***V.V.Rotkin***
Selforganization of the fullerene complexes on solution 335

NT-1.19p *A.B.Vorob'ev, A.K.Gutakovsky, **V.Ya.Prinz**, V.A.Seleznev, V.L.Kuznetsov, Yu.V.Butenko, A.B.Sharaya, E.M.Moroz, V.N.Kolomiichuk*
A technology for fabricating two- and one-dimensional ensembles of supermagnetic nanoparticles 339

NT-1.20p ***A.E.Zhukov**, V.M.Ustinov, A.Yu.Egorov, A.R.Kovsh, A.F.Tsatsul'nikov, M.V.Maximov, B.V.Volovik, A.A.Suvorova, N.A.Bert, P.S.Kop'ev*
Strained quantum islands of InAs in an (In,Ga)As/InP matrix . . . 341

Nanostructure technology-2

NT-2.01i *V.V.Aristov, S.V.Dubonos, B.N.Gaifullin, A.A.Svintsov,* ***S.I.Zaitsev***
Three dimensional e-beam lithography 345

NT-2.02p *V.D.Khavryutchenko, E.A.Nikitina,* ***E.F.Sheka***
STM-simulated chemical modifying of the alpha-C:H film 351

NT-2.03p ***Yu.E.Lozovik,*** *S.V.Chekalin, A.I.Ivanov, V.O.Kompanets, D.V.Lisin, Yu.A.Matveets, S.P.Merkulova*
Femtosecond laser pulse nanolitography using STM tip 352

NT-2.04p ***I.Maximov,*** *N.Carlsson, P.Omling, P.Ramvall, L.Samuelson, W.Seifert, Q.Wang, A.Forchel, K.Kerkel*
Processing of a MOVPE-regrown sub-100 nm InP/GaInAs quantum point contact 354

NT-2.05p *P.Radojkovic, Th.Gabriel,* ***M.Schwartzkopff,*** *E.Hartmann*
Manipulation of nanoparticles with the STM 357

NT-2.06p *I.P.Soshnikov, A.V.Lunev, M.E.Gaevski,* ***L.G.Rotkina,*** *N.A.Bert*
Fabrication of the selforganized nanostructure with ion and neutral beam etching 361

NT-2.07p ***D.Wang,*** *K.L.Wang*
Nanostamp lithography: a new process for fabrication of nanostructures 365

Quantum wires and quantum dots

QWR/QD.01i ***A.A.Odintsov,*** *Y.Tokura, S.Tarucha*
Transport of interacting electrons in modulated quantum wires and carbon nanotubes 368

QWR/QD.02i ***N.N.Ledentsov***
Submonolayer insertions in wide bandgap matrices: New principles for optoelectronics 374

QWR/QD.03p *O.A.Aktsipetrov, E.A.Gan'shina, S.V.Gushin,* ***T.V.Murzina,*** *T.V.Misuryaev, K.Pedersen*
Optical second harmonic spectroscopy of Co magnetic quantum dots 330

QWR/QD.04p *M.V.Baidakova, V.I.Ivanov-Omskii, V.I.Siklitsky, A.A.Suvorova, A.A.Sitnikova, A.V.Tolmatchev,* ***S.G.Yastrebov***
Structure of copper nanoclusters embedded in a-C:H 383

QWR/QD.05p ***K.Chernoutsan,*** *V.Dneprovskii, V.Karavanskii, O.Shaligina, E.Zhukov*
Time-resolved luminescence of porous n-InP 387

QWR/QD.06p *V.Dneprovskii,* ***E.Zhukov***
Nonlinear optical properties of semiconductor quantum wires . . . 391

QWR/QD.07p *P.V.Giugno, L.Vasanelli, R.Cingolani, A.Continenza,* ***V.G.Baru,*** *A.Chernushich, V.Jitov, V.Luzanov*
Size-dependence of the crystal structure of CdSSe nanocrystallites embedded in glass 395

QWR/QD.08p ***E.G.Guk,*** *M.E.Levinstein, V.A.Marikhin, L.P.Myasnikova, S.L.Rumyantsev*
Macroscopic electric properties of polydiacethylene nanostructures 399

QWR/QD.09p *P.K.Kashkarov, E.A.Konstantinova, A.V.Pavlikov,* ***V.Yu.Timoshenko***
Dielectric effect on exciton dynamics in silicon quantum wires . . 403

QWR/QD.10p ***V.V.Klimov,*** *V.S.Letokhov*
Dynamics and radiation of a charged particle moving in a carbon nanotube 407

QWR/QD.11p *A.A.Lipovskii, E.V.Kolobkova,* ***V.D.Petrikov***
Hole spectrum in CdTe quantum dots 411

QWR/QD.12p *A.A.Lipovskii, E.V.Kolobkova,* ***V.D.Petrikov***
Optical transitions in PbSe quantum dots 415

QWR/QD.13p ***S.I.Pokutnyi,*** *I.P.Guk, G.V.Semenova*
Size quantization of exciton in quasi-zero-dimensional semiconductor structures 417

QWR/QD.14p *S.G.Romanov, A.V.Fokin, V.I.Alperovich,* ***V.Y.Butko,*** *R.M.De La Rue*
Photoluminescence in opal-based photonic crystals doped with semiconductor 421

QWR/QD.15p ***A.N.Rubtsov***
The role of zero-point fluctuations in the nonlinear optical response of nanostructures 425

QWR/QD.16p ***M.Tkach,*** *I.Pronyshyn, O.Makhanets*
Electron spectrum in quantum superlattice with axial symmetry . . 429

QWR/QD.17p ***M.Tkach,*** *V.Holovatsky, O.Voitsekhivska, M.Mikhalyova*
Exciton-phonon interaction in spherical nanoheterosystem CdS/HgS/H_2O 433

QWR/QD.18p *G.Zegrya, V.Golovach, A.Konstantinovich,* ***M.Tkach***
Electron and hole spectra in ellipsoidal nanoheterostructure (quantum dot) 437

Silicon based nanostructures

SBNS.01i ***M.Asada,*** *M.Watanabe, W.Saitoh*
Metal/insulator/semiconductor heterostructure quantum-effect devices on Si substrate 440

SBNS.02p *N.T.Bagraev, E.I.Chaikina, W.Gehlhoff, L.E.Klyachkin, I.I.Markov, A.M.Malyarenko*
Lasing oscillations in silicon quantum wires 444

SBNS.03p *N.T.Bagraev, L.E.Klyachkin, A.M.Malyarenko, B.G.Podlaskin, N.A.Tokranova*
Multielement photodetector multiscan: random telegraph signal in single-electron tunneling transport 448

SBNS.04p *N.T.Bagraev, W.Gehlhoff, L.E.Klyachkin, A.M.Malyarenko, A.Naeser*
Self-assembly quantum wires created by impurity dipole ordering in silicon 452

SBNS.05p *E.V.Ostroumova, A.A.Rogachev*
Current instabilities in the Auger transistor 456

SBNS.06p *O.Sreseli, D.Goryachev, G.Polisski, L.Belyakov, F.Koch*
Carrier transport and mechanism of porous silicon electroluminescence in electrolytes 460

SBNS.07p *V.Yu.Timoshenko, B.V.Kamenev, J.Rappich, Th.Dittrich*
Optical study of silicon nanostructure evolution 463

SBNS.08p *V.G.Zavodinsky, I.A.Kuyanov*
Electronic structure of Au-Si quasi one-dimensional systems . . . 466

Single electronics

SE.01i *J.S.Tsai, Y.Nakamura, C.D.Chen*
The potential of aluminum single electron devices — A floating-gate memory and its higher temperature operation . . . 467

SE.02i *A.N.Korotkov*
Fluctuations in single-electron tunneling 471

SE.03p *S.A.Gurevich, D.A.Zakheim, V.V.Horenko, T.A.Zaraiskaya, E.M.Tanklevskaya*
Room temperature hysteresis behavior of IV-curves and memory effects in granular metal-dielectric films 474

SE.04p *V.A.Krupenin, D.E.Presnov, M.N.Savvateev, H.Scherer, A.B.Zorin*
Noise in metallic SET transistor with an island isolated of the substrate 477

SE.05p *N.S.Maslova, S.I.Oreshkin, V.I.Panov, S.V.Savinov, A.Depuydt, C.Van Haesendonck*
Observation of charge effects on semiconductor surface by low-temperature scanning tunneling spectroscopy 480

SE.06p *Yu.A.Pashkin, Sh.Farhangfar, J.P.Toppari, J.P.Pekola*
Experimental investigation of the influence of the electromagnetic environment on charging effects in ultra-small tunnel junctions . . 484

SE.07p *S.G.Romanov, A.V.Fokin, D.K.Maude, J.C.Portal*
Single-electron transport in a lattice of InSb quantum dots 488
SE.08p ***A.A.Tager**, M.Moskovits, J.M.Xu*
Correlated charge transfer and cross-tunneling in coupled nanowire junctions array 492
SE.09p ***A.S.Trifonov**, V.V.Khanin, E.S.Soldatov, S.P.Gubin, S.A.Yakovenko, G.B.Khomutov*
Investigation of single-electron effects in nanostructures on the base of single metallorganic clusters 494

Tunneling phenomena

TP.01i *E.E.Vdovin, **Yu.V.Dubrovskii**, Yu.N.Khanin, N.S.Novoselov, T.G.Andersson, P.Omling, S.-B.Carlsson*
"Gamma-X" tunneling in GaAs/AlAs/GaAs heterostructure 497
TP.02p ***N.S.Averkiev**, V.A.Berezovets, I.I.Farbshtein, G.E.Pikus, N.I.Sablina*
Peculiarities of the weak localization of the 2D holes in the quantum well on (1010) surface of tellurium 498
TP.03p ***D.G.Baksheyev**, D.Lenstra, O.A.Tkachenko, V.A.Tkachenko*
Photon-induced full electron transparency of double and triple quantum-well structures 499
TP.04p *I.A.Devyatov, **M.Yu.Kupriyanov***
AC Josephson effect in a SIS tunnel junctions with localized states in the barrier 501
TP.05p ***M.N.Feiginov**, V.A.Volkov*
AC response of the tunnel junctions substantiated by the junction plasmons 505
TP.06p *Yu.N.Khanin, **E.E.Vdovin**, Yu.V.Dubrovskii, T.G.Andersson*
Tunnel resonance's in structures with a step-like barrier 508
TP.07p ***G.M.Minkov**, O.E.Rut, A.V.Germanenko*
Edge anomaly in tunneling of electron into p-type semiconductor 512
TP.08p ***A.Zakharova***
Interband tunneling in RTS with type II heterojunctions 516

2D electron gas

2DEG.01i ***V.M.Pudalov***
Global phase diagram for the quantized Hall conductor 520
2DEG.02i ***S.I.Dorozhkin***
Properties of two-dimensional hole systems 525
2DEG.03i ***Yu.M.Galperin**, H.Totland, F.A.Maao*
Acoustoelectric effects in quantum constrictions 531

2DEG.04p *P.I.Birulin, S.P.Grishechkina, Yu.V.Kopaev, S.S.Shmelev, V.T.Trofimov,* ***N.A.Volchkov***
Single-gated mobility modulation transistor 537

2DEG.05p *I.L.Drichko, A.M.Diakonov, V.D.Kagan, A.M.Kreshchuk, T.A.Polyanskaya, I.G.Savel'ev,* ***I.Yu.Smirnov****, A.V.Suslov*
The 2DEG heating by electric field of surface acoustic wave . . . 541

2DEG.06p ***T.S.Lagunova****, T.I.Voronina, M.P.Mikhailova, K.D.Moiseev, A.E.Rosov, Yu.P.Yakovlev*
Transition from semimetal to semiconductor in type-II p-GaInAsSb/p-InAs heterojunctions 545

2DEG.07p ***L.K.Orlov****, J.Leotin, F.Yang, Yu.Arapov, N.Orlova*
Quantum cyclotron resonance of 2D holes in Ge layers of Ge-$Ge_{1-x}Si_x$ heterostructures 549

2DEG.08p *D.A.Romanov, E.B.Gorokhov, V.A.Tkachenko,* ***O.A.Tkachenko***
Magnetic states of two-dimensional electrons near the intersection of quantum well by slipping plane 553

2DEG.09p ***V.A.Sablikov****, S.V.Polyakov*
Optical-beam-induced currents in modulation doped heterostructures 557

2DEG.10p *O.A.Tkachenko,* ***D.G.Baksheyev****, M.B.Wojtsekhowski, V.A.Tkachenko*
Microwave driven dynamic barriers in uniform 2DEG as electron beam splitters and interferometers 559

2DEG.11p ***M.V.Yakunin****, Yu.G.Arapov, G.I.Harus, V.N.Neverov, N.G.Shelushinina, O.A.Kuznetsov*
Peculiarities of the quantum magnetotransport in a wide potential well $Ge_{1-x}Si_x$/p-Ge/$Ge_{1-x}Si_x$ 561

Author Index 573

* A camera ready copy of the abstract had not been received by the submission deadline.

Quantum Transport in Semiconductor-Coupled Superconducting Junctions

Hideaki TAKAYANAGI

NTT Basic Resaecrh Laboratories
3-1, Morinosato-Wakamiya, Atsugi-shi, Kanagawa
243-01 Japan

We investigate normal transport of superconducting junctions which couple with a two-dimensional electron gas (2DEG) in the semiconductor heterostructure in the ballistic transport regime. Subharmonic energy-gap structures, enhancement of the quantized conductance in a ballistic quantum point contact, and resistance minimum as a function of gate voltage in a two-gated junction are observed. These phenomena originate from Andreev reflection that an incident electron is refelcted as a hole at the supercondcutor-2DEG interface.

1 Introduction

A semiconductor-coupled superconducting junction has been studied for more than twenty years in a long history [1] of studies of quantum transport in superconductor-normal-metal (S-N) or S-N-S junctions. In 1985 an epoch-making technology was developed: the critical-current control by gate voltage.[2,3] A gate-fitted semiconductor-coupled Josephson junction is a very strong tool for the study of quantum transport concerned with superconductivity, since the electron state in the semiconductor can be changed systematically by varying the gate voltage. The p-type InAs-coupled junction has provided the interaction effects associated with Anderson localization on the critical current [4] and mesoscopic fluctuations of the critical current.[5] This type of device has also been studied from the viewpoint of a Josephson field effect transistor (JOFET).[6,7]

At the first stage of the study of a semiconductor-coupled junction, a semiconductor in the diffusive transport regime ($\ell < L$) was used. Here, ℓ is the mean free path in the semiconductor and L is the sample size. A superconducting junction coupled with a semiconductor heterostructure in the ballistic transport regime ($\ell > L$) has been developed along with progress in the semiconductor crystal growth technology. [8,9] The combination of the gate-control and high-mobility semiconductor has resulted in interesting quantum phenomena: quantization of the critical current in a superconducting quantum point contact,[10] Fabry-Pérot interference of the critical current,[11] and focusing of Andreev-reflected holes.[12] The combination has also provided a JOFET with a voltage gain of over 1.[13]

In this paper, we report normal transport concerned with Andreev reflection in a superconducting junction coupled with a semiconductor heterostructure in the ballistic transport regime. Superconducting transport in the junction will be reported elsewhere.[14]

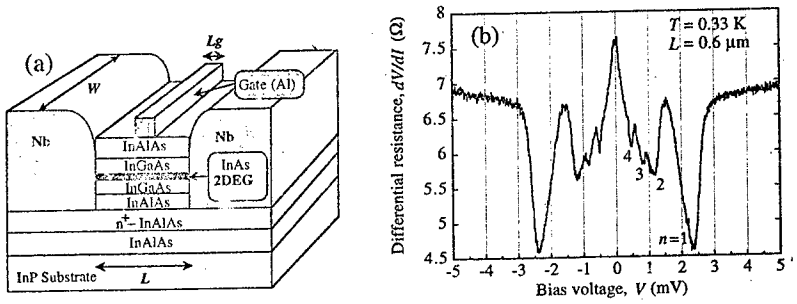

Figure 1: (a) Schematic view of a typical semiconductor-coupled Josephson junction. A supercurrent can flow through the 2DEG between the superconducting Nb electrodes. (b) Measured subharmonic energy-gap structures due to multiple Andreev reflection in a junction shown in (a).

2 Junction Structure

Figure 1(a) illustrates a typical structure of the semiconductor-coupled Josephson junction. The junction uses an InAs-inserted-channel inverted $In_{0.52}Al_{0.48}As$ / $In_{0.53}Ga_{0.47}As$ modulation-doped heterostructure as the normal metal. The heterostructure used in this study was grown by molecular beam epitaxy (MBE) on an Fe-doped semi-insulating (100) InP substrate. All InGaAs and InAlAs layers were lattice matched to InP. We fixed the InAs quantum-well thickness at 4 nm and the insertion position (the distance between the InAlAs spacer layer and the InAs quantum well) at 2.5 nm.

The charge distribution in the heterostructure was obtained by solving the Schrödinger and Poisson equations self-consistently. The calculated results showed clearly that a two-dimensional electron gas (2DEG) is well confined in the inserted InAs layer. The sheet carrier density N_S, mobility μ, and the effective mass $m*$ for the 2DEG were respectively measured at 10 K as 2.3×10^{12} cm^{-2}, 111,000 cm^2/Vs, and 0.45 m_e by Hall measurement, where m_e is the free electron mass.[15] This high mobility of the 2DEG seems to be attributed to a decrease in scattering due to ionized impurities and interface roughness. We also used another heterostructure with the same structure but different N_s and μ. N_s and μ were measured to be 2.4×10^{12} cm^{-2} and 31,000 cm^2/Vs, respectively. The mean free path of the 2DEG ℓ is 2.8 μm for the first heterostructure and 0.8 μm for the second one.

We used Nb as the superconducting electrode. Nb has a critical temperature of about 9 K and an energy gap of 1.5 meV. The fabrication process of the junction is not described here; details of the device fabrication are reported elsewhere.[16] We only note that the rf sputter cleaning of the layers from the undoped InGaAs to the undoped InAlAs before the Nb deposition is essential to obtain a supercurrent.[17] The supercurrent flowed through the 2DEG due to the superconducting proximity effect or Andreev reflection. From the measured values of N_S and m^*, the coherence length $\xi_N = \hbar v_F / 2\pi k_B T$ in the clean limit was calculated to be 1.2 μm at 1 K, where v_F is the Fermi velocity of the 2DEG. Therefore, if the distance between the two superconductors L is shorter than the mean free path of the 2DEG mentioned above, the S-N-S junction belongs to the clean limit ($\ell > \xi_N$) with ballistic

transport ($\ell >> L$). As shown in Fig. 1(a), the junction has a gate located directly on the heterosturucture and shows a high controllability of both the critical current and the junction normal resistance by gate voltage.[13]

3 Normal transport in the context of Andreev reflection

3.1 Multiple Andreev reflection

We will first show one of the most typical phenomena in the ballistic S-N-S junction: mutiple Andreev reflection (MAR). An incident electron from the normal-metal (N) side is reflected as a hole at a S-N interface. This is Andreev refelction and this effect provides an increase in the conductance of a S-N junction.[18] Consider a S-N-S junction with a zero potential difference between two superconductors ($V = 0$). The electron and hole can travel infinite times between two S-N interfaces. This results in a supercurrent. Eventhough $V > 0$, the electron and hole can travel many times between two interfaces provided $V < 2\Delta/e$, where Δ is the energy gap of the superconductor. MAR can be observed in the form of subharmonic energy-gap structures on the current-voltage characteristics. The first observation of such structures in a semiconductor-coupled junction was reported in a Nb-Si-Nb system.[19] This was followed by a junction reported in this paper.[9]

Fig. 1(b) shows a measured differential resistance-bias voltage ($dV/dI - V$) curve for a junction with $L = 0.6$ μm. Dip structures were observed near voltages eqaul to $2\Delta/ne$, with $n = 1, 2, 3, 4$. A careful observation of the $dV/dI - V$ curve gives us a structure for $n = 5$. These structures are subharmonic energy-gap structures due to MAR. The mean free path of the used 2DEG was 0.8 μm. Therefore, it is shown that even a junction with $L \approx \ell$ shows high-order subharmonic structures at a low temperature.

If the considered energy E is less than Δ/e, the Andreev reflection probability $A(E)$ and the normal reflection probability $B(E)$ satisfies the condition that $A(E) + B(E) = 1$. Real junctions always have non-zero $B(E)$ because of the Shottoky barrier at the interface or the difference in the Fermi velocity between the superconductor and the normal metal. It is noted that a normal reflection at the S-N interface is essential for the observation of subharmonic energy-gap structures.[20]

3.2 Conductance of a superconducting quantum point contact

It is well known that a quantum point contact (QPC) shows a quantized conductance in units of $2e^2/h$.[21,22] This is the experimental confirmation of the Landauer formula $G_N = 2e^2/h \sum_n T_n$, where T_n is the transmission eigenvalue. A similar equation was obtained for the conductance of a S-N junction: $G_A = 4e^2/h \sum_n T_n^2/(2 - T_n)^2$, provided that $A(E) = 1$ and $B(E) = 0$.[23] This equation predicts that a QPC having a S-N interface with a perfect Andreev reflection shows the conductance doubling $G_A = 2G_N$ because T_n is 1 or 0.

Figure 2 (a) shows a SEM photograph of a superconducting quantum point contact (SQPC). The used semiconductor heterostructure was the same as that in Fig. 1 (a) with $\ell = 2.8$ μm. A SQPC consists of a split gate between two S-N interfaces. It was theoretically predicted that the critical current of a SQPC was quantized instead of its conductance quantization. [24,25] Quantization of the critical current was observed experimentally by using a SQPC shown in Fig. 3 (a).[10] Then what is the behavior of the conductance in a SQPC ?

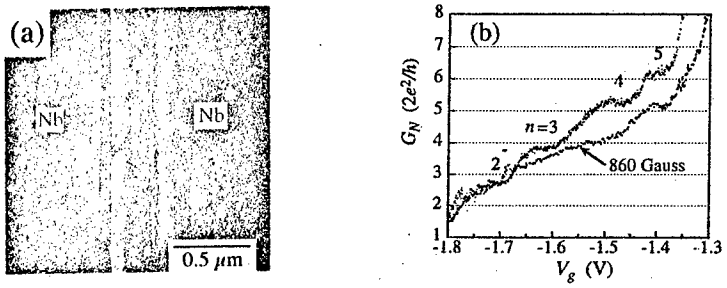

Figure 2: (a) SEM photograph of a superconducting quantum point contact. (b) Zero-bias conductance in a superconducting quantum point contact as a function of gate voltage.

Fig. 2 (b) shows a measured zero-bias conductance in a SQPC as a function of gate voltage applied to the split gate. It is shown that the step height is a little bit larger than $2e^2/h$ but is not double of $2e^2/h$. This is because the real S-2DEG interface has a non-zero value of $B(E)$ as discussed above.

Andreev reflection is very unique in the sense that the reflected hole returns in the direction from which the incident electron came (retro reflection). This retro reflection results in the enhancement of the conductance in a SQPC. Therefore, if the retro reflection is broken by a magnetic field, the conductance step height will approach $2e^2/h$. Fig. 2 (b) also plots the conductance of the same SQPC with a magnetic field of 860 Gauss. The reduction of the step height is clearly seen. However, the step for $n = 2$ did not change and this behavior is not yet well understood.

3.3 Resistance minimum in a S-2DEG junction with two gates

A Nb-InGaAs contacts showed the differential conductance peak around zero voltage.[26] This effect was explained by Andreev reflection[27] and by the proximity effect[28]. In order to observe the conductance peak (or resistance minimum), disorder in the N region is essential because the elastic scattering inceases coherent Andreev reflection. The calculation based on the reflectionless tunneling theory showed that the disorder can be replaced by a tunnel barrier, assuming ballistic motion between this barrier (barrier 1 with the transparence Γ_1) and the other barrier at the S-N interface (barrier 2 with the transparency Γ_2).[29] According to the calculation, the resistance of a NI_1NI_2S junction shows a minimum as a function of the transparency of barrier 1, where I_i denotes barrier i ($i = 1, 2$). We reported on the resistance characteristics in a gated S-N junction. Gate voltage could change the transparency of the gate structure and the resistance showed a minimum as a function of gate voltage.[30]

The calculation also shows that the high transparency of barrier 2 (a large value of Γ_2 for the S-N interface) never provides the resistance minimum. If Γ_2 can be decreased, however, the resistance minimum will appear again. We have fabricated and measured a S-N junction shown in Fig. 3 (a) in order to confirm this. The junction has two gates. Gate 2 works to change the effective value of Γ_2. Therefore, gate 2 was fabricated very close to the S-

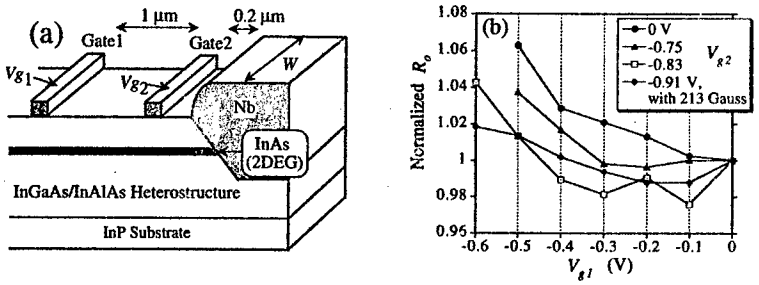

Figure 3: (a)Junction structure with a two-gate configuration. (b) Zero-bias resistance in the junction as a function of gate voltage 1.

N interface. Gate 1 works as a tunnel barrier. Fig. 3 (b) shows the measured zero-bias resistance R_0 of the junction as a function of gate voltage applied to gate 1, V_{g1}, with changing another gate voltage applied to gate 2, V_{g2}. As clearly seen, when $V_{g2} = 0$, R_0 shows a monotonic increase as increasing V_{g1}. However, as increasing V_{g2}, R_0 becomes to show a clear minimum value. This indicates that an increase in V_{g2} results in a decrease in Γ_2 and the resistance minimum in R_0 gradually appears.

We have also measured R_0 with a magnetic field B of 213 Gauss. As shown in the figure, R_0 still showed a minimum eventhough its value became slightly smaller. $B \ll h/eS$ is required to observe the conductance enhancement when it is due to the elastic scattering in the disorder, where S is the area of the junction. 213 Gauss is strong enough to break the coherence in the diffusive motion. But for a ballistic motion, the trajectories of the Andreev-reflected hole enclose no magnetic flux and no magnetic field dependence is expected.[29] A ballistic motion occurs between the interface and gate 1, because the used 2DEG has a ℓ of 2.8 μm. So as theoretically predicted, the resistance minimum showed no magnetic field dependence.

4 Conclusions

Quantum phenomena in normal transport of mesoscopic-scale superconductor-semiconductor junctions were reported: subharmonic energy-gap structures, conductance enhancement in a superconducting quantum point contact, and resistance minimum in a two-gated junction . These phenomena that originate from Andreev reflection could be observed by the combination of the gate control technology and the high-mobility semiconductor heterostructure. This combination will continue to provide new and interesting quantum phenomena in the context of Andreev reflection.

Acknowledgments

It is a pleasure to acknowledge my collaborators in this field: E. Toyoda, T. Akazaki, J. Nitta, and H. Nakano. I have greatly benefitted from discussions with Dr. B. J. van Wees, Dr. A. Furusaki, Dr. Y. Ishii, Dr. T. Enoki, and Dr. K. Arai. I also thank Dr. T. Izawa and Dr. N. Matsumoto for their encourgement through this work.

References

1. K.K. Likharev, *Rev. Mod. Phys.* **51**, 101 (1979).
2. H. Takayanagi and T. Kawakami, *Phys. Rev. Lett.* **54**, 2449 (1985).
3. T. Nishino *et al*, *IEEE Electron Dev.* **6**, 297 (1985).
4. H. Takayanagi, J. B. Hansen, and J. Nitta, *Phys. Rev. Lett.* **74**, 162 (1995).
5. H. Takayanagi, J. B. Hansen, and J. Nitta, *Phys. Rev. Lett.* **74**, 166 (1995).
6. A.W. Kleinsasser and W.J. Gallagher, *Superconducting Devices*, eds. S.T. Ruggiero and D.A. Rudman (Academic, San Diego, 1990).
7. A.F. Volkov and H. Takayanagi, *Phys. Rev.* **B35**, 15162 (1996).
8. C. Nguyen, J. Werking, H. Kroemer, and E.L. Hu, *Appl. Phys. Lett* **57**, 87 (1990).
9. J. Nitta,T. Akazaki, H. Takayanahi, and K. Arai, *Phys. Rev.* **B46**, 14286 (1992).
10. H. Takayanagi, T. Akazaki, and J. Nitta, *Phys. Rev. Lett.* **75**, 3533 (1995).
11. H. Takayanagi, T. Akazaki, and J. Nitta, *Phys. Rev.* **B51**, 1374 (1995); H. Takayanagi and T. Akazaki, *J. Phys. Soc. Jpn.* **34**, 4554 (1995).
12. H. Takayanagi and T. Akazaki, *Phys. Rev.* **B52**, R8633 (1995).
13. T. Akazaki, H. Takayanagi, and J. Nitta, *Appl. Phys. Lett.* **68**, 418 (1996).
14. B. J. van Wees and H. Takayanagi, to be published in *Mesoscopic Electron Transport*, eds. L.P. Kouwenhoven, G. Schön and L.L. Sohn (Kluwer Academic Publishers, The Netherlands).
15. T. Akazaki, J. Nitta, H. Takayanagi, and T. Enoki, *Appl. Phys. Lett.* **65**, 1263 (1994).
16. H. Takayanagi and T. Akazaki, *Jpn. J. Appl. Phys.* **34**, 6977 (1995).
17. H. Takayanagi, T. Akazaki, and J. Nitta, *Semicond. Sci. Technol.* **8**, S431 (1993).
18. A. F. Andreev, *Sov. Phys. JETP* **19**, 1228 (1964).
19. D. R. Heslinga*et al*, *IEEE Trans. Mag.* **27**, 3264 (1991).
20. M. Octavio *et al*, *Phys. Rev* **B27**, 6739 (1983).
21. B. J. van Wees *et al*, *Phys. Rev. Lett.* **60**, 848 (1988).
22. D. A. Wharam *et al*, *J. Phys.* C **21**, L209 (1988).
23. C. W. J. Beenakker, *Phys. Rev.* **B46**, 12841 (1992).
24. C. W. J. Beenakker and H. van Houten, *Phys. Rev. Lett.* **66**, 3056 (1991).
25. A. Furusaki, H, Takayanagi, and M. Tsukada, *Phys. Rev. Lett.* **67**, 132 (1991).
26. A. Kastalsky, L.H. Green, J.B. Barner, and R. Bhat, *Phys. Rev. Lett.* **64**, 958 (1990).
27. B.J. van Wees *et al*, *Phys. Rev. Lett.* **69**, 510 (1992).
28. A.F. Volkov, A.V. Zaitsev, and T.M. Klapwijk, *Physica* C**210**, 21 (1993).
29. J.A. Melsen and C.W.J. Beenakker, *Physica* B**203**, 219 (1994).
30. H. Takayanagi, E. Toyoda, and T. Akazaki, *Proc. LT-21*, 2507 (Prague, 1996) .

Weak 2D-localization effects in multilayer heterostructures and highly anisotropic crystals

Yu.G.Arapov, G.I.Harus, A.N.Ignatenkov, N.K.Lerinman, V.N.Neverov, A.I.Ponomarev, L.D.Sabirzyanova, N.G.Shelushinina
Institute of Metal Physics, RAS, 620219 Ekaterinburg, Russia

N.A.Babushkina
Kurchatov Institute, Russian Science Center, 123182 Moscow, Russia

Introduction

The interference effect for electrons diffusing along a closed path and the time-reversed one results in weak localization corrections to the conductivity of disordered conductors at low temperatures [1]. These corrections to the metallic conductivity are of the order of $(k_F l)^{-1}$, $\hbar k_F$ being the Fermi quasimomentum and l being the elastic mean free path. If magnetic field normal to the motion of carrier is applied the interference is destroyed because of the phase shift between the corresponding amplitudes. In a two-dimensional (2D) system this causes negative magnetoresistance for the field perpendicular to the plane but no effect for the field parallel to the plane. This anisotropic magnetoresistance has been observed in a number of 2D system, such as thin films or two-dimensional channels of MOS structures. We are presented here the evidence of 2D weak localization effects in the conductance of $Ge/Ge_{1-x}Si_x$ multilayer heterostructures and highly anisotropic single crystals $Nd_{2-x}Ce_xCuO_{4-\delta}$.

Results and discussion

a) *$Ge/Ge_{1-x}Si_x$ ($x=0.03$)*

We have investigated the diagonal ρ_{xx} and Hall ρ_{xy} resistivities as functions of magnetic field B (up to 12T) and temperature (T=0.1÷20K) for multilayer $Ge/Ge_{1-x}Si_x$ heterostructures with a p-type conduction in the Ge layers. The conductivities per layer $\sigma_\square$ at B=0 and T=0.1K, hole sheet densities N_S, mobilities μ and some other parameters of three samples are listed in Table 1.

Fig.1 shows the conductivity per one layer for investigated samples as a function of log$T$. The fact that $\sigma_\square$ varies logarithmically with T for $0.1 \le T \le 12$K is an indication that quantum corrections due to a weak localization or an electron–electron interaction are important. The localization correction in 2D system may be written as [1]:

$$\Delta\sigma_\square(T) = -\frac{e^2}{\pi h}\ln\frac{L_\varphi}{l} = -\frac{e^2}{\pi h}p\ln\frac{T}{T_0}, \qquad (1)$$

where $L_\varphi = \sqrt{D\tau_\varphi}$, D being the diffusion coefficient and $\tau_\varphi \sim T^{-p}$ is a phase-breaking time. A best fit to the lines for T=(0.1÷12)K gives exponents in the temperature dependence of τ_φ close to p=1 or p=2 which correspond to electron-electron scattering mechanism of phase relaxation in "pure" (p=2) or "dirty" (p=1) limits [2]. The estimate of the phase coherence length gives $L_\varphi \sim 10^{-4}$cm at T=2K.

Table 1

Sample $Ge/Ge_{1-x}Si_x$	Number of layers	Layer thickness, Å	$\sigma_{\square}\times10^4$, Ω^{-1}	$\mu\times10^{-4}$, cm^2/Vs	$N_s\times10^{-11}$, cm^{-2}	m^*/m_0	k_Fl
$1123a_6$	15	190	4.0	1.4	2.6	0.104	10.3
$1124b_3$	27	200	5.6	1.0	2.4	0.107	14.4
$1125a_7$	36	190	6.8	1.7	2.4	0.100	17.5

The magnetic field effect in the 2D weak localization theory for $B<<B_{tr}$ is given by [3]:

$$\Delta\sigma_{\square}(B)=\frac{e^2}{\pi h}\left[\psi\left(\frac{1}{2}+\frac{B_\varphi}{B}\right)-\psi\left(\frac{1}{2}+\frac{B_{tr}}{B}\right)+\ln\left(\frac{B_\varphi}{B}\right)-\ln\left(\frac{B_{tr}}{B}\right)\right], \qquad (2)$$

where $B_\varphi=\hbar c/4eL_\varphi^2$, $B_{tr}=\hbar c/2el^2$ and ψ is the Digamma function. The equation (2) was derived in the framework of diffusion approximation as for $B<<B_{tr}$ closed paths with many collisions are important. Weak localization effect beyond the diffusion approximation for $B>B_{tr}$ has been treated by Dyakonov [4]. According to [4] the asymptotic high field ($B>>B_{tr}$) behavior is $\Delta\sigma\sim B^{-1/2}$.

Fig.2 shows the resistivity ρ_{xx} as a function of B at different temperatures for one of the $Ge/Ge_{1-x}Si_x$ samples. The suppression of localization effect by magnetic field perpendicular to the layers of heterostructure leads to the negative magnetoresistance for $B \le 1$T at $T \le 12$K. In the investigated samples $Ge/Ge_{1-x}Si_x$ the mean free path $l\cong10^3$ Å and $B_{tr}\cong0.03$ T. Fig.3 shows the fit of curves $\sigma_{\square}(B)$ to the numerical calculation of Dyakonov for $1\le B/B_{tr}\le30$. The absolute value of quantum correction to the conductivity was extracted from this fit: $\Delta\sigma=(1.9\div2.2)\ e^2/\pi h$ at $T\cong(1.1\div2.7)$K. To compare, the estimated values of $\Delta\sigma$ for AlGaAs/inGaAs/GaAs quantum wells are in the range $(1.6\div2.3)e^2/\pi h$ [5].

b) ***$Nd_{2-x}Ce_xCuO_{4-\delta}$ ($x=0.18$, $x\cong0.12$)***

The crystallographic structure of $Nd_{2-x}Ce_xCuO_{4-\delta}$ is the simplest among the superconducting cuprates: each copper atom is coordinated to four oxygen atoms in a simple planar structure without apical oxygen. The single crystal may therefore be regarded as an analog of a 2D system: a collection of 2D conducting CuO_2 planes separated from each other by a distance $d \approx 6$ Å [6]. In accordance with such a structure, $Nd_{2-x}Ce_xCuO_{4-\delta}$ single crystals have a high anisotropy factor of the resistivity in the normal phase $\rho_c/\rho_{ab}\cong10^4$.

In the superconducting sample $Nd_{1.82}Ce_{0.18}CuO_{4-\delta}$ (T_c=6K) the normal state transport at low T is hidden unless a magnetic field $B>B_{c2}$ is applied (the second critical field $B_{c2}\cong3$T at T=2K). We have destroyed superconductivity by a field perpendicular to CuO_2 planes and observed the logarithmic upturn in the normal state resistance at low T (Fig.4) and negative magnetoresistance in fields higher than B_{c2} (Fig.5).

For non-superconducting sample $Nd_{1.88}Ce_{0.12}CuO_{4-\delta}$ we have measured the resistance in perpendicular and parallel fields at 1.9 and 4.2 K for B up to 5.5 T. We observed a highly anisotropic negative magnetoresistance (Fig.6). The curves for perpendicular field may be fitted by the functional form (2) predicted by 2D weak localization theory in

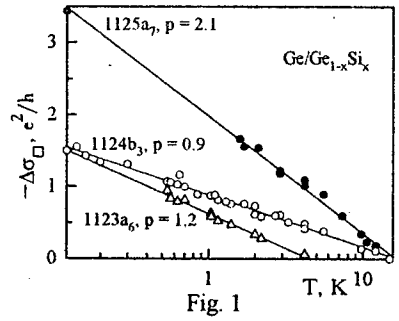

Fig. 1

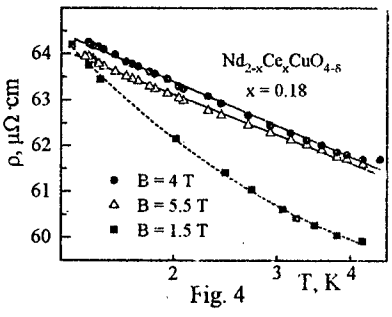

Fig. 4

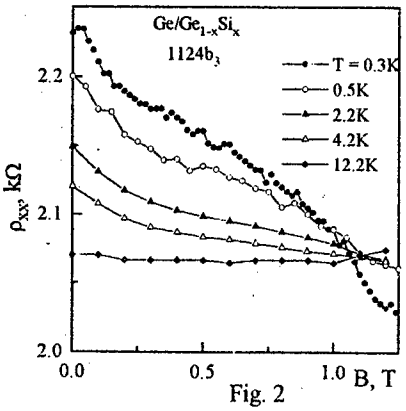

Fig. 2

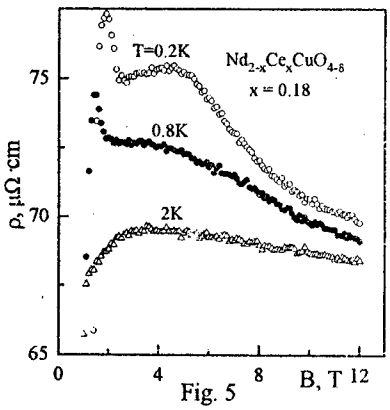

Fig. 5

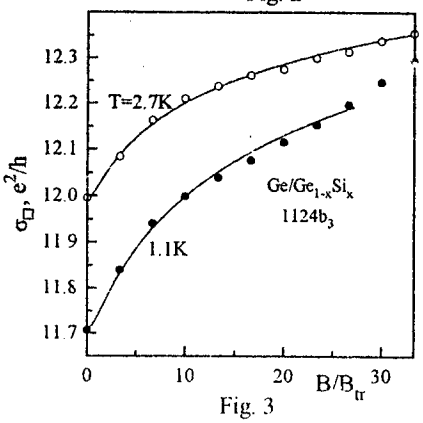

Fig. 3

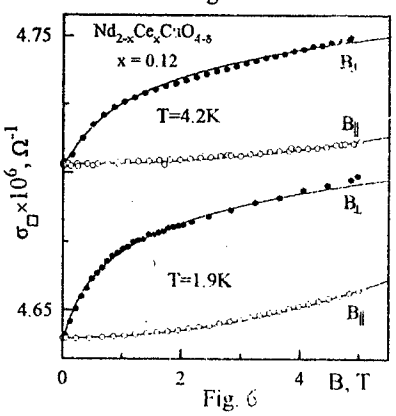

Fig. 6

diffusion approximation ($B_{tr} \cong 20$ T and then we have $B \ll B_{tr}$). From the fit we have L_φ=770 Å at T=1.9K.

The effect of weak negative magnetoresistance in fields parallel to CuO_2 planes(Fig.6) we explain including the finite thickness (d) corrections to the strictly 2D theory [7]:

$$\Delta\sigma_{\square}(B_{\parallel}) = \frac{e^2}{\pi h} \ln\left(1 + \frac{d^2 L_\varphi^2}{3\lambda^4}\right), \qquad (3)$$

where $\lambda^2 = c\hbar/eB_{\parallel}$. By fitting (3) to the parallel field curve at T=1.9K we estimate the effective thickness of a conducting CuO_2 layer: $d \cong 1.5$ Å. Thus all our data confirm that $Nd_{2-x}Ce_xCuO_{4-\delta}$ crystal may be described as a set of almost decoupled 2D metallic sheets.

Conclusions

Thus, the 2D weak localization effects manifest themselves as in the artificial $Ge/Ge_{1-x}Si_x$ so in the natural $Nd_{2-x}Ce_xCuO_{4-\delta}$ multilayered systems with a true metallic conduction in a layer ($k_F l \geq 10$). The essential parameters typical of investigated samples are listed in Table 2. One can see that both systems are really two-dimensional relative to the effect of weak localization: $d/L_\varphi \ll 1$. Moreover the conditions of carrier confinement $k_F d \sim 1$ are also fulfilled.

Table 2

Sample	N_S, cm^{-2}	k_F, cm^{-1}	l, cm	d, Å	L_φ(2K), cm	$k_F l$	$k_F d$	d/L_φ	B_{tr}, T
$Ge/Ge_{1-x}Si_x$	2.4×10^{11}	1.2×10^{6}	1.2×10^{-5}	200	1×10^{-4}	14	2.8	2×10^{-2}	3×10^{-2}
$Nd_{2-x}Ce_xCuO_{4-\delta}$	6.6×10^{14}	6×10^{7}	4×10^{-7}	1.5	7×10^{-6}	24	0.9	2×10^{-3}	20

While the values of parameter $k_F l$ are close to each other in two materials more than an order of magnitude difference in mean free path values l (and so in k_F values) takes place. As a consequence we have nearly three orders of magnitude difference in the values of the characteristic field B_{tr}. It allowed us to investigate the localization corrections not only in traditional low field region $B \ll B_{tr}$ where diffusion approximation is valid but also in interesting high field region $B > B_{tr}$ where closed paths with only a few collisions are essential.

This work is supported in part by the RFFI, Grant № 95-02-04891 and the Russian Program FTNS, Grant № 1-065/3.

[1] P.A. Lee, R.V. Ramakrishnan, Rev. Mod. Phys. **57**, 293 (1985).
[2] B.L. Altshuler, A.G. Aronov, D.E. Khmelnitsky, J. Phys. C **15**, 7367 (1982).
[3] S. Hikami, A. Larkin, Y. Nagaoka, Progr. Theor. Phys. **63**, 707 (1980).
[4] M.I.Dyakonov, Solid State Commun. **92**, 711 (1994).
[5] M.I.Dyakonov, A.Zduniak, W.Knap, Int. Conf. on Electron Localization and Quantum Transport in Solids, Extended abstracts, Jaszowiec, Poland, 1996, p.209.
[6] A. Kurmaul, J.S. Moodera, P.M. Tedrow, A. Gupta, Physica C **177**, 415 (1991).
[7] B.L. Altshuler, A.G. Aronov, Zh. Eksp. Teor. Fiz. Pis'ma **33**, 515 (1981).

HIGH-TEMPERATURE MESOSCOPICS AND QUANTUM QUASI-1D PERCOLATION-LIKE CONDUCTIVITY OF STRONGLY DISORDERED FIELD-EFFECT SYSTEMS

B.A.Aronzon[a], D.A.Bakaushin[b], N.K. Chumakov[a], E.Z.Meilikhov[a], V.V.Ryl'kov[a,b], and A.S.Vedeneev[b]

[a]Russian Research Center "Kurchatov Institute", 123182 Moscow, Russia
[b]Institute of Radioengineering & Electronics, 141120 Fryazino, Moscow reg., Russia

Mesoscopic phenomena accompanied by quantization of conductance were found to be characteristic feature of quasi-2D MIS FETs with high concentration of built-in charges.

INTRODUCTION

Disordered systems with the exponentially wide spread of local conductivities are known to have percolation-like behaviour [1]. For systems of this type, the length of conductance self-averaging is characterized by the correlation radius L_c and defines the size of cells of the percolation cluster [2]. If the system sizes are about of L_c, self-averaging fails and the system becomes to be mesoscopic one. Commonly, the mesoscopic effects are observed in the case of hopping conductivity when the temperature T is low enough [3]. However, as it will be shown below, mesoscopic effects can be observed at relatively high temperatures ($T \approx 77 \div 300$ K), even in structures of macroscopic sizes exceeding L_c, or in low-channel FETs, disordered due to built-in charge of high concentration N_t in the under-gate insulator.

EXPERIMENTAL

The MNOS structures with inversion n-type channel were fabricated on the low-doped Si-substrate. The under-gate insulator, the 320 A thick Si_3N_4 and the 50 A thick SiO_2 layers, provides controllable recharging of electron traps at the SiO_2-Si_3N_4 interface. The field-effect curves, i.e. the channel conductance G dependence on the gate potential V_g, measured at different N_t are shown in Fig.1. The insert illustrates the effective (apparent) electron state density N_{ss} calculated formally using standard field-effect approach [4]. The Hall-effect measurements were also carried out (Fig.2).

In FETs, when N_t becomes much higher than $\sim 10^{12}$ cm^{-2}, $G(V_g)$ curves manifest an additional threshold V_{tl} independent of N_t (Fig.1). When the $V_g \sim V_{tl}$, a peak-like peculiarity of the apparent N_{ss} spectrum appears at $G \sim e^2/h$ regardless of variations T or N_t. The result contradicts to the concept of localized electron states formed by FP [5].

Notice that in analogous Si-MNOS structures with sizes exceeding L_c, the effect of this kind was not observed, and $N_{ss}(G)$-functions were in accordance with the theory [5] (insert at Fig.2). The Hall effect in those structures manifested a threshold-like character. With V_g reducing, the Hall-effect voltage dropped and became zero when the inversion channel conductivity turned to less than $\sim e^2/h$. Disappearance of the Hall effect was accompanied by appearance of mesoscopic fluctuations of transverse voltage drop between the Hall-potential probes [6].

Analogous peaks of $N_{ss}(G)$-functions at $G \sim e^2/h$ were observed at $T \approx 77$ K in GaAs-AlGaAs HEMTs and GaAs MESFETs disordered due to FP of ionized donors in doped layers. Conductivity quantization was also found in back-gated Si-SiGe selectively doped hetero-structures with quasi-2D hole channel at $T = 0.35$ - 4.2 K (the channel length and width were 200 μm and 20 μm respectively).

DISCUSSION

Our consideration is based on the percolation theory [1] applied to the case of free-electron transport in quasi-2D systems disordered by the strong FP [5]. We also account of the natural anisotropy of the percolation system conductance: when the structure length L is about L_c while its width W is much more compared with the latter, the conductance G is controlled by the existence of relatively low-probable (but low-resistant) single percolation path shunting the source-to-drain space [7]. This shunting is more essential if W/L ratio is higher and FP is stronger, that was confirmed by our computer simulations.

In the case of Si-MNOS FETs the percolation-like conductivity occurs that results in two-threshold-like $G(V_g)$ curves. The first threshold V_{tl} is associated with appearance of the low-resistant percolation path, while the second one is caused by FP screening followed by the transition to effective medium [1,5].

We consider the physical picture as follows. At $V_g \leq V_{tl}$ (low concentration of electrons in the FET channel), statistic fluctuations of the built-in charge density form low-resistant regions with the local potential much lower than the average level. These regions are connected each to other with high resistant passing bonds forming the only percolation path with the length of about L. The path resistance is controlled by the most resistant passing (bonding) region. It is of principal for our case that FP correlation function naturally defines two spatial scales. There are mac-

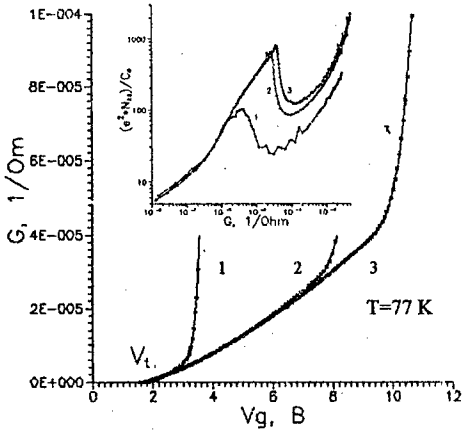

Fig. 1. Field-effect curves for Si-MNOS transistor (L=5μm, W=50 μm) at different concentration of built-in charge, N_t≈2.5·10^{12} (1), 5.3·10^{12} (2), and 6.5·10^{12} cm^{-2} (3). The insert shows effective electron state density spectrum $N_{ss}(G)$, C_0 is the undergate capacitance.

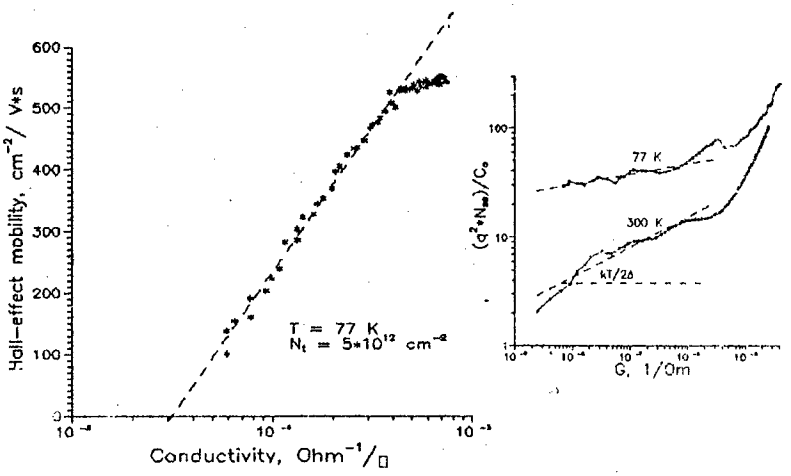

Fig. 2. Hall-effect mobility vs. channel conductivity. The insert illustrates the effective electron state density spectrum, Δ~40 meV is the characteristic energy scale of the FP.

roscopic scale, about the screening radius R_s, and the microscopic one, about the average distance between the electron channel and built-in charge planes [5]. The first scale determines a size of regions with reduced local potential, while the second one controls the passing region size (30-100 A) which is comparable with the electron wave-length and thus the passing regior resistance is quantized. That is why the percolation path above mentioned leads to experimentally observed additional threshold V_{tl} and to the quantum nature of the conductance at $V_g \sim V_{tl}$. When V_g rises, non-linear electron screening of FP becomes stronger. This leads to decreasing R_s with simultaneous lowering L_c and results in transforming initially quasi-1D percolation system into quasi-2D effective medium at $G \geq e^2/h$.

At last notice the identity of field-effect curves in weak-inversion regime and independence of their thresholds on the built-in charge density. It means the principal possibility of creating a new type of reproducible radiation-proof short channel transistor structures based on the strongly disordered low-dimensional systems.

ACKNOWLEDGEMENT

The work was partly supported by the RFBR grant 96-02-18429, Russian foundation for "Physics of Solid Nanostructures" 1997, and INTAS grant 93-1403.

REFERENCES

[1]. B.I.Shklovskii and A.L.Efros. Electron Properties of Doped Semiconductors (Spring-Verlag, New York, 1981).

[2]. M.E.Raikh and I.M.Rusin, Sov.Phys.JETP, **65** 1273 (1987).

[3]. A.O.Orlov et al., Sol.St.Com. **72** 743 (1989).

[4]. E.H.Nicollian, J.R.Brews. MOS Physics and Technology (Willey, New Your, 1982).

[5]. V.A.Gergel' and R.A.Suris, Sov.Phys.JETP, **57** 415 (1983).

[6]. B.A.Aronzon, D.A.Bakaushin, V.V.Ryl'kov, A.S.Vedeneev, and J. Leotin. Proc. Intern. Symposium "NANOSTRUCTURES: Physics and Technology" St.Petersburg 1996.

[7]. A.I.Yakimov et al., Phys.Low-Dim.Str., **6** 75 (1994).

Nonbackscattering contribution to the weak localization

A. P. Dmitriev, I. V. Gornyi and V. Yu. Kachorovskii
A. F. Ioffe Physico-Technical Institute,
Polytechnicheskaya 26, St.Petersburg, 194021, Russia

We show that the enhancement of backscattering responsible for the weak localization [1] is accompanied by reduction of the scattering in other directions. A simple quasiclassical interpretation of this phenomenon is presented in terms of a small change in the effective differential cross-section for a single impurity. The angular dependence of this modified cross-section for the case of zero magnetic field and the short-range impurity potential is presented in Fig. 1.

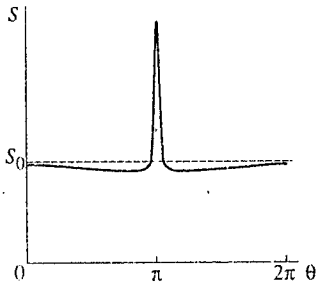

Fig 1.

The positive peak near $\theta = \pi$ corresponds to the enhancement of backscattering described by the so called "fan" diagrams (Fig. 2a) while the "hat" diagramms in Fig. 2b are responsible for the decrease of the scattering rate in other directions.

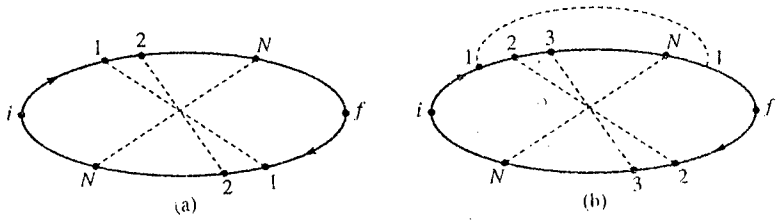

Fig 2.

The "hat" diagrams were considered in many works, but their importance was not emphasised and a clear quasiclassical interpretation of processes corresponding to these diagrams was never given. Moreover in Ref. [2] it was claimed that a quasiclassical interpretaiton of these processes is not possible.

We show that the process described by "hat" diagrams, can be easily interpreted quasiclassically. An electron starting from point i reaches point f by two ways:
(1) consecutively scattering by impurities $1, 2, \ldots, N$ and finally by impurity 1 again,
(2) scattering in the opposite order by impurities $N, N-1, \ldots, 2$, and having no collisions at all with impurity 1.
The phase difference of the two paths ending at the point f depends on the lengths of the intervals $(i,1),(1,2),(N,1),(1,f)$ and $(i,N),(2,f)$, and is given by

$$\Delta\phi = k_F(|\mathbf{r}_1 - \mathbf{r}_i| + |\mathbf{r}_2 - \mathbf{r}_1| + |\mathbf{r}_1 - \mathbf{r}_N| + |\mathbf{r}_f - \mathbf{r}_1| - |\mathbf{r}_N - \mathbf{r}_i| - |\mathbf{r}_f - \mathbf{r}_2|). \qquad (1)$$

Let us fix the positions of the points $i, 1, f$ and then integrate over the coordinates of the impurities $2, N$. Because of the phase stationarity requirement the contribution to the conductivity arises only from the configurations in which the points N and 2 lie close to the lines $1-i$ and $1-f$ respectively in angles of the order of $(k_F l)^{-1/2}$ (see Fig. 3), where k_F is the Fermi wave vector, l is the mean free path.

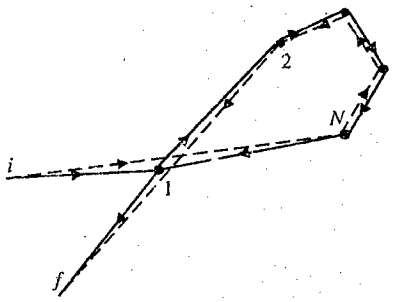

Fig 3.

In this configuration $\Delta\phi$ is equal to zero. It is clear from Fig. 3 that the process described by "hat" diagrams can be interpreted as a coherent changing of the scattering by the impurity 1 at angle θ. In order to obtain the scattering reduction one should add to $\Delta\phi$ an additional scattering phase acquired during the first way after two collisions with impurity 1 and take into account the phase factor arising due to integration over the impurity positions near the stationary phase configuration. The resulting phase difference between the two ways is equal to π.

Now an isotropic scattering cross-section S_0 should be replaced by the modified scattering cross-section $S(\theta)$ which has the following form:

$$S(\theta) = S_0 + C\Delta(\pi - \theta) + S_1(\theta). \qquad (2)$$

The second term in the right hand of Eq. (2) corresponds to the coherent backscattering at small angles of the order of $(k_F l)^{-1}$. The function $\Delta(\pi - \theta)$ is concentrated in this angle and the integral

of it over θ is equal to 1. The quantity C is proportional to the total probability of return W which in the diffusion approximation is $W = \ln(L_\phi/l)/(\pi l^2)$, here L_ϕ is phase breaking length. The function $S_1(\theta)$ is negative and corresponds to a decrease of scattering at angle θ, being described by the diagrams in Fig. 2b. This function may be expressed through the total probability $W(\theta)$ for an electron to return to the origin at an angle θ to the initial direction of propagation.

It is easy to see that the reduction of elastic scattering time due to the coherent backscattering is exactly compensated by its enhancement due to the reduction of the scattering at other angles. At the same time, since the differential cross-section is anisotropic due to the quantum corrections (see Fig. 3), the transport scattering time τ_{tr} changes and does not anymore equal to the elastic scattering time. This is the physical reason which leads to the quantum corrections to conductivity of the order of $(k_F l)^{-1}$. We stress that the description of weak localization in terms of cross-section changing is possible only when the "hat" diagrams are taken into account. If only the backscattering is considered, one gets the correction to τ_{tr} which is two times greater than correct one.

The reduction of the scattering at the arbitrary angles leads to the decrease of the quantum correction to the conductivity. Within the diffusion approximation this decrease is small because the cross-section $S_1(\theta)$ is almost isotropic. The anisotropic part of $S_1(\theta)$ arises mainly due to triangle trajectories. Taking into account the diagramms in Fig. 2b leads to the appearance of an additional factor 1/2 in the argument of the logarithm in the expression for quantum correction to conductivity.

A similar consideration is also possible when magnetic field is applied. In the high-field limit, when the diffusion approximation is not valid, only triangle paths are important [3, 4] and $S_1(\theta)$ is strongly anisotropic. Thus the contribution of the diagrams of Fig. 2b differs from that of the "fan" diagrams by the numerical factor only.

We calculate numerically the quantum correction to the conductivity for the total range of the classically weak magnetic fields.

References

[1] B. L. Altshuler, A. G. Aronov, D. E. Khmelnitskii and A. I. Larkin in: Quantum Theory of Solids, ed. I. M. Lifshits, MIR Publishers, Moscow (1982)

[2] M. B. Hastings, A. D. Stone, H. U. Baranger Physical Review B, **50**, 8230 (1994)

[3] V. M. Gasparian and A. Yu. Zuzin, Fizika Tverdogo Tela, **27**, 1662 (1985)

[4] M. I. Dyakonov, Solid State Com. 92, 711 (1994); A. Cassam-Chenai and B. Shapiro, J. Phys. I France **4**, 1527 (1994)

RESONANT CONDUCTANCE OF INTERACTING ELECTRONS IN OPEN MESOSCOPIC STRUCTURES

V.A.Sablikov[1] and B.S.Shchamkhalova

Institute of Radio Engineering and Electronics, Russian Academy of Sciences, Vvedensky sq.1, Fryazino, Moscow district, 141120, Russia

We have investigated AC conductance of interacting electrons in a quantum wire structure and found that the electron-electron interaction produces an appreciable effect in the frequency dependence of the conductance, especially, in the real part of the impedance. The repulsive interaction results in the increase of the resistivity, while the inter-electron attraction leads to an opposite effect. This phenomenon is caused by the reflection of boson-like excitations of the Luttinger liquid inside the quantum wire at the contacts with the leads.

INTRODUCTION

It is recognized now that the Coulomb interaction is of crucial importance for the electron transport in nanostructures. The prominent example of its manifestation in low-conducting structures, whose conductance is lower than e^2/h, is the Coulomb blockade. The present paper deals with an open mesoscopic system (such as quantum wire structure) which are highly conducting, so the Coulomb blockade does not appear therein. However in these structures the electron-electron interaction is very important as well. It makes the electron motion be strongly correlated which results in breaking down the 1D Fermi liquid concept. Instead of this, a strongly correlated state of the Luttinger liquid appears with boson-like elementary excitations. Investigation of the Luttinger liquid behavior in mesoscopic semiconductor structures has attracted a great deal of attention [1]. A very important problem is the experimental confirmation or rejection of Luttinger liquid states in low-dimensional structures. Recent theoretical considerations [2-4] show that the Luttinger liquid does not manifest itself in the DC conductance of quantum channels. This finding agrees with the experiment [5].

We propose that AC conductance may be a tool which will allow one to find the Luttinger liquid behavior of interacting electrons since AC transport is strongly dependent on the charge and current distribution inside the structure [6]. With this in mind we use the Luttinger liquid approach to investigate the AC conductance of a model structure which is represented by a quantum wire coupled to two electron reservoirs those serve as leads (see Fig.1).

THE MODEL

The Luttinger liquid approach allows one to consider low-energy excitations in 1D interacting electron systems. In the most simplest case where the electron-electron interaction may be considered as short-range one and back-scattering may be neglected, the standard bosonization technique gives simple relations for the observable values of charge density $\rho(x,t)$ and particle current $j(x,t)$ in terms of the boson phase field $\Phi(x,t)$

$$\rho(x,t) = -\frac{e}{2\pi}\frac{\partial\Phi}{\partial x}, \qquad j(x,t) = \frac{e}{2\pi}\frac{\partial\Phi}{\partial t}.$$

[1]E-mail: vas199@ire216.msk.su

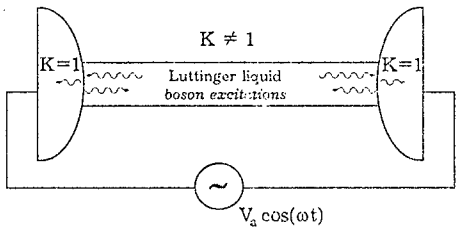

Fig. 1. A model of quantum wire structure. Curled lines show the boson excitations generated inside the wire by the external AC field. The excitations are reflected at the wire ends because their velocity is different in the electron liquids of the wire and the reservoirs.

In terms of the boson field the Hamiltonian becomes

$$H = \frac{1}{8\pi}\int_{-L/2}^{L/2} dx\, v\left[K^{-1}\left(\frac{\partial\Phi}{\partial x}\right)^2 + K\Pi^2\right],$$

where Π is the momentum conjugate to Φ, and K is the interaction dependent parameter

$$K = \left(1+\frac{U}{2\varepsilon_F}\right)^{-1/2},$$

U is the interaction potential between neighboring electrons and ε_F is the Fermi energy. When the interaction is repulsive $K<1$, while $K>1$ corresponds to an attraction.

The boson excitations are pair excitations of the electron above ε_F and hole below ε_F. They move similar to sound waves, whose velocity v is renormalized by the interaction since the latter dictates the compressibility of 1D electron liquid.

As a model of open mesoscopic structure, we consider the system as an inhomogeneous Luttinger liquid. Inside the wire the interaction parameter $K\neq 1$ and the velocity is $v = v_F/K$ (v_F being the Fermi velocity), inside the reservoirs, where the electrons can be considered as free ones, K=1 and v=v_{F0}.

THE IMPEDANCE

The motion equation for the Luttinger liquid driven by an external electric field $E(x)\exp(-i\omega t)$ was solved straightforwardly without specifying the function $E(x)$. In the specific case of E=const in the wire, we have obtained following expression for $\Phi(x,t)$ inside the wire

$$\Phi(x,t) = \frac{2evKE}{\omega^2}\left[-1+\frac{K\cos(qx)}{K\cos(qL/2)-i\sin(qL/2)}\right]\cdot e^{-i\omega t}, \qquad (1)$$

where $q=\omega/v$.

The current in the external circuit is found as

$$j = \frac{1}{V_a}\int_{-L/2}^{L/2} dx\, E(x)\, j(x,t)$$

Using equation (1) the admittance becomes

$$Y(\omega) = \frac{2e^2K}{hqL}\left[i + \frac{1-r}{qL}\frac{1-e^{iqL}}{1-re^{iqL}}\right],$$

where $r = (1-K)/(1+K)$ is the reflection coefficient of the boson excitation at the points $x = \pm L/2$ where the wire contacts with the reservoirs.

The low frequency limit of $Y = Y_0 \equiv e^2/h$ is independent on the interaction (in agreement with Ref. [2-5]). However, the interaction effect is essential in the frequency dependence of AC conductance. Of most interest is the frequency behavior of the impedance $Z = 1/Y$, which is shown in Fig.2 for three interaction parameter. The case of $K = 1$ corresponds to the absence of the electron-electron interaction. It is worth to note that in this case the present result coincides exactly with straightforward calculations based on the one-electron Schrödinger equation [7].

In all the cases, the real part of Z shows strongly oscillating behavior versus the frequency. At resonant frequencies $\mathrm{Re}Z = 0$ together with $\mathrm{Re}Y = 0$. The electron-electron interaction manifests itself in the shape of resonances. The repulsive interaction gives rise to narrowing of the resonances while the attraction makes the resonances be more wider which results in the appearance of resistance peaks on the background of the relatively high conductance.

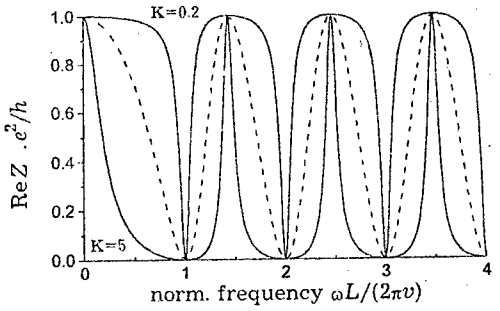

Fig. 2. Frequency dependence of ReZ for repulsive interaction ($K = 0.2$), attractive interaction (K=5) and noninteracting electrons (dashed line). The frequency is scaled by the time for an electron to transit the wire with the interaction-renormalized velocity.

The resonances occur when the frequency is equal to the inverse of the time for an electron to transit the wire length with the velocity $v = v_F/K$ renormalized due to the electron interaction: $\omega = 2\pi nv/L$ (n is an integer). Under the resonance condition, an integer number of charge waves is kept within the wire length. The charge density is concentrated only inside the wire. In the course of time $\rho(x,t)$ is redistributed in such a way that the particle current through the contacts is absent. This is the reason for which $\mathrm{Re}Y = 0$ at the resonant frequency.

The effect of the electron-electron interaction on the resistance and the shape of the resonance curve is caused by the reflection of the boson-like excitations at the wire ends. Under AC conditions, the distribution of the boson field generated by external electric field inside the wire is dependent on the interference of the excitation waves reflected at the contacts of the quantum wire with the reservoirs where their velocity is different (see Fig.1). The resulting distribution

of the charge density is dependent on the reflectance phase, i.e. on whether $r > 0$ ($K < 1$) or $r < 0$ ($K > 1$).

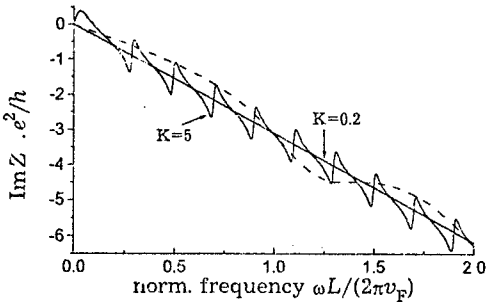

Fig. 3. Frequency dependence of ImZ for repulsive interaction ($K = 0.2$), attractive interaction (K=5) and noninteracting electrons (dashed line). The frequency is scaled by the time for an electron to transit the wire with the Fermi velocity.

The imaginary part of Z is practically always negative (see Fig.3) which corresponds to an inductance. The exception is low-frequency region in the case of $K > 1$. An interesting feature is that in the case of the repulsive interaction, ImZ is approximately proportional to ω which allows one to say about a frequency-independent effective inductance

$$L_{eff} = \frac{hL}{2e^2 v_F}.$$

This work is supported by the Russian Program 'Physics of solid state nano-structures' (grant No 97-1054) and Russian Foundation for Basic Research (grant No 96-02-18276).

REFERENCES

[1] J. Voit, Reports on Progress in Physics, **58**, 977 (1995)
[2] D. I. Maslov and M. Stone, Phys.Rev. B, **52**, R5539 (1995)
[3] V. V. Ponomarenko, Phys.Rev. B, **52**, R8666 (1995)
[4] I. Safi and H. J. Schulz, Phys.Rev. B, **52**, R17040 (1995)
[5] S. Tarucha, T. Honda, and T. Saku, Solid State Commun., **94**, 413 (1995)
[6] M. Büttiker and T. Christen, in "Quantum Transport in Semiconductor Submicron Structures", ed. by B. Kramer, NATO ASI Series, Vol. **326**, 263-291 (1996)
[7] V.A.Sablikov, E.V.Chensky, JETP Lett.,**60**, 397 (1994)

METAL NANOPROBE INDUCED ELECTROSTATIC QUANTIZATION IN NEAR SURFACE DELTA-DOPED GaAs STRUCTURE AT 300 K

S.Yu.Shapoval, V.L.Gurtovoi, V.V.Valyaev, V.V.Sirotkin
Institute of Microelectronics Technology, Russian Academy of Sciences
142432 Chernogolovka, Moscow region, Russia

I.A.Smirnova

Institute of Solid State Physics, Russian Academy of Sciences
142432 Chernogolovka, Moscow region, Russia

At the nanometer length scale, confinement in the vertical direction in semiconductors can be controlled epitaxially through the use of multilayered structures. Using nanolithography, additional lateral confinement can be achieved by fabricating submicron lateral structures. Unfortunately, due to limitation of nanolithography now it is practically impossible to create semiconductor structures with electrical contacts and lateral sizes of 10-20 nm. Lateral confinement can greatly extend our ability to control electron energy levels in semiconductor devices at room temperature, when the maximum size of the device of order of 5-10 nm.

Application of the sharp probes (tip radius of the order of 1-5 nm) in tunneling experiments near the surface of semiconductor results in lateral confinement of flowing current. Thus, electrostatic lateral confinement induced by a nanoprobe could solve the problems of lithography limitations, i.e., create both electrical contact to the semiconductor structure and lateral confinement of order of 5-20 nm (which depends on tip radius, applied voltage and tip-sample distance).

Two types of structures were studied. The first consists of n^+-GaAs substrate, 500 nm n^+-GaAs buffer layer, 5 nm unintentionally doped (UID) layer , Si-doped delta-layer with a concentration of 2×10^{12} cm^{-2}, 5 nm UID layer and 5 nm n^+ cap-layer. Two upper layers of the structure is a region where lateral electrostatic quantization is expected to occur. The second structure consists of thick n^+-GaAs epilayer on n^+-GaAs substrate.

W-nanoprobes were electrochemically etched and usually had tip radius of 2-5 nm [1]. IV-characteristics were measured on an SPM with disabling feedback and positive voltage on the tip (in air at T=300 K). Differential-conductance was calculated from IV-characteristics by digital differentiation.

Numerical solution of Poisson equation has shown that the bias on the tip creates a lateral confining potential in two upper layers of the structure (total thickness of 10 nm). This potential is approximately parabolic with equidistant energy levels. As is well known, there is only one energy level in V-shape potential well of delta-doped GaAs with concentration 2×10^{12} cm^{-2}. Therefore, periodic conductance oscillations as a function of bias voltage will appear when energy levels in surface lateral confining potential coincide with energy level in delta-well.

IV-measurements were done in sample points, where tip-surface barrier potential is higher than 1 V, which means that this surface point is contamination free. We observed reproducibly two types of oscillations in differential conductance for the structure with delta-well. For bias voltage from 0 to 1V, a period of oscillation was about 0.1 V. The period was dependent on tip-sample surface distance. These oscillations we connect with lateral quantization. For higher bias voltage (>2 V), the period of oscillations was more than 0.5 V, which could be attributed to field-emission resonances due to standing waves between the tip and sample. The field-emission-resonances are usually observed for voltage higher than the barrier potential [2]. For the second type of samples only field-emission-resonances were observed.

References

1. V.Dremov, V.Mararenko, S.Shapoval and O.Trofimov, Sharp and clean tungsten tips for STM investigations. Nanobiology, **3**, 83 (1994).

2. R.S.Becker, J.A.Golovchenko and B.S.Swartzentruber, Phys.Rev.Lett. 55, 987 (1985).

Inverted magnetoresistive oscillations in mesoscopic aluminum films

I.N. Zhilyaev, S.G. Boronin, S.V. Dubonos, I.A. Sosnin
Institute of Microelectronics Technology, Russian Academy of Science
Chernogolovka, Moscow District, 142432, Russia

In simply-connected aluminum thin-film structures in a perpendicular magnetic field H, the resistance oscillations with a period close to the quantum of magnetic flux through the area of the structure were observed [1]. This means that when Abrikosov vortices penetrate into mesoscopic superconducting film, the film behaves similarly to a Little-Parks (LP) thin-film interferometer.

We report the measurements of such structures at larger currents through them. The film of several tens of nanometers in thickness were evaporated thermally onto silicon substrate. Micron-size structures with narrow connecting lines (their width was 100–200 nm) were patterned with e-beam lithography. The measurements were carried out using standard four-probe technique in superconducting transition region (temperature was about 1.2 K).

At larger currents through the structure we have found a behavior which could be described rather as inverted when compared with the LP oscillations: the structure of the resistance curves vs H consists of sharp minima, rather than maxima, i.e., the phase of the observed oscillations is opposite to the LP oscillations on a decreasing background.

We propose explanation of new inverted oscillations on the base of the work [2]. At larger currents the structure consists of two parts: normal and superconducting (connecting lines and, respectively, film). The penetration length of nonequilibrium quasiparticles from normal connecting lines to superconducting film oscillates when H changes. Because of this the resistance of the N-S boundary oscillates and gives the oscillations observed. This mechanism explains also the decreasing background.

The work is supported by Program "Physics of Solid State Nanostructures" and INTAS.

References

[1] I.N. Zhilyaev, I.A. Sosnin, S.V. Dubonos, S.G. Boronin, V.V. Ryasanov, *JETP Lett.*, **64**, 608 (1996).

[2] I.N. Zhilyaev, I.A. Sosnin, P. Tuset, K. Fossheim, *Phys. Rev. B*, **54**, R9658 (1996).

Magnetoresistance oscillations in ring-tunnel junction structure

I.N. Zhilyaev and S.G. Boronin
Institute of Microelectronics Technology. Russian Academy of Science
Chernogolovka, Moscow District, 142432, Russia

We present here the study of magnetoresistance of aluminum structure composed of a ring tied with tunnel junction in superconducting transition region with the magnetic field direction perpendicular to the ring plane.

The film of several tens of nanometers thick were evaporated thermally onto silicon substrate. The structures were patterned with e-beam lithography. The Al-Al tunnel junctions were fabricated by oxydation of aluminum in a single vacuum cycle, using a two-angle deposition-oxydation-deposition cycle [1]. The width of lines composing these structures was within 100–200 nm range. Tunnel junctions area amounted several hundredths of square microns and their resistance was several thousand Ohms. Tunnel junction - ring distance was equal to 0.5 μm, the ring diameter being of order 1 μm.

In studying the behavior of the resistance of these structures in a magnetic field we observed the oscillations with the period equal to a quantum of magnetic flux through the ring area. Shape of the oscillations observed resembled that of the Little-Parks ones. Their amplitude was very large and had the value of about 100 Ohms. On the contrary, the amplitude of Little-Parks oscillation found for separate ring was equal to several tenths of Ohms.

One could suggest the following mechanism of magnetoresistance observed in the ring-tunnel junction structure. The order parameter of a ring is known to oscillate in magnetic field when the field changes, resulting in resistance oscillations of the ring (Little-Parks effect). In addition, the oscillations of order parameter of the ring influence directly the critical current of tunnel junction, resulting from nonlocality effect [2], and yield an added increase of oscillations amplitude.

Thus, we have found a new quantum interferometer structure. It should be noted that we indirectly have observed a new transistor effect with the voltage gain of order 100-1000.

The work is supported by Program "Physics of Solid State Nanostructures" and INTAS.

References

[1] G.J. Dolan, *Appl. Phys. Lett.*, **31**, 337 (1977).

[2] N.E. Israeloff, F.Yu, A.M. Goldman, R. Bojko, *Phys. Rev. Lett.*, **71**, 2130 (1993).

New magnetoresistive oscillations in connecting lines of ring structures

I.N. Zhilyaev, S.G. Boronin, S.V. Dubonos
Institute of Microelectronics Technology, Russian Academy of Science
Chernogolovka, Moscow District, 142432, Russia

It has been reported [1] that the nonlocality effect take place in mesoscopic superconducting stuctures under the conditions when coherence length of pairs is comparable to the structure size. Magnetoresistive oscillations in connecting lines accompany the Little-Parks ones which are the magnetoresistive oscillations of aluminum ring in superconducting transition region.

In the present work we report on the measurements of magnetoresistance of similar aluminum ring structures. When carrying the current through the structure we found that depending on the point on superconducting transition the oscillations of two different types may be observed on the connecting lines: those of the type found earlier in [1] and new oscillations.

The films of several tens of nanometers in thikness were evaporated thermally onto silicon substrate. The ring structures with the lines of 100-200 nm in width were patterned with e-beam lithography. New oscillations have the same period as those in [1] which is equal to quantum of magnetic flux through the area of ring but they have a new phase.The phase of new oscillations is such that maximum is observed at magnetic field $H = 0$. It differs from the situation in [1] where minimum is observed at $H = 0$.

We suppose that the new oscillations are caused by nonequilibrium penetration of quasiparticles into superconductor. There is nonuniformity of order parameter in our ring structure because the structure consists of different parts which are ring and connecting lines. The order parameter changes smoothly in connecting lines at some distance from the ring. Such gradient of order paramter gives additional resistance in nonequilibrium conditions (see [2]). With changing magnetic field the last resistance oscillates and gives the oscillations observed.

The sort of oscillations in a given point of a superconducting transition depends on relative values of oscillation amplitudes caused by the mechanism described in the work [1] or by the new mechanism.

The work is supported by Program "Physics of Solid State Nanostructures" and INTAS.

References

[1] N.E. Israeloff, F.Yu, A.M. Goldman, R. Bojko, *Phys. Rev. Lett.*, **71**, 2130 (1993).

[2] I.N. Zhilyaev, I.A. Sosnin, P. Tuset, K. Fossheim, *Phys. Rev. B*, **54**, R9658 (1996).

INTERWELL RADIATIVE RECOMBINATION IN n-i-n AlGaAs/GaAs DOUBLE QUANTUM WELLS

V.B.Timofeev

Institute of Solid State Physics, Russian Academy of Science
142432 Chernogolovka, Russia

Investigations of coupled double quantum wells (DQW) and superlattices (SL's) in semiconductor heterostructures have gained considerable interests during the last decade [1-5]. In part this interest arises from expectations that their electronic properties might be used in optoelectronic techniques. On the other hand, the physical interest in these systems is strongly related to their excitonic properties, which have attracted considerable attention both with respect to the single excitonic problem and the exciton-exciton interaction. In the case of biased DQW (n-i-n or p-i-n DQW structures under applied or build-in electrical field) one of attractive possibilities is related with interwell excitons in which electron and hole are separated between different QW's [3,4] These interwell excitons should demonstrate a long radiative decay time and due to that these excitons can be accumulated to a high densities and can be cooled to low enough temperatures. The intriguing collective phenomena are expected for interwell excitons in high density limit and low temperatures [6-9]. Observation of some collective phenomenon related with interwell excitons was announced recently in [5].

The main goal of presented talk is to demonstrate that the radiative recombination phenomena in the case of n-i-n AlGaAs/GaAs DQW's under applied electrical bias are developing within other scenario.

1. First of all we should emphasize that random potential fluctuations at low enough temperature forces carries (nonequilibrium or equilibrium) to be localized in the plane of DQW's. Such localization in plane of QW should occur if concentration of carriers is less than critical concentration of localized states which, of course, modifies from sample to sample. This critical concentration determines a mobility edge and is directly related with metal-insulator transition in considered DQW's systems (typically, concentrations of localized states varies in the range from $10^{10}cm^{-2}$ in good samples and to $10^{11}cm^{-2}$ or even more in worse one). So, in DQW under applied bias photoexcited electrons and holes, if their concentrations are less than critical number, are,first of all, localized in spatially separated wells (Stark localization), but besides of this localization these carriers should be

localized in planes of wells due to the random potential fluctuations. In the case of biased systems - nin or pin DQW or SL's - the origin of these fluctuations is mainly related to ionized residual impurities located in barriers (AlGaAs in considered case). So, if density of nonequilibrium carriers, electrons and holes, somehow created in DQW, are less than critical numbers of localized states the radiative recombination in this regime is directly connected with recombination of localized e-h pairs in plane. Of course the recombination process has the tunneling nature under consideration. Localized nonequilibrium electrons and holes are weakly bound in corresponding wells so their radiative recombination process is analogues to donor-acceptor pairs recombination in bulk semiconductors. But in the considered case it is better to say about Radiative Recombination of Quantum Confined Electron-Hole Localized Pairs.

It is possible to imagine from general point of view the main properties of such interwell recombination process and behaviour of corresponding luminescence spectra. The shape of luminescence spectrum is a convolution of distribution functions of localized in neighbouring wells electrons and holes interacting via Coulomb potential. So, in principal it should be quite broad luminescence band reflecting an amplitudes of random potential fluctuations and a wide range of interwell electron-hole space separation (Coulomb attraction term). In fact high energy side of luminescence band corresponds to the shorter interwell electron-hole distances, and hence to the stronger attraction between pairs. In turn low energy side corresponds to larger interwell distances, and therefore to weaker electron-hole interaction. This luminescence band can be simply tuned in a wide spectral range under variation of applied bias according to the Stark term in Hamiltonian -(-eFz). Because localized electrons and holes, participating in recombination processes, are weakly bound therefore corresponding luminescence band under applied magnetic field, perpendicular to planes, behaves as recombination of almost free electron-hole pairs. And finally: time-resolved experiment under pulsed excitation should demonstrates a movement of luminescence band (with some redistribution in shape) to lower energy side with time delay.

2. Now we turn to the regime when electron (or hole) concentrations in wells are above mobility edge (i.e. larger than critical concentration of localized states). This regime was definitely realized in n-i-n DQW . So, in n-i-n DQW 2D electron gas appears in one of well at high enough applied bias, more than 0.7 V. Appearance of 2D degenerate electron gas is proved: 1) by direct observation of Landau level quantizations in PLE spectra in the energy region higher that hh1 exciton (see Fig.1); 2) by direct observation of Landau level quantization of

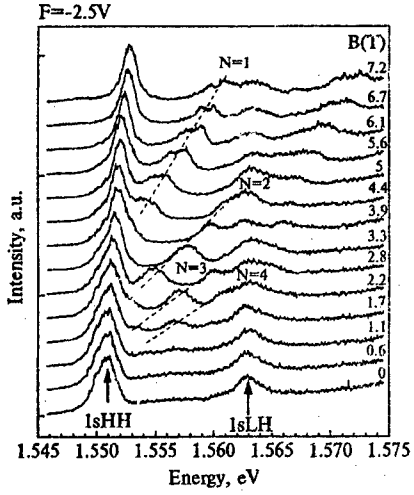

Fig. 1

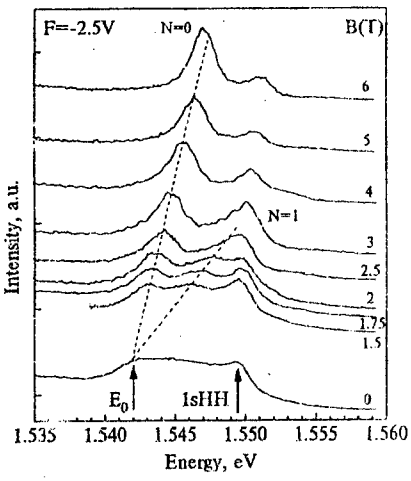

Fig.2

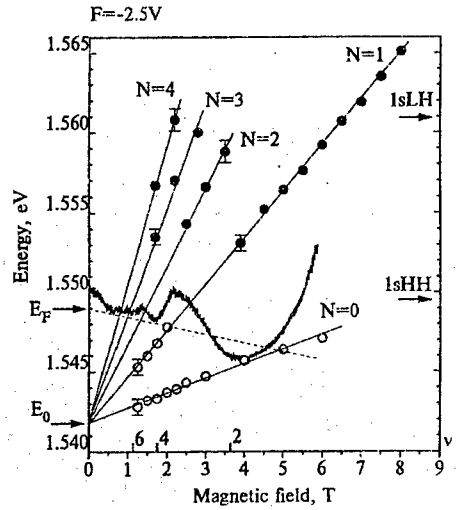

Fig. 3

luminescence band, corresponding to recombination of 2D-electrons with holes in neighbour wells (see Fig.2) and, finally, 3) by observation of optical analogue of Shubnikov oscillations of the luminescence intensity, detected at the Fermi edge of 2D- electron gas [9]. Fermi edge of 2D-gas at given applied bias is pinned by energy position of intrawell excitons, 1s HH, of neighbour QW. So, Fermi energy can be changed only by applied bias. Laser excitation does not influence on 2D-electron density, at least in the range 10 mkWt - 2 mWt of excitation power. Summary of these experiments are plotted on Fig.3. On this Figure: solid dots correspond to PLE data, open dots to PL data and solid noisy curve is Shubnikov oscillations of the luminescence intensity, detected at Fermi edge, under magnetic field variations.

Above described techniques were used for the investigations of 2D-electron gas behavior under variation of applied bias in the wide range. It was found that free 2D-electron gas disappears at applied bias lower than 0.7 V. With the use of these investigations the critical concentration corresponding to mobility edge was found equal $5 \cdot 10^{10} cm^{-2}$ [2].

Finally we would like to emphasize that studied n-i-n DQW can be used for investigations of Coulomb correlations of spatially separated electron-hole layers in ultra quantum regime.

References

1. Y.J.Chen, E.S.Kotcles, B.S.Elman, and C.A.Arimento, Phys.Rev. B36, 4562 (1987)
2. M.N.Islam, R.L.Hillman, D.A.Miller, D.S.Chemla, A.C.Gossard, and J.H.English, Appl.Phys.Lett. 50, 1098 (1987)
3. J.E.Golub, K.Kash, J.P.Harbison,, and L.T.Florez, Phys.Rev. B41, 8564 (1990)
4. T.Fukuzawa, E.E.Mendez, and J.M.Wang, Phys.Rev.Lett. 64, 3066 (1990)
5. L.V.Butov, A.Zrenner, G.Abstreiter, G.Boehm, and G.Weimann, Phys.Rev. Lett. 73, 304 (1994)
6. Yu.E.Lozovik and V.Yudson, Zh.Eksp.Teor.Fiz. 71, 738 (1976)
7. D.Yoshioka and MacDonald, J.Phys.Soc.Jpn. 59, 4211 (1990)
8. X.M.Chen, and J.J.Quinn, Phys.Rev.Lett. 67, 895 !1991)
9. I.V.Kukushkin and V.B.Timofeev, Advances in Physics, 45, 147-242 (1996)

Inhomogeneous Broadening Effect on the Exciton-Light Coupling in Quantum Wells

A.V. Kavokin and M.R. Vladimirova
A.F. Ioffe Physico-Technical Institute, 26, Politechnicheskaya, 194021, St Petersburg, Russia
L.C. Andreani and G. Panzarini
INFM-Department of Physics "A.Volta", University of Pavia, I-27100, Pavia, Italy

Exciton resonances in semiconductor nanostructures are usually inhomogeneously broadened due to interface or alloy compound fluctuations. Still there was no clear understanding whether inhomogeneous broadening effects are qualitatively different from the homogeneous broadening effects and how to distinguish between both.

In this work, we have solved the Maxwell equations for light incident on a quantum well (QW) taking into account the non-local contribution of an inhomogeneously broadened exciton resonance to the dielectric polarization. It has been assumed that the exciton resonance frequency distribution is described by a Gaussian and associated with the in-plane disorder in a QW.

In the framework of a linear non-local response theory Maxwell equations for a light-wave normally incident at the single quantum well in the vicinity of the exciton resonance frequency can be written in form

$$\nabla\times\nabla\times\mathbf{E}=\frac{\omega^2}{c^2}\mathbf{D}, \tag{1}$$

where

$$\mathbf{D}(z)=\varepsilon_\infty\mathbf{E}(z)+4\pi\mathbf{P}_{exc}(z),$$

$$\mathbf{P}_{exc}(z)=\int\chi(z,z')\mathbf{E}(z')dz',$$

the non-local susceptibility

$$\chi(\omega,z,z')=\chi(\omega)\Phi(z)\Phi(z'),$$

where $\Phi(z)$ is the exciton envelope function taken with equal electron and hole coordinates, z is the normal to QW plane direction. Taking into consideration only the ground exciton state, one can write in the absence of the inhomogeneous broadening

$$\chi(\omega-\omega_0)=\frac{\varepsilon_\infty\omega_{LT}\pi a_B^3\omega_0^2/c^2}{\omega_0-\omega-i\gamma}, \tag{2}$$

where ω_0 is the exciton resonance frequency, γ is its homogeneous broadening due to nonradiative processes, ω_{LT} is the exciton longitudinal-transverse splitting in a bulk material, a_B is the bulk exciton Bohr radius.

Solving Eq.(1) using the susceptibility (2) and supposing for simplicity the background dielectric constants in the well and barrier to be equal, one can obtain the amplitude reflection and transmission coefficients in form

$$r=\frac{i\Gamma_0}{\tilde{\omega}_0-\omega-i(\gamma+\Gamma_0)},\quad t=1+r, \tag{3}$$

where the exciton radiative damping rate

$$\Gamma_0=\frac{k\omega_{LT}\pi a_B^3}{2}\left[\int\Phi(z)\cos kz\,dz\right]^2, \tag{4}$$

$$\tilde{\omega}_0 - \omega_0 = \frac{k\omega_{LT}\pi a_B^3}{2}\iint dzdz' sink|z-z'|\Phi(z)\Phi(z') << \Gamma_0, \qquad (5)$$

$$k = \frac{\omega}{c}\sqrt{\varepsilon_\infty}\,.$$

Supposing that due to inhomogeneous broadening the exciton resonance frequency is described by Gaussian distribution function and neglecting possible dependence of the exciton envelope function on energy one should substitute the resonant dielectric susceptibility $\chi(\omega)$ (2) by a function

$$\tilde{\chi}(\omega) \equiv \frac{1}{\sqrt{\pi}\Delta}\int d\nu\chi(\omega-\nu)\exp\left[-\left(\frac{\nu-\omega_0}{\Delta}\right)^2\right] = \frac{i\varepsilon_\infty\omega_{LT}\pi^{3/2}\omega_0^2 a_B^3}{c^2\Delta}e^{-z^2}erfc(-iz), \quad (6)$$

where

$$z = \frac{\omega-\omega_0+i\gamma}{\Delta} \qquad (7)$$

and $erfc(z)$ is a complementary error-function.

Here we have supposed that $\Delta, \gamma > 0$. Solving Eq.(1) with the susceptibility (6) one can obtain instead of Eq.(3)

$$r = -\frac{\sqrt{\pi}\Gamma_0 e^{-z^2}erfc(-iz)}{\Delta + \sqrt{\pi}\left(\Gamma_0 + i\left(\tilde{\omega}_0-\omega_0\right)\right)e^{-z^2}erfc(-iz)}. \qquad (8)$$

In the following we will assume $\tilde{\omega}_0 - \omega_0 \approx 0$.

In the case of small inhomogeneous broadening one can use the expression

$$e^{-z^2}erfc(-iz) \to \frac{i}{\sqrt{\pi}z}$$

and Eq. (8) reduces to Eq. (3); one can also derive the absorption coefficient of the quantum well as

$$A(\omega) \equiv 1 - |r|^2 - |t|^2 = \frac{2\gamma\Gamma_0}{(\omega_0-\omega)^2 + (\gamma+\Gamma_0)^2}, \qquad (9)$$

so that the integrated absorption is

$$\int d\omega A(\omega) = \frac{2\pi\gamma\Gamma_0}{\gamma+\Gamma_0}. \qquad (10)$$

In case of inhomogeneous broadening the integrated absorption appears to be dependent also on Δ.

Fig. 1 shows the integrated over the frequency excitonic absorption in 1 QW, 5 and 10 equally spaced QWs as function of the inhomogeneous broadening parameter Δ. The solid lines have been obtained assuming zero homogeneous broadening while the dashed lines show the calculation with $\hbar\gamma$ =0.1 meV. We have always taken $\hbar\Gamma_0$ =0.026 meV, the period d=10 nm. The integrated absorption of light in single and multiple QWs is found to increase with enhancement of either homogeneous or inhomogeneous broadening: only when broadening is larger than the exciton radiative width does the integrated absorption attain the saturation value expected from the exciton oscillator strength and number of the QWs. This behavior is similar to that of exciton-

polariton absorption in bulk semiconductors [1,2], but in the present case it is not due to a spatial dispersion effect.

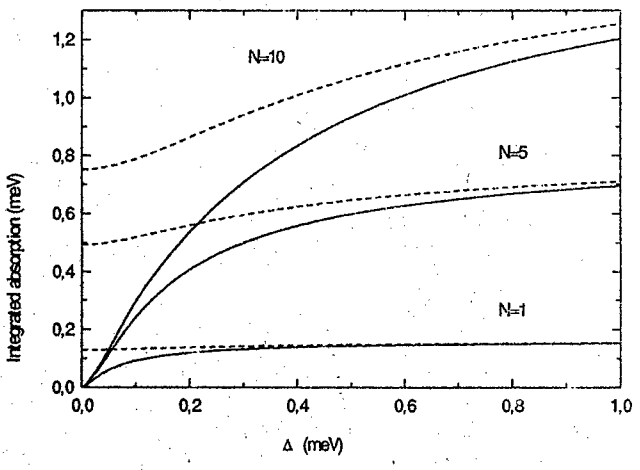

Fig.1

A qualitative difference between homogeneous and inhomogeneous broadening effects can be revealed in time-resolved spectra.

Time-resolved reflection and transmission spectra from the single quantum well have the same shape because the corresponding amplitude coefficients are related by $t=1+r$. For example the time-resolved transmission in case of incident delta-pulse is described by a function

$$G(\tau)=\int\frac{d\omega}{2\pi}\exp(-i\omega\tau)t(\omega). \qquad (11)$$

The experimentally detectable quantity is the integrated intensity of light which is proportional $|G(t)|^2$. In case of no inhomogeneous broadening $G(\tau)$ can be calculated analytically:

$$G(\tau)=-\Gamma_0\exp\left[-(\gamma+\Gamma_0+i\omega_0)\tau\right]\ \ (\tau>0). \qquad (12)$$

Results of the numerical calculation of the time-resolved transmission spectrum of the single QW in the presence of inhomogeneous broadening are shown in Fig. 2. One can see that the inhomogeneous broadening gives rise to pronounced oscillations in the time-resolved signal, which is a qualitatively new effect in comparison with what is known for the case of only homogeneous broadening. What is the origin of oscillations?

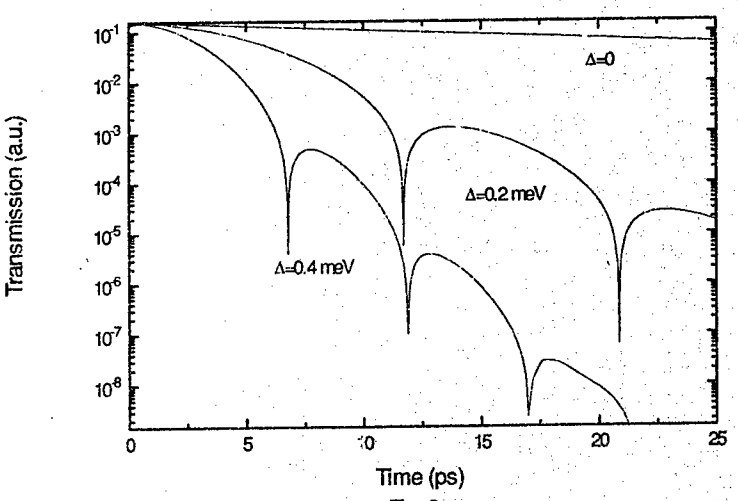

Fig. 2

To obtain an intuitive physical understanding of the effect, let us consider a wave packet composed by a set of plane waves with amplitudes proportional to $\exp\left(-\left(\frac{\omega-\omega_0}{\Delta}\right)^2\right)$, which is a simplified analogy of the wave packet emitted by an inhomogeneously broadened exciton. As a zeroth order approximation let us suppose all these waves to have the same phase. Since

$$e^{i(\omega_0+\nu)t}+e^{i(\omega_0-\nu)t}=2e^{i\omega_0 t}\cos\nu t,$$

the time-dependent integrated signal is given by a function

$$G(t)\propto\int_0^\infty d\nu e^{-\frac{\nu^2}{\Delta^2}}\cos\nu t=\frac{\sqrt{\pi}}{2}\Delta\exp\left(-\frac{\Delta^2t^2}{4}\right), \qquad (13)$$

which describes an initial Gaussian-like decay of the transmitted signal. The origin of the minima and oscillations is in the frequency dependence of the phase of the emitting oscillators. As one can see from Eq.(8) or, more directly, from Eq.(3), the phase of the reflection coefficient of light changes from π to $-\pi$ as one tunes the frequency across the exciton resonance. The interference of the light waves emitted with the different phases results in the oscillations of the time-resolved transmission and reflection. In the first order and in the case of a strong disorder, one can approximate the phase as a function of frequency by

$$\varphi\approx\operatorname{arctg}\frac{\nu}{\Delta}, \qquad (14)$$

where $\nu=\omega-\omega_0$. In this case

$$G(t) \propto \Delta^{-1}\int_0^{\infty} dv e^{-\frac{v^2}{\Delta^2}}(\Delta\cos vt - v\sin vt) = \frac{\sqrt{\pi}}{2}\Delta\exp\left(-\frac{\Delta^2 t^2}{4}\right)\left[1-\frac{t\Delta}{2}\right]. \quad (15)$$

Thus we see that even in this oversimplified model the interference of modes having a different phase in case of inhomogeneous broadening causes the pronounced nonmonotonity of the time-resolved signal which has a minimum (zero) at $t = \frac{2}{\Delta}$.

Analytically, the oscillations of a time resolved signal for a single QW can be obtained if instead of the Gaussian one takes the following frequency distribution function to be substituted in the dielectric susceptibility (6):

$$f(x) = \frac{\Delta^3}{\pi}\frac{1}{(x-\omega_0)^4 + \Delta^4}. \quad (16)$$

One can show that in this case the oscillations appear if $\Delta > 2\Gamma_0$ and have a period

$$T = \frac{4\pi}{\sqrt{\Delta^2/4 - \Gamma_0^2}}. \quad (17)$$

In order to generalize this formalism for the case of multiple quantum wells (MQWs) one should derive the amplitude reflection and transmission coefficient of MQW in terms of the single QW reflection and transmission coefficients (8). This can be done using a transfer matrix method. At normal incidence, in the basis of amplitudes of in-coming and out-going light waves the transfer matrix across the period of MQW structure has a form

$$\hat{M} = \frac{1}{t}\begin{bmatrix} (t^2 - r^2)e^{ikd} & re^{-ikd} \\ -re^{ikd} & e^{-ikd} \end{bmatrix}, \quad (18)$$

where d is the period of the structure. The eigenvalues of this matrix can be written in form

$$e^{\pm iQd} = \left(m_{11} + m_{22}\right)\Big/ 2 \pm \sqrt{\left(m_{11} + m_{22}\right)^2/4 - 1}, \quad (19)$$

where m_{11} and m_{22} are the diagonal elements of the matrix $\hat{M}$. The eigenvectors of this matrix can be represented as

$$I_{\pm} = \begin{bmatrix} 1 \\ a_{\pm} \end{bmatrix}, \quad (20)$$

where

$$a_{\pm} = \frac{re^{ikd}}{e^{-ikd} - te^{\pm iQd}}.$$

Representing the light wave inside the structure as a linear combination of two eigen vectors and using the Bloch theorem one can obtain the amplitude reflection and transmission coefficients of the MQW in form

$$\begin{aligned} r_{MQW} &= \frac{a_+ a_- \left(1 - e^{2iNQd}\right)}{a_- - a_+ e^{2iNQd}}; \\ t_{MQW} &= \frac{(a_- - a_+)e^{iNQd}}{a_- - a_+ e^{2iNQd}} e^{-ikd}. \end{aligned} \quad (21)$$

The eigen frequencies of exciton polaritons in the structure must satisfy the equation

$$a_+ e^{iNQd} = a_- e^{-iNQd}. \quad (22)$$

Substituting the amplitude coefficients (21) into Eqs. (9,11) one can obtain, respectively, the absorption and time-resolved transmission spectra of the MQW.

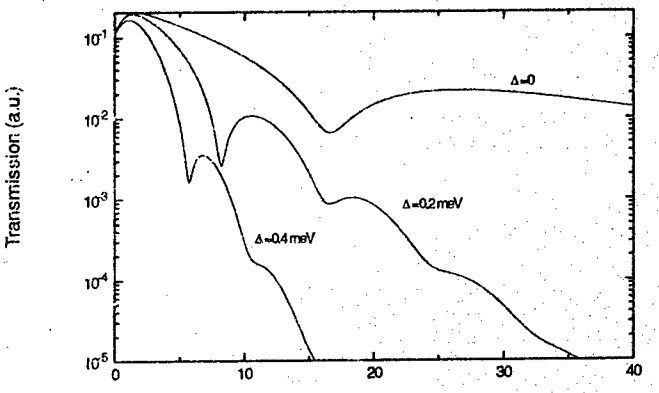

Fig. 3

Fig. 3 shows the time-resolved transmission spectra for a periodical structure containing 5 QWs with the same parameters as before. The spectra are always non-monotonic, while in the absence of the inhomogeneous broadening the oscillations are originated from the optical coupling of excitons in different QWs [3], while in the presence of inhomogeneous broadening additional oscillations appear connected with interference of light waves emitted by excitons from the upper-wing and from the lower-wing of the inhomogeneous distribution and having different phases.

For multiple QWs, QWs in a microcavity and an exciton resonance in a thick film of bulk, in general, increase of the disorder induces decrease of the period of oscillations and makes the decay of the signal faster.

In conclusion, the developed formalism has allowed to investigate theoretically the inhomogeneous broadening effect on the complete set of the optical characteristics of the structure.

A.V. Kavokin and M.R. Vladimirova gratefully acknowledge the financial support from the Russian Foundation for Basic Research, grant INTAS 93-3657-Ext and the Volkswagenstiftung.

References:

[1] A.S. Davydov, *Theory of Solids* (Nauka, Moscow, 1976).
[2] V.A. Kosobukin, R.P. Seisyan, S.A. Vaganov, Semicond. Sci. & Technology, **8**, 1235 (1993).
[3] T. Stroucken et al., Phys. Rev. Lett. **74**, 2391 (1995).

Phase diagram, superfluidity and exciton spectra in double quantum well system

Yurii E.Lozovik
Institute of Spectroscopy, 142092 Moscow region, Troitsk, Russia, e-mail: lozovik@isan.msk.su

Systems with spatially separated electrons and holes in coupled quantum wells (CQW) are interesting in connection with their possible superfluidity manifesting itself as persistent longitudinal electric currents along each well, and besides that with Josephson-type phenomena and unusial properties in strong magnetic fields. In the report recent results concerning the system will be presented.

The properties of excitonic liquid phase in the system of spatially separated electrons (e) and holes (h) in CQW are considered. The energy of the ground state of the exciton liquid as a function of the density of electrons and holes at different separations D between e- and h-layers is obtained. The quantum phase transition exciton gas-exciton liquid due to D decreasing is studied.

At $D < 1.1$ the energy of the liquid phase is greater than the energy of a single exciton, so the exciton liquid is a stable phase in this region and the exciton gas is a metastable phase (all distances are given in units of 2D exciton radius at $D = 0$). At $D = 1.1$ first order quantum transition exciton liquid-exciton gas takes place. The minimum of the energy as function of e-h density corresponding to exciton liquid survives corresponding to metastable phase in the region $1.1 < D < 1.9$. At $D > 1.9$ the liquid phase becomes absolutely unstable and the exciton density is determined only by external conditions. Excitonic gas is metastable at any D and stable at $D > 1.9$ due to dipole-dipole repelling of excitons with spatially separated e and h.

At small densities biexcitons and biexciton ions and other complexes (particularly charged ones) with spatially separated electrons and holes are also exist at small D (some of them become stabilized in strong magnetic fields). They also have interesting transport properties along layers.

The supefluid density of the exciton system as function of D and carrier density is calculated using ladder approximation for rare exciton gas and BCS-type approximation for dense exciton system. The temperatures of appearance of the superfluidity in the system (Kosterlitz-Thouless transition) decreases as function of D.

For the anisotropic 2D e-h CQW system metal-insulator quantum transition is studied. Crystallization in two-layer e-h and e-e systems is analized.

Influence of the magnetic field on exciton spectra and on superfluidity in two-layer system is analized in detail. Particularly e-h system with one half Landau filling is studied.

Josephson-type phenomena and electromagnetic properties of two-layer system are considered.

For the anisotropic 2D e-h system in CQW Mott metal-insulator quantum transition is analized. The problem of magnetoexciton localization is considered. The derivation of the magnetoexcitonic relaxation time and diffusion constant is presented. Drag effects in the two-layer e-h system due to Coulomb e-h scattering and to the presence of indirect excitons is analized. Drag of spatially separated electrons and direct excitons in CQW due to polarization interactions are also considered. Experimental data conserning the problem will be discussed.

The work was supported by grants of Program "Physics of Solid Nanostructures", Russian Foundation of Basic Research and by INTAS.

Exciton-polariton behaviour of the absorption edge of thin GaAs crystals with the "super-quantum" thickness

G. N. Aliev, N. V. Luk'yanova, R. P. Seisyan
Ioffe Physico-Technical Institute, Russian Academy of Sciences
Polytechnicheskaya 26, 194021, St Petersburg, Russia

At $T = 1.7$ K the optical absorption of pure GaAs samples with thickness $d = 0.4$–4.4 μm has been investigated at the region of the exciton-polariton resonanses. Strong changes in the spectral behaviour of the absorption edge due to exciton-polariton processes are revealed as the sample thickness decreases. Dependence of the integral absorption on the thickness is considered as a result of competition of the optical processes in two diffrent sample regions: near-surface region, where the integral absorption saturates due to increasing damping parameter in the electric field and central region, where exciton-polariton is not perturbed.

1 Introduction

High quality thin semiconductor films frequently exhibit properties quite different from those of bulk crystals at the region of the exciton-polariton resonanses. Especially this is valid for "super-quantum" region $a_x \lesssim d \lesssim l^*$, where a_x is Bohr radius for exciton and l^* is exciton-polariton mean free path length. The aim of this work is the optical absorption investigation of free pure crystals of "super-quantum" thickness, using GaAs as an example.

2 Experimental data

We have studied high quality gas-phase epitaxial (GPE) layers of GaAs ($n \approx 5\times10^{14}$ cm^{-3}, $\mu_{77} \lesssim 140000$ cm^2/V s) grown on the (100) GaAs substrate. To measure the transmission spectra we etched the substrates so that the thickness of epitaxial layers has been reduced from 10 μm up to 0.4 μm[1]. The samples were placed free in the glass box and immersed in pumped liquid helium at 1.7 K. Sulphide passivation of the surfaces was carried out just before measurements on separate samples. The sample thickness d was estimated from an optical density D in the spectral continuum region as $d = D/\alpha^*$, where α^* was taken 8×10^3 cm^{-1}.

The samples of thickness $d > 2$ μm demonstrated an ordinary behaviour with clearly expressed members of exciton series, quasicontinuum, continuum and exciton-impurity complex [1]. The linewidth of the exciton ground state was about 0.3–0.5 meV and it increased as the sample size decreased, so that the excited exciton states and bound exciton states became undetectable (Fig. 1). The passivation of the samples had no effect on the optical density in the continuum region while it enhanced the excitonic absorption line and induced its shift of about 0.4 meV to higher energies without any important changes in the linewidth. The decrease in the sample thickness to 0.3 μm

[1] The samples of the different thickness were prepared by N. D. Il'inskaya.

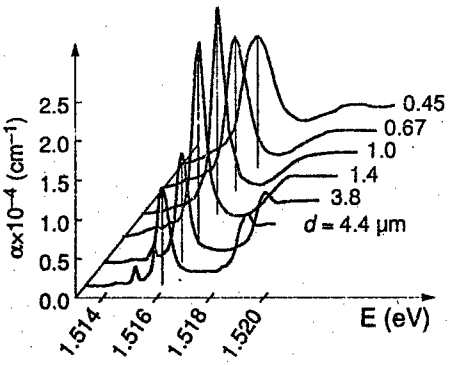

Fig 1. Excitonic absorption spectra of GaAs samples with different thicknesses.

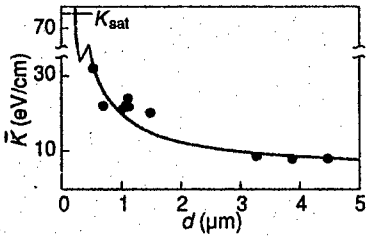

Fig 2. Integral absorption $\bar{K}$ versus the sample thickness d. Solid line is the result of fitting procedure according to exp. (1), $K_1 = 5$ eV/cm, $K_s = 74$ eV/cm, $d_s^* = 0.11$ μm.

resulted in a small lower-energy shift of the line, while the optical absorption behaved unusually. The substantial rise of line amplitude has been observed along with line broadening and insignificant shift.

3 Discussion

Absorption coefficient α obtained from transmission spectra in the area of exciton resonances due to its thickness dependence is found to be not a constant of material but a constant of definite sample only. The spectral behaviour of the excitonic structure can be better understood if we take into account the surface electric field F_s induced by the surface charge Q_{ss} and regions of the volume charge at the surfaces d_s. Under constant surface condition, the decrease in the total thickness d does not influence $2d_s$ and decreases d_1, where the excitonic states are not perturbed. In the regions d_s a nonuniform electric field $F(x)$ exists and for the range $F(x^*) > F_I = R/e\,a_x$, where e is the electron charge, R is the exciton binding energy it ionizes the exciton, while in the other part of d_s, it induces the nonuniform Stark shift. This explains the short-wave-length

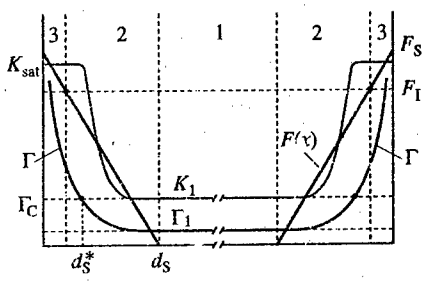

Fig 3. Electric field distribution, integral absorption, damping parameter of the thin semiconductor sample of "super-quantum" thickness (model).

shift after the passivation, which corresponds to the average field about 800 V/cm, and the long-wave-length shift and broadening of lines when the sample thickness decreases because of the enhancement of the relative contribution of the near-surface regions up to $d = 2d_s$. In this case one can expect a strong dependence of the measured absorption coefficient $\tilde{\alpha}$ on the thickness $\tilde{\alpha}(\omega) = \alpha(\omega)(1 - 2\delta\alpha_1(\omega)d_s/\alpha(\omega)d)$, where $\delta\alpha_1$ is the near-surface absorption coefficient averaged on d_s. It looks like a hyperbolic function and, for exciton maximum position ω_0, could only increase with rising d. Experimentally we have observed an opposite dependence. A better understanding can be gained by integration of the absorption coefficient over the frequency. The behaviour of the integral absorption K which is proportional to the exciton oscillator strength, is shown in Fig. 2. We stress that this characteristic is not sensitive to the inhomogenious broadening and, therefore, to the Stark effect. In spite of this the figure shows the increase in $K(d)$ from 8 eV/cm to 33 eV/cm as the thickness decreases from $d > 4.4$ μm to $d = 0.45$ μm. This is in a good agreement with dependence of the integral absorption on temperature [2, 3] exhibiting a strong increase in K to the critical temperature T_c followed by its saturation. This is strongly governed by the longitudinal-transverse splitting constant Δ_{LT} proportional to the oscillator strength: $K = (\pi/c\hbar)\sqrt{\varkappa_0}\Delta_{LT}\hbar\omega_0$, where $\varkappa_0$ is a background dielectric constant. The substitution of bulk GaAs parameters yields $K \equiv K_{sat} = 70$ eV/cm. The 7-fold decrease in K, observed at $d \gtrsim 3\mu$m, corresponds to the maximal variation of K in the temperature dependence [2] at the same samples as those studied in this work and manifests the exciton-polariton processes playing an important role when $\Gamma < \Gamma_c$, $\Gamma_c = 2\hbar\omega_0\sqrt{2\varkappa_0\Delta_{LT}/Mc^2}$, where M is the translational excitonic mass. In this case there is no real absorption of light and Bouguer law can not be applied. The measured "absorption coefficient" is governed by the dissipative damping Γ. In [2] the increase in Γ is associated with the change in temperature due to the exciton-phonon scattering, while, in the present case, it is caused by an electric field. From the common consideration we can offer the following expression for the integral absorption of thin sample:

$$\tilde{K}(d) = K_1 + 2\frac{d_s^*}{d}K_s\left(1 - \frac{K_1}{K_s}\right), \qquad (1)$$

where K_s is averaged integral absorption coefficient of the surface regions and K_1 is one for inside region of sample. A good agreement between (1) and experimental data was reached by choice

of $K_1 = 5$ eV/cm at $K_s \approx 74$ eV/cm and $d_s^* \approx 0.11$ μm. It is remarkable that K_s practically coincides with theoretical value of K_{sat}, and ratio $K_s/\bar{K} \approx 7$ is the same as in [2], where the temperature broadening of the exciton line was studied. Thus the obtained data testify the exciton-polaritonic character of the light propagation through the sample central region where $F = 0$. Damping parameter rapidly increases as $\Gamma \approx \Gamma_1 + A\,R f^{-1} \exp(-4/3f)$, where A is a numerical coefficient, R is exciton binding energy and $f = F/F_l$ in the near-surface areas 2 and 3 (Fig. 3), leading to the loss of spacial dispersion and K saturation when $\Gamma > \Gamma_c$. To estimate Γ_1 it is possible to use results of [4] for the exciton-polariton with spacial dispersion:

$$K = \frac{2}{\pi}\left[\arctan\left(g/\sqrt{1-g^2}\right) + g\sqrt{1-g^2}\right] K_{sat}, \qquad (2)$$

where $g = (\Gamma/\Gamma_c) \leq 1$. According to (2) K depends on g almost linearly, and saturates at $\Gamma > \Gamma_c$. At $\Gamma << \Gamma_c$ dissipative damping is $\Gamma = \pi K \Gamma_c / 4 K_{sat}$. Using obtained data we can estimate: $\Gamma_1 = 0.02$ meV ($\Gamma_c = 0.24$ meV). So, the transition from Γ_1 to Γ_c and correspondingly from K_1 to K_{sat} takes place in relatively narrow crystal region. This justifies dividing the crystal on three parts and using the expression (1) where $d_s^* \lesssim d_s$.

4 Conclussion

The investigations showed an influence of the exciton-polariton processes on light transmission through perfect semiconductor crystal thin plate of "super-quantum" thickness. These processes were displayed by a substantial increase in the sample transmittance in the region of exciton resonances up to $\Gamma \geq \Gamma_c$, where Γ was acting dissipative damping. This condition was reached in our experiments due to electric field, whereas in [2, 3] that was made by the temperature variations.

Acknowledgements

This work was supported by Russian Basic Research Foundation (grant No. 96-02-17935).

References

[1] R. P. Seisyan, *Spectroscopy of Diamagnetic Excitons*, Moscow: Nauka, 1984 (in Russian)

[2] V. A. Kosobukin, R. P. Seisyan, S. A. Vaganov, *Semicond. Sci. Technol.*, **8**, 1235–1238 (1993)

[3] G. N. Aliev, O. S. Coschug-Toates, V. A. Kosobukin, R. P. Seisyan, S. A. Vaganov, *Proc. SPIE*, ed. J. Singh, p. 561 (1995)

[4] N. N. Akhmediev, *Sov. Phys. JETP*, **4**, 1534–1543 (1980)

HOMOGENEOUSE BROADENING OF NEUTRAL AND NEGATIVELY-CHARGED EXCITON LINES IN MODULATION-DOPED QWs.

G.Astakhov, V.Kochereshko, D.Yakovlev, A.Platonov

A.F.Ioffe Physico-Technical Institute RAS, 194021, St.Petersburg, Russia

T.Wojtovicz, G.Karczevski, J.Kossut

Institute of Physics Polish Academy of Science PL02608 Warsaw, Poland

W.Ossau, G.Landwehr

Physikalisches Institut der Universitat Wuerzburg, 97074, Wuerzburg, Germany

Homogeneous linewidth of exciton, negatively-charged exciton (trion) and exciton cyclotron resonance state (ExCR) were studied by analyze of reflectivity and photoluminescence excitation (PLE) spectra in modulation-doped quantum well (QW) structures.

$CdTe/Cd_{0.7}Mg_{0.3}Te$ quantum well structures grown by molecular beam epitaxi on (100) oriented GaAs substrates were used for this study. The structures were modulation-doped with Iodine in the barrier at the distance of 100A from QW. The electron concentration in QWs was of the order of 10^{11} cm^{-2}.

A strong circular polarization of exciton, trion and ExCR lines in magnetic fields in Faraday geometry were observed in reflectivity and PLE. The sign of the circular polarization of the exciton line was the same as for the ExCR line and was opposite to the sign of the trion polarization. The degree of the polarization was observed to decrease with the temperature and described by Boltzmann factor $\exp(-\Delta E / kT)$ that reflects the leveling of the electron Zeeman sublevels population. We explain the the polarization of exciton line by the difference of homogeneous broadening of the exciton for two circular polarization in the presence of magnetic fields. This difference can be initiated by two reasons (i) spin dependent exchange scattering of excitons by free electrons and (ii) fast trapping of exciton by free electron into trion state.

We analyzed also the temperature dependence of the integral intensity for exciton, trion and ExCR reflectivity (absorption) lines. The strong difference of these dependencies have been found to support the idea of the spin dependent exciton - electron scattering.

Photon-induced lifting of the degeneracy of excitonic states in coupled microcavities

A. Armitage, M.S.Skolnick, T.A. Fisher, D.M. Whittaker, and J.S. Roberts
Department of Physics, The Hicks Building, Sheffield S3 7RH, UK
V.N. Astratov, M.A. Kaliteevski, A.V.Kavokin, and M.R.Vladimirova
Ioffe Physicotechnical institute, 26 Polytechnicheskaya, 194021, St-Petersburg, Russia
L.C. Andreani,
INFM-Department of Physics 'A. Volta', University of Pavia, Italy
G. Panzarini
INFM-Department of Material Science, University of Milano, Italy

1. Introduction

Semiconductor microcavity (MC) with quantum wells (QW) [1,2] and vertical cavity surface emitting lasers [3] are attracting increasing interest, what is stimulating design of nowell multi-cavity structures allowing divers types of interactions between photon and exciton. In the double cavity structure shown in Fig.1 the photon field of two MC are coupled through a common mirror that gives rise to a splitting between otherwise degenerate cavity modes. Coupling of cavity modes with excitonic states of QWs placed within the cavities have to lead to the modification of eigen-modes behavior.

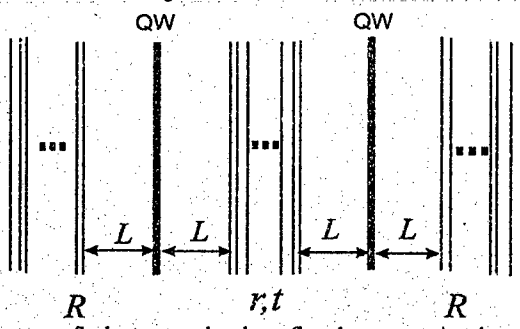

Fig.1. Scheme of the structure

Such structure has been first demonstrated and experimentally investigated in 1994 by Stanley et al. [4]. *Two modes behavior at room temperature and three modes behavior when either of two optical modescouple to QW exciton* is shown in that paper. In this paper we present first result on observation and study of light-matter interaction in coupled MCQW involving the behavior of *four modes, i.e. two exciton and two photons*. This behavior clearly manifests itself as an appearence of four peaks in reflectivity spectra of coupled MCQW under resonance conditions.

2. Experiments

The coupled QMC structure consists of a pair of one wavelength GaAs cavities separated by the common AlGaAs/GaAs distributed Bragg reflector (DBRs). The outside mirrors are also AlGaAs/GaAs DBRs. Three 10 nm-wide InGaAs QWs are located in the center each cavities. The optical length of each of the cavities is designed to match at 4K the wavelength of the lowest energy heavy-hole exciton transition involving the first heavy hole and electron states

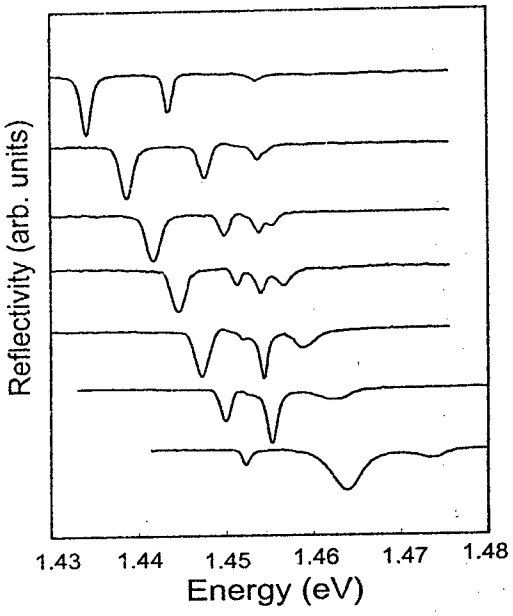

Fig.2. Reflectivity spectra for a coupled semiconductor microcavity at 5 K taken at different angles of incidence (φ).

The reflectivity spectra were measured using white light illumination. Three mode behavior can be seen in the upper spectrum in Fig.2 taken at normal incidence. The low-energy and central peaks originate from two coupled cavity modes splitted by approximately 9 meV. The high-energy heavy-hole exciton peak is observed at 10 meV to higher energy from the central peak. This peak is relatively weak since at these energies it is only weakly coupled to the cavity modes.

In order to investigate extensively an anticrossing between the QW exciton and each of the two coupled cavity modes it is necessary to tune the exciton-photon interaction over 30-40 meV. The angular dependent reflectivity technique was empoyed to wider the range of the mode tuning. This technique relies on the strong shift of the cavity modes to higher energy with angle of incidence (φ) due to the in-plane dispersion of the cavity photon modes whereas the exciton energy is angle independent [2]. An additional advantage of angular dependent techniques is that tuning is achieved without the application of any external perturbation which may influence the nature of the electronic states involved.

As illustrated in Fig.2 the clear anti-crossing behavior between the exciton and both cavitie modes is observed. For $20>\varphi>30$ the exciton resonates with both cavities modes simultaniously that is accompanied by the formation of previously unreported four peak structure in reflectance spectra. For $\varphi>40$ (see lower spectrum), the cavities linewidths are found to increase strongly with angle. This broadening arises from incresed damping of the both cavity modes, and reduction of the cavity finesse, as the cavity modes move progressively into the excitonic continuum.

3. Theory

Dispersion equation for polaritonic modes in layered structure, surronded with two planes with amplitude reflection coefficient R_1 and R_2 can be written in a form (1), which has come from the boundary conditions: there is no light incident from outside:

$$A\begin{pmatrix}1\\R_1\end{pmatrix} = \hat{M}\begin{pmatrix}R_2\\1\end{pmatrix} \qquad (1),$$

where $\hat{M}$ is transfer matrix of light through the structure in the basic of amplitude of incoming and outgoing waves, A is a constant.
From (1) one can obtain excluding A:

$$R_1 R_2 M_{11} + R_1 M_{12} - R_2 M_{21} - M_{22} = 0 \qquad (2).$$

In the case of simmetrical structutre (2) has a form:

$$R^2 M_{11} + R(M_{12} - M_{21}) - M_{22} = 0 \qquad (3)$$

where components of $\hat{M}$ are:

$$M_{11} = \exp(4i\Phi)a^2 b - 2\exp(2i\Phi)ar_{QW}r - r_{QW}^2 ,$$
$$M_{12} \exp(2i\Phi)abr_{QW} + ar - r_{QW}^2 r + \exp(-2i\Phi)r_{QW} ,$$
$$M_{22} = \exp(-4i\Phi) - br_{QW}^2 - 2\exp(-2i\Phi)r_{QW}r ,$$
$$M_{12} = - M_{21} . \qquad (4)$$

Here $a = t_{QW}^2 - r_{QW}^2$, $b = t^2 - r^2$, t,r and t_{QW} ; r_{QW} are the amplitude transmission and reflection coefficiens of common mirror and quantum wells respectively, $\Phi = n_c L\omega / c\cos\varphi$ is the phase gained by light propogating QW to mirror, φ - incidence angle, ω - light frecuency, n_c- cavity refractive index, c-light velocity.
Equation (3) can be rewritten in factorized form

$$[X(t+r) + Z][X(t-r) - Z] = 0 \qquad (5)$$

where first term conserns to the branches generated with symmetrical opical state while the second conserns to the antisymmetrical optical state [2]. Here $X = \exp(2i\Phi)Ra + r_{QW}$, $Z = Rr_{QW} - \exp(-2i\Phi)$. This equestion has 4 roots conserning to 4 polaritonic branches, but the number of dips in reflection spectra can differ for differnt structures depending on nonradiativer broadering of exciton and transmision coefficient of common mirror.

Figures 3 and 4 shows the positions of polariton modes obtained using eq. 5 and positions of dips in calculated reflection spectra for two model structures with differnt common mirrors. Parameters of the structures are choosen so that the frequency of uncoupled cavity mode is in resonance to exciton frequency when incidence angle is 30°.

Two different cases can be realized: when the splitting of two coupled optical modes is not very large, four dips are observable in reflection spectra (Fig3.). If splitting of cavity modes is large (Fig.4) one can see only three dips in reflection spectra.

This effect can be simply understood in terms of a simple model of coupled oscillators. Suppose that two MCs are identical so that both photon eigenmodes have the same frequency ω_m in the absence of coupling; let γ_c be the decay of each single cavity mode. Coupling between the two photon modes is described by the equation:

$$(\omega_m - \omega - i\gamma_c/2)^2 = V_{opt}^2, \qquad (6)$$

where V_{opt} is the coupling constant governed by the transmittivity of the common mirror [5]. The width of the coupled cavity modes is reduced by a factor of two, due to the fact that each cavity mode decays on one side only of the coupled structure. Solving (6), one obtains the symmetric and antisymmetric solutions:

$$\omega_{\pm} = \omega_m \pm V_{opt} - i\gamma_c / 2 \qquad (7).$$

Considering multi-QWs embedded in each cavity as a single QW we can describe the two-fold

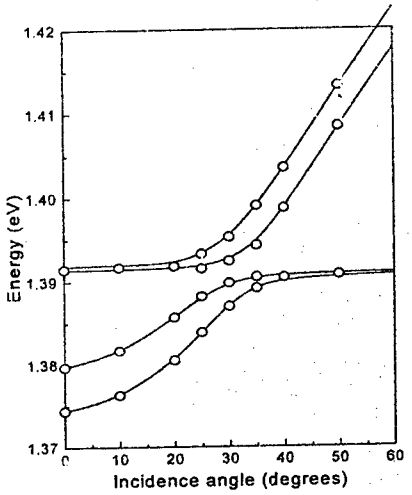

Fig. 4. Energies of polaritonic modes (lines) and position of the dips in reflection spectra (circles) as a function of incidence angle

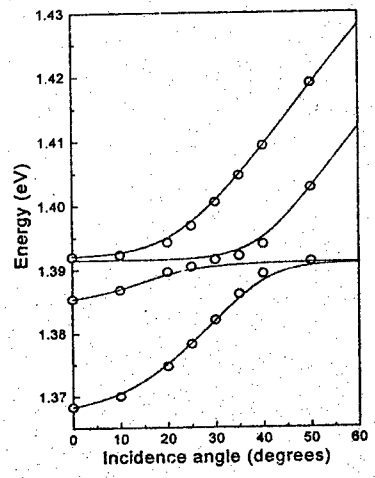

Fig. 4. Energies of polaritonic modes (lines) and position of the dips in reflection spectra (circles) as a function of incidence angle

degenerate lowest exciton by the symmetric and antisymmetric eigenfunctions:

$$|s\rangle = (|QW1\rangle + |QW2\rangle)/\sqrt{2} \quad (8a),$$

$$|a\rangle = (|QW1\rangle - |QW2\rangle)/\sqrt{2} \quad (8b),$$

where |QW1> and |QW2> are the single exciton wave functions in first and second QWs. Evidently the symmetric exciton state only interacts with the symmetric photon mode, and the antisymmetric exciton only interacts with the antisymmetric photon mode. Therefore the dispersion of cavity polaritons in this case is given by two independent equations:

$$(\omega - \omega_0 - i\gamma)(\omega - \omega_1 - i\gamma_c/2) = V^2 \quad (9a)$$

$$(\omega - \omega_0 - i\gamma)(\omega - \omega_2 - i\gamma_c/2) = V^2 \quad (9b)$$

where ω_0 and γ are the frequency and non radiative broadening of the exciton, V is the exciton-photon coupling constant.

The best condition for the observation of the whole set of coupled MCQW are provided under condition $V_{opt} \sim V$, which are satisfied in our experiments (See also Fig.3). When $V_{opt} >> V$, (what is the case of [4]) the shifts of the energies of symmetrical and antisymmetrical exciton states can not be simultataneously strong enough to resolve the related dips in reflection spectra (Fig.4).

This work was supported in part by RFBR and "MNTP Nanostructures".

References:

1) C. Weisbouch, M.Nishioka, A.Ishikava, Y.Arakawa, Phys. Rev. Lett. **69**, 3314 (1992)
2) E.L.Ivchenko, M.A.Kaliteevski, A.V.Kavokin et al., JOSA B, **13**, 1061 (1996)
3)Kawaguchi, IEE Proc. J. Optoelectron., **140**, 3 (1993)
4) R.P. Stanley, R.Houdre, U.Oesterle, M.Ilegems, C.Weisboush, Appl.Phys.Lett., **65**(16), 2093 (1994)
5) M.A. Kaliteevski, Journal of Tech. Phys., in press (1997)

SPLITTING AND ORDER OF EXCITON RADIATIVE LEVELS IN GaAs/AlAs SUPERLATTICES: A LINK TO THE INTERFACE MORPHOLOGY

P.G. Baranov, N.G. Romanov, [1]
A. Hofstaetter, B.K. Meyer, A. Scharmann, C. Schnorr and W. von Foerster, [2]
F.J. Ahlers, and K. Pierz [3]

[1] A. F. Ioffe Physico-Technical Institute, Russian Acad. Sciences, 194021 St. Petersburg, Russia
[2] 1. Physics Institute, University of Giessen, Heinrich-Buff-Ring 16, D 35392 Giessen, Germany
[3] Physikalische-Technische Bundesanstalt, Braunschweig, Germany

One of the most important problems connected with the growth of quantum wells (QW) and superlattices (SL) is the structural disorder on the atomic scale which occurs at the interfaces and determines to a large extent optical and electrical properties of the grown structures. The characterization of interface quality is important in order to obtain information needed for the optimization of growth processes and device performance. Since pattern sizes are atomic ones, the geometry must be controlled down to the sub-monolayer level.

For a long time the principal tool for investigations of interfacial perfection has been photoluminescence which uses confined excitons as local probes for the interface microscopic structure [1]. Optically detected magnetic resonance (ODMR) and exciton level-anticrossings (LAC) can provide more detailed information on the excitons. g-factors and exchange splittings in both type II and type I GaAs/AlAs SL have been measured with high accuracy (see [2,3] and references therein). It was shown that ODMR and LAC can be applied for characterization of the SL period and the QW width [4]. On the basis of LAC and ODMR studies the order of the exciton radiative levels in type II SL was directly linked to the interface at which the exciton is localized [5]. This made possible separate investigations of the opposite interfaces [6]. In type I SL in which the exciton radiative lifetime is too short to use ODMR exciton exchange splitting was measured from LAC [3,7].

In the present paper we report results of a LAC and ODMR study which demonstrated different composition profiles of the opposite interfaces and allowed to reveal the preferential orientation of lateral interface islands in GaAs/AlAs QW and SL.

In type Ii GaAs/AlAs SL in which the electron and the hole are spatially separated in the adjacent AlAs and GaAs layers the four energy levels of heavy-hole excitons are split due to low local symmetry of the interfaces. The order of radiative levels is reversed for the opposite interfaces. As it was shown by LAC and ODMR in [5] the lowest radiative level emits light polarized along [110] for excitons localized at the normal (AlAs on GaAs) interface and along $[1\bar{1}0]$ for excitons localized at an inverted (GaAs on AlAs) interface. Fig.1a shows LAC spectra and the exciton energy level schemes in a SL 18.6 Å GaAs/ 23.2 Å AlAs grown without interruptions with the substrate kept at 600°C. LAC was recorded within the high-energy part of

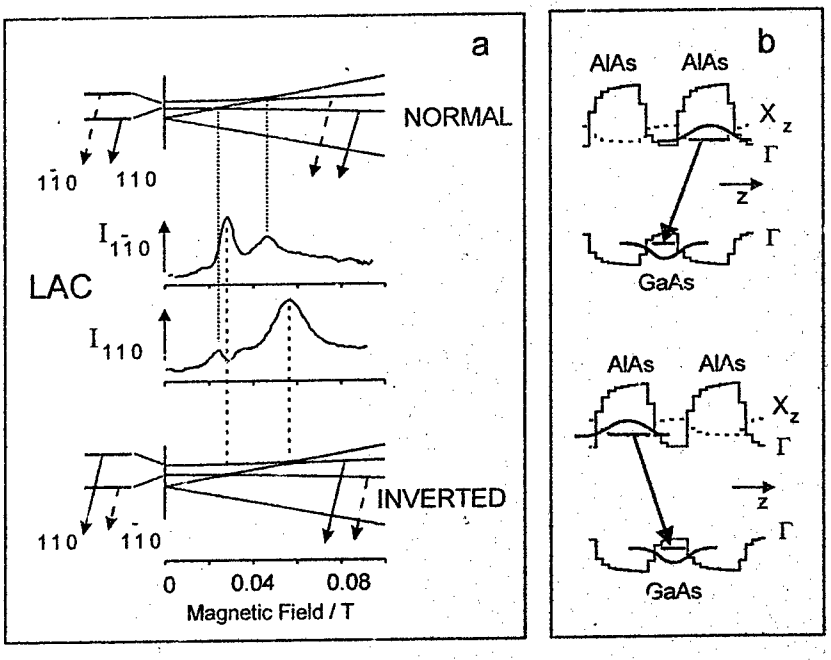

Fig.1 a) Energy levels and level anticrossing spectra of excitons localized at the normal and inverted interface in type II GaAs/AlAs SL: b) Band structure and recombination at opposite interfaces in type II SL calculated with the interface composition profiles from [8].

the luminescence line by monitoring the [110] and [$1\bar{1}0$] components of emission with magnetic field along the SL growth direction [001]. As shown in the figure two sets of LAC signals belong to excitons localized at the normal and inverted interfaces and differ in the exchange splitting: excitons at the inverted interface have approximately 20% larger splitting. This is also confirmed by ODMR spectra.

The observed difference of the exchange splittings can be explained by different composition profiles of the opposite interfaces. Numerous studies have shown that the interfaces in GaAs/AlAs SL are never abrupt and are not symmetrical due to different surface segregation rates of Ga and Al [8]. Using the envelope-function method (program ECA4) [9] we have calculated the electron and hole wavefunctions in a SL with the same GaAs and AlAs widths and the composition profile deduced from surface chemical analysis for GaAs/AlAs structures grown at 600 °C [8]. The calculated SL band alignment is shown in Fig.1b. To obtain exciton localization at one type of interface, two model SL with a period consisting from four layers having different widths and different sequence were constructed similar to Ref. 5. Calculations

showed that the ratio of the exchange splittings of excitons localized at the normal and inverted interfaces is in very good agreement with the measured one. This confirms the validity of the interface composition profile [8] which follows from the surface segregation model.

Relative amplitudes of LAC signals can be considered as a measure of relative concentrations of excitons localized at the opposite interfaces. From LAC spectra shown in Fig.1a we can conclude that in this type II SL grown without interruptions with the substrate temperature 600 °C there is approximately 2.5 times more excitons localized at the inverted interface than at the normal one. The ratio of the LAC signals of excitons localized at the opposite interfaces changes with the growth interruptions and can be also used for characterization of the interface roughness.

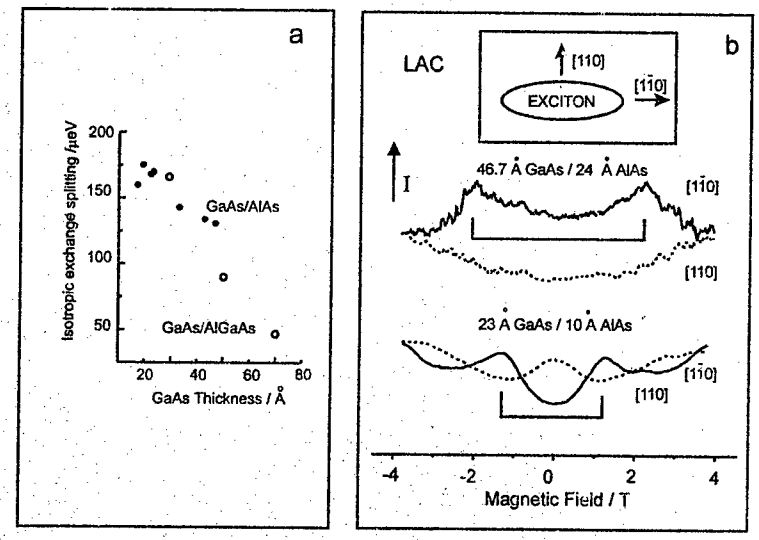

Fig.2 a) Isotropic exchange splitting in type I GaAs/AlAs SL (black circles) and GaAs/$Al_{0.3}$ $Ga_{0.7}$ As QW (open circles); b) Exciton LAC in two different type I SL recorded by monitoring linearly polarized emission

Application of LAC spectroscopy to type I GaAs/AlAs SL and GaAs/$Al_{0.3}Ga_{0.7}As$ QW allowed to measure the exciton isotropic exchange splitting which is much larger than in type II SL and varies with the GaAs thickness as shown in Fig.2a. The splitting of radiative levels in type I structures was believed to be absent because of axial symmetry of the excitons. However, measurements of LAC by monitoring linear polarization of emission revealed the existence of a splitting between radiative levels. Fig.2b shows LAC recorded in two type I GaAs/AlAs SL by monitoring [110] and [1$\bar{1}$0] components of emission. LAC signals are seen in [1$\bar{1}$0] polarization

which proves that the exciton radiative levels are split apart, the lowest level being polarized along $[1\bar{1}0]$.

Recently it was theoretically shown that the anisotropic localization potential leads to a splitting of radiative levels of localized excitons [10]. The polarization of the split sublevels is determined by the shape of the exciton envelope function and the lowest state is polarized along the longer axis of the function. Thus we can conclude that the exciton envelope functions in type I SL under study are elongated along $[1\bar{1}0]$ (see inset in Fig.2b) due to $[1\bar{1}0]$ oriented interface defects. This is in agreement with the studies of the interface morphology with the use of scanning tunneling microscopy (STM) in GaAs/AlAs structures grown under similar conditions. STM studies of GaAs surface showed that islands and monolayer step holes are greatly elongated along $[1\bar{1}0]$ direction [11]. The preferential orientation of interface islands along $[1\bar{1}0]$ was also demonstrated in a recent high-resolution optical investigation of single quantum dots[12]. Studies of LAC allow to observe such an orientation via broad luminescence lines of SL.

In conclusion, LAC measurements in linearly polarized light allowed to prove different composition profiles of normal and inverted interfaces in type II GaAs/AlAs SL and to reveal an anisotropy of the interfaces and the preferential orientation of interface islands along $[1\bar{1}0]$ in type I GaAs/AlAs SL.

We are indebted to B.P.Zakharchenya and E.L.Ivchenko for fruitful discussions. This work was supported in part by the Volkswagen foundation under grant No. I/70958 and the Russian Foundation for Basic Research under grant No. 96-02-16927.

References

1. M.A. Herman, D. Bimberg, and J. Christen, *J. Appl. Phys.* **70**, R1 (1991).
2. Solid State Commun. **87**, 649 (1993).
3. P.G. Baranov and N.G.Romanov in: *The Physics of Semiconductors ed. J.Lockwood* (World Scientific, 1994) v. 2, p.1400.
4. P.G.Baranov, N.G.Romanov, I.V.Mashkov, G.B.Khitrova, H.M.Gibbs and O.Lunges, *Phys. Solid State* **37**, 1648 (1995)
5. P.G.Baranov, I.V. Mashkov, N.G.Romanov, C.Gourdon, P.Lavallard and R.Planel, *JETP Letters* **60**, 445(1994).
6. P.G.Baranov, N.G.Romanov, A.Hofstaetter, A. Scharmann, C. Schnorr, F.J. Ahlers, and K.Pierz , *JETP Letter* **64**, 754 (1996).
7. N.G.Romanov, P.G. Baranov, I.V. Mashkov, P. Lavallard and R.Planel, *Solid State Electronics* **37**, 911 (1994).
8. R. Teissier, *Thèse de Doctorat de l'Université Paris YI*, Paris 1992.
9. J.M.Moison, C.Gilles, F.Houzay, F.Barthe, and M. Van Rompay, *Phys. Rev.* **B40**, 6149 (1989).
10. S.V. Goupalov, E.L. Ivchenko and A.V. Kavokin, 9th Int. Conf. on Superlattices, Microstructures and Microdevices, Liege 1996, Abstr., p. MoPPT-14.
11. J.Sudjiono, M.D.Johnson, C.W.Snyder, M-B.Elowitz, B.G.Orr, *Phys.Rev.Letters* **69**, 2811 (1992).
12. D.Gammon, E.S.Snow, B.V.Shanabrook, D.S.Kaster, and D.Park, *Phys.Rev.Letters* **76**, 3005 (1996).

A NEW APPROACH TO THE POLARITON PROBLEM IN HETEROSTRUCTURES. THE CORRECT BOUNDARY CONDITIONS AND OPTICAL REFLECTION AT AlGaAs/GaAs-HETEROJUNCTIONS

G.F. Glinskii, K.O. Kravchenko

St.Petersburg Electrotechnical University
Prof. Popov str. 5, St.Petersburg, 197376 Russia
Fax: (812)-234-3164, E-mail: root@me.etu.spb.ru

The optical reflection under normal and angular incidence from AlGaAs/GaAs heterojunction near exciton resonance of GaAs has been investigated. The problem has been solved in terms of 11×11 matrix equation for polariton envelope functions, which was derived from the quantum field microscopic theory. The equation includes a $\Gamma_6 \otimes \Gamma_8$-exciton block, a Γ_{15}-photon block (Maxwell equations) and an exciton-photon interaction operator. The effective mass approximation has been used with the correct boundary conditions taking into account δ-corrections, that mix the polariton states at the interface.

1. INTRODUCTION

The effects of exciton-photon mixing (polariton effects) have a considerable influence on the reflection spectra near the exciton resonance. Usually these effects are taken into account by introduction of non-analytical long-range electron-hole interaction, which leads to a longitudinal transverse exciton splitting. Following solving of the Maxwell equations for the transverse field and taking into account the dielectric constant $\varepsilon(\omega,k)$ gives the polariton dispersion branches. In the present paper we use a general equation for the exciton-photon system, which is obtained by quantum field microscopic theory [1-3].

To calculate the reflection spectra one must know the boundary conditions for exciton and photon wave functions. The problem of correct boundary conditions at heterojunctions was being widely discussed recently. The so called "symmetrized" boundary conditions which are commonly used can not be considered correct. Therefore the boundary conditions we obtained are based on the exciton-photon equation for the heterosystem and the interface symmetry (fig. 1).

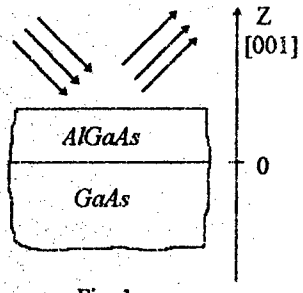

Fig. 1

2. POLARITON EQUATION

According to [1-3] an equation describing the interaction between exciton and photon can be represent in terms of the Green's function. Within the effective mass approximation in

A^3B^5 semiconductors when the main exciton states $\Gamma_6 \otimes \Gamma_8$ are decomposed by the short range exchange interaction into irreducible $\Gamma_{15} \oplus \Gamma_{12} \oplus \Gamma_{25}$ states the polariton equation has the following form:

$$\begin{array}{c|ccc|c} & \Gamma_{15} & \Gamma_{12} & \Gamma_{25} & \Gamma_{15} \\ \hline \Gamma_{15} & & & & \\ \Gamma_{12} & & K^{-1} & & \Gamma \\ \Gamma_{25} & & & & \\ \hline \Gamma_{15} & & \Gamma & & D^{-1} \end{array} \cdot \begin{array}{|c|} \hline \Phi \\ \hline A \\ \hline \end{array} = 0, \qquad (1)$$

where $K^{-1} = \hbar\omega - H_{ex}$ is the inverse exciton Green's function, H_{ex} is 8×8-exciton Hamiltonian, D^{-1} is the inverse photon Green's function, Γ is the exciton-photon coupling matrix operator, Φ is an exciton wave function, A is an electromagnetic field vector potential.

In contrast to the exciton in a homogeneous semiconductor the exciton Hamiltonian H_{ex} which takes into account a heterointerface is no longer determined by the three like Luttinger's parameters. It can be shown that it is to be described by four constant determining a $k \cdot p$-interaction of Γ_{15} hole states with Γ_1, Γ_{12}, Γ_{15}, Γ_{25} bands. The Hamiltonian also includes constant and $k \cdot p$-dependent electron and hole interface $\delta(z)$-corrections, which can be obtained by the perturbation theory. The corrections describe a short range interface influence and lead to a mixing of the exciton states at the interface. The results obtained in the present work are in agreement with ones of Burt [4], Foreman [5] and Ivchenko [6].

D^{-1} is modified by background dielectric constant inverse photon Green's function which corresponds to the Maxwell equations taking into account the short range $\delta(z)$-interface corrections similar to the ones for the exciton.

3. BOUNDARY CONDITIONS AND OPTICAL REFLECTANCE

The polariton wave functions boundary conditions can be obtained from the Hamiltonian using its Hermiticity (the current conservation). The Green's operator (1), which we obtained by the $k \cdot p$-theory, takes into account non-commutativity of the position dependent band parameters and the momentum operator. It helps to avoid an ambiguity for boundary conditions and therefore any symmetrization becomes unnecessary. As an example the Γ_{15} hole envelope function boundary conditions for (001) heterointerface when we neglect interaction with other states have the following form for $z = 0$ interface (fig. 1):

$$\bar{\psi}(+0) = \bar{\psi}(-0),$$

$$\left(\hat{J}_z \bar{\psi}\right)\Big|_{z=+0} - \left(\hat{J}_z \bar{\psi}\right)\Big|_{z=-0} = A_z \bar{\psi}(0),$$

where

$$\hat{J}_z = \begin{bmatrix} (-1+\beta_3+\beta_4)\frac{1}{i}\frac{\partial}{\partial z} & 0 & (\beta_3-\beta_4)k_x \\ 0 & (-1+\beta_3+\beta_4)\frac{1}{i}\frac{\partial}{\partial z} & (\beta_3-\beta_4)k_y \\ (\beta_1-2\beta_2)k_x & (\beta_1-2\beta_2)k_y & (-1+\beta_1+4\beta_2)\frac{1}{i}\frac{\partial}{\partial z} \end{bmatrix},$$

$$\hat{A}_z = \frac{i}{a_0}\begin{bmatrix} m_1-m_2 & m_3 & 0 \\ m_3 & m_1-m_2 & 0 \\ 0 & 0 & m_1+2m_2 \end{bmatrix} + \begin{bmatrix} 0 & 0 & -(n_1k_x+n_2k_y) \\ 0 & 0 & -(n_1k_y+n_2k_x) \\ n_1k_x+n_2k_y & n_1k_y+n_2k_x & 0 \end{bmatrix},$$

here

$$\beta_i(z) = \frac{2}{m}\sum_q \frac{\left|\langle \Gamma_{15}\| \hat{p} \|\alpha_i, q\rangle\right|^2}{E_q^{\alpha_i}(z) - E^{\Gamma_{15}}}, \quad (\alpha_1=\Gamma_1, \alpha_2=\Gamma_{12}, \alpha_3=\Gamma_{15}, \alpha_4=\Gamma_{25}),$$

m_i and n_i are parameters describing short range $\delta(z)$ interface corrections, m_3 determines the heavy-light hole and exciton mixing at the interface even under normal incidence,
a_0 is the lattice constant.

Using the equation (1) and the boundary conditions we numerically calculated the optical reflectivity spectra for AlGaAs/GaAs heterojunction (fig. 1) under normal and angular incidence.

4. ACKNOLEDGEMENTS

The authors are grateful to E. Ivchenko for a valuable discussions of boundary conditions.

REFERENCES

[1] Z.G. Koinov and G.F. Glinskii, J. Phys. A 21, 3431 (1988).
[2] G.F. Glinskii and Z.G. Koinov, Phys. Stat. Sol. (b) 155, 501 (1989).
[3] Z.G. Koinov and G.F. Glinskii, Phys. Stat. Sol. (b) 155, 513 (1989).
[4] M.G. Burt, J. Phys. Condens. Matter 4, 6651 (1992).
[5] B.A. Foreman, Phys. Rev. B 48, 4964 (1993).
[6] E.L. Ivchenko, A.Yu. Kaminski, U. Rössler, Phys. Rev. B 54, 5852, (1996).

Hopping relaxation of localized excitons in quantum wells studied by time-resolved photoluminescence spectroscopy

L.E. Golub, S.V. Ivanov, E.L. Ivchenko, A.A. Kiselev,
T.V. Shubina, A.A. Toropov
A.F. Ioffe Physico-Technical Institute, 194021 St. Petersburg, Russia
J.P. Bergman, G.R. Pozina, B. Monemar
University of Linköping, S-581 83 Linköping, Sweden
and
M. Willander
University of Gothenburg/Chalmers University
S-412 96 Gothenburg, Sweden

In [1] we have developed a theory of low-temperature energy relaxation of localized excitons and calculated photoluminescence (PL) spectra under steady-state and short-pulse optical excitation in semiconductor quantum wells (QW's). In the simplest model, we assumed

$$w(\varepsilon,\varepsilon',r)=\omega_0 e^{-2r/a}\,\theta(\varepsilon-\varepsilon')\,,\qquad g(\varepsilon)=g_0 e^{-\varepsilon/\varepsilon_0}\,, \tag{1}$$

where ε is the exciton localization energy, $w(\varepsilon,\varepsilon',r)$ is the exciton transfer rate for the $\varepsilon\to\varepsilon'$ transition between the sites separated by the distance r, $\theta(x)$ is the Heaviside function, $g(\varepsilon)$ is the density of localized states; $\omega_0, a, g_0, \varepsilon_0$ are constant parameters. The recombinati n lifetime τ_0 was also assumed to be a constant. In the time-resolved PL spectra excited by a short pulse, the red shift of the spectral peak, $\hbar\omega_m$, with increasing the time delay, t, is described by

$$\hbar\omega_m(t)=\hbar\omega_m^{st}+\varepsilon_0\left(2\ln\frac{\ln\omega_0\tau_0}{\ln\omega_0 t}-\alpha\right), \tag{2}$$

where $\hbar\omega_m^{st}$ is the PL peak position under steady-state excitation and $\alpha\approx 0.08$.

In the present work we apply the theory for the description of real experimental data. The samples studied were $Zn_{1-x}Cd_xSe/ZnSe$ QW heterostructures grown by molecular-beam

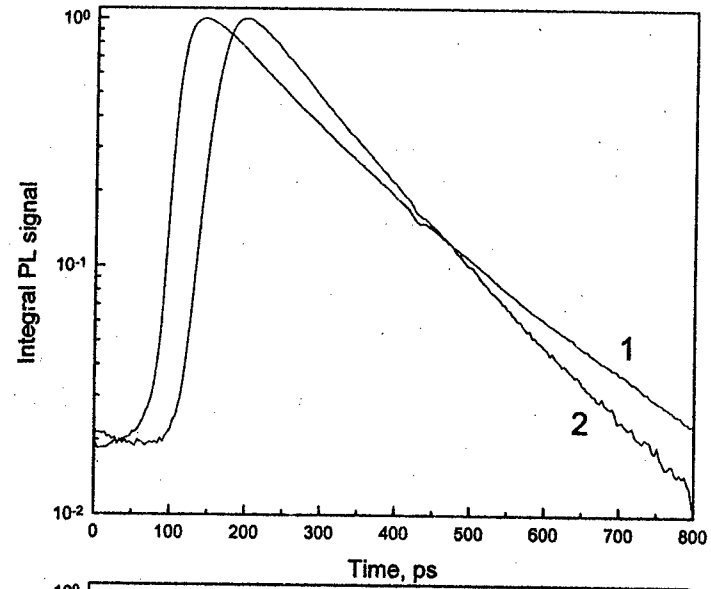
Integral PL signal
10⁰
10⁻¹
10⁻²
0
100
200
300
400
500
600
700
800
Time, ps
1
2

Fig. 1

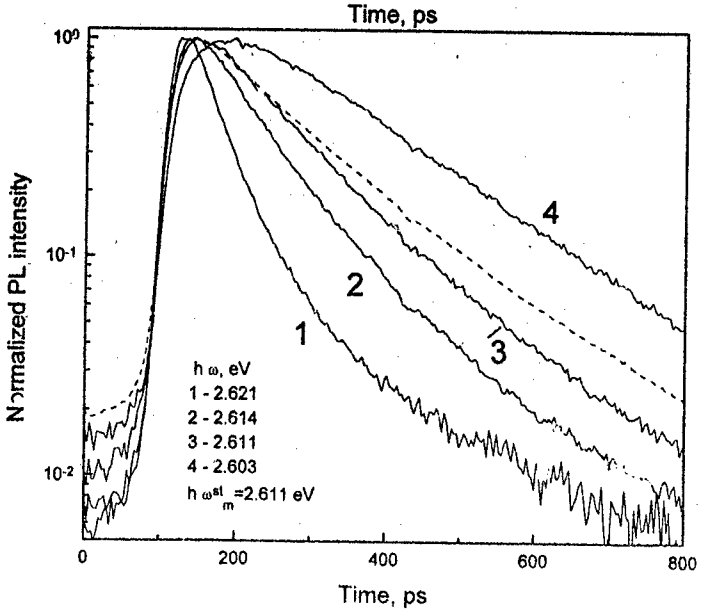
Normalized PL intensity
10⁰
10⁻¹
10⁻²
0
200
400
600
800
Time, ps
1
2
3
4
h ω, eV
1 - 2.621
2 - 2.614
3 - 2.611
4 - 2.603
h ω^st_m =2.611 eV

Fig. 2

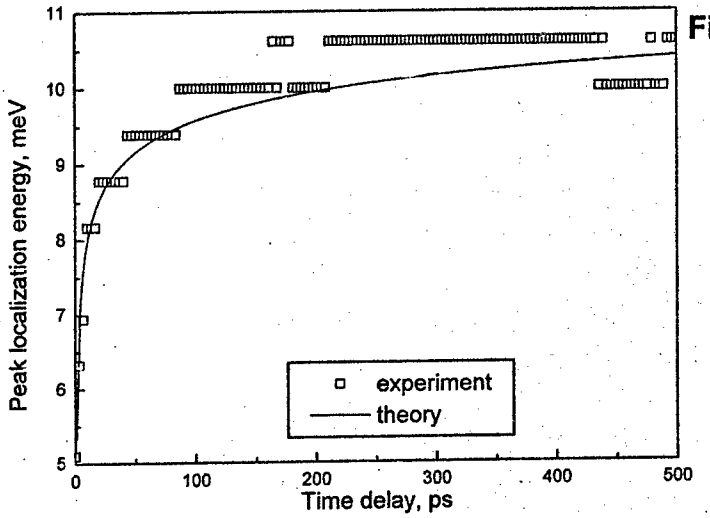
Peak localization energy, meV
Time delay, ps
experiment
theory

Fig. 3

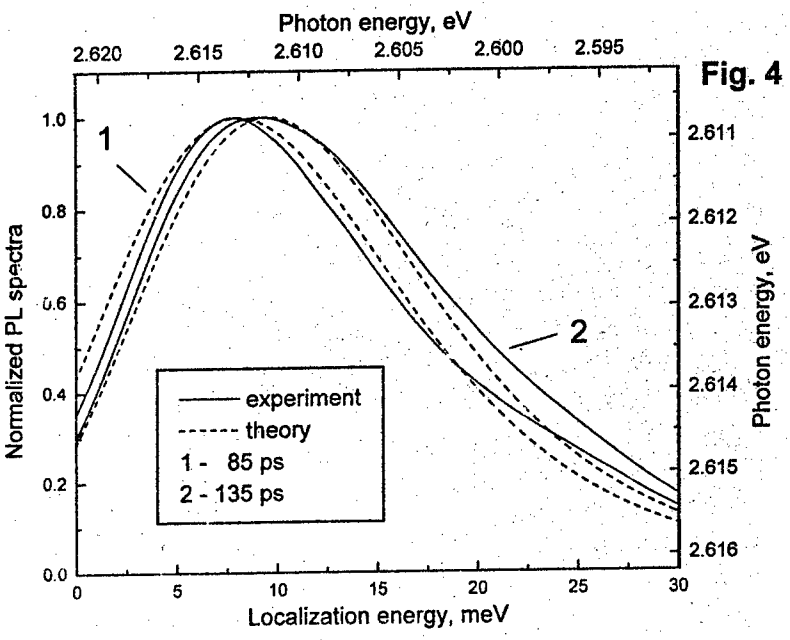
Photon energy, eV
Normalized PL spectra
Photon energy, eV
Localization energy, meV
1
2
experiment
theory
1 - 85 ps
2 - 135 ps

Fig. 4

epitaxy on (001) GaAs substrates. The structures comprised five ZnCdSe QW's of different widths ranging from 20 Å to 100 Å. The picosecond time-resolved PL measurements were performed with the samples placed in a pumped bath cryostat (T = 2 K). The double-frequency mode-locked tunable titanium sapphire laser was used as a radiation source with the pulse duration of 10 ps. The PL spectra were detected by a Hamamatsu synchroscan streak camera with a resolution not worth than 20 ps.

Fig. 1 shows the integral PL intensity, $\int I(\hbar\omega, t)\, d\hbar\omega$, as a function of time referred to an arbitrary origin. Curves 1 and 2 were measured respectively on 20-Å $Zn_{.8}Cd_{.2}Se$/ZnSe and 20-Å $Zn_{.88}Cd_{.12}Se$/ZnSe QW's. One can see that in the both cases the integral PL decay is monoexponential with the lifetime $\tau_0 = 400$ ps (curve 1) and 270 ps (curve 2). In Fig. 2 we show the time-dependent spectral intensity $I(\hbar\omega, t)$ measured at four different energies $\hbar\omega$ for the $Zn_{.8}Cd_{.2}Se$/ZnSe QW, the dashed curve coincides with curve 1 in Fig. 1, $\hbar\omega_m^{st} = 2.611$ eV is the peak position for the steady-state PL. The time dependence of $I(\hbar\omega)$ at higher energies is essentially non-exponential and demonstrates that, for excitons with small values of localization energy, the acoustic-phonon-assisted hopping prevails over the recombination.

The temporal shift of the PL peak is shown in Fig. 3. The solid curve is calculated by Eq. (1), for $\omega_0 = 10^{13}$ s^{-1} the best fit is obtained for $\varepsilon_0 = 2$ meV. The theoretical and experimental PL spectra for the time delays 85 ps and 135 ps are presented in Fig. 4. A good agreement between the shapes of solid and dashed curves confirms the above value of ε_0. Taking a value of $\varepsilon_m^{st} = 10$ meV for the Stokes shift between the PL and PLE peaks we find $N\pi(a/2)^2 = 1.4$, where $N = g_0\varepsilon_0$ is the total density of localized states.

Thus, the presented set of experimental data can be effectively described by the kinetic theory [1]. Note that previously only the temporal shift of the PL peak (in CdTe/ZnTe QW's) was used for comparison with theory [2].

Financial support of this work was provided by the Russian Foundation for Fundamental Research (code 96-02-17849) and by the Volkswagen Foundation.

References

[1] L.E. Golub, E.L. Ivchenko, A.A. Kiselev, Proc. Int. Symp. 'Nanostructures: Physics and Technology', St. Petersburg 1995, p. 114; J. Opt. Soc. Am. B **13**, 1199 (1996).

[2] H. Kalt, J. Kollet, S.D. Baranovskii, R. Saleh, P. Thomas, Le Si Dang, J. Cibert, Phys. Rev. B **45**, 4253 (1992).

Excited States of Localized Excitons in Quantum Well Structures: Long-Range Exchange Splitting

S.V. Goupalov, E.L. Ivchenko and A.V. Kavokin
A.F.Ioffe Physico-Technical Institute, Russian Academy of Sciences, 194021 St.Petersburg, Russia

In semiconductors the exchange interaction between an electron and a hole consists of the short-range and long-range terms [1]. The latter can be as well considered as arising due to the macroscopic electric field induced by the pair excitation. For the heavy-hole exciton in a GaAs/$Al_xGa_{1-x}As$(001) QW structure the short-range exchange interaction splits the fourfold degenerate level $e1$-$hh1(1s)$ into a radiative doublet with the angular momentum component $m = \pm 1$ and two close-lying nonradiative singlets. If such an exciton is localized at an anisotropic island of well width fluctuation the doublet is split by the long-range exchange into two linearly-polarized sublevels [2]: $|x\rangle = \left(|1\rangle + e^{i\phi}|{-1}\rangle\right)/\sqrt{2}$, $|y\rangle = -i\left(|1\rangle - e^{i\phi}|{-1}\rangle\right)/\sqrt{2}$, where the axes x and y (or the phase ϕ) are determined by the island shape. Recently Gammon et al. [3] have observed such splittings in photoluminescence spectra from single islands. They also measured photoluminescence excitation (PLE) spectra in the same optical near-field regime and found that the localized-exciton excited levels revealed a doublet structure with the doublet components polarized along the in-plane [110] and [1$\bar{1}$0] directions. For the ground and four excited states, the splitting $\Delta = E_{1\bar{1}0} - E_{110}$ varied as -25, $+41$, $+45$, -22 and -47 μeV respectively. In the present work we have calculated values of Δ for the excited states of an exciton localized by a rectangular island of the well-width monolayer fluctuation. The exciton envelope function is approximated by

$$\Psi(\mathbf{r}_e, \mathbf{r}_h) = F(X,Y)\,\varphi_{1s}(\rho)\,\varphi_{e1}(z_e)\,\varphi_{hh1}(z_h). \qquad (1)$$

Here $\varphi_{e1}(z_e)$, $\varphi_{hh1}(z_h)$ describe the electron and heavy hole size quantization, $\varphi_{1s}(\rho)$ is the in-plane relative motion envelope function ($\vec{\rho} = \vec{\rho}_e - \vec{\rho}_h$), and $F(X,Y)$ is the in-plane center-of-mass envelope. The splitting between the $|x\rangle$ and $|y\rangle$ states is given by

$$\Delta \equiv E_x - E_y = \frac{\hbar\Gamma_0}{S}\sum_{q>k}\frac{q_x^2 - q_y^2}{k\sqrt{q^2-k^2}}\,f^2(\mathbf{q})\,, \qquad (2)$$

where x, y are the axes of the rectangular island, $f(\mathbf{q}) = \int d\mathbf{R}\, e^{-i\mathbf{qR}}\, F(X,Y)$, S is the sample area, $k = (\omega/c)\sqrt{\varepsilon_b}$, ε_b is the dielectric constant, Γ_0 is the radiative damping rate for a free exciton in the perfect QW. The function $F(X,Y)$ was found as a solution of the two-dimensional Schrödinger equation

$$\left[-\frac{\hbar^2}{2M}\left(\frac{\partial^2}{\partial X^2} + \frac{\partial^2}{\partial Y^2}\right) - V\theta\left(\frac{L_x}{2} - |X|\right)\theta\left(\frac{L_y}{2} - |Y|\right)\right] F(X,Y) = -\varepsilon\, F(X,Y), \qquad (3)$$

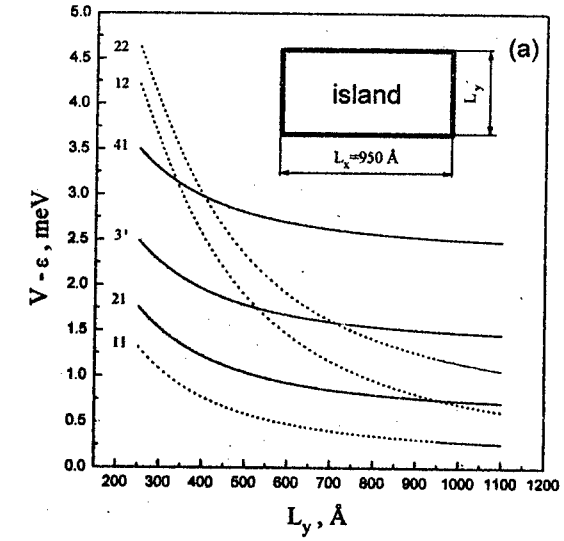
(a)
island
L_y
L_x=950 Å
22
12
41
3'
21
11
V - ε , meV
L_y , Å

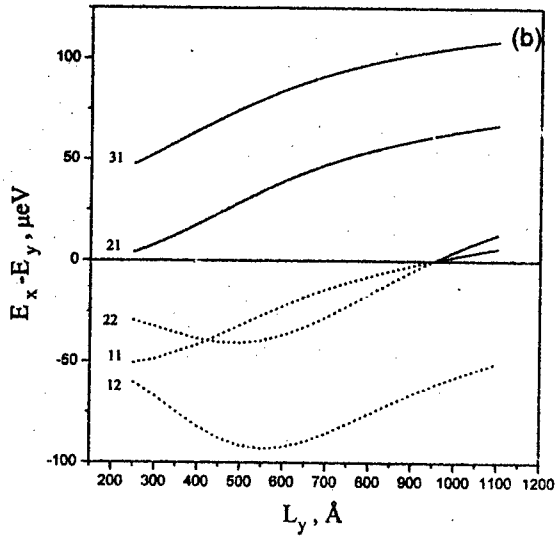
(b)
31
21
22
11
12
E_x-E_y , μeV
L_y , Å

Fig. 1

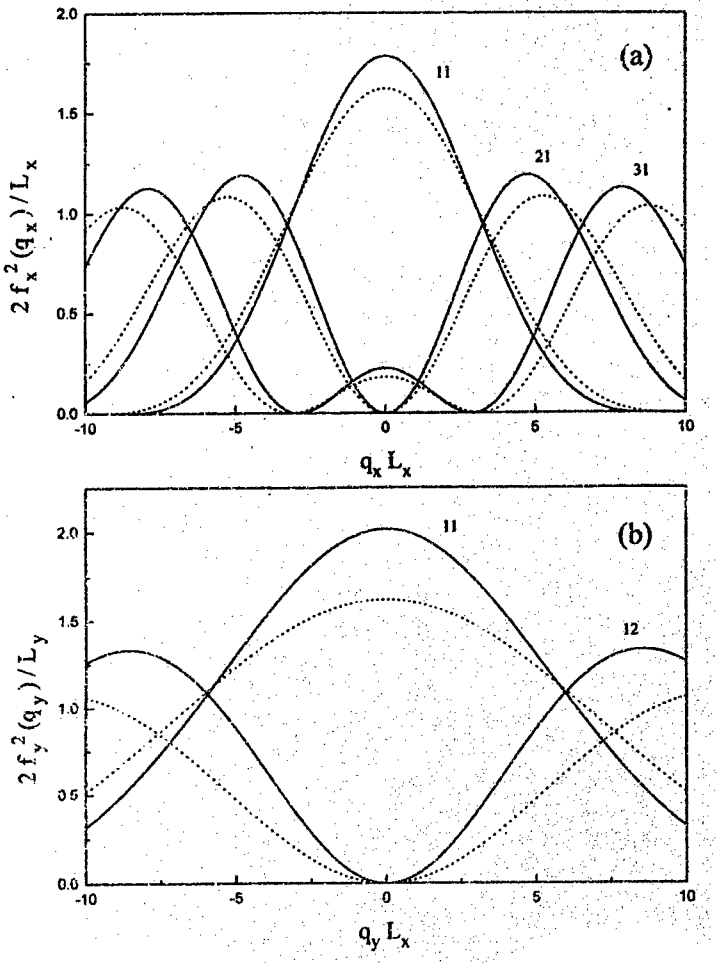

Fig. 2

where L_x, L_y determine the extensions of the rectangular island, M is the mass of translational motion of the exciton as a whole in the QW plane, V is the energy difference between the $1s$–exciton levels in the two perfect QW's differing in the width by one monomolecular layer, ε is the localization energy referred to the free-exciton energy in the wider QW, $\theta(t) = 1$ if $t > 0$ and $\theta(t) = 0$ if $t < 0$. While calculating the splitting Δ we used the approximation of the factorized envelope function [4] and took $F(X, Y)$ as a product $F_x(X)\, F_y(Y)$, where $F_x(X)$, $F_y(Y)$ are found self-consistently from Eq.(3). The localized states $|lj\rangle$ are labelled by two integer quantum numbers, e.g. 11, 21, 22 etc., describing the exciton in-plane confinement in the x and y directions.

Fig. 1 gives (a) the energy of the localized exciton and (b) the splitting Δ as a function of L_y for a fixed value of $L_x = 950$ Å and for a 28-Å GaAs/AlGaAs QW. The difference $V - \varepsilon$ is the localized-exciton energy referred to the free exciton energy in the wider QW. The parts of curves in Fig.1 corresponding to negative and positive values of $\Delta = E_x - E_y$ are shown by dashed and solid lines respectively. The sequence of signs for the splittings of the ground and excited levels observed in [3] is reproduced in Fig. 1 for values of L_y lying between 450 Å and 500 Å. One can see from Eq.(2) that the sign of Δ is determined by the shapes of $F_x(X)$ and $F_y(Y)$, in particular by the difference of the averaged values $\langle q_x^2 \rangle$ and $\langle q_y^2 \rangle$. Fig. 2 demonstrates Fourier transforms, $f_x(q_x)$, $f_y(q_y)$, of these functions for the 11, 21, 31, 12 states (solid curves, $L_y = 450$ Å). Dashed curves are Fourier components of these functions calculated in the approximation of infinite barriers ($V \to \infty$). Note that the solid and dashed curves in Fig. 2*a* are very close to each other while in Fig. 2*b* they deviate remarkably. It should be mentioned that, for ideal rectangular shape of the island, the localized-exciton states $|lj\rangle$ with even l or/and j are forbidden and they can be observed in PLE spectra only due to the shape distortion. The alternative explanation of the experiment [3] can be based on the assumption that the observed excited states are the ground states of excitons localized by different rectangular islands which are located close to each other. In this case the oscillator strengths for the ground and excited exciton states should be comparable. Moreover, the islands should be elongated along both the [110] and [1$\bar{1}$0] axes in order to obtain the varying signs of Δ. However, a scanning tunneling microscope image of a growth-interrupted GaAs surface shows [3] that the one-monolayer-high islands are aligned along only one axis [1$\bar{1}$0].

We acknowledge partial support by the Russian Foundation of Fundamental Research (code 95-02-06038) and the Volkswagen Foundation grant.

[1] G.E. Pikus and G.L. Bir, *Zh. Eksp. Teor. Fiz.* **60**, 195 (1971); **62**, 324 (1972)

[2] S.V. Goupalov, E.L. Ivchenko, and A.V. Kavokin, Proc. Int. Symp. 'Nanostructures: Physics and Technology', St. Petersburg 1996, p. 322; Abstract Workbook of ICSMM-9, Liege, Belgium, 1996, p. MoPPT-14.

[3] D. Gammon, E.S. Snow, B.V. Shanabrook, D.S. Katzer, and D. Park, *Phys. Rev. Lett.* **76**, 3005 (1996).

[4] G. Bastard and J.Y. Marzin, *Solid State Commun.* **91**, 39 (1994).

COHERENT CONTROL OF EXCITON SPIN IN QUANTUM WELLS

P. Le Jeune, X. Marie, T. Amand, M. Paillard, F. Romstad, J. Barrau, M. Brousseau
Laboratoire de Physique de la Matière Condensée, INSA-CNRS,
Complexe Scientifique de Rangueil, 31077 Toulouse cedex 4 (FRANCE)

We present a method to measure the optical dephasing time of excitons in semiconductor quantum wells by time-resolved Photoluminescence (PL) spectroscopy.

A sequence of two 1.2 ps optical pulses split from the same Ti:Sa laser source, right (σ^+) and left (σ^-) polarized, excite the heavy hole excitons (XH) resonantly in a very high quality GaAs/AlAs Multiple Quantum Well structure (L_W= 10 nm) at T=10 K. This excitation pulse sequence is produced by a Mach-Zender type interferometer which can control the pulse separation on two different time-scales : a coarse tuning allows to set the time delay (t_1) between the two pulses on a picosecond time scale; a fine tuning (t_2), on a femtosecond time scale, allows to control very accurately their relative phase around t_1. For instance, when the two excitation pulses overlap in time ($t_1 = 0$), interference effects will create linearly polarized light : if $t_2 = n.\frac{\lambda}{c}$ ($(n+\frac{1}{2}).\frac{\lambda}{c}$), n integer, the linear light polarization $P_E = \frac{\Sigma^X - \Sigma^Y}{\Sigma^X + \Sigma^Y}$ will be equal to 1 (-1) ; Σ^X and Σ^Y denote the intensities of the X and Y linear polarisation components of the excitation light. The XH exciton states are described, as usual, using the basis set $|J_z\rangle = |S_z + J_{hz}\rangle$, with the electron spin state $S_z = \pm 1/2$, and the heavy hole total angular momentum projection $J_{hz} = \pm 3/2$ (the growth axis Oz is chosen as the quantization axis). The σ^+ and σ^- pulses creates then $|J_z = +1\rangle$ and $|J_z = -1\rangle$ excitons respectively. Light polarized linearly in the X or Y direction creates a coherent superposition of $|+1\rangle$ and $|-1\rangle$ states called linear excitons which are labeled $|X\rangle$ and $|Y\rangle$, with $|X\rangle = \frac{|+1\rangle + |-1\rangle}{\sqrt{2}}$ and $|Y\rangle = \frac{|+1\rangle - |-1\rangle}{i\sqrt{2}}$

The time-resolved exciton PL is recorded by up-converting the PL signal in a $LiIO_3$ non-linear crystal with the beam generated by a synchronously-pumped optical parametric oscillator. The linear polarization $P_L = \frac{I^X - I^Y}{I^X + I^Y}$ of the exciton luminescence is recorded systematically 4 ps after the second excitation pulse to avoid any back-scattered light from the sample surface (I^X and I^Y denote the intensities of the X and Y linear polarization components of the luminescence).

We performed first the experiment with t_1=0. Figure (1a) shows the exciton linear polarization (P_L) as a function of the fine tuning t_2. In this case, the exciton polarization oscillations merely reflect the excitation light polarization, as the linearly polarized excitation light creates directly linear exciton states $|\psi_\varphi\rangle = \cos\left(\frac{\varphi}{2}\right)|X\rangle + \sin\left(\frac{\varphi}{2}\right)|Y\rangle$, with $\varphi = \frac{2\pi c}{\lambda} t_2$.

Figure (1b) shows the result of the experiment with t_1 = 6.66 ps. In that case, there is no time overlap between the two pulses. As can be seen the linear polarization oscillations, though attenuated, are still present. They originate from the interaction of the second pulse with the coherent excitons created by the first pulse. The first pulse, σ^+–polarized, creates $|+1\rangle$ excitons which give rise to a macroscopic polarization coherent with the external field. The second pulse, σ^-–polarised, will again create $|\psi_\varphi\rangle$ exciton states if the coherent macroscopic polarization created by the first pulse is not lost.

Figure (2) displays the minima and maxima of the linear polarization oscillations as a function of t_1. The decay reflects then directly the exciton decoherence, usualy characterized by the optical dephasing time T_2. We checked that, as expected, no linear polarization can be measured at any time delay when the sample is excited by the first pulse or by the second pulse independently.

We alto performed the same kind of experiment with a sequence of two linearly polarized excitation pulses. When they are cross-polarized, the exciton spin interferences result in circularly polarized luminescence for $t_1 < T_2$. When they are co-polarized, constructive or destructive coherent exciton interferences modulate the exciton population, which leads to photo-luminescence intensity oscillations. This last configuration gives similar results as in the reflectivity coherent control experiments described in [1].

To conclude, we have presented a technique which allows the measurement of the exciton optical dephasing time in semiconductor hetero-structures by time-resolved photoluminescence spectroscopy. In contrast to the widely used non-linear techniques as Four Wave Mixing, our method relies on the linear response of the material.

Acknowledgements: We thank R. Planel and V. Thierry-Mieg for the growth of very high quality samples. Part of this work has been supported by a NATO contract. HTECH.CR4 .

[1] A.P. Heberle et al., Phys. Rev. Lett., 75, 13 (1995).

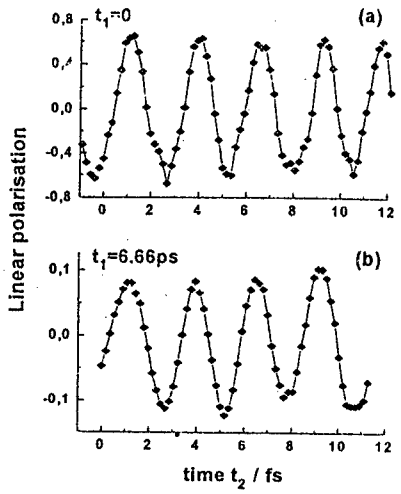

Figure 1: Linear polarisation oscillations of the XH exciton luminescence versus the dephasing between the two excitation pulses. Time delay between σ^+ and σ^- pulses: (a) t_1=0, (b) t_1=6.66 ps. The excitation photon energy is set at resonance with the XH exciton (1.568 eV).
The total incident energy density is about 20 nJ/cm^2 per pair of excitation pulses. The dots are experimental data (solid line is a guide to the eyes).

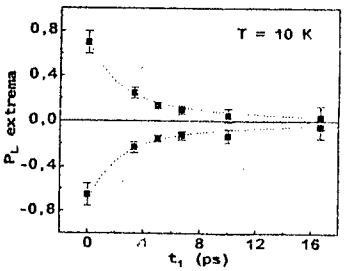

Figure 2: Decay of the linear polarisation extrema versus time delay t_1. The experimental data are shown as dots with error bars (the dashed line is a guide to the eyes).

Resonant Faraday Rotation in a Semiconductor Microcavity

A.V. Kavokin, M.R.Vladimirova, M.A.Kaliteevski,
Ioffe Physicotechnical Institute, 124021, Polytechnicheskaya, 26, St.-Petersburg, Russia
O.Lyngnes, J.D.Berger, H.M. Gibbs and G. Khitrova
Optical Sciences Center, University of Arizona, Tucson, AZ85721, USA

Faraday rotation at quantum well exciton resonances is enchenced in a microcavity due to multiple round-trips of light between mirrors when the cavity mode is strongly coupled to the exciton and is accompanied by a resonant redistrbution of signal between right - and left-circural polarizations. We observe a 3° Faraday rotation in the reflection spectrafrom an (InGa)As/GaAs quantum well micocavity in 11 Tesla magnetic field when the cavity mode is resonant with either heavy or light-hole exciton.

Although the first works on the magneto-optics of normal mode coupling in semiconductor microcavities have appeared very recently, a number of striking effects have alredy been found [1-4]. Herein we present the study of the magnetic field effect on the polarization of light propagating in semiconductor microcavity.

It is well known that plane of polarization of linearly polarized light experiences a Faraday rotation as it propagates through a semiconductor in the presence of a magnetic field. This effect is enhenced in the vicinity of an exciton resonance, and its magnitude is governed by the exciton *g*-factor and oscillator strength. The resonant Faraday rotation in transmission has been studied recently for semimagnetic quantum well (QW) system, where excitons have giant *g*-factor due to their exchange interaction with magnetic ions [5]. Detected rotation angles were of the order of tens of millidegree for a double QW system and are expected to be much less in similar nonmagnetic QW.

Our idea was to amplify the Faraday rotation effect by placing the QW in a microcavity and tuning the cavity mode onto resonance with QW excitonic transition. The rotation is strongly amplified due to multiple round-trips of light between two mirrors during the lifetime of the exciton polariton mode.

For experimental studies two identical 8 nm $In_{0.04}Ga_{0.96}As$ QWs were grown inside a $3\lambda/2$ microcavity with symmetric 99.6% reflectivity mirrors consisting of 14 and 16 ½ period GaAs/AlAs Bragg mirrors. The QW were placed ain the antinode of the intracavity field. By moving across the sample, the cavity mode could be brought into resonance with different exciton transitions. Reflection measurements were performed in Faraday geometry at T=1.8 K using superconducting magnet. Detailed information about the sample one can find in [3].

Fig. 1 shows the theoretical and experimental microcavity reflection spectra in 11.25 Tesla magnetic field detected in σ_- and σ_+ circular polarization, linear polarization and linear cross-polarization, i.e. detected in the linear polarization orthogonal to the polarization of incident light. The cavity mode is coupled to the *e1-lh1* exciton resonance which experiences the Zeeman splitting of 1.3 eV. One can see that the positions of the spectral dips are substantially different in σ_- and σ_+ circular polarization which results in the appearence of a resonant signal in the linear cross-polarization. Also is seen a series of strong dips corresponding to optically coupled bulk GaAs exciton-polariton states in the cavity and mirrors. The total thickness of GaAs layers is about

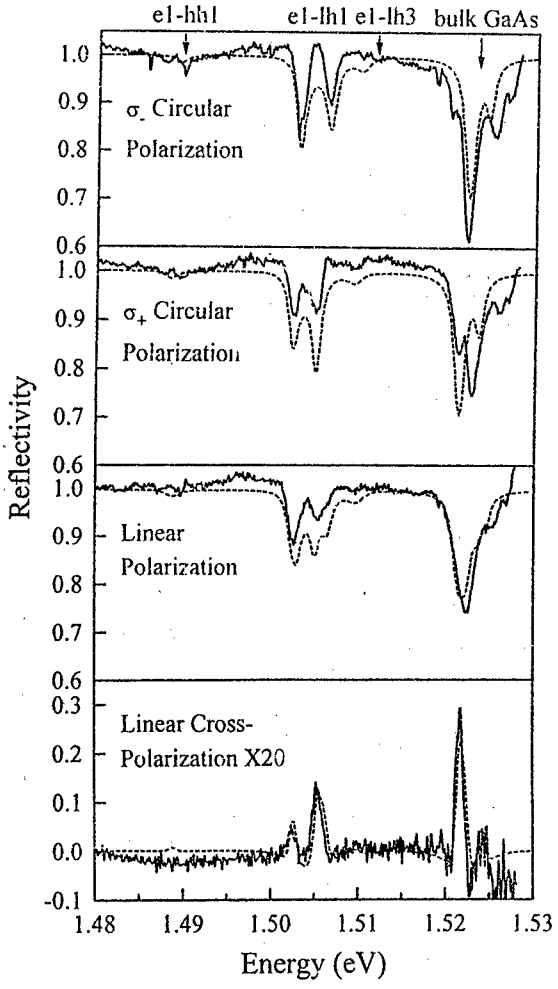

Fig.1 Measured (solid) and calculated (dashed) microcavity reflection spectra in 11.25 Tesla when the cavity mode is tuned to the *e1-lh1* exciton resonance in σ_- and σ_+ circular polarization, linear polarization, and linear cross- polarization.

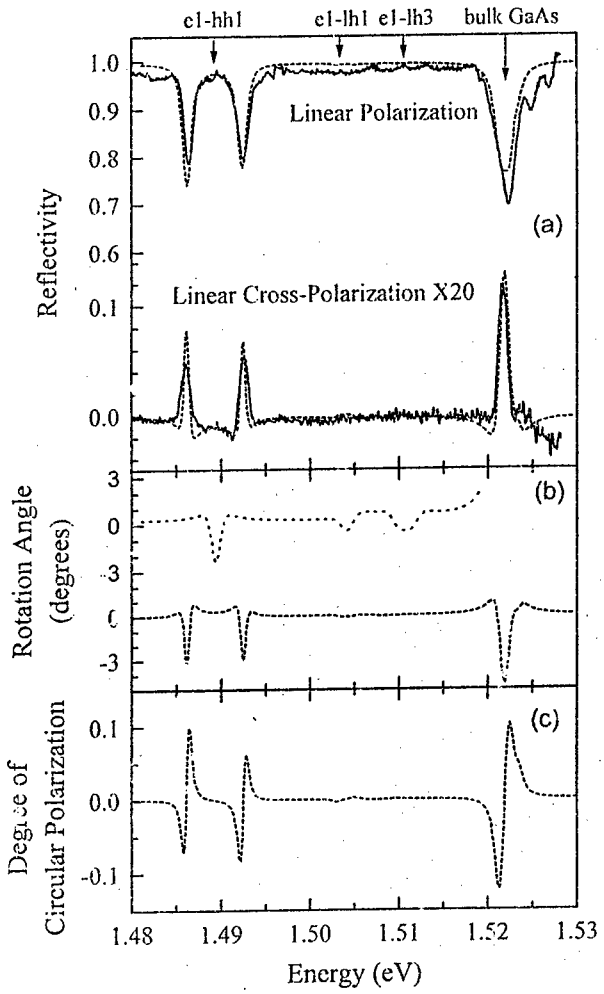

Fig.2 (a) Measured (solid) and calculated (dashed) microcavity reflection spectra in 11.25 Tesla when the cavity mode is tuned to the *e1-hh1* exciton resonance linear polarization, and linear cross- polarization. (b) Calculated Faraday rotation angle and (c) degree of circular polarization (dashed line). Dotted line in (b) shows Faraday rotation angle in transmission through central cavity layer.

2μm, whereas the total thickness of two InGaAs QW in the cavity is only 16 nm. Nevertheless, the Qws resonant signal in linear cross polarization, which is a measure of the Faraday effect has the same order as bulk exciton resonance, even though it has less than 1% of the path lelength. When we tune the cavity mode away from theQW exciton resonance, the resonant signal in the linear cross -polarization vanishes.

Although the Zeeman splitting of *e1-hh1* excitonic transition (0.6 meV) is much less the the splitting of *e1-lh1* exciton (1.3 meV) we can see substantial signal in cross-polarization when cavity mode tunned to *e1-hh1* resonance (Fig.2). This is becouse the *e1-hh1* oscillator strength is tree times stronger then that of *e1-lh1*.

Excelent agreement between theory and experiment allows us to obtain with good accuracy the Faraday rotation angle and the degree of circular polarization in reflection for linearly polarized incident light (Fig.2 b,c). The dotted line in Fig. 2b shows the calculated Faraday rotation angle for one -way propagation trough the central cavity layer with two QWs. The rotation angle is strongly increased at the cavity polariton eigenmode frequencies. This is accompanied by the appearence of an uncompensated circulary polarized component of light (Fig 2c). The rotation angle from the whole microcavity has the opposit sign comparing to rotation angle of light inside the cavity.

In conclusion, semiconductor microcavities provide a resonant amplification of the Faraday effect due to multiple round trips of light intensity between σ_- and σ_+ polarized components. Experimentally, the resonant Faraday rotation has been measured in linear cross-polarized reflection spectra of the microcavity with two embedded InGaAs/GaAs QWs.

For the details, we refer the reader to [6,7].

We gratefully asknowledge RFBR and MNTP "Nanostructures".

References:

1) J.Tgnon, P.Voisin, C.Delande, M.Voos, R.Houdre, R.P.Stanley, U.Oesterele, *Phys. Rev. Lett.*, **74**, 3967 (1995)
2) T.A.Fisher, A.M.Afshar, M.S. Skolnick, D.M.Whittaker, J.S.Roberts, *Phys. Rev. B*,**53**, R10459 (1996)
3) J.D. Berger, O.Lynges, H.M.Gibbs, G.Khitrova, T.R.Nelson, E.K.Lindmark, A.V.Kavokine, M.A. Kaliteevski, V.V.Zapasskii, , *Phys. Rev. B*, **54**, 1975 (1996)
4)T. Tanake, Zhenlong Zhang, M.Nishioka, Y.Arakawa,Appl.Phys. Lett., **69**,887 (1996)
5) J.J. Baumberg, D.D.Awchalom, N.Samarth, H.Luo, J.K.Furdina, *Phys. Rev. Lett.*,**72**, 717 (1994)
6) A.V. Kavokin, M.R.Vladimirova, M.A.Kaliteevski, O.Lyngnes, J.D.Berger, H.M. Gibbs and G. Khitrova, *Phys. Rev. B*, 1997, to be published.
7) M.A.Kaliteevski, A.V.Kavokin, P.S.Kop'ev, *Semiconductors*, **31** (7), 1997, in press

COMBINED EXCITON-ELECTRON PROCESSES IN MODULATION DOPED QW STRUCTURES

V.Kochereshko[1],D.Yakovlev[1,2], W.Ossau[2], G.Landwehr[2], T.Wojtowicz[3], G.Karczewski[3], J.Kossut[3]

[1]*A.F.Ioffe Physico-Technical Institute Russian Academy of Sciences, St.Petersburg, Russia*

[2]*Physikalisches Institut der Universität Würzburg, 97074 Würzburg, Germany*

[3]*Institute of Physics Polish Academy of Sciences PL02608 Warsaw, Poland*

Bound exciton-electron complexes (X^-) and resonant exciton-electron states (ExCR) have been studied in modulation-doped QWs with two-dimentional electron gas of low density.

CdTe/$Cd_{0.7}Mg_{0.3}Te$ heterostructures grown by molecular-beam epitaxy on (100) oriented GaAs substrates were used for the studies. The structures were modulation-doped with Iodine in the barrier at the distance of 100 Å from the QW. The electron concentration in QWs was varied for different samples from 0 to $10^{11}cm^{-2}$. Photoluminescence (PL), photoluminescence excitation (PLE) and reflectivity spectra were studied in magnetic fields up to 7.5T at 1.6K.

PL, PLE and reflectivity show strong emission and absorption lines related to the negatively charged exciton-electron complexes (trions). The trion line (X^-) is strongly polarized in PLE and reflectivity spectra and is nearly unpolarized in PL spectrum. This reflects the fact that the ground state of the trion is a singlet. X^- line presents in doped structures only and dominates the PL spectra with the increase of electron concentration. In the reflectivity it can become even stronger than the exciton line. On the contrary the intensity of the exciton line was observed to be always larger in PLE spectra. These facts indicate very large rate of exciton trapping into the trion state. This rate can even be much higher then the rate of exciton radiative recombination.

PLE and reflectivity in the presence of magnetic fields show also combined exciton cyclotron resonance (ExCR) lines caused by photocreation of exciton and simultaneous excitation of backround electron between Landau levels (LL). We observed two such transitions in our samples. One (ExCR1) from the lowest LL (N=0) to the next (N=1) and second (ExCR2) from the lowest LL to the LL with N=2. We have found that the intensity of ExCR1 line can even exceed the intensity of exciton line in reflectivity spectra. This reflects very large contribution of such processes to the dielectric function. In doped structures at zero magnetic field a high energy wing of exciton line is additionaly broadened due to the exciton-electron scattering. Magnetic fields suppress the scattering processes, the broadening of exciten line gets smaller and ExCR lines appear at the high energy side of the exciton line. In PL spectra of doped structures we observed a line caused by the shake up process connected with the annihilation of exciton with simultaneous excitation of background electron between Landau levels.

Pecularities of the light hole transitions in substrate-free stressed heterosystem (In,Ga)As/GaAs with MQWs

S.I. Kolchanovskii, K.Moumanis, M.E.Sasin, R.P. Seisyan
A.F. Ioffe Physico-Technical Institute, 26 Politechnicheskaya, 194021, Russia

1. Introduction

Low-dimensional structures based on (In,Ga)As/GaAs heterosystem have attracted an increased attention during recent years. First of all, this is because in a range of In compound x=0÷0.3 these QWs belong to the mixed type I - type II class, so that the QW represent an attracting potential for an electron and a heavy hole and repulsing potential for a light hole. The heavy-hole exciton transitions clearly are spatially direct while the nature of light-hole excitons is not evident. In pronounced type II QWs excitons are spatially indirect which makes their oscillator strength much smaller than the exciton oscillator strength in type I QWs. However, optical spectra of (In,Ga)As/GaAs QWs show pronounced light hole exciton transitions, which contradicts with the model of spatially indirect excitons [1,2]. The "Coulomb well" model resolves this problem supposing that the light hole excitons are spatially direct.

Electron-hole attraction is described in this model by introducing of one-dimensional effective potential created by electron which confines the light hole in normal to QW plane direction. For the first time an additional hole confinement in QWs due to its Coulomb attraction to the electron has been described theoretically for the case of type I QW with infinite barriers in [3]. The "Coulomb well" has been supposed parabolic, which yields equidistant hole energy levels. The parabolic approximation provides good agreement with experimental data on the fine excitonic structure in 0-dimensional microcrystals CdS and CdSe where the model of infinite barriers is reasonable. In our case, however, there is no barriers for the light hole at all, so that the approach to description of the "Coulomb well" effect should be substantially modified.

Experimentally, "Coulomb well" effects on the excitonic spectrum can be revealed in the fine structure of excitonic transitions which requires very narrow spectral lines and correspondingly high quality samples. In this paper we report a magnetooptical study of record quality MBE grown (In,Ga)As/GaAs samples, prepared in Optical Science Center, University of Arizona, and kindly placed at our disposal by H.Gibbs and G.Khitrova. For optical measurements substrates were completly removed by chemical etching.

2. Theoretical background

Consider first single particle electron and hole energies in strained (In,Ga)As/GaAs QWs. Thin $In_xGa_{1-x}As$ layers are lattice matched to the GaAs substrate which results in the band gap increase and splitting between heavy and light holes so that the potential well gets deeper for heavy holes and vanishes for light holes. Assuming the ratio of hydrostatic strain constants for conduction and valence bands Q_e^H [2] one can write equation for the electron, heavy and light hole band energies as:

$$E_c = E_g^{GaAs} - \Delta E_c(x) + \frac{Q_e^H}{1+Q_e^H} a_x (2-\lambda_x^{100}) \frac{x}{13.9+x} \quad ,$$

$$E_{hh} = \Delta E_v(x) - \frac{a_x\left(2-\lambda_x^{100}\right)}{1+Q_e^H}\frac{x}{13.9+x} + |b_x|\left(1+\lambda_x^{100}\right)\frac{x}{13.9+x},$$

$$E_{lh} = \Delta E_v(x) - \frac{a_x\left(2-\lambda_x^{100}\right)}{1+Q_e^H}\frac{x}{13.9+x} - |b_x|\left(1+\lambda_x^{100}\right)\frac{x}{13.9+x}\left[1+\frac{9}{4}\frac{|b_x|}{\Delta_0(x)}(1+\lambda_x^{100})\frac{x}{13.9+x}\right] \quad (1)$$

Here $\Delta E_{c(v)}(x)$ is conductor (valence) band parts of the E_g change with x, a and b are constants of deformation potential, λ_x^{100} is parameter depending on elastic constants [2]. The difference in condition between free samples and samples on substrate is manifested by the relative shift of the lines. Fig. 1 demonstrates also the condition of strain of the GaAs barrier layers in free samples measured by exciton line shift δE and splitting Δ_s. Defining them by the most intensive edge lines, we can calculate GaAs deformation ε

using data of Ref.4: $\Delta_c = 2b(1+\lambda)e = 6.43e$, $\delta E = a(2-\lambda)e = -9.7e$, what gives mean experimental values of e=4.3 10^{-4} and 5.8 10^{-4} for NMC 21 and NMC 11 respectively. This means that the lattice parameter $\tilde{a}$ of the GaAs on substrate plane is extended, so that $\tilde{a} = \tilde{a}_1 + \Delta\tilde{a}$,and this partly induces a decrease of strain e_1 in (In,Ga)As layer $e_1 = e_0 + e(\tilde{a}_0/\tilde{a}_1)$, where e_0 is an initial strain in (In,Ga)As layers, and $\tilde{a}_0$ and $\tilde{a}_1$ are lattice constants of free GaAs and (In,Ga)As at given x, respectivly. So the difference between two conditions of the samples is approximately equal to the barrier layer deformation: $\Delta e = e_1 - e_0 = ek$, where k=5.6512/(5.6512-0.4x)≈1. This allows to write for the shift, Δ_1 and Δ_2 of HH1E1 and LH1E1, respectively:

$$\Delta_1 = a_x\left(2-\lambda_x^{100}\right)e - |b_x|\left(1+\lambda_x^{100}\right)e,$$

$$\Delta_2 = a_x\left(2-\lambda_x^{100}\right)e + |b_x|\left(1+\lambda_x^{100}\right)e\left[1 - 9|b_x|\left(1+\lambda_x^{100}\right)\left(e_0+e_1\right)/4\Delta_{0x}\right]. \qquad (2)$$

Calculating the strain induced splittings of exciton lines we haven't taken into account quantization of exciton-polaritons [5] which changes differently light and heavy hole peak positions. Anyway, the correspondence between calculated and experimental values can be accepted as satisfactory.

3. Samples and experimental technique.

In order to reveal the "Coulomb well" effects the $In_xGa_{1-x}As/GaAs$ QWs with x=0.05÷0.08 have been chosen for two reasons. First, according to calculation, they should exhibit the simplest excitonic spectrum since there is only one confined electron state in the QW of width less then 100A; second, low Indium concentration provides best quality of samples and ultra-narrow spectral lines. To exclude strain relaxation effects the barriers in multiple QW structures have been grown much thicker than wells. Parameters of the studied samples NMC 21 and NMC 11 were x=0.045 and 0.062, L_z=90 and 88A, L_b=822 and 758A, respectively. There were also samples with higher In concentration for an additional measurements. $Al_xGa_{1-x}As$ 0.5 μm thick stop layers allowed to remove completely the substrates by chemical etching. Free samples have been immersed into the pumped liquid helium cryostat in the magnetic field up to 7.5 T. Magnetoabsorption measurements have been performed at the normal incidence of light.

4. Experimental Results

Optical transmission spectra of two samples with x=0.045 and 0.062 measured either before or after the substrate removal are shown in Fig.1. Free samples exhibit much more spectral details. Two kinds of spectral lines having different scales of absorption modulation can be distinguished. The low amplitude lines

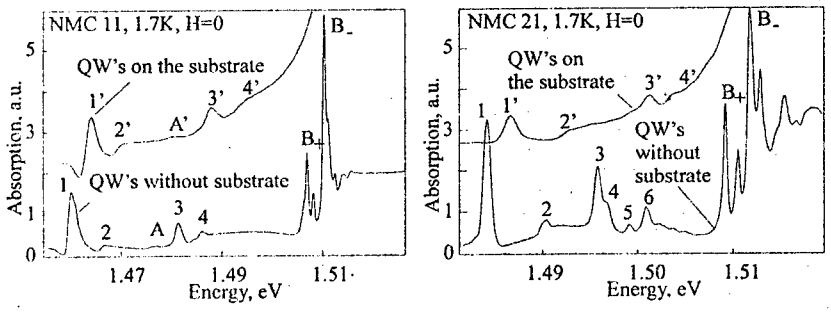

Fig.1 Absorption spectra of MQW (In,Ga)As/GaAs, samples NMC 11 (x=0.062)and NMC 21 (x=0.045); 1, 1' - HH1E1(1s), 2,2'' HH1E1(2s), 3,3' - LH1E1, 6 - LH3E1, B+ and B- are light and heavy hole excitons in GaAs barrier layer.

correspond to the transitions to the (In,Ga)As well electron level, while stronger spectral features correspond to the transitions in the GaAs barrier layers. The later features are characterized by complex multy-peak system of transitions and could be described in the terms of the exciton-polariton branch quantization combined with weak strain effects [5]. In the spectra taken before substrate removing many details are failed, naturally including all details of GaAs barrier behavior. All peak positions in the free samples are found longwave shifted ones by about 2.5-6.6meV. The shift is different for heavy and light hole transitions. Hereafter we will discuss the low-amplitude lines associated with quantum well transitions. These lines in their turn can be separated in two groups: two lines are associated with HH1E1 exciton ground (1s) state and first excited (2s) state, and the series of lines corresponding to the light hole exciton states. It is worth to note that for such a small In contents there are no other allowed optical transitions in the system according to the calculated energy scheme. The fan diagram taken in magnetic fields is shown in Fig.2. It is clearly seen that there is one group of lines with very typical behavior for magnetoexciton in QWs [6] which may easily be associated with HH1E1 excitons.

The most interesting is the behavior of the light hole exciton lines which could be extracted mentally by excluding of all above discussed HH1E1 exciton lines. First of all the light-hole exciton does not form its own fan diagram and is only weakly dependent on the magnetic field. Moreover the same behavior in the magnetic field is demonstrated by the second light hole line shifted in respect to the ground state transition similarly to the first excited (2s) state of HH1E1 exciton. At stronger fields two lines of doublet are diverging in RCP and converging in LCP like if they have opposite signs of g-factor. This effect is only seen in free samples while in samples having a substrate the dependence of two light-hole states on the magnetic field is quasi-parallel. Very weak resemblance of fan diagram appears in spectra of samples with higher In content, but all Landau levels in it are also show a doublet structure. And last, sometimes weak equidistant "fine structure" is detectable at energies higher doublet lines.

5. Discussion

Heavy hole exciton transitions dominate in the magnetoabsorption spectra. Fan diagrams are typical for well-to-well transitions in the magnetic field [6]. To restore true Landau fans one has to add individual binding energies to the all experimental point positions. The reconstruction of Landau fans in the units $y = \hbar\omega_0(l + 1/2)$, where ω_0=eH/mc is free electron cyclotron energy, proportional to the magnetic field H, is shown in Fig.2 by black circles. This reconstruction confirms choice of experimental points belonging to the light holes. Theoretical data obtained in [1,2] makes possible calculation of Coulomb well configuration and of oscillatory energy levels in it. The main parameters of such a well weakly depend on well parameters and for our samples NMC 21 and 11 the total depth occurred to be about V_o=12-17meV, first level position is LH1=-12.5-15meV and splitting between LH1 and LH3 oscillatory light hole levels is ΔE_{osc}=2-5meV, respectively. The width of Coulomb well on half maximum is about 200A. It is substantially more then L_z and partly overlap barriers. Taking into account mixing of light hole states of well and barrier and exciton binding energies calculated in Ref.1 we can establish quite good agreement with experiment for doublet splittings, whereas it is obvious that LH1 level position is too high and comparable with sum of

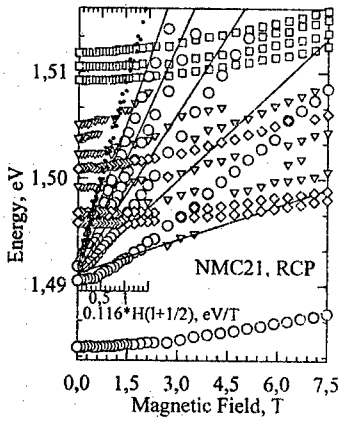

Fig.2 Fan diagrammes of NMC 21 as an example, RCP, T=1.7K. Rectangles are of GaAs barrier first maxima, circles are of HH1E1, rhombuses are of LH1E1 and LH3E1 and triangles are of additional transitions in the LH - E1 system magnetoexciton maxima. Solid lines are calculated positions for HH1E1 Landau level transitions and black circles are for E(y) reconstruction of HH1E1 transitions (short scale).

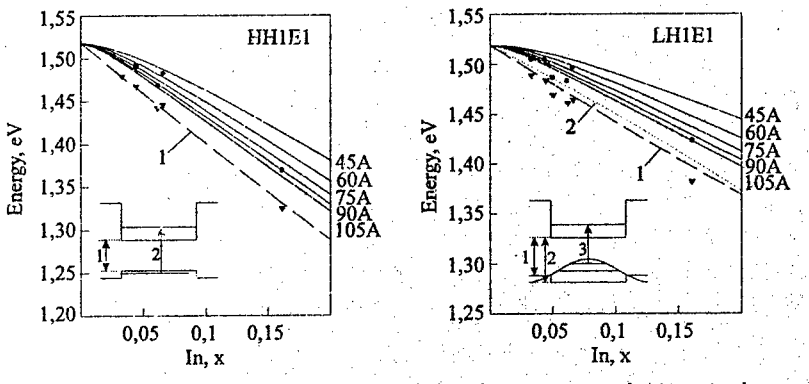

Fig.3 HH1E1 and LH1E1 transition positions vs x. Black circles are experimental points, triangles are corresponding reconstructed $E_g(x)$ points for heavy and light holes. Theoretical $E_g(x)$, direct for heavy holes (1) and indirect (1) or direct (2) for light holes , are given by dashed and dotted(2) curves, solid curves represent quantum level transitions. Transitions are schematically shown on insets.

$\Delta E_c, \Delta E_{hh}$ and ΔE_{lh} To overcome this contradiction an additional study of samples with higher x was undertaken. The results are shown in Figures 3a and 3b. where simultaneously with experimental points for HH1E1 and LH1E1 transitions belonging to the samples with different x and L_z, curves for $E_g(x)$, E_c and E_{lh} are plotted (eq.1). Subtracting from the experimental energy positions values of quantum well energy levels E1 and HH1 we can reconstruct $E_g(x)$, E_c and E_c+E_{lh}. The agreement for HH1E1 is remarkable and experimental mistake does not overcome ±2meV, while experimental points for LH1E1 are near corresponding curves for low In concentrations x<0.05 and substantially lower for higher concentrations x>0.05. Shift achieves here 14-18meV, and this explains all contradiction. Indeed, Coulomb well calculation in [1,2] don't take into account shallow position of electron level causing confinement, which occurs to be essential at x<0 .05. Only for higher x the theory [1,2] becomes quantativly valid whereas at the lower In concentrations it remains valid only qualitatively. Exactly calculating LH3 position as regards to valence band top in GaAs barrier and taking into account its splitting due to deformation e and barrier - well light hole mixing we can obtain method of g-factor estimation for the oscillatory levels, which seems to give an answer on question about the reason of its different signs in RCP and LCP spectra.

References

[1] R.P.Seisyan, A.V.Kavokin, S.I.Kokhanovskii, A.I.Nesvizhskii, M.E.Sasin, M.A.Sinitsin, B.S.Yavich. *Semicond. Sci.& Technol.* **10**, 611(1995)

[2] A.V.Kavokin, S.I.Kokhanovskii, A.I.Nesvizhskii, M.E.Sasin, R.P.Seisyan, A.P.Egorov, A.V.Zhukov, V.M.Ustinov. *Fiz. Tekh. Poluprov.* 1997 *[Semiconductors]*, in press.

[3] Al.L.Efros. *Fiz. Tekh. Poluprov.* **20**, 128(1986) [*Sov. Phys. Semicond.* **20** 808(1986)]

[4] G.N.Aliev, N.V.Luk'yanova, R.P.Seisyan. *Phys. Solid State* **38**, 590(1996)

[5]G.N.Aliev, N.V.Luk'yanova R.P.Seisyan, M.R.Vladimirova, V.N.Bessolov, H.Gibbs, G.Khitrova. in Proc. of ISCS-23, ed. R.Suris & M.Shur,1997, in press.

[6] A.V.Kavokin, A.I.Nesvizhskii, R.P.Seisyan. *Fiz. Tekh. Poluprov.* **27**, 971(1993) [*Semiconductors*, **27**, 530(1993)].

Anomalous effect of magnetic field on the indirect exciton in GaAs double quantum wells.

V.V.Krivolapchuk, D.A.Mazurenko, E.S.Moskalenko, N.K.Poletaev and A.L.Zhmodikov

A.F.Ioffe Physical-Technical Institute, Russian Academy of Sciences, 194102, St.Petersburg, Russia

T.S.Cheng and C.T.Foxon

Department of Physics, University of Nottingham, University Park NG7 2RD, Nottingham, UK

Abstract. We report the studies of exciton photoluminescence (PL) spectra from slightly asymmetric double quantum wells (QW) of GaAs in the presence of magnetic field perpendicular to the QW's plane. The experiments were carried out in the "indirect regime" in which structure is biased in such a way that indirect exciton (IX) transition has the lowest energy position in PL. The magnetic field induced changes in PL are revealed mostly as shifts of IX line position in energy which differ markedly from those observed previously. In particular the magnetic field induces shift of IX line to lower or higher energies depending on sign and value of bias voltage across the structure. Possible microscopic mechanisms of this anomalous behaviour are discussed.

Samples and experimental arrangement. The samples were taken from wafer NU1117 consisting of 1 μm GaAs buffer layer followed by three DQWs. The structure was grown in Nottingham University by MBE at T=630^{O}C on 0.4 mm thick (001) semi-insulating GaAs substrate. The thickness of the narrow barriers of $Al_{0.33}Ga_{0.67}As$ between two QW in DQW is 3.82 nm and that of the thicker barriers between DQW is 20.35 nm. The widths of the QWs in DQW differ by 2 ML (0.57 nm) with layer widths (QW/barrier/QW in nm) of 20.07/3.82/1.95, 10.18/3.82/9.61 and 8.20/3.82/7.63. A constant electric field (V_{dc}) was applied across the whole structure (Fig. 1a) between two indium contacts deposited on the substrate surface and the sample's face with QWs. The latter contact was made with single pin hole providing the possibility to excite photoluminescence (PL) in DQWs which was studied by means of using double-grating monochromator combined with photon-counting system. The samples were illuminated by He-Ne laser beam (λ = 730.3 nm) providing the below barrier PL excitation and bath temperature was kept as low as 4.2K.

The magnetic field **B** (up to 5T) was applied in the growth direction, ie parallel to the V_{dc} (Fig. 1a). V_{dc} was kept negative providing relative shift of band structure in DQW system (Fig. 1b). This is the case of "indirect regime" which is characterized by the lowest energy position in PL of indirect exciton IX (electron in wide and hole in narrow QW) relative to the direct exciton transition DX (electron and hole are both situated in the wide well) - see Fig. 1b.

Experimental results. In the present contribution we concentrate on results obtained on DQW of widths 10.18/3.82/9.61 nm which PL spectrum taken at B=0 and V_{dc}=-0.4V is shown in Fig.2a. The spectrum consists of DX line ($h\nu$=1.555 eV), line of DX bound on the impurity (BDX) [1] and IX line accompanied by the line of localized IX (LIX) [2]. The spectral position of both latter lines in PL is determined by the value of electric field across the DQW and varies linearly with external V_{dc} [2] in the bias range $-0.4<V_{dc}<0$ V. Further decrease of V_{dc} ($V_{dc} < V_o = -0.4$ V) results only in negligible change in position of IX and consequently electric field in DQW due to the appearance of large (up to several μA) electric current through the whole structure.

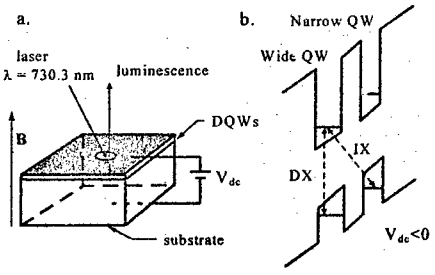

Fig. 1. Experimental setup (a) and energy band diagram in the "indirect regime" (b)

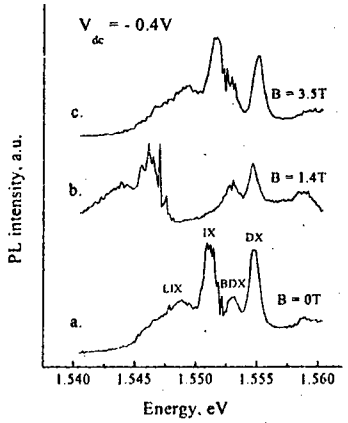

Fig. 2. PL spectra taken at $V_{dc}=V_0=-0.4$V at B=0T (a), 1.4T (b) and 3.5T (c).

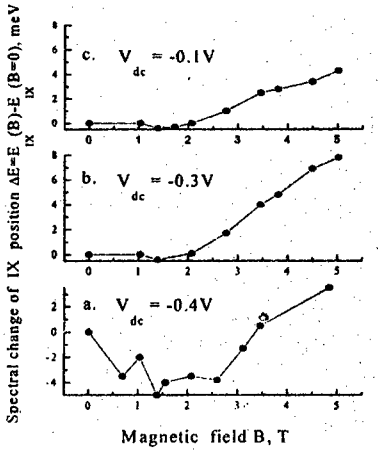

Fig. 3. ΔE versus B at V_{dc}=-0.4V (a), -0.3V (b) and -0.1V (c).

Applied magnetic field **B** shifts IX and LIX lines to lower energies (Fig. 2b) while leaves spectral positions of DX and BDX unchanged. Further increase of **B** results in shift of IX (as well

as LIX) to opposite side, ie to higher energies (Fig. 2c). The shift of IX line spectral position versus **B** value is shown in Fig. 3 for three different V_{dc}s in terms of $\Delta E = E_{IX}(\mathbf{B}) - E_{IX}(\mathbf{B}=0)$ dependence on **B**.

Discussion. Coming to the discussion it is important to note that ΔE only increases (remaining positive) in the whole range of **B** at $V_0 < V_{dc} < 0V$ (see Fig. 3 b and c). This bias range corresponds to the regime where no electric current across the whole structure was detected. In contrary at V_{dc}s when electric current starts ($V_{dc} \approx V_o = -0.4$ V) magnetic field induces decrease in ΔE followed by its corresponding increase when **B** exceeds 2T (see Fig. 3a). The fact that magnetic field shifts IX line to down energies (Fig. 3a) means that more electric field is applied across the DQW at nonzero **B** comparing to the case when **B** is switched off (at the same fixed V_{dc}). Thus we conclude that **magnetic field blocks the electric current** across the device. At other V_{dc}s no current occurs (at **B**=0) and hence nothing to be blocked. So the magnetic field induces only positive shift of ΔE (Fig. 3b and c).

The positive shift of IX line position was reported earlier [3,4] and explained in terms of diamagnetic shift of IX. Really in low magnetic fields $\hbar\omega_c < E_D^{IX}$ (where $\hbar\omega_c$ is the cyclotron frequency 1.73 meV/T for electrons with $m=0.067m_0$ and E_D^{IX} =3.3 meV is the IX binding energy [2]) $\Delta E = \alpha \times \mathbf{B}^2$, where $\alpha \sim (1/E_D^{IX})^2$ [3]. But at high magnetic fields $\hbar\omega_c > E_D^{IX}$ spectral position of IX ground state which is detected in luminescence should follow Landau levels position [3], namely

$$E_{IX}(\mathbf{B}) = E_{IX}(\mathbf{B}=0) + 1/2\{\hbar\omega_c^e + \hbar\omega_c^h\} - E_D^{IX}(\mathbf{B}), \quad \text{where} \quad E_D^{IX}(\mathbf{B}) \sim (d^2 + \lambda_B^2)^{-1/2} \qquad (1)$$

where d is effective interwell electron-hole separation in the two QW's and λ_B is the magnetic length.

Indeed as it is seen in Fig. 3 ΔE begins to acquire positive shift when **B** value exceeds 2T which corresponds to the high magnetic field regime, namely $\hbar\omega_c^e \geq 3.46$ meV which exceeds $E_D^{IX}(\mathbf{B}=0) = 3.3$ meV.

Thus we conclude that sign of IX line shift is determined by two opposite contributions:

(i) low energy shift is due to the magnetic field induced total or partial blockade of electric current, and

(ii) high energy shift is due to the diamagnetic contribution to ΔE.

Evidently **(i)** can be detected under specific conditions, namely when current passes across the whole structure and hence contribution from **(i)** is essential only when $V_{dc} < V_0$. As concerns **(ii)**, it should be active at any values of V_{dc} if only $\hbar\omega_c > E_D^{IX}$ condition is satisfied. As it follows from Fig.3 the absolute values of ΔE positive shift induced by magnetic field are V_{dc} value dependent. This can be explained in terms of binding energy E_D^{IX} dependence on d (1) which in turn can be strongly affected by bias voltage magnitude across the DQW [5] via the electric field induced changes in electron and hole wavefunctions overlap in the growth direction.

The mechanism of electric current blockade by **B** is unclear, further experiments are needed to reveal the role of magnetic field. However, the fact that we detect electric current through the whole structure under laser illumination means that free charges (electrons, holes) created in GaAs QWs as well as in the buffer layer and the substrate pass particularly through the AlGaAs barriers where no free charges are generated as a result of underbarrier excitation. One of the possible mechanisms of this is considered as: the charges tunnel through the barriers being trapped (as an intermediate step) on impurities which are located in AlGaAs barriers. The effectiveness of these processes depends on lateral (in plane of QW) spread of the charge wavefunction - the larger spread is, the more efficient trapping becomes. Magnetic field applied perpendicular to the QW's plane localizes carriers in the in-plane direction on typical space size of λ_B, thus decreasing probability of charge trapping and this eventually leads to current quenching.

In conclusion we have observed anomalous influence of **B** on the IX line spectral position. Particularly the sign of magnetic field induced shift of IX line is V_{dc} value dependent. This is assumed to be due to the magnetic field induced blockade of electric current through the whole device.

Acknowledgements. We are grateful to Prof. A.A.Kaplyanskii, Prof. R.A.Suris, Prof. O.V.Konstantinov and Dr. D.R.Yakovlev for interesting discussions, to Dr. A.V.Akimov for attention to experiments and to Prof. L.J.Challis for fruitful collaboration. This work was funded by the INTAS-94-395 and the Russian Foundation for Basic Research (96-02-16952a).

REFERENCES.

1. The origin of this line is attributed to DX bound on charged impurity in AlGaAs barrier. For more details see paper by E.S.Moskalenko, A.L.Zhmodikov, A.V.Akimov, A.A.Kaplyanskii, L.J.Challis, T.S.Cheng, O.H.Hughes, Annalen der Physik, **v.4**, (1995), p.127 and references therein.

2. D.A.Mazurenko, A.V.Akimov, E.S.Moskalenko, A.L.Zhmodikov, A.A.Kaplyanskii, L.J.Challis, T.S.Cheng, C.T.Foxon, Acta Physica Polonica, **v.90**, N.5, (1996), p.895

3. M.Bayer, V.B.Timofeev, F.Faller, T.Gutbrod, A.Forchel, Phys.Rev.B **v.54**, N.2, (1996), p.8799

4. L.V.Butov, A.Zrenner, G.Abstreiter, A.V.Petinova K.Eberl, Phys.Rev.B **v.52**, N.16, (1995), p.12153

5. F.H.Peeters, I.E.Gobub, Phys.Rev.B **v.43**, N.6, (1991), p.5159

The influence of real carriers on the optical Stark effect in GaAs/AlGaAs superlattice.

K.Litvinenko, A.Gorshunov, V.I.Grinev, J.M.Hvam*, V.G.Lyssenko.

Institute of Microelectronics Technology
Russian Academy of Sciences, Chernogolovka, 142432 Russia

The influence of manybody effects, which occurs due to the presence of real carriers, on the optical Stark effect (OSE) are investigated in GaAs multiple quantum wells by spectrally resolved differential transmission spectoscopy. The OSE for excitonic resonances have been investigated in great detail for nonresonant excitation [1-3]. For the nonresonant configuration, effests such as coherent oscillations, blue shift, and adiabatic following, known from atomic physics, have been demonstrated. However, for resonant excitation both virtual and real carriers are excited and a complicated interplay of the OSE and manybody effects occurs.

The sample under investigation is a 20 period $GaAs/Al_{0.3}Ga_{0.7}As$ multiple quantum well structure with wells of 80Å and barriers of 20Å. After MBE growth the sample is lifted off the substrate and mounted on a sapphire disk for transmission experiments. A liquid helium cryostat was used to maintain a sample temperature of 5K during the experiments.

Pulses of 100 fs from a passively mode-locked Ti:Sapphire laser were used for the pump-probe transmission experiments. The pulses were split in to paths a variable delay for the probe beam. The transmitted probe beam was dispersed in a 0.6 m spectrometer and recorded with a multichannal analyser, resulting in a resolution better than 0.1 meV throughout the spectral range of the experiment.

The absorption spectrum of the sample and the laser spectrum for excitation below and above the exciton resonance are shown in Fig.1. The heavy hole exciton (HHX) and light hole exciton (LHX) resonances are clearly resolved together with the onset of the heavy hole continuum. The superlattice miniband width is estimated to be 23 meV and thus exceeds the binding energy of the heavy hole exciton of the isolated quantum well. This results in a strongly anisotropic three-dimensional medium with modified optical properties. However, the linear absorption can be calculated by a method using a fractional dimensional approach [4]. We shall use the adopted generalized Elliot formula [5] to fit the experimental data.

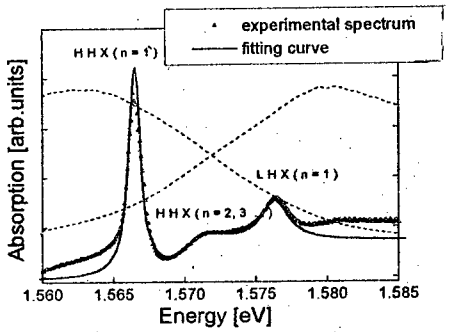

Fig.1. Absorption spectrum of sample and the laser spectrum for the two detuning.

Results from fits with the generalized Elliot formula are shown in Fig.2. The broadening of exciton resonance is proportional to the carriers density and can be used as a measure of this value. For the case of resonant excitation one can see an overshoot of the exciton density during pulse overlap. This shows the presence of virtual carriers in the sample during pulse overlap. For the case of nonresonant exitation, the presence of both real and virtual carriers is clearly demonstrated in pronounced overshoot of the HHX broadening at pulse overlap. This additional carrier density results in the unique temporal behavior of the exciton binding energy. For a long negative time delay a small blue shift of exciton binding energy can be explained by the OSE for both excitation conditions. When the time delay becomes shorter, the real carriers should start to play an important role. As it was shown in Ref.6, the influence of free carriers due to phace space filling (PSF) effect results in the decreasing of the binding energy (see Fig.2). Near zero delay we observed a rapid increasing of the exciton binding energy for the case of nonresonant excitation. Since the carrier density is not significantly changed at τ=0, the rapid modification of the binding energy is a result of the scattering of free carriers. After scattering the electrons and the holes do not occupy the same places in the k-space and, consiquently, can not take a part in the PSF effect. Thus, for short positive time dalay the exciton binding energy may be even bigger, than its nonexcited value, due to exchange and corralation effects and interaction with the electro-magnetic field.

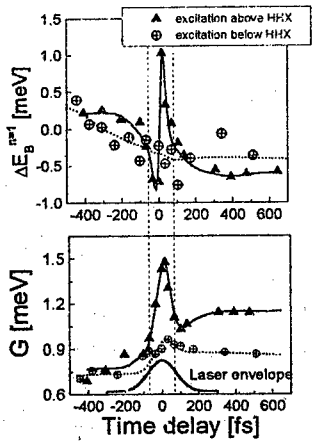

Fig.2. The change of the exciton binding energy and the exciton linewidth as a function of the time delay. The carrier density is estimated to be $1.4 \cdot 10^{11} cm^{-2}$ for the excitation below HHX, and $4.4 \cdot 10^{10} cm^{-2}$ for the excitation above HHX.

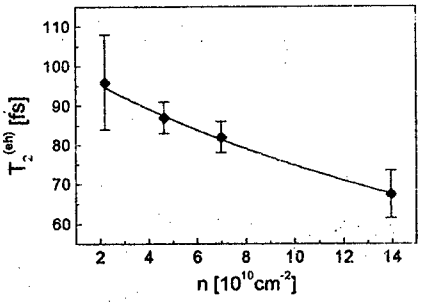

Fig.3. The dependence of relaxation time of the electron-hole plasma on the carrier density.

The time distance between the maximum red and blue shift of the binding energy is proportional to the relaxation time $T_2^{(eh)}$ of electron-hole plasma. In Fig.3 one can see the relaxation time $T_2^{(eh)}$ as a function of carrier dencity. The simples model explaining this dependence is the kinetic model of electron gas. According with this model the relaxation time is inversly proportional to carrier density: $1/T_2^{(eh)} \sim N$ [7]. This approximaion is quite good discribed our experimental data. It means that for our experimental condition the influence of Coulomb interaction can be niglected [8].

We experimentaly investigated the dependence of binding energy on the carrier density for a fixed time delay (τ=500 fs) and obtained that the effective exciton Mott density equals $2.4 \cdot 10^{12}$ cm^{-2}.

This work was supported by the INTAS-RFBR 95-0576 and the Russian Fund for Fundamental Research (Grant № 96-02-05046).

References

[1] A.Mysyrowicz, D.Hulin, A.Anton tti, A.Migus, W.T.Masselink, H.Morkock, Phys.Rev.Lett. **56**, 2748 (1986)

[2] W.Knox, J.B.Stark, D.S.Chemla, D.A.B.Miller, S.Schmitt-Rink, Phys.Rev.Lett. **62**, 1189 (1989)

[3] R.Binder, S.W.Koch, M.Lindberg, W.Schäfer, F.Janke, Phys.Rev.B. **43**, 6520 (1991)

[4] P.Lefebvre, P.Cristol, M.Mathieu, Phys.Rev.B **48**, 17308 (1993)

[5] K.Litvinenko, D.Birkedal, V.G.Lyssenko, J.M.Hvam, "Abstracts of Inv. Lectures on 23 International Conference on the Physics of Semiconductors. Berlin, Germany - July 21-26, 1996

[6] D.Huang, J.-I.Chyi, H.Morkoç, Phys.Rev.B. **42**, 5147 (1990)

[7] A.Honold, L.Schultheis, J.Kuhl, C.W.Tu, Phys.Rev.B. **40**, 6442 (1989)

[8] J.Feldmann, T.Meier, G.von Plessen, M.Koch, E.O.Gobel, P.Tomas, et al. Phys.Rev.Lett.70(20), 3027(1993)

Excitonic states in type-I and type-II quantum well structures based on beryllium chalcogenides

A.V.Platonov[2], D.R.Yakovlev[1,2], U.Zehnder[1], V.Kochereshko[2], W.Ossau[1], F.Fischer[1], Th.Litz[1], A.Waag[1], and G.Landwehr[1]

[1]*Physikalisches Institut der Universität Würzburg, 97074 Würzburg, Germany*
[2]*A.F.Ioffe Physico-Technical Institute Russian Academy of Sciences, St.Petersburg, Russia*
E-mail:platon@semimag.ioffe.rssi.ru

We present an optical investigation of the novel heterostructures based on beryllium chalcogenides with both a type-I and a type-II band alignment. In quantum well (QW) structures with type-II band alignment (BeTe/ZnSe) we observed strong exciton transition involving electron confined in the conduction well band and holes localized in the valence band barrier (both in ZnSe layer). Behaviour of exciton properties in this kind of structure as function of temperature and magnetic field was compared with a QW structure with type-I band alignment (ZnSe/BeZnSe).

Semiconductor heterostructures based on beryllium chalcogenides are relatively new and very promising materials for applications and for fundamental investigations. Recently these compounds were successfully used for creating a laser emitting diode in a blue range[1]. But at present a limited number of papers about basically properties of such heterostructures is available. At the same time Be-containing semiconductor compound allow to grow high quality QW structures with positive and negative valence band offset and with a wide range of offset values (up to 2.0 eV). Therefore, these structures increase faculties for the band-structures engineering. Also a large value of exciton binding energy make a set of fine effects as easy observable for instance a negatively charged exciton [2].

The studied structures were grown by molecular-beam epitaxy on GaAs substrate with (100) orientation. Two samples were fabricated:

sample 1: 70-Å-thick ZnSe/ZnBeSe QW, which has the type-I band alignment, i.e. electron and holes have a minimum of energy in ZnSe layer. The structure was slightly doped by In the barrier layer.

sample 2: 160-Å-thick ZnSe/BeTe QW. This system has a type-II band alignment with a very large confinement potential for electrons (about 2.0eV), which are localized in ZnSe, and for holes (0.9eV), which have the minimum of their energy in BeTe layers.

Reflectivity and photoluminescence spectra(PL) at temperature 1.6 K for samples 1 and 2 are presented in fig.1(a,b), respectively.

For the type-I QW the reflectivity spectrum shows three resonance's, which can be identified as excitons with heavy hole, with light hole and bound exciton on a donor or negatively charged exciton [2] (which are not spectrally resolved). At low temperatures the dominating peak in a PL (2.822eV) spectrum corresponds to the bound exciton state.

A strong resonance is at the energy exceeding the ZnSe band gap observed for the type-II structures in the reflectivity spectrum. BeTe has a direct band gap of about 4.2eV hence we identify the resonance as a transition between electron, which is confined in ZnSe QW, and the hole from a quasi-localized above-barrier state.

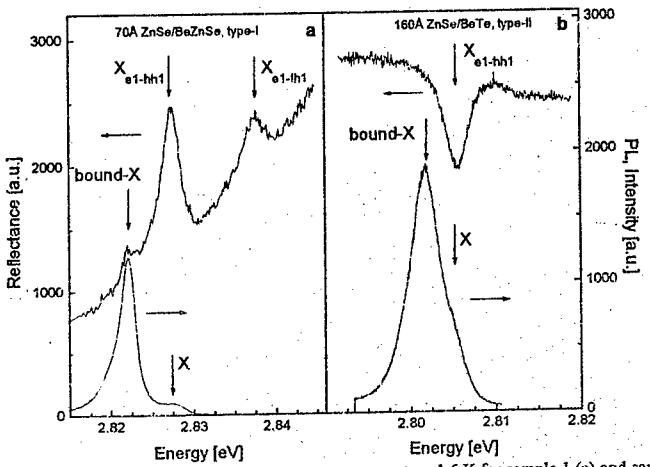

Fig.1. Reflectivity under normal incidence and PL specra at temperature 1.6 K for sample 1 (a) and sample 2 (b).

By fitting the reflectivity spectra to analytical expressions [3] we found the following exciton parameters for the type-I QW: resonance energy ω_0=2.828 eV, oscillator strength ω_{lt}=1.2 meV, damping Γ=1.3 meV; and for the type-II QW: ω_0=2.805 eV, ω_{lt}=1.05meV, Γ=1.6 meV. The comparable oscillator strength of the type-II and type-I QWs and a relatively small exciton damping for type-II evidence the strong hole localization in the ZnSe-layers, i.e. in the above barrier states. By using magneto-reflectivity measurements we also estimated an exciton binding energy for both structures: $E_x^I = 30\ meV$, $E_x^{II} = 25\ meV$. Summarised all facts mentioned above we can conclude that in the studied type-II structure electrons in QW and holes which are localized above the barrier create an excitonic state with similar parameters as in the type-I QWs.

We also measured temperature dependencies of the exciton linewidth for both structures. The drastically increase of this quantity for the type-II QW was observed at a low temperature (T<100K) range in comparison with the type-I QWs and bulk materials. This effect is explained by enhancement of the acoustical phonon scattering for the above barrier state in the type-II QWs. The results of model calculations of such enhancement are in a good quantitative agreement with the experimental data.

Acknowledgements: This work has been supported in part by the Volkswagen Foundation and by the Russian Foundation for Basic Research grant No.95-02-04061a.

References:

[1] A.Waag, F.Fisher, Th.Litz, et.al., Appl.Phys.Lett., **70**(3), 1997

[2] K.Kheng, R.T.Cox, V.P.Kochereshko, K.Seminadayar, Superlattices and Microstructures, **15**, 253, (1994).

[3] E.L.Ivchenko, P.S.Kop'ev, V.P.Kochereshko et.al., Sov.Phys. Semiconductors **22**(3), 784, (1988); E.L.Ivchenko, G.E.Pikus "Superlattices and Other Heterostructures", Springer Seria in Solid-State Sciences Vol.110, Springer-Verlag (1994).

SCREENED EXCITONS IN QUANTUM WELLS

Mikhail E. Portnoi[a,b] and Ian Galbraith[a]

[a]*Physics Department, Heriot-Watt University, Edinburgh EH14 4AS, United Kingdom*
[b]*A.F.Ioffe Physico-Technical Institute, St.Petersburg, Russia*

The large exciton binding energy in wide-gap semiconductors and quantum wells favours excitonic gain processes for which no satisfactory theoretical treatment exists. A knowledge of the balance between excitons and free carriers is important in determining the dominant gain process. It is known that a naive application of the Mott criterion for the metal-insulator transition as well as the use of a law of mass action are insufficient, as screening of excitons by the electron-hole plasma and strong scattering of particles within the plasma both play a crucial role. A simple formalism to study simultaneously bound states in a screened potential and scattering of charge carriers by the same potential is needed.

We apply a variable-phase approach [1] known from scattering theory to study scattering and bound states in an attractive Coulomb potential, statically screened by a two-dimensional (2D) electron gas. Levinson's theorem, which connects the number of bound states in a given potential with the scattering phase shifts of a slow particle, is generalised to the 2D case. This theorem is used for bound-state counting and a hitherto undiscovered simple relation between the number of bound states and the screening radius is found.

A proper account of scattering eliminates discontinuities in thermodynamic properties of the electron-hole system whenever bound states disappear due to screening. Consistent treatment of bound states and scattering allows us to estimate the distribution of electron-hole pairs between correlated and free-carrier states.

In what follows we consider a simple case in which a screened charge resides in the same plane as a screening 2D electron gas. This geometry is appropriate to the problem of screened excitons in a narrow quantum well. We assume that an attractive potential is created by a point charge e at the origin and use throughout this paper excitonic Rydberg units where length and energy are scaled, respectively, by the effective Bohr radius a^* and Rydberg Ry^*. In these units and geometry the Thomas-Fermi expression for the statically screened potential in the electron plane [2] is

$$V_s(q) = -4\pi/(q+q_s)\,, \tag{1}$$

where q_s is the 2D screening wavenumber. Eq. (1) is the 2D analogue of the Yukawa potential. Taking the 2D Fourier transformation of Eq. (1) yields in real space

$$V_s(\rho) = -2\left\{\rho^{-1} - q_s\int_0^\infty dq J_0(q\rho)/(q+q_s)\right\}\,, \tag{2}$$

where $J_0(q\rho)$ is the Bessel function, and $\rho=(x^2+y^2)^{1/2}$ is the in-plane distance from the origin.

To describe the application of the variable-phase method in 2D we consider a particle moving with energy $E=k^2$ in the potential $V(\rho)$ which has radial symmetry. At large distances from the scattering center, the radial wave function satisfies the free Bessel

equation, whose general solution is

$$R_m(\rho) = A_m[J_m(k\rho)\cos\delta_m - N_m(k\rho)\sin\delta_m] \stackrel{\rho\to\infty}{\longrightarrow} A_m\left(\frac{2}{\pi k\rho}\right)^{1/2}\cos(k\rho-(2m+1)\pi/4+\delta_m), \tag{3}$$

where m is the absolute value of the projection of the angular momentum onto the symmetry axis of the potential, δ_m is the scattering phase shift, $J_m(k\rho)$ and $N_m(k\rho)$ are the Bessel and Neumann functions, respectively. In the variable-phase method A_m and δ_m are considered not as constants but as functions of the distance ρ. The phase function, $\delta_m(\rho)$, is the phase shift produced by a potential cut-off at a distance ρ. Then the scattering phase shift can be obtained as a large distance limit of the phase function $\delta_m(\rho)$, which satisfies the following first-order, non-linear differential Riccati equation originating from the radial Schrödinger equation:

$$\frac{d}{d\rho}\delta_m(\rho) = -\frac{\pi}{2}\rho V(\rho)[J_m(k\rho)\cos\delta_m(\rho) - N_m(k\rho)\sin\delta_m(\rho)]^2 \tag{4}$$

with the boundary condition $\delta_m(0) = 0$.

The screened Coulomb potential $V_s(\rho)$, defined by Eq. (2), behaves like ρ^{-1} at small distances and like ρ^{-3} at large distances. Such behaviour allows the application of the variable-phase method to this potential.

Figure 1 shows the k dependence of the phase shifts δ_m obtained by the numerical solution of Eq. (4) for the screened Coulomb potential $V_s(\rho)$ with $q_s = 1/5$.

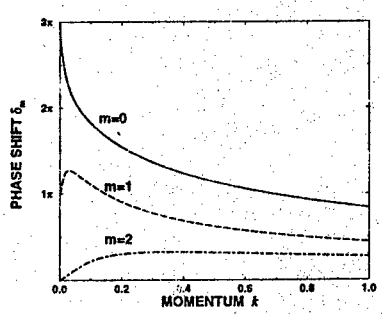

Figure 1: Scattering phase shifts versus in-plane wave vector k for a 2D particle in an attractive Coulomb potential screened by a 2D electron gas. Screening length $r_s = 1/q_s = 5$.

The distinctive feature of this plot to which we draw attention is that in the low-energy limit, $k \to 0$, the scattering phase shift is an integer number of π:

$$\lim_{k\to 0}\delta_m = \nu\pi\,. \tag{5}$$

This behavior may be understood recalling Levinson's theorem [3] which connects the zero-energy scattering phase shift with the number of the bound states for non-relativistic particles

in 3D. We expect that this fundamental theorem holds also in 2D in the form of Eq. (5), where ν is the number of bound states for a given m. Despite its appeal, Levinson's theorem has not been widely used to enumerate bound states since there exists an ambiguity in the usual definition of δ_m, being defined only up to mod(π). However using the variable phase approach avoids this problem since the phase function is uniquely defined by Eq. (5) for all ρ.

In Fig. 2 the number of bound states, obtained as the low-energy limit of the scattering phase shift in units of π , is plotted as a function of the screening length $r_s = 1/q_s$ for the potential V_s . As the screening length increases, the potential supports more bound states and these new bound states appear at critical values of the screening length indicated by the steps. One can see from the location of these steps that the ν-th bound state for a given m appears at the critical screening length, given by a simple formula

$$(r_s)_c = (2m+\nu-1)(2m+\nu)/2 , \quad \nu = 1, 2, \ldots . \tag{6}$$

This intriguingly simple relation has, to our knowledge, never been reported despite numerous calculations of the binding energy in the screened Coulomb potential, since conventional numerical methods for the binding energy calculation fail for extremely shallow energy levels. Note that for $m = 0$ the first bound state appears immediately at $(r_s)_c = 0$, corresponding to the fact that there is always at least one bound state in any symmetric 2D attractive potential. Using Eq. (6) we can simply evaluate how many bound states the 2D statically-screened Coulomb potential will support for any value of m .

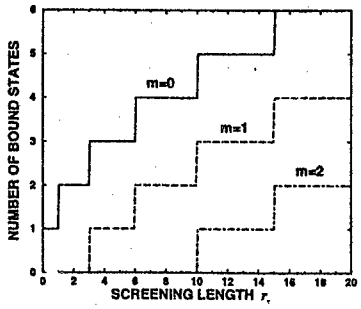

Figure 2: Number of bound states, calculated as the low-energy limit of the phase shift, plotted versus the screening length r_s . New steps appear at $(r_s)_c = (2m+\nu-1)(2m+\nu)/2$, $\nu = 1, 2, \ldots$.

For many applications (e.g., in a partition function calculation) the value of the binding energy, not just the number of bound states, is important. The variable-phase method provides an elegant and efficient solution of the eigenvalue problem as well. To approach this problem we recall that for the states with negative energy the wavenumber k is imaginary, $k = i\kappa$, and we introduce the function $\mu_m(\rho,\kappa)$ vanishing in the origin and satisfying a non-linear equation

$$\frac{d}{d\rho}\mu_m(\rho,\kappa) = -\frac{\pi}{2}\rho V(\rho)\left[I_m(\kappa\rho)\cos\mu_m(\rho,\kappa) + \frac{2}{\pi}K_m(\kappa\rho)\sin\mu_m(\rho,\kappa)\right]^2 , \tag{7}$$

where $I_m(\kappa\rho)$ and $K_m(\kappa\rho)$ are the modified Bessel functions of the first and second kind, respectively. The functions $I_m(\kappa\rho)$ and $K_m(\kappa\rho)$ represent two linearly independent solutions of the free radial-wave Schrödinger equation for the negative value of energy, $E = -\kappa^2$, and $\cot\mu_m$ characterizes the weights of the diverging (I_m) and converging (K_m) solutions as $\rho \to \infty$. For the bound state the diverging solution vanishes, implying the asymptotic condition

$$\mu_m(\rho \to \infty\,, \kappa_\nu) \;=\; (\nu - 1/2)\pi\;, \quad \nu = 1, 2, \;\ldots\;. \tag{8}$$

Here ν numerates the bound states for a given m and $(\nu - 1)$ is the number of non-zero nodes of the radial wave function.

The two-body interaction part of the partition function of interacting 2D Boltzmann particles is given by

$$Z_{int} \;=\; \sum_m C_m \left\{ \sum_\nu \exp(-E_{m,\nu}/k_BT) + \frac{1}{\pi}\int_0^\infty dp \frac{d\delta_m}{dp} \exp(-p^2/2\mu k_BT) \right\}\;, \tag{9}$$

where μ is the reduced mass, $C_0 = 1$, $C_m = 2$ for $m \geq 1$. Eq. (9) is a 2D analog of the Beth-Uhlenbeck formula and it can be derived in the same fashion as in the 3D case [4].

An important consequence of Levinson's theorem for statistical mechanics of a 3D plasma is a removal of discontinuity in partition function whenever a bound state disappears due to screening [5,6]. Exactly the same happens in a 2D case if the contribution from phase shifts is properly taken into account. Integrating by parts and using Levinson's theorem in the form of Eq. (5) we can rewrite Eq. (9) as

$$Z_{int} = \sum_{m,\nu} C_m[\exp(-E_{m,\nu}/k_BT) - 1] + \frac{1}{\pi\mu k_BT}\int_0^\infty \left(\sum_{m=0}^\infty C_m\delta_m \right) exp(-p^2/2\mu k_BT) pdp\;, \tag{10}$$

where the double sum in the first term ranges only over bound states. Thus the zero-energy part of the phase shift integral exactly cancels the zero-energy part of the bound state sum, removing the discontinuity in Z_{int} as a function of the interaction strength. The variable-phase method allows to calculate both terms of Eq. (10) with the same accuracy.

For the calculation of the degree of ionisation, electron-electron and hole-hole repulsion should be taken into account [6]. The repulsion term partially compensates the integral term in the partition function and it can be also calculated using the variable-phase method. Finally, the degree of ionisation of 2D electron-hole plasma (which characterizes the balance between correlated states and free quasiparticles) can be calculated in a wide range of densities and temperatures.

[1] F. Calogero, *Variable Phase Approach to Potential Scattering*, Academic Press, 1967.
[2] T. Ando, A. B. Fowler, and F. Stern, Rev. Mod. Phys. **54**, 437 (1982).
[3] N. Levinson, K. Dans. Vidensk. Selsk. Mat. Fys. Medd. **25**, 3 (1949).
[4] E. Beth and G. E. Uhlenbeck, Physica **4**, 915 (1937).
[5] F. J. Rogers, Phys. Rev. A **4**, 1145 (1971).
[6] R. Zimmermann, *Many-Particle Theory of Highly Excited Semiconductors*, Teubner-Texte zur Physik - Band 18, BSB Teubner, Leipzig (1987).

Single photon state generation and detection: single photon turnstile device and solid state photomultiplier

Jungsang Kim[1], Hirofumi Kan[2], and Yoshihisa Yamamoto[1,3]
[1] ERATO Quantum Fluctuation Project, E. L. Ginzton Laboratory,
Stanford University, Stanford, CA 94305, U. S. A.
[2] Central Research Laboratory, Hamamatsu Photonics Inc,
Hamamatsu, Shizuoka, Japan
[3] NTT Basic Research Laboratories,
Atsugi, Kanagawa, Japan

The idea about utilizing quantum mechanics to perform cryptography and computation has drawn a lot of interest in recent years [1]. Several schemes and systems to realize these ideas were proposed, and demonstrated. One of the most practical schemes to realize quantum cryptography is to use photons, encoding the information in the polarization of the photon [2, 3]. Quantum computation can also be performed in optical systems, and a prototype logic gate was demonstrated using single photons and a high-Q optical cavity [4]. However, in all of these schemes thus demonstrated so far, the source of photons was either highly attenuated laser or light emitting diode, or one of the photon pairs generated by parametric down-conversion process. The arrival time of the photons in these sources are determined by the Poisson statistics, and is totally random. The lack of ability to control the generation times of the photons imposes limitation on the efficiency of these schemes.

Generation of single photons with well-defined time interval is crucial in improving the efficiencies of these schemes. The generation of such photon states imply highly non-classical quantum statistics of light, as the photons need to be anti-bunched in time domain. It was proposed recently that such photon states can be generated by a mesoscopic light emitting diode with high quantum-efficiency [5]. The nonlinear Coulomb interaction of electrons and holes (Coulomb blockade) in such a device is utilized to achieve regulated pumping of the active region with a single electron and a single hole.

Detection of single photons carrying quantum information need to be detected with high quantum efficiency. Current technology to detect single photons is to use either a photomultiplier tube (PMT) or a Si avalanche photodiode (APD) in Geiger mode. However, the quantum efficiency of PMT's are generally limited to below 15%. Si APD's can detect photons with high ($\sim$ 80%) quantum efficiency and relatively good time resolution ($\sim$ 50 ns), but have large excess noise factors. This results in compromise between quantum efficiency and low background dark count.

In this work we report some progress in the field of *single photonics*, where we attempt to fabricate good source and detector for single photons.

The first effort is the fabrication of single photon turnstile device, which is the source for photons with well-defined generation time. This is the proposed mesoscopic p-n junction that is pumped with resonant tunneling [5]. First, p-n junction was carefully designed and grown by molecular beam epitaxy of GaAs/AlGaAs multilayers. Then, we fabricated sub-micron scale devices by

electron beam lithography and electron cyclotron resonance reactive ion etching (ECR-RIE). We have observed light emission from these mesoscopic devices down to 0.6 μm in diameter. Some of the devices show sharp discrete peaks in the resonant tunneling current and associated photon output, strongly indicating that the inhomogeneous broadening is resolved. Such photon emission from "quantum dots" produced by local potential fluctuations could be utilized to demonstrate anti-bunching of photons in time domain.

The second effort is to come up with an alternative device in photon counting. We characterize relatively new devices used for photon counting, called Si solid state photomultipliers. They utilize impact ionization of electrons from shallow impurity band to conduction band as the multiplication process. The quantum efficiency of these detectors are reported to be close to those of Si APD's, and the intrinsic time resolution can be much better than Si APD's. The biggest advantage of this device is its low excess noise factor, which results in narrow dispersion in pulse height distribution. We have measured the excess noise factor of this device to be very close to unity, implying that the avalanche multiplication process in these devices is essentially noise-free [6]. We have also demonstrated that the fast avalanche multiplication process in these devices can be utilized to achieve photon counting with 3 ns time resolution. This is more than an order of magnitude better than what can be achieved with Si APD's. This detector also proves to be a strong candidate in loop-hole-free test of Bell's inequality using entangled photon states generated by parametric down-conversion process.

References

[1] For review, see T. P. Spiller, *Proc. of IEEE*, **84**, 1719 (1996) and references therein.

[2] C. H. Bennett and G. Brassard, *Sigact News*, **20**, 78 (1989).

[3] J. Breguet, A. Muller and N. Gisin, *J. Mod. Opt.*, **41**, 2405 (1994).

[4] Q. A. Turchette, C. J. Hood, W. Lange, H. Mabuchi, and H. J. Kimble, *Phys. Rev. Lett.*, **75**, 4710 (1995).

[5] A. Imamoglu and Y. Yamamoto, *Phys. Rev. Lett.*, **72**, 210 (1994).

[6] J. Kim, Y. Yamamoto, and H. H. Hogue, to be published in *Appl. Phys. Lett.*

Dynamics of Semiconductor Microcavity Modes in Femtosecond Time Scale.

Yu.E. Lozovik, A.L. Dobryakov, V.M. Farztdinov, S.A. Kovalenko*,
Yu.A. Matveets, E.A. Vinogradov.

Institute of Spectroscopy, Russian Academy of Sciences, 142092 Troitsk, Moscow region.
**Max-Planck-Institut fur Biophysikalishe Chemie, P.O.Box 2841, D-3400 Gottingen, Germany.*

Dynamics of semiconductor microcavity modes in ZnSe-metal structure was investigated by femtosecond pump-supercontinuum probe spectroscopy in wide spectral region 300-800 nm. The powerful laser pump pulse excites electrons of metal (i.e. boundary of the microcavity) and of ZnSe layer (by two-photon absorption and absorbtion of second-harmonics generated photon). Photoinduced changes of dielectric function of metal transform the boundary condition. It leads to shift of frequencies of cavity modes to red region of spectrum. Another contribution to change of boundary condition is connected with tunneling of excited electrons through Schottky electron barrier into ZnSe layer. The generation of coherent phonon oscillations (LO-phonon mode 250 cm^{-1} and TO-phonon mode 200 cm^{-1}) in ZnSe was detected.

Nonlinear optical nanostructures now attract growing attention not only because they provide interesting phenomena for the study of nonequilibrium systems but because they constitute the basis of numerous promising phenomena suitable to all-optical signal-processing schemes. There is considerable interest in understanding of nonlinear optics of

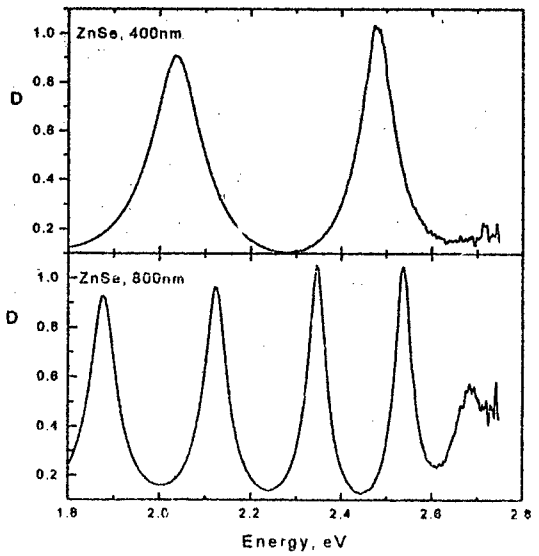

Fig 1. Linear response of ZnSe film on C-quartz substrate

thin film planar resonator structure (nonlinear Fabry-Perrot resonator). These structures are the simplest physical system to consider change of boundary conditions of microcavity during propagation of ultrashort laser pulses through planar resonator structure and to elucidate the role of nonlinear processes and coherent interaction. The system is also perspective for study of nonstationary Casimir effect, i.e. parametric photons and other excitations generation due to laser pulse induced abrupt change of the boundary (see [1] and references therein).

ZnSe film with thickness 400 and 800 nm on the metal Cr-quartz substrate (as planar resonator structure) was used to study dynamics of semiconductor cavity modes in femtosecond time scale. By femtosecond pump-supercontinuum probe spectroscopy the excitation and relaxation of semiconductor cavity modes of ZnSe film were investigated. The excitation with photon energy $\hbar\omega_{pump}$= 2.34 eV at room temperature was conducted by optical pulses of 50 fs duration and with pulses frequency repetition ~ 2 Hz. The photoinduced response (difference reflectivity ΔR) was studied in wide spectral region $\hbar\omega_{probe}$=1.6-3.2 eV by supercontinuum probe pulses with delays from -0.2 to +3 ps with time step 7 fs.

ZnSe film on the metal Cr-quartz substrate is planar resonator structure. The typical linear response of this structure is shown in Fig.1. (for ZnSe film with thickness 400 and 800 nm on the metal Cr-quartz substrate). Note that ZnSe film is transparent in the frequency region of pump $\hbar\omega_{pump}$= 2.34 eV and only the two-photon absorption is possible (energy gap for ZnSe is 2.8 eV).

There are different time scales of processes under investigation. One of them is connected with the excitation of electrons of metal (i.e. boundary of the microcavity). During the time of order pulse duration powerful pump pulse create the nonequilibrium electron distribution. It leads to the ultrafast change of the effective boundary conditions on ZnSe-metal interface for eigenmodes of microcavity. Another contribution to changes of boundary conditions is connected with tunneling of nonequlibrium excited electrons under (and partly through) Schottky electron barrier into ZnSe layer. The typical value of this barrier is ~ 1 eV. At the time delays of the order of pulse duration electrons penetrates in ZnSe layer on depth of hundreds Å. By electron-electron interaction the quasiequilibrium state is established. The typical time of establishment of quasiequilibrium electron state is the time of order of tenth fs. We can consider that electron

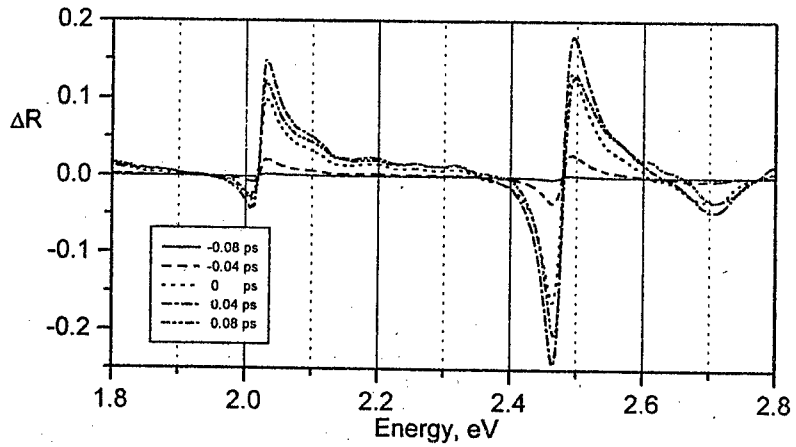

Fig2.a. Temporal evolution of difference reflectivity of ZnSe (400 nm) film on Cr - quartz substrate from -80 fs to 80 fs with time delay step dt=40 fs.

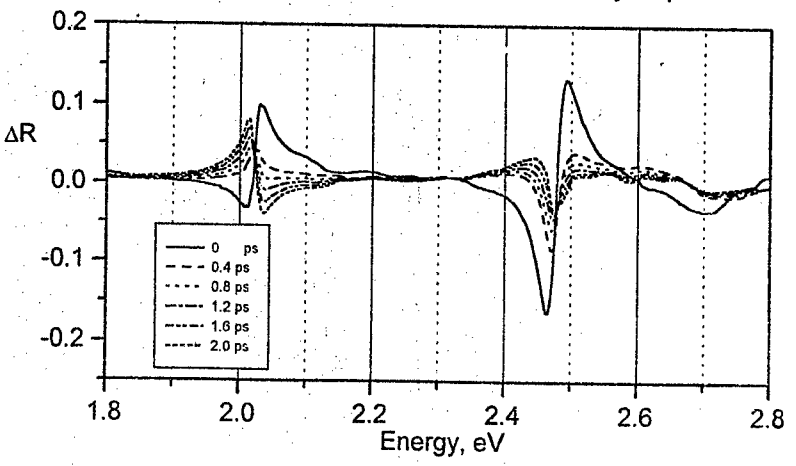

Fig2.b. Temporal evolution of difference reflectivity of ZnSe (400 nm) film on Cr - quartz substrate from 0 ps to 2 ps with time delay step dt=0.40 ps.

temperature is 10^3 K at this time and so the Schottky barrier becomes inpenetrable for most of quasiequilibrium electrons after that time. Photoinduced changes of dielectric function transform the boundary condition. It leads to observable shift of frequencies of cavity modes to red region of spectrum (see Fig.2, Fig3).

Another contribution (during the time of order pulse duration) is connected with two-photon absorption. It is interesting to note that it is possible the generation of second harmonic on metal interface and one-quanta absorption from this generation may be essential too.

The spectral dependence of two-photon absorption is directly connected with semiconductor cavity modes (and repeat its linear response, see Fig.1.). The contribution from two-photon adsorption changes the real part of dielectric function. This change of dielectric function of ZnSe film leads to the modification of difference reflectivity and quality agree with experimental signal (see Fig2, Fig3). It is interesting that the time of establishment of the microcavity modes τ_c (of the order path time of the microcavity) may be largerthan the time of observed difference spectra evolution in the time region considered above. This fact may be important for the observation of nonstationary Casimir effect [1].

The last time scale is connected with electron-phonon interaction and heating of lattice by electron system. The changes of dielectric function due to these process (after the time of order of 1 ps) lead to large shift of cavity modes and to establishment of new spectral position of these modes.

The generation of coherent phonon oscillations in ZnSe was detected (LO-phonon mode at 250 cm^{-1} and TO-phonon mode at 200 cm^{-1}). There are different possibilities for mechanism of this generation. One of them is connected with parametric pumping due to nonstationary Casimir effect. Another ones may be connected with laser pulse stimulated Raman scattering and simultaneous by with local electric field near ZnSe-metal interface due to tunneling of electrons through Schottky electron barrier. It is interesting to note that the spectral dependence of amplitude of these oscillation is directly connected with linear response.

In conclusion note that femtosecond laser pulses make it possible to manipulate of the boundary conditions for microcavity modes and to modify the temporal, spectral and spatial properties of the structures. This is promissing for possible applications of the method used for

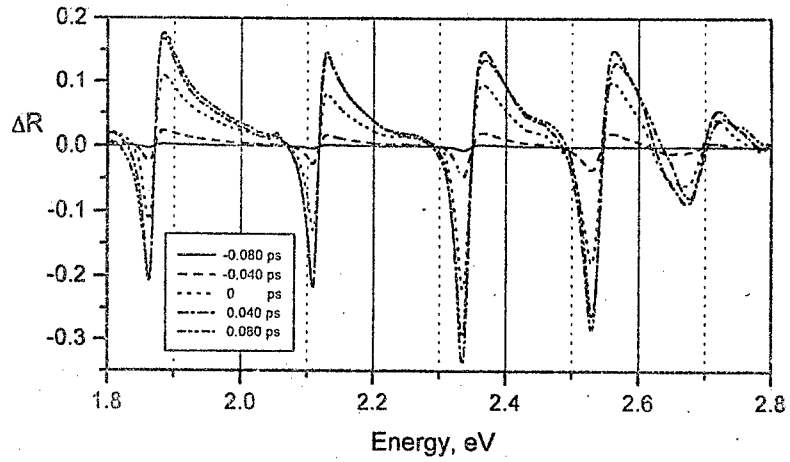

Fig.3.a. Temporal evolution of difference reflectivity of ZnSe (800 nm) film on Cr-quartz substrate from -80 fs to 80 fs with time delay step dt=40 fs.

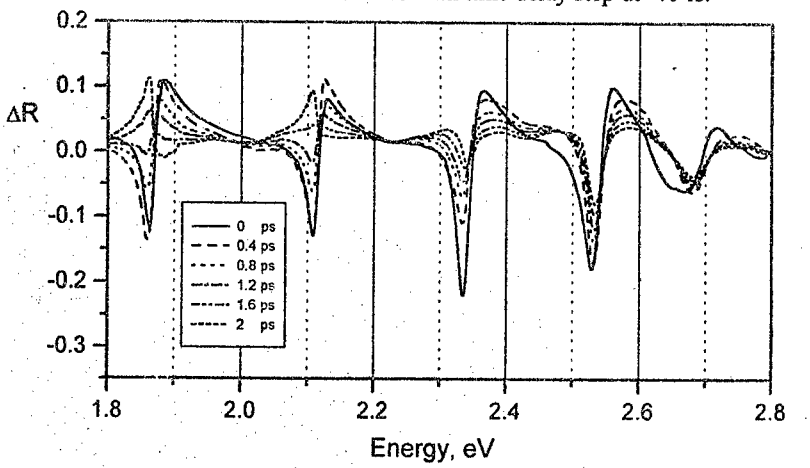

Fig.3.b. Temporal evolution of difference reflectivity of ZnSe (800 nm) film on Cr-quartz substrate from 0 ps to 2 ps with time delay step dt=0.4 ps.

all-optical processing. Particularly femtosecond spectroscopy of nanostructures permits to investigate the processes of parametric pumping of cavity modes, coherent phonon generation etc.

The work is supported by Programm " Physics of Nanostructures", Russian Foundation of Basic Research and INTAS.

1. Yu.E.Lozovik, V.G.Tsvetus, E.A.Vinogradov, *Parametric Excitation of Vacuum by Use of Femtosecond Laser Pulses*, Physica Scripta, **52**, 184-190, 1995.

Triple magnetopolarons in quantum wells

V. I. Belitsky† and M. Cardona‡, A. Cantarero‡,
L. I. Korovin§ and I. G. Lang§, and S. T. Pavlov¶
† Max Planck Institut für Festkörperforschung, Heisenbergstrasse 1, D-70569 Stuttgart, Germany
‡ Departamento de Física Aplicada, Universidad de Valencia, E-46100 Valencia, Spain
§ A. F. Ioffe Physico-Technical Institute, 194021 St. Petersburg, Russia
¶ P. N. Lebedev Physical Institute, 117924 Moscow, Russia

During the last years, a new wave of attention to the Johnson-Larsen effect[1] has been stimulated by investigations of low-dimensional structures where both electronic and vibrational excitations show size-quantized features.

Resonant coupling between pure electronic and mixed electron-phonon states lifts the degeneracy at all crossing points of the dispersion branches for bare excitations. As a result, double and triple polaron splittings appear in the vicinity of points where two and three branches cross at $\omega_{eH} = \omega_{LO}$, respectively. Although the double magnetopolaron has been investigated in detail for both bulk and low-dimensional structures, the crossing point of three energy branches, located higher in energy, has not received much attention.[2]

Schematically, the triple magnetopolaron (TMP) wave function can be written as

$$\Theta_p^{(3)} = a_{0p}^{(3)}\Psi_2\psi_0 + a_{1p}^{(3)}\Psi_1\psi_1 + a_{2p}^{(3)}\Psi_0\psi_2, \tag{1}$$

where Ψ_n are electron wave functions with the Landau number $n = 0, 1, 2$, ψ_N the wave function of the phonon subsystem with $N = 0$, 1 and 2 LO-phonons, respectively. The TMP wave function Θ is characterized by an index $p = a$, b, and c that corresponds to the splitting of the triply degenerate state into three energy levels $E_a^{(3)}$, $E_b^{(3)}$, and $E_c^{(3)}$.

We separate the electron-phonon interaction into two parts as

$$V = V^{res} + \Delta V\,, \tag{2}$$

and assume that V^{res} has non-zero matrix elements only for resonant transitions between states which become degenerate, i.e., between the states (n, N) and $(n-1, N+1)$ when $\hbar\omega_{eH} = \hbar\omega_{LO}$. Close to the resonance $\hbar\omega_{eH} = \hbar\omega_{LO}$ there are no other states but polarons. The residual interaction ΔV is a small perturbation which can give transitions between polaron states accompanied by emission of one LO-phonon. Note that the separation of the interaction into two parts is relevant only in the vicinity of the resonance $\omega_{eH} \sim \omega_{LO}$ where the resonant part V^{res} cannot be treated as a perturbation.

The qualitative understanding of the TMP can be achieved with the help of a schematic picture for the case of exact resonance $\omega_{eH} = \omega_{LO}$. This corresponds to the crossing point of three bare energy branches $(n = 2,\ N = 0)$, $(n = 1,\ N = 1)$, and $(n = 0,\ N = 2)$. Let us approximate the matrix elements for the resonant part of the electron-phonon interaction by two constants M_{10} and M_{21} which are proportional to the square root of the coupling constant and correspond, respectively, to the phonon-assisted transitions $n = 1 \to n = 0$ and $n = 2 \to n = 1$. One sees that the following matrix equation may be used to visualize the key features of the TMP:

$$\begin{pmatrix} E_0 & M_{21} & 0 \\ M_{21}^* & E_0 & M_{10} \\ 0 & M_{10}^* & E_0 \end{pmatrix} \times \begin{pmatrix} a_1 \\ a_2 \\ a_3 \end{pmatrix} = E \times \begin{pmatrix} a_1 \\ a_2 \\ a_3 \end{pmatrix}. \tag{3}$$

where we put $E_0 = E_1 = E_2$ for the energy of the triply degenerate unperturbed state.

The three eigenvalues of Eq. (3) are $E_\pm = E_0 \pm \Delta/2$ and $E = E_0$, with $\Delta = 2\sqrt{|M_{21}|^2 + |M_{10}|^2}$. They correspond to the eigenvectors

$$\left(\frac{M_{21}}{\sqrt{2}\Delta}, \pm\frac{1}{\sqrt{2}}, \frac{M_{10}^*}{\sqrt{2}\Delta}\right), \quad \left(\frac{M_{10}}{\Delta}, 0, -\frac{M_{21}^*}{\Delta}\right). \tag{4}$$

Three important conclusions can be drawn from this qualitative description. First, there is one unshifted state $E = E_0$ of the resonant TMP which does not have the component $n = 1$, $N = 1$. Second, the TMP wave function is a mixture of bare states weighted with coefficients which are independent of the coupling constant of electron-phonon interaction as it is seen from Eq. (4). Finally, the energy splitting Δ is proportional to the square root of the electron-phonon coupling constant. Below we give the general equations for the TMP wave functions and energies which confirm qualitatively this simplistic picture when $\omega_{eH} = \omega_{LO}$.

To obtain the equations for the TMP wave function and eigenenergies, we take the interaction V of electrons with confined phonons to have the general form

$$V = \sum_\nu \left[C_\nu(\mathbf{r}_\perp, z)b_\nu + C_\nu^*(\mathbf{r}_\perp, z)b_\nu^+\right], \tag{5}$$

$$C_\nu(\mathbf{r}_\perp, z) = C_\nu e^{i\mathbf{q}_\perp \mathbf{r}_\perp}\xi_\nu(z), \tag{6}$$

$\nu \equiv (\mathbf{q}_\perp, j)$ labels the phonon from branch j with the in-plane wave vector $\mathbf{q}_\perp$, $\mathbf{r}_\perp$ is the in-plane co-ordinate and $C_\nu \sim \alpha^{1/2}$, where α is the Fröhlich coupling constant.

Applying a procedure similar to that of Ref. [3] we find that the TMP wave function can be written as

$$\Theta_{k_y}(x, y, z, Y) = \mathcal{C}\left(\Theta_{k_y 0} + \Theta_{k_y 1} + \Theta_{k_y 2}\right), \tag{7}$$

where

$$\Theta_{k_y 0}(x, y, z, Y) = \Psi_{2k_y}(x, y, z)\psi_{ph0}(Y), \tag{8}$$

$$\Theta_{k_y 1}(x, y, z, Y) = (E - E_0)\sum_\nu \Phi(\nu)\exp\left[ia_H^2 q_x (k_y - q_y/2)\right]\Psi_{1k_y - q_y}(x, y, z)\psi_{ph\nu}(Y), \tag{9}$$

$$\begin{aligned}\Theta_{k_y 2}(x, y, z, Y) &= \frac{E - E_0}{E - E_2}\sum_{\nu_1\nu_2}\Phi(\nu_1)\exp\left\{ia_H^2\left[q_{1x}(k_y - q_{1y}/2) + q_{2x}(k_y - q_{1y} - q_{2y}/2)\right]\right\} \\ &\times\ U_{10}^*(\nu_2)\Psi_{0k_y - q_{1y} - q_{2y}}(x, y, z)\psi_{ph\nu_1\nu_2}(Y),\end{aligned} \tag{10}$$

$E_0 = (5/2)\hbar\omega_{eH}$, $E_1 = (3/2)\hbar\omega_{eH} + \hbar\omega_{LO}$, $E_2 = (1/2)\hbar\omega_{eH} + 2\hbar\omega_{LO}$, and $\mathcal{C}$ is the normalization constant. The function $\Phi(\nu)$ and the TMP energy E have to be found from two coupled equations

$$\Phi(\nu)\left[(E - E_1)(E - E_2) - A_{10}^2\right] - \frac{E - E_2}{E - E_0}U_{21}^*(\nu) - \sum_{\nu_1} R(\nu, \nu_1)\Phi(\nu_1) = 0, \tag{11}$$

$$(E - E_1)(E - E_2) - A_{10}^2 - \frac{E - E_2}{E - E_0}A_{21}^2 - \sum_{\nu\nu_1} U_{21}(\nu)R(\nu, \nu_1)\Phi(\nu_1) = 0, \tag{12}$$

where the matrix element

$$U_{nn'}^*(\nu) = C_\nu^* M^*(\nu)K_{nn'}\left(a_H q_x - a_H q_z\right), \tag{13}$$

$$M(\nu) = \int_{-\infty}^{\infty} dz \xi_\nu(z) \varphi_m^2(z) \,, \tag{14}$$

$$\begin{aligned} K_{nn'}(\mathbf{p}) &= K_{nn'}(p_x, p_y) = \left[\frac{\min(n!, n'!)}{\max(n!, n'!)}\right]^{1/2} i^{|n-n'|} \exp\left(-\frac{p^2}{4}\right) \left(\frac{p}{\sqrt{2}}\right)^{|n-n'|} \\ &\times \exp\left(i(\phi - \pi/2)(n-n')\right) L_{\min(n,n')}^{|n-n'|}(p^2/2) \,, \end{aligned} \tag{15}$$

$\mathbf{p}$ is a two dimensional vector, $p = \sqrt{p_x^2 + p_y^2}$, $\phi = \arctan(p_y/p_x)$, and $L_{n'}^{n}(t)$ is the Laguerre polynomial. The function $R(\nu, \nu')$, related to diagrams with crossing phonon lines,[4] and A_{ij} are

$$A_{ij}^2 = \sum_\nu |U_{ij}(\nu)|^2 \;, \quad R(\nu, \nu_1) = U_{10}(\nu_1) U_{10}^*(\nu) \exp\left(i a_H^2 [\mathbf{q}_1 \times \mathbf{q}]_z\right) \,. \tag{16}$$

When three energy branches cross at a certain energy the interaction leads to the splitting into three energy levels. From here on, the corresponding TMP wave functions Θ, their energies E, and the coefficients $\Phi(\nu)$ and C are labeled with the index p.

Close to the resonance $|\omega_{eH} - \omega_{LO}| \sim \Delta$, where Δ is the TMP splitting at the resonance point, the TMP wave functions $\Theta_{k_y,p}$ and the energies E_p can be found by iterations with respect to $R(\nu, \nu_1)$ under the assumption that the contribution of terms with R in Eqs. (11) and (12) is relatively small. However, there is no small parameter in the iteration procedure and the smallness of terms with R is only numerical.

We proceed to consider the TMP under conditions of exact resonance $\omega_{eH} = \omega_{LO}$. In this case, $E_0 = E_1 = E_2$. We thus use the notation E_0 for all three energies and provide $\Phi_p(\nu)$, E_p, and $\Theta_{k_y,p}$ with a superscript res. Under condition $E_p \neq E_0$, the Eq. (12) for the TMP energies reduces to

$$(E_p^{res} - E_0)^2 - A_{10}^2 - A_{21}^2 - \sum_{\nu\nu_1} U_{21}(\nu) R(\nu, \nu_1) \Phi_p^{res}(\nu_1) = 0 \tag{17}$$

and Eq. (11) for the function $\Phi_p^{res}(\nu)$ becomes

$$\Phi_p^{res}(\nu) \left[(E_p^{res} - E_0)^2 - A_{10}^2\right] - U_{21}^*(\nu) - \sum_{\nu_1} R(\nu, \nu_1) \Phi_p^{res}(\nu_1) = 0 \,. \tag{18}$$

From Eq. (17) it is clear that there are only two solutions $E_p^{res} = E_0 \pm \Delta/2$, which correspond to levels $p = a$ (plus) and $p = c$ (minus). It follows from Eq. (18) that

$$\Phi_a^{res}(\nu) = \Phi_c^{res}(\nu) \equiv \Phi^{res}(\nu) \,. \tag{19}$$

We have two coupled equations for Δ and $\Phi^{res}(\nu)$

$$\Phi^{res}(\nu) \left[(\Delta/2)^2 - A_{10}^2\right] - U_{21}^*(\nu) - \sum_{\nu_1} R(\nu, \nu_1) \Phi^{res}(\nu_1) = 0 \,, \tag{20}$$

$$(\Delta/2)^2 - A_{10}^2 - A_{21}^2 - \sum_{\nu\nu_1} U_{21}(\nu) R(\nu, \nu_1) \Phi^{res}(\nu_1) = 0 \,. \tag{21}$$

According to Eqs. (7)-(10), the TMP wave functions for levels $p = a, c$ have the form of

$$\Theta_{k_y p}^{res} = \frac{1}{\sqrt{2}(\Delta/2)} \frac{\Theta_{k_y 0} + \Theta_{k_y 1p}^{res} + \Theta_{k_y 2}^{res}}{\sqrt{\sum_\nu \Phi^{res}(\nu) \Phi^{res}(\nu)}} \,, \tag{22}$$

where the function $\Theta_{k_y 0}$ has been defined in Eq. (8) and the function $\Theta^{res}_{k_y 1p}$ depends on p and is given by

$$\Theta^{res}_{k_y 1p} = \pm\frac{\Delta}{2}\sum_{\nu}\Phi^{res}(\nu)\exp\left[ia_H^2 q_x\,(k_y - q_y/2)\right]\Psi_{1k_y-q_y}(x,y,z)\psi_{ph\nu}(Y)\,, \tag{23}$$

where plus and minus correspond to $p = a$ and $p = c$, respectively. The function $\Theta^{res}_{k_y 2}$ is independent of p and can be written as

$$\Theta^{res}_{k_y 2} = \sum_{\nu_1\nu_2}\Phi^{res}(\nu_1)\exp\left\{ia_H^2\left[q_{1x}(k_y - q_{1y}/2) + q_{2x}(k_y - q_{1y} - q_{2y}/2)\right]\right\} \times U^*_{10}(\nu_2)\Psi_{0k_y-q_{1y}-q_{2y}}(x,y,z)\psi_{ph\nu_1\nu_2}(Y)\,. \tag{24}$$

Equations (20) and (21) can be solved by iterations with respect to R. In the lowest order we find

$$\Delta_0 = 2\sqrt{A_{10}^2 + A_{21}^2},\ \Phi_0(\nu) = \frac{U^*_{21}(\nu)}{\sum_\nu |U_{21}(\nu)|^2}\,. \tag{25}$$

Since $\Phi_0(\nu) \sim U^{-1}$ and $\Delta \sim U$, we conclude that all three functions $\Theta_{k_y 0}$, $\Theta^{res}_{k_y 1p}$, and $\Theta^{res}_{k_y 2}$ defined above are of the same order of magnitude and $\sim \alpha^0$. The splitting $\Delta \sim \alpha^{1/2}$ coincides with the splitting of the double magnetopolaron. The same dependences on the coupling constant have already been found from the qualitative picture of Eq. (4). Note that in a bulk semiconductor $\Delta \sim \alpha^{2/3}$.

Since Eqs. (17) and (18) only allow two symmetric solutions with finite deviation of energy from the unperturbed value E_0, it is clear that the energy of the third level *coincides* with this unperturbed value so that

$$E^{res}_b = E_0\,, \tag{26}$$

a result which had already been obtained heuristically from Eq. (3). It can be shown[4] also that the wave function $\Theta^{res}_{k_y b}(x,y,z,Y)$ of the unshifted state does not have component $n = 1$, $N = 1$ (see also Eq. (4)).

To summarize, the equations for eigenstates and eigenenergies of the TMP in quantum well structures have been derived in a general form. The case which involves exact resonance has been analyzed in more detail. Our theory of the triple polaron is relevant for the case when the deviation from equidistant energy separation of the three lower Landau levels is smaller than the triple polaron splitting.

References

[1] E. J. Johnson, D. M. Larsen, Phys. Rev. Letters **16**, 655 (1966).

[2] L. I. Korovin, Fiz. Tverd. Tela **13**, 842 (1971) [Soviet Phys.: Solid State **13**, 695 (1971)].

[3] I. G. Lang, V. I. Belitsky, A. Cantarero, L. I. Korovin, S. T. Pavlov, and M. Cardona, Phys. Rev. **B 54**, 17 768 (1996).

[4] I. G. Lang, V. I. Belitsky, A. Cantarero, L. I. Korovin, S. T. Pavlov, and M. Cardona, submitted to Phys. Rev. **B**.

Effect of the near-QW band bending due to QW charging on confinement of light holes in the InGaAs/GaAs strained quantum well

D.O.Filatov, I.A.Karpovich, M.V.Stepikhova

University of Nizhnii Novgorod, 23/2 Gagarin Ave, Nizhnii Novgorod 603600 Russia

W.Jantsch

Institut fur Halbleiterphysik, Johannes Kepler Universitat Linz, A-4040, Linz, Austria

In the last few years a lot of work was devoted to the study of the band structure of strained quantum well structures (QWSs) of GaAs/InGaAs which are promising for their opto-electronic applications [1]. One of the features of the size quantization spectrum in these QWSs is the strong splitting of the light hole and the heavy hole subbands due to the large GaAs/InAs lattice mismatch.

Usually the light hole subband in GaAs/InGaAs QWs is considered to be expelled out of the QW due to elastic strain so that only heavy holes are confined in the QW [2]. However, lately there appeared several papers where light hole confinement in QWs was observed experimentally [3]. Results of theoretical calculations of the GaAs/InGaAs QW's band structure are also contradictory and predict the presence or absence of the light hole ground state level in the QW depending on the band structure parameters which the model is based on. The critical parameter is the relative conduction band (CB) discontinuity Q which also determines the valence band (VB) confining potential.

The purpose of the present study is the theoretical and experimental investigation of another factor which can cause light hole confinement. It is well known [4] that an InGaAs QW built into n-GaAs usually is negatively charged which causes an additional barrier for holes which possibly may lead to confinement of the light holes.

Our theoretical study was based on the numerical solution of the one-dimensional Schrodinger equation in the effective mass approximation, taking into account the additional near-QW band bending due to charging of the QW. The CB and VB confining potentials were found from Poisson's equation treating the QW as a charged plane. The QW band structure parameters involved in the calculations, such as the InGaAs band gap and band discontinuities were calculated in dependence of the QW width and the InGaAs alloy composition taking into account the elastic strain [4].

The results of the modelling show that in the case when the QW is situated in the quasi-neutral region (QNR) of a structure the light hole ground state is always a confined one whatever the relative band discontinuity Q, and that the main contribution to the confining potential for the light holes is due to the Coulomb potential of the QW charge. It has been found that the band bending does not significantly affect the transition energies but it increases the localization of the light hole wavefunction sufficiently and thus the overlap integral of the electron and light hole wavefunction. For the square well approximation the value of the electron-light hole overlap integral is approximately 0.3, while the band bending increases it up to 0.9.

For the experiment a GaAs/InGaAs QWS with a single QW built in the QNR of the structure was grown by MOVPE on an (001) conducting n-GaAs substrate. The QW width was 4.1 nm, the In content was 0.35.

The structures were characterized by photocurrent (PC) spectroscopy and C-V measurements of Schottky barrier diodes with semi-transparent Al Schottky contacts, 500 mkm in diameter. All measurements were performed at room temperature.

In the PC spectra two peaks are observed which we attribute to the electron-heavy hole (e-hh) and to the electron-light hole (e-lh) exciton optical transitions in the QW. Identification of e-lh transition was performed by measurement of the polarization dependence of the photosensitivity (PS) in the e–hh and the e–lh absorption bands, exciting the Schottky photodiode by linearly polarized light. The structure was cleaved so that the cleaved surface crosses the Al contact. The linearly polarized incident light was directed perpendicularly to the cleaved surface so that it propagates inside the structure almost parallel to the QW plane. It is well known [5] that at the absorption edge the e–hh transition is allowed when the electric field in the incident linearly polarized electromagnetic wave E is parallel to the QW plane, but this transition is forbidden if E is perpendicular to the QW plane.

For the e-hh transition, 100% polarization dependence was observed while for the e-lh transition it is week. This allows to identify the e-lh and e-hh transitions in the PC spectrum.

Studying the dependence of the photosensitivity in the e-hh and the e-lh absorption bands on the reverse bias V it was found that when the QW is situated in the QNR both the e-hh and the e-lh PSs are increasing with V because the photoexcited excess carriers escape from the QW by thermal emission. The quantum efficiency of the light absorbed by the QW is limited by the emission rate of the minority carriers (holes).

At the beginning of depletion of the QW, a step-like decreasing of the e-lh PS occurs as compared to the e-hh PS. This was explained by the following. In the depletion process, the electric field in the QW increases stepwise [4]. Because of the heterointerface confining potential for the light holes, the light hole state becomes non-stationary because of leakage of the wavefunction into the continuous states through the triangular barrier. The latter is decreased by the field. So we observe transitions from the continuous states of the light hole band to the confined electron states.

After depletion of the QW the dependence of the PS on V saturates. This we attribute to a change in the carrier escape mechanism: when the QW is in the electric field of the Schottky barrier the main escape mechanism is tunnelling through the triangular barrier. In this case, the PS is limited by the tunnelling rate of electrons.

In conclusion, the PC spectra of the Schottky barrier diodes with a QW built in the quasi-neutral region of the structure on the reverse bias show together with the theoretical consideration of the effect of the QW charging on the QW energetic spectrum and wavefunctions that confinement of light holes in the strained InGaAs/GaAs QWs is caused mostly by the additional near-QW band bending due to QW charging.

When the QW is situated in the depleted region of the Schottky barrier only the transitions from the continuous states of the light hole band to the confined electron states can be observed because of leakage of the light hole wavefunction into the continuous states through the triangular barrier which is decreased by the electric field.

The authors are grateful to B.N.Zvonkov and E.R.Lin'kova (Epitaxial Technology Group, Physical-Technical Research Institute of University of Nizhnii Novgorod) for growing the

structure for investigations and for C–V measurements respectively and to V.Ya.Aleshkin (Institute of Physics of Microstructures, Russian Academy of Sciences) for fruitful discussions.

The work was supported by International Center for Advanced Studies in Nizhnii Novgorod (grant 96–24–02).

1. C.Weisbuch, B.Vinter. Quantum Semiconductor Structures: Fundamentals and Applications. Acad. Press, San Diego, 1991.
2. G.Ji, D.Huang, U.K.Reddy, T.S.Henderson, R.Houdre, H.Morkoc. *J.Appl.Phys.* **62**, 3366 (1987).
3. X.Marie, J.Barrau, B.Brousseau, Th.Amand, M.Brousseau, E.V.K.Rao, F.Alexandre. *J.Appl. Phys.* **69**, 812 (1991).
4. V.Ya.Aleshkin, E.V.Demidov, B.N.Zvonkov, A.Murel, Yu.A.Romanov. *Fiz. Techn. Poluprovod.* **25**, 1047 (1991).
5. S.Jorda, V.Rossler. *Superlattices & Microstruct.* **8**, 481 (1990).

PEKAR POLARON IN QUANTUM WELLS, WIRES AND DOTS

I.P.Ipatova, A.Yu.Maslov, O.V.Proshina.

A.F.Ioffe Physical Technical Institute, St.Petersburg 194021, Russia

Strong interaction of an electron with longitudinal optical phonons in ionic crystals results in the electron self-trapping by the polarization field of the lattice vibrations, that is in Pekar polaron [1]. It is assumed in [1] that polaron is a macroscopic object with radius a_0 which is larger than the lattice parameter.

This paper deals with the theory of Pekar polarons in quantum wells, wires and dots. It is assumed that the characteristic size of each nanostructure L is smaller than polaron radius a_0

$$L < a_0. \tag{1}$$

Equation (1) means that the separation between levels of size quantization is larger than the polaron binding energy

$$\Delta E > \frac{\hbar^2}{ma_0^2}. \tag{2}$$

Therefore the motion of an electron in the nanostructure potential is fast and the polaron motion is slow. Unequality (2) allows to apply the adiabatic approximation to solution of polaron problem in nanostructures.

a. Quantum well.

Schrödinger equation for an electron in a quantum well with the strong electron-phonon interaction has a form

$$-\frac{\hbar^2}{2m}\triangle\Psi(\mathbf{r}) + V(z)\Psi(\mathbf{r}) + e\phi(\mathbf{r})\Psi(\mathbf{r}) + \left(\frac{\varepsilon}{8\pi}\int d^3r(\nabla\phi(\mathbf{r}))^2\right)\Psi(\mathbf{r}) = E\Psi(\mathbf{r}). \tag{3}$$

Here $V(z)$ is the one-dimensional quantum well potential, $\phi(\mathbf{r})$ in the third term is the potential of the polarization field induced by longitudinal optical phonons. The last term on the left-hand side of Eq.(3) is the energy of the electric field $\mathbf{F} = -\nabla\phi(\mathbf{r})$. Here m is the effective mass of carrier and ε is the dielectric permittivity which takes into account the inertial part of the polarization, $1/\varepsilon = 1/\varepsilon_\infty - 1/\varepsilon_0$, $\varepsilon_\infty, \varepsilon_0$ being high frequency and static permittivities, respectively.

In solving the Eq. (3), it is considered that both the energy $E_n(p_x, p_y)$ and the wave function $\Psi_n(\mathbf{r})$ of the electron on the nth level of size-quantization in the infinite quantum well are known from quantum mechanics

$$\Psi_n(\mathbf{r}) = \exp[i/\hbar(p_x x + p_y y)]\psi_n(z). \tag{4}$$

One can find the polaron solution of Eq. (3) representing the wave function $\Psi(\mathbf{r})$ as an expansion on the wave functions (4)

$$\Psi(\mathbf{r}) = \sum_{p_x,p_y,n} a_n(p_x,p_y)\exp[i/\hbar(p_x x + p_y y)]\psi_n(z) \tag{5}$$

with unknown coefficients $a_n(p_x,p_y)$. The substitution of wave function (5) in Eq. (3) results in equation for a_n

$$[E_n(p_x,p_y) - E]a_n(p_x,p_y) +$$

$$+e\sum_{p'_x,p'_y,n'} a_{n'}(p'_x,p'_y)\int dxdy\phi_{nn'}(x,y)\exp\Big[i/\hbar[(p_x-p'_x)x+(p_y-p'_y)y]\Big] = 0 \tag{6}$$

where

$$\phi_{nn'}(x,y) = \int dz\psi_n^*(z)\psi_{n'}(z)\phi(\mathbf{r}). \tag{7}$$

Unequality (2) allows to neglect in Eq. (6) by nondiagonal matrix elements between the levels of size quantization. We find finally the independent equations for the electron motion on each level of the size-quantization

$$\Big[E_n(p_x,p_y) - E\Big]a_n(p_x,p_y) +$$

$$+e\sum_{p'_x,p'_y} a_n(p'_x,p'_y)\int dxdy\phi_{nn}(x,y)\exp\Big[i/\hbar[(p_x-p'_x)x+(p_y-p'_y)y]\Big] = 0. \tag{8}$$

Here

$$\phi_{nn}(x,y) = \int dz\mid\psi_n(z)\mid^2\phi(\mathbf{r}). \tag{9}$$

It is conventional to make the Fourier transformation into coordinate representation and to find from Eq. (8)

$$-\frac{\hbar^2}{2m}\Big(\frac{d^2}{dx^2}+\frac{d^2}{dy^2}\Big)\chi_n(x,y) - e\phi_{nn}(x,y)\chi_n(x,y) =$$

$$= \Big(E - E_n(0) - \frac{\varepsilon}{8\pi}\int d^3r(\nabla\phi(\mathbf{r}))^2\Big)\chi_n(x,y) \tag{10}$$

where the notation is introduced

$$\chi_n(x,y) = \sum_{p_x,p_y} a_n(p_x,p_y)\exp[i/\hbar(p_x x + p_y y)]. \tag{11}$$

The wave function $\chi_n(x,y)$ is the slow wave function of two-dimensional polaron motion on the nth level of size-quantization.

Calculating the average energy and making the variational procedure with respect to the polarization potential $\phi(\mathbf{r})$, one can find the effective polarization potential $\phi_{nn}(x,y)$ which corresponds to the lowest energy $< E >$ for nth level of quantization

$$\phi_{nn}(x,y) = \frac{e}{2\varepsilon}\int dz\psi_n^2(z)\int \frac{d^3r_1}{\mid \mathbf{r}-\mathbf{r_1}\mid}\psi_n^2(z_1)\chi_n^2(x_1,y_1). \tag{12}$$

The electron density here is $\psi_n^2(z)\chi_n^2(x,y)$.

Schrödinger equation (10) takes the form

$$-\frac{\hbar^2}{2m}\Big(\frac{d^2}{dx^2}+\frac{d^2}{dy^2}\Big)\chi_n(x,y) - e\phi_{nn}(x,y)\chi_n(x,y) = (E-E_n(0))\chi_n(x,y), \tag{13}$$

This equation differs of standard equation for the ground state of two–dimensional polaron in that it holds for an arbitrary nth level of quantization.

Variational procedure with the electron wave function given in [2] leads to the polaron energy

$$E_n = E_n(0) - \alpha^2\hbar\omega_0(C_0 - C_1A_{nn}\frac{L}{a_0}) \tag{14}$$

where dimensionless coefficients A_{nn} are equal to

$$A_{nn} = \frac{1}{L}\int dzdz_1[\psi_n^0(z)]^2[\psi_n^0(z_1)]^2 \mid z-z_1\mid . \tag{15}$$

Here the dimensionless constant of Fröhlich interaction is

$$\alpha = \frac{e^2}{2\hbar\omega_0}\left(\frac{2m\omega_0}{\hbar}\right)^{1/2}\left(\frac{1}{\varepsilon_\infty}-\frac{1}{\varepsilon_0}\right) \tag{16}$$

where ω_0 is the optical phonon frequency, and $a_0 = \hbar^2\varepsilon/me^2$ is the polaron radius. The coefficient $C_0 = 0,4047$ was found earlier in [2], and the coefficient C_1 is obtained here and equals $C_1 = 0,0682$. In the case of infinite rectangular quantum well and $n = 1$ coefficient A_{nn} is $A_{nn} = 0,207$. Equation (14) shows that polarization of the medium is different for various levels of size quantization, and this difference is determined by the coefficients A_{nn} from Eq.(15).

b. Quantum wire.

Similar approach results in the case of quantum wire in the energy of nth level of quantization

$$E_n = E_n(0) - \frac{1}{4}\alpha^2\hbar\omega_0\ln^2\left(\frac{a_0}{LB_{nn}}\right) \tag{17}$$

where L is cross section characteristic size and the numerical coefficients B_{nn} are of the order of unity and are determined by the cross–sectional shape of the wire: $\ln B_{nn} = \int dydzdy_1dz_1[\psi_n^{(0)}(y,z)]^2[\psi_n^{(0)}(y_1,z_1)]^2\ln\Big[\sqrt{[(y-y_1)^2+(z-z_1)^2]}/L\Big]$. In case of infinite rectangular wire and $n = 1$, $B_{11} = 1,334$.

The comparison of Eq.(17) and Eq.(14) shows that the polaron effect in the case of quantum wire is more prominent because of large factor $a_0/L > 1$.

c. Quantum dot.

The quantum dot optimum polaron energy is obtained by the similar variational procedure

$$E_n = E_n(0) - \alpha\hbar\omega_0\left(\frac{\hbar^2}{mL^2}\frac{1}{\hbar\omega_0}\right)^{1/2} D_{nn}. \tag{18}$$

Here L is the diameter of the spherical dot with infinite walls and the dimensionless coefficients D_{nn} describes the polarization of the medium. It is determined by the actual form of the wave function of the electron in the dot, $\Psi_n^{(0)}(\mathbf{r})$. For instance, for $n = 1$ $D_{11} = 1,786$.

The second term in Eq. (18) depends on the ratio of the size quantization energy to the phonon energy. There are semiconductor materials where this factor is large then the unity, for example CdSe.

The most essential result is that the polaron energies are different for various levels of size quantization in all nanostructures under consideration. It means, that the optical transitions between the levels of quantization should manifest some effects similar to ones which are well known in physics of deep impurity centers in semiconductors. For example, there exist large Stokes shift between the frequencies of absorption and emission. Moreover, phonon replicas should be observed in optical transitions between size–quantization levels. These phonon replicas may have the same intensity as one for the direct electronic transition. It is quite possible that the multi–phonon transitions of this nature has been recently observed in experiment on time dependent luminescence from CdSe quantum dots in glassy matrix [3].

REFERENCES

[1] Pekar S.I. Studies in the Electronic Theory of Crystals (in Russian), Gostekhizdat, Moscow, (1951).

[2] Xiaoguang Wu., Peeters F.M., and Devreese J.T., Phys. Rev. B, **31**, 3420, (1985).

[3] ungnickel V., Henneberger F., and Puls J. Proceedings of 22-nd International Conference on the Physics of Semiconductors. Vancouver. Canada. 2011, (1994).

DETERMINATION OF THE SIGN OF THE CONDUCTION-ELECTRON g-FACTOR IN SEMICONDUCTOR QUANTUM WELLS BY MEANS OF THE HANLE EFFECT AND SPIN QUANTUM BEATS TECHNIQUES

V. K. Kalevich, B. P. Zakharchenya, K. V. Kavokin
A. F. Ioffe Physicotechnical Institute, Russian Academy of Sciences, 194021 St. Petersburg, Russia
P. Le Jeune, X. Marie, D. Robart, T. Amand, J. Barrau, M. Brousseau
Laboratoire de Physique de la Matiere Condensee CNRS-ERS 5646 INSA, Complexe scientifique de Rangueil, 31077 Toulouse cedex, France

A method of measuring the sign of the conduction electron g-factor in semiconductor quantum wells is proposed, which is based on determination of the sense of electron-spin Larmor precession by the Hanle effect or spin quantum beats techniques under oblique incidence of pump light on the sample, with the luminescence detected at an angle to the pump beam. This method has been used to measure the sign of the transverse electronic g-factor component in $GaAs/Al_{0.3}Ga_{0.7}As$ quantum wells of various widths. It has been shown experimentally that the average spin of electrons photocreated in quantum wells may not coincide with the pump light direction.

1. One of the important semiconductor parameters is the g-factor of conduction electrons. For its determination, the Hanle effect [1] and spin quantum beats [2] are widely used. In determining the sign of the g-factor by means of quantum beats, as well as in the first experiment on determination of the g-sign by Hanle effect, the polarization of the luminescence emerging from cleaved face of a crystal in the direction perpendicular to the exiting beam, has been measured. By comparing the signs of polarization of the luminescence and of the pump light one can determine the direction of electron-spin Larmor precession and, hence, the g-factor sign. However, this geometry cannot be employed in studies of GaAs/AlGaAs-type quantum wells, since luminescence in such structures is dominated by recombination of electrons with heavy holes and, by the selection rules [1], cannot be circularly polarized when viewed in the quantum well plane. These difficulties can be readily sidestepped, if one observes the luminescence in reflection at an angle to the pump beam, with the magnetic field oriented perpendicular to the excitation and detection directions, as shown in Fig.1. This geometry was proposed [3] for determination of the g-factor sign in bulk GaAs-type crystals using the Hanle effect.

The present report gives the results of the experiments [4] in which this geometry has been applied to determine the sign of the electronic g-factor in quantized films by use both the Hanle effect and quantum beats.

2. To elucidate the essence of the proposed method, consider first the situation in a bulk semiconductor.

Hanle effect

In order to determine the sign of the g-factor in a bulk unstrained semiconductor

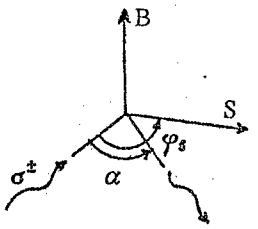

Fig.1.

subjected to cw excitation and studied in the geometry of Fig.1, one has only to obtain the dependence of the absolute value of the circular polarization degree ρ on magnetic field B. This dependence can be written [3]

$$\frac{\rho(B)}{\rho_0} = \frac{\cos\alpha + \varphi_S \sin\alpha}{1+\varphi_S^2}, \qquad (1)$$

here α is the angle between the directions of excitation and detection, ρ_0 is the degree of polarization for B=0 and α=0, and $\varphi_S=\Omega T_S = g\mu_B B T_S/\hbar$ is the angle through which the average spin $\vec{S}$ of electrons turns during the electron spin-orientation time $T_S=\tau\tau_S/(\tau+\tau_S)$. Here τ and τ_S are the electron lifetime and spin relaxation time in the conduction band. Eq.(1) takes into account that in a bulk GaAs-type crystal ρ is equal to the projection of $\vec{S}$ on the observation direction. For $\alpha\neq 0$, the $\rho(B)$ plot is not symmetrical with respect to the B=0 point. The value of ρ is larger for the magnetic field direction at which the electron spin precesses toward the luminescence observation axis.

Electron-spin quantum beats

Electron-spin quantum beats set in under coherent excitation of the two electron spin levels by a short pulse of circularly polarized light and may be considered as a result of Larmor precession of electron spins about the magnetic field $\vec{B}$ with a frequency $\vec{\Omega}_L = g\mu_B\vec{B}/\hbar$ [2]. Here, as can be easily shown, the variation of ρ with time is equal [4]:

$$\rho(t)/\rho_0 = e^{-t/\tau_S}\cos(\Omega t-\alpha), \qquad (2)$$

where $\rho_o=\rho(t=\alpha=0)$. As seen from Eq.(2), the observation of luminescence at an angle α to the pump beam results in a phase shift of the ρ oscillations. If the magnetic field direction is known, the sign of the phase shift can be used to determine that of the g-factor. The phase shift is negative for the magnetic field orientation at which, upon the pump pulse, the $\vec{S}$ begins precession toward the luminescence observation axis.

3. The above methods can be employed to determine the sign of the electronic g-factor component $g_\perp$ in the QW plane. In this case, however, an additional analysis will be required.

First, the electron orientation in a film may not coincide with the direction of the exciting beam because of the heavy- and light-hole subbands being splitted. In particular, as shown theoretically [5], under excitation of electrons from states close to the top of the heavy-hole subband ($hh\rightarrow c$ transition) their average spin at the

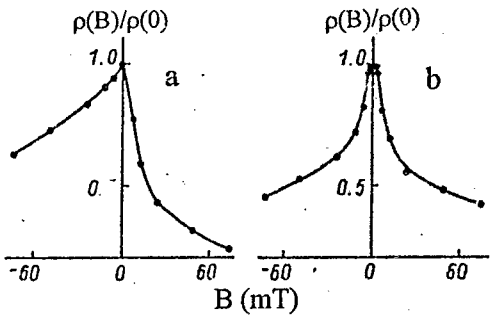

Fig.2.

moment of generation is directed along the structure growth axis for any light incidence angle. Second, the polarization of recombination radiation with participation of heavy holes (c→ *hh* transition), which predominates in the luminescence spectrum of GaAs/AlGaAs wells at low temperatures, is determined by spin projection S onto the growth axis rather than onto the luminescence observation direction, as it was the case in bulk crystals. By this reason the angle α substituted into (1) and (2) is zero for the *hh*→c, c→ *hh* transition, and the Hanle curve must be symmetrical, while the oscillations ρ(t) measured for different signs of the magnetic field must coincide. If a pump photon energy is large enough for simultaneous excitation of electrons from both the heavy- and light-hole subbands, the deviation of $\bar{S}$ from the pump direction may be neglected. In this case the Hanle curve asymmetry and the quantum-beat phase shift are retained and can be used to determine the sign of $g_\perp$.

The ρ(B) Hanle curves were measured in $GaAs/Al_{0.3}Ga_{0.7}As$ QW of thickness 100, 45, and 10Å at T=2 K. The angle between the directions of the pump light and luminescence observation outside the crystal was ~85°. The sample was positioned so that the normal to its surface coincided with the bisectrix of this angle, and the magnetic field was oriented along the crystal surface. The asymmetry of the Hanle curves obtained at a pump photon energy in excess of the light-exciton energy yielded $g_\perp<0$ for L_Z=100 Å (Fig.2a) and $g_\perp>0$ for L_Z=45 and 10 Å. The virtually complete absence of asymmetry in the ρ(B) curves measured at excitations close to resonance with the heavy exciton (Fig.2b) attests that the average spin of photoexcited electrons at the moment of excitation in QWs may not coincide in direction with the pump light.

Quantum beats ρ(t) were measured in $GaAs/Al_{0.3}Ga_{0.7}As$ MQW of thickness 120 and 30Å at T=1.7 K. Pump pulses were produced by a tunable Ti-sapphire laser with a repetition frequency of 82 MHz. Their duration, equal to 1.2 ps, defined the time resolution of the measuring equipment using parametric up-conversion.

The ρ(t) oscillations on a 120-Å thick QW at $h\nu$>XL ($h\nu$-XL=58 meV) measured for B<0 lag behind those obtained for B>0 (Fig.3a), which corresponds to

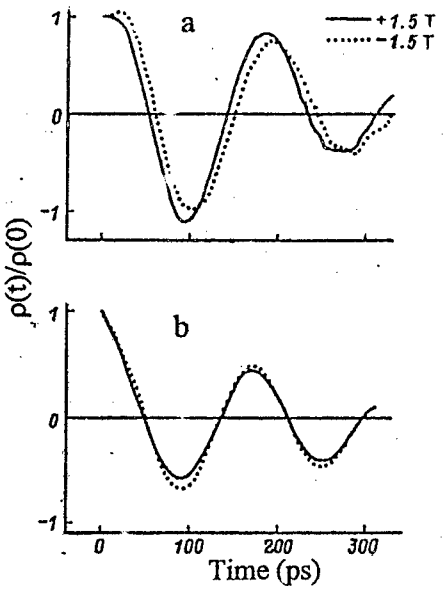

Fig.3.

$g_\perp<0$. The absence of any phase shift between the oscillations in Fig.3b measured for XH< $h\nu$ <XL implies that the average spin of the electrons excited from the heavy-hole subband is aligned with the QW growth axis.

The ρ(t,-B) beats lead the ρ(t,B) oscillations on a 30-Å thick QW at $h\nu$>XL. This corresponds to $g_\perp>0$.

Thus we have considered a method to determine the sign of the in-plane component of the conduction-electron g-factor in a QW from the shape of the Hanle curves or from the phase shift of the electron spin quantum beats. This method was applied to GaAs/$Al_{0.3}Ga_{0.7}As$ QW to find that $g_\perp<0$ in 120- and 100-Å thick wells, and $g_\perp>0$ in wells of thickness 45, 30, and 10 Å. It was shown that the average spin of optically oriented electrons in size-quantized films at the moment of excitation may not coincide in direction with the pump light.

This work was partially supported by the Russian Fundamental Research Foundation (Grant 96-02-16941) and NATO (Grant HTECH CR6 950377).

References.

1. Optical Orientation, ed. by Meier F. and Zakharchenya B., North-Holland, Amsterdam, vol. 8 (1984); Chapters 2, 5, 9, and 11.
2. Oestreich M., Hallstein S., Ruhle W. W. *Proc.23 ICPS*, Berlin, v.1, 677(1996).
3. Kalevich V. K. and Kul'kov V. D. *Opt. Spektrosk.* **52** 200 (1982).
4. Kalevich V. K., Zakharchenya B. P., Kavokin K. V., Petrov A.V., Le Jeune P., Marie X., Robart D., Amand T., Barrau J., Brousseau M. *Phys. Solid State* **39** (1997), in press.
5. M. I. Dyakonov and V. I. Perel. *Sov. Phys. Semicond.* 7,1551 (1973).

Dependence of optical spectra of superlattices on the site symmetry of impurities and defects

Yu.E.Kitaev, A.G.Panfilov

Ioffe Physical-Technical Institute, 194021 St.Petersburg, Russia

P.Tronc

Laboratoire d'Optique Physique, ESPCI, 75005 Paris, France

V.P.Smirnov

Institute of Fine Mechanics and Optics, Sablinskaya 14, 197101, St.Petersburg, Russia

The short-period $(GaAs)_m(AlAs)_n$ superlattices (SL's) with different numbers of monolayers (m,n) of parent materials (GaAs and AlAs) distinguish from each other by the arrangement of atoms over the symmetry positions (Wyckoff positions). Therefore, from the crystallographic point of view, they are distinct crystals. For each direction of growth, the SL's constitute several single crystal families specified by different space groups G_l (the same within each family). Thus, the SL's can be considered as a new class of artificially grown crystals whose structure depends on the growth direction and numbers of monolayers of constituent materials.

In previous papers [1] we performed a complete group-theory analysis of electron state symmetries in perfect $(GaAs)_m(AlAs)_n$ SL's grown along the [001], [110], and [111] directions. We predicted some variations in the optical spectra upon varying the SL period. In this paper, we extend this analysis on SL's with defect and impurity states.

The variety of different Wyckoff positions in the primitive cell of the perfect SL's is noticeably larger than in the bulk parent materials. Correspondingly, much more is the variety of positions that can be occupied by substitutional impurities or defects. For example, the metal (Ga or Al) and non-metal atoms can occupy various Wyckoff positions in the primitive cell depending both on the growth direction and numbers of monolayers. When a sample is doped, the same doping atom, which substitutes, e.g., a Ga atom at sites with different symmetries, shows different behaviour.

The aim of this work is to show how the distribution of the impurities and defects over the Wyckoff positions will manifest in the polarized optical spectra and *vice versa* how one can obtain an information from the spectra, e.g., about the sites of dopants in the lattice.

1. Crystal defect symmetries

Analyzing the electron states of point defects, we assume that the site-symmetry group Gq is not modified when a SL atom in the position q is replaced by a substitutional impurity or by a single vacancy. In case of so-called "molecular" point defects (paired impurities, double vacancies, etc.), the crystal defect (CD) occupies two atomic or interstitial positions. In this case, the symmetry of such a CD is determined by the common elements of two groups: the point group of the isolated "molecule" whose axis coincides with the line connecting the two involved SL sites and the site-symmetry group of a point on this line.

Basing on the analysis of perfect SL structures [1] we determined possible locations of the simplest CD (single ones and complexes occupying the nearest atom sites) in the SL's grown along different directions. The results are presented in Table 1. We see that, being T_d in the bulk parent materials, the site symmetry group *Gq* for point defects is lowered in the SL's down to D_{2d}, C_{2v}, C_{3v}, and C_s depending on the occupied Wyckoff position, growth direction, and numbers of monolayers. For "molecular" point defects the symmetry is lowered from C_{3v} down to C_s or even C_1.

Table 1. Possible occupation numbers (per primitive cell) for substitutional CD states in the $(GaAs)_n(AlAs)_n$

		Growth direction and space group								
		[001]				[110]				[111]
Atoms substituted	Site symmetry	D_{2d}^5 m=2k+1 n=2s+1	m=2k n=2s	D_{2d}^9 m=2k+1 n=2s	m=2k n=2s+1	C_{2v}^1	C_{2v}^7	C_{2v}^{20} m=2k+1 n=2s	m=2k n=2s+1	C_{3v}^1, C_{3v}^5
Ga	D_{2d}	1	-	1	-	-	-	-	-	-
	C_{2v}	m-1	m	m-1	m	1	-	1	-	-
	C_{3v}	-	-	-	-	-	-	-	-	m
	C_s	-	-	-	-	m-1	m	m-1	m	-
Al	D_{2d}	1	-	-	1	-	-	-	-	-
	C_{2v}	n-1	n	n	n-1	1	-	-	1	-
	C_{3v}	-	-	-	-	-	-	-	-	n
	C_s	-	-	-	-	n-1	n	n	n-1	-
As	D_{2d}	-	2	1	1	-	-	-	-	-
	C_{2v}	m+n	m+n-2	m+n-1	m+n-1	2	-	1	1	-
	C_{3v}	-	-	-	-	-	-	-	-	m+n
	C_s	-	-	-	-	m+n-2	m+n	m+n-1	m+n	-
Ga+As (Al+As)	C_{3v}	-	-	-	-	-	-	-	-	m(n)
	C_s	4m(n)	4m(..)	4m(n)	4m(n)	2m(n)	2m(n)	2m(n)	2m(n)	3m(n)
	C_1	-	-	-	-	2m(n)	2m(n)	2m(n)	2m(n)	-

From Table 1, we see that the Ga and Al atoms occupy D_{2d} sites and As occupy C_{2v} sites in the $(GaAs)_1(AlAs)_1$[001]-grown SL whereas in the $(GaAs)_2(AlAs)_2$[001] SL, the metal (Ga,Al) atoms occupy C_{2v} sites and As atoms are distributed among the D_{2d} and C_{2v} sites. If a CD substitutes, e.g., metal atoms, the optical transitions involving this impurity are to be different for these two SL's. Moreover, the behaviour of impurities substituting As atoms at different sites in the (2x2) SL will be also different. It gives a possibility to determine the sites of dopants in the lattice when analyzing the optical spectra.

Till now, the defect symmetries in quantum structures have been not adequately considered. Most of calculations of CD-state energies in quantum structures addressed the single-quantum-well problem merely, keeping the symmetry language of parent tetrahedral materials. This may have lead to misinterpretation of experimental data.

For example, the authors of [2] observed in the $(GaAs)_5(AlAs)_5$[001]-grown SL a Ga-centered point-defect state with the a_1 symmetry instead of the t_2 one they were expecting. Basing on the "nearly tetrahedral" site-symmetry of the defect, they concluded on its interstitial nature (Ga_i rather than Ga_{As}). However as one can see from Table 1, in [001]-grown SL's, there are two As sites (of D_{2d} and C_{2v} symmetry type). The former is absent in SL's with odd values of m and n. The t_2 state splits into $a_1+b_1+b_2$ or into b_2+e in the case of the C_{2v} or D_{2d} site-symmetry respectively. Thus, the observed CD may be not an interstitial defect but an C_{2v} antisite one.

2. Optical selection rules

Let the symmetry of a CD localized state be described by the irreducible representation (irrep) d_α of the CD site symmetry group Gq and the symmetry of an electron state in the conduction or valence band of the SL by the irrep D_β of the SL space group G. To determine the allowed direct transitions between the initial $d_\alpha{}^{(i)}$ and final $D_\beta{}^{(f)}$ states we subduce [3] the irrep $D_\beta{}^{(f)}$ on the site symmetry group Gq :

$$D_\beta{}^{(f)} \downarrow Gq = \sum_\gamma A_\gamma d_\gamma .$$

The dipole transition between the initial $d_\alpha{}^{(i)}$ and final $D_\beta{}^{(f)}$ states is allowed if

$$(D_\beta{}^{(f)} \downarrow Gq)^* \times d_\alpha{}^{(i)} \cap d_v \neq 0,$$

where d_v is the vector representation of the site symmetry group Gq.

When the spin-orbit interaction is taken into account, the products of double-valued irreps should be considered. Like in [1], one can obtain a relation between the selection rules when the spin-orbit interaction is taken into account and those when it is not. As a result, some forbidden transitions will become allowed whereas some allowed transition will become forbidden when the spin-orbit interaction is taken into account.

Table 2. The selection rules for CD(D_{2d})-state-to-band-state direct transitions in [001]-grown SL's. The labels of irreps in brackets refer to the case where spin-orbit interaction is not taken into account. Polarizations in brackets (parentheses) refer to transitions allowed only without (with) including spin-orbit interaction; the ones in capitals refer to the transitions allowed in both cases; small irrep labeling follows [4].

CD site	localized state	conduction/valence band state			
		$\Gamma_5[\Gamma_1]$	$\Gamma_7[\Gamma_2]$	$\Gamma_6[\Gamma_5]$	$\Gamma_7[\Gamma_5]$
D_{2d}	$\bar{e}_1[a_1(s;d_{z^2})]$	(x,y)	(x,y)Z	X,Y	X,Y(z)
	$\bar{e}_2[b_1(d_{x^2-y^2})]$	(x,y,z)	(x,y)	X,Y(z)	X,Y
	$\bar{e}_2[b_2(p_z;d_{xy})]$	(x,y)Z	(x,y)	X,Y(z)	X,Y
	$\bar{e}_1[e(p_x,p_y;d_{yz},d_{xz})]$	X,Y	X,Y(z)	(x,y)[z]	(x,y)Z
	$\bar{e}_2[e(p_x,p_y;d_{yz},d_{xz})]$	X,Y(z)	X,Y	(x,y)Z	(x,y)[z]

As an example, in Table 2, we present an extract (for CD with D_{2d} symmetry for the [001]-grown SL's) from the complete list of selection rules for transitions between localized and SL Γ states

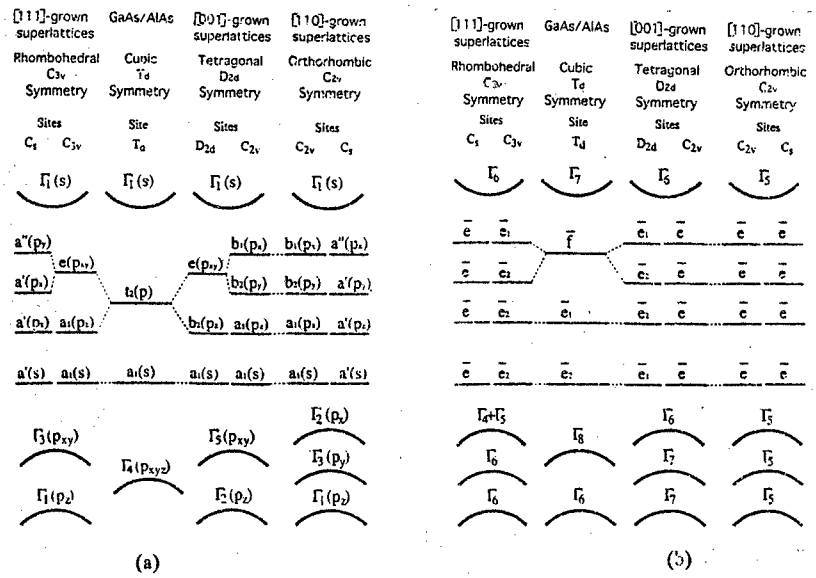

Symmetry correspondence between the CD states in bulk GaAs(AlAs) and localized at different sites in the$(GaAs)_m(AlAs)_n$ SL's grown along different directions
(a) - neglecting spin-orbit interaction, (b) - with spin-orbit interaction

displaying the modification of selection rules on including spin-orbit interaction. We consider not only *s* and *p* states of CD but also *d* ones since the latter orbitals correspond to the upper occupied states in, e.g., transition metals.

When lowering the site symmetry from T_d in GaAs, the CD states in SL are modified as illustrated by the Figure. The use of the Figure together with selection rules (Table 2) can noticeably simplify an analysis of experimental spectra. Basing on the polarization peculiarities of the spectra and comparing the line intensities, one can not only assign the lines to certain CD-level-to-SL-band transitions but also determine the sites of dopants in a lattice.

Summarizing, we have shown how the distribution of the impurities and CD over the Wyckoff positions will manifest in the polarized optical spectra. The selection rules have been established for polarized-light experiments related to single substitutional impurities, vacauces, and two-component complexes, the spin-orbit interaction being taken into account.

The authors acknowledge the HTEC.CRG 960664 NATO grant.

[1] Yu.E.Kitaev, A.G Panfilov, P.Tronc, and R.A.Evarestov, J.Phys.Condens.Matter, 9, 257, 277 (1997).
[2] J.M.Trombetta, T.A.Kennedi, W.Tseng, and D.Gammon, Phys.Rev.B 43, 2458 (1991).
[3] R.A.Evarestov and V.P.Smirnov , *Site Symmetry in Crystals: Theory and Applications*, Springer Series in Solid State Sci. vol.108 (Springer, Heidelberg, 1993)
[4] S.C.Miller and W.F.Love, Tables of Irreducible Representations of Space Groups and Co-Representations of Magnetic Space Groups (Pruett, Boulder, 1967)

Interband mixing between 2D electron and 3D heavy hole states in narrow gap semiconductor

V.A.Larionova and A.V.Germanenko

Institute of Physics and Applied Mathematics, Ural State University
Ekaterinburg 620083, Russia. E-mail: Viola.Larionova@usu.ru

Interband mixing effects attract much interest because they can play a decisive part in forming the energy spectrum of low-dimensional systems. Such is in the case for InAs-GaSb semimetallic superlattices, whose physical properties are determined by the mixing between valence band states of GaSb and conduction band states of InAs at the interfaces. Analogous situation takes place in a metal–insulator–semiconductor structure based on a narrow gap semiconductor. A small value of the energy gap in the semiconductor leads to the fact that at energies below the top of the valence band the two-dimensional (2D) states localized in a surface quantum well can mix with the valence band states and 2D carriers can tunnel from the space charge region into the valence band states in the volume of semiconductor. Due to high value of the effective mass, the probability of tunneling of 2D carriers into the heavy hole states is small. In this case the interband mixing with the heavy hole states was usually neglected. This approach is justified for semiconductors with low impurity density, because the surface potential in such materials is smooth in the shape, and the 2D states localized in the quantum well are spatially separated from the valence band by a wide region of forbidden energies.

In semiconductors with high doping level the effects of interband tunneling of 2D electrons into the heavy hole states can be stronger. The influence of these effects on the energy spectrum and broadening of the 2D states localized in the surface quantum well in the narrow gap semiconductor (HgCd)Te is discussed here.

A small value of the energy gap (E_g) in semiconductor investigated makes it necessary to employ a multiband Hamiltonian in the kP-based calculations of the energy spectrum. We started from the multiband Hamiltonian derived from Kane's model making the usual assumption that the energy difference between the valence Γ_8-band and spin-orbit split-off Γ_7-band is infinite. To consider the effects involving the heavy hole states, the interaction with remote bands has been taken into account by a standard procedure of including additional terms with γ-parameters in the Hamiltonian. An isotropic approximation has been used. We assumed the electrostatic potential ($\varphi(z)$) to be parabolic in the space charge region and constant in the volume of semiconductor.

Thus, Schrödinger equation is two independent systems of differential equations of the second order. For solving these systems boundary conditions have to be deduced. We supposed: (i) the band structure of insulator to be identical to that of semiconductor; (ii) the energy gap in the insulator to be much greater than that in semiconductor, and the conduction and valence band offsets, denoted as D_c and D_v, respectively, to exceed the value of E_g; (iii) the energy bands in the insulator to be "flat", and (iv) the structure to have a smooth insulator/semiconductor interface of width d with linear dependence of the band-edge energies on z coordinate.

Since a general solution of the Kane Hamiltonian for $\varphi(z) = const$ is known, the wave function on the insulator and semiconductor sides of the structure can be simply derived.

In the insulator it contains only the terms exponentially vanishing deep into the insulator. As to the boundary conditions on the semiconductor side we are interested in the case when the 2D state is degenerate only with the heavy hole valence band. In this case the normal component of the light hole quasimomentum is imaginary. Therefore, the wave function is a superposition of the light hole term, which diminishes exponentially deep into the semiconductor, and two oscillating terms presenting the plane wave associated with the heavy hole.

Thus, starting from the exact solution of the Kane Hamiltonian on the insulator side we numerically integrated the differential equation systems through the space charge region and chose those solutions which satisfy the boundary conditions on the semiconductor side.

It is clear that the eigenvalue problem has a continuous spectrum of solutions in the case of interest, i.e. at any energy value we can find the wave function satisfying the boundary conditions. To define the energy level associated with the resonant 2D states and its broadening caused by the interband mixing between the 2D states and heavy hole states, the Levinson's theorem has been applied.

To analyze peculiarities of the energy spectrum of 2D states arising from the interband mixing, we have performed numerical calculations using realistic parameters. They are the following: $E_g = 50$ meV, $N_A - N_D = 6 \times 10^{17}$ cm^{-3}, $\kappa = 20$. The calculations have been carried out using two sets of γ-parameters: $\gamma_1 = 2.0$, $\gamma = 0$ [1] and $\gamma_1 = 4.5$, $\gamma = 1.0$ [2]. To make identical the dispersion law of bulk electron states calculated with different sets of γ-parameters, we changed slightly the value of the momentum matrix element P from 8.0×10^{-8} eV·cm, for the first set, to 8.1×10^{-8} eV·cm, for the second one. Parameters of the insulator/semiconductor interface are the same as in [1]: $D_c = 2$ eV, $D_v = 1$ eV, and the interface width $d = 10$ Å.

Figure 1 shows the energy spectrum of 2D states calculated with different sets of γ-parameters as compared with the energy spectrum of 2D states calculated in the infinite heavy hole mass approximation with a so-called "mid-gap" boundary condition on the semiconductor side. Two branches of the energy spectrum specified by k^+ and k^- are two "spin" branches of the ground 2D subband split by spin-orbit interaction in an asymmetric quantum well. It is clearly seen from the figure that the interband mixing of 2D states with the heavy hole states results in the energy shift of 2D subbands and the broadening of 2D energy levels. The broadening is shown in Fig. 1 as hatched region. The value of broadening is different for k^+ and k^- sublevels for a fixed energy. The maximum value of the broadening is about 10 meV. It is comparable to the broadening of 2D states appearing due to tunneling into the light hole states which has been calculated in [3] for a sample with close parameters. Note that the broadening value slightly depends on the heavy hole effective mass.

Traditional experimental methods, such as galvanomagnetic investigations, volt- capacitance spectroscopy, give information about the carriers at the Fermi energy. In p-type (HgCd)Te the Fermi level lies near the top of the valence band, where the broadening of 2D states is small and therefore these methods must not be sensitive to this effect. Tunneling investigations allow to get information about the 2D states in a wide energy range including the energies, where the broadening is large. Besides, the maximum value of broadening is comparable with the cyclotron energy in magnetic fields right up to 2 T. This can result in additional broadening of resonance peaks in magneto-optical and cyclotron resonance experiments.

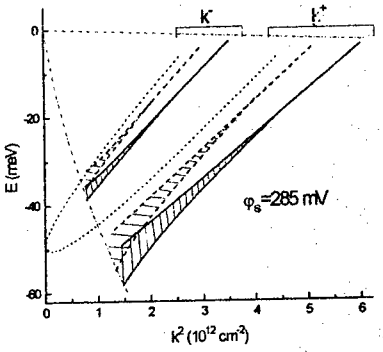

Fig.1. The energy spectrum of 2D states calculated with different sets of γ-parameters: $\gamma_1 = 4.5$, $\gamma = 1$ (the solid curves) and $\gamma_1 = 2$, $\gamma = 0$ (the dashed curves), as compared with the energy spectrum of 2D states calculated in the infinite heavy hole mass approximation (the dotted curves). The value of the surface potential is 285 mV, k^+ and k^- denote two different spin branches of the energy spectrum. The dot-dash curves show the borders of region, where the 2D states are in resonance with the heavy hole valence band.

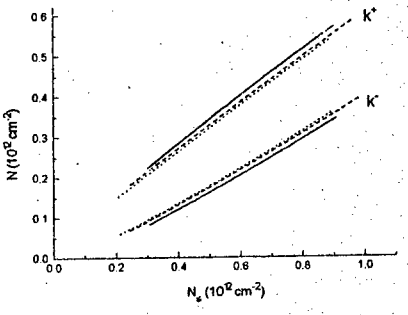

Fig.2 The dependence of the electron concentration in each 2D subband on the total concentration of 2D electrons. The notations and curve types are the same as in Fig.1.

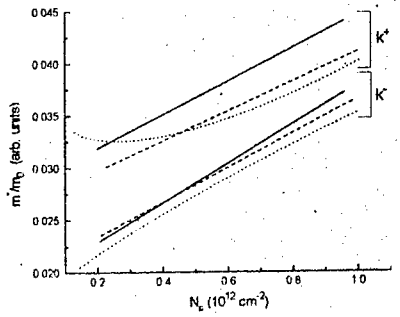

Fig.3. The dependence of the electron effective mass on the total concentration of 2D electrons.

As to the effect connected with the influence of interband mixing on the dispersion law of 2D states traditional experimental methods give no way of direct deducing a quasimomentum dependence of the energy of 2D states for a fixed value of a surface quantum well. The value of the surface potential is usually used as a fitting parameter in analyzing experimental data, for example, dependences of 2D subband concentration and the effective mass of 2D carriers on their total concentration. Figure 2 shows the relationship between 2D subband concentration and the total concentration of 2D electrons, calculated using two sets of γ-parameters and infinite heavy hole effective mass. The concentration of 2D electrons is changed by varying the surface quantum well depth from 250 to 320 mV. It is clearly seen from the figure that the interband mixing does not cause essential changes in the subband distribution of 2D electrons. One can see only slight increase in ratio between concentrations of 2D electrons in k^+ and k^- "spin" subbands with decreasing the heavy hole effective mass. Thus, in spite of the fact that the interband mixing results in shifting the energy positions of 2D subbands, it does not strongly influence the subband distribution of 2D electrons.

The effective mass of carriers is a differential characteristic of the energy spectrum and it might be more sensitive to the interband mixing effects. We have calculated the effective mass of 2D electrons $m^* = \hbar^2 k \left(\partial E/\partial k\right)^{-1}$ at $E = E_F$ as a function of their total concentration (Fig. 3). As is clearly seen for large concentration of 2D carriers ($N_S > 0.55 \times 10^{12}$ cm^{-2}) the effective mass of 2D electrons, calculated in the model taking into account the interband mixing (solid and dashed curves), is larger than that calculated with the infinite heavy hole mass (dotted curves). It is evident that the concentration dependence of the effective mass, calculated with $\gamma_1 = 4.5$, $\gamma = 1.0$ deviates mostly from the results obtained in the infinite heavy hole mass approximation. For k^+-"spin" states this difference is larger and at $N_S \simeq 10^{12}$ cm^{-2} it comes to more than 10%.

A distinctive situation occurs for small concentrations of 2D electrons ($N_S < 0.45 \times 10^{12}$ cm^{-2}) for k^+-group of states. The effective mass, calculated with γ-parameters, monotonically decreases with decreasing the total concentration, whereas the effective mass, calculated in the framework of the infinite heavy hole mass approximation, goes through a minimum, and at some value of the total concentration it becomes larger than the effective mass calculated with γ-parameters.

Thus, the presented results show that the interband mixing causes the effective mass of 2D states to be larger than that calculated in the infinite heavy hole mass approximation. This is more evident for k^+-"spin" states and for large concentration of 2D carriers. The effective mass of 2D carriers calculated with the most-used set of γ-parameters [2] differs mostly from the results of calculation, in which the interaction with remote bands is neglected. To our knowledge there are no experimental data concerning the effective mass of 2D states in highly doped narrow gap semiconductors in case, when 2D states are in resonance with the heavy hole valence band.

This work was supported in part by the Russian Foundation for Basic Research (Grant No 97-02-16168) and by the Program "Physics of Solid Nanostructures".

1. G. M. Minkov et al, Phys. Rev. B **54**, 1841 (1996).
2. Y.Guldner, C.Rigaux, A.Mycielski, and Y.Couder, Phys. Stat. Sol. (b) **82**, 149 (1977).
3. I.Nachev, Nuovo Cimento **12** D, 1143 (1990).

Scattering of holes by quantum-well heterostructures

A.F. Polupanov[1], V.I. Galiev[1], A.N. Kruglov[1], S.G. Shekhovtsov[1], E.M. Goldys[2] and T.L. Tansley[2]

1) Institute of Radioengineering and Electronics of the Russian Academy of Sciences, Mokhovaya 11, Moscow, 103907, Russia
2) Macquarie University, North Ryde, 2109 NSW, Australia

1. Introduction

In the design of quantum well (QW) devices it is important to know the eigenenergies and eigenfunctions of the QW. The envelope-function approach gives a good description of electronic and hole subbands near the zone center, is rather easy to apply and is particularly convenient if strain effects or external perturbations are to be included. Recently we have developed an efficient numerical-analytical method for finding confined states in quantum-well systems with arbitrary potential profiles, described by coupled Schrödinger equations, such as hole states in semiconductor QW [1]. In the present paper this method is extended to the case of continuum hole states. In contrast with the previous approaches, this work avoids the conventional large box approximation to confine the continuum wave functions thus giving realistic continuum hole states in a statement corresponding to the scattering problem. The expressions for the elements of the S-matrix, which describes hole scattering, are derived and its symmetry is analyzed. The method is used to study the scattering of holes in various $GaAs/GaAlAs$, $Si/SiGe$ and $GaInAs/InGaAsP$ QW heterostructures with the account taken of the inherent anisotropy, non-parabolicity, heavy- and light-hole mixing and strain effects due to the lattice-constants mismatch at the interfaces.

2. Wave functions of the continuous spectrum

We consider for definiteness the case of a single QW (barrier) with the potential profile of the general form $U(z)$, where z is a coordinate axis perpendicular to the layers in the structure. The well (barrier) extends from $z = 0$ to $z = d$. Inside the well (barrier) region, we have the following system of coupled one-dimensional Schrödinger equations, which are readily seen to be, a general form of the equations for the envelope functions of a hole in a semiconductor QW:

$$H\Psi = \left\{ a\frac{d^2}{dz^2} + b\frac{d}{dz} + c + U(z) \right\} \Psi(z) = E\Psi(z) \qquad (1)$$

Here a, b, c are independent of z $n \times n$ matrices, $\psi(z)$ an n-component wave function with the number n determined by the number of coupled bands taken into account. In the particular case of a hole, matrices a, b and c depend on the valence band parameters and on component of the momentum parallel to interfaces. It is convenient to rewrite equation (1) in the form of the first-order equation replacing the function $\psi(z)$ with the $2n$-component function $y(z) = \begin{pmatrix} \psi(z) \\ d\psi(z)/dz \end{pmatrix}$. Substituting this expression into equation (1) we obtain

$$\frac{dy(z)}{dz} = Ay(z), \quad A = \begin{pmatrix} 0 & 1 \\ a^{-1}(E - U(z) - c) & -a^{-1}b \end{pmatrix} \qquad (2)$$

where $A(z)$ is the $2n \times 2n$ matrix function constructed from the matrices a, b, c, the potential and the energy. At $0 \leq z \leq d$ solutions of (2) are constructed, as described in [1], in the form of a power series using the recurrence relations. Boundary conditions specific to the particular problem are imposed on the wave function solution at the points $z = 0, d$. For definiteness, but without loss of generality let us next consider the case when $y(z)$ should be continuous across the interfaces.

With the well (barrier) extending from $z = 0$ to $z = d$, $U(z) = 0$ at $z < 0$, $z > d$ and we designate matrix $A(z)$ in these regions by A_0. Solutions satisfying the definite conditions at $z \to \pm\infty$ are easy to find since they are superpositions of $2n$-columns (eigenvectors of the matrix A_0) multiplied by exponential functions (eigenvalues of the matrix A_0). In the case of the states of the continuous spectrum either all eigenvalues of the matrix A_0 are purely imaginary or some of them are real and some are purely imaginary.

For illustrative purposes and bravity but without loss of generality we consider the latter case with 4×4-dimensional matrix A_0 which is just the case in so-called axial approximation. The eigenvalues of the matrix A_0 are: $i\kappa, \lambda, -\lambda, -i\kappa, (\kappa, \lambda > 0)$ Let us define the fundamental matrix of the solutions of Eq.(2) at $z \leq 0$ and $z \geq d$ in terms of the following 4×4 matrix function

$$F(z) \equiv (\chi_1 \exp(i\kappa z), \chi_2 \exp(\lambda z), \chi_3 \exp(-\lambda z), \chi_4 \exp(-i\kappa z))$$

Here $\chi_k = \begin{pmatrix} u_k \\ v_k \end{pmatrix}$, with $v_k = i\kappa_k u_k$, are eigenvectors of the matrix A_0. It is convenient to consider henceforth that these vectors are normalized, *i.e.* $u_k^* u_k = 1$. Using the method of [1] and calculated $F(0)$, we obtain the 4×4 matrix function $\hat{F}(z)$ which is the solution of Eq. (2) at $0 \leq z \leq d$. Let us calculate this matrix function at the point $z = d$, then we get the 4×4 matrix $\hat{F}(d)$. Since fundamental matrices of solutions are nondengenerate it is obvious that there exists a nonsingular 4×4 - matrix Π such that $\hat{F}(d) = F(d)\Pi$. The matrix Π is therefore unambiguously defined by the relation $\Pi = F^{-1}(d)\hat{F}(d)$ To determine the wave function, corresponding to a hole in the definite band incident on the well (barrier) from the left half-space the following inhomogenuous system should be solved:

$$\Pi\,(1, \eta_+, 0, \xi_-)^t = (\xi+, 0, \eta_-, 0)^t, \tag{3}$$

These are 4 equations for 4 variables $\xi_-, \xi_+, \eta_+, \eta_-$, where ξ_- and ξ_+ corresponds to the reflection and transmission, respectively. The inhomogenous system of linear equations (3) for unknown coefficients ξ_- and ξ_+ can always be solved unambiguously. Then we have the following expressions for the in-waves at $z \leq 0$, $0 \leq z \leq d$, $z \geq d$, respectively:

$$F(z)\,(1, \eta_+, 0, \xi_-)^t, \quad \hat{F}(z)\,(1, \eta_+, 0, \xi_-)^t, \quad F(z)\,(\xi_+, 0, \eta_-, 0)^t \tag{4}$$

3. S-matrix. Reflectivities and transmissivities

It is convenient to mark in-states at a given value of E, as well as S-matrix indices by the double index $\alpha = s\tau$, where s equals $+$ or $-$ for a 'left-right' and 'right-left' incidenting hole, respectively, and τ designates a hole type (L or H). In what follows we put $-\alpha \equiv -s\tau$.

The group velocity of the τth hole is equal to $v_\tau = |(dk_\tau/dE)|^{-1}$. We multiply constructed in-states by the factor $(2\pi v_\tau)^{-1/2}$ for them to be normalized on $\delta(E - E')$ and designate them

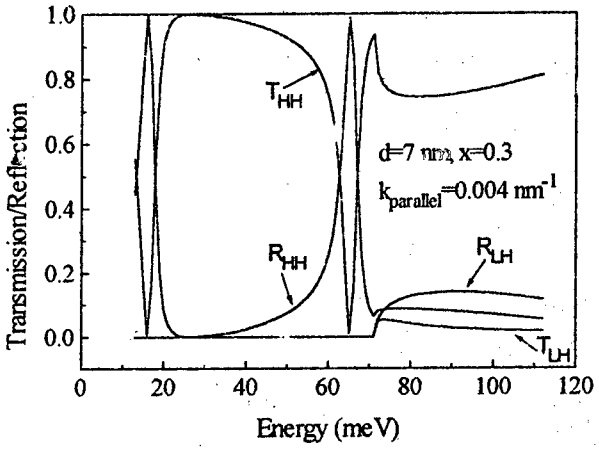

Figure 1: Reflectivities and transmissivities for a heavy hole incident from the left half-space on a single $GaAs/Al_xGa_{1-x}As$ QW

as $\Psi^{\rm in}_{\alpha E}(z)$: $\int \Psi^{\rm in*}_{\alpha E'}\Psi^{\rm in}_{\beta E'}dz = \delta(E-E')\delta_{\alpha\beta}$ Then it is obvious that the components of the S-matrix which describe holes scattering, are as follows

$$S_{\alpha,+\tau} = \xi_\alpha \left(\frac{v_{|\alpha|}}{v_\tau}\right)^{1/2}$$

Since $S_{\alpha\beta} = \int \Psi^{\rm out*}_{\alpha}\Psi^{\rm in}_{\beta}dzdE$ by defenition, and $\bar{\Psi}^{\rm in}_{\alpha} = \Psi^{\rm out}_{-\alpha}$ (here bar means complex conjugation) because the Hamiltonian under consideration is invariant with respect to the antiunitary transformation $H \to \bar{H}$, the following symmetry relation for the S-matrix holds:

$$S_{\alpha\beta} = S_{-\beta-\alpha} \tag{5}$$

Expressions for the transmissivities ($T_{\alpha\beta}$) and reflectivities ($R_{\alpha\beta}$) are readily obtained from the S-matrix elements:

$$|S_{\alpha\beta}|^2 = \begin{cases} T_{\alpha\beta}, & {\rm sgn}(\alpha) = {\rm sgn}(\beta) \\ R_{\alpha\beta}, & {\rm sgn}(\alpha) = -{\rm sgn}(\beta) \end{cases}$$

It is important to emphasize that to obtain all elements of $S_{\alpha\beta}$ and hense all transmissivities and reflectivities it is sufficient to calculate only in-solutions, corresponding to holes incident on the well (barrier) from the left half-space, due to the symmetry relation (5) and the fact that S-matrix is unitary.

The developed method has been used to examine the scattering of holes in various $GaAs/GaAlAs$, $Si/SiGe$ and $GaInAs/InGaAsP$ QW structures. By using the Luttinger

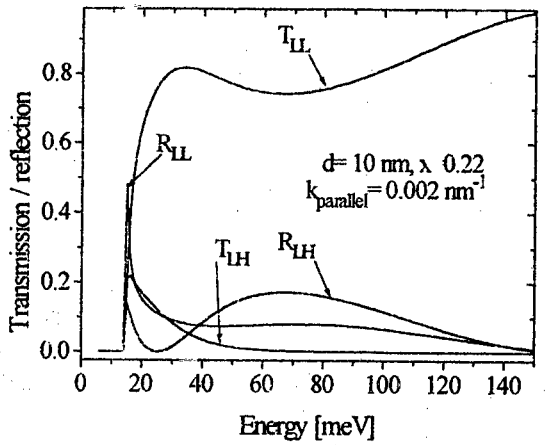

Figure 2: As Fig. 1, but for a light hole incident from the left half-space on a single $Si/Si_{1-x}Ge_x$ QW

Hamiltonian to describe the dynamics of holes close to the top of the valence band, we have taken into account exactly the band non-parabolicity, anisotropy, and heavy- and light-hole mixing.

Strain effects due to the lattice constants mismatch in $GaInAs/InGaAsP$ and $Si/SiGe$ QW structures have been taken into account using deformational constants from [2] and from the calculations of the strain-dependent band alignment of the valence bands at Si/Ge interfaces [3]. Some results of the calculations of the reflectivities and transmissivities of holes incident from the left half-space on a single QW as functions of the overbarrier energy are presented in Figures 1,2. The presence of the anti-resonances and 'resonance' peak of T_{HH} as well as nonmonotonous behaviour of T_{LL} at small energies shows the dramatic effect of both, holes coupling and strain effects on the hole dynamics in QW structures. Results depend strongly on both, allov compositions and well (barrier) widths.

Acknowledgements

A.F.P., V.I.G. and A.N.K. acknowledge the partial financial support of the Russian Foundation for Fundamental Studies, grant N97-02-16820.

References

[1] V.I. Galiev, E.M. Goldys, M.G. Novak, A.F. Polupanov and T.L. Tansley, Superlattices and Microstructures, **17** (1995) 421.

[2] S.L Chuang, Phys. Rev. **B43** (1991) 9649.

[3] C.G. Van de Walle and R.M. Martin, Phys. Rev. **B 34** (1986) 5621.

STACKING FAULTS AS QUANTUM WELLS FOR ELECTRONS IN WURTZITE GaN

Y.T.REBANE, Y.G.SHRETER AND M.ALBRECHT*

A.F.Ioffe Physico-Technical Institute, Russian Academy of Sciences,
26, Polytechnicheskaya str, 194021 St.Petersburg, Russia
* University Erlangen-Nurenberg, Erlangen, Germany

INTRODUCTION

Recent investigations of the 364 nm line in the photoluminescence spectra of GaN-epilayers have shown that it can be attribute it to extended structural defects. The reasons for this are the small value of the Huang-Rhys factor, the spatial anticorrelation of the line intensity with respect to the bound exciton (BE) line, an increase of the line intensity near the buffer layer and the disappearance of the line in thick films [1-5]. Screw dislocations [2-4] and isolated cubic phase crystallites in the hexagonal matrix [5] were suggested as possible candidates for such defects. However, a detailed microscopical investigation of GaN epilayers grown on vicinal surfaces of the SiC substrates where 364 nm line is particularly intense with respect to BE line have shown very high concentration of stacking faults [6]. This give us reasons to suggest that 364 nm line is related to excitons bound to stacking fault (SFE). In this paper we develop a theoretical model that allows to calculate the wave functions and the binding energies of SFE.

STACKING FAULT AS A POTENTIAL WELL FOR ELECTRONS

Two most common stacking faults (SF) in wurtzite GaN with an αbβaαbβ structure have the following stacking sequences αbβa<u>αbβcγb</u>βcγ (I_1), αbβa<u>αbβcγaα</u>cγaα (I_2) and αbβa<u>αbβcγaαbβa</u>αbβ (E) and corresponding Burgers vectors of surrounding dislocations are $\mathbf{b}(I_1) = 1/6[2,-2,0,3]$, $\mathbf{b}(I_2) = 1/3[1,-1,0,0]$ and $\mathbf{b}(E) = 1/2[0,0,0,1]$ [7]. It can be easily seen that they include layers of cubic phase with widths $w(I_1) = 1.5c_0$, $w(I_2) = 2.0c_0$ and $w(E) = 2.5c_0$ respectively, inserted into the host wurtzite crystal, where c_0 is the lattice constant. The wurtzite crystal can be considered as an uniaxially deformed along [111]-axis cubic crystal with corresponding strain $\varepsilon_{zz} = 0.612c_0/a_0 - 1$. For GaN with the lattice constants $c_0 = 5.185$ Å and $a_0 = 3.189$ Å [8] the strain is $\varepsilon_{zz} = -0.005$. This strain shifts the edges of conduction and valence bands by values $\Delta E_c = \Xi\varepsilon_{zz}$ and $\Delta E_v = (a-b)\varepsilon_{zz}$ respectively, where Ξ and a, b are the deformation potential constants for cubic GaN. The experimental values of Ξ and a, b for cubic GaN are not available. However, the combination

$$\Xi - a = dE_g/dlnV \qquad (1)$$

can be found from the experimental value of $dE_g/dlnV = -9.8$ eV[9]. The constants a and b for cubic GaN are related to deformation potential constants D_2, D_3 and D_5 for wurtzite GaN in cubic approximation by expressions

$$a = D_2 - D_3/3, \quad b = 2D_5 + 2D_3/3 \qquad (2)$$

This gives a = -14.6 eV and b = -2.1 eV for D_2 = -0.91Ry, D_3 = 0.22Ry, D_5 = -0.15Ry found from calculations of band structure of strained wurtzite GaN [10].
Then from Eqs.(1),(2) we can find Ξ = -24.4 eV. We would like to notice that the value of Ξ is much higher compare with other semiconductors $\Xi \sim$ - (4 - 8) eV [11]
Since the SFs are layers of cubic phase surrounded by wurtzite phase that can be considered as uniaxially compressed cubic phase they form potential wells for electrons. The depth of the wells is $\Delta E_c = \Xi\varepsilon_{zz}$ = 122 meV. The widths of the potential wells L depend on the interface positions between cubic and hexagonal phases that are in the range $L(I_1) = (1.0 \pm 0.5)\, c_0$ = 2.6 - 7.8 Å, $L(I_2) = (1.5 \pm 0.5)\, c_0$ = 5.2 - 10.4 Å, and $L(E) = (2.0 \pm 0.5)\, c_0$ = 7.8 - 13.0 Å. Thus, we can consider the SFs as quantum wells for electrons.

In the valence band the deformation potential a is negative and, therefore, SFs are potential barriers for holes. The widths of the barriers are the same as the widths of potential wells for electrons and the height of the barriers is $\Delta E_v = (a-b)\varepsilon_{zz}$ = 62 meV.
Thus, electrons are attracted to the stacking faults but the holes are repulsed from them and the interface between wurtzite and cubic GaN is similar to the II-type heterojunction

It should be noted that this model is semiphenomenological one. To check its accuracy we can calculate the difference in band gaps for wurtzite and cubic phases $\Delta E_g = \Delta E_c - \Delta E_v$ = 60 meV. The experimental values of ΔE_g are in the range of 90 - 190 meV [9]. Thus, the theoretical estimate based on this model is lower but in a reasonable agreement with the experimental value.

EXCITONS AT STACKING FAULTS

Since the stacking faults contain a few atomic layers the quantum effects are significant for calculation of the electron binding energy E_e at stacking fault. Thus, the binding energy can be found from a well known solution of one-dimensional Schrödinger equation for square quantum well and E_e is given by a solution of the equation

$$\sqrt{\Delta E_c - E_e}\, tg\sqrt{m_e L^2(\Delta E_c - E_e)/\hbar^2} = \sqrt{E_e} \qquad (3)$$

For the case $E_e \ll \Delta E_c$, E_e can be found in the δ-potential well approximation as

$$E_e = m_e(\Delta E_c L)^2/2\hbar^2 \qquad (4)$$

For the stacking fault of I_2-type with $L \sim$ 10 Å and m_e = 0.2 m_0 [13], the binding energy found from Eq.(4) is $E_e \sim$ 25 meV. Thus, the SFs can bound electrons even at room temperature.

The holes can be attracted to the electrons bound to the stacking faults via Coulomb force, forming excitons bound to stacking faults (SFE). The binding energy of the stacking fault exciton E_{SFE} can be estimated in an approximation that the electron at SF is immobile. An account of the

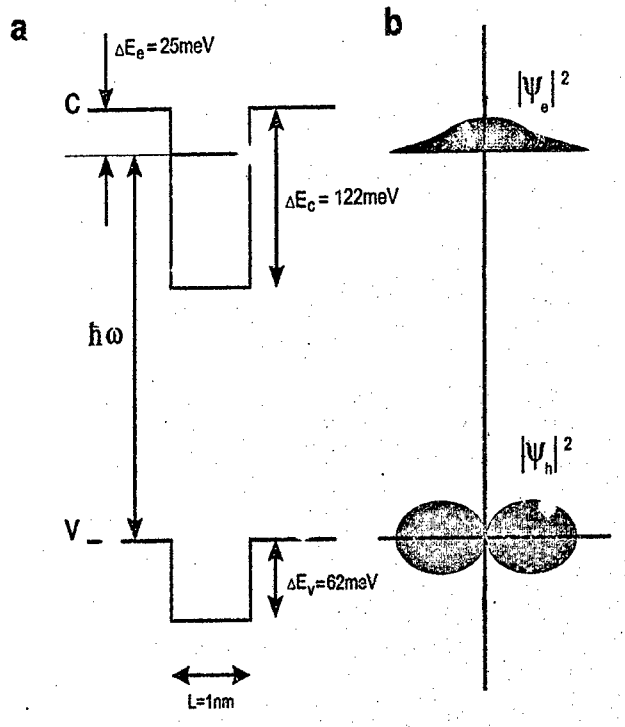

Fig.1 Schematic showing (a) the potential well of a stacking fault (I_2) embedded in a hexagonal wurtzite lattice; (b) the scheme for wave functions of electrons and holes bound to the stacking faults.

electron motion in the SF plane should reduce this energy to some extent and, therefore, this approximation gives an upper estimate for E_{SFE} . Since the SF strongly repels the hole its wave function should go to zero at SF plane. Therefore the binding energy of the hole is given by its lowest p-state in the Coulomb potential. The energy of this level is $E_0^{J=3/2,-} = 0.23\ Ry^*$, where $Ry^* = m_{hh}\, e^4/2\varepsilon^2\hbar^2$ and m_{hh} is the mass of the heavy hole, ε is dielectric constant [14]. For GaN with $m_{hh} = 1.76\ m_0$ [10] and $\varepsilon = 9$ [15], Ry* = 295 meV and the upper estimate for SFE binding energy is ~ 60 meV. From another hand the lower estimate for E_{SFE} is the binding energy of the free exciton ~ 30 meV. Thus, the binding energy of SFE is in the range E_{SFE} = 30 - 60 meV.

CONCL SIONS

A model of the exciton bound to stacking faults (SF) in GaN is suggested. It is shown that SFs are potential wells (depth ~ 120 meV) for electrons and potential barriers (~ 60 meV) for holes. The binding energy of the exciton at stacking faults is estimated as 30 - 60 meV.

On the base of this model we can attribute the line observed at ~ 3.4 eV in the h GaN samples with high density of stacking faults to the excitons bound to stacking faults. To check the model we can compare the shift of the line with respect to the h-GaN band gap $E_g - \hbar\omega = 3.5$ eV - 3.4 eV = 0.1 eV with the sum of binding energies of carriers to the stacking fault $E_{SFE} + E_e$ ~ 0.08 eV. Thus, a reasonable agreement exists between the model and the experimental data.

ACKNOWLEDGEMENTS

Y.T.R. thanks the Russian Fund of Fundamental Studies (grant no.96-02-17825-a)

REFERENCES

[1] C.Wetzel, S.Fisher, J.Kruger, E.Haller, R.J. Molnar, T.D. Moustakas, E.N.Mokhov, and P.G.Baranov, Appl.Phys.Lett., 68, (1996) 2556.

[2] Y.G.Shreter and Y.T.Rebane, Proccedings of the 23d International Conference on the Physics of Semi nductors, Berlin, V.1.D.22, p.2937 (1996)

[3] Y.T.Rebane and Y.G.Shreter, Proccedings of 23d International Symposium on Compaund Semiconductors, Astoria Hotel, St.Petersburg, Russia September 23-27, 1996 (in press)

[4] Y.G.Shreter, Y.T.Rebane, T.J.Davis, J.Barnard, M.Darbyshire, J.W.Steeds, W.G.Perry, M.Bremser and R.F.Davis Proccedings of MRS Fall Meeting, Boston, December 2-6, 1996, in press.

[5] W.Rieger, R.Dimitrov,D.Brunner, E.Rohrer,O.Ambacher and M.Stutzman, Phys.Rev., B, to be published.

[6] M.Albrecht, S.Christiansen, G.Salviati, C.Zanotti-Fregonara, Y.Rebane, Y.Shreter, Proc. MRS Spring Meeting, S.Fransisco, 2-7 April, 1997, to be published.

[7] P.Vermart, P.Ruterana and G.Nouet, Phil. Mag. a 75, 239 (1997)

[8] H.P.Maruska and J.J.Tietjen Appl. Phys. Lett. 15, 327 (1969)

[9] P.Perlin, I.Gorczyca, N.E.Christensen, I.Grzegory, H.Teisseyre, T.Suski Phys.Rev. B 45, p 13307-13 (1992)

[10] M. Suzuki and T.Uenoyama J.Appl.Phys. 80, 6868-6874 (1996)

[11] C.C Van de Walle Phys.Rev. B 39, pp.1871-1883 (1989).

[12] S.Strite and I .Markoc J.Vac.Sci. Technol. B 10, pp 1237-1266 (1992)

[13] A.S.Baker and M.Ilegems, Ph Rev., B7, 743 (1973)

[14] Y.Rebane, Phys.Rev., B48, 11772 (1993)

[15] H.Markoc, S Strite, G.B.Gao, M.E.Lin, B.Sverdlov, and M.Burns, J.Appl.Phys. 76, 1363 (1994)

EXCITON COMPLEXES IN MULTI-VALLEY SEMICONDUCTORS

A.A. ROGACHEV

A.F.Ioffe Physical-Technical Institute, 26 Polytechnicheskaya, St.-Petersburg, 194021, Russia

Excitons in multi-valley semiconductors form up to six or even more different excitonic molecules. These molecules are strongly bound and consist of electron-hole pairs of high density. In the paper we try to demonstrate the fact that the diagram of the gas (excitons and excitonic molecules) - excitonic liquid phase transition also obeys to the standard phase diagram while at a corresponding scaling it describes all gas-liquid phase transitions for simple liquids. Being very close to hydrogen atoms the excitons may form excitonic molecules and excitonic liquid [3,4]. Both such species have been experimentally observed ([1,2] and a lot of citations in these books). If exciton molecule consists of two excitons its binding energy differs from hydrogen molecule only by the structure factor equal to $\varepsilon^{2} m_{ex} / m_{O}$ where m_{ex} is the exciton reduce mass and ε is the dielectric constant. The problem of exciton molecules in a multi-valley semiconductors such as *Ge*, *Si* and some *III-V* -semicoductors is much more complicated one. Both germanium and silicon as well have multi-valley structure in the both conduction and valence bands. This can radically alter the energetic structure of e-h complexes (multiexciton complexes, polyexcitons and exciton molecules in present literature are synonyms). Degeneracy of conduction band is 8 in case of germanium and 12 in case of silicon. In *Ge* and *Si* the valence band structure is fourfold degenerate at Γ point with splitting on heavy and light holes. In the case of both donors and excitons the ground state of hole is fourfold degenerate. It is also probably true for the case of polyexcitons because they can be treated as having spherical symmetry. The density of condensed liquid also increases with the number of valleys. The exciton binding energy in a molecule (or in an excitonic complex) is close to that in exciton drops. However, being in essence the smallest possible drops, the polyexcitons have a smaller binding energy than the liquid drops for the same reason why small drops have always a smaller binding energy. Let us consider a model of polyexciton in which the number of valleys in both the conduction and valence bands is equal to γ . This means that we suppose the presence of γ of statistically independent electrons and holes. Actually γ can not be very large because of the overlap of exciton regions occupied in k-space.

We also suppose that $m_e = m_h = 2\,m_{ex}$. Wavefunctions of electrons and holes are identical, and so the charge density is equal to *zero* and correspondingly the potential energy calculated in the Hartry approximation vanishes. The kinetic energy E_k for the hydrogen-like wavefunctions is equal to $\frac{\hbar^2}{m_e r^2}$. In this approximation the stability of the excitonic molecule is determined only by the correlation and kinetic energies. The exchange energy is small, since electrons and holes from different valleys have different quantum numbers. The correlation energy of an electron and hole is equal to $\frac{e^2}{\varepsilon \cdot r_s}$, where $r_s = \sqrt{\frac{\varepsilon \cdot E_k}{6\pi \cdot e^2 n}}$ and $n \approx \frac{\gamma}{r^3}$. The ground state energy of electron-hole pairs in polyexciton containing 2γ excitons is equal to

$$-E_g = \frac{e^2}{e\sqrt{\frac{nr}{\gamma}}} - \frac{\hbar^2}{m_{ex} r^2} \qquad (1)$$

Minimizing E_g we find size of the molecule r, accordingly there are $r \approx \gamma^{-1/3} r_h$ and $-E_g \approx \gamma^{2/3} R_y$, where $R_y = \frac{1}{4}\frac{e^4 m_e}{\varepsilon^2 \hbar^2}$. The ground state energy of exciton liquid which calculated in the same approximation is also proportional to $\gamma^{2/3}$.

A little bit more involved calculation shows that in case of silicon there are polyexcitons containing two, three, four, and eleven together with twelve excitons. In an exciton the ground state is splited into the spin states ±3/2 and ±1/2. In this consideration we neglect this splitting. Then g-factor of an exciton will be 48 for silicon and 32 for germanium. In the ground state of excitonic molecules there are 4 hole states and much more electron states. An experiment shows [2] that excitonic complexes bound on donors contain 6 holes. However 2 holes are in the excited state, which is more likely to be Γ_7^+.

This model shows another stability island of near 11 and 12 excitons. The experiment, however shows that 5 and 6 exciton molecules exist. At present there is a problem how to differ molecules with large number of exciton from small e-h drops. For this reason it is difficult to define exactly the temperature in the triple point of the phase diagram. The phase diagram shown in Fig.1 is obtained free energy from experimental data [7]. It was supposed that a molecule with more than 4 excitons is not essential for the phase diagram.

In the part of the phase diagram related to smaller density of electron-hole pairs phase border N between gas + liquid and gas may be determined as

$$N = n_{ex} + \sum_{z=2}^{z=4} n_{ex}^{z} \left(\frac{2\pi\hbar^2}{kTm_{ex}}\right)^{\frac{3(z-1)}{2}} z^{\frac{3}{2}} \frac{g(z)}{g_{ex}^{z}} exp\left(\frac{E_z}{kT}\right), \qquad (2)$$

where $n_{ex} = g_{ex}\left(\frac{m_{ex}kT}{2\pi\hbar^2}\right)^{3/2} exp\left(-\frac{E_l}{kT}\right)$,

$g(z)$ is g-factor of exciton molecule, which consists of z excitons, E_l is the energy of exciton in e-h drop, E_z is the energy of exciton molecule formed from z free excitons. If exciton atom consists of up to 4 excitons, g-factors are g_{ex} =48, g_2 = 396, g_3 = 800, g_4 = 495.

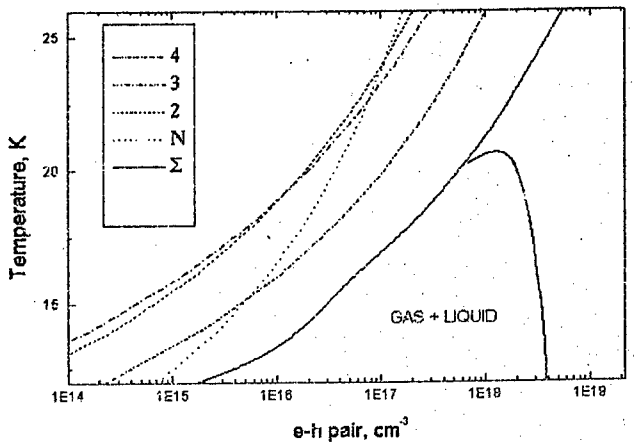

Fig.1 The exciton gas and liquid diagram. Σ -line is the border between gas and gas + liquid. Other lines are: biexcitons, triexcitons and tetraexcitons.

Distribution of polyexcitons in quantum wells on energy levels depends on the nature of polyexcitons, i.e. either they are bosons or fermions. The polyexciton spin is determined by the sum of spins of electrons and holes. Electrons within one valley are fermions. Electrons in a

polyexciton can be located in different valleys and can behave themselves as bosons. Two electrons from different valleys but with the same spins can be located in point. This is also related to holes, with spins 1/2 and 3/2 as well. The stability of polyexcitons is based on this property. At first glance it is obvious that if the polyexciton spin is equal to zero, it is a boson. If concentration of excitonic complexes in a quantum well is less than that at which the Mott criterion is fulfilled and temperature is low enough , all complexes are located on the lowest energy level of the well. The modified Mott criterion , to which polyexciton system obeys, is discussed in [6]. At high density polyexcitons transform into excitonic liquid drops, and electrons and holes are, of course, fermions.

Thus, transition from the system, which is determined by the Bose-statistics, to the system determined by the Fermi-statistics is conditioned by the fulfillment of the Mott criterion, i.e. by the transition from gas consisted of polyexciton to the electron- hole liquid.

In such an experiment it is desirable to use three-dimensional quantum well , since lowering down the dimentionality of the quantum well, as a rule, decreases the degeneracy degree of electron and hole energy levels. If the three-dimensional well has small linear dimensions ("dot"), electrons behave themselves as individual particles, since the Coulomb corrections are small. However in many cases the Coulomb corrections play a decisive role, for example, when the quantum well is shallow enough and does not capture an electron-hole pair (exciton), but can capture polyexcitons.

The work are supported by RFFI 97-02-18106 , FTNS 95-1011 and INTAS 94-789 grants.

References

1. C.D. Jeffries and L.V.Keldysh, Eds.of Electron-Hole Droplets in Semiconductors (North-Holland, , msterdam,1983).
2. A.A.Rogachev, in: Handbook on Semiconductors, Completely Revised Edition, Edited by T.S.Moss, Volume 1 (Elsevier Science Publishers B.V., 1992), p.449
3. S.A.Moskalenko, Opt. & Spekt. osk., v.5, 147 (1958).
4. V.M.Agranovich and B.S.Toshich, Zh.Eksp & Teor.Fiz., v..53, p.149 (1967).
5. A.A.Rogachev, Ann. de Physique, v.20, C2-389, (1995).
6. A.A. Rogachev, The 23rd Int. Conf. on Physics of Semiconductors, Vol.1, p.173, World Scientific, (1996).
7. M.L.W. Thewalt, V.A. Karasyuk, D.A. Harrison and D.A. Huber, *ibid.*, p.341.

POLARIZATION ANOMALIES IN LUMINESCENCE AND ELECTRON EMISSION FROM HIGHLY DOPED SEMICONDUCTOR STRUCTURES WITH SPLITTED VALENCE BAND

A.V.Subashiev and E.P.German
Department of Experimental Physics, State Technical University, 195251 St.Petersburg, Russia

The optical electron spin orientation in semiconductor structures has been extensively studied in recent years (see e.g. [1,2]). In quantum well (QW) structures and in compressively strained (in the plain of the heterointerface) semiconductor layers (SL) the valence band 4-fold degenerate Γ_8 state is splitted into only 2-fold spin-degenerate states Γ_6 (heavy-hole subband) and Γ_7 (light hole subband), the heavy-hole band being moved up. Therefore when the electrons are excited by circularly polarized light at the absorption edge from the heavy-hole subband a fully polarized final electron state is formed. The electron polarization up to 90 % was observed in polarized luminescence from quantum well structures [3] and from strained layers [4] and in polarized electron emission experiments on the strained structures [5] and superlattices [6].

At higher energies light holes contribute to the absorption, and smaller polarization is obtained, since the direction of the spin orientation is opposite for the electrons excited from the edge of heavy-hole and light-hole bands.

High polarization of the emitted electrons have made strained GaAs layers and GaAs-based superlattices with a surface activated in the negative electron affinity state an effective source of highly polarized electrons for high-energy physics applications [7].

In the report we consider the optical spin orientation of the electrons in highly p-doped semiconductor structures with splitted valence band in the case when the edge absorption is modified by the hole Fermi-distribution in the valence band. We point out that at low temperatures when the top of the heavy-hole band is empty, the absorption edge is shifted via the Moss-Burstein effect. Then, near the edge the transitions from the light-hole band can predominate, while at higher energies large contribution of the heavy-hole band changes the sign of the average polarization to the opposite. Thus, abrupt changes in the electronic polarization and, consequently, in the polarized luminescence and photoemission are predicted.

The strained structure energy band diagram illustrating the qualitative reasoning above is plotted in Fig. 1. It is readily seen that the light-hole absorption edge is lower in energy than the heavy-hole edge when $E_F(1+m_{hh,\perp}/m_c) > \Delta$. Here E_F is the heavy-hole Fermi energy, m_c is conduction band effective mass, $m_{hh,\perp}$ is the heavy-hole splitted band transverse effective mass, and Δ is the valence band splitting caused by the stress. Since $m_{hh,\perp}/m_c > 1$ the effect is shown to be observable in the samples with $\Delta \geq 20$ meV at acceptor concentrations $p \geq 10^{18}$ cm^{-3} and $T \leq 77$ K.

When temperature is raised, the Fermi-level shifting and the smearing of the Fermi-distribution lead to the heavy-hole domination in the edge absorption, and the spin orientation becomes a smooth function of the excitation energy and does not change its sign.

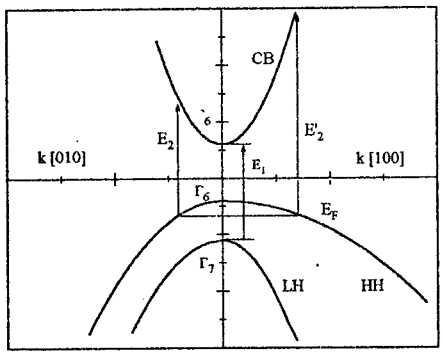

Fig.1 Energy bands for a strained (100) GaAs layer as a function of wave vector k along and perpendicular to the strain axis. The onset of the optical transitions from the splitted light-hole (E_1) and heavy-hole (E_2,E_2') valence band states to the top of the conduction band Γ_6 are shown by the vertical arrows, E_F being Fermi energy.

We have considered the circularly polarized light absorption in QW and in SL p-doped GaAs structures with different doping level on a $Ga_{1-x}P_x$ substrate, oriented along [100] axis with the valence band splitted by the lattice constant's mismatch. We assumed that as a result of heavy doping the excitonic effects are screened, and are negligible. The attainable values of valence subband splitting Δ and the hole Fermi energy are much smaller than the spin-orbital valence band splitting, therefore Luttinger model for valence band states is applicable. The average concentration of electrons excited from slitted valence band states in the conduction band in a unit time in a state with spin up and spin down have been calculated.

The electron polarization at the excitation moment is given by

$$P = P_h \frac{K_h}{K_l + K_h} + P_l \frac{K_l}{K_l + K_h} \qquad (1)$$

Here K_h and P_h (K_l and P_l) are the absorption coefficient and the electron polarization for the electron excitation from the heavy-hole (light-hole) band. The resulting electron polarization depends on the relative contribution of the light- and heavy-hole bands.

The absorption coefficient of GaAs strained layer with the band splitting $\Delta = 30$ meV calculated at temperature T = 4 K for several hole concentrations is shown in Fig. 2. The light-hole contribution and the heavy-hole contribution to the absorption are shown separately by the dashed lines. As expected, the onset of the heavy-hole transition is shifted to the high energy with the rise of the hole concentration. Note the square-root heavy-hole absorption coefficient energy dependence at the absorption edge, which results from anisotropy of the hole spectrum in the stressed layer. The anisotropy reduces the absorption coefficient up to the excitation energy $\hbar\omega = E_g + E_F(1 + m_{h,\|}/m_e)$ where $m_{h,\|}$ is the heavy hole mass in unstressed GaAs.

The results of the electron polarization calculation are depicted in Fig. 3. Separate contributions of the heavy-hole and light-hole transitions are shown by dashed lines. For small values of hole concentration the electron polarization is high and positive up to the doubled band-splitting energy, where the light-hole contribution

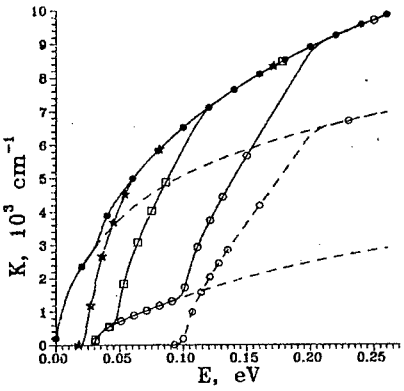

Fig. 2 Absorption coefficient versus excitation energy E = $\hbar\nu$ -- E_g in a strained heavily p-doped GaAs layer for several doping concentrations at T=4 K: (•) p=10^{16} cm^{-3}, (⋆) p=5×10^{17} cm^{-3}, (□) p=10^{18} cm^{-3}, (o) p=3×10^{18} cm^{-3}, and (dotted lines) separate contributions of HH and LH bands.

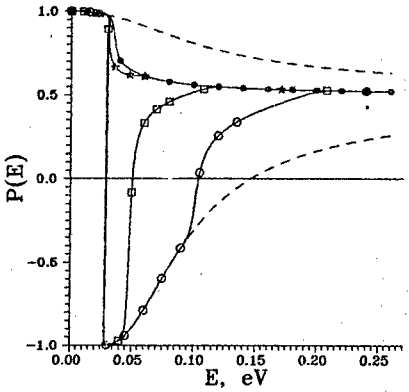

Fig. 3 Electron spin polarization as a function of the optical excitation energy in a strained heavily p-doped GaAs layer at T=4 K: (•) p=10^{16} cm^{-3}, (⋆) p=5×10^{17} cm^{-3}, (□) p=10^{18} cm^{-3}, (o) p=3×10^{18} cm^{-3}, dotted lines - separate contributions of HH and LH bands.

starts to reduce it. When Fermi - energy is larger than 0.5Δ the anomalous rapid changes of polarization from negative values are clearly seen. Note the changes of the heavy-hole contribution energy dependence in the case of high hole concentration, originated from the anisotropy of the hole spectrum.

The energy dependence of the electronic polarization below the interband transition edge is highly sensitive to the specific features of the fluctuation potential, the percolation level position and the electron spin relaxation mechanism. Still, the spin relaxation effects do not smear the polarization anomaly, but only specify the red-side edge of the polarization curves.

The energy at which the polarization changes it's sign is very sensitive to the Fermi-level position, and therefore to the band tailing density of states. We have calculated the Fermi energy for as a function of hole concentration (i) neglecting band tailing (ii) including band tails in so-called Halperin - Lax model [8], (iii) accounting for the tailing in modified quasiclassical approach, proposed in Ref. [10]. The most pronounced difference is found when the band splitting and the Fermi energy are of the same order of magnitude as the band tail states energy. For the acceptors in GaAs with high ($\approx$ 30 meV) ionization energy the values are found to be quite close.

The results of the electron polarization calculation for the GaAs QW structure for the 5 nm QW width are presented in Fig. 4. Separate contributions of the first heavy-hole subband (HH1) the first light-hole subband (LH1) and the second heavy-hole subband excitations are shown by dashed lines. The anomalous rapid changes of polarization from negative to

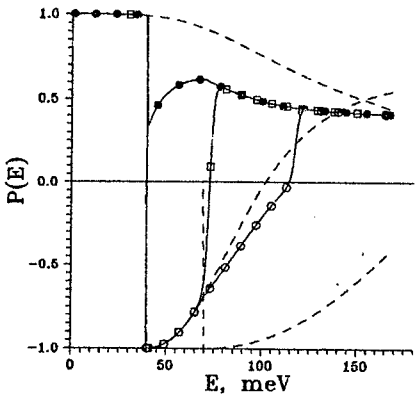

Fig.4 Electron spin polarization as a function of the optical excitation energy in a 5 nm-width QW GaAs structure at T=4 K: (•) $p=10^{11}$ cm^{-2}, (□) $p=1.5^{12}$ cm^{-2}, (o) $p=1.5 \times 10^{12}$ cm^{-2}, dotted lines - separate contributions of transitions from HH1, LH1 and HH2 subbands.

positive values are strongly pronounced for the hole concentration $p \geq 10^{12}$ cm^{-2}.

In conclusion, we have shown that in QW and strained layer structures with splitted valence band the electronic polarization can have anomalously strong dependence on the excitation energy, doping and temperature. The results indicate high sensitivity of the polarization anomaly to the fluctuation potential.

This work is supported by CRDF Grant No. RPI-351. The partial support by the RFBR (Grant No. 96-02-19187a) and by INTAS, project 94-1561, is also gratefully acknowledged.

References.

[1] C. Herman, H.-J. Drouhin, G. Lampel et al., Photoelectronic Processes in Semiconductors, Activated to Negative Electron Affinity In: *Spectroscopy of Nonequilibrium Electrons and Phonons*, edited by C. V. Shank and B. P. Zakharchenya, (Elseiver Science, B.V., 1992) p. 135.

[2] D. N. Mirlin and V. I. Perel', Hot-Electron Photoluminescense under Continuous-Wave Pumping, in *Spectroscopy of Nonequilibrium Electrons and Phonons*, edited by C. V. Shank and B. P. Zakharchenya, (Elseiver Science, B. V., 1992) p. 269.

[3] A. M. Vasil'ev, F. Daiminger, J.Straka, Superlatt. and Microstruct. **13**, 97 (1993).

[4] H. Horinaka, D. Ono, W. Zhen et al., Jpn. J. Appl. Phys. **34**, 6444 (1995).

[5] T. Maruyama, E.L.Garwin, R.Prepost, G.H.Zalapac, Phys.Rev. **B 46** ,4261(1992).

[6] T. Omori, Y. Kurihara, Y. Takeushi, M. Yoshioka et al., Jpn. J. Appl. Phys. **33**, 5676 (1994).

[7] *Proceedings of the workshop on photocathodes for polarized electron sources for accelerators*, SLAC-432 (January, 1994).

[8] B. I. Shklowski and A. L. Efros, *Electronic Properties of Doped Semicondutors* (Springer, Berlin, 1984).

[9] P.-V. Meigham. Rev. Mod. Phys., **64**, 755 (1992).

[10] O. A. Mezrin, O. V. Konstantinov, and N. S. Averkiev, Sov. Phys.-Semicond. **21**, 310 (1987)

The effect of the heterojunction abruptness on the one-band envelope-function method

E. E. Takhtamirov and V. A. Volkov
Institute of Radioengineering and Electronics of RAS Mokhovaya str. 11, 103907 Moscow, Russia

It is derived the one-band Hamiltonian for the Γ-point electrons in (001) heterostructures, non-graded interfaces, composed of III-V related lattice-matched semiconductors. The position-dependent effective mass parameters are included in the effective Hamiltonian. The accuracy of the Hamiltonian is specified. The effects caused by abruptness of heterojunctions are discussed.

The effective-mass approximation based on the envelope-function method is widely used to describe the dynamics of electrons in perturbed crystals. Still it is absent received firm basement under the approximation for semiconductor structures with position-dependent chemical composition. Considerable recent attention has been paid to the following two problems: 1) the correct choice of the kinetic energy operator comprising the non-commutative operators of the momentum and the effective mass, and 2) principal applicability of the envelope-function method to description of electron states in structures with abrupt heterojunctions. This is the case even for the simplest situation concerning the one-band Hamiltonian.

In Ref. [1] it was derived the effective conduction-band Hamiltonian for heterostructures with graded heterojunctions taking into account the position-dependent effective mass. Further it was shown and reported [2] that for abrupt heterojunctions the envelope-function equations have additional terms, which originate from the rapid change in periodic potential, that are not exponentially small. That is why even the all-band set of the $\mathbf{k}\cdot\mathbf{p}$ envelope-function equations becomes merely asymptotically exact. The requirement on desirable locality (differential form) of the envelope-function equations brings about further limitations in accuracy of the method. This way, it is necessary not only to include such terms into the Hamiltonian, but also estimate accuracy of all approximations made to assure correctness of consideration. This is the purpose of the present work.

Let us consider a (001) structure with a single heterojunction formed with related lattice-matched zinc-blend symmetry semiconductors. We adopt the following simple model for the lattice potential:

$$U = U_1 + G[U_2 - U_1] \equiv U_1 + G\delta U,$$

$U_1 \equiv U_1(\mathbf{r})$ and $U_2 \equiv U_2(\mathbf{r})$ are the periodic extended to the entire structure potentials of the left- and right-hand materials respectively, $G \equiv G(z)$ is the form-factor of the heterojunction: $G = 0$ if $z < -d$, and $G = 1$ if $z > d$. We assume $2d \cdot \bar{k}_z \ll 1$, where $\bar{k}_z$ is the characteristic wave number of a state in question. Having the function $G(z)$ at hand, and when the transition region of the heterojunction is much less then the characteristic wavelength of a state in question, we can specify the envelope-function equation with mathematically abrupt heterojunction (the Heaviside step-function $\Theta(z - z_0)$ substitutes $G(z)$, and $|z_0| < d$) that will be equivalent to some accuracy to the original equation. The resulting envelope-function equation including abrupt-interface-induced corrections has the following form, we set $z_0 = 0$:

$$[\varepsilon_{c0} + \Theta(z)\,\Delta U_c - \varepsilon]\,\mathrm{F}(\mathbf{r}) + \frac{1}{2} m_e^{\alpha}(z)\,\mathrm{p} m_e^{\beta}(z)\,\mathrm{p} m_e^{\alpha}(z)\,\mathrm{F}(\mathbf{r}) +$$

$$+\alpha_0 \mathbf{p}^4 \mathbf{F}(\mathbf{r}) + \beta_0 \left(\mathbf{p}_{\|}^2 \mathbf{p}_z^2 + \mathbf{p}_x^2 \mathbf{p}_y^2\right) \mathbf{F}(\mathbf{r}) +$$

$$+ d_1 \cdot [\mathbf{p} \times \mathbf{n}] \cdot \sigma \delta(z) \mathbf{F}(\mathbf{r}) + d_2 \cdot \delta(z) \mathbf{F}(\mathbf{r}) = 0. \quad (1)$$

Here ϵ_{c0} is the conduction band edge of the left-hand semiconductor, ΔU_c is the conduction band offset, $m_e(z)$ is the position-dependent band edge effective mass, $2\alpha + \beta = -1$, α_0 and β_0 are the weak non-parabolicity parameters, $\mathbf{p}$ is the momentum operator, $\mathbf{p}_{\|} = (\mathrm{p}_x, \mathrm{p}_y, 0)$; $\mathbf{n}$ is a unit vector along the z-axis, σ are the spin-1/2 matrices, $\delta(x)$ is the Dirac δ-function. The constants α, d_1 and d_2 are defined via the cumbersome expressions presented below.

The constant α:

$$\alpha = \frac{4\rho + \mu_1 + \xi}{2(\mu_2 - \mu_1 - 4\rho)}.$$

The abrupt-interface-related constant ρ is

$$\rho = \sum_{n \neq c; m \neq 0} \frac{i \langle c | \mathrm{p}_z | n \rangle \langle n \mid \delta U \sin(K_m z) \mid c \rangle}{2\pi K_m m_0 (\epsilon_{c0} - \epsilon_{n0})} \int_{-d}^{d} G'(z) \cos(K_m z)\, dz -$$

$$- \sum_{m \neq 0} \frac{\langle c \mid \delta U \cos(K_m z) \mid c \rangle}{2\pi} \int_{-d}^{d} G'(z) \left(\frac{\cos(K_m z)}{K_m^2} + \frac{\sin(K_m z)}{K_m} z \right) dz;$$

where $|n\rangle = u_{n0}$ is the periodic Bloch amplitude at the nth band edge ϵ_{n0} of the left-hand crystal for Γ point, m_0 is the free electron mass, $\hbar = 1$, $G'(z) = dG(z)/dz$, and $K_m = (4\pi m/a)$, m is an integer and a is the lattice constant. Further, μ_1 and μ_2 are the material-defined constants:

$$\mu_1 = \sum_{n \neq c} \frac{2 \cdot |\langle c | \mathrm{p}_x | n \rangle|^2 \delta U_{cc}}{m_0^2 (\epsilon_{c0} - \epsilon_{n0})^2} - \sum_{n,s \neq c} \frac{4 \cdot \langle c | \mathrm{p}_x | n \rangle \langle n | \mathrm{p}_x | s \rangle \delta U_{sc}}{m_0^2 (\epsilon_{c0} - \epsilon_{n0})(\epsilon_{c0} - \epsilon_{s0})},$$

$$\mu_2 = \sum_{n,s \neq c} \frac{2 \cdot \langle c | \mathrm{p}_x | n \rangle \delta U_{ns} \langle s | \mathrm{p}_x | c \rangle}{m_0^2 (\epsilon_{c0} - \epsilon_{n0})(\epsilon_{c0} - \epsilon_{s0})};$$

here $\delta U_{nn'} = \langle n \mid \delta U \mid n' \rangle$. And the constant ξ originates from the finite width of the transition region of the heterojunction:

$$\xi = 2\Delta U_c \left(d^2 - \int_{-d}^{d} 2G(z)\, z dz \right).$$

The constant d_1:

$$d_1 = \sum_{n,s \neq c} \frac{\langle c | \mathrm{p}_z | n \rangle \langle n | [\nabla \delta U \times \mathbf{p}]_x | s \rangle \langle s | \mathrm{p}_y | c \rangle}{4 i m_0^4 c^2 (\epsilon_{c0} - \epsilon_{n0})(\epsilon_{c0} - \epsilon_{s0})} +$$

$$+ \sum_{n \neq c; m \neq 0} \frac{\langle c | [\nabla (\sin(K_m z)\, \delta U) \times \mathbf{p}]_y | n \rangle \langle n | \mathrm{p}_x | c \rangle}{4\pi K_m m_0^3 c^2 (\epsilon_{c0} - \epsilon_{n0})} \int_{-d}^{d} G'(z) \cos(K_m z)\, dz;$$

here c is the velocity of light in vacuum. The constant d_1 depends both on the materials of heterojunctions and the grade of its abruptness.

The constant d_2 also comes from the finite width of the heterojunction and specific form of the function $G(z)$:

$$d_2 = \Delta U_c \left(\int_{-d}^{d} G(z)\, dz - d \right) +$$

$$+ \sum_{m \neq 0} \frac{\langle c \mid \delta U \cos(K_m z) \mid c \rangle}{2\pi K_m} \int_{-d}^{d} G'(z) \sin(K_m z)\, dz.$$

The total wave function expressed via the envelope is:

$$\Psi(\mathrm{r}) = u_{c0} \left(1 - \frac{1}{2} \sum_{n \neq c} \frac{|\langle c| \mathrm{p}_x |n\rangle|^2}{m_0^2 (\epsilon_{c0} - \epsilon_{n0})^2} \mathrm{p}^2 \right) \mathrm{F}(\mathrm{r}) +$$

$$+ \sum_{n \neq c} \frac{u_{n0}}{(\epsilon_{c0} - \epsilon_{n0})} \left[\frac{\langle n| \mathrm{p} |c\rangle \cdot \mathrm{p}}{m_0} + \delta U_{nc} \Theta(z) + \right.$$

$$\left. + \sum_{s \neq c, \alpha, \beta} \frac{\langle n| \mathrm{p}_\alpha |s\rangle \langle s| \mathrm{p}_\beta |c\rangle}{m_0^2 (\epsilon_{c0} - \epsilon_{s0})} \cdot \mathrm{p}_\alpha \mathrm{p}_\beta \right] \mathrm{F}(\mathrm{r}). \qquad (2)$$

We assumed that $|\langle n \mid \delta U \exp(K_m z) \mid n' \rangle|$ is of the order of $|\delta U_{nn'}|$ at finite m, the magnitude of the conduction band offset is of the same order, and the energy constant of the spin-orbit interaction is of the same order too. It is convenient to introduce the parameter $\lambda = (2m_e E_g)^{-1/2}$ depending on the characteristic bandgap E_g and the effective mass m_e (for conduction band of GaAs $\lambda \approx 6$Å). In Ref. [1] it was shown that k_z^2 is of the order of $2m_e |\delta U_{nn'}|$ the reason of necessary inclusion of the weak non-parabolicity terms into the envelope-function equation with position-dependent effective mass. During the derivation of the conduction band envelope-function equation (??) we used that small parameters are $t_1 = \lambda \cdot \bar{k}_z$, $t_2 = \bar{k}_z / K_1$ ($K_1 = 4\pi/a$) and $t_3 = d \cdot \bar{k}_z$. The accuracy of this one-band approximation does not allow to take into account all terms that are of the order of $|\delta U_{nn'}| \cdot t_1^q \cdot t_2^w \cdot t_3^v$ with $q, w, v = 0, 1, 2, 3$ and $q + w + v = 3$. This accuracy will be preserved for the structures with many layers if $L \cdot \bar{k}_z$ is of the order of unit or more, where L is the characteristic width of the layers. For wide bandgap materials ($\lambda \sim a$) the principal restriction in the accuracy originates from the going into the differential equation form for the envelope-function equation. It can be shown, that the envelope function F(r) Fourier transform $\mathcal{F}(\mathrm{k}) \propto (k_z)^{-3}$ at $k_z \to \infty$. If one includes, e.g. the term proportional to p_z^6, its contribution will be of the order of the inaccuracy, which the term will produce, appearing in going from the integro-differential envelope-function equation to the differential one. In this case this single-band approximation and any other many-band model, which pretends to consider the problem of the electron states more accurate, have generally speaking the same accuracy when the proper envelope-function equation is in the form of differential equations of finite order.

References

[1] E. E. Takhtamirov and V. A. Volkov, Semicond. Sci. Technol., **12**, 77 (1997).

[2] E. E. Takhtamirov and V. A. Volkov, Abstracts of Invited Lectures and Contributed Papers of Int. Symp. "Nanostructures: Physics and Technology", St. Petersburg 1996, pp. 330-333.

CYCLOTRON RESONANCE AND INTERSUBBAND ABSORPTION IN P-TYPE MQW Ge/GeSi HETEROSTRUCTURES IN QUANTIZING MAGNETIC FIELDS

V.Ya.Aleshkin, N.A.Bekin, I.V.Erofeeva, V.I.Gavrilenko, *M.Helm, Z.F.Krasil'nik, O.A.Kuznetsov, M.D.Moldavskaya, *V.Nikonorov and †M.V.Yakunin

Institute for Physics of Microstructures of Russian Academy of Sciences
GSP-105, Nizhny Novgorod, 603600, Russia; e-mail: gavr@ipm.sci-nnov.ru;
*Institut für Halbleiterphysik, Universität Linz, Austria
†Institute of Metal Physics RAS, Ekaterinburg, Russia

Investigations of far infrared (FIR) response of p-type strained MQW heterostructures (HS) are of significant interest from both fundamental and practical points of view. The stress resulting from the mismatch of lattice constants of well and barrier layers splits the degenerate valence band thus providing holes of low mass and high mobility in quantum wells. FIR photoconductivity connected with excitation of confined acceptors was observed in strained MQW Ge/GeSi HSs and the possibility of developing of sensitive photoelectic detector of long wavelength range of FIR region was shown [1]. In strained MQW InGaAs/GaAs heterostructures FIR emission of highly nonequilibrium hot holes at real space transfer was revealed and the new mechanism of the intraband population inversion was put forward [2]. However to the present time there have been no systematic exploration of valence band structure in strain MQW systems.

The paper is devoted to the investigation of cyclotron resonance (CR) and intersubband absorption in selectively doped p-type MQW $Ge/Ge_{1-x}Si_x$ heterostructures in quantizing magnetic fields. Earlier CR in Ge/GeSi HSs was studied in low magnetic fields up to 3 T only [3,4] (recently CR was observed in Ge/GeSi at B = 8.5T at λ = 119 μm [5]). The structures under investigation were grown by CVD technique on Ge(111) substrates. GeSi barriers were selectively doped with boron. Absorption spectra were measured by Bruker IFS 113 spectrometer optically coupled with helium cryostat with 14T superconducting solenoid. The radiation passed through the sample was detected by Si-bolometer. To reveal the field induced absorption the signal measured in the magnetic field $S(B)$ was divided by that obtained at $B = 0$.

Fig.1 represents normalized transmittance spectra of the sample #123. Four absorption lines can be identified in the spectra. The spectral positions of lines 1 and 2 are practically independent on the field. The line 3 shifts nearly linear with the field (see Fig.2). The resonant frequency of the weak absorption line 4 (it is much better pronounced in the sample #125) slightly increases with the field. The line positions for different samples are plotted in Fig.2. In the sample #125 the additional absorption line 3' was revealed. It is clearly seen that the slope of line 3 is nearly constant up to 14 T; it corresponds to the cyclotron mass of $(0.08 \div 0.09)m_0$, i.e. of the value of "classical" cyclotron mass at Fermi energy [4]. This fact is striking since in high magnetic fields the observed cyclotron energy exceeds several times the energy gap between the 1st and the 2nd hole subbands which are in addition highly nonparabolic [4]. The positions of lines 1,2 and 4 are in a good agreement with the calculated at $B = 0$ energy gaps between the 1st and the 2nd, 3rd and 4th heavy hole subbands correspondingly (bold segments in Fig.3). The above calculations were carried out taking into account the finite value of the valence band offset at the heterojunctions. In the quantizing magnetic fields the hole states in QW become zero-dimensional thus resulting in resonant transitions between subbands in contrast to the case of zero magnetic field.

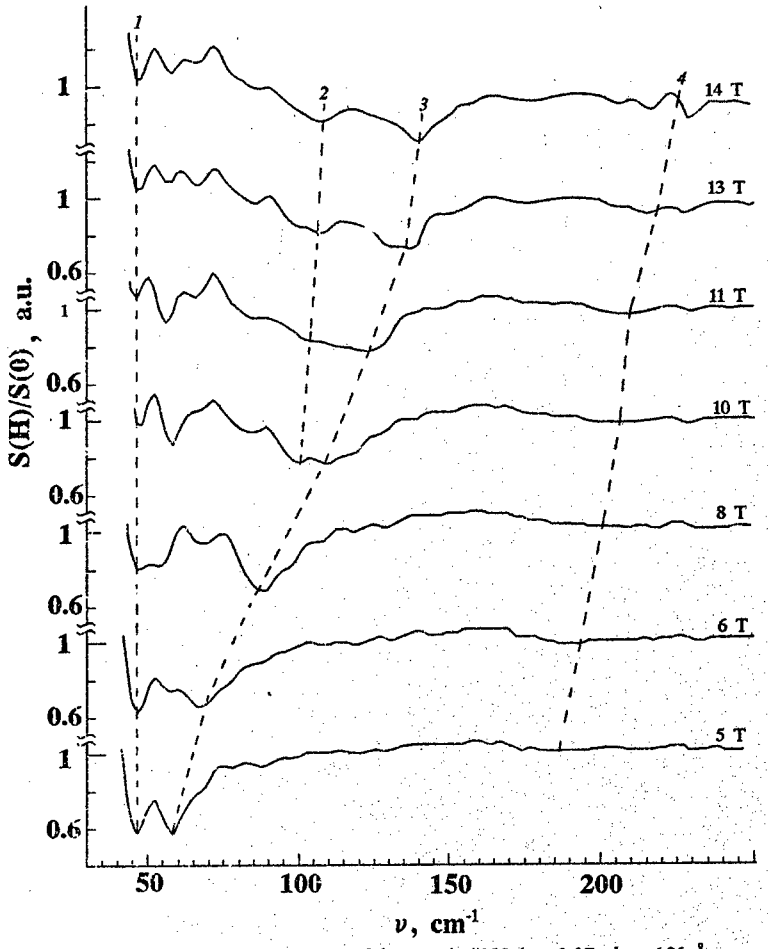

Fig.1. Normalized transmittance spectra of the sample #123 ($x \approx 0.07$, $d_{Ge} \approx 190$ Å, $P_{equiv} \approx 3.6$ kbar, $n_{QW} = 15$, $p_s \approx 2.4 \cdot 10^{11}$ cm^{-2}) in magnetic fields 5÷14 T; $T = 4.2$ K.

Calculations of the Landau levels versus magnetic field for QW with infinitely high walls using the Kohn-Luttinger approach were carried out to allow more detailed interpretation of the experimental spectra. The anisotropy of the hamiltonian was taken into account by first order perturbation theory. The results are given in Fig.3 where few lowest weakly interacting Landau levels

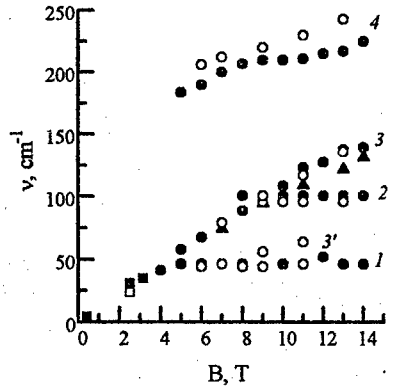

Fig.2. Spectral positions of the absorption lines versus magnetic fields of the samples #123 (•,□), #125(o,□; x ≈ 0.08, d_{Ge} ≈ 180 Å, P_{equiv} ≈ 3.6 kbar, n_{QW} = 36, p_s ≈ 2.7·10^{11} cm^{-2}), #374 (Δ; x ≈ 0.09, d_{Ge} ≈ 180 Å, P_{equiv} ≈ 1.5 kbar, n_{QW} = 6, p_s ≈ 2.9·10^{11} cm^{-2}); T = 4.2 K. Data for B < 4 T were taken from [4].

attributed to four heavy hole subbands hh1÷hh4 are presented. The discrepancy between subband edge positions calculated at B = 0 and Landau level positions at low magnetic fields is clearly seen. It originates from the assumption of infinite height of QW walls in Landau level calculations that results in the overstated energy values at $B \to 0$. Thus only qualitative comparison of these results with the experimental data is allowed. However this approach seems to give adequate description for the Landau level behavior within subband.

Landau levels in QW are classified in two independent groups designated by letters c and s (Fig.3). The only exception is the lowest levels in each subband -1(1), -1(2) ...which have the same nature as 3D states [6]. In the designation of a level the first number M = -1,0,1... numerates Landau levels within the group and the index at the letter numerates the levels with the same M

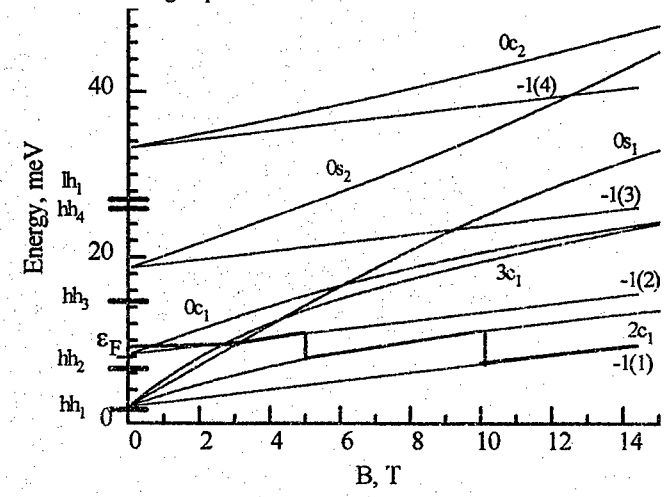

Fig.3. Calculated Landau level energies versus magnetic field for the sample #123 (for infinite height of QW). Bold segments across the energy axis indicate calculated positions of hole levels at B = 0, k = 0 in QW at finite band offset. Fermi level ε_F is shown schematically by bold line.

and c or s in the order of the increase of the energy. The levels -1(n) (n=1,2...) do not interact with other Landau levels; they linearly shift with the field with the same slope. So the lines 1 and 2 in Fig.1 which spectral positions are independent on the field can be naturally attributed to the transitions from -1(1) level to -1(2) and -1(3) levels correspondingly. The spectral position of the line 4 corresponds fairly well to the gap between hh1 and hh4 subbands. However this line exhibits a marked shift in the magnetic field (this absorption line is much better revealed in the sample #125 with greater number of QWs). This may be explained both by the transitions to 2nd Landau level in hh4 subband $0c_2$ which is relatively close to -1(4) one and by the transitions to the 1st light hole subband lh_1 that is close to hh_4 according to the correct calculations at $B = 0$ (Fig.3).

Despite the whole picture of Landau levels in QW is extremely complicated because of number of interacting levels [6] it is clearly seen from Fig.3 that the energy position of the $0s_1$ level attributed to hh1 subband has nearly constant slope versus magnetic field. This level "easily" penetrates into hh2 and hh3 subband. Such behavior results from the fact that $0s_1$ level pushes off only from the $0s_2$ one attributed to hh3 subband. The difference in the slopes of $0s_1$ and -1(1) levels corresponds to the cyclotron mass of $(0.07\div0.08)m_0$ that is in a good agreement with the observed cyclotron mass of $(0.08\div0.09)m_0$ for the line 3 (Fig.1,2). The difference in the quantum number $\Delta M = 1$ also corresponds to CR transitions within one and the same subband. Thus the striking behavior of CR line 3 which persists from millimeter wavelengths up to $\hbar\omega \approx 20$ meV is naturally explained by the existence of weakly interacting Landau levels. As far as the line 3' that was revealed in the sample #125 only (Fig.2) its spectral position corresponds to CR transitions between $2c_1$ and $3c_1$ levels (Fig.3) (in this sample the hole concentration is a little bit higher than that in #123 and the 2nd Landau level $2c_1$ seems to be populated up to 11.5 T). There is also some spectral structure resembling this line in spectrum of #123 at $B = 8$ T at $\nu = 55$ cm^{-1}. However at $B \geq 10$ T when only the lowest Landau level is populated in this sample the line is not observed in the spectra.

Thus the investigation of FIR absorption in selectively doped p-type MQW Ge/GeSi heterostructures in quantizing magnetic fields was carried out. Resonant transitions between hole subbands were revealed. CR lines resulting from transitions from two lowest Landau levels were observed. Nearly linear dependence of CR frequency on the magnetic field is shown to result from the existence of weakly interacting Landau levels.

The research described in this publication was made possible in part by FWF, Austria, project M00327-PHY; Russian Scientific Programs "Physics of Solid State Nanostructures" (projects # 1-065/3, # 2-027/4), "Physics of Microwaves" (project # 4.5), "Physics of Quantum and Wave Processes/Fundamental spectroscopy" (project #7.8) and Grant #95-02-04891 from RFBR. The authors would like to acknowledge A.V.Germanenko and G.M.Minkov for collaboration in the development of the numerical codes for Landau level calculation, Yu.N.Drozdov and L.D.Moldavskaya for x-ray investigation of the heterostructures.

REFERENCES

1. V.I.Gavrilenko, I.V.Erofeeva, A.L.Korotkov *et al.* JETP Lett. 65(2), p.209 (1997).
2. V.Ya.Aleshkin, A.A.Andronov, A.V.Antonov *et al.* JETP Lett. 64(7), p.520 (1996).
3. V.I.Gavrilenko, I.N.Kozlov, O.A.Kuznetsov *et al.* JETP Lett. 59(5), p.348 (1994).
4. V.Ya.Aleshkin, N.A.Bekin, I.V.Erofeeva *et al.* Abstr. Intern.Symp. "Nanostructures: Physics and Technology", St.Petersburg, 1995, p.271.
5. L.K.Orlov, A.V.Potapov, R.A.Rubtsova *et al.* Thin Solid Films, 1997 (in press).
6. Yu.G.Arapov, N.A.Gorodilov, V.N.Neverov *et al.* Pis'ma ZhETF. 59(4), p.247 (1994).

LATERAL ELECTRIC FIELD EFFECTS ON PHOTOLUMINESCENCE FROM InGaAs/GaAs MQW HETEROSTRUCTURES

V.Ya.Aleshkin, A.A.Andronov, D.M.Gaponova, V.I.Gavrilenko, D.G.Revin, B.N.Zvonkov[+], I.G.Malkina[+], E.A.Uskova[+]

Institute for Physics of Microstructures, RAS, 603600 N.Novgorod, GSP-105, Russia
E-mail: revin@ipm.sci-nnov.ru
[+]Physical-Technical Institute of N.Novgorod State University

In recent papers [1, 2] the far IR radiation from 2D hot holes in MQW $In_xGa_{1-x}As/GaAs$ heterostructures at lateral transport has been investigated experimentally. The remarkable nonmonotonic behaviour of the radiation intensities versus electric field were revealed under real space transfer and new mechanism of the intraband population inversion was put forward. The paper presents the first study of lateral electric field effects on the band gap photoluminescence (PL) from these heterostructures under real space transfer.

$In_xGa_{1-x}As/GaAs$ heterostructures ($0.03 < x < 0.2$, $d_{InGaAs} = 5 \div 10$ nm, $d_{GaAs} \approx 60$ nm, $n_{QW} = 20$) were grown by MOCVD technique at atmospheric pressure on semi-insulating GaAs (001) substrates. Two δ-layers of carbon were introduced at $2.5 \div 5$ nm from both sides of each $In_xGa_{1-x}As$ quantum well in GaAs barrier layers. Typical values of 2D hole concentration and mobility at T = 4.2K were of $p_s = (0.5 \div 3) \times 10^{11}$ cm^{-2}, $\mu \approx 3000$ cm^2/V·s. The lateral pulsed electric field up to 2 kV/cm $3 \div 5$ μs in duration was applied to the structure via strip electric contacts deposited on the sample surface at the distance $3 \div 4$ mm. PL was excited by continuous He-Ne or Ar^+ lasers, dispersed by monochromator and detected by cooled photomultiplier. Boxscar integrator was used for data acquisition. The laser beam was focused on the samples to a spot of 1 mm in diameter. The measurements were carried out at 4.2 K.

In strong electric fields current-voltage I(V) characteristics of wide quantum wells ($x \approx 0.2$, $d_{InGaAs} \approx 10$ nm) exhibit pronounced saturation resulting from the escape of the holes from the quantum wells into GaAs barrier layers where their mobility drops drastically [1]. In these heterostructures PL emission is caused by optical transitions between electron and heavy holes subbands in quantum wells. In the electric fields corresponding to the linear part of I(V) curve PL peak shifts to higher energy (up to 5 meV at $E \approx 0.6$ kV/cm) and broadens a little bit while the integral PL intensity remains nearly constant (Fig 1). This can be explained by the carrier heating in the quantum wells. At further increase of electric field the integral PL intensity goes down that indicates the carrier transfer to GaAs barrier

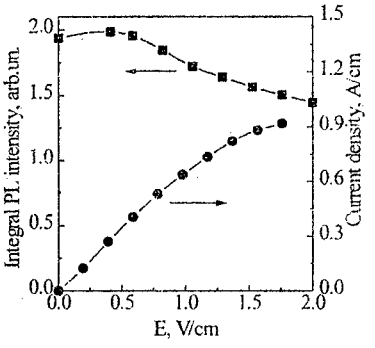

Fig.1 Integral PL intensity (■) and current density (●) versus lateral electric field for 8 nm quantum wells $In_{0.2}Ga_{0.8}As/GaAs$ heterostructures.

layers while the PL spectrum remains practically the same. The escaped from quantum wells holes can recombine only with the electrons in GaAs but this emission is undetectable because of barrier and cap-layer absorption.

In heterostructures with narrow and shallow quantum wells ($x \approx 0.1$, $d_{InGaAs} \approx 5$ nm) the energy position of the first heavy holes level in quantum well is higher than that of acceptor level in the barrier and at zero electric field holes are frozen at impurities. I(V) characteristics for these heterostructures exhibit sharp current increase at electric field of the order of 0.6 kV/cm due to impact ionisation of the acceptors [1]. Integral PL intensity in such heterostructures is nearly constant up to the acceptor breakdown, then it rapidly falls down 2 ÷ 3 times and decreases slowly afterwards with electric field increase (Fig.2).

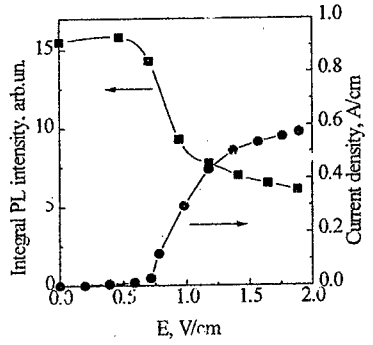

Fig.2 Integral PL intensity (■) and current density (●) versus lateral electric field for 5 nm quantum wells $In_{0.1}Ga_{0.9}As/GaAs$ heterostructures.

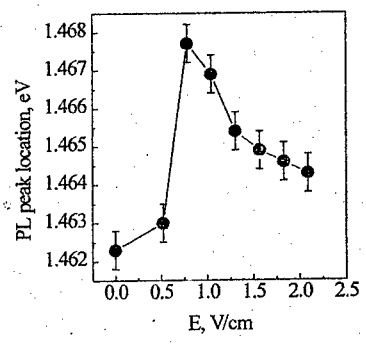

Fig.3 PL peak location versus lateral electric field for 5 nm quantum wells $In_{0.1}Ga_{0.9}As/GaAs$ heterostructures.

Before acceptor breakdown PL corresponds to the optical transitions from electron subband in quantum well to acceptor level in GaAs. These transitions are possible because the effective depth of penetration of electron wave function from quantum wells into the GaAs layers is approximately equal to the width of the spacer between heterojunction and δ-layer (also note that the concentration of acceptors is much greater than that of photoexcited holes.). The breakdown results in the hole transfer from acceptors to quantum wells. Under these conditions PL is mainly associated with the electron transitions between electron and heavy holes subbands in quantum wells. A remarkable high-energy shift (about 3 ÷ 5 meV) of PL peak is clearly observed in the fields corresponding to the breakdown (Fig.3). However under breakdown condition the electric field values are high enough for real space transfer; so the main part of holes escapes from quantum wells to GaAs. This can explain the decrease of PL intensity. With further increase of the electric field the holes are quickly withdrawn from the quantum wells to the barriers where their PL is undetectable. Some of them are captured in δ - layers thus providing the main part of the PL signal that results in the reverse shift of the PL peak.

PL peak half-widths in all investigated heterostructures proved to be very large (15 ÷ 20 meV). We suppose this is connected with the fluctuation of In composition in the excitation spot.

Thus PL in high lateral electric fields is shown to be a sensitive tool to probe hot carrier distributions and behaviour under real space transfer.

The work was supported in part by Grants # 97-02-16311 from Russian Foundation for Basic Research, # 1-064/3 from Russian Scientific Program "Physics of Solid State Nanostructures", the State Science and Technology Program "Physics of Quantum and Wave Processes" (subprogram "Fundamental Spectroscopy", Project 7.8) and # 094-842 from INTAS.

REFERENCES

1. V.Ya.Aleshkin, A.A.Andronov, A.V.Antonov, N.A.Bekin, V.I.Gavrilenko, D.G.Revin, B.N.Zvonkov, E.R.Lin'kova, I.G.Malkina and E.A. Uskova JETP Lett. 64, 7, 520 (1996).
2. V.Ya.Aleshkin, A.A.Andronov, A.V.Antonov, N.A.Bekin, V.I.Gavrilenko, D.G.Revin, E.R.Lin'kova, I.G.Malkina, E.A. Uskova and B.N.Zvonkov. Abstracts of Invited Lectures and Contributed Papers of the International Symposium "Nanostructures: Physics and Technology" St.Petersburg, 1996, p.443-446,

Infrared Second Harmonic Generation in a Generic Quantum Wire Biased with a Magnetic Field

A. Balandin,* S. Svizhenko, and S. Bandyopadhyay

Department of Electrical Engineering
University of Nebraska
Lincoln, Nebraska 68588

Abstract

We have theoretically studied second harmonic generation (SHG) and phase matching conditions in a generic semiconductor quantum wire biased with a magnetic field. A strong second-harmonic component of the dielectric susceptibility arises from the dipoles associated with transitions between three lowest magneto-electric subbands in the conduction band. Simultaneous action of a symmetric electrostatic potential (band-gap discontinuity) and an external magnetic field leads to the breaking of inversion symmetry without tilting the potential barriers thus preventing carrier escape.

It is well-known that non-vanishing second-order susceptibilities, $\chi^{(2)}$, can be obtained in semiconductor structures only if the inversion symmetry of the conduction-band potential is broken either by an external electric field or by the intentional growth of an asymmetric well. Obviously, the former is the preferred method[1] since an electric field can be continuously varied which allows one to tune the degree of symmetry-breaking and the magnitude of $\chi^{(2)}$. However, this method has a practical shortcoming. An electric field tilts the potential barriers of the well thereby allowing carriers to escape by tunneling or thermionic emission.

*The author is on leave from the Moscow Institute of Physics and Technology, Russia.

Here, we propose magnetostatic biasing to overcome this shortcoming. It will be shown that a magnetic field can break inversion symmetry without tilting potential barriers and promoting carrier escape. A transverse magnetic field applied to a quantum wire exerts a Lorentz force on an electron moving along the wire. As a result, its wave function (in any subband) will be skewed towards one edge of the wire. This skewing does not tilt potential barriers to first order. However, it effectively breaks inversion symmetry since it causes a net charge to accumulate at either edge of the wire. This leads to a non-vanishing even-order susceptibility in a symmetric structure. The skewing has another subtle effect. The degree to which the wave function is skewed is *different in different subbands* since an electron has different kinetic energies and hence experiences different Lorentz forces in different subbands. As a result, transitions between subbands whose wave functions have the same parity - which are forbidden without a magnetic field - are now allowed since the parities are altered by different amounts in different subbands by the different degrees of skewing. We should point out that this effect has similarity with the quantum confined Lorentz effect (QCLE) previously examined by Balandin and Bandyopadhyay [2] in the context of interband transitions between conduction and valence band states.

We consider a generic $GaAs$ quantum wire with a magnetic field applied perpendicular to the wire axis. The wire is approximately $150\mathring{A}$ wide. In order to evaluate the magnitude and dependence of the second harmonic generation (SHG) on the biasing field and wire geometry, we calculate the second order susceptibility using regular perturbative approach with empirical broadening parameters. The dipole elements $d_{mn}(B, W)$ for first three magneto-electric subbands are found within the framework of the electric dipole and envelope function approximations.

Fig. 1 presents the dipole moments for the lowest intraband transitions as a function of magnetic flux density. At zero magnetic field, a non-vanishing dipole matrix element occurs only for transitions between states of opposite parity (e1-e2, e2-e3). Transition dipole d_{e3-e1} has obvious non-monotonic behavior on a magnetic field. This transition is forbidden at zero field since the wave functions of the first and third subband have the same parity. At low and moderate magnetic fields, the parities are altered by the skewing of the wavefunctions and consequently d_{e3-e1} is no longer zero but increases

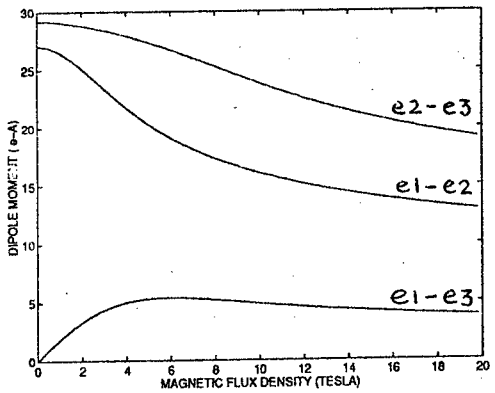

Figure 1: The dipoles of three inter-subband transitions as functions of the applied magnetic field.

with the magnetic field. The decrease at higher magnetic fields is related to the onset of Landau condensation: the traversing states ("skipping orbits") condense into closed cyclotron orbits (Landau levels) which are no longer skewed by the magnetic field to the wire edge since they have no translational velocity and hence no Lorentz force.

In Fig. 2, we show an absolute values of $\chi^{(2)}$ as a function of photon energy for two different values of the magnetic field. In our numerical calculations we have used $N = 1\ 10^{17}\ cm^{-3}$. Both susceptibility curves have pronounced peaks which correspond to magneto-electric subband transitions. The peak value of the second order susceptibility is $\chi^{(2)} = 14.5\mathring{A}/V$ for 1 tesla field (left panel); and $\chi^{(2)} = 43.1\mathring{A}/V$ for 3 tesla (right panel). The value of susceptibility increases strongly with the wire width up to $1500\mathring{A}/V$ at $500 - 1000\mathring{A}$ wide wires. Although the operation frequencies are no longer in the infrared range for these wire dimensions. This shows that relatively weak magnetic fields in quantum wires can produce similar magnitudes of $\chi^{(2)}$ as rather strong electric fields in quantum wells.

We have also calculated the absorption over the whole frequency range of interest. At resonance frequencies 72 meV and 124 meV the absorption coef-

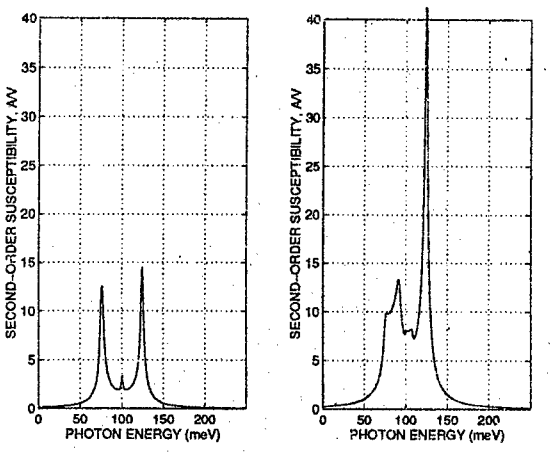

Figure 2: Second order susceptibility as a function of the photon energy for two values of the biasing magnetic field. The left panel corresponds to a magnetic flux density B=1 tesla, the right panel to B=3 tesla.

ficient $\alpha = 1.5\ 10^4\ cm^{-1}$ and $\alpha = 4.5\ 10^4\ cm^{-1}$, respectively. The absorption coefficient at twice the frequency is much less. This implies that the large portion of the pump energy will be absorbed by the structure and converted into second harmonic for which the structure is effectively transparent.

Another important factor for efficient second harmonic generation is the phase matching. Since the refractive index $n(\omega)$ of the most materials is frequency dependent, the following inequality holds $n(\omega) \neq n(2\omega)$. We will show that using a magnetic field as an additional degree of freedom, it is possible to adjust $n(\omega)$ so that at some frequencies the following holds simultaneously: $n(\omega) \approx n(2\omega)$ and $\alpha(\omega) >> \alpha(2\omega)$.

REFERENCES

[1]. M.M. Fejer, S.J.B. Yoo, R.L.Byer, A. Harwit, J.S. Harris, *Phys. Rev. Lett.*, **62**, 1041 (1989).

[2]. A. Balandin and S. Bandyopadhyay, *J. Appl. Phys.*, **77**, 5924 (1995).

GENERATION OF HIGH-FREQUENCY OSCILLATIONS IN MULTILAYER HETEROSTRUCTURES WITH NANOLAYERS

A.M.Belyantsev, A.B.Kozyrev

Institute for Physics of Microstructures of Russian Academy of Sciences
603600 Nizhny Novgorod, GSP-105, Russia

We consider the possibility of the direct effective transformation of a videopulse into a radiopulse with filling frequency of the order of 100 GHz in multilayer heterostructures (MLHS) with nanolayers where the redistribution of carriers under strong applied field occurs during the time of the order of $10^{-12} \div 10^{-13}$ sec.

Mechanism of the generation of the high-frequency oscillations is connected with the electromagnetic shock wave (EMSW) front instability to the longest period wave running in synchronism with this front [1]. The process of generation being qualitatively discussed the EMSW front in some sense can be considered as a traveling with velocity v_s source of radiation leaving behind an increasing "wake" in the form of electromagnetic oscillations running out of it with a relative velocity determined by the differences between phase $v_p = v_s$ and group velocity $(v_s - v_g)$. It is obvious from this consideration that the evolution of the "wake" of oscillations behind the EMSW front (radiopulse envelope) is determined by its elongation proportional to the distance covered by the EMSW front on NLTL, dispersive spreading, attenuation because of dissipation and nonlinear distortion.

The results of computer modeling of the transient processes arising in the course of EMSW formation on the NLTL with spatial dispersion and MLHS with nanolayers as nonlinear capacitors are presented. Evolution of the EMSW structure (excitation of the quasimonochromatic oscillations behind the ESMW front) and its spectrum on NLTL on the basis of MLHS characterized by either hysteretic (asymmetric MLHS) or single-valued functional (symmetric MLHS) capacitance-voltage characteristics is investigated. The requirements on MLHS and dispersion characteristics relevant for effective generation by EMSW of radiopulses with a high filling frequency and a relatively narrow spectrum are discussed.

MLHS-based NLTL for generation in the millimeter wave region can be realized in a planar form as a strip line whose dispersion characteristics can be controlled by the shape of the conducting metal plates. A design of such NLTL is shown in Fig. 1 *a* and its equivalent circuit diagram represented by a *LC*-circuit with capacitance cross links precisely describe its dispersion characteristics. The advantages of the NLTL with such a circuit diagram are the ease of dispersion control by means of variation of only one parameter (cross link capacitor) and the possibility to realize weak dispersion of the group velocity near the given frequency. It is the variant that has been used in the computer modeling.

The nonlinear current in symmetric (of the type considered in [2,3], see also Fig. 1 *c*) and asymmetric [4] MLHS (Fig. 1 *b*) is characterized by the capacitance ratio C_{max}/C_{min} and capacitance saturation voltage u_*.

In the case of the hysteretic nonlinearity (results of the computer modeling corresponding to the synchronism in the minimum of the group velocity are presented in Fig. 2) the nonlinear

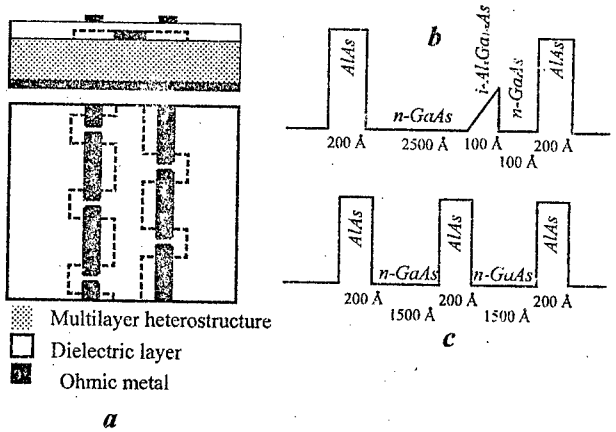

Fig. 1: a) Layout of the NLTL on the basis of MLHS
b) Conduction band profile of asymmetric MLHS
c) Conduction band profile of symmetric MLHS

medium behind the EMSW front saturates and arising oscillations propagate behind the front as in a linear medium, without distortion. In doing so the oscillations are generated strictly at the synchronous frequency and their spectral width is determined by the radiopulse width. The shape of the envelope depends significantly on the local behavior of the group velocity in the generated frequency range. The dispersive spreading is minimal and the shape of the radiopulse envelope is close to a rectangular when the synchronism $v_p(\omega) = v_s$ corresponds to the minimum of the group velocity $v_g(\omega)$. Thus the radiopulse droop comparatively fast takes stationary shape and its duration can be about 4-5 periods of generated oscillations. The radiopulse duration grows with distance because of the generation of oscillations of nearly the same amplitude.

The amplitude of oscillations behind the EMSW front u_ω is close to the magnitude of voltage of EMSW (u_s). As the results of the computer modeling show the depth of modulation in the EMSW structure depends on the parameters of nonlinear capacitance. Thus it grows with the increase of the capacitance ratio C_{max}/C_{min} and approaches 100 % for the capacitance ratio of 7÷8, i.e., the transformation of the videopulse into radiopulse is effective (the considerable part of the videopulse energy transforms into the energy of the high-frequency oscillations).

The radiopulse filling frequency can be tuned easily in a wide range both by variation of the bias voltage and by variation of the EMSW magnitude.

In the case of the transmission line whose nonlinear components are described by the single-valued function (symmetric MLHS) the propagation of perturbations behind the EMSW front takes place in a nonlinear medium .The typical results of the computer modeling for the considered case are given in Fig. 3. The characteristic frequency of oscillations in the EMSW

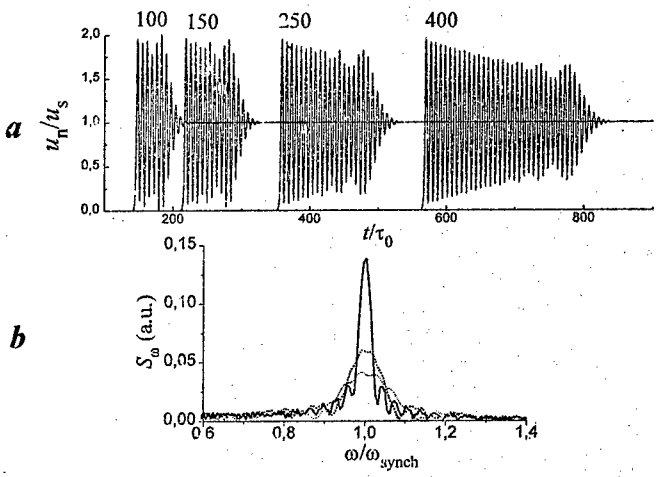

Fig. 2: Voltage waveforms at 100, 150, 250 and 400 sections (*a*) and spectra of the waveforms at 100, 150 and 400 sections (*b*) of nonlinear transmission line with nonlinear components on the basis of asymmetric MLHS.

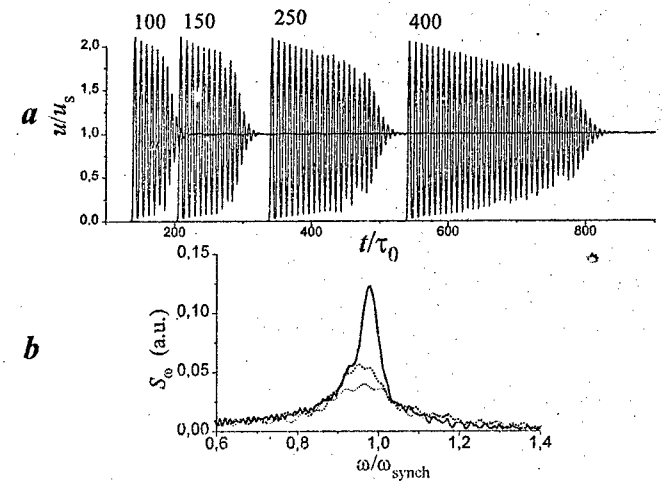

Fig. 3: Voltage waveforms at 100, 150, 250 and 400 sections (*a*) and spectra of the waveforms at 100, 150 and 400 sections (*b*) of nonlinear transmission line with nonlinear components on the basis of symmetric MLHS.

front takes place as in a nonlinear medium .The typical results of the computer modeling for the considered case are given in Fig. 3. The characteristic frequency of oscillations in the EMSW structure is determined by the synchronous frequency. However, in general, the generated radiopulse represents itself the frequency-modulated signal and the shape of oscillations is far from sinusoidal because the propagation behind the EMSW takes place in a nonlinear medium. This results in the spectral content of the generated radiopulse which in contrast to the hysteretic nonlinearity is wider and has more complicated structure. It is obvious that the higher the relative amplitude of oscillations (u_ω/u_s) and the higher the nonlinearity saturation voltage, i.e., $u_\omega \geq u_s - u_*$, the stronger the nonlinear processes manifest themselves in the spectrum of the nonstationary EMSW. It is found that to get the generation of the radiopulse with monochromatic filling and shape of the envelope close to rectangular the relative variation of the group velocity in the range of the generated radiopulse spectrum should be small and the nonlinearity behind the front should be weak (it is possible when the capacitance ratio is large and the saturation voltage is small in compare with EMSW voltage magnitude).

The generation of the radiopulse with quasihomogeneous in the wide frequency range spectrum is also possible at certain conditions.

This work was made possible under the grant from Russian Foundation for Basic Research (project N 96-02-19284).

REFERENCES

1. A.M.Belyantsev, A.I.Dubnev, S.L.Climin, Yu.A.Kobelev, L.A.Ostrovsky, "Generation of radiopulses by EMSW on ferrite transmission lines"; *ZhTF*, vol. 65, no. 8, pp. 132-142, 1995 (J. Tech. Phys.).

2. A.M.Belyantsev, A.V.Okomel'kov, "The influance of the screening effect on the nonlinear characteristics of the classic superlattices", *Fiz. Tech. Polipr.*, vol. 18, no 7, pp. 1214-1219 (1984). (Phys. Tech. Semicond.)

3. Hui Shi, W.-M. Zhang, C. W. Domier, N. C. Luhmann, Jr., L. B. Sjogren, and H. - X. L. Liu, "Novel concepts for improved nonlinear transmission line performance"; *IEEE Trans. Microwave Theory Tech.*, vol. 43, no. 4, pp. 780-789, April 1995.

4. A.M.Belyantsev, S.L.Climin, Yu.Yu.Romanova, "Dynamic behaviour of the capacitance of asymmetric multilayer heterostructure"; Abstract. 1-st Russian Conference on Physics of Semiconductors. Nizhny Novgorod (1993).

Infrared Emission from the Interface and Magnetotransport in type II Broken-gap p-GaInAsSb/p-InAs Heterojunction

M.P.Mikhailova, N.L.Bazhenov, V.A. Berezovets, A.V.Chernjaev, V.I.Ivanov-Omskii, K.D.Moiseev, , R.V.Parfeniev, V.A.Smirnov, Yu.P.Yakovlev.
A.F.Ioffe Physical-Technical Institute RAS, St Petersburg 194021, Russia

Recently, intensive electroluminescence (EL) on the type-II p-GaInAsSb/p-InAs single heterojunction has been observed and studied at T=77 K [1,2]. Two narrow luminescence peaks were observed in the spectral range of λ=3-4 μm with full width at half maximum about 10-20 meV. It was found that unusual EL is due to indirect (tunnel) radiative recombination of spatially separated electrons and holes localised in deep adjacent quantum wells at different sides of the interface. In the present work we continue studying the nature of this EL in more detail. Magnetoresistance and Hall coefficient under high magnetic fields at helium temperatures were also studied in order to confirm the existence of 2D carriers near the heterojunction interface.

Single GaInAsSb/InAs heterojunctions were fabricated using LPE technique on p-InAs (100) substrates doped with Zn up to the carrier concentration $5x10^{16}$ cm^{-3}. The wide-gap quaternary $Ga_{1-x}In_xAs_ySb_{1-y}$ layer (x=0.17, y=0.22) was lattice-matched with the substrate ($\Delta a/a=2\times10^{-4}$). This layer was also Zn-doped ($p=10^{18}$ cm^{-3}). The energy gap of the quaternary layer (E_g=0.630 eV) at T=77 K was determined by photoluminescence and photoconductivity measurements.

The EL spectrum included two band (band A - 311 meV, and band B - 384 meV) at T=77K (figure 1). As the temperature decreased, band A narrowed and shifted slightly towards higher energy (314 meV at T=4.2K). Band B split into two subbands with energies of 371 meV (B_1) and 400 meV (B_2). The intensity of band B_2 strongly increased as temperature was decreased. The shape of this band was analysed and shown to be Gaussian under "forward bi " (positive potential on InAs), but under the reverse bias the longwave edge of the band was inhomogeniously broadened. The intensity of band B_2 was shown to oscillate under magnetic field of up to 4.6 T. The energy position of this band and its temperature dependence allowed us to attribute this band to band-to-

acceptor transition in InAs. The position and shape of two other bands (A and B_1) seemed not to depend on the polarity of the applied voltage. Moreover, time-resolved spectroscopy showed that their position does not change even within 12 μs after switching off the current through the heterojunction. This fact indicates that these bands can be ascribed to transitions of 2D-electrons localised in the quantum well at the InAs-side of the interface.

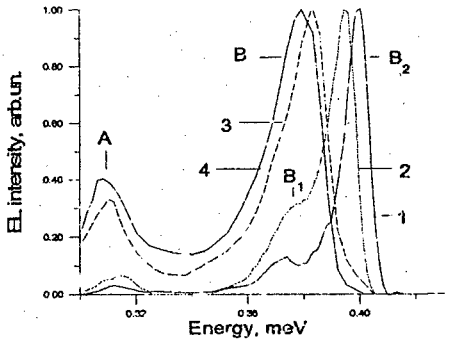

Figure 1. EL spectra under "reverse bias" at T=4.2K (1), 15K (2), 77K (3), 100K (4).

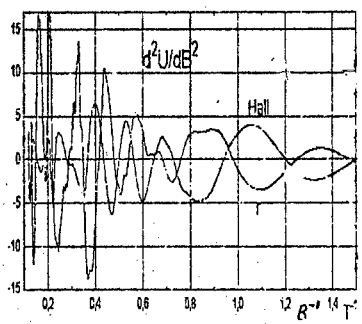

Figure 2. Oscillations of Hall coefficient and magnetoresistance versus reciprocal magnetic field.

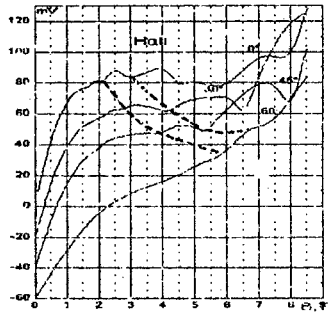

Figure.3. Hall signal versus magnetic field at various j.

In order to check whether 2D carriers can be observed in some independent experiment, the quantum oscillations of magnetoresistance and Hall coefficient have been measured at helium temperature in magnetic fields up to 9 T. The oscillating components were extracted using computer simulation. Figure 2 shows the results of this processing for the Hall coefficient and magnetoresistance. The oscillation picture was complicated and comprised three oscillating functions which was confirmed by Fourier analysis. The three oscillation periods indicated existence of several types of carriers in the heterostructure. For identification of 2D carriers we studied the dependence of these oscillations on angular orientation of the sample in magnetic field.

Figure 3 shows the Hall voltage as a function of the magnetic field B at different angles (j) between B and the normal to the surface. The Hall voltage in low magnetic fields (B <0.5T) was proportional to B and decreased with increasing the angle (~cos(j)). At higher B and j=0, the Hall signal remained nearly constant with varying the field; however, there was no such saturation region at j=60°. We attributed this phenomena to the effect of heavy holes on the Hall coefficient when the sample was rotated. Broken lines demonstrate the shift of the oscillation minima with variation of j. This evolution of the SdH picture corresponds to the two-dimensional electron system of the heterostructure. The oscillation period was found to be δ=0.0417 T^{-1}. Therefore, the electron concentration can be estimated as $n=6\times10^{11}$ cm^{-2} if one disregards spin and valley degeneration..

Thus, the results of EL study as well as the magnetotransport data obtained testify that 2D-carriers localised at the interface of p-GaInAsSb/p-InAs heterojunction participate in radiative recombination processes.

The work was supported by the International Association (INTAS), grant 94-789, as well as by the Russian Foundation for Basic Research, grant No 96-02-17841-a and the Program "Physics of Solid-State nanostructures".

References

[1]. M.P. Mikhailova, G.G. Zegrya, K.D. Moiseev and Yu.P. Yakovlev. Solid-State Electronics. 40 Nos 1-8, 673 (1996).

[2] N.L.Bazhenov, G.G.Zegya, M.P.Mikhailova, K.D.Moiseev, V.A.Smirnov, O.Yu.Solov'eva and Yu.P. Yakovlev. Semiconductors. 31, No 6 (1997) (in press).

Drift velocities, Bloch oscillations and electron impact ionization in silicon carbide superlattices

V.I. Sankin and A.A. Lepneva
A.F. Ioffe Physico-Technical Institute, Russian Academy of Sciences
Politekhnicheskaya 26, St.Petersburg, 194021, Russia
Fax: (812) 515 5747, (812) 247 1017, E-mail: sankin@widegap.ioffe.rssi.ru

The electric field being applied to a crystal results in a number of physical phenomena known under a common name of the Wannier-Stark localization (WSL). It should be noted that the theoretical problem of WSL is not finally solved and remains as a subject of discussions. Herewith the interest in the problem from the both fundamental and applied points of view is very substantial.

The results presented in this paper are different, but they are reflection the same phenomenon namely WSL in minizone spectrum conditions. In particular we will discuss impact ionization specificity, the different I–V characteristics of silicon carbide polytypes in WSL regime and the saturated drift velocities in polytypes with different superstructure parameters, at the electric field directed along the crystal axis or the superlattice (SL) axis, $F \parallel C$.

Earlier in our articles [1, 2] the results were presented which allowed to suppose that impact ionization at $F \parallel C$ was characterised by the practical absence of the electron component. But spicifical experimental difficulties did not allow to prove this supposition by direct observation of the electron impact ionization process because the conditions of pure electron excitation could not be provide at that time. The study of current-field characteristics of SiC for fields higher than 10^5 V/cm is a complicated problem because of the high electronic injection and high current density. Besides the electronic component of current should be separated from the hole component since the latter do not exhibit the behaviour inherent for WSL [1]. All these problems have been solved after the development of special tree terminal experimental structure allowing to control the current injected independently of the electric field and to make an electric field in the sample uniform [3].

Besides this experimental structure is available for investigation of impact ionization specificity because it allows to realize the impact ionization excitation by pure electron current. In this case a pulse and a direct voltage was applied to the emitter and collector of the structure. The direct voltage provide an electron injection from emitter and a high field in collector and pulse voltage provide a transport of electrons through a base in collector. An increase of pulse current was at increase of direct voltage. These changes of the pulse current can be caused by both the change of the injection level and impact ionization in collector region. The monotonous character of these changes which presented in Fig. 1 says that it is evident not caused by first reason because the impact ionization is characterized by much sharper current increase. Besides the peculiarities with NDC which arise on I–F characteristics at more strong fields are the results of electro-phonon resonances in Wannier–Stark ladder regime [4]. It is the main evidence that electron component of impact ionization is not observed to the fields almost 5000 kV/cm.

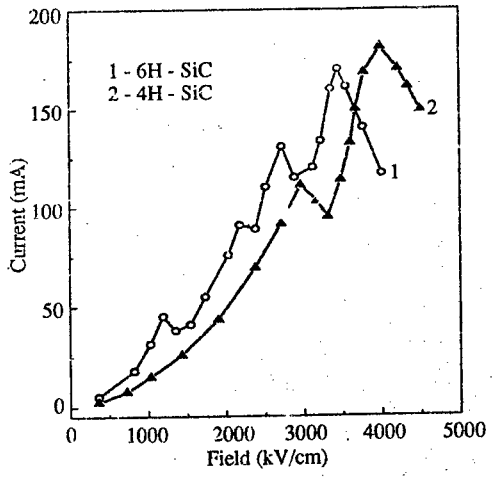

Fig 1.

These data are the evidence of assumption, which is noted above about the absence of electron component of impact ionization to some values of the electric fields. This phenomenon can be explained by suppression of an electron heating in electron-minizone theoretically described in [5].

In flight region of experimental structure, where electric field was uniform, I-F characteristics of different polytypes was investigated in strong electric field.

The most extraordinary feature of these characteristics is the NDC region (Fig. 2) associated with a some threshold field F_t specific for every polytype. For 4H, 6H and 8H t... F_t values are 2.9×10^5 V/cm, 1.5×10^5 V/cm and 1.1×10^5 V/cm respectively.

For the treatment of these results in terms of WSL the parameters included in Esaky-Tsu criterion $F_t > h/ed\tau$ should be obtained. The superlattice constants d for the three polytypes are 5 Å for 4H, 7.5 Å for 6H and 10 Å for 8H (Fig. 1b). Taking into account the similarity of electrophysical properties of the three polytypes and considering the scattering time τ for them as approximately the same one can conclude that there is a qualitative agreement between the threshold fields obtained for the three polytypes and one determined by the criterion. In other words the Esaky-Tsu criterion of NDC associated with the Bloch oscillations correlates well with F_t obtained experimentally for superlattices with periods substantially different.

The reasons mentioned above allows us to interpret the NDC obtained in the framework of WSL. However for the more accurate treatment of data the scattering time τ in a strong electric field should be determined experimentally for the three polytypes. Fortunately the experimental method used for the study allows to obtain the τ value by the analysis of the same current-field characteristic.

The idea is the following. The electronic transport in the experimental structure used for the measurements is determined by the transit-time mechanism, and the appropriate theory is suitable

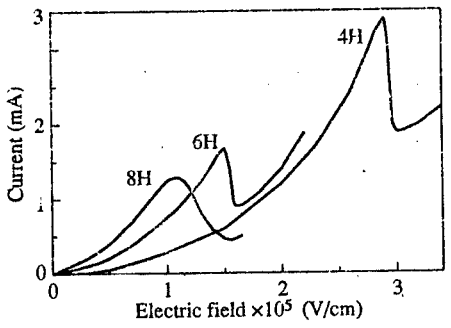

Fig 2.

for such a case. It is known that the current-field characteristic inherent for the transit-time conduction mechanism includes the region of the linear characteristic associated with the space charge limited current. This region is observed when the concentration of the carriers injected is as large as an ionized impurity concentration in the base. It is easy to show that the drift velocity is determined by the characteristic tilt tangent

$$j = 2\epsilon_s v_s V/w^2 \tag{1}$$

Here j, ϵ_s, v_s, V, w are the current density, the dielectric constant of semiconductor, the saturated drift velocity, the voltage applied to the base, and the base width respectively.

The feature of the experimental structure used for the study is an ionized impurity concentration so low that the space charge limitation of the current becomes at low current density when the electric field is insufficient for the carriers velocity saturation. Since velocity in such a case depends on the field as $v = \mu V$ (here μ is the electron mobility) the resulting law determining the current-field characteristic is run as follows:

$$j = 2\epsilon_s \mu V^2/w^3 \tag{2}$$

Thus the current-field characteristic of the experimental structure (Fig. 2) includes the following regions: the region with $j \sim V^2$ connected with the space charge limitation of the current injected (3) and the region with $j \sim V$ associated with electronic velocity saturation (2). Then on reaching the threshold electric field value the NDC associated with the Bloch oscillations arises. These regions are identified clearly in the experimental current-field (current-voltage) characteristics of the three polytypes involved into the study.

The electrophysical parameters such important as a high field mobility and saturated velocity are of great self-sufficient interest but in this study they are used for the calculation of the scattering time which can be expressed as $\tau = m\mu/e$. Values of high-field mobility μ obtained by the processing of the characteristic region with $j \sim V^2$ was found to be 3.1 cm^2/Vs, 4.5 cm^2/Vs and 6.4 cm^2/Vs for polytypes 8H, 6H and 4H respectively. The masses along the superlattice axis at such a strong field can be obtained with the formula:

$$v_s = (8E_p/3\pi m)^{1/2} \tag{3}$$

where the saturation velocity v_s can be extracted from the region with $j \sim V$ and the longitudinal optical phonon energy E_p is taken to be as high as 100 meV.

The experimental results processed this way lead to the following scattering time values: 1.75×10^{-13} s for 8H, 2.05×10^{-13} for 6H and 1.1×10^{-13} for 4H. The fault of t calculation related to variation of the base width is supposed to be about 20% or smaller. Considering these results one can conclude that the both experimentally measured parameters F_t and τ meet the Esaky-Tsu criterion.

To summarise it should be noted that the negative differential conductance was observed in a three superlattices possessing similar electrophysical properties but different periods. The threshold fields of NDC arise correlate well with the criterion of conductivity in the Bloch oscillations regime. The difference between these threshold field values is in good agreement with the difference of the superlattice constants.

The series of papers [3-4, 6] is a first study of WSL carried out with a new class of superstructure objects — natural superlattices of a hexagonal silicon carbide polytypes. The data obtained one can consider as both a serious experimental contribution to the problem of WSL and as a result very promising for superhigh frequency devices design.

From the analysis of linear region of I–V characteristics, which have been described by Eq. (1) the values of saturated electron drift velocities for 4H-, 6H-, 8H- and 21R-SiC were obtained which are approximately equal to 3.3×10^6, 2×10^6, 10^6 and 4.4×10^3 cm/sec correspondingly. The low values of velocities,which are significantly less than well known value $v_s = 2 \times 10^7$ cm/sec for $F \perp C$ [7] pay attention itself. But these values qualitatively correspond to the analogical results for artificial SL's in which localization is intrinsic property of these objects. In case of SiC polytypes, the velocity decrease is connected with decrease of the first-minizone width for the noted set of polytypes.

Thus, presented results are the convincing evidence of minizone structure of electron spectrum in SIC polytypes, which is necessary condition of FIL existence.

The partial financial support of Russian Foundation of Fundamental Research and Russian Science Program "Physics of Solid State Nanostructures" is gratefully acknowledged.

References

[1] A.P.Dmitriev, A.O.Konstantinov, D.P.Litvin, V.I.Sankin, *Sov. Phys. Semicond.* **17**, 686, (1983).

[2] V.I.Sankin, Yu.A.Vodakov, D.P.Litvin *Sov. Phys. Semicond.* **18**, 2146, (1984).

[3] V.Sankin, A.Naumov, *Superlattices and Microstructures*, **10**, 3, 353, (1991).

[4] R.A.Suris, B.S.Shamkhalova *Sov. Phys. Semicond.* **18**, 738, (1984).

[5] V.Sankin, I.Stolichnov. *JETF Letters*. **59**, 703 (1994).

[6] V Sankin, *Superlattices and Microstructures*, **18**, 4, 309 (1995).

[7] W.V. Muench and E.Petterpaul, *J. Appl. Phys.* **48**, 4823, (1977).

Simplest structures for stimulated photon emission by transitions from continuum to a quasilevel

O. A. Tkachenko, D. G. Baksheyev, M. B. Wojtsekhowski, and V. A. Tkachenko,*

Novosibirsk State University, Novosibirsk, 630090, Russia

**Institute of Semiconductor Physics, Novosibirsk, 630090, Russia*

Inelastic resonant electron transmission through semiconductor triple-barrier asymmetric structures [1] and Stark superlattices [2] has recently been predicted to be almost full due to photon-induced transitions between two or more quasilevels. In this report we will show that analogus strong response to irradiation can be produced by the structure in which electron tunneling in elastic channel is absent and which possesses only one quasilevel. Analytic solution for the time-periodic Schrödinger equation with potential in the form of a sharp step with δ-well placed at the higher potential side gives the Breit-Wigner-type formula for transmission coefficient with emission of quantum $\hbar\omega$:

$$T_{-1} = T_{\max}\frac{\Gamma_e\Gamma_i}{(E-\hbar\omega-E_0-\delta E_0)^2+\frac{1}{4}(\Gamma_e+\Gamma_i)^2},$$

where E is the energy of the electrons incident from the higher potential side, E_0 and Γ_e the quasilevel and its width in the absence of hf field, δE_0 and Γ_i the shift and broadening of the quasilevel due to inelastic decay, Γ_i being proportional to the square of hf field amplitude. Thus, one can control the probability of inelastic transitions by varying frequency $\hbar\omega$ and irradiation intensity. When $\Gamma_i = \Gamma_e$ the inelastic transmission coefficient, at the resonance $E = \hbar\omega + E_0 + \delta E_0$, reaches its maximum $T_{-1} = T_{\max}$. Analytic treatment and numerical modeling of real structures show that $T_{\max}$ can be close to unity at relatively small amplitudes of hf fields.

Such configuration can be made of an n-$Ga_{0.65}Al_{0.35}As$/GaAs/$Ga_{0.65}Al_{0.35}As$/n-GaAs structure with the voltage applied to its doped contacts to prevent from band bending [Fig. 1(a)]. Alternating voltage is provided by monochromatic infrared irradiation polarized along the growth direction of the structure. Numerical calculations show that 70%-transmission with emission of photons occurs in such structure, at optimized barrier thickness, frequency and amplitude of the high-frequency field, when cold electrons of energy E fall onto the quantum well from the higher potential side of the structure. With the account of elastic channel the transmission becomes almost full (95%) whereas it is small (4%) in the absence of irradiation [Figs. 1(b), 1(c)].

Stacking such well-in-step configurations in a single heterostructure permits of making a tunable cascade-amplifier of irradiation, and in this case inevitable technological nonuniformities of the cascades and deviating positions of quasilevels will not impede its workability. Indeed, since the electron motion above the step is classically allowed the energy of incident electron and, respectively, the frequency of the hf field are more widely variable than in resonant photon-assisted tunneling through two quasilevels E_0 and E_1 of an asymmetric triple-barrier structure [1]. In the former case the only resonant condition $E = E_0 + \hbar\omega$ must hold instead of two conditions in the latter case: $E = E_0$, $E_1 = E_0 - \hbar\omega$. It differs advantageously from single-well [3] and multiple-well [4] cascades in which photon must couple the pairs of quasidiscrete states.

Due to detailed balance, an analogous p-i-n structure with an $In_xGa_{1-x}As$ quantum well

can act, at a corresponding direct voltage, as an electron pump for electrons incident on the potential step from n-GaAs side and having the energy of the quasilevel.

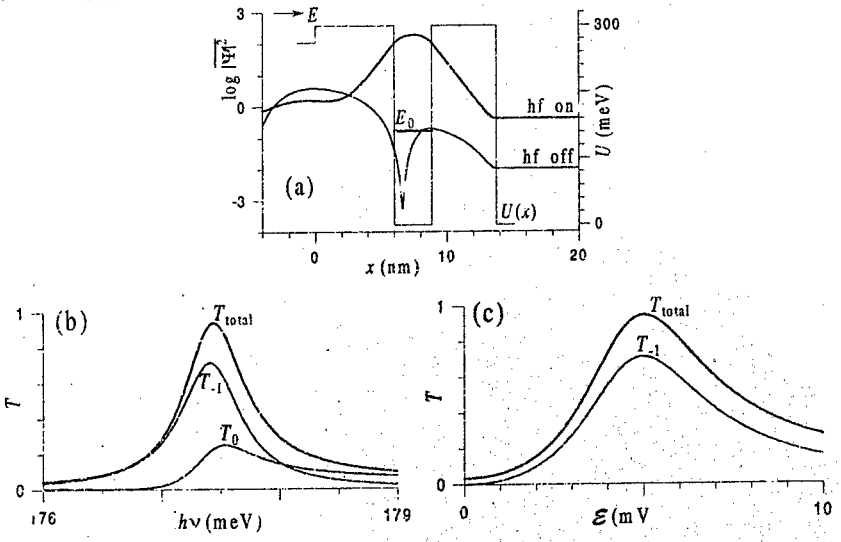

Figure 1. (a) Time-averaged probability density $\overline{|\Psi|^2}$ and potential of the structure $U(x)$. Electrons of energy $E = 320$ meV are incident from the left. Switching on hf field ($\hbar\omega = 177.5$ meV, amplitude $\mathcal{E} = 5$ mV/nm) results in strong increase of transmission. (b) Frequency dependence of elastic, T_0, inelastic, T_{-1}, and total transmission at fixed amplitude $\mathcal{E} = 5$ mV/nm. (c) Transmission at resonant frequency $\hbar\omega = 177.5$ meV versus amplitude of hf field.

The work was partly supported by Russian Foundation for Basic Research, Grant No. 96-02-1.060.

References

[1] M. Yu. Sumetskii and M. L. Felshtyn, Pis'ma Zh. Eksp. Teor. Fiz. **53**(1), 24 (1991); C. A. Stafford and N. S. Wingreen, Phys. Rev. Lett. **76** 1916 (1996).

[2] O. A. Tkachenko, V. A. Tkachenko, and D. G. Baksheyev, J. Appl. Phys. 81(4), 15 February 1997; O. A. Tkachenko, V. A. Tkachenko, D. G. Baksheyev, and A. S. Jaroshevich, in Compound Semiconductors-95, Inst. Phys. Conf. Ser. No 145 (IOP, 1996), Chapter 16, pp. 1193-1198.

[3] R. F. Kazarinov, R. A. Suris. Sov. Phys. Semicond. **6**, 120 (1972).

[4] J. Faist, F. Capasso, C. Sirtori, *et al.*, Appl. Phys. Lett. **64**, 1144 (1994).

Absorption of infrared radiation caused by bound-to-bound and bound-to-continuum direct transitions of hot carriers in simple rectangular and asymmetrical coupled multiple quantum wells.

L.E.Vorobjev, L.E.Golub*, E.A.Zibik, I.E.Titkov, D.A.Firsov, V.A.Shalygin, E.Towe+

St.Petersburg State Technical University
195251, St.Petersburg, Russia
*A.F.Ioffe Physico-Technical Institute, St.Petersburg, Russia
+University of Virginia, USA

The first results of investigations of infrared (IR) optical transmission variation due to carrier heating by longitudinal electrical field in GaAs/AlGaAs multiple quantum well (MQW) structures of two types are presented.

1. The structures of first type contained simple rectangular GaAs wells with the width L_w = 20 nm and $Al_{0.5}Ga_{0.5}As$ barriers with the width L_b = 10 nm. The MQW structures were grown on semiinsulating substrate by gas-phase epitaxy with metalorganic compounds (MOCVD). The total number of quantum wells was 400. The middle layer of each barrier was doped by acceptors such that the surface hole concentration was $p_s = 2 \cdot 10^{11}$ cm^{-2} . Hole mobility was μ = 3200 cm^2/V·s at T = 77K. The depth of quantum well was about 260 meV.

The main goal was to investigate the spectral and polarization dependences of IR radiation modulation due to hole heating by longitudinal electric field. Investigations were carried out in multipass waveguide geometry in the spectral region λ = 4...9 μm. In this region both bound-to-bound and bound-to-continuum transitions are possible. (Transitions are shown at Fig.1). Hole heating in longitudinal electric field results in hole redistribution among subbands. Thus, the light absorption is changed in electric field.

The equilibrium spectra of IR radiation absorption were investigated at different lattice temperatures. Optical modulation spectra for light of *s*- and *p*-polarization were studied at different values of electric field. The comparison of these spectra allowed us to determine the hot hole temperature as a function of electric field.

The absorption spectra obtained experimentally and the results of theoretical calculations are compared.

2. Structure of second type represents the selectively doped system consisted from two quantum wells of different width divided by tunnel-transparent barrier (see Fig. 2). The central 10 nm region of wide barrier was doped with Si providing sheet carrier concentration $N_s = 5 \cdot 10^{11}$ cm^{-3}. The number of structure periods was 150. This structure was grown by method of molecular beam epitaxy (MBE) on semiinsulating GaAs substrate. According to the calculations the energy positions of quantum levels measured from bottom of deep well are: ε_1 = 84 meV,

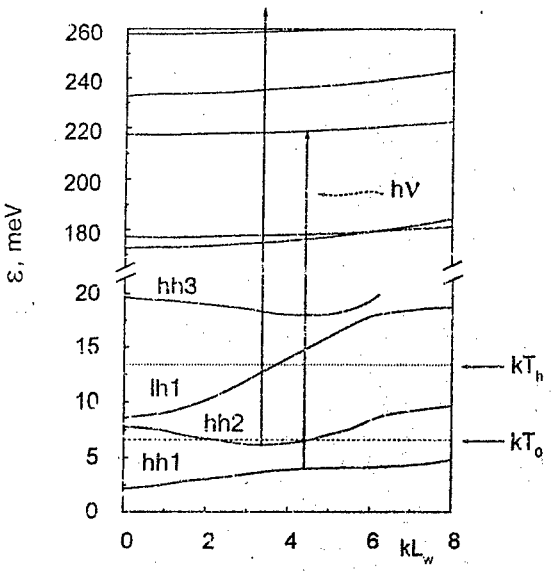

Figure 1. The diagram of bound-to-bound and bound-to-continuum optical transitions of holes.

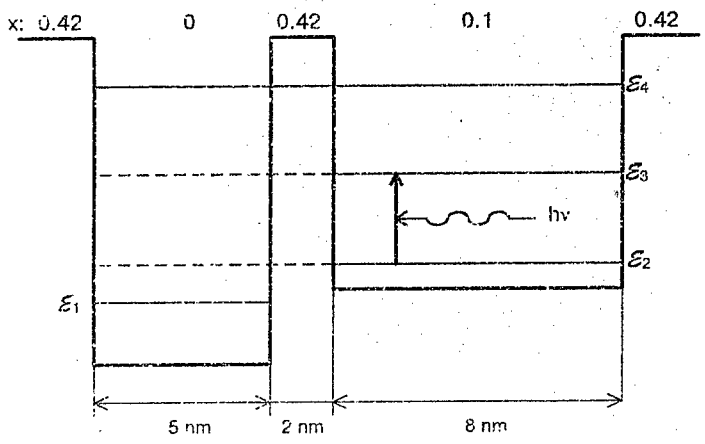

Figure 2. The energy diagram of tunnel-coupled quantum well structure GaAs/$Al_xGa_{1-x}As$ (without considering space charge effects).

ε_2 = 130 meV, ε_3 = 237 meV, ε_4 = 322 meV.

The equilibrium IR absorption spectra for such structures were measured for light of *s*- and *p*-polarization in multipass waveguide geometry (see inset in Fig. 3). Difference between these spectra is shown in Fig.3. One can see the spectra transformation with temperature due to electron redistribution between energy subbands.

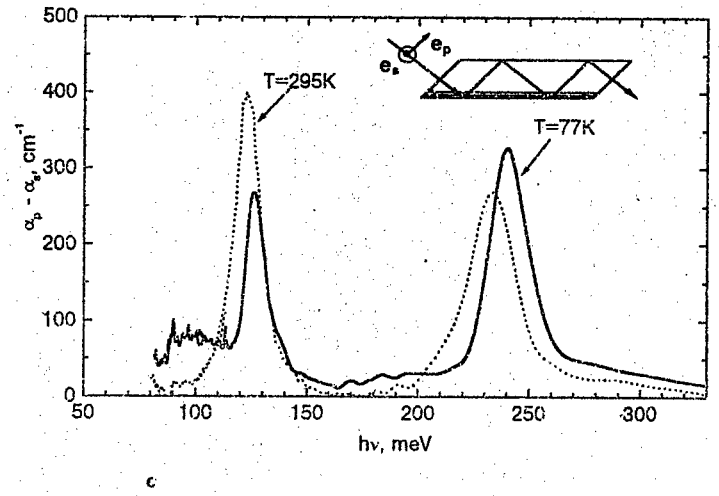

c

Figure 3. The equilibrium light absorption spectra for structure with tunnel-coupled wells. The unit polarization vectors for light of p- and s-polarization are shown in the inset.

The strong heating longitudinal electric field results in transitions of electrons in real space from narrow well into wide one (the electrons occupied level ε_2). Therefore optical absorption appears in the region $\hbar\omega \approx \varepsilon_3 - \varepsilon_2$.

We investigated experimentally dependence of absorption modulation on heating electric field at λ = 10.6 and 9.6 μm and analyzed it. Comparing the variation of absorption coefficient due to electron heating in electric field and the temperature dependence of equilibrium absorption at the same wavelength we determined the electron temperature as a function of electric field.

This work was supported by Russian Foundation for Basic Researches (Grant No. 96-02-17404a), INTAS-RFBR (Grant No. 615i96), Ministry of Science and Technology (Program "Physics of Solid State Nanostructures, Grant No. 1-093/4).

Emission and absorption of FIR radiation by hot electrons in simple rectangular and asymmetric tunnel-coupled quantum wells

L.E.Vorobjev, S.N.Danilov, D.V.Donetsky, Yu.V.Kochegarov, I.E.Titkov, D.A.Firsov, V.A.Shalygin

St.Petersburg State Technical University
195251, St.Petersburg, Russia

V.N.Tulupenko

T.Shevchenko Kiev National University, Ukraine

G.G.Zegrya

A.F.Ioffe Physico-Technical Institute, Russia

E.Towe

University of Virginia, USA

The results of investigations of new optical phenomena connected with intra- and intersubband transitions of hot electrons in selectively doped GaAs/AlGaAs quantum wells of two types are presented. Electron heating was caused by electric field applied along the layers of structures.

1. The quantum wells of the first type were simple rectangular GaAs wells of width L_w = 6 nm. The $Al_{0.22}Ga_{0.78}As$ barriers was 14 nm in width. The central 6 nm thick region in barrier was doped with Si to provide at T = 77 K the carrier concentration $N_s = 3x10^{11}$ cm^{-3}, carrier mobility was about 3400 cm^2/(V·s). The structure had 150 wells. The layers were grown with MBE on semiinsulating GaAs substrate. We used p-Ge FIR hot hole laser as the source of light and multipass geometry in investigations of structure transmittance.

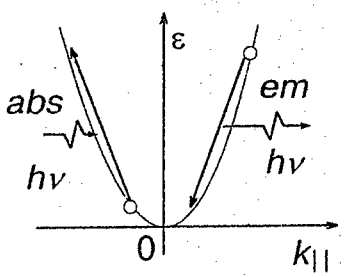

Figure 1. The diagram of intrasubband optical transitions in rectangular quantum well.

There are two energy levels of size quantization in these wells, one of them is near the top of the well. In such well the emission and absorption of FIR radiation connected with indirect transitions of hot electrons within the first energy subband (see Fig. 1) were studied. The emission spectra in the range of 70...350 μm are presented in Fig. 2 and the dependence of modulation of radiation with λ = 90 μm is shown in Fig. 3. The sign of modulation corresponds to reduction of absorption. The calculations of emission spectra and change of absorption was carried out taking into account various scattering mechanisms: polar phonon emission, impurities, e-e interaction, interface roughness scattering. Results of calculations are compared with experiment.

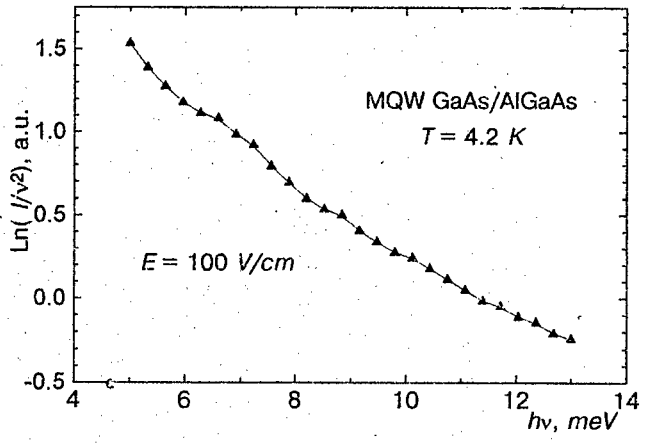

Figure 2. The emission spectra of hot electrons in rectangular quantum wells. The radiation was observed from the butt-end of the structure.

2. As quantum wells of second type we used selectively doped system consisted from two wells of different width divided by tunnel-transparent barrier (see Fig. 4). The central region of wide well was doped with Si providing sheet carrier concentration $N_s = 5x10^{11}$ cm^{-3}. The number of structure periods was 150. This structure also was grown by MBE on semiinsulating GaAs substrate. According to the calculations the energy positions of quantum levels measured from bottom of deep well are: ε_1 = 41 meV, ε_2 = 95 meV, ε_3 = 106 meV, ε_4 = 123 meV. The strong heating longitudinal electric field results in transitions of electrons in real space from narrow well into wide one. The electrons occupied levels ε_2 and ε_3 and can drop on level ε_1 emitting optical phonon (more likely from level ε_2 than from level ε_3).

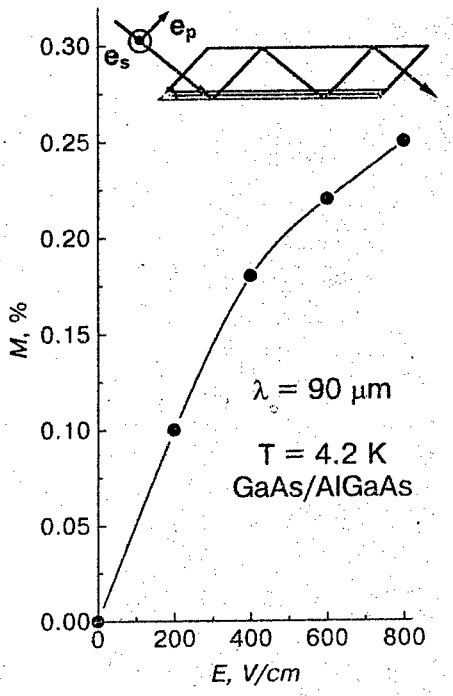

Figure 3. The modulation of absorption for light of s-polarization in strong electric field.

We have found spontaneous far-infrared emission from these structures under electron heating by longitudinal electric field and have studied emission spectra in region λ = 30...350 μm. The contributions in spontaneous emission of direct electron transitions $\varepsilon_3 \rightarrow \varepsilon_2$ accompanied by emission of photon and indirect intrasubband transitions with participating of above-mentioned scattering mechanisms are analyzed.

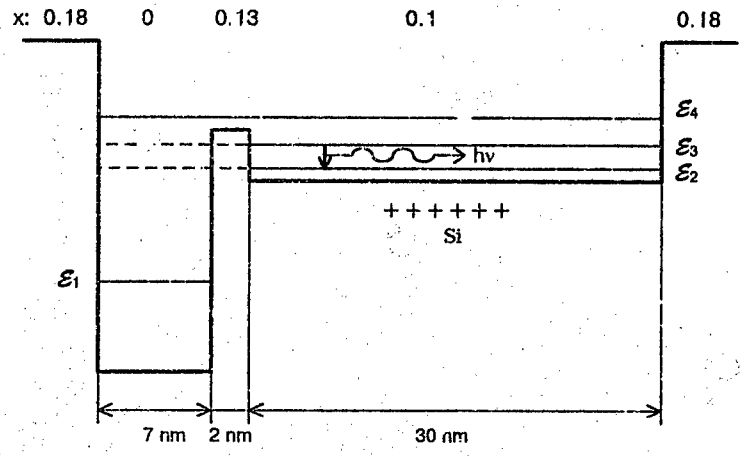

Figure 4. The energy diagram of tunnel-coupled quantum well structure $GaAs/Al_xGa_{1-x}As$ (without considering space charge effects).

This work was supported by Russian Foundation for Basic Researches (Grant No. 96-02-17404a), INTAS-RFBR (Grant No. 615i96) and Russian Ministry of Science and Technology (Program "Physics of Solid State Nanostructures, Grant No. 1-093/4).

Calculation of Thresl old Characteristics of 3 – 4 μm Compressively Strained InAlAsSb MQW Lasers

Aleksey D. Andreev and Georgy G. Zegrya

A.F.Ioffe Physical-Technical Institute of Russian Academy of Sciences,
26 Polytekhnichesl ya, St.-Petersburg 194021, Russia
Phone: +7-812-247-9367, E-mail: andreev@theory.ioffe.rssi.ru

Threshold characteristics of compressively strained $InAlAsSb$ $3-4\mu m$ MQW lasers have been studied theoretically. It is shown that the internal absorption decreases with strain, which results in weaker temperature dependence of the threshold carrier concentration. It is demonstrated that the strain considerably improves threshold characteristics of $InALAsSb$ QW laser and increases its limiting operation temperature.

High performance mid-infrared lasers operating in the $3-5\mu m$ band are highly desirable for many applications such as pollution monitoring, molecular spectroscopy and laser radar systems. Compressively strained quantum well (QW) structures based on $In_xAl_{1-x}As_ySb_{1-y}$ alloy appear to show much promise in this regard [1-3]. However the III-V mid-infrared $(3-4\mu m)$ lasers operating at room temperatur : has not been created up to now. Increasing limiting operating temperature of mid-infrared lasers is possible by choosing the optimal parameters of the multi-quantum well (MWQ) structures. In these structures the Auger recombination (AR) processes give the main contribution to the threshold current density. Therefore to increase the laser operating t emperature a decrease of AR rates is necessary. In our recent paper [4] we have shown that the AR rate is very sensitive to the variation of the QW parameters. In particular, the AR rate decreases when the compressive strain increases. In addition, the strain increases the laser gain which results in lower threshold carrier density.

The aim of the present paper is to study theoretically the effect of strain on the threshold characteristics of the MWQ $3-4\mu m$ lasers based on $In_xAl_{1-x}As_ySb_{1-y}$ alloy. It is demonstrat d that using compressively strained MQW structures considerably improves the parameters of $3-4\mu m$ $In_xAl_{1-x}As_ySb_{1-y}$ lasers.

In the present work, we study the multi-quantum well laser structure consisted of $AlAs_{0.08}Sb_{0.92}$ cladding layers, $In_{0.}Al_{0.2}As_{0.72}Sb_{0.28}$ barriers of width 100Å and $In_xAl_{1-x}As_ySb_{1-y}$ quantum wells. The QW width a and the number of QW N_{QW} were varied. Analogously to Ref. [2], the composition of the quaternary alloy of the QW we determined from the condition that the emission wavelength λ is a constant at given strain $\xi = (a_W - a_B)/a_B$ and QW width a.

For $InAlAsSb/GaSb$ heterostructures with QWs considered in this paper, the CHCC Auger process is the dominant one, since for these structures $(\Delta_{so} - E_g^{eff}) \gg T$, where Δ_{so} is the spin-orbit splitting, T is temperature. Therefore in this paper we restrict our study to the CHCC Auger process [4-7].

The calculated AR coefficient essentially depends on strain and QW parameters (QW width, barrier heights, emission wavelength) [4,6]. However the temperature dependence of the AR coefficient is weak, i.e. the Auger process is a thresholdless one [8]. Therefore the temperature dependence of AR rate is determined mainly by the temperature dependence of the carrier concentration.

In our analysis of the interband light absorption we have followed to Ref. [9]. In MQW structures considered in this paper $(\Delta_{so} - E_g^{eff}) \gg T$, therefore we have assumed that the dominant mechanism of the light absorption is that involving the electron excitation. This mechanism of the interband absorption is due to the interaction between the charge carriers and abrupt heterobarrier [9]. Therefore, the optical matrix element strongly depends on the

effectie i .rrier heights $\tilde{V}_c$, $\tilde{V}_v$ for electrons and holes [9]: $|P| \propto (3\tilde{V}_c + \tilde{V}_v)/E_g$. The effective barrier height for electrons decreases with strain. As a result the internal absorption α_i decreases with strain (see Fig. 1), which leads to a weaker temperature dependence of the threshold carrier density.

We calculate the threshold carrier concentration taking account of 3D carriers in the barrier and in the separate confinement (SC) region:

$$n_B^{3D} + n_W^{3D} = p_B^{3D} + p_W^{3D}, \tag{1}$$

where n_B^{3D} and p_B^{3D} are electron and hole concentrations in the barriers and SC region; n_W^{3D} and p_W^{3D} are electron and hole concentrations in the QW expressed in 3D units ($n_W^{3D} = n_W^{2D}/a$, $p_W^{3D} = p_W^{2D}/a$). From Eq.(1) and the threshold condition $g(\omega) = \alpha_i(\omega) + (1/L)\ln(1/R)$ we have calculated the threshold carrier density dependence on temperature. Because of strong internal absorption, the threshold carrier density has a strong non-linear temperatures dependence. However this dependence becor es more weak with increasing strain in QW (see Fig. 2).

It should be noted that there two additional important mechanisms, which lead to the strong non-linear thres old carrier density dependence on temperature. The first is the dependence of the Lorentz bandwidth δ on temperature and the second is the effect of carrier heating. However in this paper we do not consider these effects, concentrating our attention only on the effect of internal absorption on the threshold carrier density dependence on temperature.

The threshold current density consists of three contributions:

$$J_{th} = J_R + J_A + J_L, \tag{2}$$

$$J_R = B_R n_W^{2D} p_W^{2D} + J_R^{3D} \equiv J_R^{2D} + J_R^{3D} \tag{3}$$

$$J_A = C_A \left[n_W^{2D}\right]^2 p_W^{2D} + J_A^{3D} \equiv J_A^{2D} + J_A^{3D} \tag{4}$$

$$J_L = \beta J_A^{2D} + J_L^{other} \tag{5}$$

In Eqs.(3)-(5) J_R is the radiative recombination current, which is the sum of recombination currents in the well, J_R^{2D}, and in the barriers and SC regions, J_R^{3D}; B_R is the radiative recombination coefficient; J_A is the Auger current and J_L is the leakage current. First term in Eq.(5) represents the Auger induced current, which is assumed to be proportional to J_A^{2D} with the coefficient β, $0.5 < \beta < 1$. The second term in Eq.(5), J_L^{other}, is the sum of the other leakage current, which depend on the laser structure design (for example, lateral diffusive leakage). In our calculation we assume that $J_L^{other} = 0$.

Figure 3 present the dependence of the threshold current density on temperature. The Auger recombination current J_A is the dominant contribution to the total current. It should be noted that since the tem erature dependence of the AR coefficient is weak, ne main factor which determines the strong temperature dependence of the threshold current is a strong increase with temperature of the threshold concentration.

Figure 4 shows the threshold current density versus strain. The AR coefficient decrease with strain, therefore the threshold current decreases with strain.

Figure 5 shov the dependence of the internal quantum efficiency $\eta = J_R^{2D}/J_{th}$ on temperature for different values of strain. The increase of strain results in two consequences: i) weaker temperature dependence of the threshold carrier density and ii) decrease of the AR coefficient. Both these factors lead to decreasing of the Auger current and to increasing of the internal quantum efficiency. As a result the limiting operating temperature increases with strain (see Fig. 6). Thus, the increase of strain considerably improves the threshold characteristics of the mid-infrared $InALAsSb$ QW laser.

In this paper we have carried out a first-principle theoretical investigation of the threshold characteristics of the MQW mid-infrared lasers based on $InAlAsSb$ alloy. Lets summarize the main results of this work.

1. The internal adsorption decrea s with strain which leads to a weaker temperature dependence of the threshold carrier density.

2. By increasing compressive strain it is possible to decrease the threshold current, to increase the internal quantum efficiency and to raise up the limiting operating temperature of *InAlAsSb* QW lasers.

In conclusion, we note that compressive strain considerably improves the threshold characteristics of *InAlAsSb* QW lasers.

This work was partially supported by the Russian Foundation of Fundamental Research, Grant No. 96-02-17952 and State Russian programm "Physics of Solid State Nanostructures".

[1] H. K. Choi and G. W. Turner, Proc. SPIE., **2382**, 345 (1995).
[2] R. F. Nabiev, C. J. Chang-Hasnain, H. K. Choi, Semiconductor Lasers Advanced Devices and Applications, Keystone, Colorado, USA, Technical Digest Series, **20**, 31 (1995).
[3] H. K. Choi, G. W. Turner, Z. L. Liau, Appl. Phys. Lett. **65**, 2251 (1994).
[4] A.D. Andreev, G.G. Zegrya, Appl. Phys. Lett, 70, N 5, 601 (1997)
[5] G.G. Zegrya, A.D. Andreev, N.A. Gun'ko, E.V. Frolushkina. Proc. SPIE, **2399**, pp. 307-316. (1995)
[6] A.D. Andreev, G.G. Zegrya, IEE Proc. Optoelectronics, to be published (1997)
[7] A.D. Andreev, G.G. Zegrya, Semiconductors, v. 31(3), 268 (1997)
[8] G.G. Zegrya and V.A. Kharchenko, Sov. Phys. JETP, **74**, 173 (1992).
[9] G.G. Zegrya. Antimonide Related Strair 1 Layer Heterostructures, M. O. Manasreh (ed.), Gordon and Breach, Neward (1997).

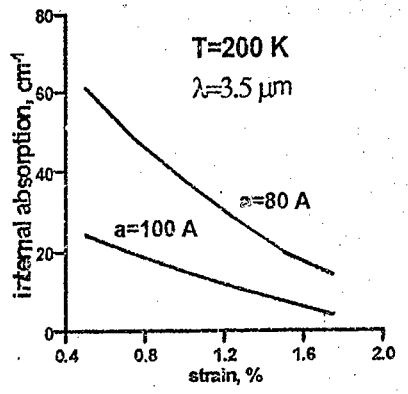

Figure 1. Internal absorption vs strain for *InAlAsSb* QW, $n^{2D} = 1 \times 10^{12}$ cm^{-2}.

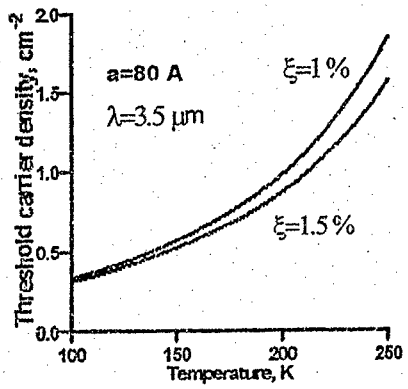

Figure 2. Threshold carrier density vs temperature for different values of strain ξ, N_{QW}=4.

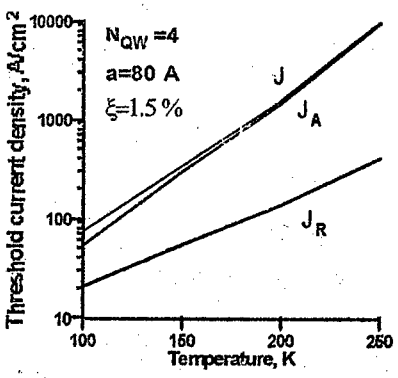

Figure 3. Threshold current density of strained MQW laser vs temperature.

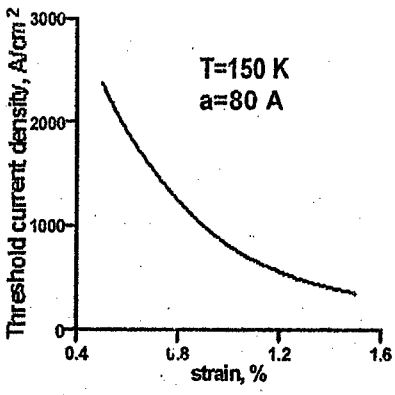

Figure 4. Threshold current density vs strain.

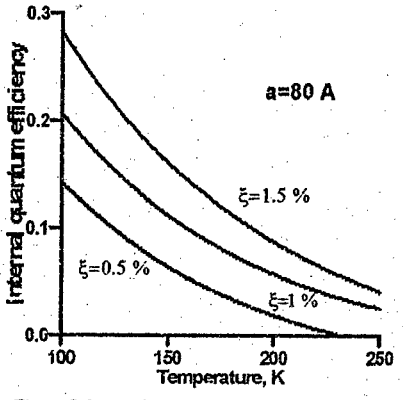

Figure 5. Internal quantum efficiency vs temperature for different values of strain, λ=3.5 μm.

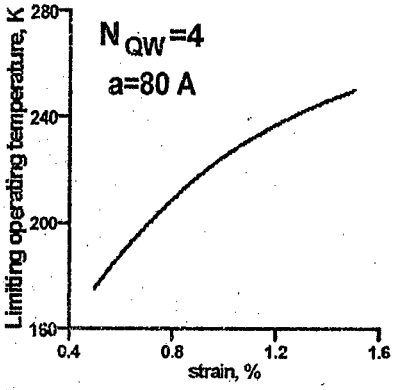

Figure 6. Limiting operating temperature vs strain for *InAlAsSb* MQW laser, λ=3.5 μm.

Effect of Strain on Auger Recombination in Type-II Quantum Wells

Aleksey D. Andreev and Georgy G. Zegrya

A.F.Ioffe Physical-Technical Institute of Russian Academy of Sciences, 26 Polytekhnicheskaya, St.-Petersburg 194021, Russia
Phone: +7-812-247-9367, E-mail: andreev@theory.ioffe.rssi.ru

Auger recombination processes in type II heterostructures with strained quantum wells (QW) have been studied theoretically. It is shown that in type-II QW there are two channels of electron and hole recombination. During the Auger recombination processes these two channels interfere destructively, which results in decrease of the Auger matrix element and the AR rate. It is shown that the Auger recombination rate essentially depends on strain. It is demonstrated that under certain conditions the Auger recombination rate can be suppressed by choosing the optimal value of strain.

Semiconductor heterostructures (HS) with quantum wells (QWs), as a heart of novel optoelectronic devices, have been studied intensively during last decade. Semiconductor HSs can be of type I or type II. In type II heterostructures the electrons and holes are separated in space, so that their recombination is possible only when either electron or hole tunnels through the heterobarrier [1,2]. Therefore in contrast to type I heterostructures, in type II HSs there are two possible recombination channels: i) an electron tunnels through the barrier and recombines with a hole localized in a QW (channel "E", see Fig. 1); ii) a hole tunnels through the barrier and recombines with an electron in a QW (channel "H", see Fig. 1). Since the tunneling probability is very sensitive both to the values of effective barrier height and effective mass, it is naturally that the rates of the elementary recombination processes in type II heterostructures with QWs essentially depend on the QW parameters.

Threshold characteristics of longwavelength lasers are determined mainly by two recombinatin processes: radiative recmbination and Auger recombination (AR). To improve temperature sensivity of 1.3--1.5 μm lasers and to raise up the operation temperature of mid-infrared ($2-5$ μm) lasers it is important to suppress the AR processes. Such kind of suppression is possible by choosing the optimal parameters of QWs. In our previous papers [1,2] we have studied the possibility of AR suppression in unstrained type II QWs. It was shown that under certain conditions the AR rate had a minimum as a function of the ratio of the barrier heights for electrons and holes [1]. However the most real heterostructures with type-II QWs are the structures with strained layers [3]. Therefore further theoretical investigations are required to find out the possibility of Auger recombination supperssion in strained type II QWs.

The aim of the present paper is to study theoretically the effect of strain on the Auger recombination processes in type II heterostructures with strained QWs. It is demonstraited that under certain conditions the AR processes can be suppressed by choosing the structure with the optimal value of strain.

In heterostructures based on III-V alloy, two channels of Auger recombination processes are important: CHCC and CHHS [2]. In the present paper, we will study only the CHCC processes. However, the main conclusion regarding interference of two channels of electron and hole recombination is also valid for the CHHS process.

The AR rate is calculated in the framework of first-order perturbation theory in electron-electron interaction: [1,2,4]. The the carrier spectrum and wave function have been derived employing the 4×4 Kane model with strain taken into account [5-7]. This model describes the main peculiarities of the carrier spectrum and wave functions in the QW: light-heavy hole mixing and non-parabolicity of the electron and hole spectrum. We introduce the strain, ξ, as $\xi = (a - a_1)/a_1$, where a_1 is the lattice constant of the material in the region $-L_- < x < 0$ (see Fig. 1), a is the in-plane lattice constant of the relaxed structure.

As w shown earlier [1-4], the overlap integrals entering the AR matrix element should be calculated in the framework of multiband Kane model taking into account non-parabolicity of the carrier spectrum dispersion. For the overlap integral I_{23} between the states of localized "2" and excited "3" electron this is important because of the following reasons. First, the wave function of the electron highly excited in the conduction band contains essential contribution from $|p>$-states of the valence band. Second, the specified overlap integral consists of contributions from three regions of integration over X: two regions of underbarrier motion of electron "2" ($x < -L_1$ $x > 0$ -- see. Fig.1) and a quantum well region ($-L_1 < x < 0$). The contributions from underbarrier motic region and the contribution from QW region compensate each other being summed. This leads to the appearance of additional small factor in the AR matrix element of the order of $(3\tilde{V}_c - |\tilde{V}_v|)/E_g$, which results in strong decrease of the AR rate (here $\tilde{V}_c$ and $\tilde{V}_v$ are the effective barrier height for electrons and holes with strain taken into account).

As noted above, in type II QWs there are two channels of the AR process (see Fig. 1). From mathematical point of view these two channels correspond to two regions of integration over x when calculating the electron-hole overlap integral:

$$I_{14} = \int_{-\infty}^{0} \psi_1^*(x)\psi_4(x)\exp(iq_x x)\,dx + \int_0^{+\infty} \psi_1^*(x)\psi_4(x)\exp(iq_x x)\,dx \equiv I_{eh}^H + I_{eh}^E. \qquad (1)$$

It is worth noting that for calculation of the electron-hole overlap integral and in order to find out the relationship between contributions I_{eh}^H and I_{eh}^E it is principally important to take account of light-heavy hole mixing in the QW. This point can be explained qualitatively as follows. Let us assume that we ignore the light-heavy hole mixing. Then the hole effective mass m_h^* does not depend on in-plane momentum q_4 and is equal to its bulk value, which is much greater that tl electron effective mass m_h^*. Therefore the characteristic damping distance of the hole wave function is $\sqrt{m^*/m_h^*}$ times smaller than that of electrons: $\kappa_h^{-1}/\kappa_h^{-1} \propto \sqrt{m_c^*/m_h^*}$. As a result, the channel "E" is the dominant and the ratio contributions I_{eh}^H and I_{eh}^E is small in case of ignoring the light-heavy hole mixing:

$$\frac{|I_{eh}^H|}{|I_{eh}^E|_{without\ mixing}} \propto \sqrt{\frac{m_c^*}{m_h^*}} \ll 1. \qquad (2)$$

The situation sig ificantly changes when we take into account light-heavy hole mixing. In this case, the hole wave function is the superposition of light and heavy hole states. The relative contributions from these two states to the hole wave function, i.e the degree of light-heavy hole mixing essentially depends on the in-plane hole momentum q_4. In particular, this mixing vanishes at $q_4 = 0$. This can be qualitatively interpreted in terms of the hole effective mass which depends on q_4: $m_h^* \equiv m_h^*(q_4)$. Consequently, the ratio (11) depends on q_4 and at definite region of q_4 can be close to unity. A detailed analysis shows that in this region of q_4 two contributions I_{eh}^H and I_{eh}^E are of the same order, but have different signs. As a results, the total electron-hole overlap integral is smaller than both contributions:

$$I_{eh}(q, \ll (I_{eh}^E(q), I_{eh}^H(q)).$$

This means that a distructive interference between two channels of electron and hole recombination takes place. This result is illustrated on Figure 2. The strain does not significantly change this effect: it can just makes this interference more or less effective, which in its turn depends on the structure parameters (barrier heights of electrons and holes, QW widths) and temperature (we do not consider here extrimely large strains).

It is also important to note that the interference between two channels considered above takes place at definite values of hole momentum q_4, at $q_4 = 0$ this interference is absent and the channel "E" is the dominant. The main contribution to the Auger rate is

given by the values of q_4 of order of either $q_4 \sim \pi/L_2$ (for narrow QWs for holes) or $q_4 \sim 1/\lambda_T = \sqrt{\hbar^2/(2m_hT)}$. Both of this values are close to region, where the interference of channels "E" and "H" occurs. Thus, the effect of interference of two channels of electron-hole recombination reduces the Auger rate.

It should be noted that the situation changes when we consider the radiative recombination rate [2]. The main contribution to the radiative matrix element gives the values of $q_h \approx q_e \approx 0$, where the interference described above is not significant. Therefore during the radiative recombination channel "E" is the dominant channel of the electron-hole recombination. Thus the interference of two channels of the electron-hole recombination practically does not reduce the radiative recombination rate.

Accurate calculation of the AR rate is possible only numerically using analitical formulars for the Auger transition matrix element [5]. The Auger rate essentially depends on the structure parameters: QW width, barrier heights, effective band gap (i.e. the emission wavelength) and strain. However, the AR rate has a weak temperature dependence, which means that the AR process in type II QWs is a threhsoldless one. In particular, decreases when the QW width L_1 or L_2 increases; the Auger rate steeply increases with emission wavelength. These dependences are analogous to that in unstrained type II structures.

Figure 3 presents the AR coefficient dependences on strain for different values of the barrier heights for unstrained structure. The analysis of these dependences shows that under certain conditions tha AR rate has a minimum at definite value of strain. This means that at certain structure parameter a suppression of AR process occurs. In paiticular, when the ratio V_c/V_v is relatively small, the Auger rate has a minimum at $\xi > 0$; the position of this minimum shifts towards smaller values of ξ when increasing the ratio V_c/V_v (remind that V_c and V_v are the barrier heights at zero strain).

The suppression of the AR rate at certain structure parameters is connected with two factor. First, the overlap integral I_{23} between the states of localized and excited electrons is reduced at definite structure parameters. Second, the overlap integral between electron and hole states is reduced at certain region of in-plane hole momentum because of destructive interference of two channels of electron-hole recombination. At some structure parameters the influence of this factors results in suppression of Auger recombination at definite strain.

In summary, we have performed a detailed theoretical analysis of Auger recombination processes in type II heterostructures with strained QWs. Let us summarize the main results of this work.

1. The overlap integral between the states of the localized and excited electrons essentially depends on the barrier heights and strain. At certain values of parameters the value of the overlap integral decreases.

2. In type II QWs there are two channels of the electron-hole recombination. These channels interfere destructively, which significantly reduces the electron-hole overlap integral.

3. At certain structure parameters (barrier heights, QW widths) the AR processes is suppressed at definite values of strain.

In conclusion, we note that the performed theoretical analysis demonstrates opportunity to control the AR rate by changing the parameters of the type II HS.

This work was partially supported by the Russian Foundation of Fundamental Research (Grant No. 96-02-17952) and by INTAS Grant No 94-1172.

[1] G.G. Zegrya and A.D. Andreev, Appl. Phys. Lett., **67**, pp.2681-2683 (1995).
[2] G.G. Zegrya, A.D. Andreev, JETP, **82**, p. 328-340 (1996).
[3] M.P. Mikhailova and A.N. Titkov, Semicon. Sci. Technol, **9**, 347 (1994).
[4] B.L. Gel'mont, Sov. Phys. JETP, **48**, 268 (1978).

[5] A.D. Andreev, G.G. Zegrya, Semiconductors, v.**31** (3), 268 (1997)
[6] A.V. Sokol'skii and R.A. Suris, Sov. Phys. Semicond., **21**, 529 (1987).
[7] E.O. Kane, J. Phys. Chem. Solids, **1**, 249 (1957).
[6] G.G. Zegrya and V.A. Kharchenko, Sov. Phys. JETP, **74**, 173 (1992).

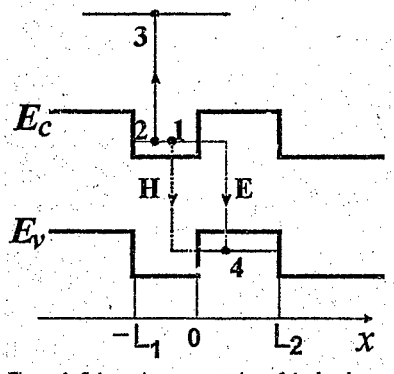

Figure 1. Schematic representation of the band diagram of type II heterostructure with QWs: number "1" and "2" denote intial states of particles, "3" and "4" denote the final states during the Auger recombination; "H" and "E" denote two possible channel of electron-hole recombination.

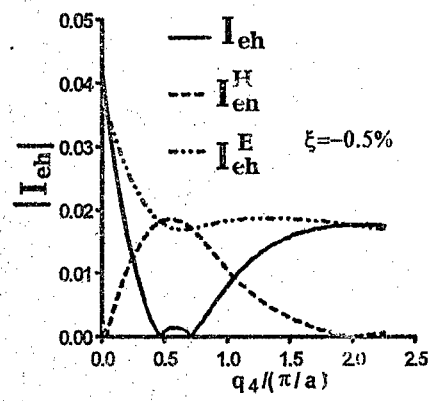

Figure 2a. Electron-hole overlap integral and contributions from two channels of electron-hole recombination, $q_1 = 0.4\ \pi/a$, $q_x = |q_1 - q_4|$, effective band gap is 0.31 eV, $\xi = -0.5\%$.

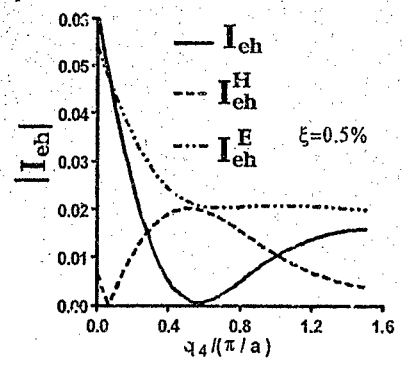

Figure 2b. The same as on Fig.2a, but at ξ = 0.5%.

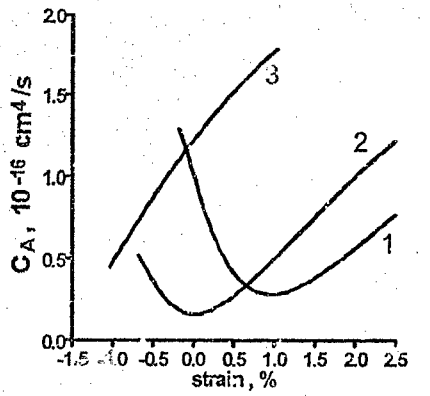

Figure 3. The dependence of the Auger coefficient on strain for different values of the barrier heights at $\zeta = 0$ %: 1 – Ve = 0.05 eV, Vv = 0.45 eV; 2 - Vc = 0.1 eV, Vv = 0.4 eV, 3 - Vc = 0.2 eV, Vv = 0.2 eV. For all three structures: T=250 K, L_1 = 60 A, L_2 = 80 A, effective band gap is 0.6 eV.

Effect of carrier recombination in the optical confinement layer on the temperature dependence of threshold current density of a quantum dot laser

L. V. Asryan and R. A. Suris

Ioffe Physico-Technical Institute, 26 Polytekhnicheskaya st., St Petersburg 194021, Russia
E-mail: asryan@theory.ioffe.rssi.ru

One of the most important expected advantages of quantum dot (QD) lasers over the conventional quantum well (QW) lasers is the weak temperature sensitivity of the threshold current [1]. Ideally, threshold current of QD laser should remain unchanged with the temperature [1]. This would be so indeed if the overall injection current went entirely into the radiative recombination in QDs. In fact, because of the presence of some nonvanishing free carrier density in the barrier regions (in the optical confinement layer – OCL), a fraction of the injection current is wasted therein. This fraction goes into the recombination processes in the OCL [2]-[10]. Recombination in the barrier regions gives rise to one more component of the threshold current [2]-[10]. Besides, the latter component, associated with the thermal excitation (leakage) of carriers from QDs to the barrier regions, depends trongly on the temperature. As a result the total threshold current should become temperature dependent [3]-[6], especially at high temperatures. This has been observed experimentally in [11].

In [4]-[10], a detailed theoretical analysis of the gain g and threshold current density j_{th} of QD laser has been given having regard to inhomogeneous line broadening caused by fluctuations in QD parameters. Both of the radiative recombinations in QDs and in the OCL have been taken properly into account. The different cases of QD filling have been revealed to occur depending on temperature, QD size fluctuations and conduction and valence band offsets at the QD–OCL heteroboundary. In view of the strong dependence of j_{th} on the parameters of the structure, optimization of the laser structure has been carried out. The key dimensionless parameter controlling the magnitudes of the minimum threshold current density and of the optimum parameters of the structure has been revealed. This parameter is the ratio of the stimulated transition rate in QDs at the lasing threshold to the spontaneous transition rate in the waveguide (barrier) region at the transparency threshold.

In this work, we give a detailed analysis (by reference to [4]-[10]) of the temperature dependence of j_{th}. Temperature dependences of both of the components of j_{th} associated with the radiative recombination in QDs and in the OCL are calculated. The relative contribution of each component to j_{th} is analyzed as a function of T. Temperature dependences of the optimum surface density of QDs and the optimum thickness of the OCL are obtained.

The threshold current density of QD laser is the sum of the current densities associated with the radiative recombination in QDs, j_{QD}, and in the OCL, j_{OCL}, [4]-[7], [9]

$$j_{th} = j_{QD} + j_{OCL}. \qquad (1)$$

We consider relatively high temperatures when equilibrium filling of QDs is the case [4]-[6]. Under the conditions of the thermal equilibrium between the electrons (holes) confined in QDs and free electrons (holes), j_{QD} and j_{OCL} are given by [4]-[7],[9]

$$j_{QD} = \frac{eN_S}{\tau_{QD}} f_n f_p \qquad j_{OCL} = ebBnp = ebBn_1p_1 \frac{f_n f_p}{(1-f_n)(1-f_p)} \qquad (2)$$

where $f_{n,p}$ are the mean electron and hole level occupancies in QDs required for attaining the peak modal gain value of $g = N_S a^2 \Gamma g_0$ *at a given surface density of QDs*, N_S (g_0 is the material gain reduced to one QD [4]–[6]); a is the mean size of QDs, Γ is the optical confinement factor in a QD layer (along the transverse direction in the waveguide), τ_{QD} is the radiative lifetime in QDs [4]–[6], b is the OCL thickness and B is the radiative constant for the OCL material.

At the lasing threshold ($g = \beta$, where β is the total loss coefficient), the population inversion in QDs, $f_n + f_p - 1$, is given by the equation

$$f_n + f_p - 1 = \frac{N_S^{min}((\Delta\varepsilon)_{inhom}, \beta)}{N_S} \tag{3}$$

where $N_S^{min}((\Delta\varepsilon)_{inhom}, \beta)$ is the minimum surface density of QDs required to attain lasing at given losses β and inhomogeneous line broadening $(\Delta\varepsilon)_{inhom}$ [4]–[7].

The free-electron and -hole densities in the OCL, n and p, are

$$n = n_1 \frac{f_n}{1 - f_n} \qquad p = p_1 \frac{f_p}{1 - f_p} \tag{4}$$

$$n_1 = N_c^{OCL} \exp\left(-\frac{\Delta E_{c1} - \varepsilon_n}{T}\right) \qquad p_1 = N_v^{OCL} \exp\left(-\frac{\Delta E_{v1} - \varepsilon_p}{T}\right) \tag{5}$$

where $N_{c,v}^{OCL} = 2(m_{c,v}^{OCL} T / 2\pi\hbar^2)^{3/2}$ are the conduction and valence band effective densities of states for the OCL material, ΔE_{c1} and ΔE_{v1} are the conduction and valence band offsets at the QD–OCL heteroboundary, $\varepsilon_{n,p}$ are the quantized energy levels of an electron and hole in a mean-sized QD (measured from the corresponding band edges) and the temperature T being measured in terms of energy.

The radiative recombination channel is primarily responsible for the temperature dependence of the threshold current density of QD laser [4]–[6]. With equations (5) for n_1 and p_1 and $B \sim T^{-3/2}$ (see equation (10) in [4] for B), the temperature dependence of j_{OCL} may be presented as

$$j_{OCL}(T) \sim T^{3/2} \exp\left(-\frac{\Delta E_{c1} + \Delta E_{v1} - \varepsilon_n - \varepsilon_p}{T}\right). \tag{6}$$

The electron and hole level occupancies in QDs at the lasing threshold (which are the analogue of the threshold carrier densities for QW or bulk lasers) become temperature dependent if the charge neutrality violation in QDs is properly taken into account.

Thus, the self-consistent consideration of the QD charge reveals the temperature dependence of j_{QD} by itself. It also leads to the extra temperature dependence of j_{OCL} through the such dependences of $f_{n,p}$ (in addition to the temperature dependence of j_{OCL} through the temperature dependence of Bn_1p_1, see equation (6)).

It should be noted that the temperature dependences of $f_{n,p}$ are much weaker compared to that of the product Bn_1p_1 (which is the exponential, see (6)). Consequently, the temperature dependence of j_{QD} is much weaker compared to that of j_{OCL}. Nevertheless, the conclusion that j_{QD} do depends on the temperature may be of great importance. The matter is that, in the properly designed QD laser structures, the recombination channel through the barrier region (OCL) states (that is the leakage current) should be suppressed. This should be at least one way to optimize the performance of QD lasers. Even so, the threshold

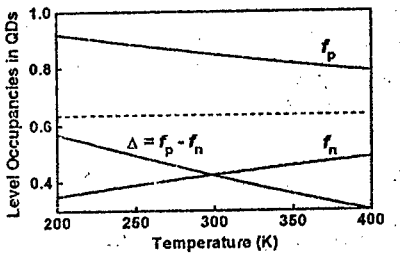

Figure 1. Electron and hole level occupancies in QDs at the lasing threshold and the difference of them *vs.* temperature.

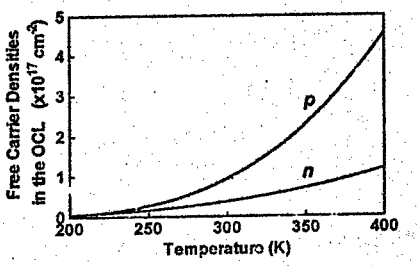

Figure 2. Free-electron and -hole densities in the OCL at the lasing threshold *vs.* temperature.

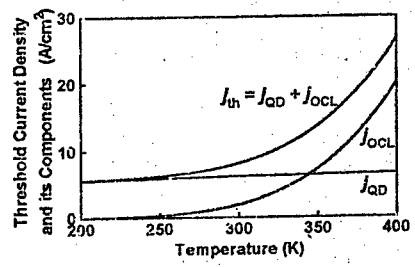

Figure 3. Threshold current density and current densities associated with the radiative recombination in QDs and in the OCL *vs.* temperature.

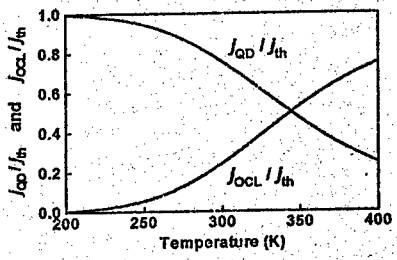

Figure 4. Temperature dependences of the relative contributions of the components to the threshold current density.

current density, being determined solely by the radiative recombination in QDs, should be temperature dependent.

To illustrate the results of calculations, we use a laser structure considered in [4, 7]. The normal (Gaussian) distribution of relative QD size fluctuations is supposed. The mean size of cubic QDs is taken to be $a = 150$ Å. The total loss coefficient, RMS of relative QD size fluctuations and OCL thickness are taken to be $\beta = 10\,\mathrm{cm}^{-1}$, $\delta = 0.05$ and $b = 0.28\,\mu\mathrm{m}$ (which is the optimum value at $T = 300\,\mathrm{K}$), respectively. The corresponding value of $N_S^{\min}$ is $2.1 \times 10^{10}\,\mathrm{cm}^{-2}$. The surface density of QDs is equal to its optimum value at $T = 300\,\mathrm{K}$ ($N_S^{\mathrm{opt}}/N_S^{\min} \approx 3.70$, [7]).

Fig. 1 shows the temperature dependence of $\Delta = f_p - f_n$ and $f_{n,p}$ at the lasing threshold. The dashed line shows $f_{n,p}$ calculated disregarding the charge neutrality violation in QDs. Δ drops slowly with the temperature; f_n and f_p tend slowly to each other. Thus, violation of the charge neutrality in QDs is suppressed with the temperature.

The free-carrier densities in the OCL (barrier regions) are plotted in Fig. 2 versus T.

Fig. 3 shows j_{QD}, j_{OCL} and j_{th} against T. At $T = 300\,\mathrm{K}$, $j_{QD} = 6.2\,\mathrm{A/cm}^2$ and $j_{OCL} = 2.0\,\mathrm{A/cm}^2$; j_{QD} and j_{OCL} become equal to each other (and equal to $6.4\,\mathrm{A/cm}^2$) at $T = 344\,\mathrm{K}$. At $T = 400\,\mathrm{K}$, $j_{QD} = 6.6\,\mathrm{A/cm}^2$ and $j_{OCL} = 20.0\,\mathrm{A/cm}^2$.

Shown in Fig. 4 are the ratios j_{QD}/j_{th} and j_{OCL}/j_{th} against T. At room temperature, the contribution of j_{OCL} to j_{th} still remains moderately small in comparison with that of j_{QD}. The former contribution increases with T. The contributions become equal to each other at $T = 344\,\mathrm{K}$ (see also Fig. 3).

The work has been supported by the Russian Foundation for Basic Research, grant No. 96-02-17952 and the Program "Physics of Solid State Nanostructures" of Ministry of Science and Technical Policy of Russia, grant No. 97-1035.

[1] Y. Arakawa and H. Sakaki, Appl. Phys. Lett., vol. 40, no. 11, pp. 939-941, June 1982.

[2] Y. Miyamoto, Y. Miyake, M. Asada, and Y. Suematsu, IEEE J. Quantum Electron., vol. 25, no. 9, pp. 2001-2006, Sept. 1989.

[3] H. Nakayama and Y. Arakawa, in Tech. Dig. 15th IEEE Int. Semicond. Laser Conf., Haifa, Israel, Oct. 1996, pp. 41-42.

[4] L. V. Asryan and R. A. Suris, Semicond. Sci. Technol., vol. 11, no. 4, pp. 554-567, Apr. 1996.

[5] R. A. Suris and L. V. Asryan, in Proc. SPIE's Int. Symp. PHOTONICS WEST'95, San Jose, CA, USA, Feb. 1995, vol. 2399, pp. 433-444.

[6] L. V. Asryan and R. A. Suris, in Proc. Int. Symp. "Nanostructures: Physics and Technology", St.Petersburg, Russia, June 20-24, 1994, pp. 181-184.

[7] L. V. Asryan and R. A. Suris, IEEE J. Select. Topics Quantum Electron., June 1997.

[8] L.V. Asryan and R.A. Suris, in Tech. Dig. 15th IEEE Int. Semicond. Laser Conf., Haifa, Israel, Oct. 1996, pp. 107-108.

[9] L. V. Asryan and R. A. Suris, in Proc. Int. Symp. "Nanostructures: Physics and Technology", St.Petersburg, Russia, June 24-28, 1996, pp. 354-357.

[10] L.V. Asryan and R.A. Suris, in Proc. 23rd Int. Conf. Phys. Semicond., Berlin, Germany, July 21-26, 1996. Editors M. Scheffler and R. Zimmermann, World Scientific, Singapore, v.2, pp. 1369-1372.

[11] N. Kirstaedter, et al., Electron. Lett., vol. 30, no. 17, pp. 1416-1417, Aug. 1994.

1.5 μm Multiquantum Well Four-Wavelength DFB Laser Array for Multigigabit/s High-Density WDM System Applications

A.G.Deryagin, V.I.Kuchinskii, D.V.Kuksenkov*, G.S.Sokolovskii, H.Temkin*

A.F.Ioffe Physico-Technical Institute, 194021, St.Petersburg, Russia
*Electrical Engineering Department, Texas Tech University, Lubbock, TX 79409

The increase in the transmission bandwidth in telecommunications has been traditionally accomplished by time-division-multiplexing (TDM) through the increase in the transmission speed. Recently, there was a considerable interest in wavelength-division-multiplexed (WDM) systems, which at the present time are believed to be cost effective compared with high transmission speed (>40 Gb/s) TDM systems [1]. Distributed feedback (DFB) laser arrays ($\lambda \approx$ 1.55 μm) are considered as key component for broadband optical networks based on high-density WDM technologies. Quantum well lasers have potentially low threshold current, narrow linewidth, low chirp and wide modulation bandwidth. This paper presents performance of the experimental four-wavelength DFB laser array.

The samples were grown on InP substrate by MOCVD. The active region contains six InGaAs quantum wells, 8 nm thick each. 4 μm wide ridge waveguide laser stripes at the separation of 250 μm are planarized by polymide. The first-order grating of the lasers was written by electron beam lithography. A coupling constant k of ~ 20 cm^{-1} was measured, resulting in the coupling constant-cavity length product (kL) of ~ 1 for the cavity length of 500μm. Difference in grating periods between adjacent lasers results in a nominal wavelength difference of 5 nm. The wavelengths of the lasers in the array are 1.5401, 1.5448, 1.5504 and 1.5558 μm, respectively. L-I curves are shown in Fig.1. At room temperature (T = 20°C) lasers have threshold currents of 20÷35 mA and slope efficiencies 0.15÷0.22 mW/mA. The typical optical spectrum of the laser is shown in Fig.2. Single longitudinal-mode operation was observed for each laser with sidemode suppression ratios of >30 dB.

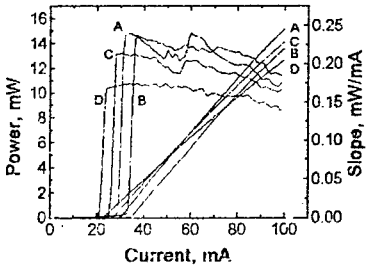

Fig.1 L-I characteristics and slopes of four-wavelength DFB LD array.

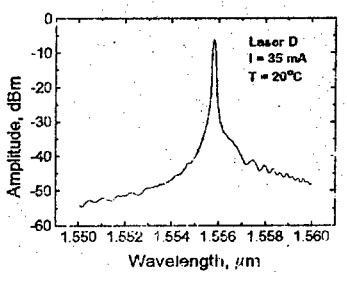

Fig.2 Typical emission spectrum of one laser in four-wavelength DFB LD array.

The laser linewidth was measured by a scanning Fabry-Perot interferometer. Fig.3 shows the measured linewidth as a function of reciprocal laser power from the front facet. The linewidth-power product was determined to be ~50 MHz·mW and the minimum measured linewidth was ~20 MHz, the value determined by interferometer resolution.

Spectral line shape for the laser operating at 8 mW output power is shown in Fig 4.

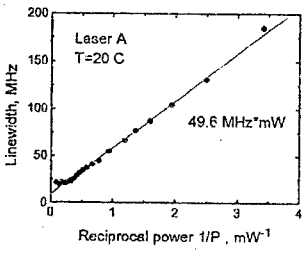

Fig.3 Measured linewidth as function of reciprocal laser power.

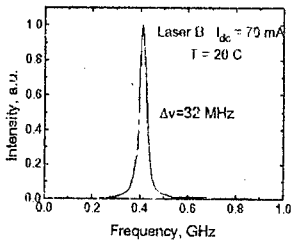

Fig.4 Optical spectrum of an individual laser.

Fig.5 shows small-signal modulation (SSM) response of the laser. The -3 dB bandwidth is 5.5 GHz.

Electrical and thermal crosstalk effects between lasers in the array are very important for the device performance. Fig.6 shows the CW thermal crosstalk, i.e. wavelength variation due to CW current injection into neighboring laser. Two curves are shown. The top curve shows the thermal crosstalk between neighboring lasers in the array (lasers separation S = 250 μm) while the bottom one was obtained for distant lasers (S = 750 μm). Compared to the previously published value of 0.003 Å/mA [2] the observed value of 0.026 Å/mA is much higher.

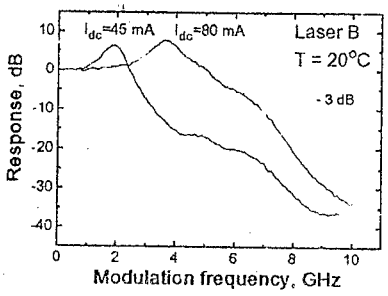

Fig.5 Small-signal modulation response.

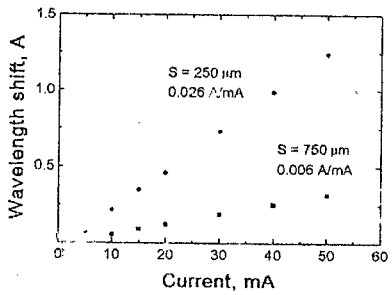

Fig.6 Dependence of the wavelength variation of a laser on the current in the adjacent laser for different spacing between lasers.

In our opinion, it can be explained as follows. First, the array under test has the 100 μm thick substrate and is mounted on a heatsink substrate-down. Thick substrate worsens the heatsinking from the active region. Second, the array had nonoptimized upper contacts serving as extra heat conductors (the distance between massive metal pads was only 60 μm). Careful device layout should substantially reduce the thermal crosstalk.

Measured electrical crosstalk between adjacent lasers is shown in Fig.7 and Fig.8. Fig.7 shows the laser frequency response on the small-signal sinusoidal modulation (-20 dBm) of the adjacent laser. First, modulation response of laser B is measured with the neighboring laser C off. Then the same is done for the case when laser C is modulated and laser B is dc biased. The amplitude difference between two values indicates the electrical crosstalk at each frequency. One can see that even in the resonance region (near 2 GHz) electrical crosstalk is less than -25 dB. Usually lasers are used under large signal modulation (LSM). Thus it is important to evaluate noise in the optical signal of the laser under LSM, caused by large signal modulation of the another laser in the array. Fig.8 shows electrical crosstalk between two adjacent lasers under large signal modulation. The signal to noise ratio was higher than 22 dB.

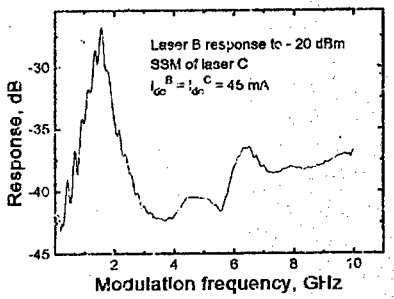

Fig.7 Small-signal modulation response for electrical crosstalk measurement.

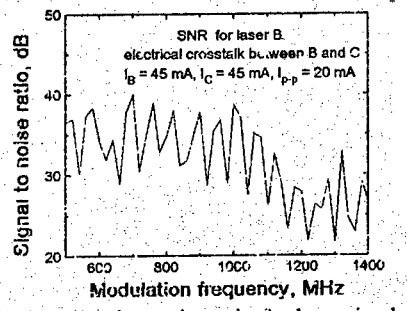

Fig.8 Signal to noise ratio for large signal modulation electrical crosstalk measurement.

In conclusion, we have demonstrated four-channel DFB LD array grown by MOCVD on InP substrate. The fabricated array showed uniform L-I characteristics (threshold current ~20÷30 mA and output power up to >20 mW). The thermal crosstalk in our devices was 0.025 A/mA. Each laser could be modulated at the speed of 5-6 Gb/s with moderate electrical crosstalk penalty (-25 dB) from adjacent laser. Such laser arrays are expected to be suitable for the fabrication of integrated optical devices for 25-30 Gb/s WDM lightwave communication systems.

References

[1] T.-P.Lee, C.E.Zah, R.Bhat, W.C. Young et al, Journal of Lightwave Technology 14, 967 (1996).

[2] L.A.Wang, Y.H.Lo, M.Z.Iqbal, J.Young, P.S.D.Lin, A.S.Gozdz, IEEE Photon. Technol. Lett 3, 965 (1991).

Modal Composition of Radiation in Room Temperature Quantum Dot Lasers

N.Yu.Gordeev, A.M.Georgievski, V.I.Kopchatov, S.V.Zaitsev, A.Yu.Egorov, A.R.Kovsh, V.M.Ustinov, A.E.Zhukov, and P.S.Kop'ev

A.F.Ioffe Physical-Technical Institute of the Russian Academy of Sciences, Politekhnicheskaya, 26, St.-Petersburg, 194021, Russia, Fax +7-812-247-10-17,E-mail address: Gordeev@switch.ioffe.rssi.ru

Nature of separate groups of longitudinal modes appearing in room temperature quantum dot lasers has been studied. It has been shown that the limited transport of carriers in the plane of active layer under conditions of a transverse channel of them in other layers leads to significant difference in gain spectra of corresponding transverse modes.

Introduction

It has been shown in numerous experiments that spectra of multimode injection lasers may be modulated with a period much broader than a period of longitudinal modes [1-4]. This phenomenon may have different interpretation. It may be concerned with some additional cavity, or separate longitudinal channels in a laser leading to "spot lasing". The effect observed in room temperature quantum dot (RT QD) lasers was especially strong. Sometimes the lasing spectrum observed under CW pumping has been decomposed into groups of longitudinal modes.

RT QD lasers have one specific property comparing with QW ones. Channeling of non-equilibrium carriers in the plane of QDs is very limited even at room temperature. The gain spectrum of such lasers is often very wide and strongly depends on pumping current density. In the case of broad area lasers having weak transverse carrier confinement it may create rather different conditions for different transverse modes.

Experimental Methods

Experimental samples were prepared as stripe geometry injection heterolasers. Initial wafers were grown as a separate confinement AlGaAs/GaAs heterostructure having 6 stacks of InGaAs QDs in the middle of GaAs waveguiding layer [5]. The stripe was formed as a 60 μm wide window in Al_2O_3 insulating layer. No mesa structures were etched. Electroluminescent spectrum of such laser is shown in fig.1. Separate groups of modes were distinguished both below and above the threshold.

By studying of similar spectra at various temperatures a spectral location of separate lasing lines and additional maximums of the superluminescence was investigated.(fig.2)

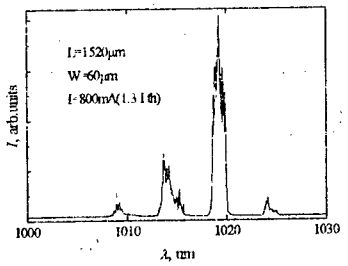

Fig.1 Lasing spectrum of RT SC QDs laser.

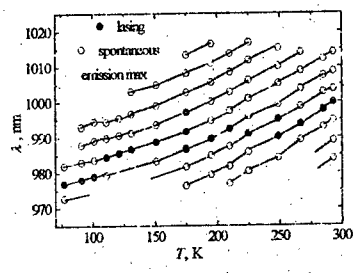

Fig.2 Temperature dependence of the lasing wavelength and spontaneous emission maxima.

To check existence of extra-cavity inside basic one formed by cleaved facets of the chip, the intensity of scattered radiation along laser stripe was studied (fig.4). To simplify the method, the fact was used that the substrate is transparent to the laser radiation. The scheme of the experiment is shown in fig.3. Such original technique was used for a first time.

Near field of lasers was studied to investigate a possibility of "spot lasing". Typical picture of near field is shown in fig.5.

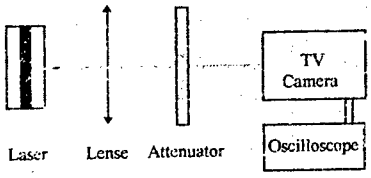

Fig.3 Scheme of the investigation of the scattered radiation along the laser stripe

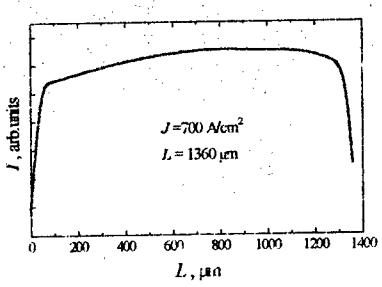

Fig 4 Intensity of the scattered radiation along the laser stripe

Spectral investigations with a spatial resolution has been used to compare spectra of different transverse modes. For this purpose radiation from different parts of the laser far field was cut and analyzed. Corresponding spectra of the central part of the far field and one of its edge are shown in fig. 6.

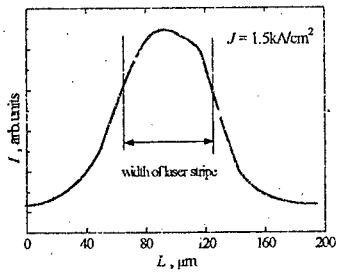

Fig.5 Near field of the laser radiation

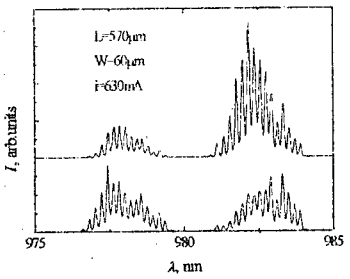

Fig.6 Lasing spectra measured in two different directions

Results

The main peculiarity of the spectra shown in fig. 1,2 is the equal distance between observed modal groups which could hardly be explained for multimode "spot lasing". The spectral interval between groups was independent from the cavity length and temperature in wide ranges. Modal groups have different threshold current. In the case of equal waveguide and output losses it means that the ratio of the corresponding modal gains changes with current.

The spectral interval between longitudinal modes significantly (12%) differs in these modal groups. For example, one modal group of the 570 μm long laser has 1.89Å modal interval, while the next one has it equal to 2.16Å.The difference makes it impossible for them to have equal optical round trip path within the cavity. Spectral location of modal groups changes with temperature. The dependence is superlinear, and does not coincide with the temperature drift of the lasing line(s) or changes in GaAs bandgap.

Concentration of photons along the cavity was close to a constant for all observed lasers. In the case of coupled cavities or some internal reflectors this value must vary. Near field of the lasers was found to be homogenous. No spots and separate channels of lasing were observed. However, the lasers emit radiation with different spectra in measured in diverse directions. This is an unconditional proye that these spectral groups belong to different transverse modes.

Discussion

The characteristic period of 5 nm in emission spectra could correspond, for instance, to 20 μm long extra cavity inside the basic one. However, it was not observed at least in longitudinal

direction. As it follows from the temperature dependence, it can not be connected with any crystal size. Otherwise it should depend on temperature as a linear function. On the other hand, different optical paths or effective refractive indexes bespeak that these groups of longitudinal modes belong to different transverse modes.

In this case it is necessary to explain why transverse modes have so different gain spectra. Obviously, transverse modes are gained by separate groups of QDs, having different pumping levels. So, in the absence of coupled cavities and separate channels of lasing located along the stripe inhomogeneous CW pumping directs to the breakdown of the emission spectra into several independent groups of longitudinal modes.

Similar structure of the spectra was observed in DHS lasers but under pulsed pumping [6], leading to dynamic inhomogeneous pumping in the transverse direction.

Conclusions

Thus, it has been shown that different transverse modes are based on different groups of QDs and have different gain spectra. The necessary condition for such situation is a significant channeling of carriers in transverse direction. It is possible because of limited transport of carriers between QDs in such laser heterostructures at room temperature.

Acknowledgments

This work is supported by the Program of Ministry of Science of Russian Federation "Nanostructures" (Project 2-001). Authors are grateful to Victor B.Khalfin for interesting discussion.

References

1. Zh.I.Alferov, D.Z.Garbuzov, N.Yu.David'uck, S.V.Zaitsev, A.B.Nivin, N.A.Strugov, I.S.Tarasov, Soviet Technical Physics Letters, , v.13(9), p.552 (1987).
2. S V.Zaitsev, N.Yu.Gordeev, M.P.Soshnikov, A.Yu.Egorov, A.E.Zhukov, V.M.Ustinov, N.N.Ledentsov and P.S.Kop'ev, OPTDM-95/SPIE, Kiev, Ukraine, proc. N2648-45, p.287 (1995).
3. S.V.Zaitsev, N.Yu.Gordeev, V.M.Ustinov, A.E.Zhukov, A.Yu.Egorov, N.N.Ledentsov, M.V Maximov, A.F.Tsatsulnikov, P.S.Kop'ev, Zh.I.Alferov, D.Bimberg, Semiconductors, v.31(5), p.27 (1997).
4. D.A.Ackerman, G.E.Shtengel, P.A.Morton, L.M.Zhang, J.E.Johnson, C.G.Bethea, L.J.-P.Ketelsen, Proc. OFC'97, p.142 (1997).
5. V.M.Ustinov, A.Yu.Egorov, A.E.Zhukov, N.N.Ledentsov, M.V.Maximov, A.F.Tsatsulnikov, N A.Bert, A.O.Kosogov, P.S.Kop'ev, D.Bimberg, and Zh.I.Alferov, Proc. Mat. Res. Soc. Symp., v.417, p.141 (1996).
6. N.Yu.Gordeev, S.V.Zaitsev, E.L.Portnoy, M.P.Soshnikov, V.P.Khvostikov. Soviet Technical Physics Letters, v.19(12), p. 88 (1993).

Influence of intervalence band absorption on characteristics of long wavelength lasers based on InAs

N.A.Gun'ko, G.G.Zegrya, Z.N.Sokolova, V.B.Khalfin

A.F.Ioffe Physico-Technical Institute, Russian Academy of Sciences.
194021 St.Petersburg, Russia

1. Introduction

In the field of the long wavelength lasers on the base of InAs great progress was achieved in the last few years [1], but working temperature and quantum efficiency of these lasers stayed much lower than for lasers working on the shorter wavelength, less than 1.5 μm [2]. It was shown that Auger recombination determined their maximal working temperature, but this did not explain the low quantum efficiency of these lasers at low temperatures ($\sim$ 77K). One peculiar feature of this laser material is that band gap (E_g) and the spin-orbital splitting (Δ) have nearly the same value. Due to this band structure the intervalence band absorption (IVA) has to be much stronger at the laser wavelength than for lasers on InGaAsP/InP, where it is important loss mechanism [3].

2. Theoretical model

We studied absorption due to transitions between the split-off band and the heavy and light hole bands, and compare the IVA with gain. Four band Kane model was safely used for calculation of the band structure, because the wavevectors of all particles involved were small. We applied the projection operator technique [4] and the following expressions for absorption coefficient were obtained:
For transitions between split-off band and heavy hole band (process 1, it takes place when $\hbar\omega > \Delta$):

$$\alpha_h^{so} = A \frac{M_{so,h}^{5/2}(\hbar\omega - \Delta)^{3/2}}{1 + \exp[\frac{M_{so,h}}{m_h}\frac{\hbar\omega - \Delta}{T} - \frac{\zeta_h}{T}]}; \qquad (1)$$

For transitions between split-off band and light hole band (process 2, it takes place when $\hbar\omega < \Delta$):

$$\alpha_l^{so} = A\frac{17E_g^2 + 20E_g\Delta + 6\Delta^2}{3E_g^2}\frac{M_{so,l}^{5/2}(\Delta - \hbar\omega)^{3/2}}{1+\exp[\frac{M_{so,l}}{m_l}\frac{\Delta-\hbar\omega}{T} - \frac{\zeta_h}{T}]}, \quad (2)$$

Where $A = \frac{2\sqrt{2}e^2\hbar\omega}{c\sqrt{\epsilon_\infty}\hbar^2\Delta^2 m_{so}^2}$, $M_{so,i} = \pm\frac{m_{so}m_i}{(m_i - m_{so})}$, $m_i = m_t$ or m_l. m_h, m_l, m_{so} are hole masses for heavy holes and split-off bands, ζ_h is holes Fermi level, ω is the light frequency and other symbols are standart . These expressions coincide with the relevant formulae from the paper [5] in the case of the nondegenerate holes. It can be shown from (1) that maximum value of the IVA is nearly independent on temperature and is function of hole concentration only. It can be seen from (1) and (2) that absorption due to process 1 when it exists, is more than ten times stronger than absorption connected with process 2 due to higher density of states. To estimate influence of the IVA on the properties of the long wavelength lasers we compare absorption due to process 1 with gain (g) (The expression for gain is taken from [6]). If we disregard Fermi-factors that are near the same in both cases we obtain for the ratio g/α:

$$\frac{g}{\alpha_h^{so}} = \frac{2}{5}\frac{E_g}{\hbar\omega - \Delta}\frac{\sqrt{m_c}m_{so}^2}{M_{so,h}^{5/2}}. \quad (3)$$

If we take $\hbar\omega = E_g$, we obtain for InAs at 77 K g/α=1.1. This great value of the IVA follows from the higher reduced density of states for transitions between heavy hole and split-off bands than for transitions between valence and conduction bands. This factor compensates small ratio $(\hbar\omega - \Delta)/E_g$, that appears because processes of the IVA are forbidden in the Γ-point of the Brillouine zone. So IVA heavily influences not only quantum efficiency but also the threshold carrier density for long wavelengh lasers. Frequency dependence of the IVA in InAs due to process 1 and 2 is presented on the Fig.1. Curves 1,1′,3,3′ correspond to expression (1) received in the first approximation at the parameter $\gamma = (\hbar\omega - \Delta)/\Delta << 1$. Curves 2,2′,4,4′ were calculated in the strict Kane model. The carrier concentrations were $6 \cdot 10^{17}\text{cm}^{-3}$ - curves 1,1′,2,2′ and $3 \cdot 10^{17}\text{cm}^{-3}$ - curves 3,3′,4,4′. It is evident that IVA can be important only if $\hbar\omega > \Delta$ when the absorption process from the heavy hole band takes place.

3. Results and discussion

We investigate the influence of the IVA on the threshold current and quantum efficiency for heterolasers with active layer from InAs. We assume standart structure

with InAs active layer with thickness $d = 0.8 - 1.5\mu$m and InAsSbP cladding [1]. Calculation are fulfilled for laser length $L = 0.03 - 0.09$cm. We disregard all other optical losses besides output losses and losses due to IVA and calculate the threshold carrier concentration from the usual equality between gain and total losses on the frequency where effective gain $(g - \alpha)$ has maximum. Quantum efficiency is determined as ratio of output losses to total losses. In InAs the value of spin-orbital splitting is nearly independent on temperature (we accept it value 0.39 eV). Band gap of InAs depends on temperature approximately lineary from 0.41 eV at 77 K till 0.35 eV at 300 K [7]. So in the temperature range 150-200 K Δ and E_g are nearly coincide. That gives a number of peculiarities on the threshold current and quantum efficiency characteristics. External quantum efficiency as function of the temperature is presented on Fig.2 for thickness of active layer 0.8 μm and 1.5 μm and for laser length 0.03 cm and 0.09 cm. The minimum at temperature 100 - 160 K could be seen for all design parameters. It should be underlined that IVA absorption increases not only due to increase of the carrier concentration but also due to displacing of gain maximum through the IVA spectrum with temperature growth.

Fig.1.

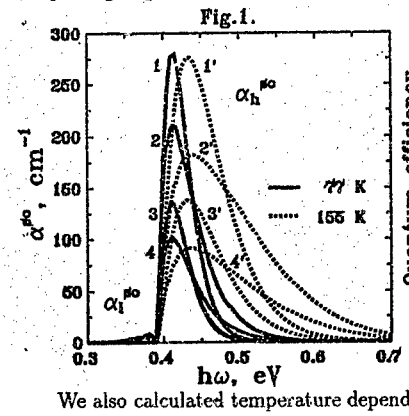

Fig.2.

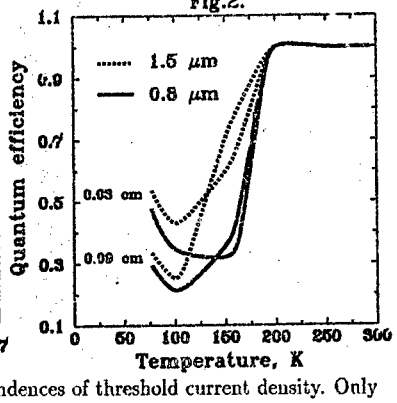

We also calculated temperature dependences of threshold current density. Only radiative recombination [8] and Auger recombination [9] were taken into account. It occurs that for all temperatures the nonradiative current is bigger then radiative, at 77 K the radiative component is near one half of the nonradiative one and only one tenth at 155 K. The calculated dependencies of the threshold current density on temperature for different heterostructures on base InAs: 1- d=0.8 μm, L=0.03 cm; 2 - 1.5 μm, L=0.03 cm; 3 - d=1.8 μm, L$\rightarrow\infty$; triangles - experimental data from [1] for heterostructure with the d= 1.8 μm, L$\rightarrow\infty$ are presented on Fig.3. Threshold current density contineously increases with temperature. Only for diodes with greatest output losses there is the region of the stabilization in the temperature

region 150-200 K. The threshold current density dependences on output losses for laser with d=1.8 μm (InAs), T= 77 K are shown on Fig.4. Triangles are experimental data from [10], contineous line is result of calculation.

Fig.3.

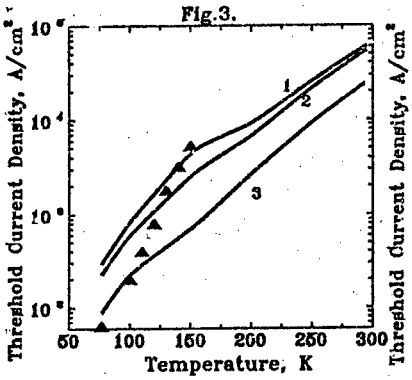

Fig.4.

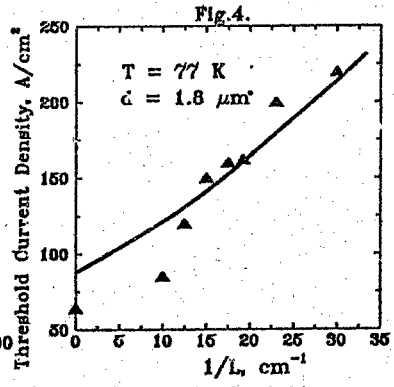

In summary we point out that the IVA heavy influences the threshold current and quantum efficiency of lasers based on InAs and can give anomalies on the temperature dependences of its characteristics. To improve the characteristics of these lasers solid solutions with $E_g < \Delta$ must be used to exclude IVA processes at all temperatures.

References

1. M. Aidaraliev, N. V. Zotova, S. A. Karandashev, B. A. Matveev, N. M. Stus', G. N. Talalakin. Infrared Phys. & Techn. **37**, 83-86, 1996.

2. P. J. A. Thijs L. F.Tiemeijer, J. J. M. Binsma, T. van Dongen. IEEE J.Quant.Elect. **QE-30**, 477-499, 1994.

3. A. R. Adams, K. C. Heasman, J. Hilton. Semicond. Sci. Technol. **2**, 761–764, 1987.

4. B. L. Gelmont. JETF **75**. 2(8), 536–544, 1978.

5. B. L. Altschuler, E. L. Ivchenko, A. N. Moskalev, G. E. Pikus, R. M. Rindin. JETF **85**, 1(17), 346–365, 1983.

6.B. L. Gelmont, G. G. Zegrya FTP **25**, 11, 2019–2023, 1991.

7.Numerical Data and Functional Relationships in Science and Technology, v. 17, Semiconductors, ed. by C. Madelung, M. Shulz, H. Weiss, 1982.

8.Quantum Well Lasers, ed. by P. Zory, Academic Press, 1993.

9. Z.N.Sokolova. Ph. D. Thesis, A.F.Ioffe PTI RAN, St.Petersburg, 1982.

10. M. Aidaraliev Ph. D. Thesis, A.F.Ioffe PTI RAN, St.Petersburg, 1992.

Phase effects in grating coupled surface emitting laser diodes.

M.A.Kaliteevski, E.L.Portnoi, G.S.Sokolovskii

A.F. Ioffe Physico-technical Institute of Russian Academy of Science, Polytechnicheskaya, 26, St-Peterburg, Russia

J.S.McKillop

LASER FARE INC., Smithfield, RI 02917

Grating coupled surface emitting semiconductor lasers (GCSEL) have many advantages comparing with the common ones emitting through the facets [1,2]. One of the main advantages of such lasers is large emitting surface and high output aperture. This results not only in the low output beam divergence [2] but also in lifting of the fundamental limit for laser output power set by 'catastrophical' degradation of the laser facets [3]. The usage of diffraction gratings for the feedback and for the radiation output allows one to get single mode laser generation with narrow linewidth [4].

The main disadvantage of GCSEL is the significant decrease of the laser efficiency because of diffraction of radiation into substrate [3]. It must be noted that sometimes second order gratings are used for the eedback because of the technological difficulties. In this case laser efficiency is lowered also by the radiation loses in the first order of diffraction [5,6]. Both these problems can be solved by placing the Bragg reflector (BR) under the waveguide layer. In spite of apparent simplicity of the described way authors of [7-10] neglect the phase relations between the wave diffracted directly in air and the other one diffracted into substrate and reflected by the BR. In this paper the rigo-

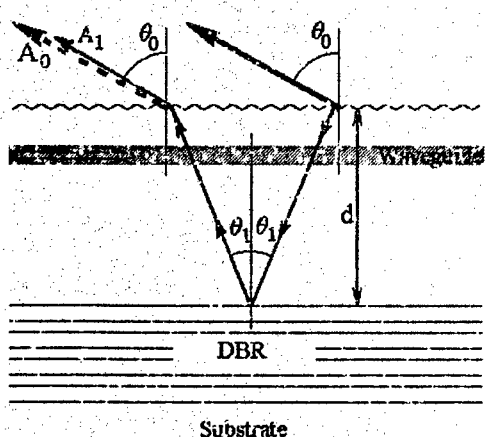

Fig.1. To calculations of phase relations in the system waveguide - surface grating - multilayer Bragg reflector.

rous calculations of the named relations are carried out and the analysis of the found effects in respect to use in laser diode's construction is done.

Let us consider diffraction of the waveguide mode on the surface grating. The wave diffracted under the angle θ_0 is the superposition of two waves (Fig.1). The first is diffracted directly in the air under the angle θ_0 with the amplitude A_0 and the second is diffracted into the substrate under the angle θ_1 and reflected by the BR with resulting amplitude A_1. We shall consider the 'negative' diffraction angles, i.e. the angles corresponding diffraction 'back'.

The phase difference between these two waves $\Delta\varphi_{01}$ is (Fig.1)

$$\Delta\varphi_{01} = 2dN_m K_0 \sin\theta_1 + 2d\bar{n}K_0 \frac{1}{\cos\theta_1} + \Delta\varphi_b(\theta_1) \qquad (1)$$

where N_m - is the effective refractive index for weveguide mode, $\bar{n}$ - the 'average' waveguide and cladding layers refractive index, d - is the distance from the grating to BR, K_0 - is wave vector of the light in vacuum, and $\Delta\varphi_b(\theta_1)$- is the phase of reflection from the BR.

When $\theta_1 \approx 0$ the phase difference can be written as follows:

$$\Delta\varphi_\perp = 2d\bar{n}K_0 + \Delta\varphi_b(0), \qquad (2)$$

One can see (Fig.2) the frequency of Bragg interference on BR the phase $\Delta\varphi_b(\theta_1)$ slightly depends on angle θ_1 [11]. At the Bragg frequency of BR when $\theta_1 = 0$ phase difference is equal 0 or π depending on the order of layer alternation [11].

The resulting intensity $I = |A_0 + A_1|^2$ depends on difference of phases of waves A_0 and A_1. In other words, BR can increase or suppress diffraction output.

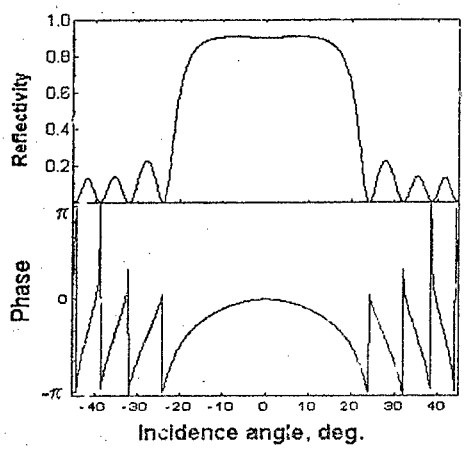

Fig.2. Reflectivity and phase of reflection from AlAs/GaAs 12 period BR with GaAs as the first and the last media for λ_0=0.9μm

It is important to note that the wave incident on the surface grating is diffracting partly 'in air', in waveguide mode and on BR. This allows to construct the high-efficiency second order distributed Bragg reflector laser diode with diffraction output through the first order surface grating. To use the monolitical epitaxial structure with multilayer BR to increase the diffraction output of this laser diode and to suppress the first order diffraction in air on the distributed Bragg reflector (Fig.3) looks like a very promising idea. The step of surface grating used for feedback can be written as:

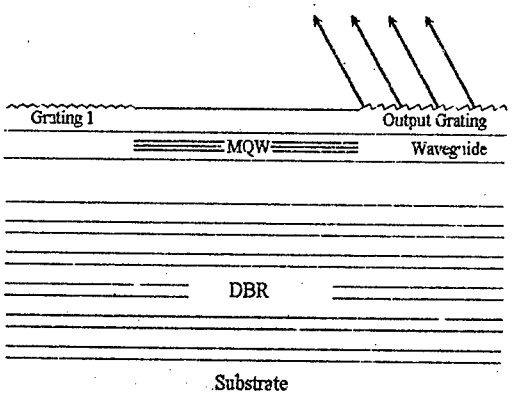

Fig.3. Proposed construction of laser diode

$$a_1 = \frac{2 \cdot \pi}{N_m \cdot K_0} \tag{3}$$

And the period of the grating used for diffraction output obeys the relation:

$$\frac{\pi}{N_m \cdot K_0} < a_2 < \frac{2 \cdot \pi}{N_m \cdot K_0} \tag{4}$$

To suppress the radiation losses in the first order on the distributed Bragg reflector and, at the same time, to enhance the output through the other surface grating the phase increment of the normally diffracted wave must differ from the one diffracted at the angle θ_1 on $(2m+1)\pi$, where m is integer. This condition using (1) and (2) can be rewritten as follows:

$$2dN_m K_0 \sin\theta_1 + 2d\bar{n}K_0\left(\frac{1}{\cos\theta_1} - 1\right) + \Delta\varphi_b(\theta_1) - \Delta\varphi_b(0) = (2m+1)\pi \tag{5}$$

When θ_1 is little and all the addends in (5) are negligible comparing to the first one. When $m = 0$, $N_m \approx \bar{n}$ (5) can be transformed to:

$$d \approx \frac{\lambda}{4 \cdot \sin\theta_1} \tag{6}$$

where λ is wavelength of light in material.

In other words, for the angle $\theta_1 = 5°$ the waveguide thickness d is about 2.5 times wavelength of light in the material. For GaAs/AlGaAs ($\lambda = 0.9$ μm , $N_m \approx \bar{n} \approx 3.5$) laser diode with the angle of output $\theta_0 \approx 20°$ the angle of diffraction 'into substrate' $\theta_1 \approx 5°$. In this case condition (5) can be satisfied when $d \approx 0.6$μm.

The work was done under financial support of the Russian Foundation for Basic Research (grant # 96-02-17836-a).

References:

1. Certificate of authorship (USSR) No 392875 with priority on July 19, 1971 Authors: Zh.I. Alferov, V.M. Andreev, R.F. Kazarinov, E.L.Portnoi, R.A.Suris, BI, No 1, 1977, p.259.
2. Zh.I. Alferov, S.A. Gurevich, R.F. Kazarinov, M.N. Mizerov, E.L. Portnoi, R.P.Seisyan, R.A. Suris, "Semiconductor laser with extremely low divergence of radiation", Sov. Phys.-Semicond. (USA), vol. 8, No. 4, p. 541-542 (1974).
3. S.Yu. Karpov, V.I. Kuchinskii, E.L. Portnoi, "Maximum output power of a semiconductor laser with diffraction output coupling", Sov.Tech. Phys. Lett. (USA), vol. 6, No.5, pp.155-157 (1980).
4. Zh.I. Alferov, A.D. Vlasov, V.I. Kuchinskii, M.N. Mizerov, E.L. Portnoi, A.I. Uvarov, "Epitaxial waveguide laser with distributed second order feedback by electron excitation" vol.3, no. 19, p. 987-990 (1977).
5. S.Yu. Karpov, "Diffraction of electromagnetic waves by periodic interfaces of arbitrary shape", vol.23, No.9, pp.1009-1013 (1978).
6. S.Yu. Karpov, M.N. Mizerov, E.L.Portnoi, V.B.Smirnitskii, "Light diffraktion by a sinusoidal interface", vol.23, No.2, pp.214-216 (1978)
7. R.F.Kazarinov and C.H.Henry, IEEE J. Quantum Electronics, QE-21, p.144-150 (1985)
8. C.H.Henry, R.F.Kazarinov, R.A.Logan, R.Yen, IEEE J. Quantum Electronics, QE-21, p.151-154 (1985)
9. A.Hardy, D.Welch, W.Streifer, IEEE J. of Quantum Electronics, v.25, No.10, pp.2096-2105 (1989)
10. D.Mehuys, R.Parke, R.G.Waarts, D.F.Welch, A.Hardy, W.Streifer, D.R.Scifres, IEEE J. Quantum Electronics, 27, p.1574-1581 (1991)
11. E.L. Ivchenko, M.A.Kaliteevski, A.V.Kavokin and A.I.Nesvizhski, J. Opt. Soc. Am. B, v.13, n.5, in press (1996)

Low Threshold (<200 μA, 300 K) Vertical Cavity Lasers Based on Vertically Coupled Quantum Dots Emitting at ~1 μm

N.N. Ledentsov*, V.M. Ustinov, A.Yu. Egorov, A.E. Zhukov, A.R.Kovsh, M.V. Maximov, P.S. Kop'ev, and Zh.I. Alferov
Abraham F. Ioffe Physical Technical Institute of the Russian Academy of Science, 194021, Polytekhnicheskaya 26, St.-Petersburg, Russia
J.A. Lott
Air Force Institute of Technology, Department of Electrical and Computer Engineering, 2950 P Street Building 640, Wright-Patterson AFB, Ohio USA 45433
D. Bimberg
Institut für Festkörperphysik, Technische Universität Berlin, Hardenbergstrasse 36, 10623 Berlin, Germany

Lasing via the exciton ground state in three-period vertically coupled InGaAs/GaAs quantum dots is realized for vertical cavity lasers. The structures include selectively oxidized AlO current apertures and AlO/GaAs reflectors. Experimental devices emit near 1.0 μm and operate continuous wave at 20°C with threshold currents below 200 μA and peak power conversion efficiencies exceeding 10 percent.

1. Introduction.

Since the first realization of lasing in self-organized quantum dots (QDs) [1, 2], an explosion of interest in the area of QD lasers occurred, as their characteristics are expected to overcome ones for best quantum well (QW) devices. Very advantageous is the application of QDs to vertical cavity surface emitting lasers (VCLs), as the lasers based on single QD can be potentially formed. In conventional planar VCLs the spectral gain width of the QW active region is larger than the free spectral range of the high finesse axial microcavity (see Fig. 1 inset). Only a fraction of the available QW spectral gain is efficiently utilized. As the dimensionallity of gain elements is reduced from QWs to QDs, material gain dramatically increases, and, moreover, band filling becomes more efficient and differential gain increases. Ideally the injected carriers concentrate into matched atomic k-states and produce gain at a single energy. The spectral linewidth of QDs is determined primarily by variations in QD size, while the true δ-function like density of states can be realized for single QD structures. The potential application of single QD VCLs, on the other hand, can be limited by very small overlap between the QD and the lightwave, which can make the modal gain insufficient to overcome losses. Previously reported QD VCLs [2-4] are in fact based on arrays of individual QDs. Even when stacked, the dots are electronically uncoupled and each has its own set of energy levels. A further improvement in optical confinement and gain efficiency is expected by replacing the uncoupled dots with vertically coupled quantum dots (VCQDs) of uniform size, as it is shown for edge-emitting structures [5]. In a VCQD stack with N periods, the ground state transition split into a narrow miniband composed of N sublevels. Nonequilibrium carriers are localized in the VCQDs and thus recombination at oxide defined apertures can be suppressed. This facilitates reduced aperture

diameters, and, together with the increased modal gain, gives the possibility of a VCL with a single VCQD stack.

This paper presents the first investigation of VCLs with VCQD active regions. The VCQDs and VCLs are designed for emission at 1.0 μm and include selectively oxidized current apertures and distributed Bragg reflectors (DBRs). This design facilitates a study of VCL performance with a variation in top DBR reflectance, by changing the number of oxidized DBR periods.

2. Experimental

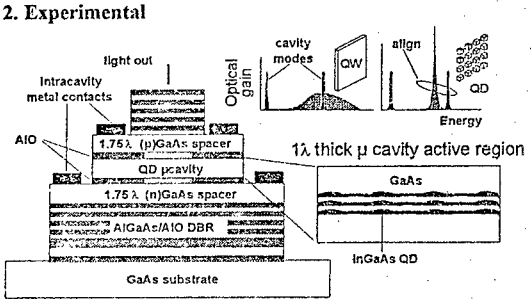

Fig. 1. Cross-section of a VCL with vertically coupled QD active region and native oxide current aperture and DBRs. Inset: Gain vs. energy for QW and QD active regions.

A cross-section of a fabricated vertically coupled QD VCL is shown in Fig. 1. The epitaxial structures are prepared by solid-source molecular beam epitaxy on (001) (n^+) GaAs substrates as described in [6]. The QDs consist of self-organized vertical stacks of InGaAs pyramidal islands formed by 1.2 nm $In_{0.5}Ga_{0.5}As$ depositions and separated by GaAs barrier layers with average thicknesses of 4 nm. The intrastack carrier wavefunctions overlap in the vertical direction resulting in extended state quantum dot potentials. Adjacent stacks are sufficiently laterally separated to be electrically decoupled. The areal stack density parallel to the growth plane is approximately $4\text{-}5\times10^{10}$ cm^{-2}. The QDs are centered in a 1λ-thick GaAs optical microcavity, whose edges are doped to 10^{17} cm^{-3}. The ends of the microcavity are composed of $Al_xGa_{1-x}As$ linearly graded from x = 0.0 up to 1.0. The microcavity is surrounded by λ/4-thick (p) and (n) AlAs layers followed by 1.75λ-thick (p) and (n)GaAs current spreading/intracavity contact spacer layers doped to 10^{18} cm^{-3}. The spacer layers are followed by DBRs composed of alternating AlAs and λ/4-thick GaAs layers. These top and bottom DBRs have 5 and 6.5 periods, respectively. The AlAs layers in the DBR, as well as those surrounding the optical cavity, are selectively oxidized to form AlO. The devices are fabricated in a manner similar to that reported in [6]. For some devices , the top 1 or 2 DBR periods are selectively wet-etched prior to oxidation. The devices reported here have approximately square current apertures of area 10x10 μm^2.

3. Results and Discussion.

Figure 2 shows the measured (solid lines) and calculated (dashed lines) reflectance of a VCL structure before and after selective oxidation. The wafers were not rotated during growth resulting in a linear variation in layer thickness. This allows a study of the affects of mismatch between cavity photon mode and peak VCQD gain. The thickness variation has minimal affect on

VECOD electroluminescence maximum intensity energy. This was verified by characterizing light-emitting diodes (LEDs) with identical coupled QD active regions.

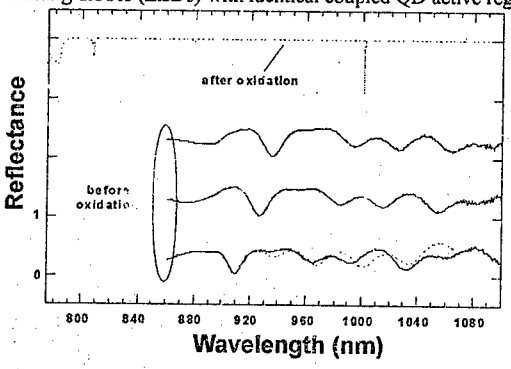

Fig. 2. Measured (solid lines) and calculated (dashed lines) reflectance spectra at normal incidence.

The calculated reflectance bandwidth of the AlO/GaAs DBRs is very large and easily covers the range 0.9 to 1.1 μm. As for VCLs with all-semiconductor DBRs, the energy of the photon mode is determined primarily by the optical thickness of the microcavity.

The room temperature (RT) continuous wave (CW) light power-current-voltage (L-I-V) and power conversion efficiency (η) characteristics of a coupled QD VCL are shown in Fig. 3. The curves are for an experimental structure emitting near 1.0 μm with 3 periods in the top DBR and an AlO aperture of about 10x10 μm^2. The threshold current is 0.27 mA and the threshold voltage is 1.26 V. The peak η is 12%. Also shown are the L-I curves for structures with 4 and 5 periods in the top DBR. As expected, the threshold current decreases to below 0.2 mA for a VCL with 5 top DBR periods but the relative output power drops drastically. The submilliampere threshold currents, along with electroluminescence measurements from QD LED test structures, indicate that the lasing proceeds via the QD ground state transition.

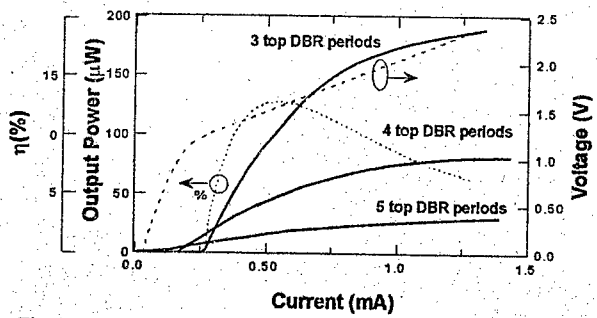

Fig. 3. Room temperature CW L-I-V and power conversion efficiency for a VCQD VCL.

The output power is relatively low because only a three-period coupled QD stack is used and the DBR reflectance is very high.

A portion of a VCL wafer is divided into two pieces parallel to the thickness gradient. One of the pieces is annealed at 700°C for 10 minutes in an overpressure of arsenic before device fabrication. This partially mixes the InGaAs dots with the GaAs barriers, resulting in a blueshift of the VCQD peak emission [7]. Post growth annealing may also reduce point defects and thus increase internal quantum efficiency. Figure 4 shows plots of RT CW threshold current versus peak emission wavelength for several VCQD VCLs located sequentially in a row. The peak emission wavelength can also be interpreted as relative position on the wafer. The solid lines are

fits to the data. The emission wavelength of the annealed VCL is indeed blueshifted with a slight decrease in threshold current.

6. Conclusion.

Surface emitting lasers based on electronically-coupled in the vertical directions quantum dots are fabricated. The performance of the first experimental VCQD VCL is comparable to that of best QW VCLs.

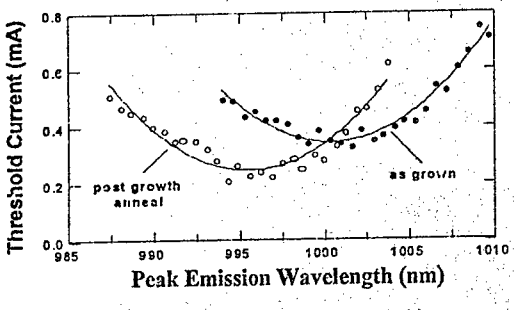

Fig. 4. Room temperature CW threshold current versus peak emission wavelength for sets of VCLs.

A significant improvement in efficiency is expected by adding AlGaAs confining layers and by increasing the number of dots in each stack, as it is shown for edge-emitting InGaAs-AlGaAs VCQD lasers emitting CW with a total power of ~1 W [8].

Acknowledgments: This work was supported by the Russian Foundation of Basic Research, the Volkswagen Foundation, and by the INTAS. The author is grateful to the Alexander von Humboldt Foundation.

REFERENCES

* also at the Institut für Festkörperphysik, Technische Universität Berlin, Hardenbergstrasse 36, 10623 Berlin, Germany

[1] N.N. Ledentsov, V.M. Ustinov, A.Yu. Egorov, A.E. Zhukov, M.V. Maximov, I.G. Tabatadze, P.S. Kop'ev, *Semiconductors* 28, 832 (1994); N. Kirstaedter, N.N. Ledentsov, M. Grundmann, D. Bimberg, U. Richter, S.S. Ruvimov, P. Werner, J. Heydenreich, V.M. Ustinov, M.V. Maximov, P.S. Kop'ev, and Zh.I. Alferov, *Electronics Letters* 30, 1416 (1994)

[2] R. Schur, F. Sogawa, M. Nishioka, S. Ishida, Y. Arakawa, Jpn. J. Appl. Phys. 35, L357-L360 (1997)

[3] H. Saito, K. Nishi, I. Ogura, S. Sugou, and Y. Sugimoto, *Appl. Phys. Lett.* 69 3140 (1996)

[4] D.L. Huffaker, O. Baklenov, L.A. Graham, B.G. Streetman, and D.G. Deppe, *Appl. Phys. Lett.* 70, 2356 (1997)

[5] N.N. Ledentsov, V.A. Shchukin, M. Grundmann, N. Kirstaedter, J. Böhrer, O. Schmidt, D. Bimberg, S.V. Zaitsev, V.M. Ustinov, A.E. Zhukov, P.S. Kop'ev, Zh.I. Alferov, A.O. Kosogov, S.S. Ruvimov, P. Werner, U. Gösele and J. Heydenreich, *Phys. Rev. B* 54, 8743 (1996).

[6] M. H. MacDougal, G. M. Yang, A. E. Bond, C.-K Lin, D. Tishinin, and P. D. Dapkus, IEEE Phot. Tech. Lett. 8(3) 310-312 (1996)

[7] A.O. Kosogov, P. Werner, U. Gösele, N.N. Ledentsov, D. Bimberg, V.M. Ustinov, A.Yu. Egorov, A.E. Zhukov, P S. Kop'ev, N.A. Bert, and Zh.I. Alferov, *Appl. Phys. Lett.* 69, 3072 (1996).

[8] Yu.M. Shernyakov, A.Yu. Egorov, A.E. Zhukov, S.V. Zaitsev, A.R. Kovsh, I.L. Krestnikov, A.V. Lunev, N.N. Ledentsov, M.V. Maximov, A.V. Sakharov, V.M. Ustinov, Zhao Zhen, P.S. Kop'ev, Zh.I. Alferov and D. Bimberg, Pis'ma v Zh. Tekhn. Fiz. 23 (1), 51 (1997) - Tech. Phys. Lett. 23 (1997).

Ultrafast excitonic saturable absorption in ion-implanted InGaAs/InAlAs multiple quantum wells.

E. Lugagne-Delpon, J.L. Oudar
France Telecom-CNET, 196 avenue Henri Ravera, F 92220 Bagneux, France
A. Shen, N. Stelmakh, J.M. Lourtioz
Institut d'Electronique Fondamentale, Bât. 220; F91405 Orsay, France

Nonlinearities associated with room temperature excitons in semiconductor quantum wells are useful for all-optical switching devices because they operate at moderate optical powers. The excitonic absorption can be bleached in a sub-picosecond timescale by exciton screening through light-induced free carriers. However the absorption recovery time is governed by the carrier population dynamics. The temporal response of the nonlinearity is thus limited by the carrier lifetime which is generally of the order of a few ns [1]. This constitutes a serious challenge for the fabrication of ultrafast optical devices. Introducing impurities in order to reduce the lifetime tends to smooth out the excitonic absorption peak because the presence of one defect per exciton volume prevents the exciton from being created. To overcome this limitation a promising approach consists in growing the samples at low temperature. However in the InGaAs/InAlAs system the introduction of additional Be-doping is found to be necessary to further reduce the carrier lifetime, and the persistence of the exciton line is unclear [2]. Another approach consists in creating recombination centres by proton irradiation [3]. We demonstrate here that irradiation with high energy heavy ions provides a very promising way to control the carrier lifetime in the InGaAs/ InAlAs system while preserving excitonic properties. The nonlinear absorption recovery time was reduced to an unprecedented value of 1.7 ps with persistence of excitonic features.

Our sample consists of a 33-period InGaAs(50 Å)/InAlAs(100 Å) superlattice grown by MBE on a semi-insulating InP substrate. The surface of the sample was irradiated with Nickel ions of 100 MeV energy, with doses ranging from 10^{10} cm^{-2} to 10^{13} cm^{-2}. Figure 1 shows the evolution of the linear absorption spectra at room temperature for increasing implantation doses. The heavy hole (HH) excitonic peak at 1.41 µm begins to broaden at doses of 10^{11} cm^{-2} but is still observable at 10^{12} cm^{-2} dose. For large implantation doses a large absorption tail appears, associated with the InP substrate. It tends to smooth artificially the excitonic features on the transmission spectra. Figure 2 shows the temporal response behaviour of the nonlinear absorption associated to the HH transition, measured by a conventional pump-probe technique with 150 fs resolution. The pump wavelength is set at 1.2 µm. One can observe a monotonous decrease of the absorption recovery time with increasing doses, from 1.6 ns for non-implanted sample down to 1.7 ps for a dose of 10^{13} cm^{-2}. The saturation

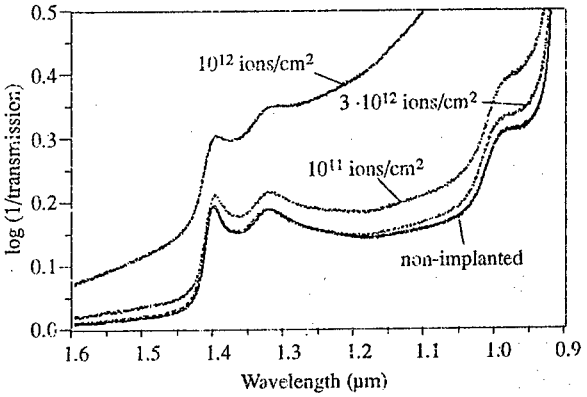

Fig. 1. Evolution of the transmission spectrum for increasing ion doses (at room temperature).

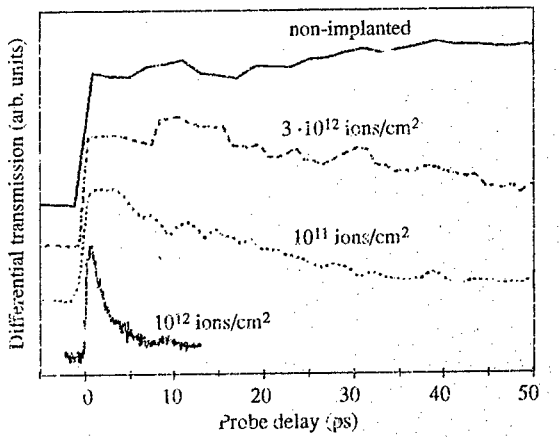

Fig. 2. Temporal response of the nonlinear HH absorption, for increasing ion doses. The pitch at 8-ps probe delay is due to a reflection of the pump on the back side of the substrate, which was not anti-reflection coated.

energy density was measured to be about 10 μJ cm^{-2}, a typical value for excitonic absorption saturation. No significant dependence with implantation dose was observed. Similar results were obtained for implantation of energetic Oxygen ions.

At high bombardment energies it is well known that the ions get implanted very deep inside the InP substrate but leave trails of defects along their travelling

direction in the top layers [4]. The defects can have a high carrier capture rate, but have only a small density per unit surface in each quantum well, allowing the persistence of the exciton line while the lifetime is reduced. Analysis by transmission electronic microscope did not lead to any observation of extended defects. Traps may thus be associated to point defects (vacancies, intersticials, ...) rather than structural ones (dislocations).

In conclusion we have realised an ultrafast saturable absorber by implantation of energetic ions in an InGaAs/InAlAs multiple quantum well. This constitutes a promising way for introducing a controllable concentration of efficient traps in order to control the carrier lifetime while preserving the excitonic properties of the semiconductor. One advantage of this approach is that the ion implantation can be realised as one of the very last steps in the fabrication process.

[1] D. S. Chemla and D.A.B. Miller, *J. Opt. Soc. Am. B*, 2, 1155 (1985)

[2] R. Takashi, Y. Kawamura, T. Kagawa and H. Iwamura, *Appl. Phys. Lett.* 65, 1790 (1994)

[3] Y. Silberberg, P.W. Smith, D.A.B. Miller, B. Tell, A.C. Gossard and W. Wiegmann, *Appl. Phys. Lett.* **46**, 701 (1985)

[4] E. Avrutin and M. Portnoi, *Sov. Phys. Semicond.* **22**, 968 (1989)

High power InGaAs/AlGaAs quantum dot laser.

M.V. Maximov, Yu.M. Shernyakov, N.N.Ledentsov[1]*, A.F.Tsatsul'nikov, Zhao Zhen, A.V.Lunev, A.V.Sakharov, V.M.Ustinov, A.Yu.Egorov, A.E. Zhukov, A.R.Kovsh, S.V.Zaitsev, N.Yu.Gordeev, P.S.Kop'ev, Zh.I.Alferov, D.Bimberg[1]

A.F.Ioffe Physical-Technical Institute, Politeknnicheskaya 26, 194021, St. Petersburg, Russia
E-Mail: maximov@beam.ioffe.rssi.ru
[1] Institut für Festkörperphysik, Technische Universität Berlin, D-10623 Berlin, Germany

Further progress in semiconductor optoelectronics is related to a great extend to quantum dot (QD) heterostructures, used, e.g. as an active region of injection lasers. Up to now it has been shown that, the lasers based on a single sheet of QDs [1] demonstrate in the low temperature range (up to 150-180 K) lasing via the QD ground state, low threshold current density (J_{th}), and ultrahigh temperature stability of J_{th} in agreement with earlier theoretical predictions. However, at higher temperatures electrons and holes are evaporated from QDs resulting in a decrease in gain and an increase in J_{th}. To improve the laser characteristics *vertically coupled* QDs (VECODS) has been used as the active media [2] of the laser. The J_{th} at 300K was shown to *decrease* dramatically with an increase in the number of QD stacks in the VECOD [3].

In this paper we report the realization of high power continuos wave (CW) operation of an injection laser with an active region based on InGaAs VECODs in an AlGaAs matrix. CW output power as high as 1W at room temperature is realized.

The laser structure was grown on (100) Si-doped GaAs substrate. It comprised a 0.4 μm-thick GRINSCH waveguide region confined by 1.5 μm-thick $Al_{0.4}Ga_{0.6}As$ emitters. A 0.6 μm GaAs p^+ contact layer was grown on top. Active region represented a VECOD structure formed by successive cycles of InGaAs QD depositions (average thickness of the $In_{0.5}Ga_{0.5}As$ deposit equals 12 Å per cycle), separated by 50 Å-thick $Al_{0.15}Ga_{0.85}As$ spacer layers at 490°C. Each VECOD is thus composed of 10 individual InGaAs islands stacked in the vertical direction. Since

*On leave from A.F. Ioffe Institute

the average thickness of the AlGaAs spacers is comparable to the QD height, the electron wavefunctions in the neighboring islands are essentially overlapping and each VECOD can be considered as a single quantum-mechanical object.

Lasers were fabricated in a shallow mesa stripe geometry. Dielectric mirrors were not used. The threshold current density (J_{th}) measured for long cavity lengths (~1100 μm) was ~290 A·cm^{-2}. The J_{th} values for the four-side cleaved samples where external losses are negligible, show much lower threshold current densities of about 100 A·cm^{-2}.

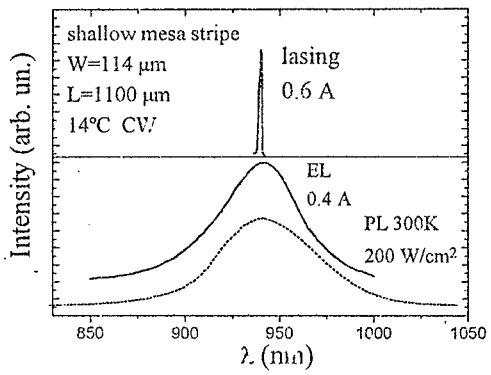

Fig.1 Photoluminescence (PL), electroluminescence (EL) and lasing spectra for the QD laser.

Photoluminescence (PL), electroluminescence (EL) and lasing spectra of the structure are shown in Fig.1. In order to measure the PL spectrum of the laser structure the upper emitter and the contact layer have been removed by wet chemical etching. The spectral position of the lasing line at current densities near the threshold corresponds to the maximum of the QD PL line (1.32 eV) recorded at 200 W/cm^2. Due to the effect of the AlGaAs matrix the InGaAs wetting layer states are placed at significantly higher photon energies of about 1.6 eV, thus the lasing definitely occurs in the range of QD transition energies. We note also that both the stimulated and lasing emissions contain both TE and TM components which points to the QD nature of the emission.

Fig.2a shows the CW light-current (L-I) characteristic of the laser at room temperature. In Fig.2b the lasing spectra at different driving currents are represented. Lasing wavelength moves towards longer wavelengths with the drive current increase. This effect is a result of the structure overheating which is estimated to be about 20°C at I=2

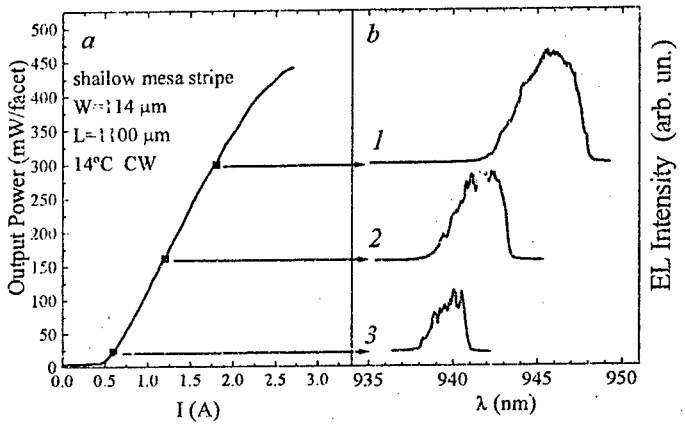

Fig.2 (a) CW light current (L-I) characteristics of the QD laser, (b) EL spectrum

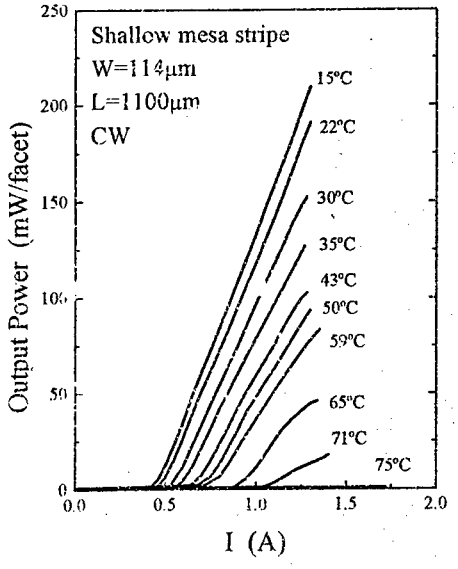

Fig.3 L-I characteristics of the QD laser measured at different temperatures.

A. Increase in the drive current results in a significant broadening of the lasing spectra. Maximal output light power for 2 facets is in the range of 0.8 -1 W at room temperature. Differential efficiency is about 50%.

Fig.3 shows the CW L-I characteristics at different heat sink temperatures. From this figure one can see that the lasing via the QD states occurs up to 70-75°C.

We further investigated the stability of the QD laser with respect to high temperature annealing. After 0.5 hour annealing at 800°C the main characteristics of the structure did not change. Thus, no considerable degradation in J_{th} and quantum efficiency occurs during the high temperature

annealing, indicating that QDs are stable. On the other hand, this observation also means that, relatively low differential efficiency is not determined by point defects due to low temperature overgrowth of QD with AlGaAs but by some other reasons. Small shift of the emission wavelength on 13nm towards shorter wavelengths we attribute to the influence of the In-Ga-Al interdiffusion processes.

To conclude, we demonstrated that lasers with an active region based on VECODs are stable and suitable for high-power operation.

Parts of this work are supported by Volkswagen Stiftung, INTAS-RFBR grant No. 95-618, RFBR grant No. 96-02-17824, N.N.L. is grateful to the Alexander von Humboldt Foundation.

1. D. Bimberg, N.N. Ledentsov, N.Kirstaedter, O. Schmidt, M. Grundmann, V.M. Ustinov, A.Yu. Egorov, A.E. Zhukov, M.V. Maximov, P.S. Kop'ev, Zh.I. Alferov, S.S. Ruvimov, U. Gösele, J. Heydenreich, „InAs-GaAs quantum dot lasers: in situ growth, radiative lifetimes and polarization properties", *Jpn. J. Appl. Phys.* **35**, 1311-1319 (1996)

2. Zh.I.Alferov, N.A. Bert, A.Yu. Egorov, A.E. Zhukov, P.S. Kop'ev, I.L. Krestnikov, N.N. Ledentsov, A.V. Lunev, M.V. Maximov, A.V. Sakharov, V.M. Ustinov, A.F. Tsatsulnikov, Yu.M. Shernyakov and D. Bimberg, „Injection heterolaser based on vertically-coupled quantum dots in a GaAs matrix", *Fizika i Tekn. Poluprovodn.* **30**, 351 (1996) - *Semiconductors* **30**, 194 (1996).

3. N.N.Ledentsov, „Ordered arrays of quantum dots" *Proc. of the 23rd Int. Conf. on the Physics of Semiconductors*, Berlin, July 21-26, 1996, ed. by M.Scheffler and R.Zimmermann (World Scientific, Singapore 1996), p.19

MBE GROWTH AND CHARACTERIZATION OF (Zn,Mg)SSe/ZnCdSe SCH SQW BLUE-GREEN LASERS WITH SHORT-PERIOD SUPERLATTICE WAVEGUIDE

S. SOROKIN, S. Ivanov, A. Toropov, T. Shubina, I. Sedova, M. Tkatchman, T. Kop'ev and Zh. Alferov

A.F.Ioffe Physico-Technical Institute of RAS, St.-Petersburg 194021, RUSSIA

Very fast progress in operating life-time of cw room temperature (RT) blue-green lasers based on II-VI wide-bandgap compounds (600 h is an unofficial record of Sony Co. to date) causes the optoelectronic community to turn again to these materials characterised by a large difference in lattice parameters of underlying binary materials and the relatively low activation energy of extended defects onset and development. The most important problems are still attributed to lowering the growth-induced defect density to 10^3 cm^{-2} by developing the more matured technology and accurate compensating the lattice-mismatch strain, as well as to a reduction of the threshold current density along with shortening the lasing wavelength by an improvement of the laser structure design.

This paper presents the results of efforts towards design and molecular beam epitaxial (MBE) growth of laser structures with strained short-period superlattice (SPSL) waveguide, lattice-matched to a GaAs substrate as a whole. The development of the strain compensation conception in II-VI laser structure design, compatible with non-interrupted growth process, is also presented along with characteristics of different injection and optically pumped blue-green RT lasers.

All the (Zn,Mg,Cd)(S,Se) quantum well (QW) heterostructures were grown by MBE on GaAs(001) substrates with a GaAs buffer layer grown in separate III-V MBE setup. The details of MBE growth and composition control of quaternary and ternary (Zn,Mg)SSe alloys have been described elsewhere [1]. Special cares were taken to control and stabilize a substrate temperature (T_S) in the (270-300)°C range, as having a dominant influence on the composition gradient of sulphur-contained II-VI compounds.

The first RT ZnSe-based separate-confinement heterostructure (SCH) consisted of ZnSSe cladding layers, thick ZnSe waveguide layers and a pseudomorphic ZnCdSe single quantum well (SQW). The main disadvantage of this construction is the noticeable lattice-mismatch between the ZnSe waveguide and GaAs substrate ($\Delta a/a \sim 0.26\%$), resulting in a misfit dislocations formation when the ZnSe thickness exceeds the critical one (~150 nm). An alternative completely pseudomorphic ZnSSe/ZnCdSe multiple QW structure showed worse optical confinement. Both lasers demonstrated RT operation under the pulse injection with a threshold current density as high as 4 kA/cm^2 [2]. A drastic improvement in the optical and electron confinement in SCH lasers has been achieved by replacing the ZnSSe claddings with wider bandgap ZnMgSSe ones, having much lower refractive index and higher conduction band offset. This structure nominally contains the ZnMgSSe cladding and ZnSSe guiding layers, lattice-matched to a GaAs substrate, and a pseudomorphic ZnCdSe SQW [3]. The lattice-matched ZnSSe and ZnMgSSe alloys have the S composition difference roughly equal to the Mg content. Different methods have been suggested to grow the pseudomorphic ZnMgSSe/ZnSSe/ZnCdSe SCH laser heterostructures [4]: (I) an

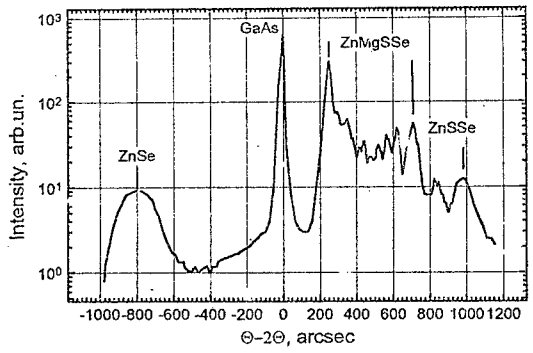

Fig. 1. Double-crystal x-ray rocking curve of the ZnMgSSe/ZnSSe/ZnCdSe SCH SQW structure grown in Mg-shutter operation regime

increase in the substrate temperature for the active and waveguide layers with respect to the cladding ones, (II) the ZnS flux variation at the ZnSSe/ZnMgSSe interface, and (III) the Mg-shutter operation regime resulting just in 1.5-2% reduction of S content in ZnSSe with respect to the quaternary layer within the T_S range of interest [1]. Though the first two methods provide the S concentration variation necessary for the lattice-matched growth, they require an undesirable rather long growth interruption near the active region, which may deteriorate the quality of the structures. The last method, realizing a conception of macro-scale strain compensation, enables one to carry out a whole process without any interruption. This regime allowed us to grow the pseudomorphic SCH SQW lasers, with the strongly stretched ZnSSe cavity and nearly lattice-matched ZnMgSSe claddings. The double-crystal x-ray rocking curve (DXRD) of such structure is presented in Fig. 1. One should note a considerable difference in ZnSSe guide and ZnMgSSe claddings peak position. However, the full width at half maximum (FWHM) values of ω-rocking curve of both layers are as low as 6 arcsec. The relatively high composition gradient of ZnMgSSe (about 450 arcsec, i. e. ~ 2% of S) is caused by T_S variation during growth using manipulator with a non-contact-type termocouple.

The elimination of growth interruption, at other optimal growth conditions, contributes significantly to the reduction of extended defect density down to 1×10^3 cm^{-2}. This value has been confirmed by plan-view and cross-sectional TEM measurements and is among the lowest values ever reported [5]. These laser structures demonstrated the RT operation under the optical (P_{th} = 25 kW/cm^2) and pulse injection (J_{th} = 800A/cm^2) pumping at λ = 520 nm.

The shortcoming of the method is a significant compressive strain introduced by the ZnSSe waveguide into the top p-ZnMgSSe:N, which turned out to initiate acceptor compensation processes during growth and did not allow one to decrease the lasing threshold. The attempts to exclude this effect by introduction of the asymmetrical waveguide, containing alternatively strained thick ZnSSe and ZnSe layers on different sides of ZnCdSe QW, were ineffective, because the abrupt stress variation near the QW resulted in breaking the structure during the laser diode processing.

To avoid stress relaxation we focused on a design of laser structures with precise nano-scale compensation of strong alternating compressive and tensile strains in the constituent layers. The strained ZnSSe waveguide was replaced with a ZnSSe/ZnCdSe SPSL, lattice-matched to cladding layers as a whole. In this case, the cadmium content in QW is equal to that in the SPSL well layers, while the sulphur content in the ZnMgSSe claddings strictly determines that in the ZnSSe barriers. It is of great importance that this SPSL can be easily realized for the wide ranges of QW and ZnMgSSe alloy compositions by choosing the proper thicknesses of the constituent SL layers and using the only shutter operation regime. Moreover, the introduction of SPSL is expected to prevent active layer from the defects penetration thus increasing the device operation lifetime.

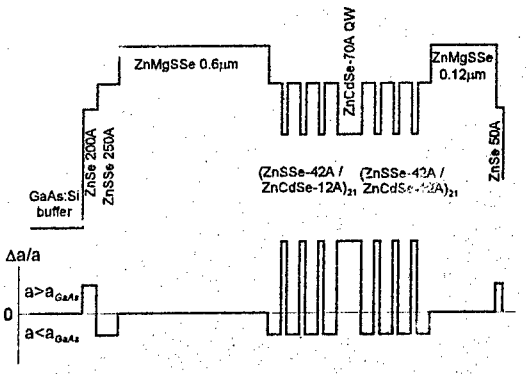

Fig.2. Schematic energy band diagram with respective strain distribution for the laser structure with SPSL waveguide.

The schematic diagram of the optically pumped laser structure with the SPSL optical cavity region is shown in Fig. 2. The structure contains 0.6μm-$Zn_{0.92}Mg_{0.08}S_{0.14}Se_{0.86}$, 70Å-$Zn_{0.88}Cd_{0.12}Se$ QW bounded with the 21 period (42Å-$ZnS_{0.12}Se_{0.88}$)/(12Å-$Zn_{0.88}Cd_{0.12}Se$) SPSL from both sides, and top 0.12μm-ZnMgSSe layer.

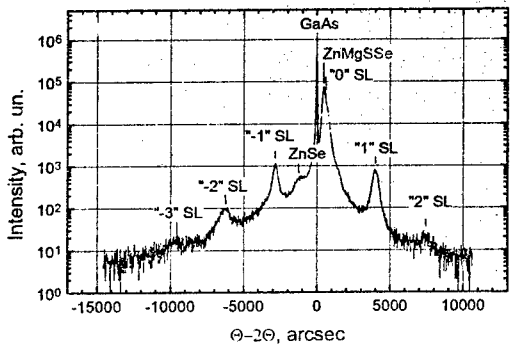

Fig. 3 Double-crystal x-ray rocking curve of the ZnMgSSe/SPSL/ZnCdSe SCH SQW structure

DXRD rocking curve of this structure is presented in Fig. 3. One can see that a zero-order SL peak practically coincides with the ZnMgSSe peak, with both being close to the GaAs substrate peak position, which indicates good lattice-matching of the whole structure. The composition gradient has been reduced significantly by using a contact-type termocouple manipulator.

The SPSL waveguides were successfully employed earlier [6] for decreasing the threshold current density in (Al,Ga)As lasers. The ZnMgSSe/ZnCdSe SPSL SCH SQW optically pumped lasers have also shown significantly improved optical and carrier confinement resulting in $P_{th} \sim 20$ kW/cm^2 at λ=490 nm (RT) and less than three times increase in P_{th} from 77 to 300K. One should especially note that the laser structure exhibits at the shorter wavelength even lower threshold power density than that of the conventional ZnMgSSe/ZnSSe/ZnCdSe SQW structure operating at 520 nm. The respective spectra of laser generation (Fig. 4) demonstrate the lasing linewidth as narrow as 6 meV at 300K.

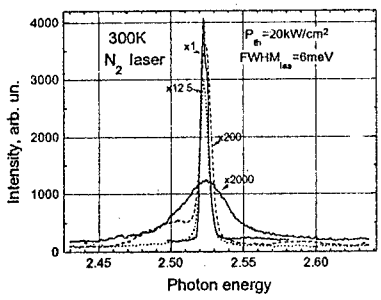

Fig. 4 The spectra of laser generation for structure with SPSL waveguiding.

In conclusion, the RT optically pumped lasers using alternatively strained ZnSSe/ZnCdSe SPSL as a waveguide have been grown by MBE. The introduction of SPSL resulted in the lower threshold power density at markedly shorter lasing wavelength as compared to the conventional ZnMgSSe/ZnSSe/ZnCdSe SCH SQW structures. The superior optical and electronic confinement as well as convenience of technological realization make the proposed design of laser active region very promising for injection device applications.

The authors are thankful to Dr. N. Faleev for XRD measurements. This work was supported in part by RFBR Grants No.97-02-18269, No.96-02-178444 and No.96-02-17911, as well as by Programm Ministry of Sciences of RF "Physics of Solid State Nanostructures" No.97-2014 and 97-1035.

References

[1] S. V. Ivanov, S. V.Sorokin, P. S. Kop'ev, J. R. Kim, H. D. Jung, H. S. Park, J. Crystal Growth 159 (1996) 16.

[2] P. S. Kop'ev, S. V. Ivanov, A. A Toropov, T. V. Shubina, S. V. Sorokin, M. V. Maximov, A. V. Lebedev, N. D. Il'inskaya, Abstracts of the International Symposium on Nanostructures: Physics and Technology, 1995, St.Petersburg, p.449.

[3] J. M. Gaines, R. R. Drenten, K. W. Haberern, T. Marshell, D. Mensz, J. Petruzzello, Appl. Phys. Lett. 62 (1993) 2462.

[4] E. S. Oh, S. D. Lee, H. D. Jung, J. R. Kim, M. D. Kim, B. J. Kim, J. K. Ji, H. S. Park, T. I. Kim, S. V. Ivanov, A.A. Toropov, and T.V. Shubina, J. Appl. Phys. 80(10) (1996) 5951.

[5] S.V. Ivanov, R. N. Kyutt, G. N. Mosina, L. M. Sorokin, S. V. Sorokin, and P. S. Kop'ev, in Proceedings 23rd International Symposium on Compound Semiconductors, St.Petersburg, (to be published in 1997).

[6] Zh. I. Alferov, A. M. Vasil'ev, S. V. Ivanov, P. S. Kop'ev, N. N. Ledentsov, M. E. Lutsenko, B. Ya. Meltser, V. M. Ustinov, Pis'ma v Z. T. Ph. 14(19) (1988).

Waveguide and Vertical-Cavity Optically Pumped Blue-Green Lasers Based on ZnCdSe/ZnSSe Superlattices and Multiple Quantum Wells

A.A. Toropov, S.V. Ivanov, T.V. Shubina, A.V. Lebedev, S.V. Sorokin, G.N. Aliev, M.G. Tkatchman, N.D. Il'inskaya and P.S. Kop'ev

A.F. Ioffe Physico-Technical Institute, 194021 St. Petersburg, Russia

We have studied both theoretically and experimentally the feasibility of using alternatively strained ZnCdSe/ZnSSe superlattices (SLs) and multiple quantum wells (MQWs) as guide and active regions of optically pumped blue-green lasers. It is shown that a proper design of the SL guide region of a ZnMgSSe/ZnSSe/ZnCdSe separate confinement quantum well (QW) laser results in better optical and carriers confinement as compared to the structure with the guide region made of a respective bulk ternary compound. With this approach, the threshold power density as low as 20 kW/cm^2 has been achieved in a room-temperature laser operating at 490 nm. A room-temperature optically pumped vertical-cavity laser has been demonstrated, utilizing a 0.68μm long ZnSSe/ZnCdSe MQW region and a short external cavity.

Currently, the continuous wave (cw) ZnSe-based lasers grown on GaAs substrates may only operate in blue-green emission region from 490 to 520 nm. The conventional design of the separate confinement single quantum well (QW) heterostructure implies a ZnCdSe quantum well (QW) placed in a ternary ZnSSe guide layer surrounded by ZnMgSSe cladding layers [1]. The composition of the quaternary alloy is usually chosen to match the lattice constant of the substrate, whereas the QW and the guide layers may be pseudomorphically strained [2]. The laser characteristics in this situation are governed by two contradictory conditions. On the one hand, the band gap of the guide layer should be small to maintain the reasonable difference in the refractive indices of the guide and cladding layers and thus to provide sufficient optical confinement. On the other hand, this band gap should be large enough to ensure the adequate band offsets needed for the electron and hole confinement in the QW. These two requirements cannot be met technologically in the devices operating at the wavelength shorter than 490 nm at 300 K mainly due to the limitation imposed by the maximum band gap of ~3.0 eV available for p-doped MgZnSSe cladding layers. The growth of a wider band-gap MgZnSSe alloy with the high enough efficiency of the p-type doping still remains difficult.

In this paper, we propose and study both theoretically and experimentally an alternative design of the laser active region, based on the employment of short-period ZnSSe/ZnCdSe superlattices (SLs). To avoid stress relaxation, attention has been paid to precise design of alternating compressive and tensile stresses in the constituent layers of the SLs. The strain in the structures is carefully balanced on the microscopic level that allows the pseudomorphic growth of high-quality strained SL regions. In particular, the feasibility of short-period SLs and extended multiple QWs (MQWs) both for the guide and active regions of the lasers has been studied.

The best optical confinement in the devices with the conventional design is consistent with the guide layer of binary ZnSe representing the lowest band gap among the ternaries. Unfortunately, the critical thickness of a ZnSe layer grown pseudomorphically to a GaAs substrate

is about 1500 Å, which is less than required for the optimal waveguide design. Furthermore, for the laser operating at 490 nm at room temperature the band offset of the heterojunction ZnSe/ZnCdSe can not provide the appropriate carriers confinement. In particular, the hole offset in this case is estimated as ~30 meV that is even less than kT at 300 K. To check the validity of our approach we have designed the ZnCdSe/ZnSSe SL with the band gap and refractive index close to the characteristics of ZnSe and estimated its feasibility for the guide layer. The entire structure is grown by molecular-beam epitaxy (MBE) on a (001) GaAs substrate and consists of a GaAs buffer layer grown by MBE in a separate chamber, 0.6μm wide ZnMgSSe bottom cladding layer with the low-temperature E_g~2.95 eV and the lattice constant closely matched to GaAs, 21 periods of (42 Å/12 Å) $ZnS_{0.12}Se_{0.88}/Zn_{0.88}Cd_{0.12}Se$ forming the guide layer, a 70 Å wide $Zn_{0.88}Cd_{0.12}Se$ QW, then 21 periods more of (42 Å/12 Å) $ZnS_{0.12}Se_{0.88}/Zn_{0.88}Cd_{0.12}Se$ and finally the 0.1μm wide ZnMgSSe top cladding layer. The $ZnS_{0.12}Se_{0.88}/Zn_{0.88}Cd_{0.12}Se$ SL is designed to have the average lattice constant matched to the GaAs one, which is confirmed by high-resolution X-Ray diffraction measurements. The ZnCdSe alloy composing the QW is chosen to gain the 300 K lasing at 490 nm. Estimations show that the optical confinement provided by the design is close to the optimal for this kind of structures.

Furthermore, the band structure calculation accounting for pseudomorphic strain in the layers confirms that the hole confinement in the QW is substantially improved as compared to the similar QW with ZnSe barriers. So, the heavy-hole band offset at the $ZnS_{0.12}Se_{0.88}/Zn_{0.88}Cd_{0.12}Se$ interface is estimated as 108 meV, which is mainly governed by the sulfur mole fraction in the ZnSSe alloy. The bottom of the lowest heavy-hole miniband in the SL, taking place at the energy 67 meV higher than the heavy-hole band edge of $Zn_{0.88}Cd_{0.12}Se$, determines the hole confinement which is about twice better than for the interface $ZnSe/Zn_{0.88}Cd_{0.12}Se$.

One more important characteristic of the guide layer is a mobility of carriers along the growth axis. In the studied sample, the carriers transport is governed by tunneling through the SL, e.g. by a minibands width. The calculated miniband widths are 72 meV, 9 meV and 104 meV for electrons, heavy holes and light holes, respectively. The small width of the heavy-hole miniband, determined by the large effective mass, is expected to make the heavy-hole transport difficult. However, bottoms of heavy- and light-hole minibands are aligned in energy with an accuracy of few meV. It means that the light-hole transport is dominant, followed by capture in the QW and energy relaxation down to the lowest heavy-hole QW level.

The laser characteristics have been studied under conditions of pulse optical pumping both at 77 K and 300 K. A nitrogen laser with a pulse width of 8 ns is used to pump lasing. In line with the calculations, the laser generation emerges at 473 nm and 491 nm at 77 K and 300 K, respectively. The threshold power density as low as 20 kW/cm^2 is observed at 300 K, which is among the best values known for ZnSe-based lasers operating near 490 nm. Only threefold change in a threshold power density is observed with the temperature increase from 77 K to 300 K that confirms an improved carriers confinement.

The SLs and extended MQW regions may also be used as an active region both in conventional waveguide-geometry lasers and in vertical-cavity lasers. In the former case, the SL region works also as a guide layer. Note that the early ZnSe-based lasers comprised ZnSe/ZnCdSe MQWs, serving as an active region and guide region simultaneously. A drawback of these devices was a considerable defect density resulting from strain relaxation in the MQW active region. In the framework of our approach, it is possible to design and grow the heterostructures with low defect concentration, which comprise coherently strained thick MQW regions. In particular, a 0.68μm

long ZnSSe/ZnCdSe MQW region with the total thickness of $Zn_{0.82}Cd_{0.18}Se$ material as large as 0.15μm has been coherently inserted in a ZnMgSSe thick layer. The QW region of this structure consists of 30 pairs of (170 Å/50 Å) $ZnS_{0.1}Se_{0.9}/Zn_{0.82}Cd_{0.18}Se$. As a whole, this region exhibits compressive strain due to some lattice mismatch with the GaAs.

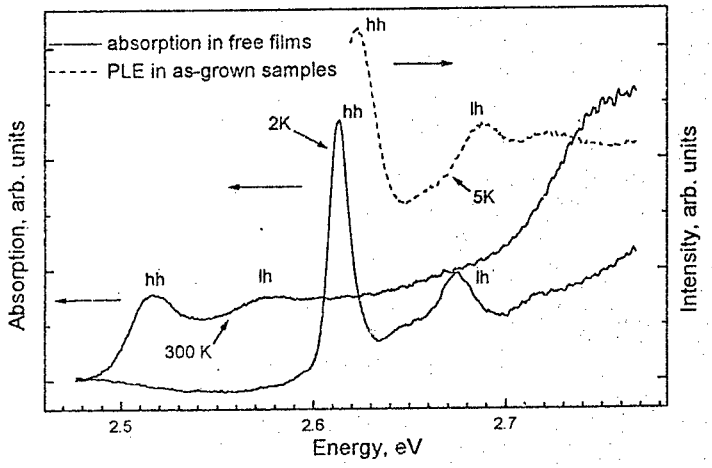

Fig.1 Absorption and PLE spectra measured in ZnSSe/ZnCdSe MQW samples

Optical properties of this structure have been studied both in as-grown samples and in free films with a chemically removed substrate. Figure 1 demonstrates absorption spectra measured in the free films at different temperatures. A sharp excitonic spectrum is clearly defined up to 300 K, confirming high quality of the structure. The dashed curve in Fig. 1 represents a low-temperature photoluminescence excitation (PLE) spectrum, measured in the same sample before removing the substrate. The removal of the substrate does not result in additional defects, but rather leads to some redistribution of strain inside the structure. In particular, it leads to a slight shift (~8 meV) of the heavy-hole exciton peak and a larger shift (~15 meV) of the light-hole exciton energy, in good agreement with the strain and band line-ups calculation.

The laser generation under optical pumping has been observed in both types of samples up to 300 K. A conventional waveguide-geometry lasing has been realized in the cleaved as-grown samples. Vertical-cavity lasers have been fabricated by inserting the free film into a short external cavity formed by the sample surface from one side and a thin quartz plate with evaporated metallic mirror from the other side. The waveguide-geometry lasers display the threshold power density of 11 kW/cm^2 at 77 K and of ~22 kW/cm^2 at 300 K. The thresholds for the vertical cavity lasers are 65 kW/cm^2 and 110 kW/cm^2 at 70 K and 300 K, respectively.

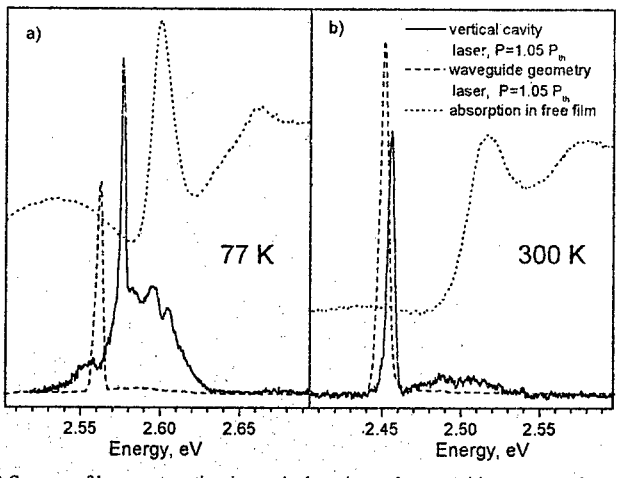

Fig.2 Spectra of laser generation in vertical-cavity and waveguide-geometry lasers

Figure 2 shows the spectra of laser generation, measured at 77 K (a) and 300 K (b) under conditions of pulsed optical pumping. The solid curves represent the spectra of the surface emitting lasers, whereas the dashed curves correspond to the waveguide-geometry lasers. The excitonic absorption peak is also displayed in Fig. 2 by the dotted curves. The wavelength of the lasing is almost the same for both types of samples at 300 K, but differs noticeably at 77 K. So, the spectra in Fig. 2 (a) display the detuning of the laser line from the exciton absorption peak of about 38 meV for the waveguide samples and of 23 meV for the surface emitting lasers. The latter value is less than the LO phonon energy (~32 meV) that neglects the possibility of an LO-phonon assisted excitonic gain mechanism and evidences in favor of a gain model based on a phase-space-filling effect of localized excitons [3].

Acknowledgements: This work has been supported in part by the Russian Foundation for Basic Research grant No. 97-02-18269a.

References:

1. J.M. Gaines, R.R. Drenten, K.W. Haberern, T. Marshall, P. Mensz, J. Petrozzello, Appl. Phys. Lett. **62**, 2462 (1993)
2. E. Oh, S.D. Lee, H.D. Jung, J.R. Kim, M.D. Kim, B.J. Kim, J.K. Ji, H.S. Park, T.I. Kim, S.V. Ivanov, A.A. Toropov, T.V. Shubina, J. of Appl. Physics **80**, 5951 (1996)
3. J. Ding, M. Hagerrot, T. Ishihara, H. Jeon, A.V. Nurmikko, Phys Rev. B **47**, 10528 (1993)

New fundamental approach to creation of mid-infrared lasers operating at high temperature

G. G. Zegrya
A.F.Ioffe Physical-Technical Institute of Russian Academy of Sciences,
26 Polytekhnicheskaya, St.-Petersburg 194021, Russia
Phone: +7-812-247-9367, E-mail: zegrya@theory.ioffe.rssi.ru

It is evident that creation of mid-infrared lasers operating at room temperature requires: (i) essential suppression of the Auger recombination processes at high temperatures to make it less or of the same order of magnitude as the radiative recombination rate; (ii) essential suppression of the internal losses for α_i to be smaller than α^*: $\alpha_i \ll \alpha^*$, where α^* are the mirror losses; (iii) leakage suppression.

The purpose of the present paper is to propose a new fundamental approach to creation of mid-infrared diode lasers operating at room temperature [1]. We will see below that within the new approach it is possible to: (i) considerably suppress the Auger recombination rate (approximately by three orders of magnitude) [2]; (ii) suppress the intraband absorption process (by two orders of magnitude); (iii) completely suppress the leakage current [1].

The essence of the new approach is the control over the Auger recombination rate (Auger engineering) and over the processes of intraband absorption. We consider deep quantum wells for both electrons and holes. The depth of the quantum wells is enough for the distance between the nearest size-quantization levels for electrons (namely, the ground and the first excited levels) to be more than the effective bandgap width $\tilde{E}_g$ (Fig.1)

$$E_{1c} - E_{0c} > \tilde{E}_g \equiv E_{0c} + E_g + E_{0h}, \qquad (1)$$

where E_{1c} is the energy of the first excited size-quantization level for electrons.

Let us now consider the CHCC Auger recombination process in such a deep quantum well under condition (1): two electrons localized on the basic level (in the states "1" and "2") interact, one of them recombining with a hole (state "3") and the other passing to the highly excited state "4" (see Fig. 1). Henceafter the highly excited electron gets between the size-quantization levels, i. e. still remains on the basic size-quantization level. This requires the longitudinal component of the momentum to change from $q_1 \sim q_T = \sqrt{2m_c T}/\hbar$ to $q_4 \approx Q = \sqrt{2m_c \tilde{E}_g}/\hbar$. The mechanism of this Auger recombination process is analogous to that in bulk semiconductors. We will later prove that this process is threshold, the Auger recombination rate depending on temperature exponentially.

Now we proceed to a more detailed description of the Auger recombination process in a deep quantum well. As a result of the Coulomb interaction of electrons in the states "1" and "2", one of them recombines with a hole passing into the state "3" while the other electron passes into the state "4", remaining on the basic size-quantization level. Such an Auger transition is possible under the condition that the electron-electron interaction is strong, since the transmitted momentum q is of the order of Q. The longitudinal component of the quasi-momentum is conserved in the process: $q_1 + q_2 = q_3 + q_4$. As a result, for the Auger

recombination rate we obtain

$$G \approx 12(2\pi)^{5/2}\frac{E_B}{\hbar}\frac{E_{0c}}{V_c}\left(\frac{m_h}{m_c}\frac{T}{E_g}\right)^{1/2}\frac{\lambda_g^3}{a^4}n^2 p\exp\left(-2\frac{m_c}{m_h^*}\frac{\tilde{E}_g}{T}\right)\left(1-\frac{m_h^*}{m_c}\frac{\delta}{\tilde{E}_g}\right), \qquad (2)$$

where $E_{th} = 2m_c\tilde{E}_g/m_h^*$, E_B is the Bohr energy, E_{0c} is the energy of ground electron state, n and p are the twodimensional concentration of electrons and holes, and $\lambda_g = \frac{\hbar}{\sqrt{2m_c E_g}}$.

Thus, we obtained an exponential suppression of the Auger recombination process in deep quantum wells ($V_c > E_g$) compared to shallow ones ($V_c \ll E_g$)).

It is interesting to compare what we derived for the Auger rate in a deep quantum well G^B (see Eq. (2)) with the expression for a shallow quantum well, G^S. Discarding the strain, we obtain

$$\frac{G^B}{G^S} \approx \frac{E_g}{V_c^B}\frac{E_g}{E_{0c}}\frac{\lambda_g}{a}\frac{T}{V_c^S}\frac{m_h}{m_c}\left(\frac{m_h}{m_c}\frac{T}{E_g}\right)^{1/2}\exp\left(-\frac{2m_c}{m_h^*}\frac{\tilde{E}_g}{T}\right), \qquad (3)$$

where V_c^S and V_c^B are the depths of deep and shallow quantum wells respectively. The ratio (3) is always less than 1. Assume $E_g = 0.4\,\text{eV}$, $V_c^B \cong 0.5\,\text{eV}$, $V_c^S \cong 0.2\,\text{eV}$, $T = 300\,\text{K}$, $a = 50\,\text{Å}$, $m_h^* = m_h/2$, we derive $G^B/G^S \sim 2\cdot 10^{-3}$, $m_h^* = m_h/2$. This ratio appears to be even smaller, since we have used an approximate expression for G^S.

We have thus shown that in deep quantum wells there can be considerable suppression of the Auger recombination rate and consequent rise in the internal quantum efficiency η.

However, the most valuable result is that under the conditions needed for the Auger recombination rate to be less than the radiative recombination rate such a deep quantum well enables a considerable suppression of the intraband absorption process.

The mechanism of the intraband absorption is appreciably different. The absorption of a photon is only possible when phonons or impurities participate, i. e. the process only occurs in second-order perturbation theory.

In the process of scattering of an electron on a LO-phonon and with account of Ref. [3] we deduce for the intraband absorption factor α_i^f

$$\alpha_i^f = \frac{8\pi}{\sqrt{\varepsilon_\infty}}\alpha_{ef}\frac{e^2}{\hbar c}\lambda_\omega^2 n\frac{\Gamma}{a}\left(\frac{\omega_0}{\omega}\right)^{3/2}, \qquad (4)$$

where α_{ef} is the electron-phonon interaction constant (Froehlich constant), moreover, $\alpha_{ef} \ll 1$; $\hbar\omega_0$ is the energy of LO-phonon. For III–V compounds we have $0.01 < \alpha < 0.1$. We should compare the expression obtained for α_i^f (4) with that for the intraband absorption factor in a shallow quantum well $\alpha_i^\perp$ (see (??)). Neglecting the strain and assuming $V_c^S = V_c^S$, $\hbar\omega = E_g$, we have

$$\frac{\alpha_i^f}{\alpha_i^\perp} \approx \frac{\alpha_{ef}}{4\sqrt{2}\pi}\frac{\hbar\omega_0}{V_c^S}\frac{(\hbar\omega_0 E_g)^{1/2}}{\varepsilon_\perp}\frac{a}{\lambda_g}. \qquad (5)$$

This ratio is always much less than unity. Using the same parameters as in estimating the relationship (3), and with account of the fact that $\alpha_{ef} \sim 3\cdot 10^{-2}$, we obtain $\alpha_i^f/\alpha_i^\perp \approx 1\cdot 10^{-3}$. In such a structure the internal losses are therefore much less than those on mirrors. $\tilde{\alpha}_i^f \ll \alpha^*$. Assuming $\alpha^* = 30\,\text{cm}^{-1}$, we have that at $T = 300\,\text{K}$ the threshold concentration equals $2\cdot 10^{12}\,\text{cm}^{-2}$. At the same value of the parameters the Auger coefficient, according

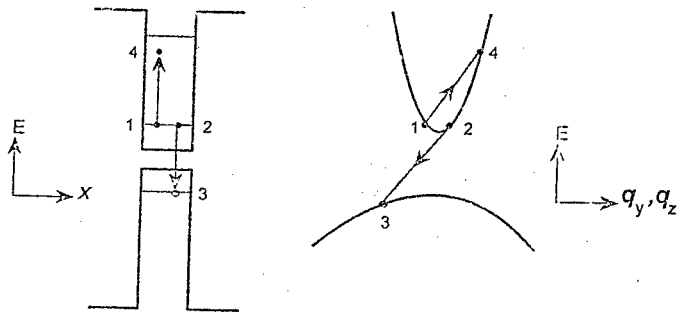

CHCC threshold Auger process in a deep quantum well, shown schematically: (a) coordinate space, (b) momentum space.

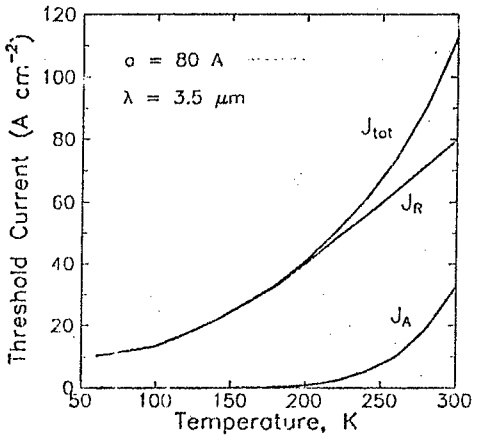

Temperature dependence of threshold current, calculated for a deep quantum well: $\lambda = 3.5\,\mu$m, $a = 80$ Å.

to Eq. (2), is $C_A^B \equiv G^B/n^2p = 2.4 \cdot 10^{-17}\,\mathrm{cm}^4/\mathrm{s}$. Thus, the Auger recombination rate equals $G^B \approx 1.92 \cdot 10^{20}\,\mathrm{cm}^{-2}\mathrm{s}^{-1}$. Consequently, the Auger recombination current equals $J_{A,th} \approx 31\,\mathrm{A/cm}^2$. Under the same conditions we have $J_{R,th} \approx 98\,\mathrm{A/cm}^2$, and the leakage current is almost zero. The threshold current density J_{th} of lasers based on quantum well does not therefore exceed $130\,\mathrm{A/cm}^2$. Then, $\eta \geq 50\,\%$. This means that such a laser can operate at room and even higher temperatures.

Fig. 2 shows the temperature dependence of the Auger current J_A and the radiative current for lasers based on deep quantum wells. The radiative current varies linearly with temperature; the Auger current is an exponential function of temperature. Nevertheless, at $T = 300\,\mathrm{K}$ we have $J_{A,th} < J_{R,th}$.

We have only considered the case of intraband absorption by holes and of CHCC Auger process. All the obtained conclusions are, however, valid for the case of holes.

It is important that the materials most appropriate for creating mid-infrared lasers based on deep quantum wells are the type-II heterostructures with quantum wells. These structures enable independent control of the distance between two size-quantization levels for electrons and holes. It is therefore possible to suppress the processes of Auger recombination and intraband absorption for electrons and holes simultaneously in type-II heterostructures.

References

[1] G. G. Zegrya, S. G. Yastrebov, Patent of Russia, Buletin of inventions, 2025010, **15**, 12 (1994)

[2] M. P. Mikhailova, G. G. Zegrya, K. D. Moiseev, et al., Proc. Soc. Photo-Opt. Instrum. Eng. **2397**, 166 (1995).

[3] V.L. Gurevich, Sov. Phys. Solid State, **4**, 1252 (1962)

THEORETICAL ANALYSIS OF AUGER RECOMBINATION MECHANISMS IN SEMICONDUCTOR QUANTUM WELLS

G.G. Zegrya, A.S. Polkovnikov

A.F. Ioffe Physico-Technical Institute RAS

In the present work we conduct theoretical investigation of main Auger-recombination mechanisms of non-equilibrium carriers in semiconductor quantum wells. It is shown that there are three different mechanisms of Auger recombination in quantum wells: (i) threshold mechanism similar to Auger process in bulk semiconductors; (ii) quasithreshold mechanism characterized by strong dependence of the threshold energy on quantum well width; and (iii) thresholdless mechanism, which is absent in bulk semiconductors. The value of the threshold energy of the first process is close to the value in bulk semiconductors and more than it may be considerably larger. On the contrary the quasithreshold Auger recombination rate slightly depends on temperature for narrow quantum wells due to rather small value of its threshold energy. That is why there are no distinct differences between the (ii) and the (iii) mechanisms in narrow quantum wells and they join to the single thresholdless process. The threshold energy of quasithreshold process increases with quantum well width and saturates near the bulk value. On the other hand the thresholdless Auger process strongly decreases with quantum well width and becomes negligible relatively the (i) and (ii) processes.

It may be shown that the matrix element of the Auger transition M splits to three different terms:

$$M = M_1 + M_2 + M_3$$

The first of them corresponds to thresholdless Auger process and it monotonly decreases as the function of in-plane momentum of the heavy hole (which is approximately equal to the transferred momentum in the Coulomb interaction). The second term corresponds to the quasithreshold Auger process and has a maximum near the threshold value of the hole momentum. However the width of this maximum is proportional to inverse quantum well thickness. Hence it doesn't coincide with the maximum of the corresponding quasithreshold Auger rate for thin quantum wells. The value of quasithreshold energy is defined by the maximum of the production of the squared matrix element and strongly decreasing distribution function of heavy holes. The first and the second term correspond to the situation, when the excited electron lays in the continuous spectrum. The third matrix element relates to the transition, when the excited electron lays in one of the localized states.

In this work we consider conditions of prevailing one or another mechanism of Auger recombination. We discuss here temperature dependences of Auger rate for quantum wells with various thiknesses.

GROWTH AND EVAPORATION OF InAs QUANTUM DOT NANOISLANDS ON GaAs (100) VICINAL SURFACES MISORIENTED TO THE [010] DIRECTION

V.P.Evtikhiev, A.K.Kryganovskii, A.N.Titkov*, V.E.Tokranov
Ioffe Physical-Technical Institute, RAS, 194021, St.Petersburg, Russia
A.Nakamura*, M.Ichida*
* CIRSE, Nagoya University, Chikusa-ku, Nagoya 464-01, Japan
KEYWORDS: quantum dots, evaporation, vicinal surface, InAs, MBE growth

Heteroepitaxial growth of strained structures like InAs/GaAs in the Stransky-Krastanov mode is now widely used in order to obtain quantum dot islands (QDs) which offer genuine three-dimensional carriers confinement. The formation of QDs was initially suggested to be driven mainly by the energetics, a necessity to minimize the total energy. However, recently an important role of adatom migration and incorporation / detachment kinetics in the formation of the QDs ensembles has been shown [1,2].

In our work we present new observations on the importance of the kinetic effects in the QDs formation. We have performed MBE growth of the InAs QDs on the GaAs (001) vicinal surfaces misoriented to the [010] direction. On such surfaces there appear multiatomic steps going to the [110] and [-110] directions. The crossing of these steps may create on the surface a net of small terraces, completely separated one from another by the step edges and efficient suppresion of the adatom migration in any direction along the surface should be expected. Our study has revealed considerable transformation of the InAs QDs ensemble with the surface misorientation to the [010] direction.

We have also performed partial evaporation of InAs QDs in UHV. It was found that evaporation of the QDs occurs nonuniformly. The evaporation creates a crater at the center of QDs with obvious faceting of the inner and outer walls along the main crystallographic planes demonstrating selective detachment kinetics.

Experimentally, It have been performed ambient AFM observations of the 2.3ML thick InAs layers MBE grown on the GaAs (001) epilayers exactly oriented and misoriented to the [010] direction up to 6 degrees. After the QDs growth termination some samples were annealed at 350C in MBE chamber without As flux.

It was found that misorientation to the [010] direction, indeed, leads to the creation on the surface of the dense net of individual terraces which number is increasing and area is decreasing with the misorientation angle. The misorientation by 3 degree already creates the situation when the adatom migration between terraces is practically blocked and on the each terrace QDs grow only from the material deposited on that terrace. The sizes of QDs and their ordering are now determined by the size and lateral distributions of the terraces on the vicinal surface. All that results in the suppresion of QDs coalescence, increase in their density, reduction of sizes, more narrow size distribution and new character of the lateral ordering.

Nonuniform character of the QDs evaporation we relate to the nonhomogeneous accumulation of elastic strain energy in QDs, especially near the interface with GaAs surface. In general, evaporation process opens an additional opportunity for the release of the strain energy via initial evaporation of the areas undergoing larger strains. Observed evaporation of QDs occurs through their central parts experiencing the largest strains. Faceting of the crater

walls has different characters for small and large QDs, varies with misorientation and may be also explained considering variations in the strain distributions.

We would like also to emphasize that complete evaporation of the QDs leaves the GaAs surface patterned with the tiny wells at the former QDs positions. The width of these wells is smaller than the base diameters of QDs and the depth is comparable to the heigt of the evaporated QDs. Taking into account recent success in the growing of homogenious ensembles of QDs [3] and also the possibility of an alignment of the QDs on vicinal surfaces [4], our findings show a new method of self-organized patterning of semiconductor surfaces on the nanometer scale.

This work was performed in part under the Grant of Russian Foundation for the Basic Research and Program of Venture Business Laboratory of Monbusho in Japan. The author (A.N.T.) acknowledges very much the financial support of The Japanese Society of the Promotion of Sciences for stay in Nagoya University.

1. G.S.Solomon, J.A.Trezza, J.S.Harris, Appl. Phys.Lett. v.66(8), 991 (1995)
2. N.P.Kobayashi, T.R.Ramachandran, A.Madhukar, Appl.Phys.Lett. v.68(23), 3299 (1996)
3 V.A.Schukin, N.N.Ledentsov, P.S.Kop'ev et al., Phys. Rev. Lett. 75, 2968 (1995)
4. M.Kitamura, Y.Arakawa et al., Appl. Phys. Lett. 66, 3663 (1995)

Optical Second Harmonic Studies of Metal-Organic Gd Superlattices fabricated by Langmuir-Blodgett Technique

O.A. Aktsipetrov, G.B. Khomutov, A.A. Fedyanin, Yu.N. Moiseev, T.V. Murzina, A.M. Tishin

Physics Department, Moscow State University, Moscow 119899, Russia

Th. Rasing,

Research Institute for Materials, University of Nijmegen, Toernooveld 1 6526 ED Nijmegen, The Netherlands

K. Pedersen,

Institute of Physics, University of Aalborg, Pontoppidanstraade 103, DK-9220 Aalborg Osi, Denmark

The interests of nanoelectronics are aimed last time on searching of new materials possessing unique properties related to quantum confinement. Most attractive objects among low-dimensional systems that are intensively studied nowadays are quantum wells (QW), multiple QW, superlattices and other thin films based structures.

Langmuir-Blodgett (LB) technique is known to give a possibility to obtain films with strictly controlled optical properties and thicknesse down to monolayer. Optical second harmonic generation (SHG) is one of the most effective tools for studying thin films, including LB ones. The main advantage of this method is its extremely high sensitivity to the properties of surfaces, interfaces and low-dimensional structures. The SHG technique is known also to be effectively used for studying of structural, symmetrical and nonlinear optical properties of LB films.

In this paper the results of the SHG studies of metal-organic Gd LB films are presented.

The SHG experiments are carried out using the output of the "Mira" and "Tsunami" Ti-sapphire lasers operating at 700÷840 nm as the fundamental radiation. For the infrared experiments, the output of a Q-switched YAG:Nd^{3+} laser at 1064 nm, pulse duration of 15 ns and repetition rate of 12.5 Hz is used.

Reflected SHG signal is detected by PMT and photoncounter. The surface morphology is controlled by atomic-force scanning microscope "Nanoscop-3".

Metal-organic Gd LB films of 1-5, 28 and 35 periods are studied. Each period consists of Gd monolayer placed between two monolayers of stearic acid. The thickness of one period of the film is about 50 Å. Gd LB films are deposited on 24 periods of pure stearic acid on quartz substrate.. The structure fabricated can be considered as metallic multiple quantum wells or superlattices. The SHG response from the substrate as well as one from the pure stearic acid films is shown to be small as compared with the response from the Gd LB films.

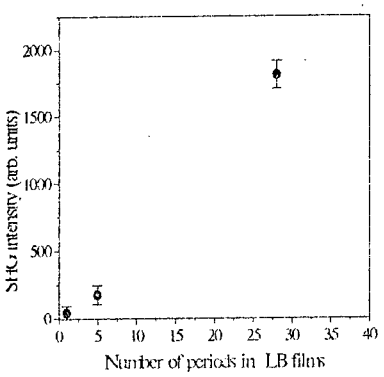

Figure 1. Thickness dependence for the s-in, s-out SHG reflected from the Gd LB films.

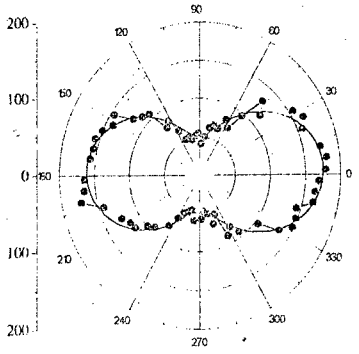

Figure 2. Polarization dependence of the SHG intensity, φ=0 corresponds to the s-polarized fundamental radiation.

The pronounced thickness dependence of the SHG intensity in reflection from the Gd LB films (Fig. 1) is obtained for various input and output polarization combinations. This indicate that the SHG response is entirely attributed to the Gd layers. At the same time, this dependence is far from being quadratic, that is typical for the incoherent SHG in irregular nonlinear systems.

The SHG response from LB films appears to be isotropic. A violation of the polarization selection rules (i.e. the presence of the isotropic s-polarized SHG) for

the reflected SHG is observed (Figure 2). These features of the SHG response testify that the LB films studied are inhomogenious and SHG should be described in terms of Hyper-Rayleigh scattering.

Transversal nonlinear optical magnetic Kerr effect is studied for Gd LB films. Magnetoinduced variations of the SHG intensity are detected for the dc magnetic fields up to 500 Gauss. These variations could be attributed to the magnetic ordered structure of Gd layers.

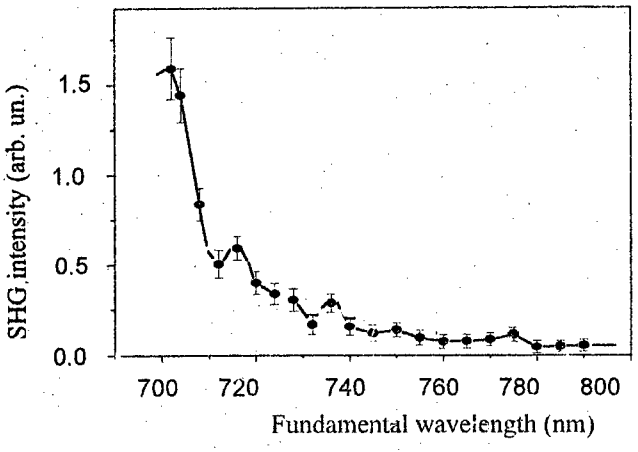

Figure 3. P-in, p-out SHG spectroscopy measured in reflection from the 28 periods Gd LB film.

The optical SHG spectroscopy is carried out in reflection from Gd LB films for various polarization combinations of the fundamental and SHG waves. Figure 3 shows the sharp rise of the SHG intensity below 730 nm and reproducible fine structure is observed. It is known that the absorption band of stearic acid is in UV spectral region. Thus the observed peculiarities of the SHG spectra can be attributed to the band structure of two-dimensional Gd layers.

Band tailing in Si delta-doped GaAs

V.Ya. Aleshkin, V.M. Daniltsev, A.V. Murel, O.I. Khrykin, V.I. Shashkin
Institute for Physics of Microstructures of Russian Academy of Sciences
GSP-105, Nizhny Novgorod, 603600, Russia;
e-mail: aleshkin@ipm.sci-nnov.ru

We have investigated the density of states of the conduction band and electron capture on deep states in Si delta-doped GaAs by modified admittance spectroscopy method. Band tails appear if Si concentration in δ-layer exceeds $6 \times 10^{12}\,\mathrm{cm}^{-2}$. The characteristic sizes of band tail and capture time rise with rising of Si concentration and change in ranges 20-80 meV and $10^{-8} - 10^{-7}$ s accordingly in our samples. It has been shown that the autocompensation is origin for saturation of the free-electron concentration at high doping densities.

Delta-doped layers in GaAs were prepared by a.p. MOCVD in system $Ga(CH_3)_3 - AsH_3 - SiH_4 - H_2$ [1] at $T = 550 \div 650$°C. Doping of GaAs was made with interrupt of GaAs growth. Bulk epitaxial GaAs was n-type with electron concentration $n \approx 10^{15}\,\mathrm{cm}^{-3}$ and Hall electron mobility $7 \times 10^3 \mathrm{cm}^2/\mathrm{Vs}$ (300 K) and $> 3 \times 10^4 \mathrm{cm}^2/\mathrm{Vs}$ (77 K). One electron trap EL2 with concentration $10^{14}\,\mathrm{cm}^{-3}$ in the epitaxial GaAs was detected by transient capacitance spectroscopy. Structures with the δ-doped layers were studied by Hall measurements and impedance measurements of the Schottky contact for frequencies 1 MHz, 10 kHz, 1 kHz at temperature range 77-360°. The Schottky contact was an evaporated aliminium circle 500 μm in diameter.

Fig.1 shows electron mobility μ dependence on free-electron concentration in the δ-layer. Solid curve represents dependence obtained by Ploog et al[2], circles and crosses represent results of our measurements. Samples with high doping densities in δ-layers ($> 6 \times 10^{12}\,\mathrm{cm}^{-2}$) have low mobility (denoted by crosses). Band tails were found only in such samples. In these samples mobility and free-electron concentration increase with rising temperature from 77 K to 300 K. Besides in such structures free-electron concentration is essentially less then concentration of the doping impurity (Si). Note that saturation and even reduction of free-electron concentration with increasing Si concentration in the δ-layer had been observed formerly [1, 2, 3].

The typical observed capacitance C and real part ac conductivity G of Schottky contact dependencies on applied voltage for structure with Si concentration in δ-layer more $6 \times 10^{12}\,\mathrm{cm}^{-2}$ are shown in fig. 2. Capacitance C(V) dependence has characteristic step-like type and G(V) dependence has sharp asymmetric peak. The reason for existence this peak is recharging deep states in the δ-layer [4]. In the structures with Si concentration in δ-layer less $6 \times 10^{12}\,\mathrm{cm}^{-2}$ peak on G(V) dependence was absent and value G was a few orders less then one in the high doped structures.

The measured dependencies G versus temperature for different applied voltages are shown on fig.3. It is well seen on fig.3 that peak of conductivity decreases and moves to higher temperatures with applied voltage increasing.

In order to describe measured dependencies of capacitance and conductivity on applied voltage and temperature we have created numerical model [6]. Numerical calculations show that if there is well defined peak on density of states (for example, the density of states is Gauss distribution with peak well separated from conduction band edge) then calculated dependence C(V) has well defined peak too. But measured C(V) dependencies are monotonic. Therefore we suggest that density of deep states in our structures monotonically decreases deep into band gap, i.e. density of states has tail. In our model we choose density of deep level in form $g(\varepsilon) = N_s/\varepsilon_0 \times \exp[(\varepsilon - E_c)/\varepsilon_0]$.

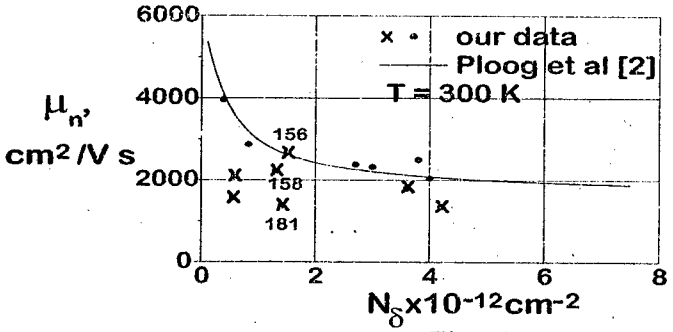

Fig. 1.

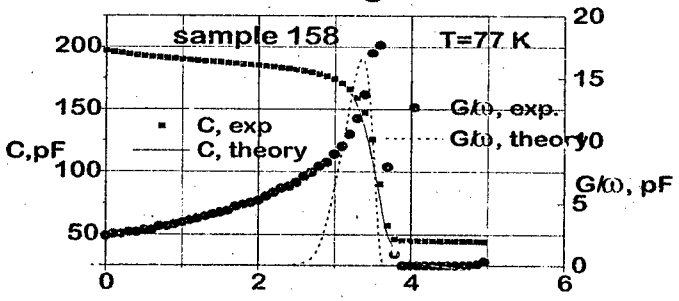

Fig. 2.

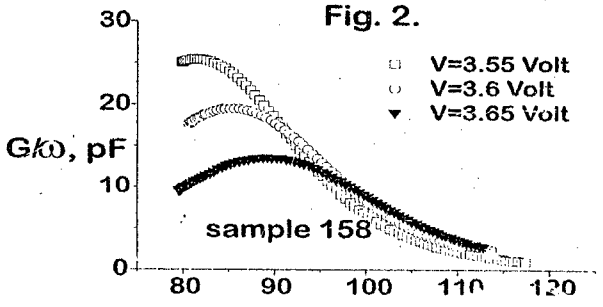

Fig. 3.

Where ε is electron energy, E_c is energy of conduction band bottom, N_s is concentration of deep states, ε_0 is tail depth.

The parameters for three samples with different Si concentration are given in the table. The values of $N_s, \varepsilon_0, \tau_0$ were chosen to provide best accordance measured and calculated dependencies C and G on applied voltage and temperature. Follow measure units are used: for N_δ and N_s — 10^{11} cm^{-2}, for ε_0 — 1 meV, τ_0 — 10^{-7} s. Note that sum N_δ and N_s is full concentration of the uncompensated donors. DX-centres decrease free-electron concentration but don't change concentration of the uncompensated donors. If the main origin for saturation of free-electron concentration is appearance DX-centres [5] then concentration of the uncompensated donors must not decrease with increasing of Si concentration. But data from the table show that both free-electron and uncompensated donor concentrations saturate with increasing Si concentration in δ-layer. Therefore autocompensation is main origin for saturation of free-electron concentration in our structures.

Table

N	SiH_4, mL/min	growth time s	Con. Si, arb. un.	300 K		77 K		N_s,	ε_o	τ_o
				μ	N_δ	μ,	N_δ			
156	20	50	1000	2670	15	2400	20	5	30	5.7
158	67	10	670	2200	13	2600	18	4	20	1.5
181	100	120	12000	1300	14	1040	15.6	9	70	8

One can see from table that concentration of deep states N_s, tail depth ε_0 and capture time τ_0 increase with increasing Si concentration in δ-layer. We suppose that these results can be explained by sharp rise fluctuations of impurity distribution when Si concentration exceed 6×10^{12} cm^{-2}. The similar phenomenon was observed in Be δ-doped GaAs with using scanning tunneling microscopy [7].

This work was supported by Russian Foundation for Basic Research under grants 95-02-05606, 95-02-05870a.

References

[1] V.M.Daniltsev, I.V.Irin, A.V.Murel, O.I.Khrykin, V.I.Shashkin Neorg. Material. **30**, 1026 (1994) (in Russian)

[2] K.Ploog, M.Hauser, A.Fischer Appl. Phys. A, **45**, 233 (1988)

[3] H.C.Nutt, R.S.Smith, M.Towers, P.K.Rees, D.J.James J. Appl. Phys. **70** 821 (1991)

[4] C.Ghezzi Appl.Phys.A **26**, 191 (1982)

[5] A.Zrenner,F.Koch, R.L.Williams, R.A.Stradling, K.Ploog, G.Weimann Semicond. Sci. Technol. **3** 1203 (1988)

[6] V.Ya.Aleshkin Semiconductors **30**, N12 (1996)

[7] B.Johnson, P.M.Koenraad, W.C.van der Vleuten, H.W.M.Salemink, J.H.Wolter Phys. Rev. Lett. **75** 1606 (1994)

Small angle X-ray study of nanostructure of ultradisperse diamond.

M.V.Baidakova, V.I.Siklitsky, A.Ya.Vul'

Ioffe Physical-Technical Inst., 26 Polytechnicheskaya, St. Petersburg 194021, Russia.

1. Introduction.

The intensive study of new nanoobjects - clusters of ultradisperse diamond (UDD), produced by detonation synthesis from carbon of explosives has begun recently [1-3].

At such synthesis diamond nanoclusters are generated at temperatures and pressures corresponding to the region of thermodynamic stability of diamond, and a cooling rate of a detonation product is high enough to exclude a reverse transition diamond-graphite after explosion.

The results of investigation of structural phase transition (SPT) in the UDD clusters at annealing in argon were published in [4]. The investigation of Raman spectra and X-ray diffraction patterns at the range of $2\theta > 10°$ have shown that the UDD cluster consists not only of crystal diamond core with the size 43 A, but also of a small amount of amorphous diamond (sp3) and graphite (sp2) phases. These amorphous phases are situated on the surface of diamond core. It was determined that the relation between amorphous and crystalline phases depends on the cooling kinetic of detonation product after explosion.

In the case of cooling in gaseous atmosphere ("dry synthesis") the amount of amorphous graphite - like phase (sp2) is significantly higher than at cooling in water environment ("wet synthesis"). This fact is due to higher probability of the reverse phase transition diamond - graphite after explosion at slower cooling.

It was shown, that the SPT in UDD begins at T=900°C i.e. at much lower temperature, than in bulk single crystals of diamond (T=1600°C). The transition begins with cluster surface, and the graphite phase arises as a set equidistant graphite nanoplates with the typical size less than 40A and the onion-like carbon is created as one of steps of this transition at temperatures higher than 1100^0C.

The investigation of the SPT was continued in this work, the attention was focused on structural modification of amorphous phase covering diamond core. The small angle X-ray scattering method (SAXS) was used for the detection of such structural modification at the scale less than 40A.

2. Experimental.

The X-ray scattering analysis was carried on the samples produced by "wet" and "dry" synthesis over the range of scattering angles θ=0.5-10°, corresponding wave vectors q were $0{,}036<q<0.8$ (A^{-1})

The intensity of the X-ray scattering was measured in reflection θ - 2θ geometry using a D-max RC diffractometer (Rigaku Cor) with Cu K_α radiation. It should be noted that this instrument has high signal-to-noise ratio which is provided by a high-brightness anode with a slightly divergent beam (10'). Simultaneously with small-angle X-ray scattering on same samples the X-ray diffraction analysis was carried out over the range $10°<\theta<60°$.

Two main parameters were determined from the data on (SAXS), the typical size of the scatter and its fractal dimension.

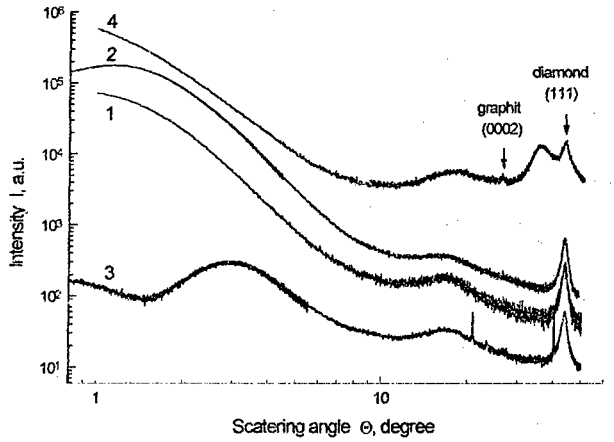

Fig.1. X-ray diffraction patterns of the UDD samples produced by "wet" synthesis and annealed in an argon atmosphere at various temperatures T: 1- no annealing, 2 - 420°C, 3-550°C, 4-1100°C. The scattering for graphite clusters united in common network is demonstrated by the curve 4.

Typical X-ray angle dependencies of the scattered intensity for the UDD samples of "wet" synthesis are shown in Fig.1.

The curve with the index "1" refers to the initial sample of the UDD (before annealing). The broad symmetrical diffraction maximum under at the scattering angle $\theta = 43.86°$ corresponds to (111) reflection of the crystallographic diamond lattice. The broad maximum (galo) is observed at $\theta = 1.1°$ and an growing of intensity of scattering radiation has been seen near to the initial beam. In [1] a suggestion was made, that this galo is similar to its nature to the first sharp diffraction peak in glasses, and can be considered as the manifestation of the correlated packing of some structural units. Two features, which can be related to the diffraction from the graphite phase, make their appearance on the X-ray diffraction pattern at large angles for the UDD samples, annealed under 1100°C, (the 3rd curve on Fig.1): (0002) graphite reflection at $\theta = 26.4°$ and galo at $\theta = 39°$.

The small angle scattered intensity I(q) is proportional to $q^{-\alpha}$, where q is a wave vector. The slope of the dependence $\ln I(q) = f(q^{-1})$ defines fractal dimensionality D. Position of maximum on I(q) curve allows one to define typical size of a scatterer [5,6].

It is known, that fractal dimensional of a volumetric fractal cluster (D) can be changed in the range from $D = 0$ to $D = 3$. It corresponds to changing of negative power α from 0 to 3. For a surface fractal cluster with $D = 2 - 3$, a negative power α is equal 3 - 4. The type, fractal

Table. X-ray small angle data for the UDD samples of "dry" and "wet" synthesis

		T °C	Type fractal	Fractal dimension D	Size a, (A)
Wet synthesis					
1	Initial		Surf	D=2.53	a=44 A
2	Ar	420°C	Surf	D=2.2	a=36-40A
3	Ar	550°C	Surf-Vol	D=2.94	a=14-16A
4	Ar	1100°C	Vol	D=2.8	a≥44A
Dry synthesis					
	Initial		Vol	D=2.84	a=52 A
	Ar	420°C	Vol	D=2.57	a=52 A
	Ar	1100°C	Vol	D=2.2	a=29 A

dimensionality and typical size of scatterer for the initial UDD samples of "wet" and "dry" synthesis before and after annealing are given in Table.

It is seen that the cooling conditions of a detonation product influence the fractal dimension D. The scatterers in the UDD matrix of "dry synthesis" are fractal clusters with fractal dimension D=2.8 and size a = 50-60 A. This result is consistent to a high probability of reverse transition diamond - graphite at the "dry" synthesis. The fact that the size of cluster of the UDD more than the size of diamond core results from the fractal nature of a scatterer. At lower graphitization probability (sample of "wet synthesis") the scatterer has a fractal surface (the fractal dimension D=2.53) enveloping a diamond core of 44 A in size. It is seen from the table data that at annealing the fractal dimension of a scatterer for samples of "wet synthesis" reduces, and at the temperature of 550°C the type of scattering fractal cluster is changed (fractal clusters modify they dimension to D=2.94, a=15A). These clusters unite into larger aggregates forming a graphite network. Annealing makes the fractal clusters of the samples of "dry synthesis" more friable and reduces its dimension to D=2.2, a=30 A for the annealing at 1100°C.

It would be emphasized that samples of two types of the syntheses are distinguished only by the amount of amorphous phase, formed on diamond core. Diamond cores are identical by structural parameters and by size. Consequently the small angle X-ray scattering occurs on the shell covering diamond core. This shell is comprised of amorphous graphite-like phase. From the comparison a diameter of fractal scatterer with the size of diamond core it is seen that the thicknesses of shells are different for samples produced by "wet" and "dry" synthesis. Our evaluation of the shell thickness gives about 5A for the sample of "dry" synthesis and less then 1 A for the sample of "wet" synthesis.

As can be seen from the table data on the volumetric fractal scatterer having highly developed surface is formed after the annealing at 1100°C no matter what was the type of scatterer in initial samples. This fact confirms the statement [4] that phase transition diamond-graphite is caused by transformation of (111) planes of a diamond core at this temperature. The resulting structures do not have either three-dimensional crystallography lattice or strong chemical bonds with diamond core (onion-like carbon), so in terms of fractal geometry these structures are "friable" volumetric fractals.

To summarize it was shown for the first time that the surface of nanoclusters of the UDD has fractal structure. The nature of changes in fractal dimension is studied during the structural phase transition diamond - graphite in an inert atmosphere.

This work have been done in the framework of the grant RFBR N 96-02-19445, at the support of the St.Petersburg United Research Centre. One of the authors (V.I.Siklitsky) has worked at the support of grant RFBR N 97-02-18110, and Arizona University grant.

References

1. G.V.Sakovich, V.D.Gubarevich, F.Z.Badaev, P.M.Brylyakov, O.A.Besedina. Doklady Akademii Nauk , v.310, p.402 (1990).
2. A.Ye.Alexensky, M.L.Baidakova, M.E.Boiko, V.Yu.Davydov, A.Ya.Vul'. Proc. of 3rd International Conference on the Applications of Diamond Films and Related Materials. Maryland, USA, August 21-24, 1995, p.457.
3 E.D.Obraztsova, K.G.Korotushenko, S.M.Pimenov, V.G.Ralchenko, A.A.Smolin, V.I.Konov, and E.N.Loubnin. NanoStructured Materials v.6, p. 827 (1995).
4. A.Ye.Alexensky, M.L.Baidakova, A.Ya.Vul', V.Yu.Davydov, Yu.A.Pevtsova.Fizika tverdogo tela, v.39(6), 1997.
5. O.Glatter. J.Appl.Cryst., 12, 166 (1979)
6. V.I.Siklitsky, V.I. Ivanov-Omskii, M.V. Baidakova. Diamond (and other wide band-gap) Composites, NATO Advanced Research Workshop, St.Petersburg, 1996, (in press)

Characterization of Si/Ge/Si quantum wells based on negative capacitance effect

A. P. Boltaev, N. N. Loiko and M. M. Rzaev
P.N.Lebedev Physical Institute, Russian Academy of Sciences
Leninsky prosp.53, 117924, Moscow, Russia

The electronic and optical properties of Si/Ge QW structures are primarily determined by the valence- and conduction-band discontinuities. The heterojunction band offset for Si/Ge interfaces has been investigated by several groups. Keuch et al [1] estimated the band discontinuities from reverse-bias capacitance measurements to be $\Delta E_v = 0.39 \pm 0.04$ eV. Margariondo et al [2] reported a valence-band offset of 0.2 eV based on photoemission studies. Mahowald et al [3] obtained 0.4 ± 0.1 eV based on the same technique. Such considerable spread in values in-data is due to the strain present in Si and Ge epitaxially grown layers as a result of the large lattice mismatch between silicon and germanium. Because the valence-band offset has not yet been accurately determined experimentally, in this paper we offer an additional method for the band offset measurements based on the negative capacitance effect studies in Si/Ge QW structures [4]. The samples used in the experiments were grown on (III) oriented p-type (10 Ωcm) Si wafers in Si MBE system with two electron beam evaporators for silicon and germanium deposition. Prior to the QW structure growth, a 90 nm-thick Si buffer layer was grown at 850 °C. The active layers of the structures consisted of 3 undoped germanium QWs separated by 20 nm-thick undoped silicon barriers grown at 500 °C. The samples were distinguished by the Ge well thickness, which were 5, 7, 9, 12 and 15 nm respectively. Finally a 20 nm-thick undoped Si cup layer was grown.

For the current-voltage ($I-V$) and capacitance-voltage ($C-V$) measurements to the samples, a sawtooth signal voltage of negative polarity with the amplitude up to 10 V and the 1000 s periodicity together with sinusoid signal voltage (with amplitude up to 5 mV and various frequency from 20 Hz to 100 kHz) were applied. The experimental $I-V$ and $C-V$ characteristics for Si/Ge QW structure with 12 nm-thick wells and I mm^2 In ohmic contact were measured at 98 K. By the band diagram designing it has been taken into account that In work function is 3.8 eV, and Ge and Si affinities are 4 eV and 4.05 eV respectively [5].

We considered that the voltage droped across the buffer layer and the substrate was -0.75 V. The estimation of this value was made on the assumption that the current through the substrate and the buffer layer is caused by hole thermoelectronic emission through the potential barrier formed between the third well and Si substrate ($e\varphi \approx 0.95$ eV). The other part of voltage, $V_w = -1.7\,\mathrm{V} - (-0.75\,\mathrm{V}) = 0.95\,\mathrm{V}$, drops across the whole active region of the QW structure. The current through the quantum wells is due to the movement of electrons injected from the ohmic contact. Moving over the potential barrier formed at heterojunction between contact and cup layer electrons are arrived to the first well from the ohmic contact. Because Ge well width in our case is 12 nm and carrier mean free path for Ge is 10 nm [5] the whole electrons pass through the potential barrier and fall to the well. Then, due to the thermoelectronic emission, the electrons from the first well pass the barrier attributed to the band discontinuity and come step by step into the second and third wells. From the other side of the sample, holes are received to the third well, where a hole-electron recombination takes place. The electrons should be accumulated in the QW by such carrier transport through the sample. This causes a delay in current change. The structure with inertial conductivity are characterized by arising of negative capacitance [6]. The value of negative

capacitance is defined by the charge accumulation in the structure. The negative capacitance is given by:

$$C_{\text{neg}} = \frac{Q_w}{V} \tag{1}$$

where Q_w is the charge accumulated in the well and V is the bias.

As it has been discussed before, the current through the first and second wells is due to the electron thermoemission and is described by the following equation:

$$I = e_T Q_w \tag{2}$$

where e_T is the thermoelectronic emission rate. In the case of Boltzman statistics, the emission rate can be get as follows [7]:

$$e_T = \frac{8kT}{\pi h} \exp\left[-\frac{\Delta E_c - E_1}{kT}\right] \tag{3}$$

where k is the Boltzman constant, T is the temperature, h is the Plank constant, ΔE_c is conduction band discontinuity and E_1 is the ground state energy in the QW.

According to the estimation of negative capacitance, we obtain the electron concentration in the QW N_w to be less than $4 \times 10\,\text{cm}^{-2}$ and the density of states of ground state to be about $3 \times 10^{12}\,\text{cm}^{-2}$. Thus, using eq. (1), one can find the current I from the experiment and estimate the charge carrier concentration in the well Q_w from negative capacitance measurements. For the considered case of $V = -1.7$ V, $I = 6 \times 10^{-5}$ A and $C_{\text{neg}} = 10^{-7}$ F obtained at the frequency $f = 30$ Hz we have an emission rate of $e_T = 4.1 \times 10^2\,\text{s}^{-1}$ and a distance between conduction-band discontinuity and ground state $\Delta E_c - E_1 = 0.21$ eV.

Therefore for the Si/Ge structure with the well width $d_w = 12$ nm, a conduction band discontinuity $\Delta E_c = 0.25$ eV was obtained. It is clear that to define a valence-band discontinuity (ΔE_v) it is necessary to create a hole injected contact to the QW structure.

The work was supported by Russian State Scientific Programs "Physics of Solid State Nanostructures" (Grant No. 97-1050) and "Technologies and Devices of Micro- and Nanoelectronics for the future" (Grant No. 130/57/1), and RFBR (Grant No. 95-02-04450).

References

[1] T.F.Keuch, M.Maenpaa, and S.S.Lau, *Appl. Phys. Lett.* **39**, 245 (1981).

[2] P.H.Mahowald, R.S.List, W.E.Spicer, and P.Pianetta, *J. Vac. Sci. Technol.* **B3**, 1252 (1985).

[3] W.A.Harrison and J.Tersoff, *J. Vac. Sci. Technol.* **4**, 1068 (1986).

[4] A.P.Boltaev, Yu.V.Kopaev, N.V.Kornyakov, N.N.Loiko, N.N.Sibeldin, M.M.Rzaev, and I.I.Zasavitskii, *Nanostructures 96* International Symposium, p 416, St.Petersburg, Russia, 24-26 June 1996.

[5] S.M.Sze, *Physics of Semiconductor Devices* (Wiley, New York, 1981).

[6] N.A.Penin, *Semicond.*, **30**, 340, (1996).

[7] K.Schmalz, I.N.Yassievich, H.Rucker, H.G.Grimmeiss, H.Frankenfeld, W.Mehr, H.J.Osten, P.Schley, and H.P.Zeindl, *Phys. Rev. B*, **50**, N19, 14287, (1994).

Carrier accumulation in As cluster contained LT GaAs layers

P.N. Brounkov *, A.V.Chernigovsky, A.A. Suvorova, V.V.Chaldyshev, N.A.Bert, S.G. Konnikov
A.F. Ioffe Physico-Technical Institute, Polytechnicheskaya 26, 194021, St.-Petersburg, Russia

V.V.Preobrazhenski , M.A.Putyato , B.R.Semyagin
Institute of Semiconductor Physics, 630090 Novosibirsk, Russia

Gallium arsenide grown by molecular beam epitaxy (MBE) at low temperatures (LT-GaAs) has attracted a great deal of attention due to their unique properties. The material exhibits very high electrical resistivity [1] and extremely short (femtoseconds) carrier lifetime. The major feature of LT-GaAs is a high arsenic (As) excess (up to 1.5 at. %) resulting in a high concentration of intrinsic point defects, such as arsenic antisite (As_{Ga}), arsenic interstitial (As_i), gallium vacancies (V_{Ga}), and their complexes. After high temperature annealing the excess As leads to the formation of As nanoclusters built in the GaAs matrix [1]. At present two models, namely, the deep level defects model [1] and the "buried Schottky" model [2] compete to explain semi-insulating behaviour of LT-GaAs.

In the present paper, we apply capacitance spectroscopy technique to study Schottky barrier structure being a 0.1 μm-thick LT-GaAs layer sandwiched between two doped 0.5 μ-thick n-GaAs buffers grown at conventional temperatures [4]. The capacitance-voltage (C-V) characteristic of this structure has a step-like shape (Fig.1a). The width of a region of the quasi-constant capacitance is proportional to the concentration of electrons (n_{LT}) swiped out from LT-GaAs layer with increasing of the reverse bias on the structure [3]. The apparent concentration profile (Ncv-W) calculated from the C-V characteristic has a peak at the depth W corresponding to the position of the LT-GaAs layer (Fig.1b). This behaviour of C-V and Ncv-W characteristics shows accumulation of electrons within and depletion around the LT-GaAs layer [3]. The width of the depletion region around the LT-GaAs layer is temperature independent (Fig.1b), whence it follows that the full negative charge located within the LT-GaAs layer is independent on temperature too. This seems to contradict the fact that the decreasing of the temperature from 370 K to 77 K results in the decreasing of the width of quasi-constant region of the capacitance from 20 V to 4.5 V (Fig.1a). From numerical analysis of the temperature dependence of the C-V characteristics [3] we found that the value of n_{LT} is reduced from 1.4×10^{17} cm^{-3} at T=370 K to

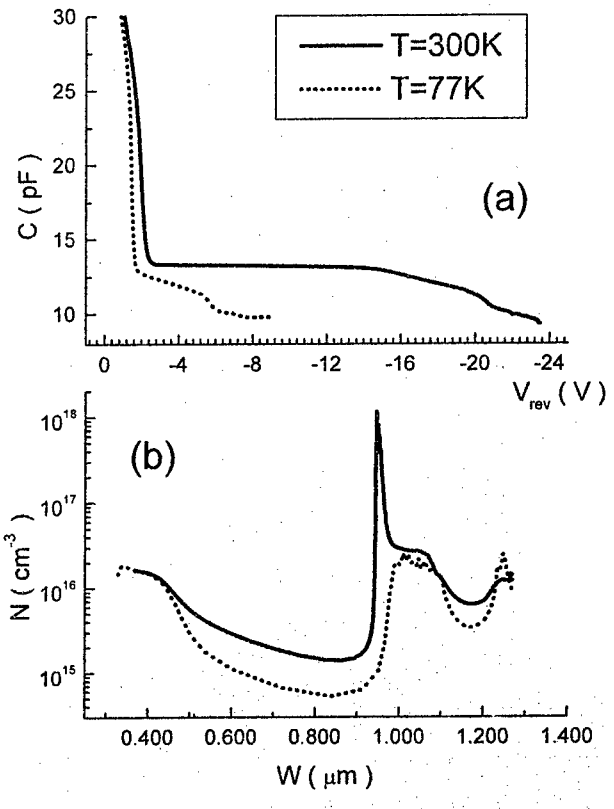

Fig.1 C-V (a) and N_{cv}-W (b) characteristics of the structure with As cluster contained LT-GaAs layer.

2.6×10^{16} cm^{-3} at T=77 K. The activation energy of this process E_{act}=0.6 eV agrees closely with the activation energy of the main deep donor trap related with As_{Ga} defect, which has a high concentration in LT-GaAs layers [5].

The structure of LT-GaAs layer was examined by use of transmission electron microscopy (TEM) technique. Cross-sectional TEM images showed that observed As clusters

are up to 10 nm in size. The concentration of the clusters was estimated to be as high as $4x10^{16}$ cm^{-3}. The TEM measurements are in a quite good agreement with the value of n_{LT} determined from C-V characteristic at T=77 K since at low temperatures electrons freeze out on deep donor trap, hence the full charge of deep donor traps is equal to zero and does not depend on the reverse bias.

In summary, the As precipitates formed in LT-GaAs was shown to act as a trap for electrons.

REFERENCES

1. D.C.Look et al Phys.Rev.B **42**, 3578 (1990)
2. A.C.Warren et al Appl.Phys.Lett. **57**, 1331 (1990)
3. P.N.Brounkov et al J.Appl.Phys. **80**, 864 (1996)
4. N.A.Bert et al Semicond.Sci.Technol. **12** , 51 (1997)
5. C.H.Goo et al Appl.Phys.Lett. **69**, 2543 (1996)

FREEZING OF ELECTRONS IN InAs/GaAs VECQDs AT LOW TEMPERATURES

P.N. Brounkov *, A.A. Suvorova, M.V.Maximov, A.F. Tsatsul'nikov, A.E.Zhukov, A.Yu.Egorov, A.R. Kovsh, S.G. Konnikov
A.F. Ioffe Physico-Technical Institute, Polytechnicheskaya 26, 194021, St.-Petersburg, Russia

T.Ihn, S.T.Stoddart, L.Eaves, and P.C.Main
Department of Physics, University of Nottingham, NG7 2RD Nottingham, United Kingdom

In recent years there has been great interest in the study of properties if heterostructures with quantum dots (QDs) formed as a result of the transformation of an inherently unstable two-dimensional coverages [1]. Additionally, it was shown that the QDs may be used as sressors to form next layer of QDs, if the thickness of the spacer is lower than 100 Å [1-4]. In this case QDs will be vertically stacked, vertically aligned and electronically coupled in the growth direction [3-4]. It has been demonstrated that vertically coupled QDs via tunneling (VECQDs) are suitable for fabrication of zero-dimensional Esaki-Tsu superlattices and cascade lasers [1].

In this paper we report on capacitance-voltage (C-V) study of a structure with a Schottky barrier on a n-type layer containing an array of VECQDs. The studied samples based on I type heterostructure InAs-GaAs were grown by MBE on doped n^+-GaAs substrate. The array of VECQDs consists of three sheets of InAs QDs. The 50 Å thick of GaAs spacer was inserted between InAs islanding layers. The InAs QDs were formed *in situ* as the result of the transformation of an elastically strained InAs layer with effective thickness 1.7 ML on lattice mismatched GaAs layer. The structures were capped with 0.5μm thick GaAs layer. The cap and buffer layers were uniformly doped with Si at a level of about $2x10^{16}$ cm^{-3} except two 100 Å thick undoped spacers at both sides of VECQDs layer.

The measurements of the C-V characteristics were performed in the range of frequency from 10kHz to 1 MHz using an HP4274A RLC meter. The amplitude of the measuring signal was equal to 10 mV.

The C-V characteristic has a step (Fig.1a). Using the depletion-layer approximation, we calculate the apparent concentration profile (N_{CV}-W) from C-V characteristic, which has a peak at a value of W corresponding to the depth of the QD plane (Fig.1b). According to the model presented in Refs.[5,6] the height and width of a step on the C-V characteristic depends on steady state occupation of the electron levels in QDs and this value, in turn , is determined at a fixed temperature by the sheet concentration N_{qd} of QDs and the Fermi-Dirac function depending on the relative positions of the quantum electron level in QDs (E_{qd}) and of the bulk Fermi level (E_F) in the matrix [5,6]. The sheet concentration of QDs was measured by use of transmission electron microscopy (TEM) (001) plan-view image of the sample ($N_{qd} = 5x10^{10}$ cm^{-2}), thus from analysis of temperature dependent C-V characteristics we can extract the energy spectra of levels in QDs[5,6]. From the fitting of C-V characteristics we have found that the density of electron states in VECQDs may be described by Gaussian distribution with the center at $E_{qd} = 70$ meV from the bottom of conduction band of GaAs and dispersion of $\Delta E_{qd} = 80$ meV.

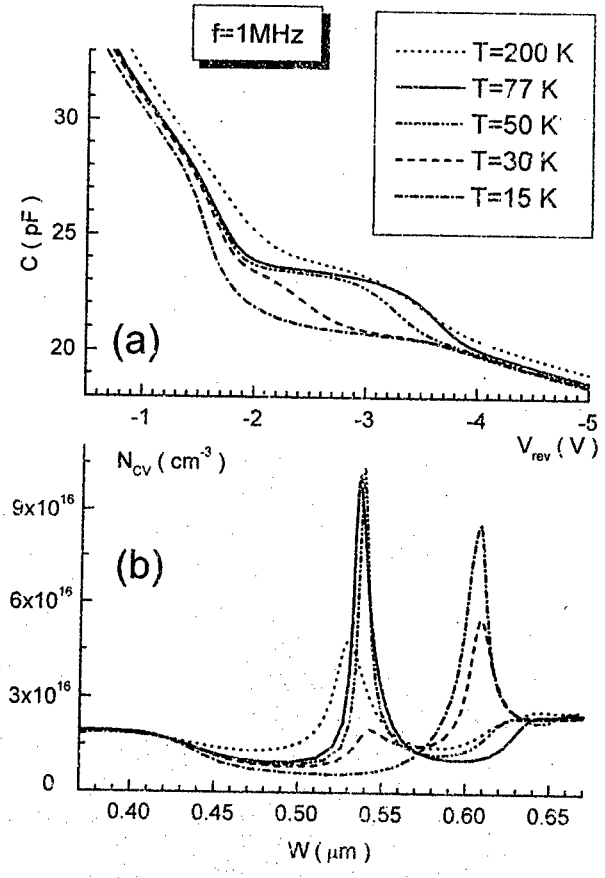

Fig.1 C-V (a) and N_{cv}-W (b) characteristics of the structure with QDs measured in the temperature range from 15 K to 290 K.

The present model quite correctly describes the experimental C-V and Ncv-W characteristics at the temperature higher than 70 K. However, discrepancy between the model and experimental data was observed at T<70K, when are suppressed step in the C-V characteristic and peak in the Ncv-W profile (Fig.1a,1b), appropriate to the accumulation of electrons in the plane with QDs.

In our opinion , this is due to the fact that the capacitance of the QD structure was derived from equation $C = \Delta Q / \Delta V$, based on the "quasi-static approach" , i.e., temporal change

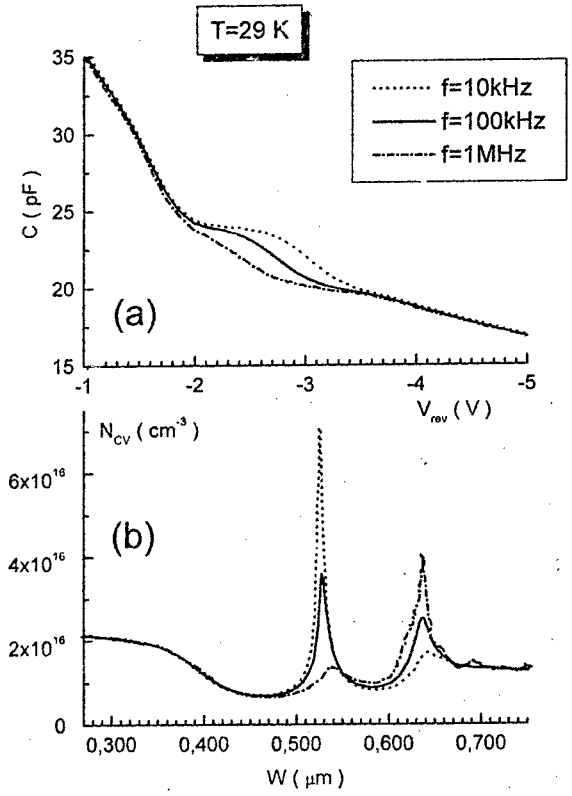

Fig.2 C-V (a) and N_{cv}-W (b) characteristics of the structure with QDs at T=29 K measured in the frequency range from 10kHz to 1MHz .

in the charge variation ΔQ caused by the increment of the reverse bias ΔV was neglected. However, in practice, the capacitance is measured by means of superimposing a small oscillation signal dV_{osc} at a frequency *f* on the applied *dc* reverse bias V_{rev}. It should be taken into account that the dV_{osc} modulates the charge at both the space charge region (SCR) edge (dQ_{3D}) and at the point where the Fermi level crosses electron level in QDs (dQ_{qd}). From the theoretical treatment of C-V characteristics of QD structure [5,6] it follows that in the region of quasi-constant capacitance (from -1.0 V to -2.5 V (Fig.1a)) the change in SCR width dW due to the increment of the reverse bias dV becomes so small that dQ_{qd} dominates dQ_{3D}, i.e. C_{qd} is

higher than C_{3D} (Fig.1a). As the temperature goes down from 70K to 15K the quantum part of capacitance C_{qd} is decreases (Fig.1a)., despite to the fact that the occupation of QDs tends to be saturated. At T=15 K Cq disappears at all (Fig.1a). It means that at T=15 K the thermionic emission rate of electrons from QDs is much lower than the angular measurement frequency $2\pi f$ (f = 1MHz Fig.1a), i.e. freezing of electrons on QD level takes place. To remove electrons from QDs at T=15 K it takes to apply higher electric field so that the electrons leave the QDs by tunneling through a narrow triangle potential. In the presence of the electric field a potential of constant slope along the direction of the field vector is superimposed on the potential of QD binding the electron. Estimation showed that in the case of high electric field ($\approx 4 \times 10^5$ V/cm) a narrow triangle potential ($\approx$ 25 Å) is formed so that the electrons are leaving the QDs by tunneling escape. This process becomes dominant at low temperatures (T<50 K) when the thermionic emission rate of electrons is negligibly small with respect to angular measurement frequency $2\pi f$ (f = 1MHz Fig.1a). Changing the frequency of a measuring signal it is possible to control a ratio between thermal and tunnel parts of capacitance (Fig.2a,2b).

It was found that the freezing of the carries in the sheet of VECQDs at low temperatures is the distinctive property of the 0D systems and it is not observed in quantum-well structures [7].

This work was supported by the program INTAS-RFBR-95 -618.

REFERENCES

[1] N.N.Ledentsov *et al* 1996 Proceedings of the *ICMSS 7, Solid State Electronics* **40** 785-798
[2] A.Yu.Egorov *et al* 1996 *Semiconductors* **30** 879-883
[3] A.F.Tsatsul'nikov *et al* 1996 *Semiconductors* **30** 953-958
[4] G.S.Solomon *et al* 1996 Phys.Rev.Lett. **76** 952-955
[5] P.N.Brunkov *et al* 1996 *Semiconductors* **30** 492-496
[6] P.N. Brounkov *et al* 1996, *Proceedings of ICPS 23*, in *The Physics of Semiconductors* ed. by M.Scheffler and R.Zimmermann (World Scientific, Singapore) 1361-1364
[7] P.N.Brounkov, T. Benyattou, G. Guillot 1996 *J.Appl.Phys.* **80** 864-871

LOCAL ELECTRONIC CHARACTERIZATION AND FORMATION OF NANOSCALE SILICON STRUCTURES USING SCANNING RESISTANCE MICROSCOPE

A. A. Bukharaev, N. I. Nurgazizov

Kazan Physical Technical Institute, Sibirsky Tract, 10/7, Kazan, 420029, Russia
e-mail: bukh@dionis.rfti.kcn.ru

It is well known that scanning tunnelling microscopy (STM) allows to study the surface topography and electronic properties of conducting and semiconducting materials with atomic and nanosize space resolution. However with the help of STM it is impossible to study nonconducting materials. The nonconducting materials, alongside with conducting materials, are successfully studied by scanning force microscopy (SFM), however, it is impossible to investigate the electronic properties of a surface using usual SFM.

This shortage is away at SFM with conductive probe, which combines in self virtues STM and SFM. Such microscope now usually name a scanning resistance microscope (SRM), as during scanning in a contact mode alongside with a surface relief a spreading resistance in a point of tip-surface contact is measured.

The experiments were performed by advanced P4-SPM-MDT scanning force microscope with two different types of conductive probes. One of them was fabricated ourselves from W wire of diameter 80 micrometers. In order to produce sharp probe tips, the W probe were electrochemically etched. Other conductive probes were the heavily doped W coated commercially silicon cantilevers. A bias voltage from 1,5 to 3 V was applied to conductive probe during scanning and current flowing between the probe and sample was measured in order to delineate regions with different surface conductivity. Topography image and current image were obtained simultaneously from the same place of a surface (two-window operating mode). Measurements current-voltage characteristics in given points of a surface were also taken. Experiments were carried out in ambient air. Before measurements were taken, a hydrogen-terminated silicon surface was prepared by "spin-etching" method, were silicon oxide cover layer is removed by metering drops of HF-ethanol solution onto rapidly spinning wafer in nitrogen atmosphere [1].

Two types of Si samples were investigated by SRM.

First there were the 900 nm periodic surface structures of varying conductivity obtained by pulsed interference laser modification of a implanted silicon surface. The transformation between low and high conductivity is activated by laser stimulated local recrystallization of amorphous silicon, as was shown earlier using STM [1]. SRM measurements in a two-window mode have allowed to observe correlation between a surface relief and current-image. One-dimensional areas with high conductivity in width about 300 nm were observed on the SRM current-images. Space resolution of SRM was about 10 nm.

Second type of Si nanostructures were obtained by SRM itself using method based on the electrical field-enhanced oxidation on silicon surfaces [2,3]. The silicon nonconductive oxide patterns of a given configuration were formed by exposing in air the H-passivated Si surfaces to an electric field which is generated by conductive SRM tip at a negative voltage bias above 5 V. The SRM current images were obtained immediately after writing using the same tip that wrote the oxide pattern. Nonconducting lines of width as small as 200 nm were achieved using the home made W wire cantilevers. It was very easy to distinguish the regions with different conductivity using the current-voltage curves measured in given points of surface. Unfortunately the mechanical and electrical stability of the W coated silicon cantilevers was insufficiently for their long-duration use in SRM.

In summary, it has been demonstrated that scanning resistance microscopy is promising method for study the surface nanostructures of varying conductivity. We think that improving of SRM by highly conductive and mechanically stable ultrasharp probes can allow to realise the local electronic characterization of such interesting objects as quantum dots and wires.

The work is partially supported by Program "Physics of solid state nanostructures" (grant N 1-073/4) and by Russian Ministry of Sciences and Technologies (grant N 143/57/4).

References

[1] A.A.Bukharaev, V.S. Lobkov. et al. Optics and Spectroscopy 79(3), 385, (1995).

[2] E.S. Snow, P.M.Campbell, Appl.Phys.Lett. 64 (15), 1932 (1994).

[3] L. Tsau, D.Wang, K.L.Wang, Appl.Phys.Lett. 64 (16), 2133 (1994).

SCANNING FORCE MICROSCOPY AND MAGNETIC IMAGING OF NANOMETER-SIZED FERROMAGNETIC SPHERICAL NICKEL PARTICLES

A. A. Bukharaev, D. V. Ovchinnikov, E. F. Kukovitskii, N. I. Nurgazizov

Kazan Physical Technical Institute, Sibirsky Tract, 10/7, Kazan, 420029, Russia
e-mail: bukh@dionis.rfti.kcn.ru

In data storage industry there has been a great progress in developing magnetic recording media with high storage capacity and reliability. In this connection recently there has been considerable interest in submicron single ferromagnetic particles. Ferromagnetic fine particles have a large variety of applications, for example in magnetic record media. The magnetic properties of isolated particles, such as their remanent magnetizations and their reversal processes, are of great importance and have been widely modelled and also have been investigated experimentally.

Earlier we have obtained small ferromagnetic Fe particles created by ion bombardment in SiO_2 layers and investigated by means of ferromagnetic resonance, Messbauer spectroscopy of conversion electrons, optical spectroscopy, magnetooptics, X-ray phase analysis and electron microscopy [1]. Both magnetic and optical properties of such layers were governed by the shape and dimensions of the particles, and the number of defects in them.

The samples containing the nanometer-sized nickel particles deposited onto fused silica were investigated in this work. The following procedure was used to obtain such detached nickel nanoparticles on the supporting substrate surface. Carbon nanotubes produced by the catalytic decomposition of some hydrocarbons over nickel catalyst were deposited on the surface of fused silica substrate. The catalytic nickel particles on the tips of nanotubes have been retained on the substrate after hydrogenization of the carbon material. These particles were transformed into nickel droplets by heat treatment at ~800°C.

Scanning force microscopy (SFM) and its modifications are one of the best and powerful instruments for investigations of such objects. In particular one can diagnose magnetic properties of submicron ferromagnetic particles by means of magnetic force

microscope (MFM). It is necessary to know the particles real sizes and shapes for correct quantification of MFM-images, however. This is a well-known problem, because SFM-image is a convolution of the tip and sample. One may define required parameters using a simple algorithm of true images reconstruction of nanoparticles and tip shape. The main feature of this numerical deconvolution method is the possibility of absolutely true surface reconstruction if SFM tip contacts all points of the surface during scanning. Even if the above condition was not fulfilled the reconstructed images are essentially closer to the original surface. Detailed description of this deconvolution method is presented in [2].

The SFM-images of the nanometer-sized nickel particles deposited onto fused silica substrate have been successfully obtained by means of the P4-SPM-MDT scanning probe microscope using Park Instruments cantilevers.

The shape of the SFM tip has been extracted from the SFM-images of the nanometer-sized calibrated latex spheres. The nickel particles real sizes and shapes have been determined using tip shape information with deconvolution procedure. Nickel particles shapes have turn out to be close to spherical, and diameters have been in range of 20 - 200 nm that is in accordance with transmission electron microscopy results.

Magnetic force microscopy (MFM) is a high-sensitivity and high-resolution instrument which is suitable for investigations of such objects. It has been predicted theoretically and confirmed experimentally that sufficiently small magnetic particles naturally assume uniformly magnetized states that is why they are ideal objects for MFM investigations. We suppose the smallest nickel particles to be uniformly magnetized after application external magnetic field. As far as the particles have spherical shapes it very simplifies imaging quantifications. We have modelled MFM imaging of ultrafine ferromagnetic particles by means of computer simulation on the described samples.

The work is partially supported by Program "Physics of solid state nanostructures" (grant N 1-073/4) and by the Russian Basic Research Foundation (grant N 96-02-16323).

References

[1] A. A. Bukharaev, A.V. Kazakov, et al., Sov. Phys. Solid State, 33 (4), 578, (1991).

[2] A. A. Bukharaev, D.V. Ovchinnikov et al., Russian Microelectronics, 1997, *in press*.

RAMAN SPECTRA AND PHONON DISPERSION CURVES OF WURTZITE GaN AND AlN

V.Yu.Davydov, Yu.E.Kitaev, I.N.Goncharuk, A.O.Lebedev, A.N.Smirnov, and A.M.Tsaregorodtsev
Ioffe Physical Technical Institute, St Petersburg 194021 Russia
Tel. (812)247-9911, Fax:(812)247-1017, e-mail: vdav@ramand.ioffe.rssi.ru
M.B.Smirnov and A.P.Mirgorodskii
Institute for Silicate Chemistry, St Petersburg 199155, Russia
O.K.Semchinova
LFI Universitat Hannover, Schneiderberg 32, 30167 Hannover, Germany

I. Introduction

Group III-V nitride semiconductors (GaN, AlN and $Al_xGa_{1-x}N$) have recently attracted considerable attention because of their great potential for development of optoelectronic devices for the blue and UV spectral regions. GaN, AlN and their alloys have very close lattice constants and strongly differing band gaps (from 3.4 eV for GaN to 6.2 eV for AlN at room temperature). These properties make them ideal for heteroepitaxy. Recently $Al_xGa_{1-x}N$/GaN MQW structures were grown by MBE, and now great efforts are directed towards fabrication of $Al_xGa_{1-x}N$/GaN superlattices. At present, there is a growing need for precise non-destructive characterization of these nanostructures.

One of the most efficient, sensitive, and direct techniques which can be used for the quantitative characterization of semiconductor nanostructures is Raman spectroscopy. To characterize low-dimensional structures, the knowledge of dispersion phonon branches $\omega(\mathbf{k})$ in bulk materials is necessary because they determine the behaviour of acoustic and optical phonons in these structures, in particular, the phenomena of the acoustic phonon " folding" and "confinement" of optical phonons. Typically, the data on $\omega(\mathbf{k})$ are obtained by the neutron scattering technique. However, because of the absence of GaN and AlN crystals of suitable sizes for neutron experiments, there are no experimental data on dispersion of phonon branches in these compounds. This difficulty can be overcome by analyzing the phonon density of states (DOS) which can be measured by the second-order Raman scattering and which is closely connected with $\omega(\mathbf{k})$.

The aim of our investigation is to obtain the phonon dispersion curves $\omega(\mathbf{k})$ for wurtzite GaN and AlN. Our approach is based on the lattice dynamical calculations and their subsequent comparison with the Raman scattering data and with the group-theory analysis of phonon symmetry and optical selection rules to establish the reliable lattice-dynamical model.

II. Experiment

GaN and AlN layers were grown on the (0001) a-Al_2O_3 substrate, using chloride-hydride-vapor-phase epitaxy (CHVPE). Details of this technique were described in [1]. The samples investigated here were an undoped 10 μm thick GaN layer with the free carrier concentration of about 1×10^{17} cm^3 and an undoped 4 μm thick AlN layer. X-ray data reveal that both layers have a wurtzite structure with the (0001) axis parallel to the growth direction. The Raman spectra of GaN and AlN layers were measured at T=300K and at T=6K using a double grating monochromator and an Ar^+ laser (λ = 488 nm) as a source of excitation. A backscattering and a

90-degree scattering geometries were used. The accuracy of measuring phonon frequencies was about 0.2 cm^{-1}.

The first-order polarized Raman spectra for GaN and AlN obtained at room and cryogenic temperatures show an excellent agreement with the selection rules for the wurtzite structure, which points to a high quality of the samples. The investigations of the frequency dispersion of the polar modes as a function of their propagation direction have revealed a good agreement with the specific features of behavior of phonons in the crystals where electrostatic forces dominate over anisotropic short-range forces. The Γ-point phonon frequencies obtained in this work are summarized in Table I.

Table I

Mode	GaN		AlN	
	T=300K	T=6K	T=300K	T=6K
E_2^1	144	143.6	248.6	248.4
A_1(TO)	531.8	533.8	611	613.8
E_1(TO)	558.8	560.2	670.8	673.4
E_2^2	567.6	569	657.4	660
A_1(LO)	734	736.6	890	894
E_1(LO	741	744	912	917

We have also measured the second-order Raman spectra of GaN and AlN samples. The spectral region investigated contains the overtone and combination parts of acoustic and optical phonons. This is a high-order scattering process, and all the phonons throughout the Brillouin zone (BZ) can become Raman active. It can be shown that, under definite conditions, the second-order Raman spectrum is not only proportional to the combined phonon DOS but also gives the information on one-phonon DOS. For example, in the case of dominating overtone scattering, the experimental second-order Raman spectrum times $\{\omega/[n+1]\}^2$, where n is the phonon occupation number at $\omega/2$, will be very close to the one-phonon DOS (except the obvious scaling the frequency axis by a factor of 2). We have performed polarized second-order Raman-scattering experiments to compare the experimental data with the derived selection rules. All second-order Raman spectra were measured at low temperatures to exclude the phonon occupation numbers.

The DOS tends to become very large at the critical points at the BZ boundaries. For this reason, we have tried to interpret our results in terms of scattering by phonons at high-symmetry K and M points at the BZ edge.

III. Group-theory analysis

The symmetry of phonons in the wurtzite 2H-GaN and AlN crystals was determined using the method of induced band representations of space groups [2]. This method allows one to connect by symmetry the local atomic displacements of particular atoms in the primitive cell and normal modes throughout the BZ. GaN and AlN with the wurtzite structure belong to the space group C_{6v}^4($P6_3mc$) with two formula units per primitive cell. Both Ga(Al) and N atoms occupy 2b sites of symmetry C_{3v}. The results of the group-theory analysis are presented in Table II.

Table II

Atom	q	β	Γ (000) C_{6v}	K $(\frac{1}{3}\frac{1}{3}0)$ C_{2v}	M $(\frac{1}{2}00)$ C_{2v}
Ga(Al)	2b	$a_1(z)$	1,4	3	1,4
N	$(\frac{1}{3}\frac{2}{3}z)$ C_{3v}	e(x,y)	5,6	1,2,3	1,2,3,4

In Table II, column 1 contains atoms occupying the Wyckoff position q given in column 2 together with its coordinates and site symmetry group. Columns 4-6 contain indices of small irreducible representations (irreps) induced by those irreps β (column 3) of the site symmetry group according to which the local atomic displacements (x,y,z) are transformed. (The

small irreps are labeled according to [3].) The induced representations determine symmetries of phonons at the symmetry points of the BZ given together with their coordinates and small groups in the headings of column 4-6. The sets of normal modes at the symmetry points of the BZ are obtained by summation of contributions of all the atoms in the primitive cell. As a result, we have

$\Gamma = \Gamma_{ac} + \Gamma_{opt} = 2(\Gamma_1 + \Gamma_4 + \Gamma_5 + \Gamma_6) = 2(A_1+B_1+E_1+E_2)$,

$\Gamma_{ac} = \Gamma_1 + \Gamma_5 = A_1 + E_1$; $\Gamma_{opt} = \Gamma_1 + 2\Gamma_4 + 2\Gamma_5 + \Gamma_6 = A_1+2B_1+E_1+2E_2$,

$K = 2(K_1+K_2+2K_3)$; $M = 2(2M_1+M_2+M_3 + 2M_4)$.

The A_1 and E_1 optical modes are both Raman and IR active and both the longitudinal (LO) and transverse (TO) components can be observed in the Raman spectra. The two E_2 modes are only Raman active and the two B_1 are silent modes.

We see that from the point of view of symmetry both atoms, Ga(Al) and N, contribute equally to all the modes. From Table II, one can also establish the symmetry behavior of particular phonon branches. One can see that there are two phonon branches (Γ_1, Γ_4) - K_3 - (M_1, M_4). This means that two doubly degenerate K_3 -modes split in the Γ - K and K-M directions transforming into two pairs of Γ_1 and Γ_4 modes and two pairs of M_1 and M_4 modes, respectively..

Next, we derived the selection rules for the second-order Raman scattering. Because of complexity, we give only some extracts from the complete list. For example, the overtones $[K_1]^2$ and $[K_2]^2$ are active in the xx, yy, zz polarizations, whereas $[K_3]^2$ as well as all the overtones of the M-point modes are active in xx, yy, zz and xy. The combinations of M_1xM_3, M_1xM_4, M_2xM_3, M_2xM_4 are active in the xz and yz polarizations, whereas M_1xM_2 and M_3xM_4 are active in xx, yy and xy.

IV. Lattice dynamical simulation

To simulate the crystal dynamics we have developed a phenomenological model based on the pair-wise interatomic potentials and rigid-ion Coulomb interactions. The ionic charge values were chosen to reproduce the observed LO-TO splitting. The short-range potentials included the second neighbour contributions. The potential parameters were determined by fitting the calculated BZ-center frequencies and the elastic constants to the experimental ones. Then the phonon dispersion curves and the DOS function were calculated by scanning throughout the BZ. Such a simple model offers an essential advantage of being applicable to complex polyatomic systems. It enables us to reproduce reasonably well the observed first-order spectra and provides the phonon DOS function which is in an perfect agreement with the observed second-order Raman spectra. All the calculations were performed by the CRYME program [4].

V. Results and discussion

The combined analysis of the dispersion curves using the experimental data, lattice dynamic calculations, and group-theory results is a self-consistent procedure.

Figure 1 shows the calculated phonon dispersion curves for GaN and AlN. Using the selection rules in combination with the phonon dispersion curves $\omega(\mathbf{k})$ we have assigned the maxima in the polarized second-order Raman spectra to the phonons of definite types of symmetry. As a result, we obtained the frequencies of the optical phonons at the symmetry points of the BZ. Our results show that the A_1(TO), E_1(TO) and $E_{2(high)}$ phonons in both GaN and AlN have a nearly flat dispersion, whereas the A_1(LO) and E_1(LO) phonons have a very large dispersion throughout the BZ. This is in a complete agreement with the calculated dispersion curves.

The acoustic phonon region is more complex for the interpretation if it is based on second-order

Raman spectra only. For GaN, we can make an additional test for validity of calculations by comparing the calculated one-phonon DOS function with the experimental one obtained from the disorder-induced Raman scattering. This approach is valid since for disordered state all the phonons are allowed to participate in the scattering and the Raman spectrum should display the entire DOS function weighted by the transition matrix elements involved in the photon-phonon coupling during the scattering process. In our case, we investigated Er (1 MeV, $\Phi=1\cdot10^{14}$ ion/cm^2)-implanted GaN. The spectrum of the Er-implanted GaN reveals the energies of acoustic zone-boundary phonons and the silent B_1 modes which are forbidden in the first-order Raman spectra.

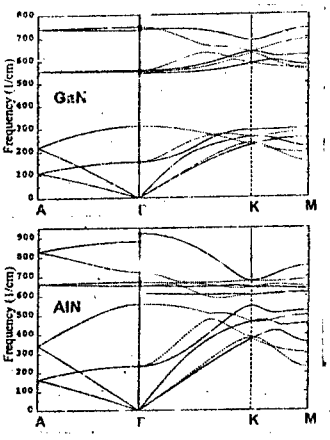

FIG. 1

Figure 2 shows the calculated phonon DOS function for GaN (a), the Raman spectrum of the Er-implanted GaN (b), the second-order Raman spectrum of non-implanted GaN sample with scaling the frequency axis by a factor of 1/2 (c), and the first-order Raman spectrum of the latter sample(d). It is clearly seen that there is a good correspondence between the calculated DOS function and the disorder-induced Raman spectrum of Er-implanted GaN. This is an additional evidence in favour of the validity of calculated dispersion curves for GaN. A similar study of Er-implanted AlN is in progress.

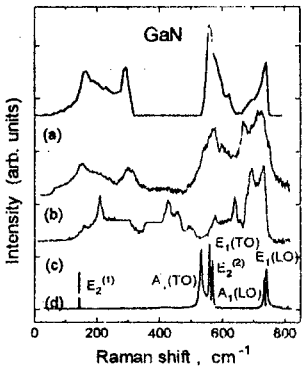

FIG. 2

To summarize, using a combination of three different methods (Raman scattering, lattice dynamical simulation, and group theory analysis) we have obtained, for the first time, the phonon dispersion curves in bulk GaN and AlN crystals. This approach appears to be efficient for the study the lattice dynamics of GaN/AlN superlattices and other low-dimensional structures based on these compounds.

The authors are grateful to Dr. N.A.Sobolev for giving us a possibility to carry out measurements on Er-implanted GaN sample.

This work was partly supported by Russian Program "Physics of Solid State Nanostructures".

References

[1] F.Bugge, A.N.Efimov, I.G.Pichugin, A.M.Tsaregorodtsev, and M.A.Chernov. Cryst.Res.Technol 22, 65 (1987)

[2] R.A.Evarestov and V.P.Smirnov, *Site Symmetry in Crystals: Theory and Applications*, ed. by M.Cardona, Springer Series in Solid State Sciences, Vol 108 (Springer, Heidelberg, 1993)

[3]. S.C.Miller and W.F.Love, *Tables of Irreducible Representations of Space Groups and Co-representations of Magnetic Space Groups* (Pruett, Boulder, 1967)

[4]. M.B.Smirnov, A.P.Mirgorodsky, and P.E.Quintard, J.Mol.Structure 348, 159 (1995)

PRECISION MAGNETOMETRY ON A NANOMETER SCALE

S.V. Dubonos
Institute of Microelectronics Technology, the Academy of Sciences, 142432 Chernogolovka, Russia

A.K. Geim
Research Institute for Materials, University of Nijmegen, 6525 ED Nijmegen, The Netherlands

1 Introduction

Hall probes have been employed in studies of magnetic properties of materials for several decades. We have extended the Hall technique further and used submicron probes for studies of individual microfabricated samples which are placed controllably in the sensitive area of the probe. Another important development is that we have been able to link the detected Hall signal to the sample magnetisation. The present sensitivity of the technique allows us to register changes less than 10^5 μB and further improvement down to 10^3 μB is straightforward. The detection of the single electron spin is arguably within experimental reach. In several regimes including mesoscopic superconductors, it has principal advantages over the alternative techniques such as μ-SQUIDs [1] and μ-mechanical cantilevers [2].

2 Experimental devices

Figure 1 shows a scheme of our devices. It is a multi-terminal wire microfabricated from a conventional GaAlAs heterostructure with a two dimensional electron gas (2DEG). We employ the 2DEG as it has a very large Hall coefficient. For the present studies of mesoscopic superconductors, relatively large Hall probes (from 1 to 1.5 μm) were found most suitable, although probes as small as 0.3 μm can be reliably fabricated from GaAlAs heterostructures. Using another round of electron-beam lithography, superconducting Al disks of various sizes are placed in the centres of different Hall crosses. Note that there is no electric contact between the superconducting samples and the 2DEG embedded at $\approx$100 nm below the heterostructure surface.

An example of the Hall signal in the presence of a superconducting particle is shown in Fig.2 (magnetic field is perpendicular to the 2DEG). The low-temperature curve exhibits a strong asymmetric hysteresis as well as a fine step-like structure which is barely noticeable on the scale of the figure but can be easily resolved after subtracting a background (e.g. see the

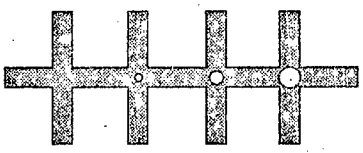

Figure 1: The sketch. of working device: 2DEG Hall crosses (grey) with Al dots of different size in the centre (white).

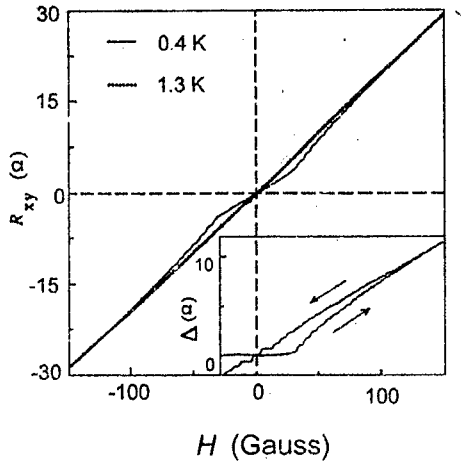

Figure 2: Hall response in the presence of a 1.2μm Al disk in the cross junction, at temperatures below (solid curve) and above (dots) the superconducting transition. Inset: fine structure becomes already visible after subtracting a linear background.

inset). For the same Hall probe but at temperatures above the superconducting transition temperature T_c or for a Hall probe without a superconducting sample, we observe a linear dependence of Hall resistivity R_{xy} on magnetic field H (dotted line). These raw data already indicate that magnetic properties of individual superconducting particles are accessible by our technique.

3 Hall Probes as Micro-Fluxmeters

The presence of a magnetic particle in the cross junction causes an inhomogeneous magnetic field distribution, and the Hall resistance generally depends on details of this distribution. However, if electron flow is uniform, the simple formula

$$R_{xy} = < B > /nc \qquad (1)$$

holds, where $< B >$ is the average field inside the Hal cross. In the case of a microscopic junction, electrons can enter into the side leads and the electron flow is no longer uniform. For a diffusive Hall cross, this can give rise to different contributions to R_{xy} from different regions of such a probe. In our experiment, we have performed analytical and numerical calculations of the ballistic Hall effect and found that Eq. (1) is modified only by a numerical coefficient and holds within the accuracy of few %. The average magnetic field $< B >$ is proportional to $\int Bdxdy$, i.e. the measured signal is proportional to the flux Φ through the characteristic area S of the Hall cross. Therefore, one can consider our Hall probe as micro-fluxmeters, similar to e.g. SQUIDs, but with a very small detection loop. In our experiment, S is only about 2 μm^2. The difference between Hall resistances measured by probes with and without a particle yields the area magnetisation

$$4\pi M = < B > -H \qquad (2)$$

The amplitude of this signal rapidly decays with decreasing the ratio between the particle and junction sizes.

4 Comparison of Hall micromagnetometry with alternative techniques

Finally, we will compare our experimental approach with μ-cantilever and μ-SQUID techniques which can be considered as alternatives for magnetisation measurements of submicron superconductors. The noise level in our experiment is not frequency dependent and corresponds to changes in magnetic field of about 0.1 G. This yields the flux sensitivity $\delta\Phi \approx 10^{-2}\phi_0$ for the area ≈ 2 μm^2. Also, the field resolution of $\delta B \approx 0.1$ G for a superconducting disk with the typical volume $V \approx 0.1$ μm^3 implies magnetisation changes $\delta M = \delta BV/4\pi \approx 10^{-15}$ erg/G or 10^5 μ_B.

The resolution of the state-of-the art μ-SQUIDs with a detection loop of the order of 1μm can be as high as $10^{-6}\phi_0$ at low frequencies [1]. However, such a sensitivity is not sustained even for moderate sweeps of few hundred Gauss and the flux noise reduces the resolution to

only about ϕ_0 [1]. We conclude that experiments similar to ours would not be feasible using SQUIDs. The basic reason is that it would be very hard to distinguish between magnetic fluxes entering into a superconducting sample and into the superconducting detection loop.

Magnetic resonance force microscopy uses micromechanical cantilivers which provide a remarkable torque sensitivity of 10^{-12} erg·cm [2]. One can imagine a submicron superconducting particle placed on the tip of such a cantilever. To detect changes in magnetisation $\delta M \approx 10^{-15}$ erg/G, an applied magnetic field in excess of 1 kG would be required. This makes mesoscopic superconductivity inaccessible, also for this technique.

Fabrication of ten times smaller Hall probes with the same sensitivity δB is a straightforward experimental task. This would correspond to the sensitivity $\delta\Phi \approx 10^{-1}\phi_0$. Furthermore, closely following speculations of Sidles et al about ultimate micro-SQUIDs and cantilevers [2], we note that a single electron located at $d = 5$ nm above a Hall probe creates the magnetic field $B \approx \mu_B/d^3 = 0.1$ G. Then one can imagine a metal Hall probe of the size of about 20 nm fabricated by electron-beam lithography, employing e.g. the contamination resist. Using a metal (e.g. Bi) instead of a 2DEG considerably decreases the response in terms of Ohms/G but does not seem to influence the field sensitivity. Therefore, we believe that using Hall magnetometers even the detection of a single-electron moment is within experimental reach and does not require further technological advances as in the case of SQUIDs and micro-cantilevers.

References

[1]. V. Chandrasekhar et al, *Phys. Rev. Lett.* **67**, 3578 (1991); W.Wernsdorfer et al, *J. Magn. Mater.* **145**, 33 (1995).
[2]. J.A. Sidles et al, *Rev. Mod. Phys.* **67**, 249 (1995).

High-Resolution X Ray Diffraction Study of Perfect InAs-GaAs Superlattice Grown by Molecular-Beam Epitaxy at Low Temperature

N.N.Faleev, V.V.Chaldyshev, A.E Kunitsyn. V.V.Tretyakov,
A.F.Ioffe Physico-Technical Institute, 194021 St.Petersburg, Russia

V.V.Preobrazhenskii, M.A.Putyato, B.R.Semyagin
Institute of Semiconductor Physics, 630090 Novosibirsk, Russia

Introduction

InAs-GaAs superlattices have attracted much attention during the last few years due to interesting physical phenomena related to 2D electron confinement in the deep and narrow quantum wells[1]. When the superlattice is grown by molecular-beam epitaxy (MBE), the substrate temperature is normally chosen within the range from 400 to 500°C. This is a compromise between a strong increase in defect concentration at low temperature and smoothing the interfaces at high temperature resulted from indium segregation and diffusion effects (600°C is much more appropriate for MBE of high-quality GaAs films)[1]. It seems to be interesting, however, to study InAs-GaAs superlattice grown at very low temperature (say, 200°C), when a very high arsenic excess (~1 at.%) is incorporated into the growing film[2,3]. In this case, the thin InAs layers inserted in GaAs matrix should act not only as electron (hole) quantum wells, but also should pin arsenic clusters being formed by excess arsenic upon annealing[4,5]. Thus, an additional As-GaAs superlattice can be formed that spatially coincides with the initial InAs-GaAs superlattice.

In this paper we report the results of high-resolution x-ray diffraction (HRXRD) study of the InAs-GaAs superlattice grown by MBE at 200°C. We show that this superlattice is quite perfect in as-grown state in spite of a very high concentration of excess-arsenic-related point defects. Its smoothing resulted in disappearance of x-ray diffraction patterns are, however, observed after annealing that causes arsenic precipitation and indium diffusion.

Experimental

The InAs-GaAs superlattices were grown by MBE at 200°C in a dual-chamber 'Katun' system on semi-insulating GaAs(100) substrates. The thin InAs insertions in the GaAs matrix were produced by interrupting the Ga beam and using an In beam. Thus produced layers contained 1 monolayer of InAs. The distance between the InAs layers was 30 nm. One part of the samples was kept as-grown, the others were annealed at 500 and 600°C for 15 min. The annealing was carried out under As overpressure in the MBE setup.

Electron probe microanalysis (EPMA) was employed to measure the average In concentration and to assess arsenic excess in the films. Concentration of arsenic antisite defects was measured using a characteristic near-infrared optical absorption (NIRA). X-ray diffraction study were carried out using Ge double-crystal diffractometer adjusted for (004)reflection of $CuK_{\alpha 1}$ radiation. The precise measurements of the lattice mismatch and assessment of the crystal lattice perfection were made using ω-scan mode with opened detector. Wide-angle measurements of x-ray diffraction in ω-2θ mode were carried out with a narrow receiving slit in the front of the detector in order to diminish the influence of the diffuse scattering.

Results and Discussion

Fig. 1 shows double-crystal rocking curves in a vicinity of (004) GaAs reflection for the InAs-GaAs superlattices in as-grown state and after annealing at 500 or 600°C. Two main peaks and many additional interference fringes are clearly seen. The right main peak corresponds to the substrate reflection. The left peak, marked as «0SL», corresponds to the periodic structure of InAs and GaAs epitaxial layers. In the as-grown sample, the angle difference between 0SL and substrate-related peaks is determined by two reasons. The one of them is lattice expansion produced by the excess-arsenic-related point defects. The other is lattice expansion resulted from InAs layers inserted in the epitaxial film. The annealing of the samples leads to a shift of 0SL peak since the well-known phenomena of the lattice relaxation due to precipitation of excess-arsenic-related point defects[3]. Therefore, the lattice mismatch in the annealed samples can be mainly attributed to the indium content. That allows us to deduce the average InAs content in the film and then to calculate the arsenic excess using Vieu's calibration[4]. The data obtained from the rocking curves are shown in table 1. The average InAs content was found to be 0.8-0.9 %, that is in a good agreement with our EPMA data (1.0±0.1 %). The arsenic excess of 0.6 % was found to be well consistent with that estimated by EPMA and with our NIRA measurements of arsenic antisite defect concentration (0.9×10^{20} cm^{-3}).

The multiple pronounced interference fringes (fig.1) and parameters of the main peaks (table 1) evidence that the as-grown InAs-GaAs superlattice is quite perfect, planarity of the interfaces and surface is very high, and parameters of the periodic structure are

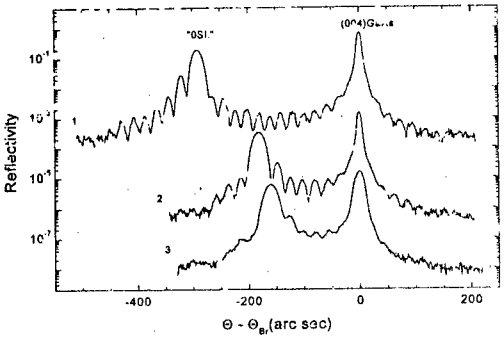

Fig. 1. Double-crystal x-ray rocking curves for as-grown (1) and annealed (2, 3) InAs-GaAs superlattices in a vicinity of GaAs(004) reflection. Annealing temperatures are 500°C (2) and 600°C (3)

Table 1

	Substr. FWHM (arc. sec) /K_{refl}	"0SL" FWHM (arc. sec) / K_{refl}	$\Delta\Theta_{I-S}$ (arc. sec)	$\Delta a/a_{\perp}$	ΣT_{str} nm	T_{SL} nm	X_{As}	X_{InAs}	T_{InAs} (A)
as-grown	9.60/ 0.682	20.20/ 0.195	-280	2.10 10^{-3}	920 ± 20	30.0 ± 1.0			
T_a= 500°C	8.70/ 0.722	22.90/ 0.165	-180	1.35 10^{-3}	850 ± 40	27.0 ± 2.0	0.6%	0.90%	2.45
T_a= 600°C	16.50/ 0.410	24.30/ 0.155	-160	1.19 10^{-3}	790 ± 80	26.5 ± 3.0	0.6%	0.80%	2.10

uniform in the whole superlattice. The annealing results in smoothing the interference patterns and decreasing their number. In addition, the annealing at 600°C causes an appreciable broading of the substrate-related peak and a essential decrease in its intensity.

In order to determine the superlattice period and to elucidate the structure transformation upon annealing, we performed HRXRD study in a wide angle range using both ω-2θ mode and ω-mode. Coherent ω-2θ rocking curves for the as-grown and annealed samples are shown in fig.2.

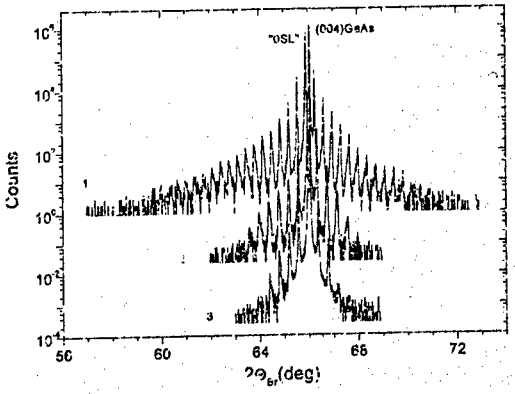

Fig.2. Coherent ω-2Θ rocking curves for as-grown (1) and annealed (2, 3) InAs-GaAs superlattices. Annealing temperatures are 500°C (2) and 600°C (3)

One can see a large number of superlattice-related interference reflections in the rocking curve of the as-grown sample. The anneal-related features mentioned above are also clearly seen in fig.2. These are a considerable smoothing of the supersmucture-related peaks and their disappearance at large angles. When compared to the rocking curve for the as-grown sample, the area of the pronounced interference picture is two time less for the sample annealed at 500°C and three time less for the sample annealed at 600°C.

An analysis of the rocking curves obtained in the ω-mode showed that the diffuse scattering is localized in a vicinity of (004) GaAs reflection and is rather weak. The scattering defect density is estimated as $3.5\text{-}5.0\times10^{9}$ cm^{-2} in the as-grown sample and in the sample annealed at 500°C and growth up to $1\text{-}2\times10^{10}$ cm^{-2} in the sample annealed at 600°C. The correlation length in the (001) plane decreases from 25-30 nm to 15-16 nm. That indicates an increase in the density of the defects involved in the diffuse scattering.

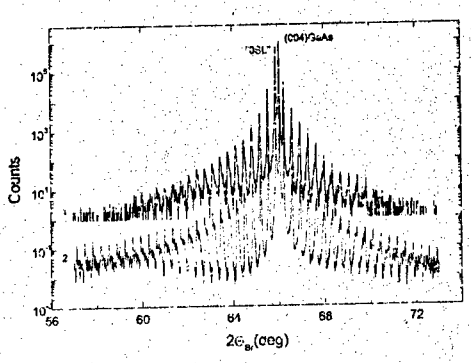

Fig.3. Experimental (1) and calculated (2) rocking curves for InAs-GaAs superlattice grown at 200°C. Reflection (004), $CuK_{\alpha1}$ radiation.

X-ray rocking curve for an InAs-GaAs superlattice with abrupt interfaces and 30 nm thick GaAs layers was calculated in the dynamic approach. In the calculations, the lattice parameters of both InAs and GaAs layers were slightly increased in order to fit the lattice expansion induced by excess arsenic. Fig.3 shows the calculated rocking curve in comparison with the experimental one for the as-grown sample. We can conclude that the curves in fig.3 are close to each other. This is a strong evidence for the low-temperature grown InAs-GaAs superlattice being fairly perfect in the as-grown state in spite of the very high concentration of excess-arsenic-related point defects. A probable reason of this fact is that excess arsenic primarily occupies positions in the cation sublattice and its diffusivity is low at 200°C. This is consistent with the weak diffuse scattering detected for all the samples. The post growth annealing causes excess arsenic diffusion and precipitation. Nanoscale arsenic clusters located at InAs layers have been observed in the annealed samples by transmission electron microscopy. The precipitation should induce a considerable roughness of the thin InAs layers. In addition, an essential smoothing of the interfaces should occur as a result of indium diffusion upon annealing. These phenomena seems to be the reasons for the partial disappearance of the interference fringes in the annealed samples.

Conclusions

The x-ray diffraction (HRXRD) study of the InAs-GaAs superlattice grown by MBE at 200°C has shown that this superlattice is quite perfect in as-grown state in spite of a very high concentration of excess-arsenic-related point defects. A large number of strong superstructure-related interference reflections and low diffuse scattering have been observed. The experimental rocking curves are close to a calculated ones. The post-growth annealing has led to partial disappearance of the x-ray diffraction fringes. This effect seems to be a result of arsenic precipitation and indium diffusion. The average indium content and arsenic excess have been deduced from HRXRD data. They are found to be well consistent with the values obtained by EPMA and NIRA techniques.

Acknowledgment

The authors are grateful to Dr. N.A.Bert and Dr. Yu.G.Musikhin for TEM data. The research was supported by Russian Foundation for Basic Research and by Russian Ministry of Science under programs: "Physics of Solid State Nanostructures" and "Fullerenes and Atomic Clusters".

References

[1] *Molecular Beam Epitaxy and Heterostructures*, Ed.by L.L.Chang and K.Ploog, Martinus Nijhoff Publishers, (Dordrecht, Boston, Lancaster, 1985).

[2] M.Kaminska, Z.Liliental-Weber, E.R.Weber, T.George, J.B.Kortright, F.W.Smith, B.Y.Tsaur, and A.R.Calawa, Appl. Phys. Lett., 54, 1831(1989).

[3] N.A.Bert, A.I.Veinger, et al., Phys.Solid State 35, 1289(1993).

[4] M.R.Melloch, N.Otsuka, K.Mahalingam, C.L.Chang, P.D.Kirchner, J.M.Woodall, and A.C.Warren, Appl. Phys. Lett. 61, 177(1992).

[5] N.A.Bert, V.V.Chaldyshev, D.I.Lubyshev, V.V.Preobrazhenskii, and B.R.Semyagin, Semiconductors 29, 1170(1995).

[6] X.Liu, A.Prasad, J.Nishio, E.R.Weber, Z.Liliental-Weber, and W.Walukiewicz, Appl. Phys. Lett. 67, 279(1995).

ATOMIC FORCE MICROSCOPY OF A3B5 HETEROSTRUCTURE DROPS.

V.A.Fedirko*, M.D.Eremtchenko*, O.I.Khrykin and V.I.Shashkin****

*) Moscow State University of Technology "Stankin",
3a Vadkovski per., Moscow, 101472, Russia
**) Institute for Physics of Microstructures of RAS, Nizhnii Novgorod, 603600, Russia.

INTRODUCTION

The development of advanced techniques to control compound semiconductor micro- and nano-structures parameters and to assess their property is of great importance. The scanning probe microscopy (SPM) provides new possibilities for surface analysis and diagnostics with very high resolution. The SPM is a near field technique which is based on the interaction between a sharp microtip and the surface atoms and molecules while scanning a portion of a sample area [1].. Different physical parameters resulting from the origin of the interaction force between the tip and the surface can be probed. The atomic force microscopy (AFM) in various modes of operation enables probing van der Waals force, lateral friction force and elastic deformation force [2], and allows surface heterogeneity imaging [3]. The resolution up to several manometers in the scanned plane can be realised with a sharp enough probing tip while the relief height resolution may be as high as several Angstroms. Earlier we reported on SPM characterisation of GaAs/AlGaAs superlattices [4]. In this paper we report on the AFM analysis in air of surface InGaAs/GaAs dot heterostructures.

EXPERIMENTAL

The samples with GaAs/InGaAs heterostructures were obtained by the metallorganic chemical vapour deposition (MOCVD) process with the EPIQUIP-502RP equipment. Epitaxial growth was carried out in the H2 - Ga(CH3)3 - AsH3 gas medium, trimethylindium was used as indium source material. The heterostructures were grown in an atmospheric-pressure vertical reactor with the induction heating of substrate. The mole fraction x of InAs varied from 0.4 to 0.66. We used both semi-insulating and low-resistant GaAs substrates 2° misoriented with respect to (100) plane in the (110) direction. with the buffer GaAs layer of about 0,5 mkm. The growth temperature varied from 450°C to 600°C range for GaAs and from 450°C to 650°C for InGaAs for different samples.. The growth conditions enabled the formation of InGaAs drops on the GaAs surface.

We used a SPM device produced by "NT-MDT" (Russia) in our experiments. NT-MDT silicon cantilevers for AFM measurements were used. The probe tip radius was about 10 nm with the cone angle 20°. Tapping mode alongside with phase contrast technique were applied to reveal the details of a surface structure and to get rid of artefacts. Surface relief and phase contrast images were registered simultaneously. The phase contrast technique enables imaging of the chemical composition over the scanned surface due to the difference of the interaction between a probe and the surface atoms [3]. Pt-C replicas of the surface were analysed by TEM with JEOL JEM-2000.

RESULTS AND DISCUSSION

The AFM relief image of the sample H124 is presented at Fig.1, while Fig.2 shows the phase contrast image of the same area of the surface. The grows temperature for InGaAs was 550°C, $x \approx 0{,}66$. The drops are nearly semiellipsoidal objects, their size about 200×300 nm in plane and 100 nm in height. All the drops of the array are oriented in the same direction. Scanning of the large area up to 20×20 mkm has not revealed any regular dot location. The phase contrast image corresponds to relief image and corroborates that the drop substance differs from that of the buffer. The tops of the drops are flattened in Fig.2 which affirms that the phase contrast does not result from the changes of the surface relief curvature. Fig.3 represents the TEM replicas' image of the same sample. It correlates well with the AFM pictures though it is clear that the AFM enables to more adequate imaging and measuring of the drops.

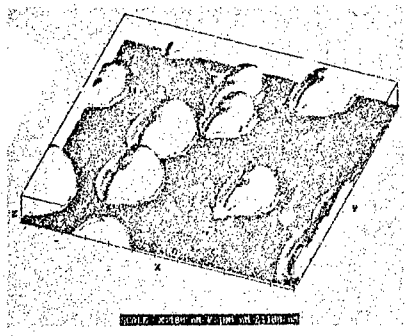

Fig.1. AFM relief image of H124 sample.

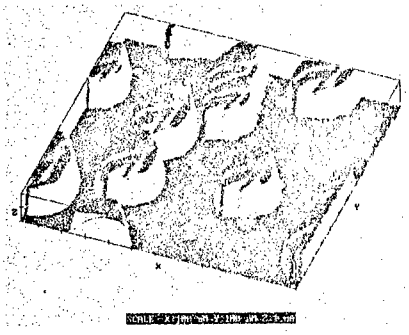

Fig.2. AFM phase contrast image of H124.

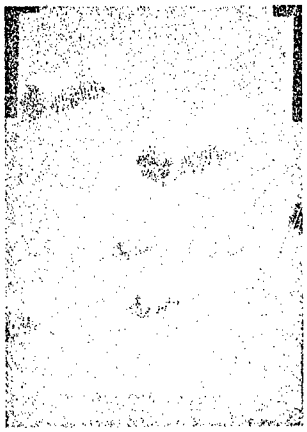

Fig.3. TEM image of H124 sample.

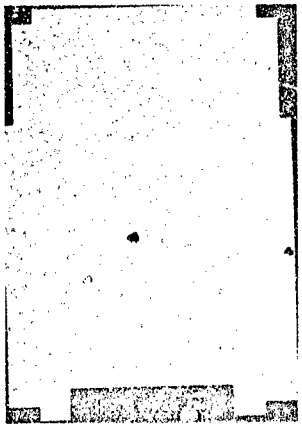

Fig.4. TEM image of H122 sample.

Fig.5. AFM relief image of H122 sample.

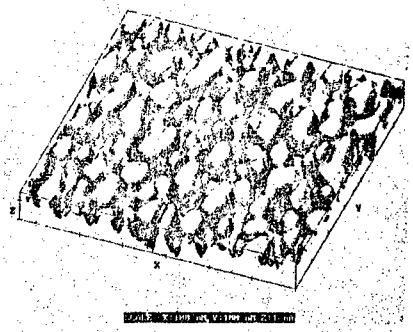

Fig.6. AFM phase contrast image of H122.

Fig.4. represents TEM image of H122 sample, while Figs.5,6 show the AFM surface relief and phase contrast picture of the same area of that sample. The grows temperature for InGaAs was 450°C, $x \approx 0{,}66$. The drops' size is about 20 - 50 nm in plane and less then 10 nm in height but they are very well distinguished. The array is more disoriented. The phase contrast image is in a good agreement with the relief image. One can see that the AFM picture correlates with the TEM image of Fig.4 but allows to distinguish much smaller details of the surface morphology.

CONCLUSION

We have shown that the AFM technique in air is effective for the surface analysis of compound semiconductor nanostructures. The tapping mode of operation allows non-destructive characterisation of nanoscale surface objects and reduces the image distortion due to lateral forces. The phase contrast technique also enables to exposure the heterogeneity of a surface. The spatial resolution up to 10 nm can be achieved.

The work was partially supported by the Russian Government program 'Actual problems of physics of condensed matter: surface atomic structures', project N 973.22.

REFERENCES.

1. Atomic force microscopy/scanning tunnelling microscopy, S.M. Cohen, M.T. Bray, and M L. Lightbody, eds., US Army Natick Research, Development, and Engineering Center, MA (1994).
2. D. Parrat, F. Sommer, J.M. Solleti, T.M. Duc, J.Trace and Microprobe Technique, 13(3), 343, (1995)
3. Q. Zhong, D. Innis, K. Kjoller, V.B. Elings, Surf. Sci. Lett. 290, L 688, (1993).
4. V.A. Fedirko, M.D. Eremtchenko, Material Science & Engineering B (1996).

Capacitance methods for investigation and design of MBE grown multi-layer nanometer structures and microwave devices

M.F.Kokorev*[1], A.Yu.Egorov**, N.A.Gordina***, A.G.Kuzminkov*, N.A.Maleev***, V.I.Presnov***, V.M.Ustinov**, A.F.Zhukov**

*Radioengineering and Electronics Department, State Electrotechnical University
Prof.Popova 5, 197376 St. Petersburg, Russia
**A.F.Ioffe Physico-Technical Institute, Russian Academy of Sciences
Politekhnicheskaya 26, 194021 St Petersburg, Russia
*** Svetlana-Electronpribor, Close Stok Company
Engelsa 27, 194156 St. Petersburg, Russia

GaAs Schottky barrier diodes and transistors are currently widely used devices in high-performance analog and microwave systems. They usually have sub-micron barrier electrodes and nonuniform doping multi-layer structures with layer thicknesses of ~100-1000 Å. Accurate non-destructive characterization of these devices is extremely important for the progress of GaAs technology.

Electrical measurements are an attractive, non-destructive way of determining the device structure parameters (doping profile, barrier electrode dimension, carrier mobility et al.). Undoubtedly, capacitance-voltage (C-V) method is most widely used for electrical doping profiling. For this method the small-signal capacitance of a depletion layer is mesuared as a function of a reversed biased voltage V. Then, the *apparent* doping profile can be found by the application of a simple formula $N_{ap}(W) = (1/e\varepsilon\varepsilon_0)\times [C^3/(dC/dV)]$ where C(V) is the measured capacitance per unit area and $W = \varepsilon\varepsilon_0/C(V)$. The standard C-V method has the following disadvantages [1]:

1. the abrupt depletion approximation was used to derive the data interpretation formulae; this leads to error in the determination of step profiles;
2. the measured data must be differentiated, leading to a considerable noise sensitivity.

To alleviate these disadvantages, the concept of inverse modelling has been proposed [1]. Inverse modelling is implemented by minimisation of the difference between measured and simulated device behaviour by iterative adaptation of the parameter values. A practical disadvantage of inverse methods is that the computational requirements may be quite high.

We have recently presented a new C-V technique for evaluating multi-layer step profiles [2]. The main points of this method are as follows:

1. Determination of the apparent doping profile and dN_{ap}/dV using smoothing.
2. Condition dN_{ap}/dV = max (or min) gives the bias voltages V_i when the mean positions of a modulated space-charge $W(V_i) = \varepsilon\varepsilon_0/C(V_i)$ are closed to positions of the step boundaries z_i. The determined values z_i are used as starting parameters in following optimisation procedure.
3. To extract layer doping levels and correct its position, we use optimization procedure with the convergence criteria

$$\frac{1}{M}\sum_{k=1}^{M}\left(N_{ap}(V_k) - N_{sim}(V_k)\right)^2 \le \Delta$$

where V_k is applied bias voltage (k = 1,2,...M), $N_{sim}(V)$ is simulated apparent profile, and Δ is specified error value. We use $N_{ap}(V)$ dependence instead of C(V) one usually used This approach provides efficiency and fast convergence of the presented procedure, since $N_{ap}(V)$ is determined by local part of the doping profile only. Another feature of the present method is a new numerical technique for C(V) and $N_{sim}(V)$ calculation instead of usually used "quasistatic approach" [1]. This technique provide calculation dC(V)/dV and $N_{sim}(V)$ with extremely high accuracy.

The other important problem for sub-micron devices is the influence of the parasitic capacitances. The fringe capacitance C_f and pad capacitances C_{pad} both degrade the performance of short-gate length MESFETs. These values can be extracted from S-parameter measurements of FETs those are pinched off [3].

Recently we have proposed a new approach to solve this problem [4]. Our method is based on the measurement of the C-V characteristics for FETs with different gate widths and Schottky diode test structures. The total measured gate capacitance for the gate-source or gate-drain diode of zero bias FET is given by

$$C_g(V) = C_{ch}(V) + C_f(V) + C_{pad},$$

where C_{ch} is the gate-channel capacitance. Assuming that the depletion-layer edge under the gate is flat, we can write:

$$C_{ch}(V) = L_g \times W_g \times Cb(V)$$

where L_g is the gate length, W_g is the active gate width and Cb is the measured low-frequency Schottky diode capacitance per unit area. For small negative gate voltages ($0>V>V_{th}/2$, V_{th} - threshold voltage), the fringe capacitance depends only slightly on the gate bias [5]. Using this fact we have

$$L_g = [C_g(V+\Delta V)-C_g(V)]/[W_g \times (Cb(V+\Delta V)-Cb(V))].$$

The contribution from the pads are best eliminated by measuring FETs with different gate widths W_g, fitting the measured capacitances to linear function of W_g, and substracting the resulting intercept. Finally, the fringe capacitance vs gate voltage can be founded. The method is valid for recessed gate structures with an arbitrary doping profile and surface-state; it may be applied to MESFET and MODFET analyses [4].

In this work we demonstrate the application of the proposed capacitance methods for investigation of multi-layer non-uniform doped nanometer structures and microwave FETs optimization for parasitic capacitances reduction. Fig.1. shows the results for our C-V profiling method in comparison with the classical C-V method. It is clearly seen that the classical C-V method is not able to represent the sharpness of the steps. The spatial resolution of our method may be 10-20A. It shows a good accuracy, stability, and convergence.

Using capacitance measurements and new numerical technique for C(V) calculation we designed multi-layer step doped FET structures (Fig.2). All investigated structures were grown by MBE. The process sequence for device fabrication has been described elsewhere [6] and is listed below:

a) ohmic contact metal evaporation, lift-off and ohmic metal alloy;
b)device isolation by mesa etching or ion implantation;
c) gate formation by E-beam lithography and subsequent lift-off;
d) device passivation;

e) overlay metallization.

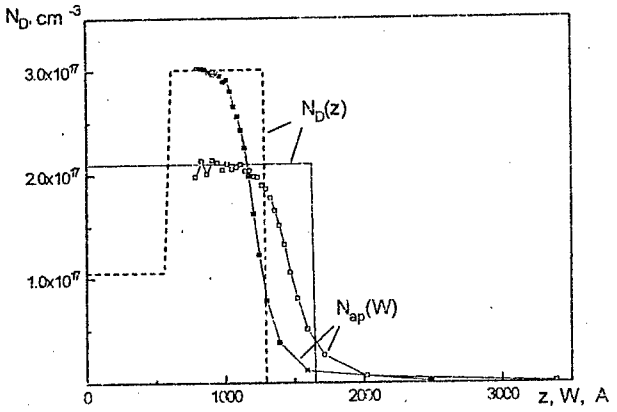

Fig.1. Classical CV method and proposed extraction method results.

Table 1 gives the main characteristics of the different FETs (W_g = 200μm). The step doped and multi-layer step doped FETs have high transonductance linearity ($\Delta g_m/g_m$ ratio of 2-3 times lower then those of typical uniformly doped GaAs MESFET) combined with high gate breakdown voltage and low fringe capacitance. The designed FETs are attractive for low-phase-noise oscillators and low-harmonic-distortion applications.

Table 1.

Parameter	Uniformly doped FET	Step doped FET	Multi-layer step doped FET
Gate length, μm	0.45	0.7	0.75
Saturation current, mA	51	60	65
Gate-drain breakdown voltage, V (I_g=10μA)	7.5	14	17
Total gate capacitance, pF	0.28	0.34	0.30
Fringe capacitance, pF	0.12	0.09	0.07
Pads capacitance, pF	0.04	0.04	0.04

Thus the present capacitance methods may be effectively used for investigation and design of multi-layer non-uniform doped structures and sub-micron microwave devices.

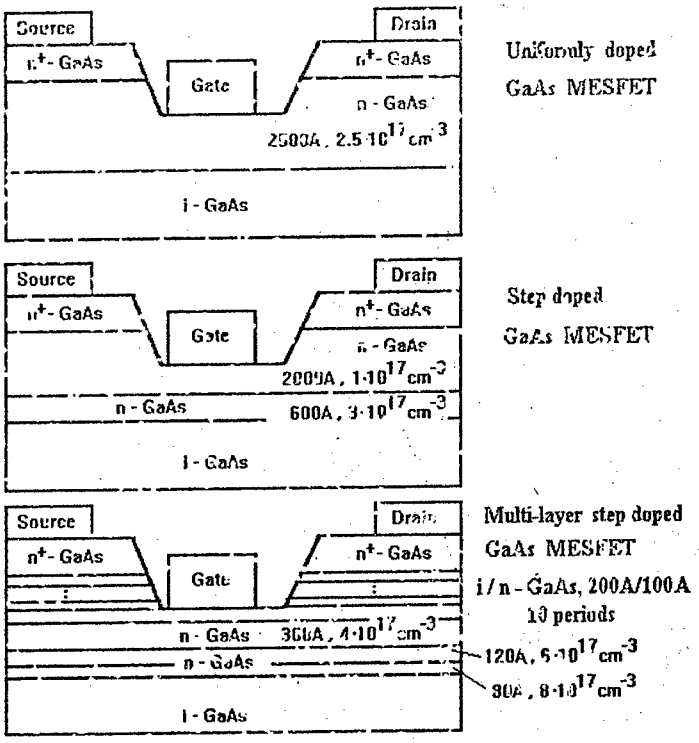

Fig.2. FET structures

1. G.J.L.Ouwerling // Solid-State Electronics, v.33, 1990, pp.757-771
2. M.F.Kokorev, N.A.Maleev, V.M.Ustinov, A.Yu.Egorov, A.E.Zhukov // Int. Symp. Nanostructures: physics and technology:Abstracts.- St.Petersburg,1996,pp.161-164.
3. R.Anholt, S.Swirhun // IEEE Trans. Microwave Theory and Techn., v.39, 1991, pp.1247-1251.
4. M.F.Kokorev, N.A.Maleev // Solid State Electron.,v.39,1996,pp.297-302.
5. R.Anholt // Solid State Electron.,v.34,1991,pp.515-520.
6. V.M.Ustinov, A.Yu.Egorov, A.E.Zhukov, P.S.Kop'ev, V.A.Krasnik, N.A.Maleev // Microelectronica, V.23,1994, pp.13-18.

Capacitance-voltage profiling of heterostructures with quantum wells at different temperatures

M.A.Melnik, A.N.Pikhtin, A.V.Solomonov, V.I.Zubkov, F.Bugge*

St. Petersburg Electrotechnical University
Prof. Popov str. 5, St.Petersburg, 197376, Russia
*Ferdinand-Braun-Institut fur Hochstfrequenztechnik, Berlin

Structures containing single quantum wells were investigated by C-V profiling at different temperatures. The structures were grown by MOVPE on GaAs-substrates and had the active zone as a high power laser diode [1]. The layer sequence of the structures is shown in Fig.1.

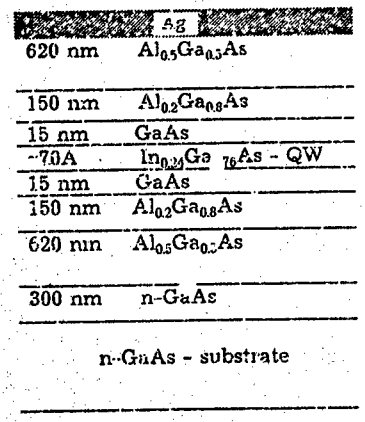

Fig.1. Layer sequence of structure being tested (Sample #020126)

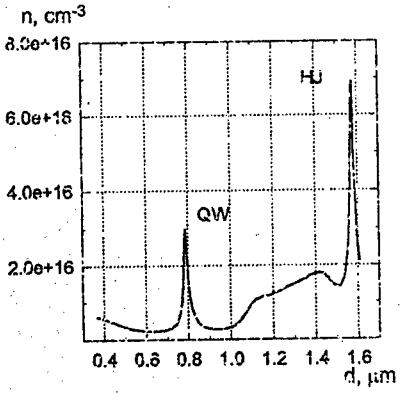

Fig.2. Apparent profile of electron concentration in the sample with QW (#020126, T=300K)

The layers except 300 nm n-GaAs were specially undoped and Schottky barriers were fabricated on the top of the structures.

Fig.2 shows measured by C-V - techniques the carrier distribution in the sample containing single QW. When derived the free carrier concentration we took in mind different values of dielectric constant ε in the layers. The first narrow peak at depth 785 nm (Fig.2) from Schottky-barrier corresponds to the carriers accumulated in the $In_xGa_{1-x}As$ quantum well and the second one to $Al_{0.5}Ga_{0.5}As$ / GaAs - heterojunction. We have measured carefully the C-V response of the QW at different temperatures. The results are presented in Fig.2. The height of QW-peaks (n_{max}) and the half-width Δ of the peaks as a function of temperature can

be seen in insert in Fig.3. It should be noted that Debye length in these materials

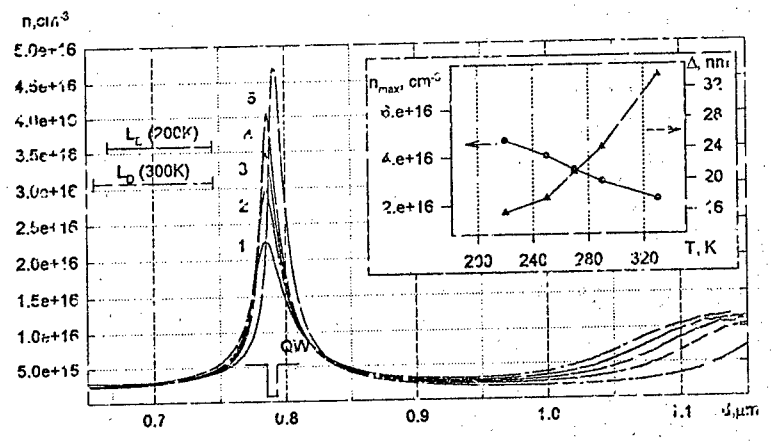

Fig.3. Temperature dependence of apparent carrier profile across the QW (1 - 330K, 2 - 290K, 3 - 270K, 4 - 250K, 5 - 220K).
Insert: Amplitude of the peaks and their half-width as a function of temperature.

is about 150 nm at T=300K and 80 nm at 200K (dopant concentration of GaAs-layer was approximately $2*10^{15}$ cm^{-3}). It means that sub-Debye resolution took place. The width of the concentration peaks were some larger than the geometric width of the quantum well itself because of the Debye smearing. It's interesting that other heterojunctions were not displayed, because of the QW had completely depleted the surrounding areas.

In the intentionally doped structures the isotype heterojunction p-$Al_{0.2}Ga_{0.8}As$ /p-$Al_{0.5}Ga_{0.5}As$ was studied into details. The hole distributions near the heterojunction derived from C-V-measurements at various temperatures are shown in Fig. 4 by solid lines. The amplitude of accommodation layer's signal increased on 60% when the temperature changed from 290K down to 120K. To obtain the value of valence-band offset we ran a numerical simulation of C-V-profiles by solving the Poison's equation. The incomplete ionisation of holes in $Al_xGa_{1-x}As$ was taken into consideration [2]. The results of the fittings for five temperatures are also shown in Fig.4 by bold symbols. The value of valence-band discontinuity (ΔE_v) in p-$Al_{0.2}Ga_{0.8}As$ /p-$Al_{0.5}Ga_{0.5}As$ was 39% of the total band-gap offset at room temperature. We found that the relative value of ΔE_v was temperature dependent. ΔE_v changed monotonously from 39% to 35% when the temperature decreased from 300K to 120K. Basing on the data [3] we found the absolute values of valence-band offsets as it shown in Fig.5.

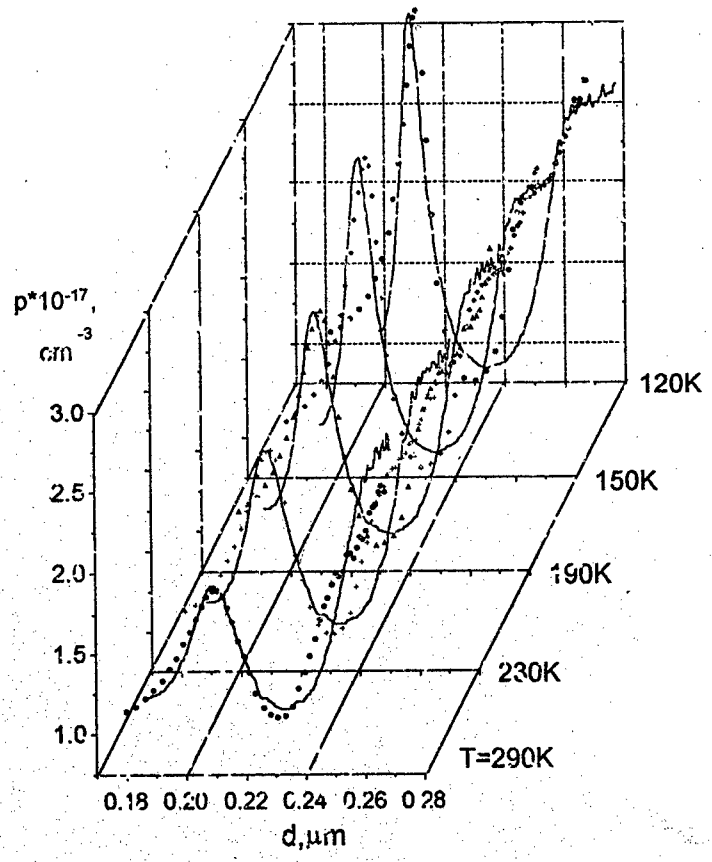

Fig. 4. The apparent carrier (hole) profiles of p-$Al_{.02}Ga_{.98}As$ /p-$Al_{.35}Ga_{.65}As$ - heterojunction (solid lines) and fitted curves (symbols) at different temperatures.

In addition, the temperature dependence of total band-gap offset ΔE_g is presented in Fig.5. One should be noted that the temperature coefficient of ΔE_v is larger than of ΔE_g. The nature of this phenomenon is discussed.

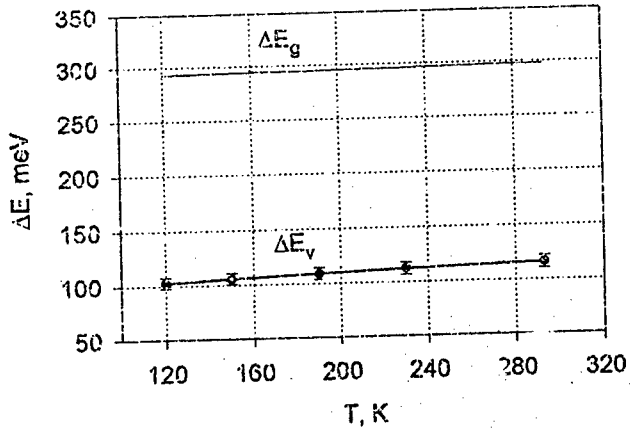

Fig.5. Temperature dependence of valence-band offset ΔE_v and total band-gap offset ΔE_g of the p-$Al_{0.2}Ga_{0.8}As$ /p-$Al_{0.5}Ga_{0.5}As$ - heterojunction.
Error bars for calculated ΔE_v are shown.

References

1. F.Bugge, G.Erbert, A.Knaurer, I.Rechenberg, U.Zeimer, M.Weyers. 23 Int. Symp. on Compound Semiconductors. - St.Petersburg, Russia, 1996. - Summaries, p.96.
2. M.A.Melnik, A.N.Pikhtin, A.V.Solomonov, V.I.Zubkov, F.Bugge. 23 Int. Symp. on Compound Semiconductors. - St.Petersburg, Russia, 1996. - Summaries, p.62.
3. Adachi S. J. Appl. Phys., 54, 1844 (1983).

Capacitance and current characterization of GaAs with InAs quantum layer/dots

A.V.Murel, V.M.Daniltsev, O.I.Khrykin, V.I.Shashkin
Institute for Physics of Microstructures , Russian Academy of Sciences
GSP 105, 603500, Nishn/ Novgorod, Russia
e-mail: murel@ipm.sci-nnov.ru

Nowadays significant attention is paid to research of quantum dots self-organizing processes in strained heterostructures. In this paper we report the results of a study of GaAs/InAs/GaAs heterostructures, grown by metallorganic chemical-vapor deposition (MOCVD) carried out by the electrical methods. The thickness of an InAs layer in them was varied in a wide range. Optical investigations of these structures were published earlier [1].

The GaAs/InAs epitaxial heterostructures were grown in gas environment, H_2-Ga $(CH_3)_3$-AsH_3, at atmospheric- pressure in a vertical reactor with the induction heating of a substrate. Trimethylindium was used as indium source material. We used both semi-insulating, and low-resistant GaAs substrates, 2°-misoriented with respect to the [100] plane in the (110) direction. The growth temperature was varied in the limits 550-650°C for GaAs and 450-650°C for InAs. The test structures were essentially epitaxial layers n-GaAs of 0.5 microns thickness with electron concentration $(1.5\text{-}3)\times10^{17}$ см$^{-3}$. At depth L≈0.15 microns from the surface, a layer with an InAs content depending on duration and rate of the deposition was built in. Earlier studies by the electron and tunnel microscopy methods revealed growth of small - several tens nanometers - islands. For the electrical research, diodes with Schottky barriers (SB) of 500 microns diameter were made by thermal deposition of aluminium through a metal mask. Capacitance-voltage (C-V) characteristics measured on frequencies 1MHz, 10 and 1 kHz, current-voltage (I-V) characteristics were registered in a range of currents $10^{-12} \div 10^{-1}$ A. Measurements were carried out at temperatures 300, 78 and 4 K.

C-V measurements.

The built - in InAs layers were placed at such a distance from SB that at a zero bias voltage the width of the space-charge region (SCR) W (0) was less than the L. C-V looked like typical structures containing quantum layers (quantum wells and dots), i.e. we observed a step of capacitance when SCR SB reaches quantum layers [2,3]. In fig. 1 the experimental CV-profiles of structures with various thicknesses of a InAs layer, expressed in effective monolayers (ML), are given, which were derived from C-V plots, measured at 78 K. For a level of concentration of carriers in a matrix 2×10^{17} см$^{-3}$ the peak in a CV-profile, connected with a quantum layer, is resolvable from thickness 0.5 ML InAs. The estimation of surface electron charge density n_w in a quantum plane was carried out either by numerical integration of the peak in the CV-profile, or from the size of the plato on dependences $1/C^2$ (V) [3]. In fig. 2 the dependence of n_w on effective thickness of a quantum layer for three temperatures of measurement is given. Up to 2ML there is a sharp increase in n_w due to intensive growth of the number of islands. From 2ML to 4ML, the growth of islands proceeds in size rather that in number. It is supposed [4] that at excess of thickness 6ML, the islands reach the critical sizes, which is accompanied by formation of dislocations, probably, defects, overlapping and coalescence of islands. Nevertheless, n_w does not decrease, but at large ML a stronger temperature dependence n_w (T) is displayed.

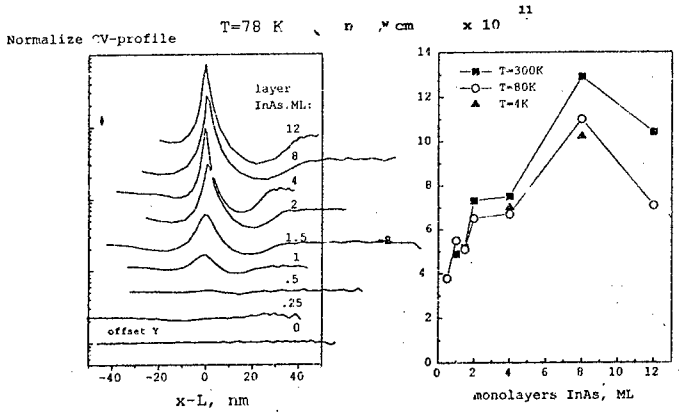

Fig.1. C-V profiles of heterostructures with various InAs thicknesses (in ML), normalized to carrier concentrations in the GaAs matrix. The coordinates in x are arranged relative to the quantum layer, on the y axis - the curves are shifted.

Fig.2. Dependence of surface concentration of confined electronов n_w in the quantum layer on its thickness (in ML).

I-V-T measurements

With higher reverse bias voltages the quantum layer becomes a part SCR of a semiconductor and can influence the transport of carriers in a cross direction due to their emission and capture, and also because of potential barriers. Fig. 3 shows the reverse I-V of structures with various thicknesses of the InAs layer. It is seen that the reverse current is really increased up to 5 orders in comparison with the structure without a InAs layer. The I-V dependence changes its character at large ML. It is most clearly seen on temperature dependences I-V-T (fig. 4). The bottom series of curves is characteristic for samples with a small thickness of a quantum layer (0.5-1.5 ML). At small voltage (up to -1V) appropriate, according to the C-V data, to an arrangement of a quantum layer outside the SCR, a strong temperature dependence of a current is observed, caused by the process of overcoming by electrons of the barrier on the interface metal / semiconductor, which makes 0.75-0.8 eV from the CV and IVT measurements. When with an increase of a bias voltage the quantum layer gets in a field SCR, the temperature dependence of current becomes weak. And, accordingly, the derived activation energy falls practically down to zero at a rather large bias voltage and low temperatures. Out of all possible mechanisms of increase of a current, the most probable one is growth the of the current components connected with minor carriers. The source is thermogenerated holes in a quasi-neutral region of a semiconductor, which fall in the potential well of the quantum layer and are extended to the area of contact by application of electrical field to the latter. Further they overcome the potential barrier by means of thermo-emission at high temperatures and tunneling - at low T, thus reaching the metal - semiconductor interface and

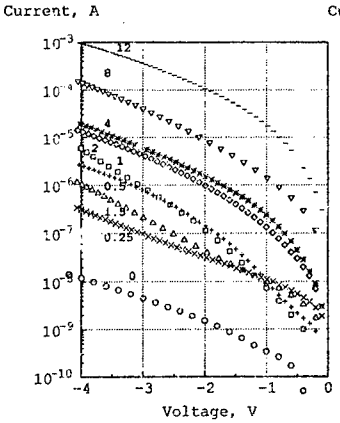

Fig.3. Reverse I-V for structures with various thickness of a InAs quantum layer (in ML).

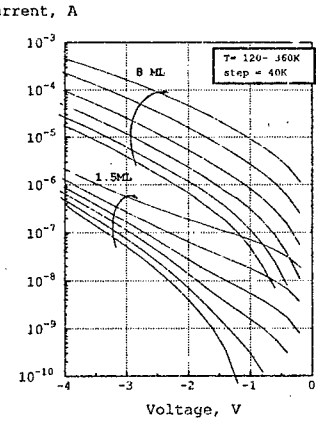

Fig.4. Temperature dependences I-V for two types heterostructures:
Bottom - 1.5 ML, top - 8 ML InAs.

making the major contribution to the reverse current. Then, the activation energy is supposed to characterize the process of hole emission from the potential well of the quantum layer.For samples with thicknesses 2-12 ML, the character I-V dependence changes (top series of curves in fig. 4), the activation energy of carrier transport practically ceases to depend on a bias voltage, and the curves straighten in coordinates lg I vs $V^{1/2}$. Such character of dependence is usually associated with conductivity caused by the Pool-Frenkel effect for emission with traps, facilitated by an electrical field [5]. It is obvious that it is connected with formation of quantum islands of critical sizes, their coalescence and thus arising defects. On the basis of the above experimental data it is possible to assume that defect- or dislocation-free quantum layers and/or dots will be formed up to thickness ≤1.5 ML, and further the defects manifested are formed most likely on the islands boundaries.

Thus, capacitance research has allowed to determine the characteristics of quantum layers, related to the major carriers (confined electrons), in potential wells, while the measurements of cross conductivity characterize emission of minor carriers, i.e. holes from quantum layers/dots.

The work was supported by RFBR, grant N95-02-05870 and Program "Physics of Solid-State Nanosuructures"

References

1. *V.Ya.Aleshkin,S.A.Gusev,V.M.Danil'tsev et al* Internat.Symp."Nanostructures", St.Peterburg, Russia, 24-28 June, 1996, p.148.
2. *V.Ya.Aleshkin,E.V.Demidov,A.V.Murel et al.* Fiz.Tehn.Poluprovod.,25,N6,1991,pp.1047-1052.
3. *P.N.Brunkov,S.G.Konnikov,V.M.Ustinov et al.* Fiz.Tehn.Poluprovod., 30, N5, 1996, p.924.
4. *A.Yu.Egorov,A.E.Zhukov,P.S.Kop'ev et al.* Fiz.Tehn.Poluprovod., 30, N8, 1996, p.1345.
5. *R.B.Hall* Thin Solid Films, 8, N4, 1971, p.435.

RADIO-FREQUENCY MODULATED REFLECTANCE IN SEMICONDUCTOR HETEROSTRUCTURES WITH 2D ELECTRON GAS

O.A.Ryabushkin

Institute of Radio Engineering and Electronics , Russian Academy of Sciences, Vvedensky sq. 1, Fryazino, Moscow District, 141120, Russia, E-mail: roa228@ire216.msk.su

We have observed strong effect of the amplitude-modulated ac electric field on reflectance spectra of probing light beam in GaAs/AlGaAs heterostructures. This phenomenon is shown to be due to the availability of 2DEG and excitons in buffer layer of the GaAs. It may be used as a basis of modulation spectroscopy which can be named as

radio-frequency or microwave modulated reflectance (RMR or MMR)

provides information about electrons and excitons of conducting layers with very low energy of external action being required.

The heterostructure under the investigation is placed between the plates of the capacitor across which ac voltage is applied of the frequency 1-30 MHz (Fig.1). One plate (nearest to 2DEG) has a hole through which the probing light beam falls on the sample and RMR spectra are obtained. The amplitude of the ac voltage was varied from 0 to 300 V, with the inter-electrode distance being 1 mm. The external ac electric field causes the spatial redistribution of the free charge carrier density along the heterostructure depth (Fig.2). There are some effective ways in which external ac electric field E_{ac} redistributes the electron density. One possibility is that the electric field is normal to the heterostructure layers. It disturbs the potential energy of the electrons across the layers and the position of the quantum levels in the quantum well. When E_{ac} is directed to the 2DEG layer from the GaAs bulk (Z- direction), the quantum level moves up so the barrier that separate 2DEG from doped layer of AlGaAs is lowered. Hence the electrons go to the wide well in AlGaAs and the total number of electrons in GaAs buffer is diminished. E_{ac} of opposite direction (-Z) forces the remaining electrons to move deep into the GaAs buffer. In such a way under the action of E_{ac} the free electron charge density is strongly redistributed in heterostructure giving rise to modulation the refrective index or attenuation index in the range of energy near interband critical points (CP's). The exciton states in GaAs bulk the more sensitivity to the change of the electron concentration. For this reason the more strong effect of the amplitude-modulated ac

electric field on reflectance spectra of probing light beam in GaAs/AlGaAs heterostructures near energy excitons recombination.

The samples used in our experiments were the modulation-doped heterostructures $GaAs/Al_xGa_{1-x}As$ ($x \approx 0.2 - 0.3$) grown by molecular beam epitaxy with parameters commonly used for the high-electron mobility transistors. The samples are characterized by their wide buffer layer (L_b) of the GaAs. The mutual arrangement of the capacitor with the sample and fibers is illustrated in Fig.1. Radio-frequency voltage $V(t) = V_0(1+\cos\Omega t)\cos\nu t$ is modulated in the amplitude and then is applied across the capacitor. Modulation frequency Ω is $\sim 2*10^3$ Hz, ν is high - or superhigh - frequency $10^5 - 10^{10}$ Hz. Variations in the modulation frequency from 10^2 Hz to 10^4 Hz does not substantially affect our results.

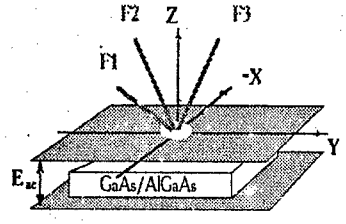

Fig.1. The spatial arrangement of the sample and the fibers. Electric field Eac is perpendicular to the surface of the heterostructures

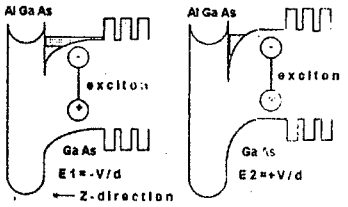

Fig.2. Energy diagram of the heterostructure with 2D electron gas under the action of external ac electric

Electric field strength in the capacitor is defined as $\mathbf{Eac}=V_0/d$ (d is the spacing between the capacitor plates, $d \sim 1$ mm). The fiber F1 is aligned in coordinate plane XZ and is directed at angle $\sim 45^0$ to the structure surface. Being rigidly bound with the sample this fiber forms the exciting light spot of ~ 100 μm in diameter. A little part of the exciting light intensity is reflected to be used for control the pump intensity. The exciting light beam from He-Ne laser ($\lambda = 633$ nm) is mechanically chopped at $1.5 \cdot 10^3$ Hz. The fibers F2 and F3 are used to measure both the photoluminescence (PL), photoreflectance (PR) and RMR intensities. It worth to emphasize that we don't use any laser excitation when the RMR is measured. The temperature of the sample can be controlled in the range from T1 = 290K to T2 = 77K. It is shown from the PL spectra that the electron temperature (T_e) is independent of the electric

field strength if the Eac < 500V/cm. We observed the strong difference between PR and RMR spectra measured at room temperature not only in the vicinity of the E_gGaAs but $E_gAlGaAs$ band gaps too (Fig.3). It must be emphasized that RMR spectrum in the vicinity of the $E_gAlGaAs$ is absent in the sample with width of the buffer layer L_b ~ 1μm. The RMR and PR spectra measured in the sample with the L_b ~ 0.015μm at T2 = 77K are shown in Fig.4. RMR spectra have a complex structure in the wide range of energy.

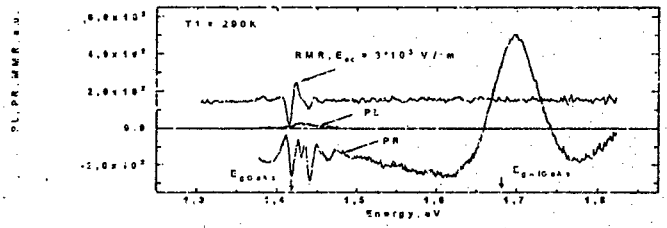

Fig.3. PL. PR and RMR spectra for the sample with L_b ~ 1μm *at T1=290K after computer processing. The PR and RMR are displaced below and above zero correspondingly*

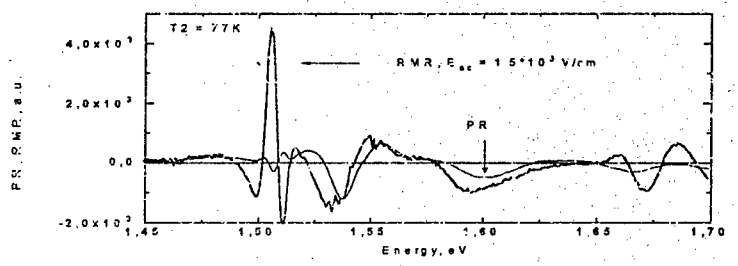

*Fig.4. The RMR (Eac = 1.5*10³V/cm) and PR spectra for the sample with* L_b ~ 0.015μm *at T2=77K*

A comparison between these spectra shows that the most distinction is observed only in narrow region (ΔE ~ 20meV) close to the energy E ~ 1.508eV (Fig.5).The temperature dependence RMR spectrum for this sample is more drastic. Increasing the temperature from T1 to T2 increased the signal of the RMR more than thousand times.

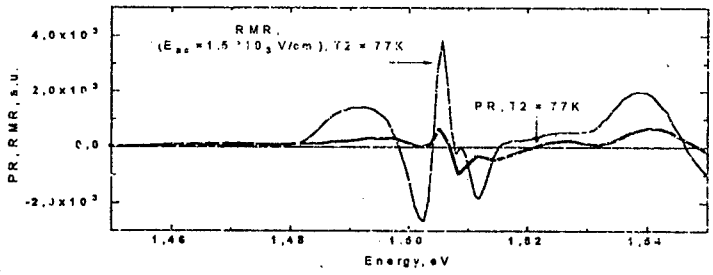

Fig.5. The RMR and PR spectra for the sample with $L_b \sim 0.015\mu m$ *at* $T2=77K$ *and* $E_{ac}=1.5*10^3 V/cm$, *with a resolution spectrometer* $\Delta E \sim 0.7mV$

The investigations of the RMR open up new opportunities for applications as a new kind of the modulation spectroscopy designed for the contactless characterization technique of highly conducting layers in semiconductor heterostructures. Commonly used photoreflectance or electroreflectance technics require much more power action on the object than the RMR. In RMR case radio - frequency or microwave radiation power is substantially lower than the light pump in PR and PL. In addition, there are large variety of radio-frequency or microwave generators and amplifiers (in contrast to light sources), which enables us to devise a new techniques for measurements of the RMR or MMR spectra. On the other hand the streng effect of modulated ac electric field on a reflectance of light gives a new possibility in the design of the appropriate high-speed optical modulators.

Acknowledgments

I would like to thank V.A. Sablikov for helpful discussions and encouragement in the course of this work.

This work is supported by Russian Foundation for Basic Research (grant 96-02-18476-a) and Russian Ministry of Science under the Program "Physics of solid state nanostructures".

DEEP LEVEL TRANSIENT SPECTROSCOPY OF THE InAs/GaAs VERTICALLY COUPLED QUANTUM DOT LASERS STRUCTURES

M.M.Sobolev, A.R.Kovsh, V.M.Ustinov , A.Yu. Egorov, A.E. Zhukov, M.V. Maximov and N.N. Ledentsov
A.F.Ioffe Physical Technical Institute, 194021 St. Petersburg, Russia

Recently, there has been considerable interest in studies of carrier localization in quantum dot (QD) heterostructures [1-3]. A remarkable progress in this area was achiveved recently when direct growth methods involving self-organization phenomena on crystal surfaces were developed [1]. First injection laser with low current density and high temperature stability based on InAs and InGaAs quantum dots in GaAs matrix were created at A.F.Ioffe Institute [2]. Additionally, the formation of new type of QDs structures i.e. vertically coupled QDs via tunneling suitable for fabrication of cascade laser has been demonstrated. At the same time the specific growth conditions of the QDs (low temperatures of the deposition) must stimulate to generation of the point defects in the vicinity the QDs due to a local stoichiometry variation during the growth of a heteroepitaxial layer, and which acts as centers of the capture and of the nonradiative recombination. At near room temperature the thermal emission of the carriers from quantum dots and they retrapping by the defects must causes to decrease of the quantum efficiency of the radiative recombination and degradation of the lasers. In this work we report on the deep level transient spectroscopy (DLTS) and capacitance-voltage (C-V) studies of InAs/GaAs vertically coupled quantum dot (VECOD) structures inserted in an active region of laser diode. The QDs are formed self-organized in a p-type GaAs matrix during molecular beam epitaxy.

From C-V profiles the spatially localization associated with QDs has been determined (Fig.1). We

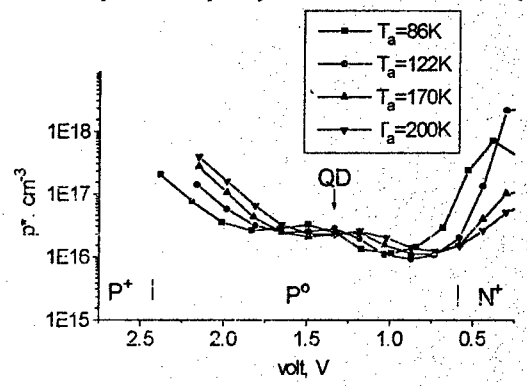

Fig.1 The apparent carrier concentration profile of the InAs/GaAs vertically coupled quantum dot (VECOD) laser structure obtained from 1 Mhz C-V measurements.

apply different combinations of bias voltages V_b and of filling pulse voltages V_f to perform the DLTS study of the regions below, coincident, and above the layer with VECODs. The measurements has demonstrated clear signal due to localization of carriers in QDs. Additionally,

some concentration of deep traps ($\approx 10^{11}$ cm^{-2}) has been revealed in the region spatially coincident with QDs. Our investigation show that point defects forming at low temperature GaAs growth during multiple InAs-GaAs deposition cycles were like those forming in GaAs under Ga-rich condition. Among them are a antisite double acceptor Ga_{As} with ionization energies 77 and 230 meV from the valence-band edge [4] and HL5 defect with energies 390 meV. We found that DLTS spectra are changed dramatically for isochronous annealing temperatures below and above 245 K and for cooling conditions $V_f>0$ or $V_b=0$ (Fig.2). After annealing at $T_a>245K$, apart from

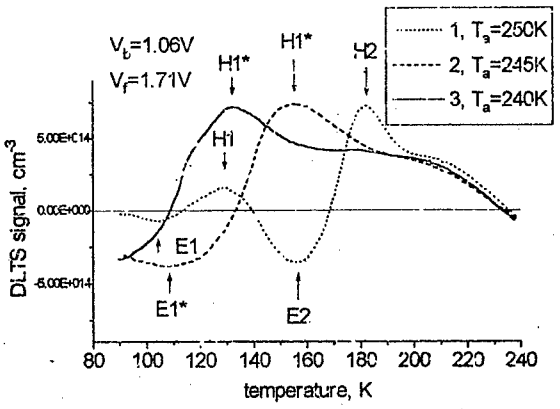

Fig.2. DLTS spectra of InAs/GaAs vertically coupled quantum dot structures at the various isochronous annealing temperatures T_a and preliminary cooling conditions $V_f>0$.

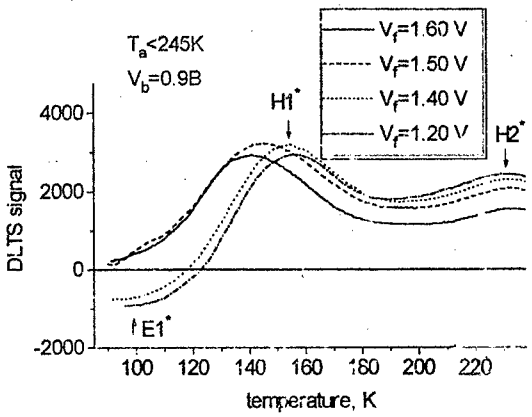

Fig.3. DLTS spectra of InAs/GaAs vertically coupled quantum dot structures at the various V_f and after annealing at Ta<245K and preliminary cooling conditions $V_f>0$.

Table

Deep level No	Energy, mev	Cross section, cm^2	Identification and origin
$T_a > T_{ac}$			
E1	111	$1.7x10^{-17}$	
E2	235	$1.3x10^{-14}$	EL14(Ni) [5]
E3	426	$4.2x10^{-16}$	Ni_{Ga} [6]
H1	194	$2.5x10^{-16}$	
H2	390	$1.8x10^{-13}$	HL5 [7]
H3	420	$1.6x10^{-14}$	HL4(Cu) [7]
$T_a < T_{ac}$			
E1*	110	$5.2x10^{-16}$	
H1*	194	$2.5x10^{-18}$	
H2*	420	$1.6x10^{-14}$	HL4(Cu) [7]

well-known for GaAs EL14 and HL5 levels, E1 electron and H1 hole levels were observed (Table). After annealing at T_a<245K the peaks, related to these levels, disappeared and other broader E1* and H1* peaks appeared. The position of the H1* peak in DLTS spectra depended on values of V_f, annealing temperature T_a, cooling conditions (V_f>0 or V_b=0) (Fig.3) and optical illumination A thermal activation energy of the H1*level also varied from 132 to 199meV with V_f, T_a. After illumination and cooling at V_f >0, when the carriers from QDs photoexcited, peak are shifted towards the position measured at V_f =0. The effects observed demonstrate that formation of an additional potential barrier takes place and H1* level is not a metastable defect. The position of the H1 peak in DLTS spectra depends on the V_b value (Fig.4.). On contrary, the amplitude and shape of the peak are not changed. A energy of the H1 level varied from 89 to 194 meV. A energy of the E1 and E1* are coincident and equals 110meV. Our results allowed us to conclude that H1, E1 and H1*, E1* levels are related with the same VECOD. At annealing at T_a<245K and cooling at V_f>0 QDs are occupied

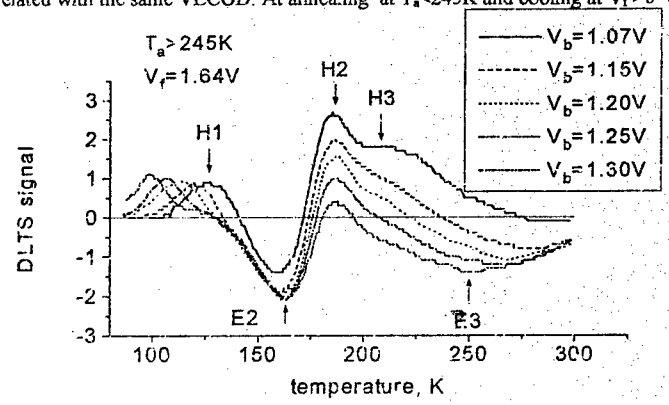

Fig 4. DLTS spectra of InAs/GaAs vertically coupled quantum dot structures at the various V_b and after annealing at T_a>245K and preliminary cooling conditions V_b=0.

by carriers. Coulomb interaction between the charged QDs and deep centers located in regions close to QDs takes place and dipoles are formed. The electrostatic potential caused by these dipoles is superimposed to the QD potential barriers caused by conduction and valence band discontinuities. The carriers from deep levels can tunnel into quantum dots from which they were previously thermally evaporated. This effect is responsible for the appearance of the broad band in DLTS spectra which replaces the EL14 and HL5 levels. At annealing temperatures T_a >245 K QDs the carriers are evaporated from QDs and dipoles can not be formed. In this sense, the observed shift of the energy is connected with an effect of lowering of the potential barrier for carrier emission from VECODs and with tunneling through its due to p-n junction-induced electric field.

References

[1] N.Kirstaedter, N.N.Ledentsov, M.Grundmann, D.Bimberg,V.M.Ustinov, S.S.Ruvimov, M.V.Maximov, P.S.Kop'ev, Zh.I.Alferov, Electron Lett., **30**, 1416, (1994).

[2] V.M.Ustinov, A.Yu.Egorev, A.R.Kovsh, A.E.Zhukov, M.V.Maximov, A.F.Tsatsul'nikov, N.Yu.Gordeev, S.V.Zaitsev, Yu.M.Shernyakov, N.A.Bert, P.S.Kop'ev, Zh.I.Alferov, N.N.Ledentsov, J.Böhrer, D.Bimberg,A.O.Kosogov*, P.Werner, U.Gosele, Proc. 9 Int. Conf. On MBE, Aug. 5-9, 1996, Malibu, USA, Abstrct Book, p.3.1 (to be published in Jornal of Crystal Growth ,vol. 175, (1997).

[3] S.Anand, N.Carlsson, M-Epistol, L.Samuelson, W. Seifert , Appl. Phys. Lett. **67**, (1995).

[4] Ph_Won Yu, W.C.Mitchel, M.G.Mier, S.S.Li, W.L.Wang.Appl. Phys.Lett., **41**, 532 (1982).

[5] L. Samuelsoson,P.Omling,H.Titze, and H.G.Grimmeis. J.Cryst.Growth, **55**, 164 (1981).

[6] D.L.Partin, J.W.Chen, A.G.Milnes, L.F.Vassamillet, J.Appl.Phys, **50**, 6845 (1979).

[7] A.Mitonneau, G.M.Martin A.Mircea. Electron.Lett., **13**, 666 (1977).

Degradation of SCH QW and GRIN SCH QW with short period superlattices GaAs/AlGaAs lasers grown by MBE

V.E.Tokranov, V.P.Evtikhiev, E.Yu. Kotelnikov, I.V. Kudryashov, D.V. Prilutsky, N.N. Faleev

A.F.Ioffe Physico-Technical Inststute, Russian Academy of Sciences, St. Petersburg, Russia

In our work we investigated an effect of laser heterostructures crystal quality to the reliability of separated confined heterostructre with quantum well (SCH QW) lasers. Two types of SCH QW laser heterostructures have been choosen for the investigations. The schematic kind of structures is presented on fig.1. The first type is an area of generation, which represents GaAs quantum well (QW) with barriers, formed by the solid solution AlGaAs. The second type differes by that the barriers are formed by a short period binary superlattice AlAs/GaAs. The structures are grown by an MBE method. For each type there was specially grown a number of structures at various modes of growth, which were selected and controlled by the RHEED method.

High resolution X-ray diffractometry was applied for initial diagnostics of obtained heterostructures: a widely used method for research of various heterostructures [1]. The method has the high spatial resolution, comparable for a certain type of heterostructures to the resolution of transmission electron microscopy, high sensitivity to crystal structural perfection, making possible to study peculiarities of of epitaxial growth mechanisms and defects generation in heterostructures [2].

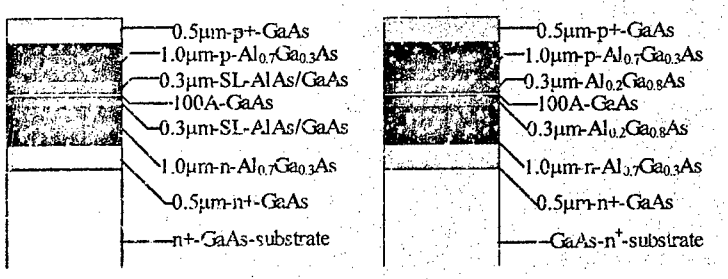

Type II Type I

Fig1 Schematical kind of the grown heterostructures.

Structure	I_{thr}	η	Type	Lifetime	static Debay-Waller factor
	A/cm²	%		(hours)	cladding QW layer
A254	200	35	I	10	-
A219	250	34	I	80	0.67
A224	220	35	I	200	0.92
A327	175	40	II	2900	0.99
A309	180	40	II	2500	0.97

Table 1. Comparison of the static Debay-Waller factor for cladding QW layers, threshold current density, differential quantum efficiency and type of heterostructure with lifetime of lasers.

Preliminary analysis of X-ray diffraction curves (RC), received for all researched laser heterostructures confirmed that all heterostructures have high crystal perfection. Epitaxial layers are planar with the sharp interfaces, density and size of structural defects are not this large to introduce nonplanarity of layers. The volume strain and diffuse scattering resulted (in conditions used for measuring) in the smoothness of interference fringes and broadening of the main diffraction peaks. On fig.2 there are shown experimental and calculated characteristic RCs. The difference in parameters of experimental RCs from the calculated ones (the comparison was performed from the factors of reflection of the basic structural peaks - from the substrate cladding quantum well and emitter layers) is at good agreement with the form of curves, which indicates an existence of crystal defects of mainly dot or claster types in the investigated heterostructures. For precise fitting the parameters of calculated curves was used the static Debay-Waller factor without consideration of the size of defects. The values of obtained static Debay-Waller factors are submitted in table 1.

There were also manufactured laser diodes from the heterostructures investigated by X-ray method. They have a form of a stripes of 100мкм in width and 700мкм in length with SiO_2 isolation and mirrors formed by cleaving without special coatings. The diodes were mounted on heatsinks with the p-layer located downwards. The devices are characterized by the good threshold characteristics in the range 180-250 A/см² and differential quantum efficiencies in the range 70-80%. These data demonstrate high quality grown heterostructures. For each heterostructure there was estimated the average lifetime for a series of laser diodes at an emitting power of 0.4W on each mirror, which is shown in table 1. The analysis of degraded lasers has shown that degradation is caused by development of defects of dark lines in the field of generation.

The comparison of the static Debay Waller factor for various layers with the lifetime of lasers shows that crystal lattice perfection of cladding QW layers determined from X-ray date by means of the static Debay-Waller factor correlates well with the degradation characteristics of laser diodes. And though the obtained data do not permit to estimate quantitatively the density and size of growth defects, as far as detailed measurements of diffuse part of scattered X-ray radiation are necessary for this purpose, for qualitative estimations of the degradation characteristics of laser structures is seemed well correctly appiying the double crystal difractometry and the static Debay-Waller factor as basic parameter for an estimation of structural perfection. The lifetime of laser diodes has appeared to be sensitive to the value of the static Debay-Waller factor, while such

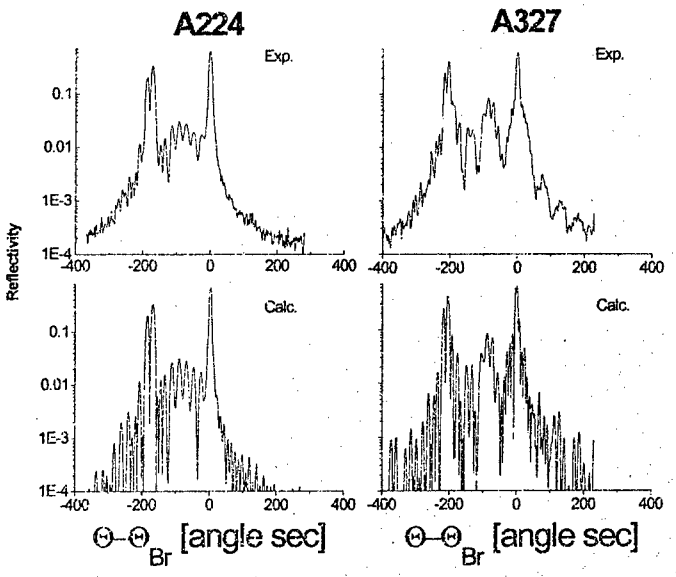

Fig.2. Experimental (top) and calculated (bottom) RCs for heterostructure A224(type I) and A327 (type II).

features as a threshold current and the differential quantum efficiency are not affected by the wide variation of crystal perfection of the quantum well cladding layers. The higher crystal perfection is reached by applying a binary superlattice AlAs/GaAs as a cladding layer instead of a solid solution AlGaAs (as shown at Table 1). Obtained result shows tha applying the shoi. period binary superlattices permits to obtain higher quality semiconductor heterostructures at wide range of growth parameters in comparison with heterostructures based on the solid solution AlGaAs.

This work was supported by the Russian Foundation for the Basic Research (Grant N97-02-18153).

References.

1.M.A.G.Halliwell and M.H.Lyons, J. Cryst. Growth, **68**, (1984), 523.
2. V.G.Gruzdov, A.O.Kosogov, N.N.Faleev, Techn.Phys.Lett., **20**(7), (1994), 561.

Fabrication of silicon quantum dots by pulsed-gas plasma processes and their properties

Shunri Oda
Research Center for Quantum Effect Electronics
Tokyo Institute of Technology
O-Okayama, Meguro-ku, Tokyo 152, Japan

We have proposed a novel method for the fabrication of nanocrystalline silicon (nc-Si) quantum dot structures with size less than 10nm and a very small spread of size (1nm).[1-4] Nanocrystalline silicon is formed by very-high-frequency plasma decomposition of silane [5] and coalescence of radicals. The basic idea for the formation of uniform structure is separation of the nucleation and the crystal growth processes. We have introduced hydrogen gas pulse into a silane plasma, that enhances nucleation of nc-Si particles. The nuclei grow in size in the silane plasma during the off state of hydrogen gas supply. The next hydrogen gas pulse forces nc-Si particles grown in the previous cycle out of the plasma cell into the deposition chamber and the next nucleation of nc-Si is enhanced simultaneously.

Nanocrystalline silicon particles can be deposited onto any kind of substrate at room temperature. Typically, as substrates we used carbon microgrids for TEM measurements, quartz for photoluminescence measurements [6] and thermal oxidized silicon with patterned polycrystalline silicon electrodes for electrical measurements. Nanocrystalline silicon particles are not stick firmly onto the substrates but adsorbed by the Van der Waals force. Hence the position of nc-Si particles can be manipulated by AFM tip while observing the image. We have also found that nc-Si particles are deposited preferentially at the steps of substrate surfaces.

Natural oxide which covers the surface of nc-Si plays very important role in the characteristics of nc-Si. First, the oxide serves as a potential barrier which controls charge and energy quantization, and tunneling current. Second, the oxide passivates the surface dangling bonds resulting in reduction in electron traps and enhancement of luminescence efficiency. Third, the oxide serves as glue for nc-Si to fix to the substrates.

Electrical properties of nc-Si were measured using nanostructured electrodes with a very small gap of 25nm prepared by EB lithography and ECR reactive ion etching. [7] Current-voltage characteristics from a single dot and an array of multiple dots were measured at various temperature between 77-300K. Some of the structures in I-V curves can be interpreted by a model of single electron tunneling.

1. S. Oda and A. Otobe, Materials Research Society Symp. Proc. **358**, 721 (1995).
2. M. Otobe and S. Oda, Materials Research Society Symp. Proc. **377**, 51 (1995).
3. A. Itoh, T. Ifuku, M. Otobe and S. Oda, Materials Research Society Symp. Proc. **452**, in press (1997).
4. T. Ifuku, M. Otobe, A. Itoh and S. Oda, Jpn. J. Appl. Phys. **36**, in press (1997).
5. S. Oda, Plasma Sources Sci. Technol., **2**, 26 (1993).
6. Y. Kanemitsu, S. Okamoto, M. Otobe and S. Oda, Phys. Rev. **B55**, R7375 (1997).
7. A. Dutta, M. Kimura, Y. Honda, M. Otobe, A. Itoh and S. Oda, Jpn. J. Appl. Phys. **36**, in press (1997).

Fabrication, characterization and manipulation of aerosol clusters

Knut Deppert, Sven-Bertil Carlsson, Tobias Junno, Martin H. Magnusson, Jan-Olle Malm, Chatrin Svensson, and Lars Samuelson

Lund University, Solid State Physics and Inorganic Chemistry 2
Box 118, S-221 00 Lund, Sweden

INTRODUCTION

Nanometer-scale semiconductor crystals are of considerable interest due to their electronic quantum-size effects. However, the fabrication of such structures remains difficult regarding both the size and the size uniformity. A large deviation in particle diameters will average out the quantum-size effects. Several attempts have been made to produce this type of nanocrystals. All these attempts are characterized by the fact that the nanocrystals are bound in one or the other way to surrounding material. Most of those methods result in nanocrystals with wide size distributions. In this paper we present a new fabrication route to produce size-selected III-V semiconductor nanocrystals via a simple, reliable, and efficient aerosol route.

Another interesting feature of aerosol produced nanocrystals is that they after deposition can be repositioned in a controlled way by using an atomic force microscope (AFM). The AFM technique which allows the fabrication of arbitrary two-dimensional structures can be an approach to nanocrystal electronic devices. Here we demonstrate the ability to manipulate aerosol particles as small as 10 nm in diameter.

METHOD

The fabrication route utilizes the formation of an aerosol of ultrafine group-III particles. The aerosol is formed by evaporating the metal in a tube furnace and subsequent cooling down the vapor. The aerosol particles are charged and size selection takes place in a differential mobility analyzer (DMA). This instrument is a conventional tool in aerosol technology for both the fabrication of size-selected test aerosols and the measurement of aerosols. It size-selects by balancing the mobility of charged particles in an electric field with the force of the gas used to flush unwanted particles. The size distribution reached is mainly depending on the gas flows and can be very narrow, e.g. ±5%. The monodisperse group-III aerosol is then mixed with a group-V containing gas and sent into a second furnace for reaction. After the reaction furnace, the particles produced may be deposited on a substrate by means of an electric field. The reaction process can be monitored with a second differential mobility analyzer. Figure 1 shows a schematic diagram of the process. Since this approach includes the reaction of aerosol particles and a self-organized growth of a new compound, all in the aerosol phase, we call this process aerotaxy [1].

The nanocrystals are produced using an aerosol generator setup similar to that used in previous studies [2]. Experiments were performed with either gallium or indium as source material. The metal was placed in a tube furnace and heated up to a suitable temperature (about 1100°C) resulting in a sufficiently large number of particles with a diameter below 20 nm. The particles were transported with hydrogen as carrier gas via a charging device and a DMA into a second tube furnace. Before entering the furnace a flow of either ammonia, phosphine or arsine

was mixed to the aerosol flow. The hydride flow was kept small thus not altering the aerosol flow conditions. However, the number of hydride molecules to the total number of metal atoms in the reaction zone was of the order of 10^6 to 10^7.

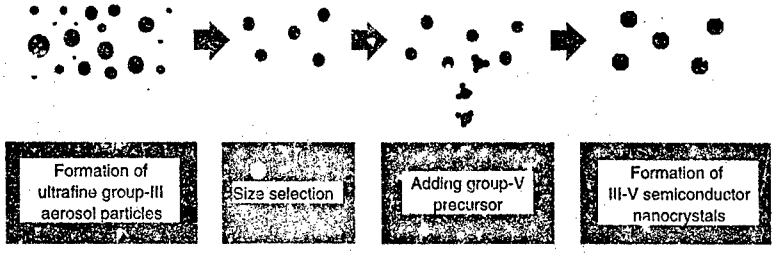

Fig. 1: Schematic diagram of the aerosol generation, sizing and reaction process.

We used a Topometrix Explorer 1000 AFM operated in ambient air for imaging and manipulation. Electron-beam deposited tips of radii down to 10 nm were used to achieve high resolution and avoid picking particles on the tip. The procedure for moving a particle is as follows: (i) The position of the particles on the surface are imaged by scanning in the non-contact mode. In this mode the lateral forces between tip and sample are sufficiently low to avoid unintended movements of the particles. (ii) Scanning is then interrupted and the tip is positioned close to the particle of interest. (iii) By moving the tip along a line crossing the center of the particle with the feedback loop turned off it will push the particle ahead, instead of following its contours as in normal imaging mode. In this way the AFM tip can reposition an individual particle several hundred nanometers without interacting with any other particles on the surface. (iv) The feedback loop is turned on again and a new image is scanned in order to reveal the effects of the manipulation.

RESULTS

The kinetics of the growth of the nanocrystalline semiconductors is deduced from the dependence of the nanocrystal formation on temperature and reactants flow. Figure 2 shows one example for the reaction of indium droplets with phosphine. This analysis leads to a consistent picture and a good understanding of mechanisms involved (indicated in figure 2). The first step is a decrease of particle diameter caused by evaporation processes. The evaporation signature disappears once the reaction of the metal with the hydride is seen to begin whereas without a hydride present the particle diameter, and even the particle concentration, decreases further. The reaction of the small droplets starts at low temperatures, lower than expected from investigations of vapor-phase growth processes. However, the temperature range for the reaction is depending on the chemistry of the hydride. The use of ammonia demands a high temperature while arsine as well as phosphine react at a much lower temperature.

After the reaction step, a stable plateau is reached where the diameter of the particles is almost constant. Here, all metal in the particle has reacted with the hydride and formed the compound material. The size of the final nanocrystal is in a self-limiting fashion dependent on the diameter of the introduced size-selected droplet. With further increasing temperature, the

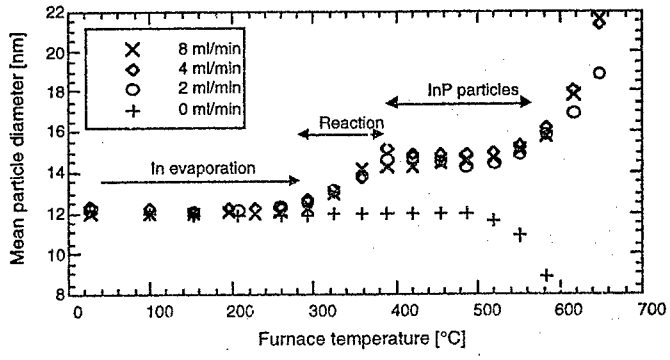

Fig. 2: Plots of the mean particle diameter of the reaction of indium particles with phosphine for different temperatures and varying phosphine flow.

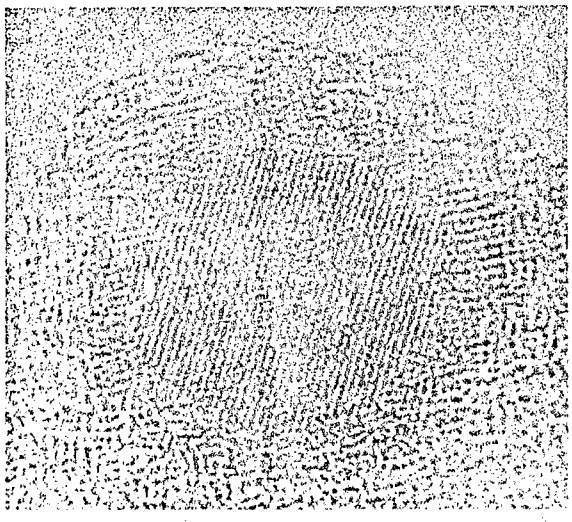

Fig. 3: Transmission electron micrograph of an indium nitride nanoparticle about 12 nm in diameter.

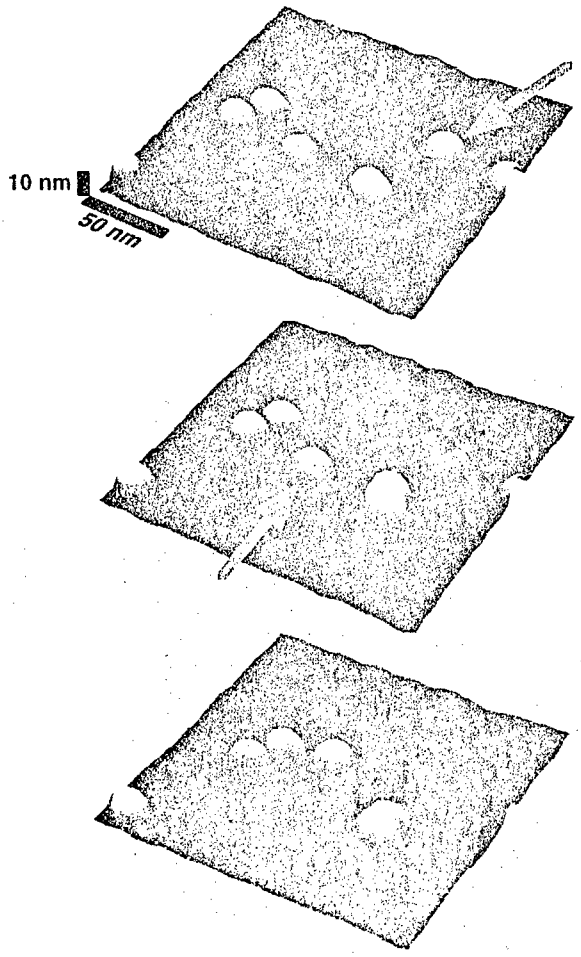

Fig. 4: Illustration of the controlled repositioning of 10 nm indium particles with an atomic force microscope.

particle diameter increases again. This process can be attributed to a homogeneous cracking of the hydride in the gas phase and subsequent condensation of the group-V component on the already existing III-V particle, thus leading to an increase in the particle diameter.

In addition to investigations of the kinetics of the formation, extended investigations of produced nanocrystals by electron microscopy and other techniques were carried out to get a more complete picture on the formation of the particles. This included the determination of the crystal structure, the size, and the composition of the particles. The final III-V particles exhibit a good crystallinity, although dependent on the process conditions, figure 3 shows one example. The tracing of the group-V content of metal droplets reacting with a hydride at various temperatures shows the development of the formation of the III-V nanocrystals during the process.Figure 4 shows a sequence of images where two 10 nm aerosol produced In particles are manipulated on a GaAs surface. The arrows indicate the directions of the tip movements. By measuring the widths of two particles as separate and after they have been brought together we are able to estimate their true lateral size [3]. In the case of the In particles in Fig. 4 such measurements gave a lateral size equal to their height, 10 nm, indicating a spherical shape.

SUMMARY

To summarize, we were able to fabricate size-selected nanocrystals of different III-V compounds in a diameter range below 20 nm using the aerotaxy method. Utilizing the reaction of either ammonia, phosphine or arsine with either gallium or indium droplets GaN, GaAs, InN and InP clusters, respectively, were formed. Our approach opens the possibility to produce size-selected semiconductor nanocrystals with considerable freedom in composition and size. It will allow new types of self-assembly and control of quantum dots.

REFERENCES

[1] K. Deppert, J.-O. Bovin, J.-O. Malm and L. Samuelson, J. Crystal Growth 169 (1996) 13.

[2] K. Deppert, H.-C. Hansson, I. Maximov, L. Samuelson and A. Wiedensohler, Appl. Phys. Lett. 64 (1994) 3293.

[3] T. Junno, K. Deppert, L. Montelius and L. Samuelson, Appl. Phys. Lett. 26 (1995) 3627.

Preparation and investigation of one to three unit cell thick YBCO particles by AFM and magnetic measurements

E Blinov†, V G Fleisher†, H Huhtinen‡, R Laiho‡,
E Lahderanta‡, P Petrii‡, Yu P Stepanov†, and L Vlasenko†
† Department of Solid State physics,
A F Ioffe Physico-Technical Institute, 194021 St Petersburg, Russia
‡ Wihuri Physical Laboratory, University of Turku, 20014 Turku, Finland

Nanocrystalline $YBa_2Cu_3O_{7-\delta}$ powders have been prepared by a citrate gel modification of the sol-gel technique. Using relatively low temperature $T = 790\,^{\circ}C$ and a process of extracting oxygen and reoxydizing the precursor powder it was possible to avoid cintering of the particles. According to x-ray powder diffraction analysis the particles have orthorhombic structure pertinent to the $YBa_2Cu_3O_7$-phase. Measurements made by atomic force microscopy show that they have flat shape with two maxima in the thickness distribution, one at 1.2 nm ($\sim$ 1c) and the other at 3.8 nm ($\sim$ 3c), corresponding to one or three orthorhombic unit cell lengths of the crystal. The average width of the particles is 40 nm. A similar value could be obtained from XRD measurements and the width of microwave absorption line around zero applied field.

MBE growth and characterization of ferromagnetic MnAs layers on CaF_2:Si(111)

Bansalchikov A.G.[a], Baidakova M.V.[a], Zakharchenya B.P.[a], Saito K.[b], Sokolov N.S.[a], Suturin S.M.[a], Tanaka M.[b]

a) A.F.Ioffe Physico-Technical Institute, 194021 St.Petersburg, Russia
b) Department of Electronic Engineering, The University of Tokyo, Japan

Studies of epitaxial growth and properties of ferromagnetic thin films on semiconductors are very attractive because of possibility to integrate magnetic with semiconductor in the same electronic device [1]. The integration is expected to lead to quite new element base for opto- and microelectronics. Among known ferromagnetics, MnAs is the one that complies reasonably with the requirements which should be met for such kind of applications. Although investigations of polycrystalline MnAs magnetic films deposited on amorphous substrates were started a long ago, epitaxial MnAs layers on Si(100) and GaAs(100) were grown quite recently [2,3]. In these studies, it was found that conditions of formation of ferromagnetic / semiconductor interface influence greatly to structural and magnetic properties of grown layers.

In this paper, we investigate growth, crystalline structure and magnetic properties of epitaxial MnAs films on heteroepitaxial CaF_2/Si(111) substrates, that have been thoroughly studied before [4,5] , as well as on As-Si(111) substrates. It is demonstrated that by means of molecular beam epitaxy (MBE) such ferromagnetic films may be grown with high crystalline quality and well pronounced magnetic properties.

All the heterostructures were grown in a small research MBE system at Physico - Technical Institute. After conventional chemical treatment, Si substrates were loaded into the growth chamber where they were annealed at 1250°C to evaporate silicon oxide. This procedure allows to obtain atomically clean Si(111) surface with 7x7 superstructure. Crystalline quality of substrate as well as growth of both buffer layer and ferromagnetic film were monitored *in situ* by reflection high energy electron diffraction (RHEED) at electron energy 15keV. The RHEED patterns for $[1\bar{1}0]$ and $[11\bar{2}]$ azimuths showed streaks indicating the corresponding layer to be a single crystalline with surface being smooth in atomic scale. A profilometer was used to measure film thickness. For #702, #703, #717 structures (See Table 1) , MnAs was deposited at 300°C on a 10 nm thick pseudomorphic CaF_2 buffer layer. The buffer layer was grown by two-step technique [5]. In other structures As-Si(111) surface was prepared following the method described in Ref. 2. In order to protect the grown layers from possible ambient contamination, MnAs film was covered with a few monolayers of CaF_2.

Table 1 Structural and magnetic parameters of the MnAs films.

Sample	Thickness, nm	$t_{\perp}$, nm	Strain $\varepsilon, 10^{-3}$	Tilt $\omega, 10^{-3}$ rad	c, Å base phase	H_C, Oe	M_S, emu/cc	M_R, emu/cc
702	750	15	0.4	2.3	5.71 (2)	30	700	130
703	400	40	1.2	2.7	α-MnAs (000L)	60	1100	750
717	380	>60	1.3	4.0		-	-	-
718	150	40	2.6	9.7	5.714(2)	-	–	–
722	160	45	1.6	5.0	α-MnAs(000L)	-	–	–
714	90	40	2.8	7.0	5.62(1) β-MnAs(001)	700	450	240

The samples were studied in single crystal geometry on High brilliance D/max P.C system (Rigaku Corp) X-ray diffractometer with copper target. The primary beam divergence was less than 5 arc. min. To determine both film crystallinity and its phase content, X-ray rocking curves were taken in wide angle range.

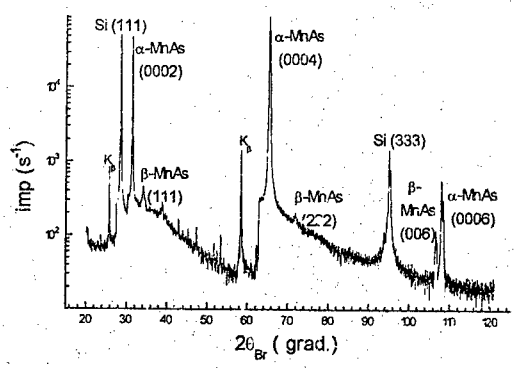

Fig.1 X-ray diffraction curve obtained from MnAs film on CaF_2/Si(111) substrate (sample #717).

Fig.1 presents a typical X-ray rocking curve obtained from a MnAs/CaF_2/Si(111) heterostructure (sample #717). Presence of (0002), (0004) and (0006) peaks on the curve shows that a single crystalline MnAs film was obtained with a hexagonal structure and (000L) growth direction. Pairs of peaks in several diffraction orders indicate that two phases are present in the film. Positions of main diffraction peaks give for the lattice parameter c value of 5.714±0.002Å that is the same as in α-MnAs. Smaller peaks on the tails of the main peaks correspond to

orthorhomboedral structure of β-MnAs which is close to that of α-MnAs [2]. The observed peaks originate from diffraction on (111) and (001) planes of paramagnetic phase. The distinctive features in rocking curves are also present for other samples where α-MnAs with hexagonal structure and (000L) growth direction seems to be the dominant phase while the β -MnAs phase proportion is less than 10%. The sole exception is provided by sample #714 where the β-MnAs phase dominates with lattice parameter c=5.62Å and prevailing growth of grains along (001) direction. The (000L) oriented α-MnAs phase and (111) oriented β-MnAs phase grains could be also observed in a small proportion.

For more detailed study of film structural quality, ω and (ω,2ω) rocking curves were measured in the vicinity of diffraction peaks of the dominant phase. The results were treated in mosaic-block crystal model. Grain size along the direction normal to substrate ($t_\perp$), microstrain existing in grains (ε), and grain misorientation (ω) were estimated and listed in Table 1. One can see that films grown on a CaF_2 buffer layer have better crystalline quality evaluated by smaller values of microstrain inside the grains and less misorientation of the latter. It is worth noting that grains of the second phase are two times smaller and have less perfect structure.

The surface morphology of the grown films was measured with an atomic force microscope (AFM) P4-SPM-MDT-16 operating in contact topography mode. Fig.2 presents AFM images of samples #702 and #722 grown on CaF_2/Si(111)(a) and As-Si(111)(b) respectively.

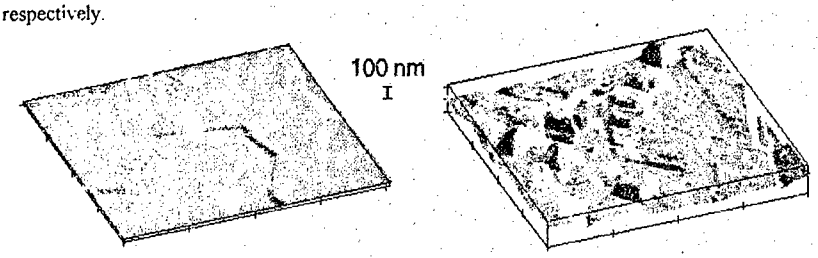

(a) (b)

Fig.2 AFM images of samples #702 (a) and #722 (b). Scanned area 4 μ x 4 μ. Maximum height deviations are 30nm for (a) and 250nm for (b). Note for (a) typical height deviation is only 10nm.

Characteristic six-fold faceting observed on the images confirms the X-ray results described above. One can see the film grown on CaF_2 buffer layer is much smoother with typical deviation of the height only 10 nm. Besides, it was found that 4° misorientation of substrate surface with respect to Si(111) plane for sample #714 leads to formation of phase with a distorted pseudo-cubic structure. This is in agreement with X-ray diffraction measurements indicating that β-MnAs (001)-oriented phase prevails in the sample.

The magnetization of 3x1x0.3 mm size pieces of the studied samples was measured at room temperature with an alternating gradient force magnetometer in the same way as was described in Ref. 2. Fig.3 shows the (M-H) curves for samples #702 and #714 in the geometry of $\overline{H}$ being parallel to $[11\bar{2}]$ direction. The #702 film appeared to be isotropic in the plane of substrate as opposed to the #714 sample whose magnetic properties in the same plane were found to be quite anisotropic. The parameters of (M-H) magnetization curves for several samples are presented in the Table 1. Here, H_c stands for coercive field, M_r and M_s - for remnant and saturation magnetization respectively. It is seen that the value of H_c for #702 is twice less than that of #703 and almost an order of magnitude less than H_c for #714. It is also small comparing with the values obtained in Ref. 2. It is worth to mention that small value of H_c is known to indicate high structural quality of the material. The saturation magnetization M_s of #702 sample appears to be higher than that of #714 which can be due to the presence of β-phase in the latter sample.

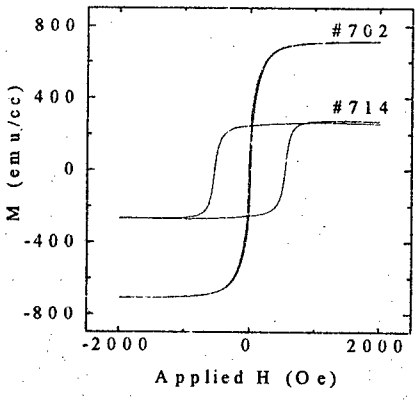

Fig.3 Magnetization as a function of applied field

Thus comparing structural and magnetic properties of epitaxial MnAs films grown on CaF_2/Si(111) and As-Si(111) substrates, we conclude that those properties strongly depend on the nature of buffer layer and are considerably better for the films grown on CaF_2.

The authors wish to thank N.N.Faleev and V.P.Ulin for useful discussions. They are also thankful to Y.V.Shusterman for his help in AFM measurements which were performed on a microscope produced by 'NT-MDT". We would like also to acknowledge support of the Russian Ministry for Research and Technical Politics in acquiring the microscope used in the above study.

References

[1] G.Prinz. Science, 250, 1092 (1990)
[2] K.Akeura, M.Tanaka, T.Nishinaga, T.De Boeck. J.Appl.Phys., 79(8), 4957 (1996)
[3] M.Tanaka, J.P.Harbison, G.M.Rothberg J.Cryst.Growth 150, 1132 (1995)
[4] L.J.Schowalter and R.W.Fathauer, CRC Crit.Rev.Solid State Mater.Sci. 15, 367 (1989)
[5] N.S.Sokolov, J.C.Alvarez and N.L.Yakovlev. Appl.Surf. Sci., vol.60/61, 421,(1992)
[6] T.S.Argunova, R.N.Kyutt, M.P.Scheglov and N.N.Faleev. J.Phys. D: Appl.Phys 28, A212(1996).

EFFICIENCY OF TWO-DIMENSIONAL PRECIPITATION AND EVOLUTION OF As CLUSTER SYSTEMS IN LOW TEMPERATURE GROWN GaAs FILMS DELTA-DOPED WITH INDIUM.

V.V.Chaldyshev, N.A.Bert, A.A.Suvorova,
A.I .Ioffe Physico-Technical Institute, 194021 St.Petersburg, Russia

V.V.Preobrazhenskii, M.A.Putyato, B.R.Semyagin
Institute of Semiconductor Physics, 630090 Novosibirsk, Russia

Introduction

Gallium arsenide grown by molecular-beam epitaxy at low temperature (LT GaAs) has attracted a great deal of attention during the last few years [1-5]. The main feature of this material is a high arsenic excess (~1 at.%) incorporated into the growing films in the form of point defects. A subsequent annealing (at 500°C or higher temperature) leads to precipitation of excess arsenic. The annealed LT GaAs exhibits semi-insulating properties with extremely short carrier lifetime. Therefore, it is attractive for several device applications.

It is typical for conventional LT GaAs films that the As clusters are randomly distributed over the film bulk [1-5]. However, it has been shown that two-dimensional arrays of As clusters can be formed using Si or In delta-doping [6-9]. In the latter case, the formation of the cluster sheets can be combined with uniform donor or acceptor doping of GaAs matrix [8,9]. Arsenic clusters are electrically active [10] and, therefore, two-dimensional cluster sheets could be used in device structures. For that the information is necessary on the evolution of the As cluster sheets upon annealing.

In this paper we report the results of transmission electron microscopic study of the structure of two-dimensional sheets and compare the Ostwald ripening rate in 2D and 3D arrays of As clusters built in the GaAs matrix.

Experimental

The LT GaAs films were grown by molecular-beam epitaxy (MBE) at 200°C in a dual-chamber 'Katun' system on semi-insulating GaAs(100) substrates. The films were uniformly doped with Si donors or Be acceptors. Shallow impurity concentration was as high as 7×10^{17} cm^{-3}. Undoped LT GaAs films were grown as well. Indium delta-layers in the growing films were produced by interrupting the Ga beam and using an In beam. Depending on In deposition time, thus produced delta-layers contained from 10-2 to 1monolayer of InAs. The distance between In delta-layers was varied from 20 to 60 nm. In order to form As clusters, the samples were divided into four parts, one of which was kept as-grown, the others were annealed at 500, 600, and 700°C for 15 min. The annealing was carried out under As overpressure in the MBE setup.

Electron probe microanalysis, x-ray diffraction measurements, and near-infrared optical absorption study showed that all the samples were of high crystalline quality. The arsenic excess in the samples was found to be approximately 0.6 at.%. It was slightly lower in the Si and Be-doped samples than in the undoped one. Cross-sectional specimens for transmission electron microscopy (TEM) were prepared using conventional procedure of mechanical grinding and polishing followed by Ar^+ ion milling. A Philips EM420 instrument operating at an accelerating voltage of 100 or 120 kV was utilized in the TEM study.

Results

Fig.1 shows a cross-sectional TEM micrograph of a sample with built-in indium delta-layers separated by undoped 40 nm thick GaAs spacers. The sample was annealed at 500°C. Two-dimensional arrays of arsenic clusters are clearly seen in the image. The positions of these sheets coincide with those of In delta-layers. The cluster density in 2D system is $(6\text{-}8)\times10^{11}$ cm^{-2}. In a vicinity of the two-dimensional arrays, the GaAs matrix is depleted by clusters. However, many clusters are dispersed far from the sheets. Such a random three-dimensional cluster system is typical for conventional LT GaAs.

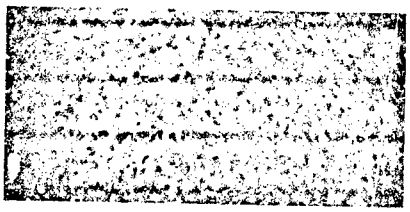

Fig.1. Cross-sectional TEM micrograph of LT GaAs film grown at 200°C and annealed at 500°C for 15 min. Two-dimensional sheets of As clusters are formed at indium delta-layers separated by 40 nm thick LT GaAs spacers doped with Si.

Two-dimensional arrays of As clusters have been observed in all the samples annealed at 500, 600, and 700°C, where indium content in the delta-layers was equal or higher than 0.2 monolayer. Fig.2 shows the details of the array structure in a Be-doped LT GaAs sample annealed at 600°C. It is clear from this figure (as well as from Fig.1) that the spatial distribution of the clusters is centered in the vertical direction at a line which corresponds to the indium delta-layer location. However, each individual cluster is more or less shifted from the centered position. Therefore, the average thickness of the array is larger than the size of a single cluster (even the biggest). It can be approximately evaluated as the double average cluster diameter. This approximation has been found to be valid in all the samples investigated. The characteristic structure of two-dimensional arrays remains similar in spite of the fact that the average cluster diameter varies from 2-3 to 10-12 nm due to acceptor or donor doping and different annealing temperature of the samples.

It can be seen from Fig.1 and 2 that the clusters in two-dimensional sheets are bigger than those in the surrounding matrix. This difference was found to be stronger at higher In content in the delta-layers. According to the fundamental law of Ostwald ripening, we should expect that the clusters in 2D system will grow and their neighbors from 3D system will dissolve with increasing duration or with elevating temperature of annealing. This process should give rise to formation of cluster-free spacers in between two-dimensional cluster sheets. We did observe such a completely ordered cluster system in LT GaAs with In delta-layers of 0.5 and 1 ml, when the spacers were as thin as 20 nm and the annealing temperature was 500 or 600°C [8,9]. One could expect formation of much thicker cluster-free spacers, when the annealing temperature is elevated, say, up to 700°C. However, a peculiarity of Ostwald ripening in the 2D system, which we discuss below, does not live up to this expectation at least in the case, when indium content in the delta-layers is as high as 0.5 ml.

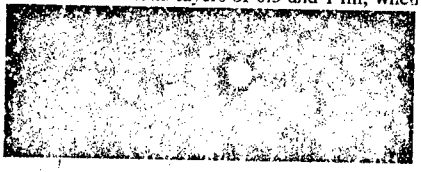

Fig.2. TEM image of As cluster sheet formed at In delta-layer in LT GaAs. The sample was uniformly doped with Be. It was grown by MBE at 200°C and annealed at 500°C for 15 min. The height of the image area is 25 nm.

Fig.3 shows the average cluster volumes, $\pi d^3/6$, for 2D and 3D cluster arrays as a function of the annealing temperature. In the case of the 3D system, the average volume increases rapidly (exponentially). In accordance to Lifshits-Slezov theory [11]:

$d^3 \sim Dt$,

where t is the annealing duration (constant in our experiments) and D is the diffusion coefficient of the excess arsenic dissolved in the GaAs matrix. It is well known that the diffusion coefficient depends on the temperature exponentially. Thus, equation (1) accounts for the exponential growth of the average cluster volume in the 3D system with elevating temperature.

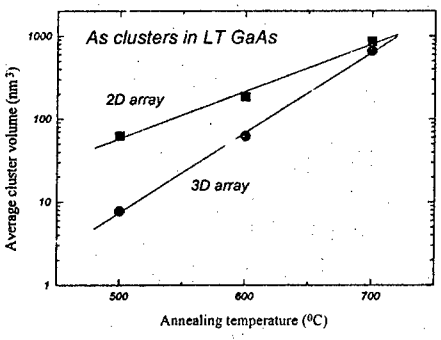

Fig.3. Average volume of As clusters in 2D and 3D systems as a function of annealing temperature. The data correspond to the undoped LT GaAs film grown at 200°C.

The data in Fig.3 prove that the cluster growth rate is lower in the 2D system than in the 3D one. There seems to be the following reason for that. A big cluster in the 3D system is surrounded by small ones and accumulates excess arsenic from all the directions due to decay of small neighbors. In contrast, a big cluster in the 2D system has many big neighbors, which are located at the same cluster sheet, and the majority of which do not dissolve Therefore, the big cluster in the 2D system accumulates excess arsenic, for the most part, due to decay of small neighbors from the 3D system. Thus, it attracts excess arsenic only from a fairly narrow spatial angle.

The effect observed considerably limits the thickness of the cluster-free spacers which can be produced between two-dimensional cluster sheets. For our samples, the clusters in 2D and 3D systems appear to be the same size upon annealing at 700°C for 15 min. After that happened, the clusters in between the sheets would be never dissolved. As a result, the initially ordered spatial distribution of As clusters will transform into a random one. This order-to-disorder

Fig.4. Cross-sectional TEM micrographs for the same LT GaAs sample annealed at 600°C (a) and 700°C (b). The sample with In delta-layers separated by undoped 20 nm thick spacers was grown at 200°C.

transition will be additionally enhanced by increasing thickness and roughness of the 2D arrays. The process described here is illustrated in Fig.4, which shows cross-sectional TEM images of the same LT GaAs sample annealed at 600 and 700°C. The annealing at 600°C results in formation of thin and flat cluster sheets at In delta-layers separated by 20 nm thick matrix, which is almost cluster-free. In contrast to that the annealing at 700°C leads to a random distribution of As clusters over the bulk.

Conclusions

Two-dimensional sheets of arsenic clusters were formed using indium delta-doping of GaAs films grown by molecular-beam epitaxy at low temperature and subsequent annealing. At Ostwald ripening stage the As cluster sheets were found to be as thick as the double average cluster diameter. The growth rate of As clusters was found to be lower in the 2D system than in the 3D one. Increasing roughness of the two-dimensional sheets and the difference between the growth rate in 2D and 3D systems of As clusters in GaAs matrix caused the transition in the spatial cluster distribution from artificial ordering to random.

Acknowledgment

The work was carried out under Russian National Programs: "Physics of Solid State Nanostructures" and "Fullerenes and Atomic Clusters". It was also supported by Russian Foundation for Basic Research.

References

[1]F.W.Smith, A.R.Calawa, C.L.Chen, M.J.Mantra, and L.J.Mahoney, *Electron Dev, Lett. 9*, (1988) 77 .

[2]M.Kaminska, Z.Liliental-Weber, E.R.Weber, T.George, J.B.Kortright, F.W.Smith, B.Y.Tsaur, and A.R.Calawa, *Appl. Phys. Lett. 54*, (1989) 1831.

[3]M.R.Melloch, K.Mahalingam, N.Otsuka, J.M.Woodall, and A.C.Warren, *J. Cryst. Growth 111*, (1991) 39.

[4]N.A.Bert, A.I.Veinger, et al., *Phys.Solid State 35*, (1993) 1289.

[5]N.A.Bert, V.V.Chaldyshev, et al., in M.O.Manasreh, H.J.von Bardeleben, G.S.Pomrenke, and M.Lannoo (eds.) *Physics and Applications of Defects in Advanced Semiconductors*, (*Mat. Res. Soc. Symp. Proc. 325*, 1994), p.401.

[6]M.R.Melloch, N.Otsuka, K.Mahalingam, C.L.Chang, P.D.Kirchner, J.M.Woodall, and A.C.Warren, *Appl. Phys. Lett.* 61, (1992) 177.

[7]T.M.Cheng, C.V.Chang, A.Chin, M.F Huang, and J.H.Huang, *Appl. Phys. Lett. 64*, (1994) 2517

[8]N.A.Bert, V.V.Chaldyshev, D.I.Lubyshev, V.V.Preobrazhenskii, and B.R.Semyagin, *Semiconductors 29*, (1995) 1170.

[9]N.A.Bert, V.V.Chaldyshev, N.N.Faleev, A.E.Kunitsyn, V.V.Tret'yakov, D.I.Lubyshev, V.V.Preobrazhenskii, and B.R.Semyagin, in E.D.Jones, A.Mascarenhas, and P.Petroff (eds.) *Optoelectronic Materials: Ordering, Composition Modulation, and Self-Assembled Structures*, (*Mat Res. Soc. Symp. Proc. 417*, 1996), p.135.

[10]A.C.Warren, J.M.Woodall, J.L.Freeouf, D.Grishkowsky, D.T.McInturff, M.R.Melloch, and N.Otsuka, *Appl. Phys. Lett. 57*, (1990) 1331.

[11]I.M.Lifshits and V.V.Slezov, Sov. Phys.-*JETP 35*, (1958) 479.

THE MECHANISM OF InAs/GaAs HETEROEPITAXIAL GROWTH DURING SUBMONOLAYER MIGRATION ENHANCED EPITAXY

G.E.Cirlin, V.N.Petrov, N.K.Polyakov, V.N.Demidov, N.P.Korneeva, A.O Golubok, S.A.Masalov, N.B.Ponomareva

Institute for Analytical Instrumentation of Russian Academy of Sciences, Rizhsky 26, 198103 St.Petersburg, Russia, Tel: ++7-812-2517377, E-mail: cirlin@ianin.spb.su

N.N.Ledentsov [a], D.Bimberg

Institut für Festkörperphysik, Technishe Universität, Berlin, Germany

(a) on leave from A.F.Ioffe Physical-Technical Institute, St.Petersburg, Russia

At present there is a great interest in formation of quantum dots directly during molecular beam epitaxial (MBE) growth for both fundamental and applied physics [1,2]. Recently, we have examined the mechanism of InAs/GaAs surface modification during submonolayer MBE at both intermediate stage (1.0 - 1.5 monolayers (ML) of InAs) and above critical thickness (more than 2 ML of InAs) when quantum dot arrays appear [3,4]. In this paper we report scanning tunneling microscopy (STM) study of InAs/GaAs morphology evolution within the interval of 1.5 - 3.0 monolayers (ML) InAs deposited during another modification of MBE which we refer to as submonolayer migration enhanced epitaxy (SMEE) [5]. The results show that different amount of InAs deposited leads to the formation of different kinds of nanostructures.

EXPERIMENTAL

Samples are grown using Russian made EP1203 machine. Singular and in some cases misoriented GaAs(100) substrates are used and during experiments they are mounted side-by-side on the same substrate holder. After the desorption of oxide layer in growth chamber the buffer GaAs slightly Be doped layer (300 nm) is MBE grown at substrate temperature T_s=550^{0}C providing (2x4) surface reconstruction for all samples. Then substrate temperature is decreased under As flux down to that, where c(4x4) surface reconstruction is appeared. After that a

desirable amount of InAs ML is deposited in SMEE growth mode. For STM measurements the samples are immediately quenched after the growth of In-contents layers. In all experiments the growth conditions during deposition of InAs layers (substrate temperature 470^{0}C, As_4/In effective fluxes ratio of about 10, growth rate for InAs is 0.1 ML/s and for GaAs is 0.6 ML/s) are maintained the same. SMEE growth procedure consists in deposition of submonolayer portions of In each followed by keeping the surface for desired time (t) under As_4 flux. Reflection High Energy Electron Diffraction (RHEED) is used for growth rates determination and to control to the spotty pattern transformation typical for three dimensional islands on the surface appearance. We have used STM setup operated at ambient pressure. The samples surface are protected with vacuum pump oil and STM experiments are carried out directly in the oil environment. Well reproducible STM images are obtained in this manner at a positive bias voltage on the sample (V_t ~ 0.5-5 V) and low tunneling currents ($I \sim 5*10^{-11}$ A). Sides of the images are always parallel to [011] and [0-11] directions.

During the experiments, we have examined the surface after deposition of InAs for three different cases: well before appearance of spotty-like patterns (1.5 ML), just after appearance of mixed streaks-spots pattern (1.75 ML) and after appearance of well-resolved spot pattern (2.0 - 3.0 ML). The surface for all three cases is controlled *in situ* by specially designed RHEED patterns registration and analysis system [6].

RESULTS

In Fig.1 a,b STM images of the surface after deposition of 1.5 ML InAs on singular and

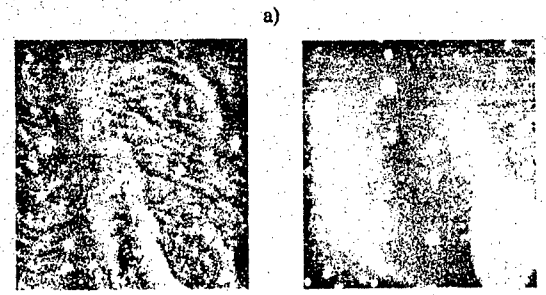

Fig.1. STM images for 1.5 ML InAs deposited on (a) singular and (b) vicinal surfaces. Scan area is 600 nm X 600 nm for both cases.

3^0 misoriented towards [011] direction (t = 30 s) are presented. The surface for this case is near-to-flat with the array of irregular one-monolayer height steps formed on singular substrate. There is no pronounced wire-like or parquet-like structures which we observe for the structures with the same amount of InAs deposited using SMBE growth mode [5].

In the next figure we present an STM-image of the surface where the deposition of indium is switched off just after appearance of the replica from three-dimensional islands are observed. For this particular case, the mean thickness of InAs deposited is 1.75 ML with t = 2 s.

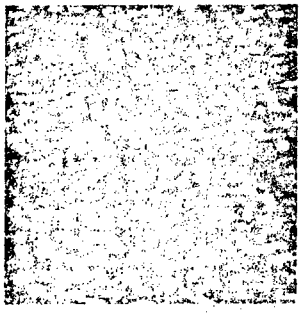

Fig.2. STM image for 1.75 ML of InAs with t = 2 s deposited on singular surface. Scan area is 360 nm X 360 nm.

As is seen from the Figure, only a small additional amount of In atoms (corresponding to~0.25 ML) deposited is required to the drastic transformation of the surface morphology as compared with previous STM images. At this stage an array of three-dimensional islands is formed. They have rectangular base shape, an average sides ratio of about 2.5 with lateral sizes ~ 5 nm and ~ 12nm along [0-11] and [011] directions. Mean surface density estimated from STM images is $1*10^{11}$ cm^{-2}. There exists an ordering of these islands along [001] direction. The islands are not uniform, they have different sizes. The same situation was observed during MBE growth experiments [7]. Our recent PL study of similar regrown structures [8] where up to three various quantum dot sizes are found for early stages of InAs/GaAs quantum dots formation during SMEE) confirm STM data.

In Fig.3 we present STM image of the surface after growth of 3 ML InAs on GaAs singular surface with t = 2 s. This amount of InAs deposited is well above the value required for the conversion of RHEED pattern into pure spotty-like picture and for the formation on the surface stable quantum dot arrays for this growth mode [5,6,8]. The feature of the image is a high average surface density ($1.1*10^{11}$ cm^{-2}) and quite uniform lateral size distribution with the main peak at 18 nm calculated from statistical cross-sectional analysis of STM data. In summary, we have observed several kinds of semiconductor nanostructures InAs on singular and vicinal

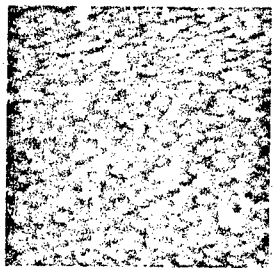

Fig. 3. STM image for 3 ML InAs deposited on singular surface with t = 2 s. Scan area is 600 nm X 600 nm.

GaAs surface during submonolayer migration enhanced epitaxy. For initial (up to 1.5 ML) stage, near-to-smooth surface is observed. Then, quantum dots are formed with different sizes along [0-11] and [011] directions with ratio ~ 2.5 (1.75 ML) and at higher InAs amount deposited (3 ML) the dots become anisotropic and uniform in lateral size.

This work is partially supported by INTAS, Program "Physics of Solid State Nanostructures" and Russian Foundation for Basic Research .

REFERENCES

1. D.Leonard, M.Krishnamurthy, C.M.Reaves, S.P.Denbaars, P.M.Petrov. Appl.Phys.Lett., 1993, v.63, p.3203.

2. N.Kirstaedter, N.N.Ledentsov, M.Grundmann, D.Bimberg. V.M.Ustinov, S.S.Ruvimov, M.V.Maximov, P.S.Kop'ev, Zh.I.Alferov, U.Richter, P.Werener, U Gosele, J.Heydenreich. Electron.Lett., 1994, v.30, p.1416.

3. G.M.Guryanov, G.E.Cirlin, A.O.Golubok, S.Ya.Tipissev, N.N.Ledentsov, V.A.Shchukin, M.Grundmann, D.Bimberg and Zh.I.Alferov, Surf.Sci., 1996. v.352-354, p.646.

4. G.M.Guryanov, G.E.Cirlin, V.N.Petrov, N.K.Polyakov, A.O.Golubok, S.Ya.Tipissev, V.B.Gubanov, Yu.B.Samsonenko, E.P.Musikhina, M.V.Maximov, N.N.Ledentsov, D.Bimberg. Abs. Int. Symp. "Nanostructures: physics and technology", St.Petersburg, Russia, June 26-30, 1995, p.405.

5. G.E.Cirlin, A.O.Golubok, S.Ya.Tipissev, N.N.Ledentsov, G.M.Guryanov. Fiz.Tekh.Poluprovodn., 1995, v.29, p.1697 (Semiconductors. 1995, v.29, p.884).

6. G.E.Cirlin, N.P.Korneeva, V.N.Demidov, V.N.Petrov, N.K.Polyakov, V.G.Dubrovskii, G.M.Guryanov, N.N.Ledentsov, D.Bimberg. In: Proc. 23th Int. Symp. on Semiconductor Compounds, St.Petersburg, Russia, 1996 (in press).

7. N.P.Kobayashi, T.P.Ramachandran, P.Chen, A.Madhukar. Appl.Phys.Lett., 1996, v.68, p.3299.

8. A.F.Tsatsul'nikov et.al., to be published.

A Thermodynamic Analysis of the Growth of III-V Compounds with Two Volatile Group V Elements by Molecular Beam Epitaxy

A.Yu.Egorov, A.R.Kovsh, V.M.Ustinov, A.E.Zhukov, and P.S.Kop'ev

A. F. Ioffe Physico-Technical Institute,
Russian Academy of Sciences,
26 Politekhnicheskaya, St.Petersburg, 194021, Russia,
phone: (812) 2479132, fax: (812) 2478640, e-mail: anton@beam.ioffe.rssi.ru

Molecular beam epitaxy (MBE) is currently widely used for the growth of III-V heterostructures. When growing ternary and quaternary III-V compounds with one volatile group V element, high accuracy of composition control is usually achieved. However, the composition control of III-V alloys containing two volatile elements (e.g. As and P), especially in the case of strained material, is more complicated problem. To explain the incorporation behavior of As and P, theoretical models have been proposed [1,2]. The advantage of thermodynamic approach is that it does not require any fitting parameters. However, by now, the application of this approach to the growth of compounds with two volatile group V elements [1,3] failed to explain some important experimental results [4]. Thus, an adequate thermodynamic model of MBE growth of multicomponent alloys is still an actual problem.

In thermodynamic models published previously MBE was considered as an equilibrium process, chemical potentials of solid and gas phases being set to be equal, and re-evaporated fluxes being treated as equilibrium those. These assumptions are not valid in the case of crystal growth which implies the transfer of substance from gas to solid phase. This means the absence of equilibrium state and, therefore, chemical potentials of these phases are not equal. This is the key point of our model unlike an equilibrium one.

The proposed model is based on the following assumptions. The MBE consider as irreversible process. The temperature of the system is a substrate one. A ternary or quaternary alloy is treated as a homogeneous mixture of constituent binaries with corresponding activity coefficients following the model of regular solution [5]. The balance between reactions of formations of binary compounds determines the composition of growing multicomponent alloy.

In the case of pseudomorphic growth the effect of strain due to lattice mismatch between the growing film and the substrate should be taken into account. The additive strain-induced Gibbs free energy leads to changes in chemical potential of the solid phase shifting the balance between the reactions of formation and, finally changing the composition of the growing layer.

Numerical calculations based on the model proposed for the GaAsP, InAsP, GaInAsP compounds were carried out at various growth temperatures and showed a good agreement with the experimental data. In particular, the fact that the alloy composition is independent on the ratio between the total flux of group III element and the total flux of group V element experimentally observed in [4] follows immediately from our model. The results of calculation are shown in figures1-3.

The proposed thermodynamic approach also allows us to consider the problem of formation of abrupt heterointerface between compounds containing different volatile elements of group V. It is well-known that a graded layer is usually formed at interface due to the substitution of the group V atoms on the crystal surface with the atoms from the incident flux. Considering the substitution reactions in the framework of our thermodynamic model reveals that As-containing surface is more stable against P exposition than the reverse case. The formation of the graded layer is shown to be strongly suppressed by the pre-deposition of thin liquid layer of group III element just prior to the interface formation. Both these results are in good agreement with the experimental data of [6].

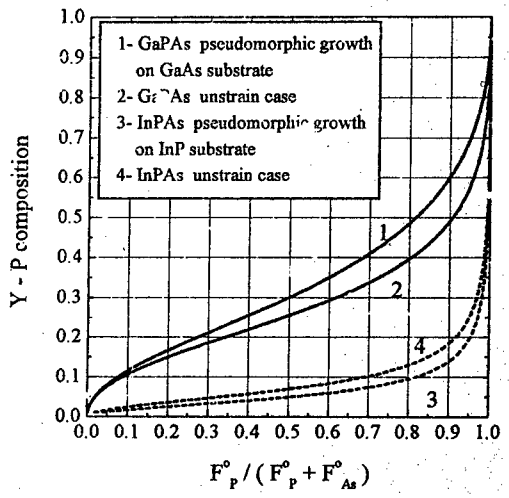

Fig.1 The dependence of y, phosporous mole fraction in GaP_yAs_{1-y} and InP_yAs_{1-y} on input flux ratio of group V elements. Tsub=520°C

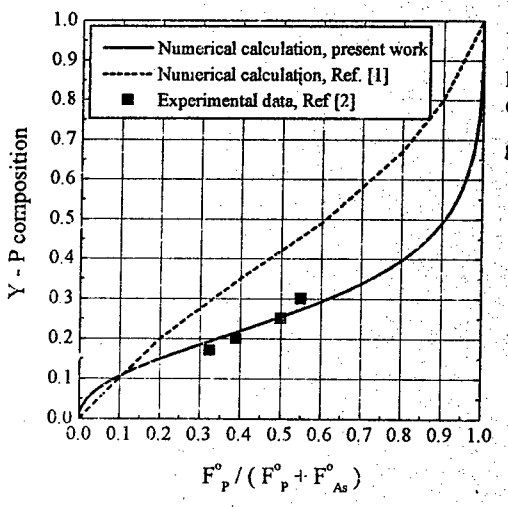

Fig.2. The dependence of y, phosporous mole fraction in GaP_yAs_{1-y} on input flux ratio of group V elements. Tsub=520°C.

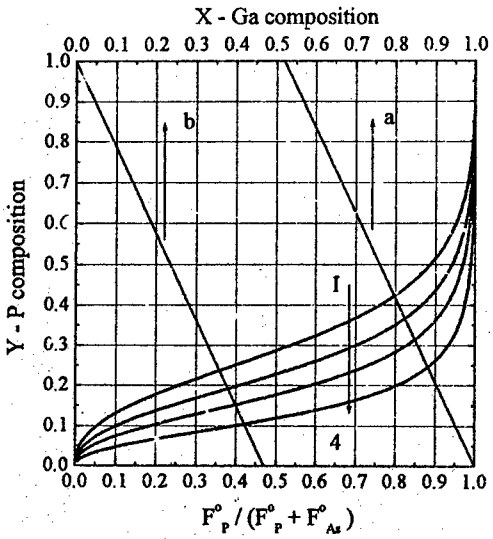

GaInPAs lattice matched to GaAs (a)

1- Tsub=577°C

2- Tsub= 477°C

GaInPAs lattice matched to InP (b)

3- Tsub=577°C

4- Tsub=477°C

Fig.3 The dependence of P mole fraction (Ga mole fraction) on input flux ratio of group V elements.

In conclusion, we have proposed the thermodynamic model of the MBE growth of III-V ternary and quaternary compounds with two volatile group V elements including the effect of strain. This model describes the dependence of layer composition and interface formation on growth conditions.

[1]. H.Seki, A.Koukitu, J.Chrystal Growth, 78, 342 (1980).

[2]. B.W.Liang and C.W.Tu, J. Appl. Phys., 74, 255 (1993).

[3]. A.Yu.Egorov, A.R.Kovsh, A.E.Zhukov, V.M.Ustinov, and P S.Kop'ev, to be published in Semiconductors (1997).

[4]. see, e.g., H.Q.Hou, B W.Liang, T.P.Chin, and C.W.Tu, Appl. Phys. Lett, 59, 292 (1991).

[5]. A.S.Jordan and M.Ilegems, J. Phys. Chem. Solids, 36, 329 (1975).

[6]. G.-J.Shiau, C.-P.Chao, P.E.Burrows, and S.R.Forrest, J. Appl. Phys., 77, 201 (1995)

For mation of three-dimensional nanometer periodic and localized defect-deformational structures and amorphyzation in solids

V. I. Emel'yanov, I. M. Panin
Physics Faculty, Moscow State University, 119899, Moscow, Russia

The theory of selforganization of three-dimensional nanometer periodic and localized defect-deformational (DD)-structures in solids subjected to action of external particle and laser beams is developed, based on the following mechanism.

Energy beam pumps into a solid a high concentration of point defects (interstitials, vacancies, electron-hole pairs). The field of defect concentration deforms the elastic continuum of the host material. In its turn the defect-induced deformation (strain) leads to self-consistent spatial redistribution of defects and after exceeding of critical value of spatially uniform defect concentration (control parameter) the DD-system makes a transition to a spatially nonuniform state. The theory of formation of one-dimensional nanometer DD-structures, based on the above physical mechanism of DD-instability, was developed in the works [1-4].

In the present treatment of the three-dimensional DD-instability we obtained the three dimensional dependence of the growth rate of unstable DD-harmonic on the direction of its wavevector and showed that it has maxima along certain crystallographic directions. The consideration of nonlinear multimode dynamics of DD-instability reveals two stages of DD-self-organization. On the first stage initially uniform angular distribution of wavevectors collapses into delta- like distributions along crystallographic directions that have maximum growth rates. On the second stage the initially uniform distributions of wavenumbers of DD-harmonics with wavevectors, oriented on the first stage along preferred crystallographic directions, collapse into delta-distributions. It is thus shown that formation of three-dimensional DD-structures occurs as a result of independent formations of one-dimensional DD-structures with wavevectors oriented along crystallographic directions with maximum growth rates. This enables to predict the geometry of three dimensional nanometer DD-structures in any particular case considered.

In treating the one-dimensional case the set of initial DD-equations is reduced to a closed nonlinear equation for selfconsistent strain, taking into account the quadratic and qubic lattice anharmonism. The exact stationary solution of this strain equation is found that gives the quantitative description of a hierarchy of processes of one and three-dimensional selforganization of steady state nanometer DD-structures (clusters and periodic structures) occurring at different values of control parameter. The geometry, periods, strain and defect distributions in DD-structures as functions of control parameter are determined.

It is shown that the formation of nanometer DD-structures occurs as a phase transition (with nonuniform selfconsistent strain being the order parameter) and is accompanied by jump-like changes of host material properties. Using the obtained analytic formula for the order parameter we calculated the critical dependencies of average defect-induced strain, crystal density and concentration of vacancy clusters (vv-centers) as functions of control parameter. The above dependencies are in agreement with corresponding experimental dependencies, recorded at the threshold of amorphyzation of crystals. Thus the threshold of formation of steady-state nanometer periodic three-dimensional DD-structures can be considered (as it was initially proposed in [1]) as the amorphyzation threshold.

References

[1] V. I. Emel'yanov, *Laser Physics*, **6**, 423 (1996).
[2] V. I. Emel'yanov, I. M. Panin, *Laser Physics*, **6**, 1071 (1996).
[3] V. I. Emel'yanov, I. M. Panin, *Izv. Akad. Nauk, ser. Fiz.*, **60**, 137 (1996).
[4] V. I. Emel'yanov, I. M. Panin, *Fiz. Tverd. Tela (Solid State Phys.)* (1997) (to be published).

A NEW PRINCIPLE OF ULTRATHIN HTSC FILM FABRICATION

I.Grekhov, V.Borevich, L.Delimova*, I.Liniichuk, A.Lyublinsky
Ioffe Institute, Russian Academy of Sciences,
26 Polytekhnicheskaya, St-Petersburg,194021, Russia
e-mail: ladel@pulse.pti.spb.su

An extremely promising application of High Temperature Superconductors (HTSC) is entirely HTSC-based microelectronics. In contrast to combination of HTSC interconnects with semiconducting active elements, the HTSC-based integrated circuit solves the problem of lowing the delay time of interconnects and can be fabricated in a single technological process. A field effect transistor with HTSC channel (SuFET) may be used as an active element in such integrated circuits. The external electric field penetrates superconductor over a distance about Thomas-Fermi electric field screening length λ (for $YBa_2Cu_3O_7$, (YBCO) $\lambda \approx 0.5$ nm; lattice constant in "c" direction ≈ 1.2 nm) which is a challenge in SuFET fabrication, since considerable modulation of YBCO channel superconducting properties can be achieved only in ultrathin films with thickness not exceeding 3 unit cells. However such decrease in the film thickness results in a drop of a zero resistance critical temperature T_{co} to the value far less than the liquid nitrogen temperature 77 K. Due to this problem there are no promising results in HTSC SuFET fabricating up to now in spite of the very intensive investigations which have been done over the world.

We have solved the problem of fabricating of ultrathin HTSC YBCO films with Tc higher than 80K. For this we offer a new buffer layer structure ($YBa_2Cu_{3-x}Nb_xO_7$, x=0.3) for ultrathin YBCO film. XRD diffraction patterns, Raman scattering spectra, scanning electron microscope images, transport properties measurements manifested that $YBa_2Cu_{3-x}Nb_xO_7$ represents a mixture of superconducting YBCO and insulating YBa_2NbO_6 grains. The proportion between superconducting and insulating volumes is determined by Nb content. For small Nb content $x < x_c = 0.29$ material is found to be superconducting with $T_c \approx 90$ K. For $x > x_c$ the material behaves as an insulator. The superconducting grains inherent the buffer layer serve as perfect nuclei for ultrathin YBCO film growth. The absence of lattice mismatching between nuclei and an incipient film yields a high quality structure at the early stage of film growth. Using the buffer layer three-unit-cell-thick YBCO film with $\Delta T_c = 90 - 80$K and four-unit-cell-thick YBCO film with $\Delta T_c = 92 - 85$K were fabricated. To our knowledge this is the best result obtained so far. Using this buffer layer, a superconductor-insulator-metal structure with four-unit-cell-thick YBCO channel ($\Delta T_c = 92 - 85$ K, $J_c(77K) = 1.6 \times 10^4\ Amp/cm^2$) and 150 nm insulator $PbZr_{0.5}Ti_{0.5}O_3$ was fabricated and showed a significant electric field effect. At the temperature 77 K, in resistive state, where a channel current was higher than the critical value, by applying a positive gate voltage $V_g = 6.06$ V the channel carrier concentration modulation (filling) up to 31% was observed. This is the last stage in elaboration of SuFET operating at the temperatures higher than 77 K.

KINETIC INSTABILITY IN THE EPITAXIAL GROWH OF SEMICONDUCTOR ALLOYS

I.P. Ipatova[1], V.G. Malyshkin[1], V.A. Shchukin[1*], A.A. Maradudin[2], and R.F. Wallis[2]

[1] *A.F. Ioffe Physical Technical Institute, St. Petersburg 19/021, Russia*
[2] *Department of Physics and Astronomy and Institute for Surface and Interface Science University of California, Irvine, CA 92697, USA*

Spontaneously formed macroscopic composition–modulated structures have been observed in numerous alloys of III–V and II–VI semiconductors grown by LPE, VPE, MOCVD, and MBE (for a review, see, e. g. [1]). Conventional attempts to explain the phenomenon have used the concept of spinodal decomposition of an alloy [2,3]. The thermodynamic theory of [2,3] developed for metal alloys deals with *closed systems* where the alloy can lower its free energy by the formation of a composition–modulated structure. The kinetics of the spinodal decomposition [3] describes the evolution of an alloy from the initial homogeneous state which is quenched to a temperature, where it is thermodynamically unstable, to a finite equilibrium state, which is the alloy with spatial modulation of composition.

Although the theory of [2,3] can be extended to bulk samples and epitaxial films of semiconductor alloys [4], one should emphasize the basic difference between formation mechanisms and observation conditions of composition–modulated structures in metal alloys, on the one hand, and those in semiconductor alloys, on the other hand. *i)* The formation of composition–modulated structures in metal alloys occurs in closed systems under long time annealing (aging). For typical temperatures of aging, $T \approx 600 - 1000^0$ C, characteristic values of bulk diffusion coefficients are of the order of $D \approx 10^{-11} - 10^{-8}$ cm^{2}s^{-1}. These diffusion coefficients are sufficiently large to promote the formation of composition–modulated structures on an accessible time scale. *ii)* Composition–modulated structures in semiconductor alloys are observed in *as–grown* samples which implies that these structures are being formed *in open systems* in the process of the crystal growth. Bulk diffusion coefficients in semiconductors at typical growth temperature ($T \approx 600^0$ C) are of the order $D \approx 10^{-19} - 10^{-16}$ cm^{2}s^{-1} [5]. These diffusion coefficients are too small to develop a composition–modulated structure during the growth time, and another kinetic mechanism than the bulk migration of atoms is needed for the structure formation.

In the present paper we study the instability which may occur in an *open system* in the process of the growth of an binary alloy $A_{1-c}B_c$, and our treatment is applicable also to the growth of a ternary semiconductor alloy $A_{1-c}B_cC$. The focus is given on the instability of the alloy growth with respect to fluctuations of composition δc. The theory linear in δc is developed, and the criterion is found that the amplitude of composition fluctuation increases with the epitaxial film thickness. This means that the growth of a homogeneous alloy is unstable, and the growth may result in an alloy with a spatial modulation of composition.

We consider the growth of an alloy from the gas phase. We study the epitaxial film on a substrate where the monolayers from the 1st to the Mth are completed, and the $(M+1)$st monolayer is the growing one. Growth on atomically smooth surfaces proceeds via the surface migration of adatoms on and via their incorporation into the growing monolayer. In the process of the growth of each Lth monolayer ($1 \le L \le M$), there appears the fluctuation of alloy composition $\delta c(\mathbf{r}; L)$, where $\mathbf{r} = (x, y)$ is the two–dimensional position vector. Since we neglect the migration of atoms in the bulk, the fluctuation of composition are "frozen" after the given monolayer is covered by subsequent monolayers.

First, "frozen" fluctuations of composition in the top completed Mth monolayer, $\delta c(\mathbf{r}; M)$, affect the migration of adatoms in the next, growing, $(M+1)$st monolayer via a short–range potential $U_{sr}^{(A,B)}(\mathbf{r}; M+1)$ acting on adatoms A and B. Second, "frozen" fluctuations in all completed monolayers $1 \le L \le M$ create, in accordance with the Vegard's rule, the long–range strain field. Therefore a long–range potential $U_{lr}^{(A,B)}(\mathbf{r}; M+1)$ appears which is proportional to the strain tensor at the surface ε_{ij}. The total potential acting on adatoms is the sum of short–range and long–range terms,

$$U^{(A,B)}(\mathbf{r};M+1)=V_{sr}^{(A,B)}\delta c(\mathbf{r};M)+V_{lr\,ij}^{(A,B)}\varepsilon_{ij}(\mathbf{r};z)\Big|_{z=Ma}, \quad (1)$$

where the coefficients $V_{lr\,ij}^{(A,B)}$ may be called deformation potentials of the adatom A or B, and a is the lattice parameter. The strain tensor may be given in terms of the static Green's tensor $G_{ij}\left(\mathbf{r}-\mathbf{r}',z,z'\right)$ of the elasticity theory for the semi-infinite medium, found in Ref. [6]. For Fourier transforms, this relation reads

$$\widetilde{\varepsilon_{ij}}\left(\mathbf{k},z\right)\Big|_{z=Ma}=\left(\frac{\partial a}{\partial c}\right)\sum_{L=1}^{M}\frac{1}{2}\left[\nabla_i\nabla'_p\widetilde{G_{jp}}\left(\mathbf{k};z,z'\right)+\nabla_j\nabla'_p\widetilde{G_{ij}}\left(\mathbf{k},z,z'\right)\right]\Big|_{\substack{z=Ma\\z'=La}}\widetilde{\delta c}\left(\mathbf{k};L\right). \quad (2)$$

The chemical potential of the rare gas of adatoms on the surface is the sum of the potential $U^{A,B}$ and of the entropy term related to the areal concentration of adatoms $N^{(A,B)}$, $\mu^{(A,B)}(\mathbf{r})=U^{(A,B)}(\mathbf{r})-T\ln(a^2N^{(A,B)}(\mathbf{r}))$. The gradient of the chemical potential in the inhomogeneous system causes the surface flux of adatoms [7], $\mathbf{j}^{(A,B)}(\mathbf{r})=-T^{-1}D^{(A,B)}\nabla\mu^{(A,B)}(\mathbf{r})$, where $D^{(A,B)}$ is the diffusion coefficient. By substituting here the expression for the chemical potential, one gets the surface flux of adatoms as a sum of the contributions of diffusion and drift: $\mathbf{j}^{(A,B)}(\mathbf{r})=-D^{(A,B)}\nabla N^{(A,B)}(\mathbf{r})-T^{-1}N^{(A,B)}(\mathbf{r})D^{(A,B)}\nabla U^{(A,B)}(\mathbf{r})$.

If there is a oversaturation in the gas phase, there appears the flux of atoms from the gas to the surface which is characterized by the deposition rate $G_0^{(A,B)}$. The concentration of adatoms and surface fluxes of adatoms may be written as sums of equilibrium quantities $N_{eq}^{(A,B)}(\mathbf{r})$, $\mathbf{j}_{eq}^{(A,B)}(\mathbf{r})$ and excess non-equilibrium quantities $\Delta N^{(A,B)}(t;\mathbf{r})$, $\Delta\mathbf{j}^{(A,B)}(t;\mathbf{r})$ caused by the oversaturation. The excess surface flux of adatoms may be written in terms of the excess areal concentration of adatoms as a sum of diffusion and drift contributions,

$$\Delta\mathbf{j}^{(A,B)}(t;\mathbf{r})=-D^{(A,B)}\nabla\Delta N^{(A,B)}(t;\mathbf{r})-T^{-1}D^{(A,B)}\Delta N^{(A,B)}(t;\mathbf{r})\nabla U^{(A,B)}(\mathbf{r}). \quad (3)$$

The excess non-equilibrium areal concentration of adatoms $\Delta N^{(A,B)}(t;\mathbf{r})$ and the excess surface flux of adatoms $\Delta\mathbf{j}^{(A,B)}(t;\mathbf{r})$ obey the continuity equation:

$$\frac{\partial\Delta N^{(A,B)}(t;\mathbf{r})}{\partial t}+\mathrm{div}\Delta\mathbf{j}^{(A,B)}(t;\mathbf{r})=G_0^{(A,B)}-\frac{\Delta N^{(A,B)}(t;\mathbf{r})}{\tau_{desorption}^{(A,B)}}. \quad (4)$$

Here $\tau_{desorption}^{(A,B)}$ is the average desorption time. We emphasize here that the deposition and desorption terms on the right hand side of Eq.(4) are particular features of an open system.

The set of coupled equations (3,4) allows to find the concentration of adatoms $\Delta N^{(A,B)}(t;\mathbf{r})$ and surface fluxes of adatoms $\Delta\mathbf{j}^{(A,B)}(t;\mathbf{r})$. Boundary conditions needed for these equations depend on the growth mechanism.

We focus on the step-flow growth on a surface vicinal to the (001) surface of a cubic crystal. A perfect vicinal surface displayed in Fig. 1 consists of (001) terraces of equal width L separated by monomolecular-height steps. Each step consists of [110] straight sections of equal length l_K separated by kinks. It was shown in Ref. [8] that the crystal growth on such a surface proceeds via kink flow and step flow, it can be stable against step bunching and step meandering, and the perfect geometry of the vicinal surface persists during the growth.

We consider fluctuations of composition where the characteristic scale of inhomogeneity r_0 is large compared to the spacing between kinks, and treat kinks as continuously distributed along steps (the so called approximation of continuous line sinks). These sinks are asymmetric with respect to lower and upper terraces since the barrier for adatoms approaching the sink from the upper terrace is higher than that for adatoms on the lower terrace. Corresponding boundary conditions at the nth line sink positioned at $x=L_n=nL$ read:

$$\Big(D\Delta N(t;\mathbf{r}) + w_+\Delta j_x(t;\mathbf{r})\Big)\Big|_{x=L_n+\eta} = 0 \qquad \Big(D\Delta N(t;\mathbf{r}) - w_-\Delta j_x(t;\mathbf{r})\Big)\Big|_{x=L_n-\eta} = 0, \quad (5)$$

where w_+, w_- are parameters of the asymmetric sink defined in Ref. [9], and $\eta \to +0$.

The set of coupled equations (3,4) subject to the boundary conditions (5) has been solved in the perturbation series with respect to the parameter U/T up to the first-order terms, and both $\Delta N(t;\mathbf{r})$ and $\Delta\mathbf{j}(t;\mathbf{r})$ have been calculated [10]. After the fluxes of both adatoms A and adatoms B attaching the line sink at the given point are known, it is possible to find the fluctuation of alloy composition $\delta c(\mathbf{r})$ which is being frozen at this point of the growing monolayer. The fluctuation $\delta c(\mathbf{r}; M+1)$ formed after the completion of the $(M+1)$st monolayer is found in the form of the linear response to the potential $U^{(A,B)}(\mathbf{r}; M+1)$ which was acting on adatoms during the growth of the $(M+1)$st monolayer. This relation reads for Fourier transforms of δc and U:

$$\widetilde{\delta c}(\mathbf{k}; M+1) = \frac{\overline{c}(1-\overline{c})}{T}\left[R^A(\mathbf{k})\widetilde{U^A}(\mathbf{k}; M+1) + R^B(\mathbf{k})\widetilde{U^B}(\mathbf{k}; M+1)\right], \qquad (6)$$

where response functions $R^A(\mathbf{k})$, $R^B(\mathbf{k})$ are determined by the kinetics of adatom migration on the stepped vicinal surface.

The set of linear equations (1,2,6) describes the dependence of alloy composition fluctuation $\widetilde{\delta c}(\mathbf{k}; M)$ on the monolayer's number M. It was shown in Ref.[10] that one may seek the solution in the exponential form $\widetilde{\delta c}(\mathbf{k}; L) \sim \exp(\gamma k a L)$. Then the inequality $\mathrm{Re}\gamma(\mathbf{k}) > 0$ yields the criterion that the fluctuation amplitude increases with the monolayer's number.

The mechanism responsible for this amplification is the drift of adatoms of the growing monolayer in the effective potential U created by the "frozen" fluctuations of alloy composition in the completed monolayers. The diffusion component of the surface flux of adatoms tends to smooth out fluctuations of composition. For high temperatures, diffusion dominates drift, and no amplification of fluctuation occurs. At a certain critical temperature T_c and at a certain wave vector $\mathbf{k}_c$ there appears amplification of the fluctuation amplitude. This temperature is the temperature of *kinetic phase transition* between the growth of the homogeneous alloy and the growth of the alloy with spatial modulation of alloy composition. At temperatures below T_c, drift dominates diffusion, and there exists a region in the k-space where fluctuations of composition increase from monolayer to monolayer.

The temperature T_c and the wave vector of the most unstable mode $\mathbf{k}_c$ are determined by the interplay of several tendencies. First, the Green's tensor from Eq.(2) is determined by the symmetry of bulk elastic moduli. Second, the symmetry of the deformation potential $V^{(A,B)}_{lr\,ij}$ from Eq.(1) is determined by the symmetry of the surface. Third, the k-dependence of the response functions $R^{(A,B)}(\mathbf{k})$ is governed by the particular kinetics of adatom migration on the stepped vicinal surface. As a result of this interplay, any direction of the wave vector of the most unstable mode of composition fluctuations ("the soft mode") is possible.

Calculations of the kinetic phase transition temperature show that T_c increases with the increase of adatom deformation potential. It means that, in contrast to the effect of long-range elastic forces on the thermodynamic instability of alloys, where they hinder the phase separation, they *favor kinetic instability*. The reason is that adatoms are attracted by domains of the surface with the excess concentration of like atoms, i. e., atoms with larger radius are attracted by domains which are under tensile strain, and smaller atoms are attracted by domains under compressive strain.

Fig. 2 displays the result of model calculations of $\mathrm{Re}\gamma(\mathbf{k})$ which have been performed for $L = 100a$, $l_k = 4a$, $w_+ = 0.01$, $w_- = 0.2$, and anisotropic deformation potential of adatoms ($V^{(A)}_{yy} = -3V^{(A)}_{xx}$, $V^{(B)}_{yy} = -3V^{(B)}_{xx}$). There is a region of unstable modes with $\mathrm{Re}\gamma > 0$ with small k_y including $k_y = 0$ which justifies the approximation of continuous line sinks.

To conclude, the kinetic mechanism is proposed of the amplification of alloy composition modulation with the thickness of the epitaxial film. Long-range elastic interaction favors

the kinetic instability and results in the increase of the kinetic phase transition temperature. For different values of material parameters, one may expect the appearance of composition-modulated structure with any orientation.

The authors are indebtful to P.S.Kop'ev for stimulating discussions. The work was supported by Russian Foundation for Basic Research, Grant No. 96-02-17943a, by National Science Foundation, Grant No. DMR-93-19404, and by the Program "Physics of Solid State Nanostructures" of Russian Ministry of Science Grant No. 2-001.

REFERENCES

* E-mail: shchukin@ton.ioffe.rssi.ru

[1] A. Zunger and S. Mahajan (1994) in: *Handbook on Semiconductors*, Ed. T.S. Moss. V. 3, Ed. S. Mahajan, Elsevier, P. 1399.
[2] J.W. Cahn. (1968) *Trans. Met. Soc.* **242** 166.
[3] A.G. Khachaturyan (1983) *Theory of structural transformations in solids*, Wiley, N.Y.
[4] I.P. Ipatova, V.G. Malyshkin, and V.A. Shchukin. (1993) *J. Appl. Phys.* **74**, 7198; (1994) *Phil. Mag. B* **57**, 557.
[5] B.L. Sharma (1989) *Defect and Diffusion Forum*, **64/65**, 1.
[6] K. Portz and A.A. Maradudin (1977) Phys. Rev. B **16**, 3535.
[7] D. Srolovitz (1989) *Acta Metall.* **37**, 621.
[8] I.L. Aleiner and R.A. Suris (1992) *Soviet Phys. Solid State* **34**, 809.
[9] R.L. Schwoebel (1969) *J. Appl. Phys.* **40**, 614.
[10] I.P. Ipatova, V.G. Malyshkin, A.A. Maradudin, V.A. Shchukin, and R.F. Wallis, to be published.

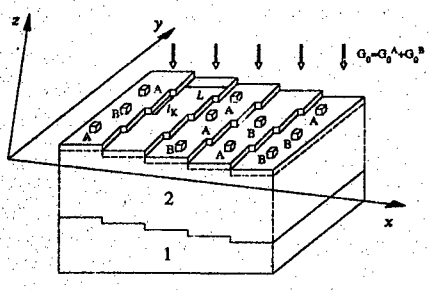

Fig. 1. Growth of an alloy on a vicinal surface; 1 — the substrate, 2 — the epitaxial film. Monolayers are defined in such a way that they repeat the stepped shape of the substrate. The dashed line depicts the top completed monolayer.

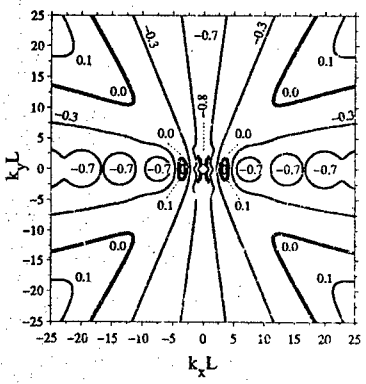

Fig. 2. Amplification coefficient $\mathrm{Re}\gamma(\mathbf{k})$ as a function of the 2D wave vector. Regions in the k-space where $\mathrm{Re}\gamma > 0$ correspond to unstable fluctuations.

Optical Er-doping of Si during Sublimational MBE

N.G.Kalugin[1], V.P.Kuznetsov[2], A.Yu.Andreev[1], M.V.Stepikhova[3], R.A.Rubtsova[2], Z.F.Krasil'nik[1]

[1] Institute for Physics of Microstructures RAS, GSP-105, Nizhni Novgorod, Russia
[2] NIFTI, Nizhni Novgorod University, 603600 Gagarin Avn., 23/3, Nizhni Novgorod, Russia
[3] Nizhni Novgorod University, 603600 Gagarin Avn., 23, Nizhni Novgorod, Russia

The region of light wavelengths 1.5 μm is an attractive field of investigatigations due to possibilities to create the effective optical fiber communication lines. There are any possible ways to create the light emitting sources for this region on the silicon-based materials: to make the GeSi based structures or to use the Er-doped Si or GeSi bulk material[1,2]. The attractive idea is to combine both this ways for fabrication of Er-doped GeSi based nanostructures with probably more high efficiency of light generation and thermal stability.

The erbium ion when incorporated in Si in the trivalent charge state, shows an intra-4*f* transition at a wavelength of 1.54 μm. This emission has been observed both under optical and electrical excitation [1,3]. The development of Er-based devices hinges on ability to efficiently incorporate optically active Er^{3+} ions into the host semiconductor material, at least ~10^{18} cm^{-3} of Er in silicon host [4] are required for fabricating of technologically useful devices. Using near-equilibrium crystal growth processes will limit impurity incorporation to the maximum solid solubility. However the solubility of Er atoms in Si is very small[5] of about 10^{14}-10^{16} cm^{-3}. Furthermore because of the low diffusion coefficient (~ 10^{-15} $cm^2 \cdot s^{-1}$ at 900° C) [6] it needs a long time and a high temperature for the conventional thermal diffusion doping. This implies that nonequilibrium processing methods must be used to obtain Er concentrations that are high enough for optoelectronic devices. The usual way of incorporating the rare earth ions and the co-doping is via implantation[3,7-9]. Energies in range of MeV and high implantation doses for erbium are needed. This leads to a high density of defects, even after thermal annealing of the samples. For high Er concentrations precipitation during annealing causes further problems. No doubth this problems will be only more considerable in the case of heterostructures. To overcome these problems, recently effort was placed on using epitaxial tachniques with *in situ* doping of erbium[10-12]. The method in use was a standard MBE: Er was evaporated from an effusion cell, an electron-beam evaporation system served as a source of Si flow. The growth chamber vacuum was $6 \cdot 10^{-11}$ - 10^{-10} mbar, the substrate temperature T = 500-600°C, and the thickness of doped layers varied in a 0.1-0.5 μm range.

The aim of present work is the studies of another MBE method - the Er doping during Sublimational MBE growth of Si. We are the first to report application of this method to growth of luminescent Si:Er layers.

It is generally recognized that the key problem in low-temperature MBE is segregation of doping impurities on a growth surface. This effect largely complicates a formation of controllable doping profiles and highly-doped layers[13,14], leads to clustering of doping impurity and, hence, to defects of a crystalline structure[14]. In the low-temperature epitaxy of Si (500-600°C) this effect was discovered in all conventional doping elements (Sb, P, As, Al, Ga, B, In) and all types of substrate orientation. Erbium is no exception. For example Ref.11 shows that due to a segregation on the Si(100) growth surface, the maximal total concentration of Er (RBS data) in deposited at 600°C layers was about $4 \cdot 10^{18}$ cm^{-3}. Accordingly at 10K the structures exhibited a

low intensity of photoluminescence at a 1.54 μm wavelength. To overcome the segregation problem, the epitaxial growth process was carried out in oxygen atmosphere ($P_{o2} \approx 10^{-9}$ - 10^{-10} mbar)[10,11]. This technique allowed to grow Si:Er layers with Er concentration about (1.5 - 4) 10^{19} cm^{-3} that featured by both electro- and photoluminescence in the 1.54 μm IR region. The authors of Ref.10,11 do not provide any data on the degree of electrical activation of Er in the epitaxial structures.

In this paper we report our study of a possibility to grow Si:Er epitaxial layers that would effectively radiate at λ= 1.54 μm, using the MBL sublimation technology without oxygen co-doping. As has already been mentioned, to this effect we need to realize the growth conditions that do not feature segregation of a doping impurity.

We have shown earlier[15] that all of the earlier investigated impurities (Sb, P, Al, As) sharply degrade in their segregation ability with a decrease in the epitaxial temperature T or with an increased growth rate V (Fig.1). Specifically, Sb segregation disapeared at T≤500 C and V≥1 μm/h. Using these regularities, we have managed to obtain uniformly doped monocrystalline layers of Si with up to $2 \cdot 10^{20}$ cm^{-3} concentration of the electrically active impurities P, As, Sb[15,16], as well as δ-doped layers[17].

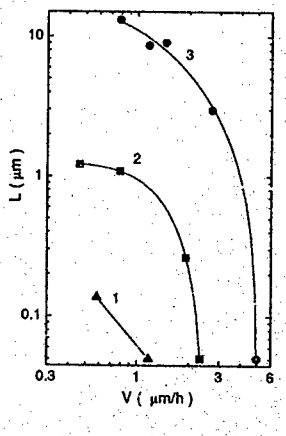

Fig.1 Dependence of the impurity concentration transition region (caused by segregation) width on the growth rate in layers doped with Al at T=500 (1), 600 (2) and 700°C (3)

In this work, Si:Er layers were grown by sublimation in a relatively low vacuum of 2 10^{-7} torr on Si(100) p-type substrates (ρ=0.005-10 Ω·cm), using the method described in Ref.14-17. Si plates Er-doped to $6 \cdot 10^{19}$ cm^{-3} (p-type conductivity) were used as a source of Si/Er vapour. Both the sources and the substrates were resistively heated, which ensures high purity of the process. This technique can be called a Sublimational MBE.

The epitaxy temperature was 400-600°C. Immediately after the growth process was over, the structures were annealed directly in a vacuum chamber at 900°C during 30 min. The concentration of the electrically active impurity in the layers was determined by the Hall method at room temperature. Studies of the PL spectra were assisted by a BOMEM DA3.36 Fourier spectrometer with a cooled InSb detector. The samples temperature was maintained at 4.2K. A Kr^+-laser (λ = 647 nm) was used as a source of exciting radiation.

The thickness of the grown Si:Er layers varied from 0.2 to 0.3 μm. All structures were of n-type conductivity with $n \approx 1 \cdot 10^{18}$ cm^{-3} and $n \approx 3 \cdot 10^{17}$ cm^{-3} for the layers grown at 400°C and

600°C, respectively Bearing in mind that the degree of electrical activation for Si:Er layers traditionally is ≤10%[18], we estimate the total concentration of Er in our layers as $\geq 10^{19}$ cm^{-3}, which indicates an almost complete capture of Er by the layer. The Hall mobility of electrons reached 317 $cm^2/V \cdot sec$ at $n = 1 \cdot 10^{18}$ cm^{-3}.

Fig. 2 demonstrates the PL spectra at 4.2K of the samples grown by the Sublimational MBE method at 600°C (a) and 400°C (b). Spectral resolution was 10 cm^{-1}, the excitation intensity was about 7 W/cm^2. In both cases the spectra exhibit a sharp peak at a 1.537 μm wavelength, which corresponds to the optical transitions from the excited $^4I_{13/2}$ to the ground $^4I_{15/2}$ spin-orbital levels of an Er^{3+} ion. The PL intensity in the structure grown at 600C is approximately the same with that in the ion-implanted Er layers[9]. The arrows labelled "C" indicate the positions of four of the five transitions related to an Er^{3+} center in the crystal matrix with cubic site symmetry, which was determined[9] as erbium ion incorporated in an interstitial site, with 4 nearest neighbors and 6 close-lying next nearest neighbors. The cubic lines in the spectrum is an evidence that Er occupies regular positions in the Si lattice and this feature clearly shows the crystal quality of epitaxial grown layers. Note that the cubic lines are not available in the PL spectra reported in Ref.11.

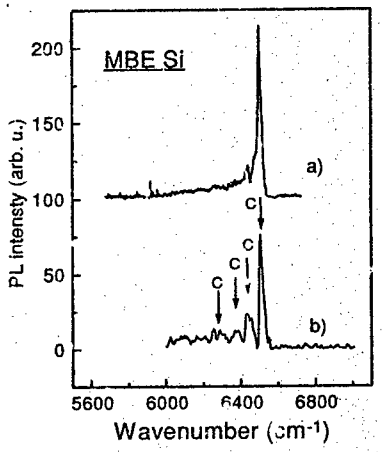

Fig.2 PL spectra of sublimation MBE grown Si: Er. The arrows mark the positions of the PL line corresponding to the cubic symmetry Er center. The curves a) and b) were obtained for the samples grown at different temperatures - 600 and 400°C respectively. The PL signal represented on the curve b) has been scaled by a factor of 2.

In conclusion, in this work we report first application of a Sublimational MBE method to grow Si layers with a high concentration of Er. The Si:Er layers (the Hall concentration of electrons is ~ 10^{18} cm^{-3}) exhibits the radiation at a 1.537 μm wavelength. According to the PL-(presence of the erbium cubic T_d centers) and the Hall effect (electron mobility) studies, the resulting layers display a fairly high quality of crystalline structure.

This work was partially supported through RFBR grant #96-02-16991 and Russian Program "Physics of solid-state nanostructures" (grant #2-027/4).

References:

[1] H. Ennen, J. Schneider, G. Pomrenke, and Axman, Appl. Phys. Lett.43, 943 (1983)
[2] L.K.Orlov, V.Ya.Aleshkin, N.G Kalugin, N.A.Bekin, O.A.Kuznetsov, B.Dietrich, G.Bacquet, G.Bacquet, J.Leotin, M.Brousseau, F.Hassen, J. Appl Phys. 80, 415 (1996)

[3] B. Zheng, J. Michel, F.Y.G. Ren, L.C. Kimerling, D.C. Jacobson, and J.M. Poate, Appl. Phys. Lett. **64**, 2842 (1994)
[4] Y.-H. Xie, E.A. Fitzgerald, and Y.J. Mii, J. Appl. Phys. **70**, 3223 (1991)
[5] H. Horiguchi, T. Kinone, R. Saito, T. Kimura, and T. Ikoma, in *Rare Earth doped semiconductors II*, Mater. Res. Soc. Symp. Proc. **422**, 81 (1996)
[6] J.S. Custer, A.Polman, and H.M. van Pixteren, J. Appl. Phys. **75**, 2809 (1994)
[7] S. Coffa, F. Priolo, G. Franzo, V. Bellani, A. Carnera, and C. Spinella, Phys. Rev. B **48**, 11782 (1993)
[8] F. Priolo, G. Franzo, S. Coffa, A. Polman, S. Libertino, R. Barklie, and D. Carey, J. Appl. Phys. **78**, 3874 (1995)
[9] H. Przybylinska, W. Jantsch, Yu. Suprun-Belevitch, M. Stepikhova, L. Palmetshofer, G. Hendorfer, A. Kozanecki, R.J. Wilson, B.J. Sealy, Phys. Rev. B. **54**, 2532 (1996)
[10] J. Stimmer, A. Reittinger, J.F. Nutzel, G. Abstreiter, H. Holzbrecher, Ch. Buchal, Appl. Phys. Lett., **68**, 3290 (1996)
[11] R. Serna, Jung H. Shin, M. Lohmeier, E. Vlieg, A. Polman, and P.F.A. Alkemade, J. Appl. Phys. **79**, 2658 (1996)
[12] H. Efeoglu, J.H. Evans, T.E. Jackman, B. Hamilton, D.C. Houghton, J.M. Langer, A.R. Peaker, D. Perovic, I. Poole, N. Ravel, P. Hemment, and C.W. Chan, Semicond. Sci. Technol. **8**, 236 (1993)
[13] H.-J. Gossman, E.F. Schubert, Crittical Rev. in Sol. Stat. and Mat.Sci. **18**(1), 1 (1993)
[14] V.P. Kuznetsov, V.A. Tolomasov, A.V. Tumanova, Kristallografiya **24**, 1028 (1979)
[15] V.P. Kuznetsov, A.Yu. Andreev, O.A. Kuznetsov et al., Phys.Stat.Sol.(a) **127**, 371 (1991)
[16] A.Yu. Andreev, V.P. Kuznetsov, V.A. Tolomasov, Sov.Tech.Phys. **32**(6), 710 (1988)
[17] V.P. Kuznetsov, A.Yu. Andreev, N.A. Alyabina, Elektronnaya Promyshlennost' **9**, 57 (1990)
[18] L. Palmetshofer, Yu. Suprun-Belevich, M. Stepikhova, Proceeding of the tenth International Conference on Ion beam modification of materials, Albuquerque, 1996 (to be published)

Lateral Ordering of Stacked Self-Assembled Islands of InAs on GaAs.

S. A. KOMAROV, G. S. Solomon *, J. S. Harris Jr.
Solid State laboratory, * Ginzton Laboratory
Stanford University, Stanford, CA 94305
email: komarov@snowmass.stanford.edu

Natural restrictions imposed on conventional lithography techniques have led to the appearance of alternative approaches for the fabrication of 0-D quantum size structures. Currently, one of the most attractive and interesting methods is the growth of self-assembled coherently strained semiconductor islands, where the dimensions and material choice of the islands create the 3-dimensional confinement. While extensive research had been devoted to the structural, optical and electronic properties of these structures, little improvement in the size uniformity and in-plane ordering has ocurred. Thus characterization on large sample areas is dominated by inhomogeneous broadening

Here we would like to report experimental evidence of improved in-plane self-organization resulting from vertically stacked self-assemled InAs islands in a GaAs matrix. Samples under investigation were grown by molecular beam epitaxy (MBE) in Stranski-Krastanow growth mode and cosisted of one, five, ten, and twenty layers of coherently strained islands of InAs with all but the last layers covered with GaAs. Ours previous studies have shown that dots in the multilayered structures form columns [1]. We have studied atomic force microscope (AFM) images of the sample surface morphology (Fig. 1) and performed real space, as well as Fourier space image processing. Along with the evolution of island size and long range surface roughness, we could clearly observe the onset of in-plane island ordering (lattice) with stacking (Fig.2). Two-dimensional Fourier spectra indicated orientation of the occuring island lattice formatior while autocovariance data provided information about the lattice parameters.

References.

1. G. S. Solomon, Y. Yamamoto, S. Komarov and J. S. Harris, Jr., Journal of Crystal Growth, Vol. 175/1-4, (1997)

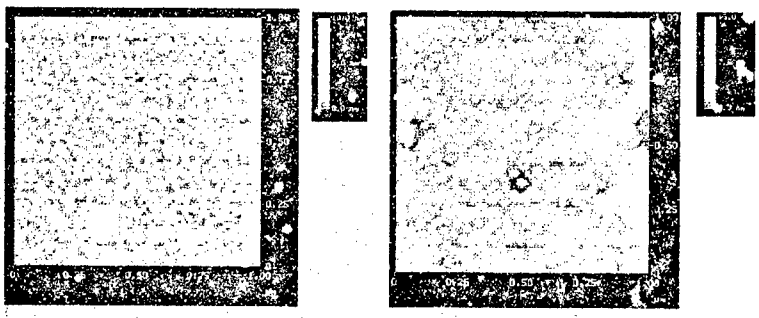

Fig.1. Visual comparison of the surface morfology of one (left) and twenty (right) layered samples of InAs self- assembled coherently strained islands on GaAs.

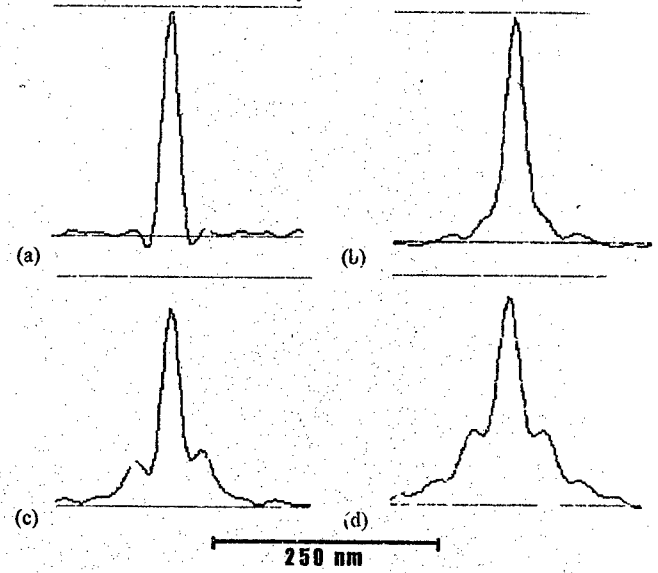

Fig.2 AFM image autocovariance (100) sections for one (a), five (b), ten (c) and twenty (d) stacked layers of InAs self- assembled islands. Length scale applies to all plots

Cluster effects in optical spectra of GaAsSb on GaAs grown by liquid phase epitaxy

A.M.Mintairov, A.S.VLASOV, V.P.Khvostikov,
P.A.Blagnov, A.A.Prokophiev, S.V.Sorokina

A.F.Ioffe Physical-Technical Institute RAS,
194021, Polytechnicheskaya 26, St.Petersburg, Russia

1. Introduction

It is well known that microstructure of nearly all III-V semiconductor alloys exhibit large scale deviation from random atomic distribution, what profoundly affects their optical properties. [1]. In our previous work [2] the strong evidence of the local phase separation (cluster effect) in relaxed mixed-cation $In_xGa_{1-x}As$ (x=0.05-0.2) grown on GaAs by MOCVD have been observed in Raman (RS) and photoluminescence (PL) spectra. The phonon modes of GaAs and partially-ordered $InGaAs_2$ clusters, together with clustering induced splitting of the band gap have been observed. While the mechanism of such cluster formations are not clear at present, one can suppose that the main driving force of it is elastic strains between substrate and epitaxial layer. In this case such clustering can be observed in other relaxed alloy systems. To prove this idea we performed the RS and PL study of anion-mixed $GaAs_{1-x}Sb_x$ alloys grown on GaAs by LPE. The other aim of this work was obtaining a material with band-gap 1.1-1.2 μm for monolithic tandem GaAs solar cell.

2. Experiment

Undoped and Te- doped $GaAs_{1-x}Sb_x$ (x~0.07-0.27) epitaxial layers (with thickness about a few microns) were grown by liquid phase epitaxy (LPE) on (001) GaAs substrates. The growth was carried out using a piston or slide boat LPE technique and the temperature-lowering method. The growth was begun at 720°C at one melt, while the furnace temperature was being lowered at 1.5°C/min down to 600°C. After it the cooling rate was increased up to 80°C/min. The growth was stopped at 350°C. As a result of a fast cooling and low temperature growth, good quality $GaAs_{1-x}Sb_x$ layers have been crystallised on GaAs substrate with x up to 0.27. The alloy composition was obtained from X-ray diffraction and microanalysis. The RS spectra were measured in the backscattering geometry using a double monochromator DFS-52 and excited with 514.5 nm Ar^+ -ion laser at room temperature. The RS spectra were analysed in $z(xy)\bar{z}$ and $z(xx)\bar{z}$ polarizations. The PL spectra were observed at 77K.

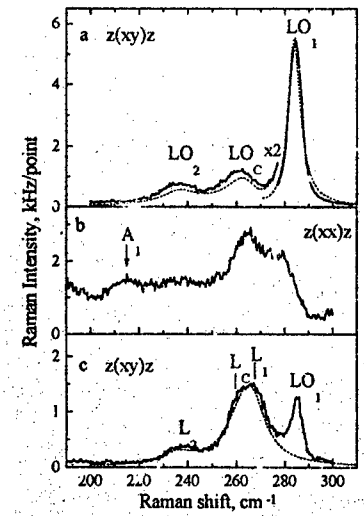

Fig.1. Raman spectra of $GaAs_{1-x}Sb_x$ layer x=0.12 (a,b), x=0.11 (c). Sample c is Te doped with electron density about $n\sim2*10^{18}$. Raman spectra were measured in the backscattering geometry in z(xy)z (a,c) and z(xx)z (b) polarizations. The solid curves are experimental and the dotted - theoretical.

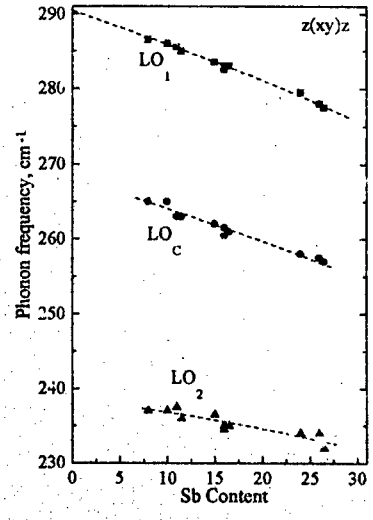

Fig.2. Dependence of phonon frequencies of $GaAs_{1-x}Sb_x$ on GaSb content, measured from Raman spectra.

3. Results and discussion

The RS spectra reveal three mode behaviour of GaAsSb optical phonons. This is evident from the appearance of the LO_1, LO_C, LO_2 bands in Fig.1,a (undoped sample, longitudinal optical phonons) and L_1, L_C, L_2 ones in Fig.1,c (doped sample, screened longitudinal optical phonons) in *(xy)* polarizations. Such behaviour takes place for all studied concentrations (Fig.2) and is similar to the InGaAs alloys [2].

The Faust-Henry factors (FHF) and oscillator strengths (OS) for $GaAs_{1-x}Sb_x$ polar optical phonons have been extracted from experimental RS spectra in the way described in [2]. The obtained values of FGF and OS are presented in table 1. And spectra calculated, using these parameters are shown in fig.1.a,c by dotted line.

Analysis of the obtained values of FHF have shown that LO_C and LO_2 phonons correspond to vibrations of Ga-As and Ga-Sb bonds of Ga_2AsSb phase, while LO_1 one corresponds to the vibration of GaAs phase. The observed parameters show that almost

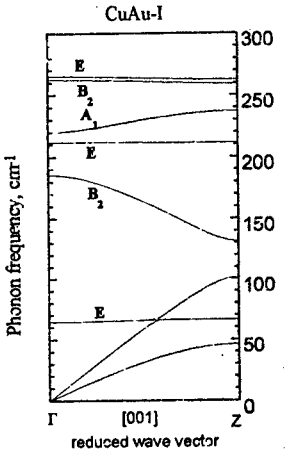

Fig.3. Phonon dispersion curves for [001] GaSb/GaAs MSL along [001] direction of Zinc blend structure, calculated in VOSM.

all Sb atoms are bounded into Ga_2AsSb phase, i.e. the content of this phase is twice the averaged Sb content.

The measurements of the RS spectra in *(xx)* polarization (Fig.1,b) reveals a strong evidence of a partial ordering of the Ga_2AsSb phase. The indication of the ordering is A_1 band at 215 cm^{-1} in Fig.1.b. Our analysis of the phonon modes and lattice dynamical calculation of a perfectly ordered ternary structures have shown that such mode exist in CuAu-I type [001]-$(GaAs)_1(GaSb)_1$ monolayer superlattice (MSL) of Ga_2AsSb clusters (Fig.3). This mode corresponds to vibrations of Ga atoms. Its frequency calculated in the valence overlap shell model (VOSM) using for corresponding consistuents bulk parameters [4] 220 cm^{-1} , is in a good agreement with experimental one. The A_1 mode have been observed by us in InGaAs alloys but at a lower frequency 211 cm^{-1}.

The calculated frequency of A_1 for InGaAs CuAu structure was 210 cm^{-1}. In InGaAs this mode corresponds to vibration of As atoms. The difference in frequencies of A_1 for GaAsSb and InGaAs is very well related with atomic mass difference of Ga (31) and As(33) and support its assignments. It should be mentioned that the intensity of *(xx)* component in GaAsSb (Fig.3) is higher than in InGaAs what probably indicate on more complex ordering structure. One of the possibilities can be chalcopyrite (CH) ordering. CH structure has the same Ga sublattice A_1 mode, but also a several modes of B_1 symmetry, which is allowed in *(xx)* polarization.

In PL spectra an additional peak B (fig.4) with lower energy of about 40-70 meV

Table 1. Parameters of the optical phonons of GaAs1-xSbx (x=0.12) found from experimental spectra.

	Type of optical phonon					
	Ga-As (GaAs)		Ga-As (Ga_2AsSb)		GaSb (Ga_2AsSb)	
	TO_1	LO_1	TO_C	LO_C	TO_2	LO_2
Frequency, cm^{-1}	268	284	263	264	236	237
Damping, cm^{-1}	12	4.2	17	17	17	17
Faust-Henry coefficient	-0.41	-0.38	-0.21	-0.25	-0.08	-0.10
Oscillator strength	1.07		0.343		0.147	

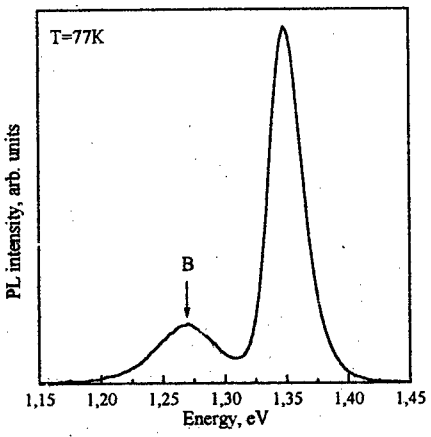

Fig.4. Photoluminescence spectrum of $GaAs_{0.89}Sb_{0.11}$ layer, measured at 77K.

have been observed. PL and Raman investigations show that the second peak B is not a result of unintentional doping. Consulting the results of RS investigations, it is naturally to assume that the additional PL peak is caused by the exciton localisation on Ga_2AsSb clusters.

The GaAsSb photo voltaic cells were prepared with Zn- diffused p/n junction. The edge of photosensitivity was shifted in such sells up to 1.2 μm.

4. Conclusion

Our RS studies have demonstrated Ga_2AsSb and GaAs cluster structure of LPE-grown relaxed $GaAs_{1-x}Sb_x$ layers (x=0.07-27). The evidence of partial chalcopyrite type ordering of Ga_2AsSb clusters was obtained from RS. The PL spectra show an additional peak with lower energy (40-70 meV), which is interpreted as emission from Ga_2AsSb clusters. The maximum content of GaSb phase of the alloys that was reached during our investigations, was about 27 % with the band gap of 1.1 eV at 77K .

This work was supported by the Russian Fundamental Research Fund (grants № 95-02-04124 and № 95-02-04126)..

References

[1] A.Zunger, and S.Mahajan, in: *Handbook on Semiconductors*, Vol.3, (Elsevier, Amsterdam, 1994).

[2] A.M.Mintairov, D.M.Muzurenko, M.A.Sinitsin and B.S.Yavich, *Semiconductors*, **28** (9), 866 (1994).

[3] A.Anastassiadou, Y.S.Rapits and E.Anastassakis, *J.Appl.Phys.*, **60** (8), 2924 (1986).

[4] P.H.Borcherds and K.Kunc, *J.Phys.C*, **11**, 4145 (1977)

Structure of InAs delta-layers in low --temperature grown GaAs

Yu.G. Musikhin, [1,2] N.A. Bert, V.V. Chaldyshev,

1. A F Ioffe Physical Technical Institute St.Petersburg Russia,194 021

A.O. Kosogov, P Werner,

2. Max - Planck Institute fuer Mikrostrukturephysik, Weinberg 2, Halle D-06120, Germany,

V.V. Preobrazhenskii, M.A. Putyato, and B.R Semyagin

3. Institute of Semiconductors Physics, Novosibirsk, Russia, 630090

Introduction

GaAs grown by molecular-beam epitaxy (MBE) at low-temperature (LT) has gained considerable interest as a very promising material with unique properties [1,2]. Earlier studies have revealed that GaAs grown by MBE at 200° C contains a strong As excess. Arsenic clusters are formed in the LT-GaAs after annealing at the temperature higher than 500°C. LT-GaAs can be used as buffer layers in field effect transistors due to high resistivity and as an active layer in ultra fast photodetectors since the carrier lifetime is very short in this material. It is generally believed that the properties of LT-GaAs are strongly affected by arsenic clusters. It has been previously shown that the clusters distribution can be controlled by inserting of thin InAs layers into LT-GaAs matrix [3, 4].

In this paper we studied the atomic structure of InAs delta-layers in as-grown LT-GaAs and its transformation after annealing. Dark-field cross-sectional transmission electron microscopy (TEM) and high resolution electron microscopy (HREM) were employed for this propouse.

Experimental

The LT MBE GaAs layers were grown in a dual-chambers 'Katun' MBE system on undoped semi-insulating GaAs substrates with (001) orientation. The substrates were prepared for growth procedure in the conventional manner. A 85 nm thick buffer layer of undoped GaAs was grown on the substrate at 580°C. Then the substrate temperature was lowered to 200°C and an LT - GaAs layer was grown at the grown rate 1 μ/h under arsenic pressure of 7×10^{-4} Pa. Indium delta layers were formed by interrupting the Ga beam for 4 s. and using an In beam at deposition rate of 0.15 monolayer per second. Thus produced, each delta layer contained approximately half a monolayer of InAs. The distance between the delta-layers was varied from 20 to 60 nm. The samples were divided into four parts, one of which was kept as grown, the others were annealed in the MBE chambers under arsenic overpressure for 10 min at 500, 600, and 700°C.

Cross-sectional TEM specimens were prepared by mechanical dimpling followed by Ar^+ ion sputtering with 4 kV energy and cooling. Some samples also were prepared by cleaving to avoid the effect of ion sputtering on the material structure. The TEM study was carried out by using Jeol 200 and Philips EM420 transmission electron microscope.

It is well known, that the (200) reflections are chemically - sensitive for fcc materials and can be used to detect composition variation using dark field technique [5]. That can be applied for observation of InAs insertions in GaAs. However, in the case of InAs delta-layers an additional contrast in the image can araise due to strain, which can cause a significant error. Therefore, we utilized both cross-sectional conventional samples and the cleaved samples with used (0-20) reflections. In the latter case, the layer projection depends on the specimen thickness (Fig.1). Approximation of this dependence toward zero allows us to derive the thickness of In

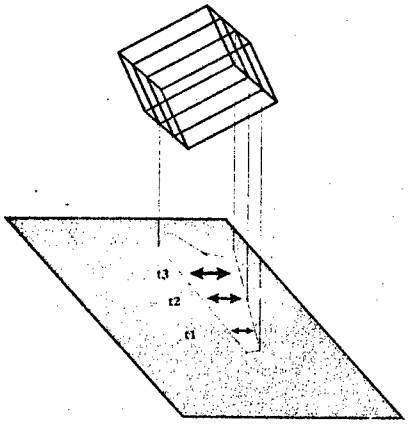

Fig.1.Sheme of the dark field experiment for measurement of InAS layer thickness in cleaved samples.

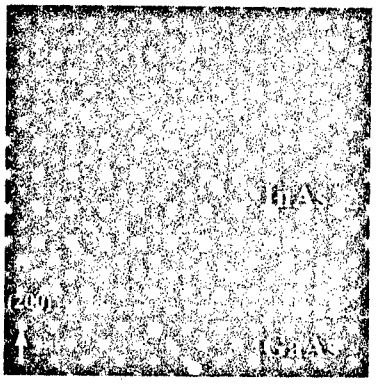

Fig.2. Simulating image of InAs layer taken at defocusing 600 nm and thickness of 50 nm.

delta layers. This data was compared with those obtained using dark field technique and by analysis of high-resolution images. The measurements of InAs delta-layer thickness from HREM image were carried out by analysis of contrast and fringes intensities corresponding to (200) and (220) planes. High resolution TEM images of InAs in GaAs matrix were simulated using McTEMP program various defocusing and specimen thickness. An example of this simulation is shown in Fig.2. One can see a pronounced contrast related to InAs insertion.

Results and Discussion

Fig3. shows the dark field TEM image of an as-grown LT-GaAs with built-in InAs delta layers. A contrast related to In delta-layer shows uniform thickness of the layers. The measurements of both conventional and cleaved samples gave equal result that the thickness of the InAs delta-layer is approximately 1nm. This value was also confirmed using HREM image. As can see in Fig.4 the InAs delta layers are as thick as 2-3 monolayers. Taking into account the (200) interplane distance in InAs, the layer thickness is equal to 0.9 nm.

Fig.3. (200) DF image of InAs layer in an as-grown samples

that spread of InAs layers occurred when In diffusion was activated upon annealing. That became significant when the annealing temperatures were higher than 600°C. TEM study showed that InAs layer thickness increases up to 8-9 monolayers after annealing at 600°C and up to 12 ML at 700°C. The delta-layer broading was accompanied by formation of As- precipitates at δ-In layers (Fig.4).

The evaluation of InAs layer thickness allows as to estimate the diffusion coefficient of In in LT-GaAs. According to [6], the InAs delta-layer spreading Δ is

$$\Delta=(4Dt)^{1/2},$$

where D is diffusion coefficient and t is annealing duration. Thus, estimated the diffusion coefficient of In in LT-GaAs matrix is 6.3×10^{-18} cm^2/s at 600°C annealing and $6.9\times10^{-17}cm^2/s$ at 700°C.

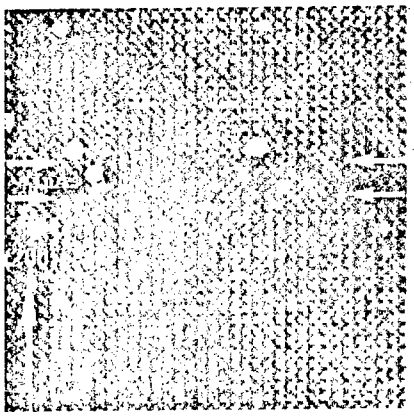

Fig.4. HREM image of InAs delta -layers in as-grown LT-GaAs

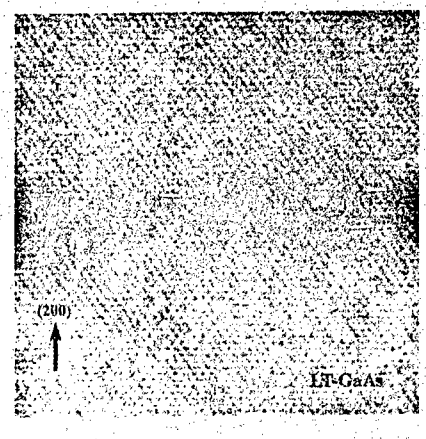

Fig.5. HREM image of As precipitates and In delta-layer in annealed samples at 600°C.

The obtained values of diffusion coefficient are approximately equal to those reported for conventional stoichiometric GaAs [7,8]. This looks rather unexpected, because very intensive diffusion processes go on in LT-GaAs under annealing. These processes result in excess arsenic precipitation and Ostwald ripening.

Summary

Using dark-field TEM and HREM we have studied the structure of InAs delta layers inserted in LT-GaAs matrix. Inspite of the fact that only 0.5 ML of InAs was deposited the real thickness of InAs delta-layers was found to be 2-3 ML in as-grown samples and it increasing upon subsequently annealing. Diffusion coefficient of In was found to be high as $6.3\times10^{-18}cm^2/s$ at 600°C and $6.9\times10^{-17}cm^2/s$ at 700°C.

Reference

[1] M.Kaminska, E.R. Weber, Z. Liliental-Weber; R leon, and Z.Rek, J. Vac. Sci. Thechnol. B7, 710, (1989)
[2] N.A. Bert, A.I. Veinger, M.D.Vilisova, et al Phys. Solid State, 35, 1289, (1993)
[3] Melloch M.R, Otsuka N, Mchalingam K, Chang C. L, Kircher P.D, Woodall J.M. and Warren A.C. Appl. Phys. Lett, 61, 177, (1992)
[4] N.A. Bert, V.V. Chaldyshev, D.I. Lubyshev, V.V. Preobrazhenskii and B.R Semyagin , Semiconductors,29, 1170, (1995)
[5] Petroff P.M, J. Vac. Sci Technol, 14(4), 973, (1977)
[6] Mallard R.E, Long N.J, Booker G.R. Scott, E.G, Hockly M, and Taylor M. J.Appl. Phys. 70(1), 182, (1991)
[7] K. S. Seo, P. K Bhattacharya, G. P. Kothiyal, and S. Hong , Appl., Phys., Lett, 49(15), 966, (1986)
[8] A O Kosogov, P Werner; U Geosele, N N Ledentsov and D Bimberg, V M Ustinov, A Yu Egorov; A. E Zhukov; P.S. Kop'ev, N.A. Bert, Apll. Phys. Lett. 69(20), 3072 (1996)

ON THE POSSIBILITY OF THE DEVELOPMENT OF VICINAL SUPERLATTICES IN QUANTUM WIRES ON SEMICONDUCTOR LOW - INDEX SURFACES

V. A. PETROV

Institute of Radio Engineering and Electronics,
Russian Academy of Sciences, Mokhovaya 11, Moscou, 103907, Russia
E-mail: vpetrov@mail.cplire.ru

As is well known, the existence of superlattice effects in quantum wells on semiconductor vicinal planes (thereafter called simple vicinal superlattices (VSL)) predicted (V.A.Petrov, 1977 [1]) and discovered independently in 1977 (T.Cole,A.Lakhani,P.J.Stiles [2]) is due to the appearance in these systems of a new cristallographic translation period in the plane of quantum wells $A >> a$ (a - lattice constant). A new translation period produces minigaps in the energetic spectrum of the particles in these systems and, as a result, different superlattice effects. At present, VSLs are developed only in 2D systems. At the same time it is known that these effects should be maximal in quantum wires when the period A appears along the axis of the wires.

In this work we suggest a new method of development of the VSL in the quantum wires. The special feature of this method is the combination of the main properties of the VSL - the separation in the system by some way of the long translation period A - with the possibility of developing this situation in the quantum wire on semiconductor *low - index* surfaces. It is easy to see that this situation is possible when the axis of the quantum wire which lies on the *low - index* surface will be oriented at the necessary angles to the basic translation vectors along the surface (Fig.1). In this case the translation symmetry of the quantum wire will be determined by its orientation on the crystal surface since the possibility of a free motion only along the axis of the wire selects in the initial two -

dimensional translation group along the surface a one - dimensional translation subgroup along the wire with the basic period A. Thus, in the two - dimensional VSL the period A along the surface is selected by the orientation *of the surface*, whereas in the one-dimensional VSL it is selected by the orientation *of the wire on the surface*. For example, if the quantum wire is realized in the MOS system with the use of a narrow gate (V.A.Petrov 1978 [3]) then the orientation of the wire will be determined simply by the appropriate orientation of the gate.

It was shown that two situations are possible in one-dimensional VSL 1.The quantum wire is developed on the surface of a single-valley semiconductor (the minimum of the energy is in the centre of the Brillouin zone) or when in multi-valley semiconductor the centres of the constant energy ellipsoids are projected onto the centre of the two-dimensional Brillouin zone. In this case the experimentally determined superlattice period coincides with the crystallographic period A.

2. If the centres of the constant energy ellipsoids in a multi-valley semiconductor are projected not to the centre of the two-dimensional Brillouin zone, then the experimentally determined period (quasiperiod) is different from the crystallographic period A. The analytic expressions of the periods and quasiperiods were obtained as a function of the angles which determine orientation of the quantum wire for the different low-index surfaces GaAs and Si. The positions of minigaps in the one-dimensional k-space were determined. It is should be noted that in the region of the particle wave function localization there are many crystallographic planes which form a superlattice energetic spectrum of the particle. Illustrative estimates of the magnitude of the minigaps for the quantum wire of the rectangular cross-section made in the weak coupling approximation demonstrate their dependence on the geometric parameters of the cross-section, on the period A (that is, on the angle of the orientation) as well as on the crystal potential.

Possible effects in these one-dimensional vicinal superlattises and their device applications are discussed.

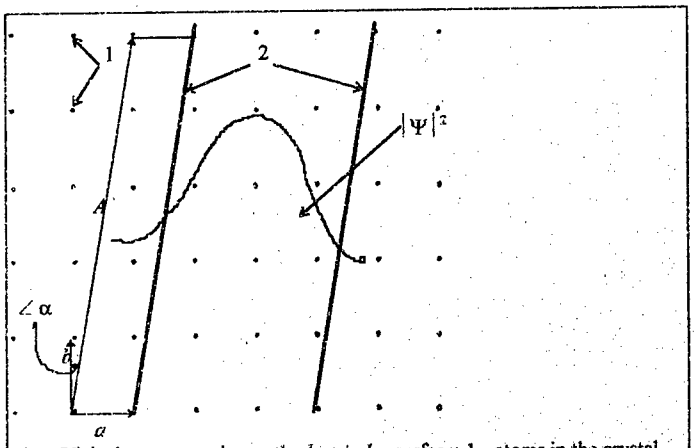

Fig.1.Vicinal quantum wire on the *low-index* surface; 1 - atoms in the crystal lattice, 2 - region of the particle wave function localization along the surface; a and b - basic translation vectors along the *low-index* surface; A- new basic translation period along the quantum wire; $\angle\alpha$ - orientation angle, which determines the period A in the vicinal quantum wire; $|\Psi|^2$ - distribution of electron density on the first quantum level along the surface in the wire.

REFERENCES

1. V.A.Petrov "Possibility of formation of one- and two-dimensional periodic superstructures in thin films and on semiconductor surfaces", 6th All-Union conf.on the Physics of Surface Phenomena in semicond.Kiev, 1977, USSR, Abstracts of Paper, Kiev, 1977, part 2, p. 80 ; Sov. Phys. Semicond. 12: 219-220 (1978).

2. T.Cole, A.A.Lakhani and P.J.Stiles, « Influence of a one - dimensional superlattice on a two - dimensional electron gas» Phys. Rev. Lett. 38, 722 (1977).

3. V.A.Petrov "Possible production of one-dimensional inversion (enrichment) channels at the semiconductor surface in an MOS - structure", Sov. Tech. Phys. Lett. 4: 285-286 (1978).

Non-stationary growth kinetics in GeH_4-Si MBE: composition abruptness at $Si_{1-x}Ge_x$/Si interface.

A. V. Potapov, L. K. Orlov

Institute for Physics of Microstructures RAS,

603600 Nizhny Novgorod, GSP-105, Russia, e-mail: potapov@ipm.sci-nnov.ru

The influence of GeH_3 molecule disintegration kinetics on compositional abruptness at $Si_{1-x}Ge_x$/Si interface in multilayer quantum size heterostructures grown by Si-GeH_4 MBE has been studied. Practical recommendations for reduction of erosion on the interface are given.

One of the main requirements on a growth technology of nanometer layer structures is obtaining of structures with extreme sharp interfaces. We have developed an epitaxy method to obtain $Si_{1-x}Ge_x$ layers from a Si atomic flow and a GeH_4 molecular flow (Si-GeH_4 MBE), which permits to grow heterostructures with thin (less than 2 nm) Ge layers [1, 2]. In particular, we have grown ($Ge/Si_{1-x}Ge_x$) superlattices [1] and structure with two quantum size Ge layers built-in $Si_{0.9}Ge_{0.1}$ alloy [2].

There are two main ways for a controlling a layer composition in our epitaxy method. The first way is the Si atomic flow manipulation, the second one - changing of the germane pressure. The first variant is more convenient in practice, as the process of changing the value of

the Si atomic flow is much less inertial than the process of changing the germane pressure. However, using the first way it is impossible to grow pure Si layers. To obtain such layers it is necessary to lower the germane pressure to a zero. Because the disintegration rates of GeH_n (n = 1, 2 ,3) molecules accumulated on a surface are limited and exponentially depend on the temperature, these molecules can for a long time be on a growing surface, especially at low growth temperatures. If Si atomic flow is continuing, a graded $Si_{1-x}Ge_x$ layer will grow instead of the Si layer even in the absence of segregation and diffusion processes. We have developed the theory of growth kinetics of $Si_{1-x}Ge_x$ alloy layers corresponding to Si-GeH_4 - MBE [1, 2].

Comparison of the experimental data and the theoretical curves has allowed to determine the value of the complete dissociation effective frequency of molecules GeH_3 $\nu_{GeH_3} = 0.5 \times \exp(-0.4/kT)$;s^{-1}) [1]. The life time of these molecules, τ, strongly grows with a reduction of the temperature and at T = 400 °C reaches the value about 2×10^3 s.

In order to simulate non-stationary processes we used a rectangular pulse of the germane pressure and a continuous flow of Si atoms. The duration of the pulse τ_p was 30 and 60 s. Thus, the transients arising after running of the germane pressure had time to disappear. Fig. 1 shows calculated distributions of Ge in layers. The uneven reduction of x immediately after the germane pulse is connected with the existence of an additional Ge atomic flow to the substrate [1, 2]. After the pulse Ge atoms on the surface are formed by thermal disintegration of accumulated GeH_3 molecules only.

For the analysis of the influence of the growth temperature (T), the Si atomic flow (F) and the germane pressure (P) on interface abruptness we shall introduce a characteristic length of a transitive area h. If the growth rate, V, is considered constant, the characteristic length h can be calculated by the formula

$$h = V\tau = 2V\exp(0.4/kT).$$

As is clearly seen from Fig. 1 and the formula, the growth temperature strongly affects the Ge distribution. At high temperatures residual Ge is located in rather narrow area. A decrease in temperature causes Ge atoms to spread to greater thickness with a simultaneous lowering of the Ge concentration level. An increase of the heterointerface erosion is basically connected with the exponential growth of the life time of GeH_3 molecules.

The increase of the Si atomic flow results in greater growth rates of layers ($V \sim F$) and, hence, in a larger characteristic length h. So, for $F = 1\times10^{15}$ $cm^{-2}s^{-1}$ and $T = 800$ °C (Fig. 1a) the length $h \approx 4$ nm, but for $F = 5\times10^{14}$ $cm^{-2}s^{-1}$ and the same temperature (Fig. 1b) $h \approx 2$ nm. Variation of the germane pressure does not have any appreciable influence on the value of h, however, it manifests itself through in change in the height of the Ge concentration jump after the germane pulse (Fig. 1b and 1c). As is shown [1, 2], the size of the Ge atomic flow is directly proportional to germane pressure. Therefore, sharper structure profiles are obtained at large values of P.

Thus, to obtain structures with extremely sharp $Si_{1-x}Ge_x$/Si interfaces by the given method one should increase germane pressure and reduce the value of a Si atomic flow. The optimum technological process seems to be that, in which after the germane pulse the value F is considerably reduced by τ. The growth temperature in this case is chosen such that the time τ is not very long and does not appreciably slow down growth of the entire structure.

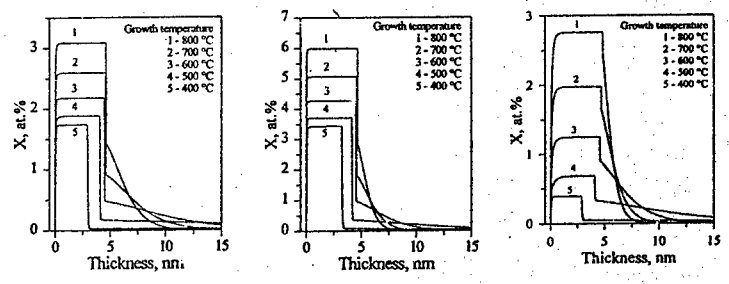

Fig. 1. Dependence of Ge content on layer thickness:

a - $P = 1\times10^{-4}$ Torr, $F = 1\times10^{15}$ $cm^{-2}s^{-1}$, $\tau_p = 30$ s;

b - $P = 1\times10^{-4}$ Torr, $F = 5\times10^{14}$ $cm^{-2}s^{-1}$, $\tau_p = 60$ s;

c - $P = 1\times10^{-5}$ Torr, $F = 5\times10^{14}$ $cm^{-2}s^{-1}$, $\tau_p = 60$ s.

References.

1. L. K. Orlov et. al. Proceedings of SIMC-9 (Toulouse, France, April 29 -May 3 1996). IEEE SIMC-9. 1996, December. P. 215.

2. L. K. Orlov et. al. Proceedings of ISCS-23 (St. Petersburg, Russia, September 23-27, 1996), to be published.

Self-organizing during film nucleation in GSMBE from silane and germane.

A. V. Potapov

Institute of Physics of Microstructures RAS,
GSP-105, 603600, Nizhny Novgorod, e-mail: potapov@ipm.sci-nnov.ru

The qualitative analysis of a formation of a new phase from silane and germane on substrates taking into account chemical reactions between surface components is made. Is shown, that for a determined ratio between surface diffusion coefficients of SiH_3 (GeH_3) molecules and Si (Ge) atoms an adatom distribution loses a stability. Thus there can arise the phenomenon of self-organizing, causing to a periodical dependence on coordinates of a nuclear concentration of the new phase. An influence of the hydride pressure and growth temperature on an opportunity of a self-organizing occurrence is analysed.

In the last years the physical properties of semiconductor quantum-size systems have attracted wide attention. In particular, due to the confinement of free carriers and excitons, quantum dots are expected to give an increase of a quantum efficiency by the enhancement of the optical electron-hole recombination strength. Especially it is important for indirect-gap materials in view of their possible applications in integrated silicon optical devices.

For obtaining of quantum dots are widely used molecular beam epitaxy and chemical vapour deposition techniques. In the present work the qualitative analysis of self-organizing effect in the silane and germane gas-source molecular beam epitaxy is made.

During the film growth from hydrides on a growing surface different chemical reactions take place. If the interaction of various components, adsorbed by a substrate, is non-linear, the stability can be lost just as it occurs in ordinary chemical

systems. As a result a conception distribution of a new phase becomes non-uniform. Moreover, the fact, that the product of the reaction undergos a phase transition, can result in the development of the instability. This instability, probably, is one of reasons, causing the non-uniform film growth.

So, I shall consider the problem on stability of a system of adsorbed atoms and molecules on the basis of a simple model. Let hydride molecules arrive on the surface (M - Si or Ge atom)

$$MH_4 + 2 \xrightarrow{f} \underline{M}H_3 + \underline{H}, \qquad (1)$$

molecular MH_3 may disintegrate by two ways

$$\underline{M}H_3 + 3 \xrightarrow{\nu} \underline{M} + 3\underline{H} \qquad (2)$$

and

$$\underline{M}H_3 + \underline{M} + 3 \xrightarrow{\varphi} 2\underline{M} + 3\underline{H}, \qquad (3)$$

thus, the atoms M are a self-catalyst. Then adatoms are built-in a crystal lattice

$$\underline{M} \xrightarrow{\gamma} M_{cr}. \qquad (4)$$

For simplicity we shall consider, that the concentration of hydrogen atoms on the surface is negligible and a quantity of conceptions of the new phase is constantly. Then for surface concentrations of molecules MH3 and atoms M it is possible to write

$$\begin{cases} \dfrac{\partial \theta_{MH_3}}{\partial t} = D\Delta\theta_{MH_3} + f(1-4\theta_{MH_3}-\theta_M)^2 - (\nu+\varphi\theta_M)\theta_{MH_3}(1-\theta_{MH_3}-\theta_M)^3 \\ \dfrac{\partial \theta_M}{\partial t} = kD\Delta\theta_M + (\nu+\varphi\theta_M)\theta_{MH_3}(1-\theta_{MH_3}-\theta_M)^3 - \gamma\theta_M \end{cases}$$

The investigation of this system revealed, that for realization of the instability the ratio between diffusion coefficients of the atoms M and molecules MH_3 k must be less than unit. In the interval (0, 1) can exist one or two areas of unstable states. On the diagram two possible situations are submitted (areas of the instability are shaded).

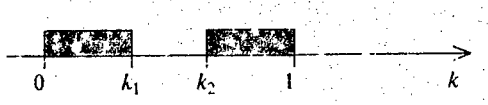

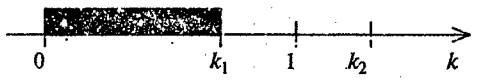

In the case of the high pressure ($f >> \varphi, \nu, \gamma$) critical values $k_{1,2}$ are approximate equal to

$$k_{1,2} \approx \frac{1}{2}\left(\gamma - \frac{27}{64}\left(\frac{1}{4}\varphi - \nu\right)\right)(f\nu)^{-\frac{1}{2}} \pm \frac{3}{16}\sqrt{\left(\gamma - \frac{27}{64}\left(\frac{1}{4}\varphi - \nu\right)\right)\left(\nu + \varphi\theta_M^*\right)}\, f^{-\frac{3}{4}}\nu^{-\frac{1}{4}},$$

$$k_{1,2} < 1 \text{ when } \gamma < 2\sqrt{f\nu} \pm \frac{3}{4}\sqrt{\frac{1}{2}\nu\left(\nu + \varphi\theta_M^*\right)},$$

here θ_M^* - the equilibrium concentration Si or Ge atoms on the substrate surface. For the pair SiH3 and Si $k \approx e^{-0.4/kT}$, that is a lot of less than 1 in the all temperature range presenting practical interest [1, 2].

Analysis shows, that near to the critical point k_1 the surface concentration of molecules MH_3 and atoms M change in anti-phase. In this case a characteristic period of non-homogeneities is

$$\lambda \propto D^{1/2} P_{MH_4}^{-1/4},$$

whence follows, that distance between non-homogeneities will grow at increase of the temperature to decrease at increase of the pressure. Conception of a new phase will be formed in those areas, where the adatom concentration exceeds some threshold significance.

The transition of the system in the steady condition will occur at infringement of the condition

$$\frac{1}{4}\varphi - \nu > 0.$$

Thus, the increase of temperature should result in failure of the instability because the speed of reaction (2) exponentially grows.

Downturn of temperature will lead to the accumulation of hydrogen on the surface. Account of this effect results in the following condition of transition in the steady state

$$\left(\frac{3}{4}-\theta_H\right)\varphi - 3\nu < 0,$$

whence it is visible, that the increase of the hydrogen concentration strengthens fulfilment of this inequality and at some significance results in that the system will be steady at any significance of parameters.

Thus, should exist an interval of temperatures, in which the process of self-organizing will be realized. At temperature below this interval the failure of instability is caused by the accumulation of hydrogen on the surface, and above - by the exponential growth of the rate of molecules SiH_3 (GeH_3) thermal disintegration.

References.

1. Gates S. M., Greenlief C. M., Beach D. B. // J. Chem. Phys. 1990. V. 93. P. 7493.
2. Ruzaikin M. P., Svechnikov A. B. Crystal growth. Edited by Givargizov E. I. and Grinberg S. A. Moscow, "Nauka", 1990, V. 18, P. 18.

Selforganization of the fullerene complexes on solution

V.V. Rotkin

Ioffe Physical-Technical Institute, 26, Politekhnicheskaya st., 194021 St.Petersburg, Russia.

(21 April 1997)

It is shown that the van-der-Waals energy of the cluster-cluster interaction in the fullerene systems is described well via the change of the plasmon energy. The energetical reason gives a guess that the solution of the single C_{60} cluster is not favorable. Contrary, the dimer solution energy is negative, which results in the supposition that the dissolving occurs via the dimerization. The possible experiment to proof the result is discussed.

After last six year efforts which are manifested by hundreds of papers on the physics, chemistry of the fullerenes and the fullerene based materials it is known a lot about the electronic structure of the single macromolecule which is the base of the different materials like the doped solids and the chemical adducts. A variety of the computational methods was used, from the *ab initio* calculation to the empirical approach to compute the energy of the inter-cluster interaction in the fullerene solid. One interesting in a review of the calculation and experiment can look at the references in [1,2].

This paper introduces the simple theoretical approach allowing to evaluate the energy of the van-der-Waals interaction in the fullerene condensed phase. The main part of this interaction is determined by the plasma modes of the solid. The same approach was used for the evaluation of the interaction of the single cluster with the different solids in [3]. The interaction of the cluster and the organic (non-polar) liquid solvent will be likewise considered below.

The optical and electrical properties of the fullerene materials allows to talk about C_{60} as the new artificial atomic unit for the nano-engineering. However the level of the fullerene technology is not high enough to be competitive with the standard electronic materials. The single cluster gives the classical example of the semiconducting quantum size dot. Relating to that it occurs interesting to know more about the stability of different fullerene complexes, namely, the dimer and other possible oligomers. As it has been declared in the abstract this theoretical paper predicts the formation of the fullerene dimer during the dissolving of the solid fullerene. The consideration, probably, correlates with the recent experiment [4], where the dimerized structures were observed in the water mixture. Even the polar liquid solvent stills beyond this theory.

1. THE ENERGY OF THE VAN-DER-WAALS INTERACTION

As usual the van-der-Waals energy is given by the shift of the plasmon zero-oscillation energy in the solid comparing with the single cluster. This shift is due to the Coulomb interaction between clusters which can be reduced to the elementary cell in the translational invariant system. The origin of the van-der-Waals forces is the same as the depolarization shift of the plasma mode frequency in the dielectric medium.

In the case of the cubic crystal and for the rotationally invariant system (liquid, for example) one can easily calculate this depolarization shift following the method of the mean field. Then the Lorentz-Lorenz approximation gives the shift including the local field effects. This is valid for the solid fullerene, which forms fortunately face-centered cubic lattice.

We calculate the mode frequencies for the face centered cubic cell with four clusters in the approximation of the dipole-dipole interaction. It was shown that the higher multipolar interaction terms can be neglected [5]. However, it is not important because of our model allows to include any multipole correction if anybody needs more accuracy.

The dipole excitation of the single cluster is elementary unit in all our consideration. It was shown that C_{60} electron density has the collective mode with the frequency about 25 eV. This is the surface plasmon on the fullerene sphere. It can be described phenomenologically [6] as well as within more sophisticated approach (see [7] and references [10-14] in Ref.[7]). So far the dipole plasmon we will use as the elementary excitation of the fullerene "super-atom" unit.

In other terms, the van-der-Waals interaction can be written using the fluctuation-dissipation theorem as the integral over the frequency of the combination of the C_{60} cluster dynamic polarizability and the dielectric function of the medium. Of coarse, in the case of the pure crystal C_{60} it is the same function. Then this integral can be evaluated in the complex plane of the frequency. The main contribution comes from the excitation having the maximal oscillator strength. It is the collective plasma mode of the cluster.

Let us remind that the frequency of the dipole plasmon can be found as the hollow metal sphere plasmon frequency:

$$\omega_1 = \omega_p\sqrt{\frac{2}{3}} \sim 22 \text{ eV} \quad \omega_p = \sqrt{\frac{240\ e^2}{mR^3}} \sim 26.9 \text{ eV}, \tag{1}$$

here ω_p is the bare plasma frequency, 240 is the number of valence electrons of the cluster, with the electron mass m and the charge e. The sphere radius R is taken ~ 3.3 Å to describe the fullerene plasmon properly. The details of the calculation can be found in [7].

Considering the fullerene solid we use the Lorentz-Lorenz approximation due to the high polarizability of the single cluster, α. A packing factor coming into the dielectric function along with the dynamic polarizability reads as:

$$\alpha(\omega) = R^3\frac{1}{1-\omega^2/\omega_1^2}, \quad \eta = 4\pi\nu\alpha(0) = 4\pi\frac{4}{d^3}R^3 \tag{2}$$

where $\nu = 4/d^3$ is the density of the clusters, $d \sim 14.2$ Å is the lattice constant. This is very common parameter in such a calculation, we take it as 0.79.

It will be very convenient to use the square of dimensionless plasma frequency $x = \omega^2/\omega_1^2$. This Lorentz-Lorenz formula gives us the plasma longitudinal frequency $\omega_L = \omega_1\sqrt{x_L} \sim 26.2$ eV along with the transverse excitation frequency $\omega_T = \omega_1\sqrt{x_T} \sim 19.6$ eV as the zero and the pole of the ϵ, the dielectric function. Then the van-der-Waals energy is the simple difference between the plasma frequency of the cluster and the modes in the solid. It reads as:

$$W = \hbar\omega_1\left(\sqrt{x_L} + 2\sqrt{x_T} - 3\right) \sim -\hbar\omega_1\frac{\eta^2}{24} \tag{3}$$

The only two parameters determining the van-der-Waals energy are the plasmon energy and the packing factor. In the expression above we used the expansion on the small η. The interplay between these parameters gives us, for example, the plasma frequency on the boundary between some mediums, in the liquid, in the medium with polarizable dopant and so on. We will discuss it at length elsewhere. Substituting the numbers into Eq.(3) one gets the van-der-Waals energy about -0.36 eV per cluster in the solid. The one of the first papers containing similar consideration to be mentioned is [8]. In the next section we will compare the result with the energy in solution.

2. FULLERENE IN SOLUTION

The plasma frequency in the solution is different from the solid phase because of the depolarization shift is much weaker in any typical organic solvent than in the solid. The reason is that the fullerene cluster has the very high frequency of this bare plasmon due to the

large number of the highly polarizable electrons. The standard medium is nearly transparent at this frequency. More precisely the dielectric function of the medium is slightly less than the unity at the frequency of C_{60} plasmon. Such a behavior of the dielectric function is not common. Probably, it was the reason that in earlier papers the depolarization shift of the plasmon of the C_{60} cluster in the dielectric liquid has been calculated improperly.

In [9] the dielectric function has not been considered, in contrary, the static permittivity has been used for the liquid surrounding the cluster. Then the boundary conditions change so that the plasma frequency depends on the permittivity of the solvent. Then the difference in the plasma frequency reads as follows:

$$\delta\sqrt{x} \simeq \frac{1}{3}(1-\epsilon), \tag{4}$$

here we expand the expression Eq.(4) on the small positive parameter $1 \gg 1-\epsilon > 0$. This is the logical way to solve the Barton model, we note that $\epsilon = \epsilon(x)$ is the function of the frequency by itself that was omitted in [9]. Then it is seen from Eq.(4) that the plasmon frequency shifts upward, that does not consist with the solubility of the fullerene.

According [7], the surface plasmon in C_{60} is the spherical oscillation of electron density σ_{LM}. For central symmetry of the cluster we use expansion of all quantities in complete spherical harmonics $P_L(r)Y_{L,M}(\Omega)$ those form a complete set on a sphere. In spherical geometry a radial jump in electric field is given by:

$$\frac{2L+1}{R}\varphi_{LM} = 4\pi\sigma_{LM}. \tag{5}$$

where $\varphi^{act} = \varphi^{ext} + \varphi^{ind} = \varphi^{ext}_{LM} + 4\pi R\sigma_{LM}/(2L+1) + \varphi^{sol}_{LM}$ is acting potential, L, M are multipole power indexes (or angular momentum and its projection onto z-axis). The selfconsistency of the calculation is proved by this acting potential including the induced potential of the C_{60} plasmon as well as the potential due to charge density induced in the solvent. We close the equation system by writing the response function for the fullerene as:

$$\frac{4\pi R}{2L+1}\sigma_{LM} = -\frac{4\pi R}{2L+1}\chi_L\,\varphi^{act}_{LM} = -\frac{\omega_L^2}{\omega^2}, \tag{6}$$

where χ is a response function of single sphere. This expression is easily obtained from classic charge liquid equations [6,7]. This consideration is more general than our $L = 1$ case of the dipole plasmon mode. However for the spherical symmetry the expression Eq.(6) holds for all multipoles.

When the induced in the solvent potential $\varphi^{sol}_{LM} = 0$ is absent, we return to the bare plasmon frequency. The corresponding bare dispersion equation reads as:

$$-\frac{4\pi R}{3}\chi_1 = \frac{\omega_1^2}{\omega^2}\frac{1}{x} = 1, \tag{7}$$

while we simply change the unity to the dielectric function including the solvent potential. It is easily seen substituting the Eq.(6) into Eq.(5) and taking the standard RPA sum. As a result the plasma frequency in the solution is:

$$\Omega(\varepsilon) = \omega_1\sqrt{\varepsilon(\Omega)} \tag{8}$$

The frequency is smaller than for the bare C_{60} that is better than the result Eq.(4).

So far we obtain the plasmon in the fullerene solid and in the solution. We will use for the dielectric function of the liquid solvent the common formula:

$$\epsilon(\Omega) = \frac{\Omega^2 - \omega_L^2}{\Omega^2 - \omega_T^2}$$

where ω_L is the typical longitudinal frequency of the $\epsilon(\Omega)$, and ω_T is the transverse frequency. With this definition the van-der-Waals energy can be written as:

$$W \sim -3/2\hbar\omega_1 \frac{\omega_L^2 - \omega_T^2}{\omega_T^2} \frac{\omega_T^2}{\omega_1^2} = -3/2\hbar\omega_1 (\epsilon_0 - 1) \left(\frac{\omega_T}{\omega_1}\right)^2 \tag{10}$$

here ϵ_0 is the static permittivity which is related to the transverse and longitudinal frequencies. The typical values for ϵ_0 is 2.3 for the benzene, 2.1 for the toluene. The van-der-Waals energy is about -0.2 eV for these solvents. So we have to conclude that by this energetical reason the solid fullerene should be more stable.

Let us consider the fullerene dimer, the similar problem was done in the [5] for the C_{119} molecule. The plasmon frequency is splitted in the axial field. Therefore the new modes bring the energy of the interaction between clusters in the dimer as the difference between the frequency of the bare plasmon and new one. Then the van-der-Waals energy of the dimer coupling reads as:

$$W \sim -3/2\hbar\omega_1 \left(\frac{R}{H}\right)^3 \left(1 + \frac{3}{2}\frac{\omega_L^2 - \omega_T^2}{\omega_T^2}\frac{\omega_T^2}{\omega_1^2} + \dots\right) \tag{11}$$

where $R \simeq 3.6$ Å and $H \simeq 8$ Å are the cluster radius and the inter-cluster distance; here the last term comes from the solvent depolarization, it is a small correction (about a percent) which will be negiected. The typical value of the van-der-Waals energy of such a dimer is about -0.7 eV.

We suppose that solvent softens the van-der-Waals forces between C_{60} clusters near the surface. Then the fullerenes form dimers near the surface. Certainly, the process has to be recalculated more accurately, including the conditions on the boundary between the fullerene solid and the solvent. We believe that these selforganized structures, probably, can be found in the solution. The Raman and IR-active phonon modes of the single cluster are splitted in the dimer like the plasmon frequency shown above. Besides that the UV irradiation of the solution can shift the equilibrium in the selforganization process because of the excitation of the single cluster plasmons.

Acknowledgments. Author thanks M.V. Korobov for the discussion which stimulate the work. This work was fulfilled within Russian research and development program 'Fullerenes and Atomic Clusters' project N 94014 and was partially supported by RFBR Grant 96-02-17926 and is carried out under the research program of International Center for Fundamental Physics in Moscow.

[1]. S.V. Kozyrev, V.V. Rotkin, Sov.- Semiconductors v.27, N 9, pp. 777-791, 1993.
[2] S.Samuel, Int.J.Mod.Phys. 7, N 22, 3877, 1993.
[3] V.V.Rotkin, Abstract on MRS-93-Fall Meeting, Boston, USA, 1993.
[4] E.V. Skokan, private communication; Moscow State University, Moscow, Russia.
[5] V.V.Rotkin, R.A.Suris, Sol.State Comm., v. 97, N 3, 183-186, 1995; V.V.Rotkin, R.A.Suris, Proc.of International Symposium "Nanostructures: Physics and Technology-95", pp.210-213, St.Petersburg, Russia, 26-30 June 1995.
[6] V.V.Rotkin, R.A.Suris, Proc. Symposium on Recent Advances in Chemistry and Physics of Fullerenes and Related Materials, Eds. K.M.Kadish, R.S.Ruoff. Pennington, 1996, p.940-959.
[7] Rotkin V.V., Suris R.A., Sov.- Solid State Physics, /bf 36, 12, 1899-1905, 1994.
[8] Lucas A.A., Gensterblum G., Pireaux J.J., Thiry P.A., Caudano R., Vigneron J.-P., Lambin Ph., Kratschmer W., Phys.Rev.**B 45**, 13694 (92).
[9] G. Barton, C. Eberlein, J. Chem.Phys. **95**, N 3, 1512-1517 (1991).

A technology for fabricating two- and one-dimensional ensembles of superparamagnetic nanoparticles

A.B. Vorob'ev, A.K. Gutakovsky, V.Ya. Prinz, V.A. Seleznev
V.L. Kuznetsov*, Yu.V. Butenko*, A.B. Sharaya*, E.M. Moroz*, V.N. Kolomiichuk*
Institute of Semiconductor Physics SB RAS, Novosibirsk 630090, Russia
*Boreskov Institute of Catalysis SB RAS, Novosibirsk 630090, Russia

Studies of structures with reduced dimensionality brought on by their intriguing physical properties are hampered by technological difficulties which arise when creating such structures. In this work, we propose a new procedure for obtaining two- and one-dimensional magnetic nanostructures which includes:

1. Production of superparamagnetic nanoparticles.
2. Preparation of a colloidal system of the nanoparticles in a dissolved polymer.
3. Fabrication of a matrix to be grouted with the colloidal solution.
4. Employment of capillary forces and an external magnetic field for providing regular arrangement of the particles in the matrix.

Recently, the possibility was shown to insert carbon or metalloorganic clusters into ultranarrow (1–100 nm-wide) slits in GaAs films [1], the slits with atomically smooth edges having been obtained with using the controllable cracking method [2]. In this paper, we show the possibility of inserting superparamagnetic particles into such slits followed by their rigid fixation in a polymer matrix.

The magnetite particles smaller than 10 nm in size are known to exhibit paramagnetic properties. They possess intrinsic magnetic moments aligned according to the direction of the applied magnetic field, the particles themselves remaining immobile. Thus, imposing a magnetic field on thin polymeric films with the superparamagnetic particles inserted into slits, one can create quasi-two-dimensional and quasi-one-dimensional systems of equally oriented magnetic dipoles.

Ultranarrow slits were controllable created in GaAs films with thicknesses ranging from 0.1 to 10 μm. The width of the slits varied from 3 to 100 nm being dependent on cracking conditions and film parameters. With the help of capillary forces, the slits were filled up either with a colloidal system of iron oxide particles in the polystirene dissolved in toluene, or with the same solution containing suspended magnetite nanoparticles (Fe_3O_4) which had been preliminarily obtained from adsorption of iron (3) acetate onto the surface of the soot followed by removal of carbon matrix. According to the specific magnetisation measurements and small angle X-ray scattering and X-ray diffraction data, the mean size of the particles was about 2 nm. Small width of the slit results in a mechanical orienting of non-spheroidal particles upon their motion inside the capillary formed by slit edges as well as in one-layered arrangement of the particles in the thin polystirene matrix. Such thin polymeric films with rigidly fixed (after removing the solvent) particles could be the object of HRTEM studies.

The samples for the HRTEM studies were prepared with using two different methods:

1. By cleaving the GaAs film along a slit with subsequent separating of the polystirene film off its edges;
2. By chemical etching of the GaAs resulting in partial uncovering of the polystirene film.

In the HRTEM images, there have been observed isolated crystalline particles with lateral dimensions from 4 to 20 nm and their aggregates. The strips in the images due to the crystal lattice of the particles corresponded to the cubic structure of magnetite. There have been observed reflexes corresponding to {111} planes (separation between strips 0.48 nm) as well as to {100} and {220} planes (0.42 and 0.29 nm, respectively).

The lower (as compared to the HRTEM data) values of the particle size yielded by the small angle X-ray scattering and X-ray diffraction techniques can be explained if we recall that it is the coherent scattering length which is determined by these methods, while the true particle size can exceed the latter. The underestimated particle sizes extracted from the specific magnetisation measurements may be related to the fact that the real shape of the particles could differ from the spheroidal one assumed in treating the data. Additionally, owing to the orienting influence of the narrow slit, it is the largest (in area) sides of the particles that turn out to be normal to the direction of the testing electron beam of microscope.

Superparamagnetic particles are known to play an important part in the magnetoreceptivity of living beings. The present works considers some application fields of the above nanostructures with superparamagnetic properties based on the principles met with in nature.

References

[1] V.Ya.Prinz, V.A.Seleznev, A.K.Gutakovsky, Novel technique for fabrication one- and two-dimensional systems, 1996 Surface Science V 361/362 (1996) p. 886-889.

[2] V.Ya.Prinz, V.A.Seleznev, A.K.Gutakovsky, Application of controllable crack formation for nanoelectronic device elements fabrication, Compound Semiconductors-23 IOP Publishing, UK, London in press.

Strained Quantum Islands of InAs in an (In,Ga)As/InP Matrix

A. E. Zhukov*, V. M. Ustinov, A. Yu. Egorov, A. R. Kovsh, A. F. Tsatsul'nikov,
M. V. Maximov, B. V. Volovik, A. A. Suvorova, N. A. Bert, P. S. Kop'ev

A. F. Ioffe Physico-Technical Institute,
Russian Academy of Sciences,
26 Politekhnicheskaya, St. Petersburg, 194021, Russia
*Phone: (812) 2479132, Fax: (812) 2478640, *E-mail: zhukov@beam.ioffe.rssi.ru*

In the present work we report on growth by molecular beam epitaxy and structural and optical characterization of strained InAs quantum islands embedded in an (In,Ga)As matrix lattice matched to an InP substrate. The onset of island growth mode after depositing 3 monolayers of InAs was revealed by transmission electron microscopy (TEM) and high energy electron diffraction (RHEED). The InAs islands formed are coherently strained and have a base length of the order of 20÷90 nm. Island formation leads to appearance of an additional dominant line in photoluminescence spectra that shifts towards lower energy with increase in effective thickness of InAs deposited. The emission of InAs islands covers the wavelength band within 1.65÷2 μm.

Remarkable improvement of the threshold current density (J_{th}) and its thermal stability have been predicted for a quantum dot (QD) laser [1]. Self-ordered quantum dots (QDs) formed in a wider band-gap matrix are promising candidates for laser applications. Up to now, structural and optical properties of (In,Ga)As QD arrays inserted into an (Al,Ga)As matrix have been studied in details. They were applied as an active region of injection lasers to achieve continuous wave operation for lasing via the QD ground state up to room temperature with output power of the order of 1 W and J_{th} values as low as 100 A/cm^2 [2]. However, the emission wavelength of QDs formed on GaAs substrates is limited within 0.9÷1.3 μm range. The extension of the wavelength range which can be achieved in QD structures up to 1.3÷2.0 μm seems to be very promising for applications in optical fiber communication and environment pollution monitoring systems.

In the present work we will show that this problem can be solved by InAs QDs inserted into an InGaAs/InP matrix. Such structures are very interesting from the fundamental point of view as well to investigate spontaneous formation of low-dimensional objects in addition to studies in (In,Ga)As/(Al,Ga)As material system.

The structures studied were grown by molecular beam epitaxy (MBE) in an InGaAs matrix lattice matched to InP. The effective thickness of InAs deposited (Q_{InAs}) was varied within 0÷13 monolayers (ML). Photoluminescence was excited by He-Ne laser (20 W/cm^2, 1.954 eV) and detected by cooled InSb photodiode.

Monitoring RHEED patterns during the InAs deposition gives an unambiguous evidence of the formation of three-dimensional islands after depositing approximately 3÷3.3 ML of InAs in a good agreement with the data reported for the deposition of InAs in an (In,Al)As/InP matrix [3] as well as of $In_{0.5}Ga_{0.5}As$-in-GaAs system [4,5] which is characterized by nearly the same lattice mismatch. However, we should note that in our case the spotty contrast in RHEED pattern is not so pronounced indicating that the islands have a lower aspect (height-to-base) ratio as compared to that in the case of (In,Ga)As-GaAs system.

Transmission electron microscopy gives a clear evidence of the presence of coherently strained InAs islands. Fig.1 shows lateral size histogram for the sample obtained by deposition of 6 ML of InAs. The average lateral size of about 50 nm is noticeably lager than the corresponding value in the case of InGaAs QDs on GaAs which can be varied 8÷20 nm [5] depending on growth condition. It should be noted that the island size extracted from TEM images in the present work may be somewhat larger than the real one due to the effect of strain fields propagating into a matrix. The similar large lateral size was obtained by atomic force microscopy for InAs islands grown by gas-

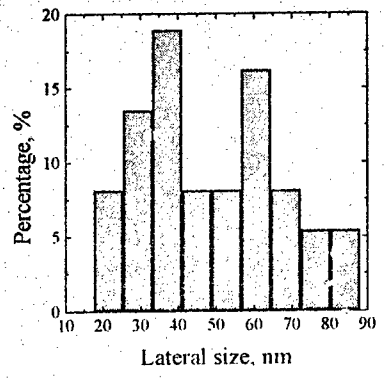

Fig.1. Lateral size histogram of the 6-ML array of InAs islands.

source MBE on GaInAsP quaternary buffer layer [6]. Typical island height of about 4÷5 nm was revealed by cross-section TEM images. In agreement with RHEED data, the islands are characterized by low aspect ratio of the order of 1:10. They lie on a few monolayer thick wetting layer of InAs.

77 K photoluminescence (PL) spectra of the structures with varied effective thickness of InAs deposited are presented in Fig.2. Island formation leads to appearance of a dominant line strongly red shifted with respect to emisssion of the (In,Ga)As matrix. PL linewidth does not depend on InAs coverage to be about 35÷37 meV. Integrated PL intensity as a function of InAs effective thickness is nearly constant until Q_{InAs}=9 ML when it starts to fall down. No PL signal was recorded for the sample of Q_{InAs}=13 ML.

PL peak position gradually shifts toward longer wavelengths with the increase in the effective thickness of InAs deposited (Fig. 3). The experimental data are compared with the results of the numerical calculation of the optical transition energy in InAs/InGaAs quantum well assuming two-dimensional growth mode [7]. It is clearly seen that the island formation lead to the remarkable red shift of PL peak position

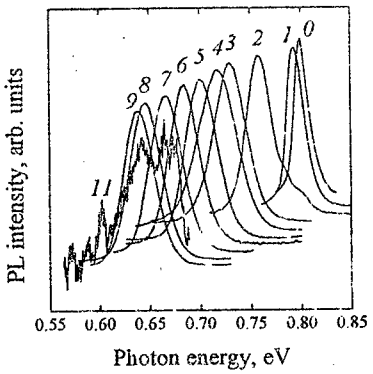

Fig.2. 77 K PL spectra of the samples with InAs effective thickness in the active region varied within 0-13 ML.

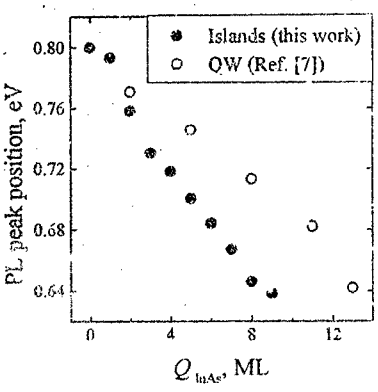

Fig.3 PL peak position (77K) for the structures with InAs islands (this work) and numerical calculation for InAs quantum well [7].

The maximum wavelength obtained in the present work (Q_{InAs}=9 ML) is as high as 1.944 μm (77 K).

The experimental data obtained can be well explained as follows. Formation of three dimensional islands in the active region results in a drastic increase in carrier localization energy owing to an extension in effective size of the active region in growth direction. At the same time, coherent growth of a strained island can be maintained until some critical size beyond which misfit dislocations are appeared. Such a plastically relaxed island does not contribute to luminescence. Thus, we can conclude that an essential part of islands excess a critical size at Q_{InAs} of about 11÷13 ML.

In conclusion, arrays of strained InAs islands in an (In,Ga)As/InP matrix were synthesized by self-organization during pseudomorphic MBE growth. Preliminary investigation of their structural and optical properties were reported on. RHEED and TEM data in a favor of island formation were presented. PL peak position up to 1.94 μm was observed at 77 K.

[1]. Y.Arakawa and H.Sakaki. Appl. Phys. Lett., 40, 939 (1982).

[2]. V.M.Ustinov, A.Yu.Egorov, A.R.Kovsh, et al., to be published in J. Cryst. Growth, 175 (1997).

[3]. S.Fafard, Z.Wasilewski, J.McCaffrey, et al., Appl. Phys. Lett. 68, 991 (1996).

[4]. P.M.Petroff and S.P.DenBaars. Superlat. Microstruct., 15, 15 (1994).

[5]. S.Ruvimov, P.Werner, K.Scheerschmidt, et al., Inst. Phys. Conf. Ser. No. 146, 31 (1995).

[6]. V.Drouot, S.Frechengues, B.Lambert, et al., Int. Conf. On InP and Related Compounds, Cape Code, MA, USA (1997).

[7]. E.Tounie, O.Brandt, and K Ploog, Semicond. Sci. Technol. 8, S236 (1993).

Three Dimensional E-Beam Lithography.

V.V. Aristov, S.V. Dubonos, B.N.Gaifullin, A.A. Svintsov, S.I. Zaitsev

Institute of Microelectronics Technology, Chernogolovka, 142432, Russia, zaitsev@ipmt-hpm.ac.ru

INTRODUCTION

Large and sophisticated electron beam lithography instruments are a necessity in modern IC production - but besides this, there are many applications which need electron beam lithography at a much smaller scale. Some of these fields are: optimizing of electron resist, integrated optics experiments, X-ray optics with zone lenses, experiments with individually created IC components, window etching in ICs for failure analysis, epitactic and galvanic experiments. Main phenomenon restricting a resolution of e-beam lithography is so called proximity effect when backscattered electrons expose places far from inlet point of e-beam. First attempts to correct proximity effect were made more than fifteen years ago [1-6]. Many studies have been done in this field, suggesting different correction methods. But no method allows to calculate a guaranteed final accuracy especially by taking into account the process of resist development, except the method of "simple compensation" which was introduced by Aristov et al [5,6].

Today, there is an increasing demand for production of real there-dimensional (3D) structures, such as blazed gratings, Fresnel lenses, diffractive optical elements, computer generated holograms, lens arrays, etc. [9-12] For these the total area has to be exposed with a continuously variable dose, which of course needs proximity correction as well. This was not available up to now. All established for proximity correction beginning from the first ones [1-4] up to recent work [13,14] aim to correct two-dimensional structures. Typical sizes of the optical elements mentioned above are in the range 100nm-10um: therefore the proximity effect correction is a crucial point for the whole design and technological procedure.

This paper describes models of exposure and development, method of proximity correction (including 3D proximity correction) and its accuracy. All this is a base of software package PROXY which enables any scanning electron microscope (SEM) to perform as an electron lithograph

EXPOSURE AND DEVELOPMENT MODELS.

Absorbed dose distribution $D(r)$, $r=(x,y,z)$, in the resist depends linearly on exposure dose $T(x,y)$. For correction it is generally assumed that D is independent on resist depth z [1] , which leads to

$$\frac{D(x,y)}{D_0} = \frac{1}{T_C}\int I(x-x', y-y')\,T(x',y')\,dx'dy'$$

D_0 and T_0 are absorption and exposure sensitivities of a resist respectively. The proximity function $I(\rho)$, $\rho=(x,y)$, is written as a sum of two Gaussians

$$I(\rho) = \frac{I_1(\rho)}{(1+\eta)} + \eta\frac{I_2(\rho)}{(1+\eta)} = \frac{1}{(1+\eta)}\left(\frac{e^{-\frac{\rho^2}{\alpha^2}}}{\pi\alpha^2} + \eta\frac{e^{-\frac{\rho^2}{\beta^2}}}{\pi\beta^2}\right), \qquad \rho^2 = x^2+y^2$$

which are interpreted as contributions of primary beam, $I_1(\rho)$, and backscattered electrons, $I_2(\rho)$. Here I, I_1 and I_2 are normalized on unity. The primary beam is concentrated in the area of radius α and the backscattered one in the area of radius β, with $\alpha<<\beta$. Factor η characterizes the contribution of backscattered electrons to the exposure in a large area. α and β are the characteristic lengths of the exposure process.

Considering first the backscattering effect only (described by β and η), it is possible (according to the arguments of [6]) to substitute the first Gaussian by δ-function. As a result the method of "simple compensation" for exposure T in point (x y) may be written (in equivalent to [5,6] form)

$$T(x,y) = (1+\eta)D(x,y) - \eta\int dx'dy' I_2(x-x', y-y')D(x',y')$$

Here the dose distribution $D(x,y)$ is defined as $D(x,y)=D_0=100\%$ inside structure Q and zero outside. Pay attention that only the second Gaussian, I_2, corresponding to backscattered electrons is used. In the formula exposures T and D are measured in percents with T_0 and D_0 equal to 100%. It was proved [14] that guaranteed accuracy of "simple compensation" determined by beam spot is about 40% of the beam radius.

3D-SIMULATION OF THE DEVELOPMENT

Liquid development of positive resists is adequately described by the model of isotropic local etching [2,7,8] which assumes that the velocity of resist boundary movement is independent of the boundary form (locality of etching) and the direction of the boundary (isotropy of etching), but defined only by development rate V at the point which the boundary passes through at a given moment. Development rate V, in turn, is defined by absorbed dose distribution D and the dose characteristic of the resist written as [2]

$$V = V_0\left(\frac{D}{D_0}\right)^{\gamma}$$

where γ is the contrast of positive resist. A numerical method for development simulation is especially fast and effective for 2D case [7,8].

REALIZATION AND EXAMPLES (2D LITHOGRAPHY)

The procedures of proximity correction and development simulation comprise a kernel of a software package PROXY. Besides this it contains an effective tool for design of structures and additional option allowing to control exposure by SEM via a special hardware called pattern generator.

In comparison to production beam lithography machines, the PROXY-SEM combination offers more flexibility in operation, more capabilities with respect to nanolithography, experimental electron beam lithography at a small fraction of the cost of currently available instrumentation. PROXY cannot be used as an IC production machine, however, PROXY offers much in fields of beam lithography research and development, especially since it is not limited to SEM's only, but to any other scanning system.

The first example is a structure which is not occasionally looks like a field transistor (Fig.1) where parts A and C simulate a source and a drain, B is a gate, parts D and E are wires situated partly far from and partly very close to large pads. The original structure was designed by PROXY graphical editor, the gate B and two slots between gate and parts A, B were designed as 200nm. Consider a situation when each point of the structure is exposed with exposure dose T equal to 150%. Development simulation shows that due to proximity effect it is not possible to obtain the structure by uniform exposure. A gate area is overexposed whereas area D with single

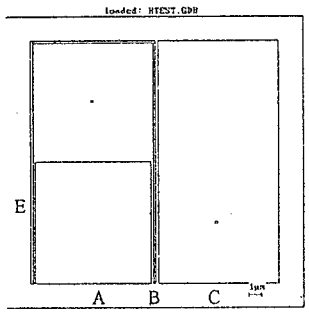

Fig.1. A test structure simulates field transistor with 0.2um gate (B), D simulates a single wire.

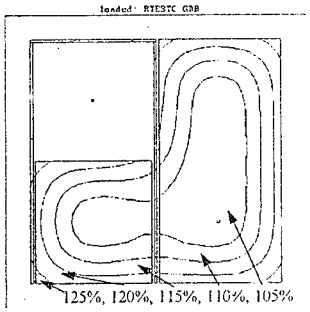

Fig.2. According to "simple compensation" (PROXY) different areas of the structure should be exposed with different time to obtain submicron features

Fig.3a. Uniform exposure does not allow one to produce the strucutre as predicted by development simulation. The gate B and the single wire D are lost.

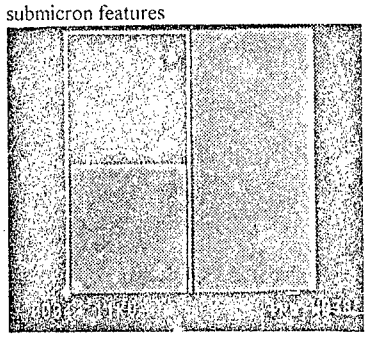

Fig.3b. E-beam lithography with exposure according to "simple compensation" allows one to create the designed structure with submicron features

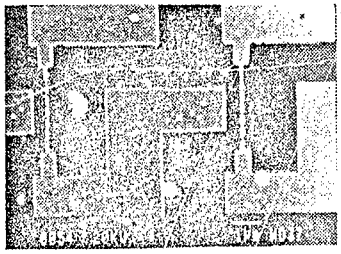

Fig.4. A part of a structure designed and created for investigation of single electron transport. Due to proximity effect the structure can no be obtained without correction

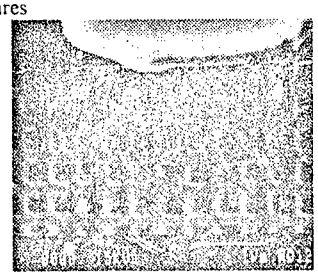

Fig.5. A part of a grid on Si produced for investigation of superconducting transition under magnetic field. Proximity correction is necessary to realize cell size comparable to coherent length of electron in Al.

standing wire is underexposed. Fig.2 shows distribution of exposure time according to "simple compensation" generated by PROXY and simulation data predicts promising result. We carried out special experiments to check correction and simulation. We used JSM-840 as a lithograph under PROXY control for exposure the structures without correction (Fig.3a) and according to proximity corrected data (Fig.3b). E-beam exposure and development of positive resist were followed by thin metal deposition and "lift off" operation so light image is Al layer. Comparison of simulated pictures with experimental ones show beautiful coincidence which confirms physical models of exposure and development, numerical algorithms and procedures implemented in PROXY and correct operation of the system at whole.

More practical structures are shown on Fig.4 (the structure was created for experiments with single electron transport and demonstrates nanometer features near large electrodes) and on Fig.5 which could not be produced without proximity correction.

3D PROXIMITY CORRECTION

The method of "simple compensation" introduced by in [5,6] has been developed as a very powerful tool for correction and simulation of proximity effects [14-16] which led to the widely used software package PROXY.

We extended this numerical calculation method for 3D correction [17,18] where a required (designed) absorbed dose D is assigned to each element of the exposed structure. Proximity 3D correction then leads to an exposure dose distribution T allowing us to produce the required absorbed dose at all places. The "3D correction" looks very similar to the "simple compensation" and consists of sequential steps. The 3D correction establishes that the dose is not constant inside the structure but is actually spatially distributed according to $D(x,y)$. As result now it is possible to produce designed relief what we call 3D lithography.

In practice we proceeded as follows. Using a graphical editor, a stepwise relief $H(x,y)$ is designed. Then the required absorbed dose $D(x,y)$ was calculated just by considering the resist contrast. After that a corrected exposure time $T^1(x,y)$ was calculated.

$$T^1(x,y) = (1+\eta)D(x,y) - \eta\int dx'dy' I_2(x-x', y-y')D(x',y')$$

We used such a procedure in iteration:

$$T^{k+1}(x,y) = (1+\eta)D(x,y) - \eta\int dx'dy' I_2(x-x', y-y')T^k(x',y')$$

Five to ten iterations are sufficient to obtain a self-consistent exposure time distribution $T(x,y)$. It demonstrates nontrivial changes in comparison with the naive noncorrected distribution proportional to $D(x,y)$. According to PROXY procedures a continuous dose distribution is approximated at the end by a stepwise function with a predefined number of steps. As a result, a structure consisting of a variety of elements (polygons) Q_i with assigned exposure dose T_i automatically appears.

TECHNOLOGY STEPS, 3D DOE EXAMPLES, AND TESTING

After exposure and development we obtained as examples stairs, linear and circular zone plates with good reproduction of the designed structure with up to ten height levels in PMMA resist of micron thickness on the Si wafer [17,18]. We estimate accuracy of pattern and relief transfer operations as 50nm in both the lateral and vertical directions. The method allows us to create lenses with high numerical aperture up to NA=0.5. Results of optical testing of the created lenses showed a focus spot about 5um in diameter with good efficiency. A prototype of a lens for practical application is presented in [18].

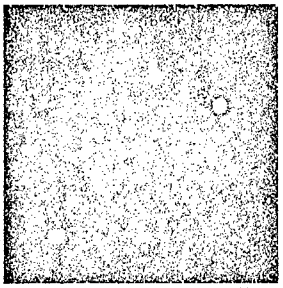

Fig.6a. A designed (desirable) image contains several tens of focal spots.

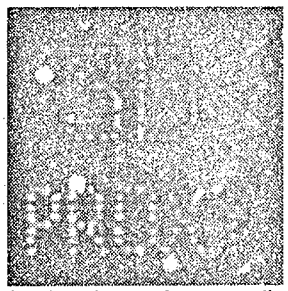

Fig.6d. An image of corresponding to the 4-level DOE.

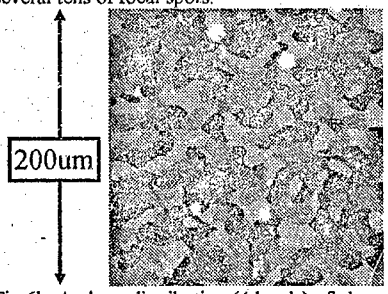

Fig.6b. A phase distribution (4 levels) of phase DOE to produce the image of Fig.3a.

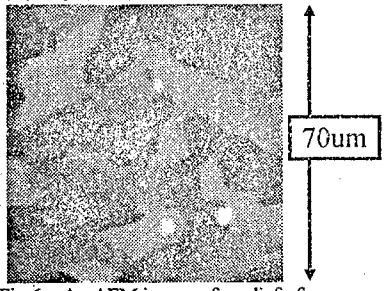

Fig.6e. An AFM image of a relief of transparent polymer DOE after copiyng from metel replica.

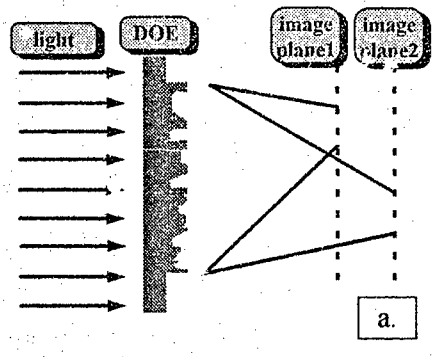

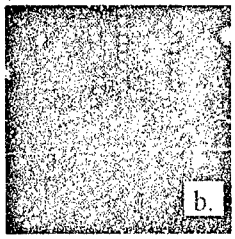

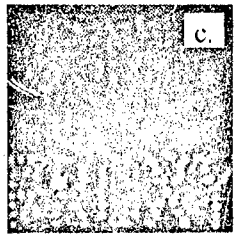

Fig.7a. A DOE with two different focal planes.
Fig.7b. An image formed by DOE(hologram) on distance = 2mm.
Fig.7c. An image formed by DOE (hologram) on distance = 3mm

The created flat lens is an example of the simplest diffractive optical elements (DOE) which transfers parallel light (laser) beam in a point. Below we present design and creation of much more complicated DOEs. Fig.6a shows a desirable image which should be formed by DOE. Fig.6b demonstrates a distribution of 4-level phase shift which should be provide by DOE to obtain the image of Fig.6a. A refractive coefficient allows one to transfer from phase shift to thickness distribution and then to absorbed dose D. Data preparing for exposure after 3D correction comprise a large set (about 10^4 elements) of polygons with assigned exposure time to each of them. Fig.6c demonstrates a part of the DOE. It clearly shows designed four levels. And finally Fig.6d shows image produce by the four level DOE of Fig.6b. One can consider the DOE as prototype of a passive beam splitter for optoelectronics applications.

Using the procedures we created a DOE Fig.7a which gives tens focuses in two different focal planes Fig.7b and Fig.7c. Another example includes a DOE with real and imaginary images and will be demonstrated during oral presentation.

REFERENCES:

[1] M.Parikh, J.Appl.Phys. 50,4371(1979).

M.Parikh IBM J. Res. Dev., 1980, v.24, N.4, p.438-451

[2] A.R.Neureuther, D.F.Kyser, and C.H.Ting. IEEE Trans. Electron Devices 1979,ED-26,p.686.

[3].D.P.Kern. Proceedings of the 9th International Conference on Electron and Ion Beam Science and Technology, edited by R.Bakish (The Electrochemical Society, Pennington, NJ, 1980), PV 80-6 491.

[4] G.Owen and P.Rissman, J.Appl. Phys. 54,3575(1983).

[5] V.V.Aristov, S.I.Zaitsev, A.A.Svintsov, Preprint, Chernogolovka, 1989

[6] V.V.Aristov, A.A.Svintsov, S.I.Zaitsev. Microelectronic Engineering 11 (1989) 641-644.

[7] S.I.Zaitsev, A.A.Svintsov, Poverkhnost',1986, N.4, p27-31.

[8] S.I.Zaitsev, A.A.Svintsov, Poverkhnost',1987, N.1, p47-52.

[9] T.Shiono, K.Setsune, O.Yamazaki and K.Wasa. J. Vac. Sci. Technol. B 5.33(1986)

[10] T.Shiono and H.Ogawa, Appl. Opt. 30.3643(1991)

[11] H.Zarzhitsky, A.Stemmer, F.Mayerhofer, and G.Lefranc. Jpt. Eng. 33.3527(1994)

[12] A Stemmer, H.Zarzhitsky, E.Knapec, G.Lefranc, and F.Mayerhofer. J. Vac. Sci. Technol. B 12,3635(1994)

[13] T.Waas, H.Eisenmann, O.Voellinger, and H.Hartmann, Microelectron. Eng. 27.179 (1995).

[14] V.V.Aristov, B.N.Gaifullin, A.A.Svintsov, S.I.Zaitsev, J.Vac.Sci.Technol. B 10, 2459(1992).

[15].V.V.Aristov, B.N.Gaifullin, A.A.Svintsov, S.I.Zaitsev, R.R.Jede, and H.F.Raith, Microelectron. Eng. 17,413(1992).

[16] S.V.Dubonos, B.N.Gaifullin, H.F.Raith, A.A.Svintsov, and S.I.Zaitsev, Microelectron. Eng. 21, 293(1993).

[17] S.V.Dubnos, B.N.Gaifullin, H.F.Raith, A.A.Svintsov, and S.I.Zaitsev, Microelectron. g. 27, 195(1995)

[18] V Aristov, S Dubonos, R Dyachenko, B Gaifullin, V Matveev, H Raith, A.Svintsov, S Zaitsev, J. Vac. Sci. Technolog. B13(6) (1995), p 2526-2628

STM-stimulated chemical modifying of the alpha-C:H film

V.D. Khavryutchenko[1], E.A. Nikitina[2], E.F. Sheka[3]
[1]Institute of Surface Chemistry, Nat. Ac. Sci., Kiev, Ukraine,
Joint Institute for Nuclear Researc, Dubna, Russia
[2]Institute of Applied Mechanics, RAS, Moscow, Russia
[3]Russian Peoples Friendship University, Moscow, Russia

Chemical reactions between an adsorbate and alpha-C:H film simulated by electric field of an STM tip were studied. The film was modeled by a supercluster containing 207 atoms and consisting of subclusters of sp2- and sp3-components according to the Robertson model [1]. Carbon tetrachloride (CT) and trichloroethylene (TCE) were considered as adsorbates. Electric field was configurated in sharp-tip and blunt-tip modes through corresponding sets of point charges. A quantum chemical software DYQUAFIELD [2] exploiting semiempirical method AM1 was used. A chemical reaction, caused a tight bonding of both adsorbate molecules with the film surface throughout a formation of grafted radical, and stimulated by electric field was observed on the diamond component of the film. The reaction is threshold and occurs at negative bias on the surface. When the bias exceeds a threshold by 1.5 time, the reaction is terminated. A graft polymerization of the CT molecules under the tip resulting in formation of nano-size hills observed experimentally is highlighted [3].

References

[1] J.Robertson, *Phil. Mag. Letts.*, **57**, 143 (1988).

[2] V.D. Khavryutchenko, V.A. Zayets, and A.V. Khavryutchenko Jr., DYQUAFIELD. (Institute of Surface Chemistry, Nat.Ac.Sci. of the Ukraine, Kiev. 1993).

[3] P.N. Luskinovich et al., *JETF Letters*, **62**, 868 (1995).

Femtosecond laser pulse nanolitography using STM tip

Yu. E. Lozovik, S. V. Chekalin, A. I. Ivanov, V. O. Kompanets,
D. V. Lisin, Yu. A. Matveets and S. P. Merkulova
Institute of Spectroscopy, RAS, 142092, Moscow r-n, Troitsk
e-mail: lozovik@alpha.isan.troitsk.ru

The nanolithography technique is proposed and realized experementally using the local field of femtosecond laser pulses enhanced in a submicron region due to lighting rod effect or to the excitation of local resonances in STM tip—substrate system. Surface topography analysis in STM mode demonstrates the controlled surface modification in a suitable regime of intensity parameters and femtosecond laser pulses focusing in the STM tip region.

The problems of creation of nanostructures, ultrahigh density recording of information, investigation and recording of ultrafast processes in nanostructures as well as finding of suitable materials and techniques for these purposes belong to the most actual basic and applied problems in semiconductor nanostructures physics.

Nanolocal research of influence of ultrashort laser pulses on the solid state surface is of interest from this point of view [1]. We used here the proposal [1] of using local electromagnetic fields enhanced in submicron region near STM tip due to the lighting rod effect or the excitation of local resonances (see, e.g.[?1) in small regions of the STM tip – substrate system for nanolithography and nanolocal research of ultrafast processes [1]. Using of ultrashort laser pulses for nanolocal studies has the following advantages. Femtosecond laser radiation allows to create non-stationary states of sample, which may lead to new *non-thermal* mechanisms of instability and photoinduced phase transitions on the surface. One of the phenomena of this kind is a specific femtosecond melting of solids (another example is appearance of the photoinduced by femtosecond laser irradiation quasi-one-dimensional surface relief with period ~1000 Å see [1] and Refs. herein). Moreover, femtosecond radiation allows realization of peak surerstrong fields without non-controlled destruction of the sample.

The surface of the sample was irradiated by femtosecond laser radiation focused in the region of STM tunnel junction. The radiation of Ti:Sa laser with wavelengths 812 and 406 nm, pulse duration 40–45 fs and repetition rate 82 MHz was used. The radiation power W was changed by means of light filters with different transmittance up to the maximal power 80–100 mW on wavelength 812 nm. The maximal power of 2nd harmonics (406 nm) was 5–7 mW. The diameter of light spot on the surface was about 1 mm. The dependence of radiation effects on exposition time was also investigated in wide range of exposition times. The angle of incidence ϑ of laser light was limited by the construction of the setup: $\vartheta \geq 76°$. The pyrolithic graphite as a sample was used.

We investigated the possibility of nanolocal laser pulse induced modification of the sample surface in the region nearly the STM tip. At the beginning we obtained the several initial images of surface by STM, reproducibility of images was checked and a lateral drift was estimated. Then we "draw" by laser pulses nearly STM tip one of the figures: point, line or X-like "letter" by means

of positioning STM tip in appropriate points and switching on the laser light. So the lines were drawn as a set of separate points. After laser pulse exposition of STM tip we take a duplicate scan of affected region to find photoinduced surface changes.

Laser irradiation effect on STM response *during* the *continuous* scanning process in STM was also studied. At first we take the initial scan, then we take the duplicate scan of the same region when the laser light of different intensities illuminated the tunnel junction. After that we take another scan without laser irradiation.

The experiments revealed the following effects:

(1) The appearance of X-like structure after drawing the letter "X" by the local laser field nearly STM tip by means of positioning STM tip in appropriate points and exposition by the laser pulses with power 6.8–8.5 mW. The whole size of long-life X-like structure was 2000×8000 Å with line thickness of the order $\sim$1000 Å and 15 Å depth.

(2) The appearance of short-lifetime groove with 200 Å width and 50 Å depth due to writing by the tip and simultaneous femtosecond laser irradiation with power 6.8–8.5 mW. It should be noticed also that the groove has continuous form unstead of consisting of the sequence of points. It is possible this feature is due to a neglegible change of value of the local electromagnetic field on the surface due to the small tip displacement.

The appearance of long-lifetime structure after the nanolocal affecting of femtosecond laser radiation demonstrates promising of nanolithography method discussed in the paper. It could be intresting to study the direct influence of laser radiation on the STM tip, tunneling and photoemission from the tip. The field enhanced in a local region near STM tip can be also used for the purposes of controlling of nanolocal chemical reactions provided by special STM tip [3] and also for the stimulation of nanolocal photochemical reactions [1].

The work was supported by grants of Program "Physics of Solid Nanostructures", Russian Foundation of Basic Research and CRDF RP2-156.

References

[1] Yu. E. Lozovik, S. P. Merkulova (to be publ.).

[2] Yu. E. Lozovik, A. V. Klyuchnik, in: "The Dielectric Function of Condensed Systems", Eds. L. V. Keldysh et. al. *Elsevier Science Publisher B.V.*,1987; A. V. Klyuchnik, Yu. E. Lozovik, A. B. Oparin, *Phys. Lett. A*, **179**, 372(1993); A. V. Klyuchnik, Yu. E. Lozovik, A. V. Solodov, *Zh. Tech. Fyz.* **65**, 6, 203–206, (1995).

[3] Yu. E. Lozovik, S. P. Merkulova et al., Phys.Lett.A **98**, 3290 (1994); Yu. E. Lozovik, S. P.Merkulova, A. M. Popov, Phys. Low-Dim. Str. **12**, 203 (1995).

PROCESSING OF A MOVPE-REGROWN SUB-100 NM InP/GaInAs QUANTUM POINT CONTACT

I. Maximov*, N. Carlsson, P. Omling, P. Ramvall, L. Samuelson,
W. Seifert, and Q. Wang
Solid State Physics, Lund University, Box 118, S-221 00. Lund, Sweden

A. Forchel, K. Kerkel, Lehrstuhl für Technische Physik,
University of Würzburg, Am Hubland, D-97074 Würzburg, Germany

Quantized conductance in a quantum point contact (QPC) attracted strong interest after its discovery in 1988 [1,2]. Because of a small size of the channel, of the order of the Fermi wavelength of an electron in a two-dimensional electron gas (2DEG), a quantization of conductance in units of $2e^2/h$ can be observed. Most of the approaches use the electrostatic definition of a QPC in GaAs/AlGaAs modulation-doped heterostructures [1,3,4]. Lateral confinement in a 2DEG can also be realized by a geometrical definition of the channel by high-resolution lithography and etching. Epitaxial regrowth of etched-out QPC would reduce scattering of electrons at the etched interface, producing a high-quality one-dimensional channel.

In this paper we demonstrate fabrication of a QPC as small as 50 nm in width and a quantized conductance in a 90 nm regrown InP/$Ga_{0.25}In_{0.75}As$ QPC at 10 K and above. The InP/GaInAs structure used in the present study is a modulation doped 2DEG system, with a mobility of 400 000 cm^2/Vs. The structure was grown by metal organic vapor phase epitaxy (MOVPE) at a pressure of 50 mbar and a temperature of 600°C. The sheet electron concentration, as measured by Hall effect at liquid helium temperature, was about $5*10^{11}$ cm^{-2}. Distance between the 2DEG and the surface was kept low, about 50 nm, to make etching easier.

The Hall bar mesa was made by optical lithography and wet etching. The QPC was formed on top of the mesa and defined using e-beam lithography at 35 kV and wet etching in $HCl:CH_3COOH:H_2O_2$ at 15 °C. 950K PMMA was used as an etch mask and the etching depth was about 80 nm. Due to the proximity effect in e-beam lithography, a 100 nm thick PMMA mask has only a limited stability during wet etching. The observed degradation of the PMMA masking properties is known to be due to increased porosity. The pores of order of 1 nm in size are formed due to release of volatile products of the main chain scission and appearance of excess free volume in the polymer film. This results in severe mask erosion and a decrease of the 2DEG mobility due to removal of the top cap layer. As a result, the smallest conducting QPC we managed to produce, was about 90 nm in width, see atomic force microscope (AFM) image in Fig. 1.

We found, that baking of PMMA above glass transition temperature (Tg=105 °C) prior to etching results in a significant improvement of its masking ability, making it possible to produce QPCs as small as 50 nm in width. Since baking of PMMA results in widening of the mask, we performed a series of baking treatments at different temperature of a test QPC-like structure and monitored widening of the mask after baking. It was found that the best baking temperature is between 110 and 130 °C for 30 min at a hot plate. To evaluate the masking properties of PMMA in $HCl:CH_3COOH:H_2O_2$ etching solution as a function of the exposure dose, we made a number of InP/GaInAs samples exposed with doses from 70 to 375 $\mu C/cm^2$. After a post-development baking at 110, 120 or 130 °C for 30 min, the samples were etched for 7 s. Etch depth in InP was measured by an AFM and plotted vs. exposure dose for the reference (unbaked) sample and the sample, baked at 130 °C, Fig. 2. The scanning electron microscope (SEM) images revealed formation of holes in InP/GaInAs at ≈100 $\mu C/cm^2$ for the unbaked sample, indicating presence of pores in PMMA. A shift to higher dose for the baked resist indicates its better masking ability compared to the reference sample.

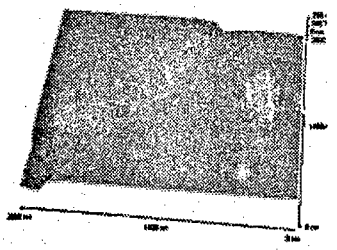

Fig. 1 AFM image of an as-etched 90 nm InP/GaInAs QPC prior to regrowth.

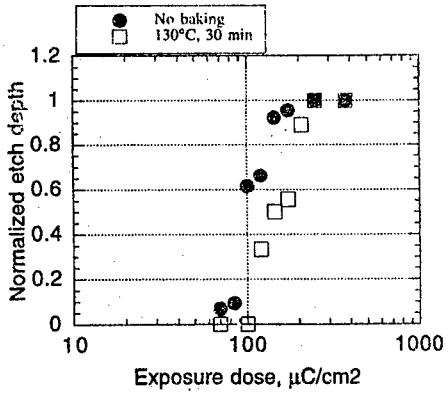

Fig. 2 Masking properties of unbaked PMMA (filled circles) and PMMA baked at 130 °C for 30 min (open squares) after etching InP/GaInAs for 7 s in $HCl:CH_3COOH:H_2O_2$ at 15 °C versus exposure dose.

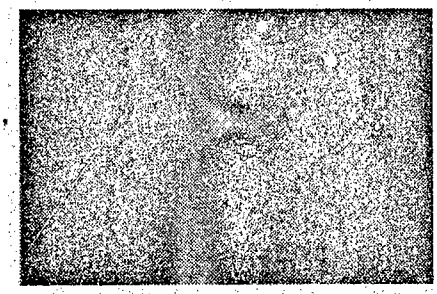

Fig. 3 A 60 nm wide QPC formed after baking PMMA at 130 °C and etching the InP/GaInAs 2DEG structure for 7 s.

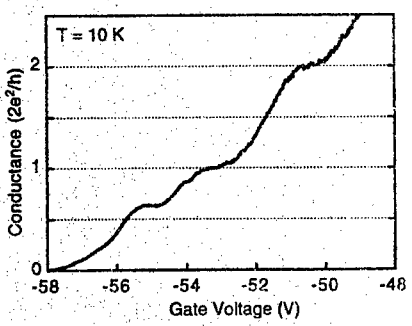

Fig. 4 Quantized conductance of MOVPE-regrown 90 nm wide QPC at 10 K.

Assuming a contribution from the back-scattered electrons of about 0.8-1 of that of the forward-scattered dose [5], one can estimate the dose in the QPC mask as 40-50 % of forward-scattered one. According to Fig. 2 it corresponds to a dose of 100-130 $\mu C/cm^2$. It is obvious from the figure that the baked PMMA is a factor of 2 more stable in this dose range as compared to the reference one.

Study of InP/GaInAs etching in $HCl:CH_3COOH:H_2O_2$ solution showed that orientation of the QPC channel along [1-10] direction results in etching profile which forms ≈130° angle between sidewalls and the surface. As a result, decrease of [1-10] channel width below 90 nm is not possible without thinning InP cap layer. On the contrary, [110] orientation allows formation of almost vertical sidewalls, but we found that QPCs in this orientation are more sensitive to baking temperature. For example, only baking at 130 °C results in formation of a 60 nm wide channel (Fig. 3), 110 and 120 °C are not sufficient to create stable PMMA mask. Slight increase of exposure dose leads to even narrow channel, about 50 nm in width.

The [1-10] 90 nm and [110] 60 nm QPC structures were regrown by low pressure MOVPE with undoped InP. MOVPE regrowth showed good surface morphology of the regrown structures, as observed by AFM and SEM. The QPC structures were characterized by transport measurements, using a top gating technique to control the electron concentration in the QPC. Typical resistance of the as-etched wire was 100 kOhm, which suggest that the electric width is smaller than 90 nm. It can readily be explained by depletion at the edge of the QPC channel. After regrowth with InP the QPCs showed an overall lower resistance than before, indicating a more defect-free interface. Fig. 4 shows a measurement of the quantized conductance of a InP/GaInAs QPC at 10K after MOVPE regrowth by 100 nm undoped InP. Details of the QPC transport measurements are published in [6].

This work was financed by Swedish Research Agencies NFR, TFR, NUTEK and SSF and the European Commission through ESPRIT IV Long Term Research, Q-SWITCH program, project number 20960. The authors would like to thank S. Lourdudoss for help with regrowth experiments and A. Bogdanov for useful discussions.

References.

1. B. J. v. Wees, H. v. Houten, C. W. J. Beenakker, J. G. Williamson, L. P. Konwenhoven, D. v. d. Marc, and C. T. Foxon, Phys. Reb. Lett., **60**, 848 (1988)
2. D. A. Wharam, T. J. Thornton, R. Newbury, M. Pepper, H. Ahmed, J. E. F. Frost, D. G. Hasko, D. C. Peacock, D. A. Ritchie, and G. A. C. Jones, J. Phys. C **21**, L209 (1988)
3. T. J. Thornton, M. Pepper, H., Ahmed, D. Andrews, and G. J. Davies, Phys. Rev. Lett, **56**, 1198 (1986)
4. A. R. Hamilton, J. E. F. Frost, et al, Appl. Phys. Lett., **60**, 2782 (1992)
5. W. M. Moreau, Semiconductor lithography. Principles, practices, and materials. (Plenum Press, New York and London, 1988)
6. P. Ramvall, N. Carlsson, I. Maximov, P. Omling, L. Samuelson,. W. Seifert, Q. Wang, and S. Lourdudoss, Appl. Phys. Lett. (submitted) (1997)

*- On leave from Institute of Microelectronics Technology, Russian Academy of Science Chernogolovka, Moscow distr. 142 432. Russia

Manipulation of Nanoparticles with the STM

P. Radojkovic, Th. Gabriel, M. Schwartzkopff* and E. Hartmann
Physics Department E16, Technical University of Munich
James-Franck-Str., D-85747 Garching, Germany

1 Abstract

One promising possibility to construct quantum effect devices is the manipulation of nanometer-sized particles using the tip of a scanning tunneling microscope (STM) for the step-by-step synthesis of structures exhibiting the desired electronic characteristics. The inert gas technique allows the preparation and the soft deposition of Ag nanoparticles on an atomically flat Si(111):H surface. It is shown that the particles can be visualized and actually be manipulated with the STM. Finally, larger compact structures can be fabricated by increasing the tunneling parameters, resulting in a sintering or even a fusion process.

2 Introduction

Devices in which the quantum nature of the electronic charge can be observed have to be built up from small structures so that the fundamental charging energy $E = e^2/2C$, characteristic for the development of the Coulomb blockade effect, is large compared to the thermal background noise [1], [2]. In view of the fabrication of devices such as the single electron transistor, different technologies are used to achieve a drastic reduction in the dimensions of the structures. For instance, electron beam lithography represents a promising technique in creating nanometer-scale structures.

Other groups are successful in oxidizing very thin metallic films grown on glassy substrates with the atomic force microscope or the STM [3]. In contrast we focus on a different approach to fabricate functional structures.

Nanometer-sized metallic particles are produced by evaporating a substance in the presence of an inert gas and subsequently deposited on a flat Si(111):H surface [2]. Upon carefully controlling the evaporation parameters, this method delivers particles with sizes between 1 and 20 nm and substrate coverages ranging from widely separated individuals up to a complete granular film.

It is shown that the particles can deliberately be displaced with the STM tip to preselected locations. Upon applying higher current values, a sintering or ripening process is induced which, at very high currents, results in a complete fusion of several neighboring particles, forming a compact structure that strongly adheres to the substrate. All particles that do not take part in the fusion process can completely be removed with the STM tip.

*e-mail: misch@physik.tu-muenchen.de

3 Experiment

The chemical preparation procedure to achieve an atomically flat Si(111) surface is described elsewhere [4]. In order to unequivocally distinct the particles from the surface structure of the carrier material, its roughness has to be much smaller than the typical particle size. The atomic step-terrace pattern of the Si substrate can clearly be seen in fig. 1 and 4. The 72-nm-wide terraces result from a 0.25° miscut of the wafer off the exact [111] direction; the bilayer steps are 0.31 nm in height.

The nanometer-sized particles are produced by an inert gas evaporation technique pioneered by Pfund in the 1930's [5]. Ag is evaporated in a W boat in the presence of a He atmosphere of $0.4 - 2$ mbar. The evaporating Ag atoms convey their energy by collisions with the He atoms. Thus, the vapor forms an oversaturated state and condensates into nanometer-sized particles, while the Si sample is held in the particle stream. Upon varying the exposure time, the coverage density can be controlled in a wide range. The particle size can be adjusted via the He gas pressure, the evaporation rate, and the distance between evaporation source and sample. The transfer between the preparation chamber and the STM recipient occurs under high-vacuum conditions, after pumping off the He.

4 Results

Keeping the particle density on the substrate quite low, distinct particles can be identified with the STM. Only for voltages of approximately 3 V and currents in the range of 100 pA, the interaction between particle and tip is sufficiently low. If the current is chosen too high, the particles will be displaced while scanning. Detailed experimental analysis revealed that particles which are attached to surface inhomogeneities, e.g. atomic steps, remain much more stable compared to those resting on the flat part of a terrace. Assuming that the particles are spherical in shape, we inferred sizes of $2 - 10$ nm solely by measuring the height of the particles in STM images. A convolution effect between the final tip geometry and the real particle dimensions inevitably leads to a broadened illustration.

Two approaches in manipulating individual particles turned out to be successful. In the so-called lateral manipulation mode, the tip is positioned *adjacent* to a selected particle and subsequently lowered by increasing the tunnel current. By moving the tip along the substrate surface, the particle can be dragged to a determined location (comparable to brushing in the macroscopic world). However, this technique fails if the substrate exhibits prominent surface inhomogeneities. Consequently, a vertical manipulation technique allows to displace particles along any desired path, independent of the nature of the substrate surface. Upon positioning the tip *above* a particle and approaching it by increasing the current or lowering the voltage, the particle couples to the tip sufficiently strong to be removed from the substrate. Following the tip movement at usual tip heights to a predefined location, the cluster can be released and redeposited by an appropriate

voltage pulse of $\sim$ 100 ns. An example for a well-controlled particle displacement is shown in fig. 1.

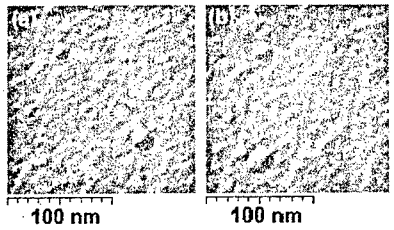

Figure 1: The lower Ag particle is moved from the right-hand side (a) to the left (b), being in a vertical line with the upper particle. The step-terrace structure of the substrate is resolved.

In a further series of experiments, the STM is operated at higher tunneling parameters (voltage, current) to locally manipulate a granular film composed of individual Ag nanoparticles. Scanning the tip with a speed of 25 nm/s at a voltage of 10 V and a current of 0.5 nA results in the formation of one-dimensional structures, as displayed in fig. 2. In that case we expect a sintering process while a neck is formed between neighboring particles. The width of these wire-like features is in the 10 nm range. A locally increased conductivity is assumed to be responsible for the appearance as elevations in the STM image.

Even higher currents can be achieved by applying (short) voltage pulses between tip and sample so that the electron flow is directed from the tip towards the particles. The duration of the pulses has to be much shorter

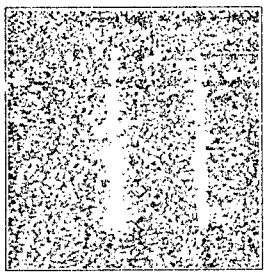

Figure 2: Two lines of sintered Ag nanoparticles. The linewidth amounts to $\sim$ 20 nm and they are 450 nm in length. The image size is 500×500 nm^2.

than the response time of our feedback circuit; consequently, the distance between tip and the granular film remains constant without disengaging the feedback loop. In fig. 3, the result of a 8.5 V pulse for 5 μs is demonstrated. The current during the pulse was at the limit of our I-V converter of 150 nA. At these exceedingly high energy densities, the particles fuse and form a 35-nm-wide feature in the upper half of the image. Comparing the volume of the fused particles with an average spheric volume of the nanoparticles and assuming mass conservation during the transition process, a filling factor if the granular film of approximately 60% can be calculated.

To show that these fused particles form a compact structure that couples strongly to the substrate, the STM tip is used to remove all those particles which did not take part in the fusion process. This is demonstrated in fig. 4, where the same fused feature

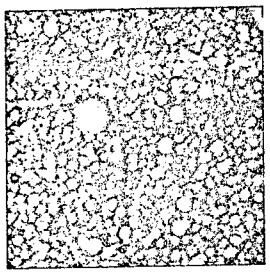

Figure 3: Fusion of several particles by applying a voltage pulse of 8.5 V for 5 μs. The image size is 250 $\times$ 250 nm^2.

Figure 4: The same field of view as in fig. 3 but after the removal of all these particles that did not participate in the fusion process.

is visible as in fig. 3. Evidently, by scanning the tip at appropriate tunnel conditions (e.g. slightly higher currents), the weakly coupling particles can completely be removed, and the characteristic structure of the underlying substrate emerges again. The "wiped out" particles have been deposited outside the field of view.

Based on the experimental findings, a current-induced melting of the nanoparticles is quite reasonable. It is expected that our results rely upon the reduction of both the melting point [6] and the thermal conductivity for nanometer-sized material. In our case, a lowering of the melting point by a factor of 3 is conceivable. Furthermore, computer calculations [7] showed that the surface atomic layer of clusters is in a highly mobile state even before the whole cluster melts. This might support our interpretation of the sintering process.

Summarizing, the combination of the inert gas technique for particle fabrication and the tip of a STM is excellently suited to synthesize single-electron devices from individual building blocks and to connect them to the outer world by forming nm-sized wires via sintering or fusion of selected particles.

References

[1] P. Radojkovic *et al.*, J. Vac. Sci. Technol. B **14**, 1229i (1996)

[2] E. Hartmann *et al.*, Proc. 2nd Russian Conf. of Semicon. Physics, Zelenogorsk 1996.

[3] K. Matsumoto *et al.*, Appl. Phys. Lett. **68**, 34 (1995).

[4] M. Schwartzkopff *et al.*, J. Vac. Sci. Technol. B **14**, 1336 (1996).

[5] A. H. Pfund, Phys. Rev. **35**, 1434 (1930).

[6] A. N. Goldstein, Appl. Phys. A **62**, 33 (1996).

[7] L. J. Lewis *et al.*, Phys. Rev. B, to be published.

Fabrication of the selforganized nanostructure with ion and neutral beam etching

I.P.Soshnikov, A.V.Lunev, M.E.Gaevski, L.G.Rotkina, N.A.Bert
A.F.Ioffe Physico-Technical Institute, 194021 Polytechnicheskaya,26 St.Petersburg, Russia

Introduction

Recently the microelectronics devices fabricated on the basis of the topological structures with conic or point elements are applied widely. The traditional method of formation of the structures using an electron beam lithography, a chemical or ion beam (plasma) etching has some disadvantages. For example, the chemical etching of the submicron elements has rather low reproducibility of the geometry profile. It is clearly displayed in the formation of relief in the mesa of the submicron size. The electronic lithography and the polishing ion etching method of the cone formation is complicated due to the problem with the stability of the masking material and the resolution. What is more important the problem of the compatibility with other technological operations of the microelectronics fabrication [1].

The authors offer the simple and reproducible method of fabrication of the submicron structure of a cone type. It bases on the formation of the surface relief by the neutral projectiles sputtering. The present paper reports the possibility of the cone relief fabrication on the wide surface and in the narrow submicron mesa by the argon neutral bombardment.

Experimental

The standard InP monocrystal plates as PhIET (PhIEO) -3 were used as samples. The surface orientation of the samples was [100], the thickness was 200-400-mkm, and the doping was about $n\sim2 * 10^{18}$ cm^{-2}. It was taken care that the received result is practically independent on the conductivity type and the doping of the samples.

Before experiment the samples were processed in chemical etchants using traditional technology for the cleaning and the removing of destructive and oxide layers [2].

The sputtering experiments were carried out in special unit fabricated on the basis of the vacuum post VUP-5 (SIA "ELECTRON", Sumy). The accelerated particle source described in [3,4] provides the argon neutral beam of the area S~10-20 cm^2 and the energy from 200 up to 700 eV and the flow density $j\sim10^{15}$ part/sec * cm^2.

The analysis of the surface relief was carried out by SEM on Series 4-88 DV100 (CAMSCAN) and EM-420 (Philips) devices.

Results and Discussion

An example of SEM image of the typical relief formed on InP with the sputtering by the argon neutralized projectiles is shown fig. 1. It consists of the exact cones that will be confirmed elsewhere [4,5]. The cone formation on InP material under particle bombardment occurs spontaneously without any microlithography. The formation process can be assigned as self organized process.

The cones received in our experiments form a submicron quasi-regular matrix on the whole sputtered surface provided that the good sample surface has been made. Topology of the typical structure is shown on the fig. 2.

The cone characteristic size analysis shows that the angle at the cone top decreases from 11° to 7° when the particle energy growing from 400 to 600 eV. No any angle dependence on the other experimental parameters (e.g. the exposition, the flow density. the conductivity type and the doping of the sample) was observed. The angle size experimental data at the various Ar projectile energies is shown on fig. 3.

The cone density has been determined from the thickness of the sputtered layer d (see fig. 4). The quasi-regular matrixes of cones has the period from 50 to 1000 nm. It is interesting that the of surface density of cones increases with increase of the inverse exposition is proportional to d^{-1}. The cone density distribution depends on the quality of the sample preparation, namely, in the case of the sample cleaned with chemical etching the distribution dispersion is makes no more than 3-5 %. The dispersion increases to 25-30 % for the mechanically polished samples with disordered layer and the oxide.

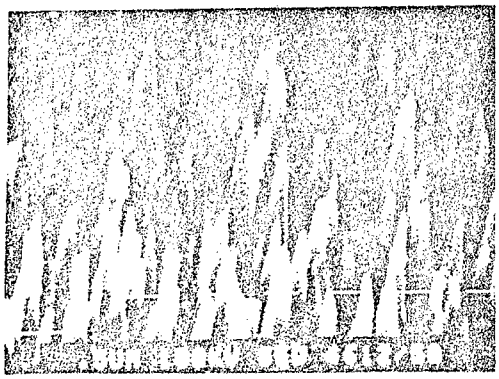

Fig.1. SEM image of the relief formed on InP by the argon neutral projectile sputtering of the layer with thickness about 3500 nm.

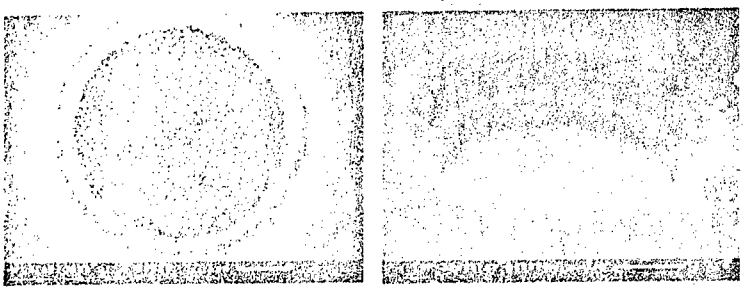

a) top b) isometry.

Fig.2. SEM image of the topology on InP in 3000 nm window after sputtering by the argon neutral projectiles of the layer with thickness about 1000 nm.

The experiment was carried out in the round window of 3000 nm diameter and in the strip lattice with the 440 nm window width. The photoresist AZ 1350 and PMMA were used as a masking covering layers. The results are collected on fig. 2. The round windows of the diameter of 3000 nm were received by the optical photolithography, and the submicron mesa stripes were received by the interference lithography. The etching Ar beam energy was 500 eV.

At the bottom of the mesa structure the formation of a cone relief occurs according to the result for the planar structure etching. The mesa interface has the submicron modulation due to the condensation from the cones. The modulation amplitude of the mesa interface does not exceed 20 nm.

We estimate the described method resolution that the given topology was possible steadily. The cone structures were formed in the mesas which have the minimal size about 100 nm.

The cone structure is formed under the projectile bombardment of the InP surface of spontaneously plasma stability from the spike emitters received by the given technology.

It was shown that the surface morphology does not vary with the sputtering in the narrow mesa having the size about 300-500 nm and more. The example of the relief formation is given on fig. 5.

The peculiarities of the relief formation with the layer sputtering were studied. In the experiment the InP layers with thickness about 100-1000 nm were used which had been made by the method of the magnetron deposition. The analysis of the surface morphology showed that the received relief is similar to the sputtering process on the massive targets. Thus, the method of the thin films sputtering can be applied for the fabrication of the topological pattern. The topological pattern can be used for the mask to get the dots and cones on the surfase using the plasma chemical (or ion beam chemical) etching.

Resume

The projectile sputtering is shown to form quasi-regular matrixes of the cone structures with the fixed distance between objects in the range from 50 to 1000 nm and the dispersion about 3-5 %. For the InP monocrystals and films received by the magnetron deposition the processes of formation of the spike matrixes have identical character.

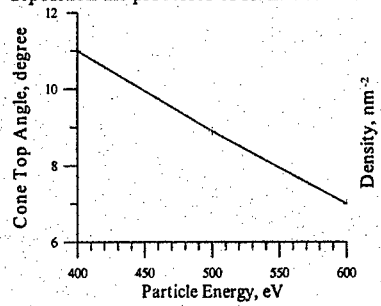

Fig.3. The cone top angle dependence Ar projectile energy.

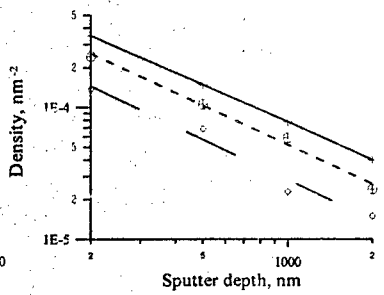

Fig.4. The cone density dependence on the thickness of the sputtered layer d by the particle energy 400 (+), 500 (⊕), 600 (□) eV.

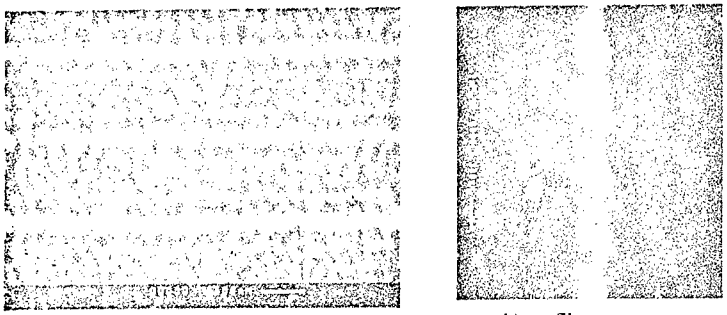

a) top; b) profile.

Fig.5. SEM image of the topology on InP in 440 nm strip window after sputtering by the argon neutral projectiles of the layer with thikness about 250 nm

The structures are self organized without any special lithography, and are made in the mesa with the minimal size about 100 nm.

The relief obtained can be used for the fabrication of electronic nanoscale devices with the cone topological elements and for the multilayer lithography mask formation. It can be used directly as the working element (for example, as the spike emitters of various type or the quantum dot).

The developed technology of formation of spike matrixes can be realized for InP and the other binary and multicomponent materials.

References

1. W.M.Moreau Semiconductor lithography, in ser. Microdevices Physics and Fabrication Technologies, Plenum Press, New York and London, 1988
2. K.Sangval, Etching of crystals, North-Holland, 1987
3. V.T.Barchenko, A.Yu Sokolovskii, Izvestia LETI, **323** (1983). 26 (in russian)
4. I.P.Soshnikov, A.V.Lunev, N.A.Bert et al. Poverhnost' **N3**, (1997)85 (in russian).
5. O.Wada, J.Phys.D, **17** (1984), 2429

Nanostamp lithography: a new process for fabrication of nanostructures

Dawen Wang and Kang L. Wang
Device Research Laboratory, Department of Electrical Engineering
University of California, Los Angeles
Los Angeles, CA 90095, U.S.A

Techniques, such as e-beam lithography, X-ray lithography, scanning probe microscopy based lithography and others, have been used to fabricate nanometer scale structures. Though it is possible to obtain nanometer scale feature sizes using the aforementioned techniques, the use of them in a high throughput microelectronics manufacture environment is still require more research. In this paper, a new process – nanostamp lithography – has been demonstrated for producing nanometer feature size nanostructures, right now 25 nm dots has been achieved by this method.

As illustrated in fig. 1, the process is a three step process. First, the polydimethylsiloxane (PDMS) stamps were cast from master molds. Mold materials can be silicon, silicon dioxide, photoresist, etc. Molds can be used repeatedly to cast stamps and stamps can be used repeatedly too to form nanostructures. Secondly, a thin layer of photoresist film was applied to the surface of a stamp by spin coating. Then the stamp and a substrate were aligned and were pressed together. After at least half an hour, the stamp was removed from the substrate carefully, which left a patterned photoresist film on the surface of substrate. In our experiment, AZ 5214 photoresist and silicon substrate were used. The thickness of the photoresist film is from about 350 nm to 1500 nm. Fig. 2 shows the atomic force microscope (AFM) images of 25 nm and 50 nm diameter pattern dots formed on the photoresist films. The patterns on the stamps are the inverse of the original patterns of the master molds. Thus the shape and size of the patterns formed on photoresist films are the same with those on the master molds. The last step is the pattern transfer. The simplest way to transfer a pattern is to etch the photoresist film back to the substrate surface by reactive ion etching (RIE) with oxygen. We developed several methods to do pattern transfer. One of them is to deposit a thin metal film (for example 15 nm Ti in our experiments) only on the top of the dots by tilted the sample for at least 45 degree during e-beam deposition. Then the photoresist film was etched back to the substrate easily by oxygen RIE. Further RIE etching with SF_6 or CH_4 can etch patterns on Si substrate directly. Fig. 3 is a AFM image of the Si dots with 50 nm diameter formed by this method.

Nanostamp lithography has several advantages. We use the stamps, not the original molds, to form nanostructures and the formation of the stamps is very simple and low cost, thus this technique can be potentially high throughput and low cost. In addition, the surface of the PDMS is very high hydrophobic, which makes it easy to remove the stamps from the photoresist films and there is no serious surface sticking problem. In our experiments, after cleaning the stamp by acetone, the photoresist can be applied on the surfaces of the stamps directly, no any release layers are needed. The whole process of applying the photoresist films onto the stamps can be performed in air and no curing or light exposure treatment is needed. The transparent of the PDMS material will help to solve the multilevel alignment problem which is the biggest challenge for all the stamping lithography. The process is compatible with current semiconductor technology.

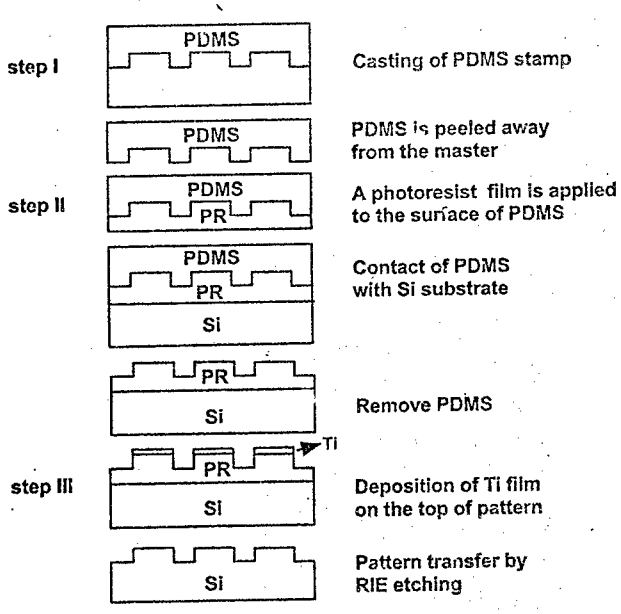

Fig. 1 Schematic of the procedure for nanostamp lithography

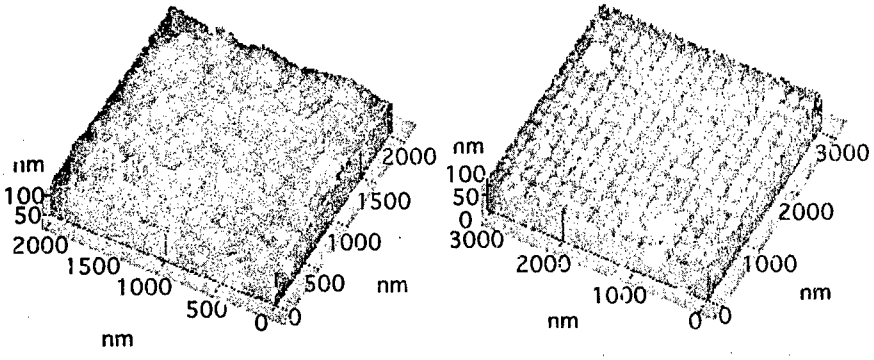

(a) (b)

Fig. 2 AFM images of (a) 25 nm and (b) 50 nm diameter pattern dots formed on a photoresist films by nanostamp lithography

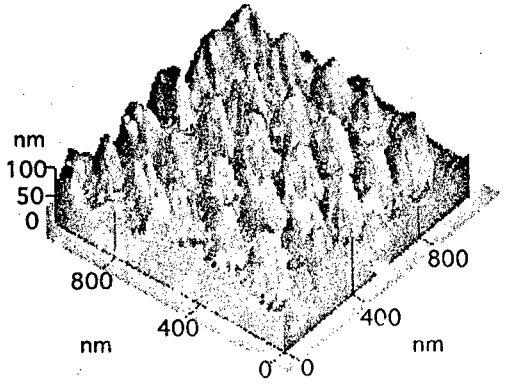

Fig. 3 AFM image of Si dots pattern with 50 nm diameter formed by nanostamp lithography followed by pattern transfer

Transport of interacting electrons in modulated quantum wires and carbon nanotubes

Arkadi A. Odintsov[1,2], Yasuhiro Tokura[3], and Seigo Tarucha[3]
[1]Nuclear Physics Institute, Moscow State University, Moscow 119899 GSP, Russia
[2]Department of Applied Physics, Delft University of Technology, 2628 CJ Delft, The Netherlands
[3]NTT Basic Research Laboratories 3-1 Morinosato-Wakamiya, Atsugi-shi 243-01, Japan

We investigate the possibility to control the electron transport on the nanometer scale by using electric field induced Mott transition in realistic periodically modulated one-dimensional systems: artificially fabricated modulated quantum wires and naturally grown carbon nanotubes. The Mott transition occurs due to the Umklapp scattering of electrons. The latter can be described by a *non-uniform* sine-Gordon-like model which incorporates also the effects of electric contacts connected to the system. For a weak Umklapp backscattering we treat the problem perturbatively and find precursors of transition to the Mott insulating state. In the opposite case the transport can be described in terms of the macroscopic quantum tunneling (MQT) of sine-Gordon solitons through the edge barrier. We evaluated the tunneling rat $\Gamma = B\exp(-A)$ as function of an effective chemical potential and temperature using instanton technique in 1+1 dimension. Interestingly, preexponential factor B increases as a power of the cutoff frequency. This enhances the tunneling amplitude, producing the effect opposite to well known orthogonality catastrophe. Numerical algorithms developed can be used for analysis of MQT in distributed and dissipative systems.

One-dimensional (1D) conductors have been attracting attention of theoreticians and experimentalists first, as a rich source of unconventional physics of interacting 1D electrons (non-Fermi liquid behavior, various types of electronic instabilities and phase transitions) and, second, as systems showing great potential for future applications (interconnects for nanodevices). Recent breakthroughs in technology have opened at least two intriguing opportunities for experimental investigation of 1D transport. First, it became possible to fabricate long and clean quantum wires. This system has been successfully used for the detection of non-Fermi liquid behavior of interacting 1D electrons [1, 2]. Second, drastic progress has been recently achieved in synthesis of single wall carbon nanotubes [3]. Coherent electron transport and single-electron effects in this system have been demonstrated in recent experiments [4].

There is a clear need to look for efficient ways to control electronic transport through new 1D systems. Analysis shows that it is technologically possible to modulate the electrostatic potential along the wire with the period $a = 2\pi/G$ of the order of the electronic Fermi wave length using selective wet etching of the donor layer. In an infinite system the electron backscattering leads to the opening of the gap at the boundary of the Brillouin zone, $G = 2k_F$. More interestingly, at half-filling, $G = 4k_F$, the Mott gap is formed due to the Umklapp scattering which occurs only in the interacting system [5, 6]. By changing the position of the Fermi level with respect to the gaps one can effectively control electronic transport through modulated quantum wire. The same idea holds also for the "armchair" carbon nanotubes where the natural periodic potential (atomic lattice) leads to the opening of the Mott gap [7, 8].

Previous researches have addressed the effect of Umklapp scattering on the transport in uniform (and formally infinite) 1D system [9, 7, 8]. In a realistic experimental layout the system (modulated quantum wire or carbon nanotube) is connected to external electric contacts which can be considered as reservoirs of non-interacting electrons. The presence of the reservoirs makes the system *non-uniform*, and drastically affects the transport even in the case of clean (not modulated) quantum wires.[10] In this work we investigate the Umklapp scattering of electrons and signatures of the Mott transition (MT) in realistic non-uniform systems.

We consider one channel modulated quantum wire adiabatically coupled to two perfect non-interacting 1D leads. The latter are aimed to model electronic reservoirs [10]. At low energies $E \ll E_F$, the system can be treated within the bosonization formalism [5, 6]. To describe the transport it is enough to consider the charge part $H = H_\rho + H_U$ of bosonized Hamiltonian, which is decoupled from the spin part. The charge part contains the standard Tomonaga-Luttinger term ($\hbar = 1$),

$$H_\rho = \int_{-\infty}^{\infty} \frac{dx}{\pi} \left\{ \frac{v_\rho(x)}{K_\rho(x)} (\nabla \Theta_\rho)^2 + v_\rho(x) K_\rho(x) (\nabla \phi_\rho)^2 \right\} \tag{1}$$

associated with the forward scattering of electrons and the nonlinear term

$$H_U = -\int_{-\infty}^{\infty} dx U(x) \cos 4\Theta_\rho \tag{2}$$

describing the Umklapp scattering. Here θ_ρ and ϕ_ρ are bosonic fields satisfying the commutation relation $[\theta_\rho(x), \phi_\rho(x')] = (i\pi/4)\mathrm{sign}(x - x')$, v_ρ is the velocity of charge excitations, and K_ρ is a standard interaction parameter of the Tomonaga-Luttinger model ($K_\rho = 1$ for non-interacting electrons). The amplitude U of the Umklapp scattering is proportional to the $2k_F$-component of the electron-electron interaction.

We will assume that the Umklapp scattering as well as the Coulomb interaction of electrons occur only in the modulated quantum wire ($0 < x < L$) which is characterized by coordinate independent parameters $(K_\rho(x), v_\rho(x)\ U(x)) = (K, v_w, U)$ in (1), (2). The parameters change stepwise at $x = 0, L$ acquiring non-interacting values $(1, v_l, 0)$ in the leads ($x < 0, x > L$) [10].

The current $I = 2e\langle\dot{\theta}_\rho\rangle/\pi$ can be found from the solution of the equation of motion supplemented with the boundary conditions [11]

$$\nabla\langle\theta_\rho \pm \phi_\rho\rangle|_{x \to \mp\infty} = \mu_{1,2}/v_l\pi \tag{3}$$

which reflect the fact that the chemical potential μ_1 (μ_2) of the left (right) reservoir determines an excess density ρ_1 (ρ_2) of rightgoing (leftgoing) electrons in the left (right) lead, $\rho_i = \mu_i/\pi v$ ($\rho_i = 0$ corresponds to half filling, $G = 4k_F$).

First, we will analyze precursors of the MT due to weak Umklapp scattering. In the absence of Umklapp scattering ($U = 0$) the solution of the equations of motion satisfying (3) has the form

$$\theta_{cl}^{(0)}(x,t) = \frac{q}{4}x - \frac{eV}{2}t \quad \text{for } |x| < \frac{L}{2}, \tag{4}$$

where $eV = \mu_1 - \mu_2$ is the DC voltage applied, and $q = 2K(\mu_1 + \mu_2)/v_w = 4k_F - G$ characterizes a deviation of electron density from half filling. The current given by this solution corresponds to

the Landauer formula, $I^{(0)} = (2e^2/h)V$. The correction ΔI to the current $I^{(0)}$ due to Umklapp process arises in the second order in the scattering amplitude U,

$$\Delta I = -2eU^2 \int_0^L \frac{dx}{\pi}\frac{dx'}{\pi} \int_0^\infty dt \sin[q(x-x') - \Omega t]\, \Im G(x,x';t), \tag{5}$$

with $\Omega = 2eV$ and $G(x,x';t) = \langle e^{4i\hat{\theta}(x,t)} e^{-4i\hat{\theta}(x',0)} \rangle$, where the average is taken over equilibrium fluctuations of the unperturbed field $\hat{\theta}(x,t)$.

We start from the "non-interacting" case $K = 1$ (where quotes imply that there is still a short range component of the Coulomb interaction, $U \propto V(2k_F) \neq 0$). From Eq. 5 we obtain the extra resistance $\Delta R = -(h/2e^2)^2 \lim_{V\to 0} \Delta I/V$ of the quantum wire due to the Umklapp scattering,

$$\Delta R = R_0 \int_0^t d\xi (t-\xi) \cos(\tilde{q}\xi) \frac{\xi \coth \xi - 1}{\sinh^2 \xi}, \tag{6}$$

where $R_0 = (2\pi U^2 v_w^2/\omega_c^4)h/2e^2$ is the scale of resistance, $t = 2\pi T L/v_w$ is dimensionless temperature, and $\tilde{q} = qv/2\pi T$ parameterizes the deviation from half filling.
In the case of half filling q=0 at low temperatures $T \ll v_w/L$ we obtain $\Delta R = (2\pi^2 R_0/3) L^2 T^2/v_w^2$. The quadratic dependence on the length L signals that the amplitudes of the Umklapp scattering sum up coherently along the wire. At high temperatures $T \gg v_w/L$ the coherence is lost on the scale of the thermal length v_w/T and the extra resistance is proportional to the length of the wire, $\Delta R = \pi R_0 LT/v_w$. Note that the temperature dependence of the extra resistance changes from quadratic to linear with increasing temperature.

Now we turn to the interacting case ($K < 1$). The temperature dependence of the resistance is determined by the behavior of the correlator $G(x,x';t)$ at the time scale $\sim 1/T$. At low temperatures $T \ll v_w/L$ this time scale corresponds to low frequencies $\omega \ll v_w/L$ at which the correlator is determined by non-interacting electrons in the leads. For this reason, the extra resistance is proportional to T^2 as in the non-interacting case; see Fig. 1. At high temperatures $T \gg v_w/L$ the behavior of the correlator $G(x,x';t)$ (10) on the time scale $1/T$ is determined by the correlations in the interacting quantum wire. The extra resistance displays interaction dependent power law behavior as a function of temperature,

$$\Delta R = \frac{\alpha U^2 v_w L}{e^2 \omega_c^{4K}} T^{4K-3}, \tag{7}$$

where $q = 0$ and $\alpha \sim 1$ (Fig. 1).

The high temperature result (7) is in agreement with the lowest order perturbative calculation of the DC conductivity of an infinite system [9]. On the other hand, it is well-known that in an infinite system at half filling the Mott gap Δ_M is formed for an arbitrarily small amplitude U of Umklapp scattering provided that the Coulomb interaction is repulsive $K_\rho < 1$.[5] At low temperatures $T \sim \Delta_M$ the perturbative result [9] breaks down and resistance starts to increase exponentially. Our results are valid at arbitrarily low temperatures for short enough quantum wires, $v_w/L \gg \Delta_M$.

Note that unlike the case of the Luttinger liquid with impurities [12] the high temperature behavior of the extra resistance (7) gives no direct indication of true low temperature properties of the system (the extra resistance decreases with decreasing temperature for $K > 3/4$, despite the formation of the Mott gap). On the other hand, the fact that the extra resistance (7) for a repulsively interacting system $K < 1$ decreases somewhat slower than in the non-interacting case

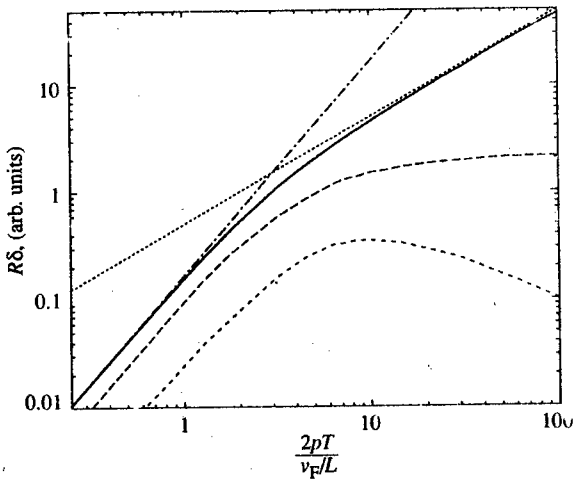

Fig 1. The extra resistance of modulated quantum wire at half filling ($q = 0$) as a function of temperature. For the curves from top to bottom $K = 1, 0.75, 0.5$.

or even increases with decreasing temperature can be interpreted as an indirect precursor of the Mott transition.

We consider now the case of strong Umklapp scattering. It is instructive to use the effective action formalism. The imaginary time Lagrangian density corresponding to (1) has the well-known sine-Gordon form,

$$L_\rho = \frac{1}{\pi K_\rho(x)} \left\{ \frac{1}{v_\rho(x)} (\dot{\Theta}_\rho)^2 + v_\rho(x) (\nabla \Theta_\rho)^2 \right\} - U(x) \cos 4\Theta_\rho. \tag{8}$$

The characteristic length in the problem is the screening length (or the size of sine-Gordon soliton), $\lambda = (v_w/8\pi K U)^{1/2}$, whereas the characteristic energy $E_0 = v_w/\lambda$ is the energy of sine-Gordon soliton up to numerical coefficient. The regime of strong Umklapp scattering corresponds to $\lambda < L$. In this case fluctuations of the field Θ_ρ in the wire region $0 < x < L$ are essentially non-gaussian and the perturbative approach is not applicable.

We decompose the action $S = S_w + S_1 + S_2$ into the wire part $S_w = \int_{-\beta/2}^{\beta/2} d\tau \int_0^L dx L_\rho$ and the actions S_i of the leads ($i = 1, 2$). Since the fluctuations in the leads are gaussian, the actions S_i can be expressed in terms of the values Θ_i of the field Θ_ρ at the ends of the wire,

$$S_i = \int_{-\beta/2}^{\beta/2} d\tau \frac{\mu_i \Theta_i}{\pi/2} + F[\Theta_i], \; i = 1, 2. \tag{9}$$

The first term in the actions S_i contains the chemical potentials of the leads. The second term ensures the fulfillment of the boundary condition (3) which becomes non-local in imaginary time.

Let us fix the chemical potential of the right lead in the middle of the Mott gap, $\mu_2 = 0$ and to consider the behavior of the system as a function of μ_1. The system is characterized by *two* threshold values of chemical potential μ_1. Below the *dynamical* threshold, $0 < \tilde{\mu}_1 < \mu_{\rm dyn} = 1/(2K)$ the minimum of the action S corresponds to a stationary solution of Euler-Lagrange equation, which describes penetration of a tail of sine-Gordon soliton into the system (we measure the energy in units E_0, $\tilde{\mu}_1 = \mu_1/E_0$). In this case the Gibbs energy of the system,

$$G(\Theta_1) = \frac{1}{\pi K}\int_0^{\Theta_1} d\Theta |\sin 2\Theta| - \frac{\mu_1 \Theta_1}{\pi/2} \qquad (10)$$

has local minima. For $|\tilde{\mu}_1| > \mu_{\rm dyn}$ such a solution does not exist. In this case the Gibbs energy decreases monotonically with Θ_1.

Addition of a sine-Gordon soliton (which corresponds to a real electron) to the system becomes energetically favorable, $G(2\pi) < G(0)$, above the *thermodynamical* threshold $\mu_{\rm therm} = 1/(\pi K)$. Below this threshold a true bulk gap halts the electrons from entering the system. This means that for

$$\mu_{\rm therm} < \tilde{\mu}_1 < \mu_{\rm dyn} \qquad (11)$$

an effective edge barrier exists for the penetration of a soliton into the system. In this regime substantial deformation energy accumulates near the edge of the system due to the presence of reservoir. Part of this energy can be released when the soliton circumvents the barrier and enters the system. Despite the existence of the edge barrier in the sine-Gordon problem was known at least since the sixties (see e.g. the paper by Kulik [13]), we are not aware about works where the tunneling through this barrier was analyzed. This analysis will be discussed in the second part of the talk.

The calculation of the tunneling rate $\Gamma = B\exp(-A)$ has been done by the instanton technique [14]. The exponent $A = S_{inst} - S_0$ is given by the difference of the the effective actions S corresponding to the instanton solution and to the stationary solution. The exponent A is a regular monotonously decreasing function of the chemical potential. The preexponential factor B is determined by the ratio of the determinants $\partial^2 S/\partial\Theta(x,\tau)\partial\Theta(x',\tau')$ taken for the two abovementioned solutions. Apart from the exponent, the preexponential factor shows power-law divergence as a function of the cutoff frequency $\omega_c \sim E_F$ producing the effect opposite to well known orthogonality catastrophe for a Luttinger liquid.

In conclusion, we have investigated transport through modulated quantum wires, with the emphasis on the observable manifestations of the Mott transition in the regimes of weak and strong Umklapp scattering. The results obtained can be generalized with minor modifications to the transport through carbon nanotubes.

We would like to thank Yu.V. Nazarov and G. E. W. Bauer for a set of useful discussions. The financial support of the Dutch Foundation for Fundamental Research on Matter (FOM) is gratefully acknowledged. One of us (A.O.) acknowledges the kind hospitality of NTT Basic Research Laboratories (Japan).

References

[1] S. Tarucha, T. Honda, and T. Saku. *Solid State Commun.*, **94**, 413 (1995).

[2] A. Yacoby, et.al., *Phys. Rev. Lett.*, **77**, 4612 (1996).

[3] A. Thess, et. al., *Science*, **273**, 483 (1996).

[4] S. Tans, *Nature*, **386**, 474 (1997).

[5] J. Voit, *Rep. Prog. Phys.*, **58**, 977 (1995).

[6] H. J. Schulz, in *Strongly correlated electronic materials: the Los Alamos Symposium, 1993* ed. K. S. Bedell et. al., Addison-Wesley, 1994, p. 187.

[7] Yu. A. Krotov, D.-H. Lee, and S. G. Louie, preprint cond-mat/9611073.

[8] L. Balents and M. P. A. Fisher, preprint cond-mat/9611126.

[9] T. Giamarchi, *Phys. Rev. P*, **44**, 2905 (1991).

[10] D. L. Maslov and M. Stone, *Phys. Rev. B*, **52**, R5539 (1995); V. V. Ponomarenko, *ibid.*, R8666; I. Safi and H. J. Schultz *ibid.*, R17040.

[11] R. Egger and H. Grabert, *Phys. Rev. Lett.*, **77**, 538 (1996).

[12] M. P. A. Fisher and L. I. Glazman, preprint cond-mat/9610037.

[13] I. O. Kulik, *Zh. Eksp. Teor. Fiz.*, **51**, 1952 (1966); *Sov. Phys. JETP* **24**, 1307 (1967).

[14] A. I. Larkin and Yu. N. Ovchinnikov, *Zh. Eksp. Teor. Fiz.*, **86**, 719 (1984); *Sov. Phys. JETP* **59** 420 (1984).

Submonolayer Insertions in Wide Bandgap Matrices: New Principles for Optoelectronics

N.N. Ledentsov*

Abraham F. Ioffe Physical Technical Institute of the Russian Academy of Science, 194021, Polytekhnicheskaya 26, St.-Petersburg, Russia, and Institut für Festkörperphysik, Technische Universität Berlin, Hardenbergstrasse 36, 10623 Berlin, Germany

New type of structures for optoelectronics is proposed and realized. The structures we refer to as „excitonic waveguides" allow an ultimate (material limited) shift towards ultraviolet spectral range. As opposite to conventional waveguides and double heterostructure lasers, no significant difference in the *average* refractive index between the cladding and the active layers is necessary, and these regions can be fabricated from the same matrix material. In this approach: (i) the waveguiding effect has a resonant nature and appears on the low energy side of the strong exciton absorption peak in agreement with the Kramers-Kronig equation; (ii) the absorption peak is induced by nanoscale island-like insertions of narrow gap material in a wide bandgap matrix, allowing to lift the k-selection rule and making the radiative annihilation of excitons possible at any lattice temperature.

1. Introduction.

Currently the structure of wide-bandgap lasers is similar to that of conventional infrared III-V lasers, in an agreement with the double-heterostructure laser geometry [1]. A using of thick layers of a wider bandgap material having a lower refractive index is assumed to be necessary. However, this wider bandgap material, lattice matched to the active layer, does not always exist, or, if exists, does not necessarily provide sufficient conductivity. The interest in the ultimate shift towards blue and UV spectral region requires a search of alternative approaches for efficient waveguiding An attractive idea is to use resonant waveguiding, which originates on the low energy side of the absorption peak due to Kramers-Kronig equation which relates the absorption with the dielectric susceptibility.

High exciton binding energies and oscillator strength and high densities required to screen excitons in II-VI and III-N materials (around 10^{19} cm^{-3}) make the resonant excitonic absorption an attractive candidate to realize this type of waveguides [2]. At the other hand, the exciton-induced lasing, resonant to the range of strongly enhanced refractive index, can be hardy realized in bulk wide-gap II-VI compounds. Free excitons with finite k-values dominating at high excitation densities and observation temperatures cannot recombine radiatively, as it was demonstrated first by Gross *et al.* [3]. More recently, ultrathin submonolayer (SML) [4] or monolayer (ML) [5] insertions were proposed to be used in excitonic waveguides. These

---

* the work is carried out in cooperation with S.V. Ivanov, I.L. Krestnikov, M.V. Maximov, A.V. Sakharov, S.V. Serokin, P.S. Kop'ev, Zh.I. Alferov, D. Gerthsen, A. Hoffmann, M. Straßburg, A. Rosenauer and D. Bimberg.

insertions are proved do form dense array of nanoscale 2D islands which can efficiently localize excitons. The structures composed of stacked ultrathin insertions result both in lifting of k-selection rule and in a strong increase in the exciton oscillator strength, providing a new possibility for lasing and waveguiding in wide bandgap matrices [6-9].

2. Growth

The crucial point to realize excitonic waveguides is related to a possibility to create nanoscale QD-like structures either isolated or electronically-coupled and providing a lateral confinement on a scale of the order of exciton diameter, what is important to break the translation symmetry of the crystal. Several approaches can be used [10]:

Two dimensional (2D) islands: Spontaneous formation of 2D ordered surface domain structures by *submonolayer* deposition has been proposed as a promising way for fabrication of QDs in materials having large effective masses of carriers and large band discontinuities, such as some of wide bandgap II-VI compounds and group-III nitrides. The driving force for the formation of nanoscale islands - is the intrinsic surface stress relaxation at domain boundaries. Atoms on the surface have different environment as compared to bulk, however they need to fit the bulk lattice parameter, the effect causing a significant *intrinsic surface stress* (τ). If two phases, having different values of τ coexist on the surface, the stress can be partially relaxed along the domain boundary. This makes the formation of ordered 2D nanoscale islands energetically more favorable, as compared to mesoscopic islands. In this way nanoscale CdSe islands having a monolayer height and lateral size of 4 nm can be formed on the surface.

Multimonolayer islands: If the energy benefit due to elastic stress relaxation at the domain boundaries overcomes the energy benefit due to complete coverage of the surface with the deposit atoms due to Stranski-Krastanow growth mode, formation of ordered array of 2D *multimonolayer islands* on *bare* substrate becomes energetically favorable. This way is proved for InGaAs growth on high-index (Al,Ga)As surfaces and for ML CdSe coverage on a ZnSe surface.

3D quantum dots. A layer of a material having a lattice constant different from that of the substrate, after some critical thickness is deposited, can spontaneously transform to an array of *three-dimensional* islands. More recently it was shown, that there can exist a range of deposition parameters, where the islands are small (~10 nm), have a similar size and shape and form dense arrays. Due to the *strain-induced renormalization* of the surface energy of the facets, the array of *equisized and equishaped* 3D islands can represent a *stable state* of the system. Interaction of the islands via the substrate makes also their *lateral ordering* favorable. If strained islands are covered with a layer of the matrix material, the islands in the second sheet are formed over the dots in the first sheet, resulting in a *three-dimensional ordered array* of QDs either isolated or strongly *vertically-coupled*. The size and the shape of islands can be changed by changing the substrate temperature, composition or the deposition mode. Assuming that 10 meV width of the QD exciton luminescence and absorption can be realized for this approach, excitonic waveguides using arrays of vertically coupled 3D QDs seem to be possible.

3D QDs formed by surface spinodal decomposition of the alloy layer. QDs can be formed by slow cooling of thick alloy layers. As a result, 3D islands appear on the surface, even the *initial* lattice mismatch between the epilayer and the substrate was absent or relaxed. Surface energetics driven surface exchange reactions also give a possibility to realize more complex *compositionally-modulated structures* in epitaxial films.

Post-growth annealing gives a possibility either to modify the shape of covered QDs, by their partial intermixing with the matrix material, or, as opposite, to fabricate QDs by *decomposing* of initially uniform *alloy layers*.

3. Characterization:

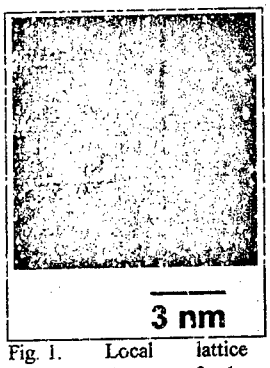

Fig. 1. Local lattice parameter image of the structure with CdSe insertions in a ZnSe matrix.

Monolayer and submonolayer insertions, most promising for QD fabrication in II-VI and III-N semiconductors, where the application of excitonic waveguides seem to be the most promising, are characterized using high-resolution transmission electron microscopy [5]. The cross-section local lattice parameter (LLP) image of the stack composed of 1 ML CdSe insertion separated by 3 nm-thick ZnSe layers is presented in Fig. 1. White color corresponds to CdSe lattice parameter in the growth direction, while the black spots indicate the ZnSe lattice parameter in the growth direction. As it can be clearly seen, the CdSe deposition results in islands having a lateral size of about 4 nm. The average thickness of the CdSe insertion in the island area obtained from numerical analysis of the LLP image is about 1.6 ML and significantly exceeds the *average* thickness of the deposit. Structural characterization of 3D QDs is performed in a number of papers [10].

4. Exciton-induced refractive index enhancement and resonant lasing.

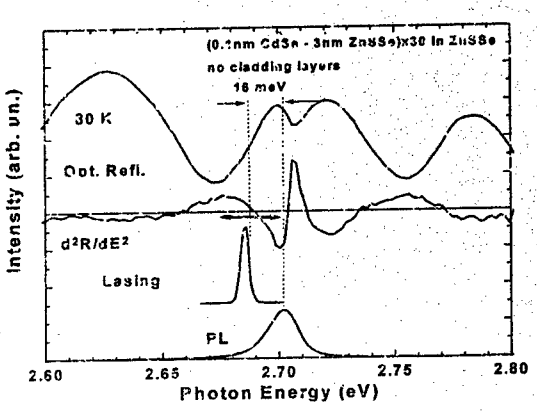

Fig. 2. Photoluminescence (PL), lasing, and optical reflectance (OR) spectra of the excitonic waveguide structure.

Photoluminescence (PL), optical reflection (OR) and lasing spectra of the structure with 30 stacks of CdSe insertions grown on top of a thick ZnSSe layer and covered by ZnSSe cap are shown in Fig. 2. The important result which follows from Fig. 1 is an extremely pronounced modulation of the OR spectra at the SL heavy-hole exciton energy, which indicates the high exciton oscillator

strength and, hence, effective refractive index modulation in the active region. Increase in the exciton oscillator strength in the array of QDs with respect to quantum wells (QWs) has been demonstrated in [11]. To describe the exciton peculiarity in OR spectrum we use the model of resonant modulation of dielectric susceptibility [12]:

$$\varepsilon(\omega) = \varepsilon_b\left(1 + \frac{\omega_{LT}}{\omega_0 - \omega - i\Gamma}\right) \qquad (1)$$

where ε_b - dielectric constant without exciton resonance; $\hbar\omega_0$, $\hbar\omega_{LT}$, $\hbar\Gamma$- exciton resonant, longitudinal-transverse splitting and damping energies, respectively. Fitting of the calculated OR spectrum to the experimental one gives the following values: $\hbar\omega_0$=2.701 eV, $\hbar\omega_{LT}$=1.9 meV and $\hbar\Gamma$=3.5 meV. The region of the exciton-induced enhancement of the refractive index and, thus, of the exciton-induced waveguiding is placed on the low-energy side from the exciton resonant energy [2]. The antiwaveguiding region is, consequently, placed on the high energy side from this energy. As it follows from Fig. 2, the lasing spectrum recorded in the waveguide geometry is 16 meV Stokes shifted with respect to the surface PL peak and the exciton resonance energy in the OR spectrum. The refractive index enhancement at lasing wavelength is estimated to be of 0.15. This value is comparable with the refractive index enhancement provided by thick (Zn,Mg)(S,Se) cladding layers.

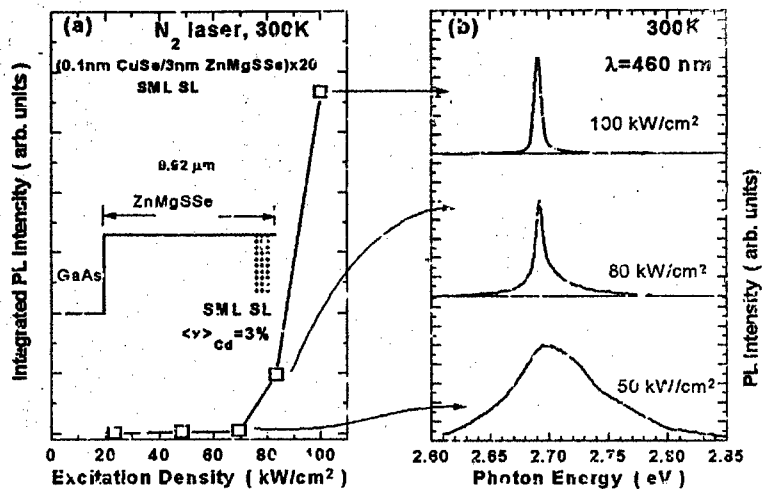

Fig. 3. Dependence of integrated PL intensity *versus* excitation density (a) and luminescence spectra (b) of the excitonic waveguide structure.

$ZnS_{0.06}Se_{0.94}$ -$Zn_{0.8}Cd_{0.2}Se$ quantum well laser structures with comparable cavity length lase at energies ~$\hbar\omega_{LO}$ (30meV) below the exciton transition revealed by PL and OR spectra, in agreement with the exciton-LO phonon lasing model [13, 14]. At room temperature this shift increases to about 100 meV [2]. For ultrathin CdSe insertions, exciton localization makes the interaction with another particle (LO-phonon, or another exciton) unnecessary, allowing the lasing to occur without additional many body interactions directly in the region of the exciton-induced waveguiding.

For CdSe insertions in a (Zn,Mg)(S,Se) matrix we were able to realize entirely exciton-induced waveguiding and lasing up to 300 K (λ = 460 nm) also without using any additional cladding layers (see Fig. 3). The estimated from the threshold density *vs* cavity length dependence the upper limit for the internal losses is comparable to that in structures with optimized cladding layers and is below 18 cm^{-1}. As a highly absorbing GaAs substrate is used, and the active layer is separated by only ~0.9 μm from the substrate, the efficient confinement of the optical mode in the excitonic waveguide is, thus, proven.

5. Gain saturation and gain suppression effects.

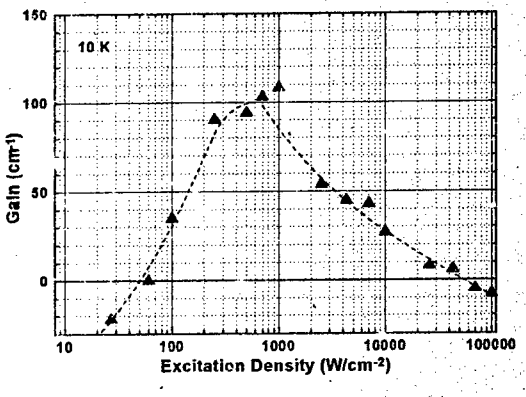

Fig. 4. Gain vs excitation density in the structure with excitonic waveguide.

Gain studies under pulsed excitation using a variable stripe length method demonstrate fast saturation of the absorption on the low energy side of exciton luminescence with excitation density (P_{exc}) and the development of a gain peak at an energy ~7-10 meV below the exciton resonance energy in the OR spectrum. Further growth in P_{exc} results in a monotonic increase in gain up to values of 100 cm^{-1}. Further increase in P_{exc} causes a gain saturation (see Fig. 4) and an appearance of a dip in the gain curve. For higher P_{exc} this dip develops to an absorption peak since, after the excitonic absorption is completely saturated, no waveguiding is possible anymore, and the emitted light is absorbed by the GaAs substrate [15]. This intriguing gain suppression effect provides unique possibilities for a new generation of devices based on optical bistability and for generation of ultrashort pulses.

6. Conclusion.

Excitonic waveguides represent a unique system with a high device potential, particularly in the ultraviolet spectral region. The recent progress became possible due to application of self-

organized growth of quantum islands by using submonolayer and monolayer deposition in the CdSe-(Zn,Mg)(S,Se) materials system.

Acknowledgments: This work was supported by the Russian Foundation of Basic Research (Grant No. 96-02-17911, 97-02-18138, 97-02-18269), and by the INTAS. The author is grateful to the Alexander von Humboldt Foundation.

REFERENCES

[1] Zh.I. Alferov, *Fizika i Tekn. Poluprovodn.* **1**, 436 (1967)
[2] Zh.I. Alferov, S.V. Ivanov, P.S. Kop'ev, A.V. Lebedev, N.N. Ledentsov, M.V. Maximov, I.V. Sedova, T.V. Shubina, A.A. Toropov, *Superlattices and Microstructures* **15** (1994).
[3] E. Gross, S. Permogorov and A. Razbirin, *J.Phys.Chem.Solids* **27**, 1647 (1966).
[4] N.N. Ledentsov, I.L. Krestnikov, M.V. Maximov, S.V. Ivanov, S.L. Sorokin, P.S. Kop'ev, Zh.I. Alferov, D. Bimberg, and C.M. Sotomayor Torres, *Appl.Phys.Lett.* **69**, 1343 (1996).
[5] N.N. Ledentsov, I.L. Krestnikov, M.V. Maximov, S.V. Ivanov, S.L. Sorokin, P.S. Kop'ev, Zh.I. Alferov, D. Bimberg, C.M. Sotomayor Torres, *Appl. Phys. Lett.* **70**, May 1996, in print.
[6] I.L. Krestnikov, M.V. Maximov, S.V. Ivanov, N.N. Ledentsov, S.V. Sorokin, A.F. Tsatsul'nikov, O.G. Lyublinskaya, B.V. Volovik, P.S. Kop'ev and C.M. Sotomayor Torres, *Semiconductors* **31**, 127 (1997) - *Fiz. Tekh. Poluprovodn.* **31**, 230 (1997)
[7] I.L. Krestnikov, M.V. Maximov, S.V. Ivanov, S.L. Sorokin, S.A. Permogorov, A.N. Reznitsky, A.V. Kornevski, N.N. Ledentsov, D. Bimberg and C.M. Sotomayor Torres, *Proceedings of the 23rd International Conference on the Physics of Semiconductors*, Berlin, Germany, July 21-26, 1996, Ed. by M. Scheffler and R. Zimmermann (World Scientific, Singapoure, 1996), v. 1, p. 3187.
[8] I.L. Krestnikov, N.N. Ledentsov, M.V. Maximov, A.V. Sakharov, S.V. Ivanov, S.V. Sorokin, L.N. Tenishev, P.S. Kop'ev, Zh.I. Alferov, *Pis'ma v Zh. Tekhn. Fiz.* **23** (1), 33 (1997) (*Tech. Phys. Lett.* **23** (1997))
[9] A.V. Sakharov, S.V. Ivanov, S.V. Sorokin, B.V. Volovik, I.L. Krestnikov, P.S. Kop'ev and N.N. Ledentsov, *Pis'ma v Zh. Tekhn. Fiz.* **23** (8), 28 (1997) (*Tech. Phys. Lett.* **23** (1997))
[10] for a review see e.g. N.N. Ledentsov, M. Grundmann, N. Kirstaedter, O. Schmidt, R. Heitz, J. Böhrer, D. Bimberg, V.M. Ustinov, V.A. Shchukin, P.S. Kop'ev, Zh.I. Alferov, S.S. Ruvimov, A.O. Kosogov, P. Werner, U. Richter, U. Gösele and J. Heydenreich, in *Proceedings MSS7*, Madrid, 1995, *Solid State Electronics* **40**, 785 (1996).
[11] M.V. Belousov, N.N. Ledentsov, M.V. Maximov, P.D. Wang, I.N. Yassievich, N.N. Faleev, I.A. Kozin, V.M. Ustinov, P.S. Kop'ev and C.M. Sotomayor Torres, *Phys.Rev. B* **51**, 14346 (1995).
[12] E.L. Ivchenko, A.V. Kavokin, V.P. Kochereshko, P.S. Kop'ev and N.N. Ledentsov, *Superlattices and Microstructures* **12**, 317 (1992).
[13] C. Benoit a la Guillaume, J.M. Denber and F. Salvan, *Phys. Rev.* **177**, 567 (1969).
[14] J. Ding, M. Hagerott, P. Kelkar, A.V. Nurmikko, D.C. Grillo, L. He, J. Han, and R.L. Gunshor, *Phys. Rev. B* **50**, 5758 (1994).
[15] A. Hoffmann et al., *to be published.*

Optical Second Harmonic Generation Spectroscopy of Co Magnetic Quantum Dots

C.A. Akʿsipetrov, E.A. Gan'shina, S.V. Gushin, T.V. Murzina, T.V. Misuryaev,
Physics Department, Moscow State University, Moscow 119899, Russia
K. Pedersen,
Institute of Physics, University of Aalborg, Pontoppidanstraade 103, DK-9220 Aalborg Ost, Denmark

Magneto-optical properties of low-dimensional structures such as magnetic nanocrystals, magnetic superlattices, thin metallic films and surfaces, etc., are a subject of high interest last years. Giant magnetoresistance, quantum confinement effects have been observed in these structures. Magnetonduced nonlinear optical properties of these structures, such as giant nonlinear optical Kerr effect are intensively studied at the moment. The method of optical second harmonic generation (SHG) is effectively used for these studies because of its unique sensitivity to the properties (including magnetic) of surfaces, interfaces, thin films, etc. It was shown both experimentally and theoretically that the magnetization of the surface or interface leads to additional contributions to the SHG in these systems.

In the present paper the results of the dc magnetic field induced SHG spectroscopy of Co magnetic quantum dots embedded in Cu films are reported.

The SHG experiments are carried out using the output of the "Tsunami" 120-fs Ti-sapphire laser operating in the wavelength range 710÷840 nm as the fundamental radiation, the laser beam being focused on the sample onto a spot of about 20 μm in diameter. Reflected SHG signal is detected by the PMT and photoncounter. For the dc magnetic field application the films are placed between the poles of the electromagnet. For the SHG infrared experiments, the output of a Q-switched YAG:Nd^{3+} laser at 1064 nm, pulse duration of 10 ns and repetition rate of 12.5 Hz is used. The SHG from the film is selected by interference filter and detected by a PMT and gated electronics.

The samples studied are Co_xCu_{1-x} films comprised by Co nanocrystals embedded in the Cu film. The relative concentration of Co in 200 nm thick films

ranges from 0.2 to 0.6. The Co_xCu_{1-x} films prior to and after the annealing are studied.

The azimuthal dependences of SHG intensity (Figures 1-3) indicate the anisotropy of the nonlinear optical properties of the film structure. SHG indicatrix are studied for p- and s-polarized fundamental radiation and for various angles of incidence, and testify that the SHG radiation is specular.

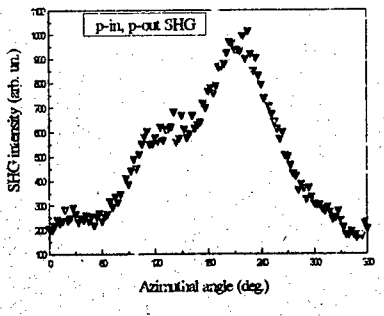

Figure 1. Azimuthal anisotropic dependence of the p-in, p-out SHG in reflection from the Co granula film.

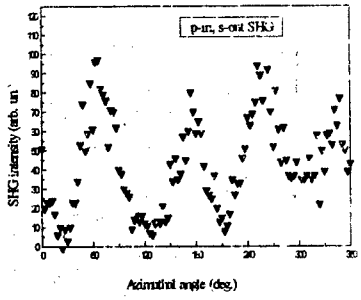

Figure 2. Azimuthal anisotropic dependence of the p-in, s-out SHG in reflection from the Co granula film.

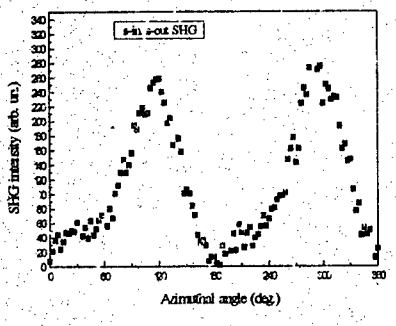

Figure 3. Azimuthal anisotropic dependence of the s-in, s-out SHG in reflection from the Co granula film.

The transversal nonlinear optical magnetic Kerr effect is studied for the Co_xCu_{1-x} films of various x values. Magnetic field induced variations of the SHG intensity appeare to be about 50 times larger as compared with the linear magnetooptical transversal Kerr effect.

Figure 4 shows the SHG spectroscopy is measured for annealed granular films (Figure 4).

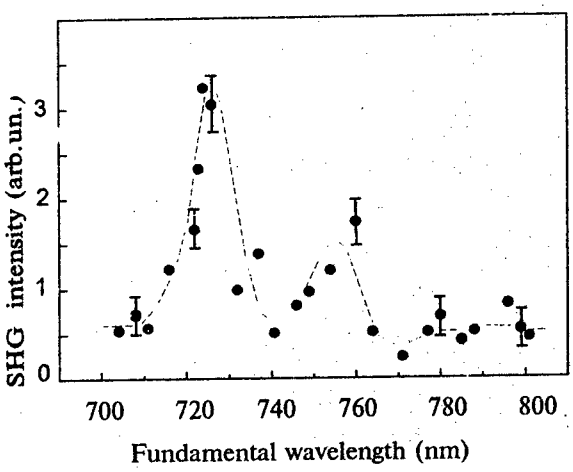

Figure . SHG spectroscopy measured in reflection from the annealed Cr granula film for p-input, p-output polarisations.

Two reproducible peaks in the SHG spectra could be attributed to the spectral properties of Co magnetic quantum dots.

Structure of copper nanoclusters embedded in a-C:H

M.V. Baidakova, V.I.Ivanov-Omskii, V.I.Siklitsky, A.A.Suvorova, A.A.Sitnikova, A.V.Tolmatchev and S.G.Yastrebov.

A.F.Ioffe Physical-Technical Institute, St.Petersburg, 194021, Russia

ABSTRACT

Transmission Electron Microscopy (TEM) (100 keV), Selected Area Electron Diffraction (SAED) and optical absorption data (0.6-5 eV) of copper-amorphous hydrogeneted carbon (a-C:H) films are presented. The size distribution functions (SDF) of copper-born clusters embedded in a-C:H were obtained both with direct observation of TEM images of clusters and from numerical analysis of optical data. Validity of optical SDF is discussed. TEM SDF is analyzed in the frames of fluctuation mechanism of early stage of cluster formation. A study of small angle X-ray scattering by the a-C:H containing copper-based clusters was performed to characterize the copper cluster structure. Fractal dimensions and sizes the cluster are estimated as a function of total copper concentration.

Keywords: nanocluster, size-distribution function, copper, fractal.

INTRODUCTION

Interest in the conductive clusters physics is stimulated partially by its possible applications to nano- and micro-electronics [1]. Using metal such as copper which is not capable of forming carbide, different kinds of conductive clusters distributed within a-C:H matrix can be formed [2,3]. The main goal of the present investigation is to process SDF of embedded in a-C:H copper-born clusters both from the optical spectra and directly from TEM images to compare them. For structural characterization of copper born clusters embedded in a-C:H a study of small angle X-ray diffraction pattern was performed.

EXPERIMENTAL

A-C:H films were produced by ion co-sputtering of graphite and copper targets in argon-hydrogen (80% Ar and 20% H_2) plasma onto KBr, amorphous quartz and silicon substrates. The optical absorption spectra (1-6 eV) of a-C:H films deposited onto amorphous quartz substrates were measured with Hitachi-U3410 spectrophotometer to characterize the microstructure of grown films by an analysis of processed optical data. Ellipsometrical measurements were performed with LEF-3m ellipsometer (1.96 eV) to find out both geometrical characteristics of grown films and their optical constants. A Philips400 TEM operating at 100 keV was used for direct observation of microstructure and electron diffraction analysis of copper-doped a-C:H films. X-ray scattering by the samples were studied with a RIGAKU X-ray diffractometer operating at a wavelength 1.541 A (Cu-Kα line) (50 kV) in reflection geometry in the range of 1.0 - 4.0 degrees.

OPTICAL STUDIES

Optical transmission spectra of copper-doped a-C:H are presented in [2]. Shape of the optical spectra shows that the dielectrical function is a result of superposition of four Lorentz oscillators as follows[3]: (1) a low-frequency oscillator associated with the free-carrier absorption; (2) a mid-frequency oscillator associated with surface plasmon excitations in insulated spherical conductive clusters; (3) a high-frequency oscillator associated with surface plasmon excitations

in non-spherical conductive clusters; (4) a high-frequency oscillator associated with the fundamental absorption of the a-C:H matrix.

The algorithm described in [2] was used to evaluate imaginary and real parts of the dielectrical function. However, SDFs of conductive copper-containing clusters embedded in a-C:H matrix were neglected in the course of calculations. In this paper we estimate SDFs of oscillators 2 and 3 by simple averaging (integration) of contribution of oscillators with their SDF weights. In accordance with [5] is reasonable to choose the SDF shape in accordance with the fluctuation theory as follows [4,5]:

$$P(D) = \frac{A}{\sqrt{2\pi}\cdot bD_{av}} \exp\left(-\left(D - D_{av}\right)^2 \Big/ 2(bD_{av})^2\right) \qquad (1)$$

Here D_{av} being the average size of the conductive cluster is a correlation length of the fluctuation, b=1[4] is a parameter; A is a constant calculated by means of the renormalization of $P(D)$. In the course of calculation it was also assumed that the relation between the relaxation time of each of the oscillator and their geometrical characteristics corresponds to a size-confined free-electrons gas model [2]. As regards to the algorithm described in [2], introduction of SDF in the model brings no additional parameters to the calculation scheme. In the course of calculations it was found that chosen distribution function fits the experimental data. As a result of fitting, we were able to find the spectral dependencies of extinction index which is shown in fig. 1. The average sizes for type(2) and type(3) copper clusters are shown in fig. 2.

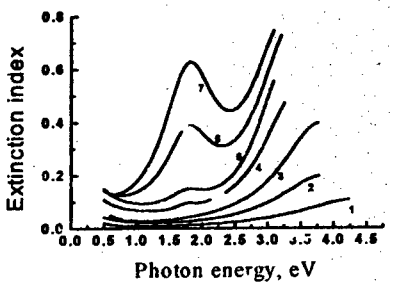

Fig. 1. The spectral dependencies of extinction index vs. copper concentration for Cu-doped a-C:H. 1-0%; 2-3%; 3-6%; 4-14%; 5-18%, 6-20%, 7-24%

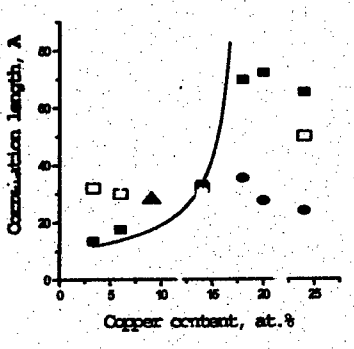

Fig. 2. The correlation length of copper-containing clusters vs. copper concentration. Full squares stand for non-spherical clusters, full circles stand for spherical clusters, line is a fit according to the percolation theory[3,4], hollow squares stand for small angular data analysis, triangle stands for mean size of copper clusters obtained from TEM image.

TEM STUDIES

The SAED pattern shows diffuse rings and the lattice spacing corresponding to each ring provides a reasonable match to the copper for a-C:H sample with 9% of copper. The size variation of copper-born nanoclusters was analyzed from TEM micrographs directly and the SDF is plotted in fig.3, full squares stand for experimental points. Full line presents the best fit to the Gaussian law (1) with b= 0.63, D_{av}=2.6 nm. Dotted curve demonstrates SDF for 9% Cu-doped a-C:H obtained from equations (1) using fitted above optical data (b=1). There is seen a reasonable agreement between optical and TEM data(fig. 2.). Rather good coincidence between optical and TEM SDF could be also ascribed in terms of early (nucleation) stage of copper-based clusters formation process. In this case average (critical) size of the cluster is a function of interface free energy per unit area σ and bulk free energy ΔG decrease per unit volume [5]: $D_{av} = 4\sigma/\Delta G$. It worth noting that at copper concentrations exceeded percolation threshold an analysis of TEM images is fairly complicated because difficulties in the spatial resolution of different geometrical forms of copper-born clusters and in this case a special analysis technique should be used

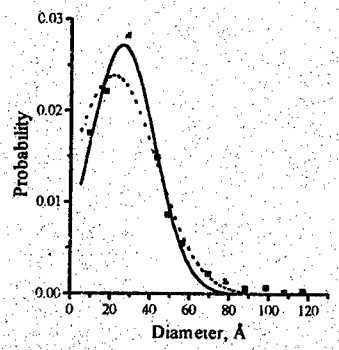

Fig. 3. SDF obtained from TEM micrograph. Full squares stand for experimental points, full line is a fitted Gaussian curve. Dotted curve is SDF obtained from optical data.

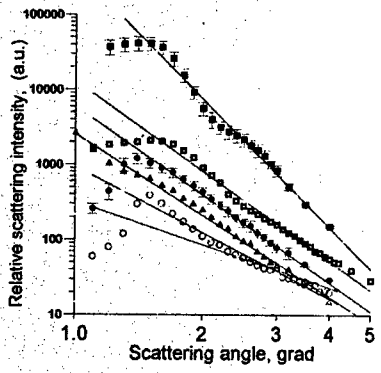

Fig. 4. X-ray scattering intensity versus scattering angle Θ for a-C:H doped with copper: ■ ■ ■ - 4% copper; □ □ □ - 6% copper; ● ● ● - 14% copper; ○ ○ ○ - 14% copper (vacuum annealed sample); ▲ ▲ ▲ - 24% copper.

X-RAY STUDIES

It was found by direct comparison of the intensity of radiation scattered by copper-free and copper-doped a-C:H films that the contribution of the a-C:H matrix is rather small, i.e., copper-based clusters embedded in the a-C:H matrix are responsible for the X-ray scattering appearing at small angles. The position of the peak in fig. 4 show that the average size of the copper- based cluster assembly is fairly well defined and the mean cluster sizes are in reasonable agreement with estimations for non-spherical clusters provided by optical measurements(fig. 2) The intensity I(q) of scattered radiation is $I(q) \sim q^{-\alpha}$, where transferred momentum $q=(4\pi/\lambda)\sin(\Theta/2)$,

Table The sample parameters.

Copper, %	Index α	Fractal dimension D	Comments
4	5.4	2.0	Scatterer with smooth boundary surfaces [8]
6	3.9	2.1	Scatterer with fractal surfaces [8]
14	3.7	2.3	------''------
24	3.6	2.4	------''------

λ is the wavelength of scattered radiation. For scatterers bounded by a smooth surface the index α is exactly 4 [6]. As evident from fig. 4. for all measured samples the scattered amplitude is indeed a power function of angle with not integer index α. The uncertainty in the exponent is about 0.1 as estimated from data reproducibility. The observed angular dependence of scattered intensity is typical for small-angle scattering by fractal structures [7,8]. We believe that the fractal structure that scatters X-rays is a material containing scatterers with smooth or fractal boundary surfaces. According to the model, at $3<\alpha<4$ the exponent α is related to the fractal dimension D of scatterers by $D=6+\alpha$ (scatterers with fractal boundaries)[7,8]. For the case $\alpha>4$, the exponent α defines the exponent $\gamma=7-\alpha$ describing the distribution P(r) of scatterers with smooth boundary surfaces of radius R [8]: $P(R)\sim R^{-\gamma}$

At low copper concentration the cluster surface is smooth and with increasing of copper content cluster surface changes its shape, i.e. the cluster surface acquires a fractal character.

CONCLUSIONS

a) Optical method of analysis of specific optical absorption bands in copper-doped a-C:H can be used to find sizes and shapes of conductive copper-containing clusters and to estimate their SDFs. b) The Gaussian curve reasonably fits experimental data of TEM SDF at copper concentration about of 9%. This indicates nucleation stage of conductive clusters formation for the samples with copper concentrations lying below the percolation threshold. c) TEM SDF at 9% copper coincide well with optical one; d)With increasing copper content copper clusters deform their shape, i.e. cluster surface acquires a fractal structure.

ACKNOWLEDGMENTS

This work was supported in part by RFBR grants N 97-03-32273-a, N 97-02-18110-a, State Russian Program "Physics of Solid State Nanostructures" and Arizona University grant.

REFERENCES

1. Li, J., Seidel,T.E. and Mayer, J.W. 1994. *MRS Bulletin* **XIX(8)**:15-18.
2. Ivanov-Omskii,V.I., Tolmatchev, A.V. and Yastrebov S.G. 1996. *Phil. Mag. B*, **73**:715-722.
3. Ivanov-Omskii,V.I., Lodygin,A.B. and Yastrebov,S.G. 1995, *Phys.Solid State*, **37(6)**: 920-922
4. Efros, A L. and Shklovskii, B.I. 1976. *Phys. Stat. Sol. B*, **76**: 475-485
5. Landau, L.D., and Lifshitz, E.M. 1981. *Physical Kinetics, Course of Theoretical Physics* Pergamon, New York.
6. Guinier, A. and Fournet, G. (1955).*Small-Angle Scattering of X-Rays*, Wiley, New-York
7. Bale, H.D. and Schmidt, P W. (1984) Small-Angle X-Ray-Scattering Investigation of Submicroscopic Porosity with Fractal Properties,*Phys.Rev.Lett.*,**53**(6), 596-599
8. Siklitsky, V.I., Ivanov-Omskii, V.I., and Baidakova, M.V. (1996), Diamond (and other wide band-gap), St.Petersburg, (to be published)

Time-Resolved Luminescence of Porous n-InP

K.Chernoutsan, V.Dneprovskii, V.Karavanskii*, O.Shaligina, E.Zhukov

Moscow St.University, Dept. of Physics, 119899 Moscow, Russia
Fax: 7-095-939-3731, E-mail: dnepr@scond.phys.msu.su
*General Physics Institute, 117942 Moscow, Russia

Time resolved luminescence of porous n- InP excited by picosecond pulses of the second harmonic ($\hbar\omega$ = 2,34 eV) of Nd-glass laser (pulse duration about 8 ps) has been investigated using streak camera with 5-10 ps time resolution.

The observed kinetics of luminescence has been explained by three mechanisms of recombination in nanostructures: linear, bimolecular and Auger process.

The samples of porous InP have been obtained by electrochemical etching of n-InP (100) substrate.

The luminescence spectra of porous InP (broad band with maximum at 580 nm Fig.1) excited by powerful picosecond pulses are shifted to the blue spectral region compared with that of the bulk. This shift allows to estimate the average size of nanostructures: the diameter is about 6 nm (4 nm) if the luminescence of quantum dots (cylindrical quantum wires) is assumed.

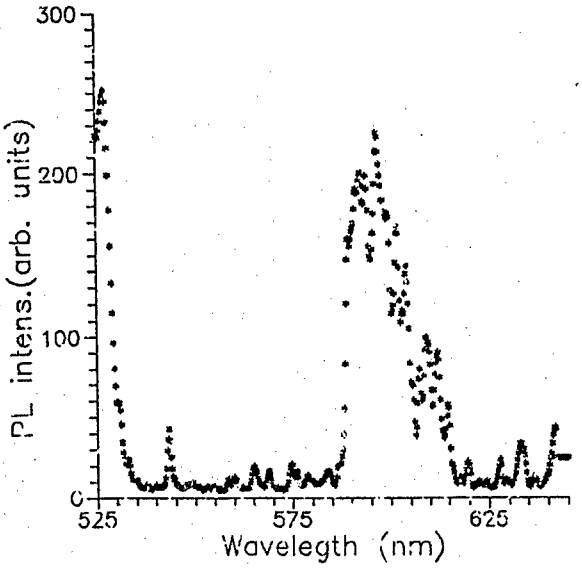

Fig.1. The spectrum of porous InP luminescence and of the trace of the pumping pulse.

The kinetic properties of the intensity of luminescence differ for low and high levels of laser excitation. In the Fig.3 the dependence of the intensity of luminescence upon time is shown for high excitation.

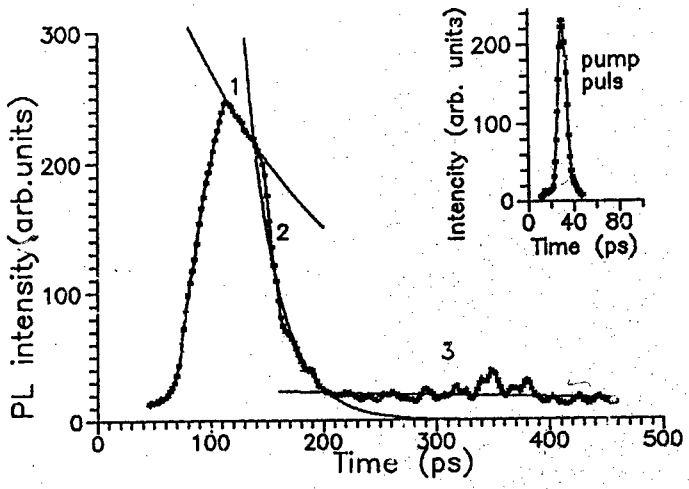

Fig.3. Time resolved intensity of porous InP at high excitation.

Three characteristic parts of the decay may be analyzed. For relatively fast first part of the decay $I \sim t^{-2}$ (the instant relaxation time of the intensity of luminescence $\tau_I = -I / (dI / dt)^{-1} \sim I^{-0.5}$). Thus taking into account that $I \sim N^2$ (N is the density of the excited carriers) one can obtain $-(dN / dt) \sim N^2$ -bimolecular recombination. For the second fast part of the decay $I \sim t^{-1}$, $\tau_I \sim I^{-1}$ and $-(dN / dt) \sim N^3$ - Auger process. The slow decay at low density of the excited carriers may be attributed to the linear recombination (τ_I = const.). The obtained results allow to suppose that the accumulation of carriers probably takes place at the first stage of the relaxation. At the intermediate level of excitation (Fig.4) the obtained results could be explained only by bimolecular and linear recombination.

The carrier confinement in semiconductor nanostructures is expected to enhanced the efficiency of photoluminescence. Probably, the highest quantum yield (60%) of quantum dots photoluminescence has been observed for InP quantum dots in colloid [1]. Our experiments have shown that the intensity of porous InP luminescence is poor. It may be because of the enhanced influence of the surface states in porous InP nanostructures (quantum dots and quantum wires). The surface states quench the luminescence through rapid surface-state trapping and nonradiative recombination of excited carriers. Another explanation of the poor luminescence of porous InP may be the retardation of carriers' relaxation in nanostructures[2] and the relative increase of nonradiative recombination probability.

The measured intensity of luminescence (I) depends upon the intensity of excitation (S) (Fig.2). It is linear at low excitation and nonlinear ($I \sim S^2$) at high excitation.

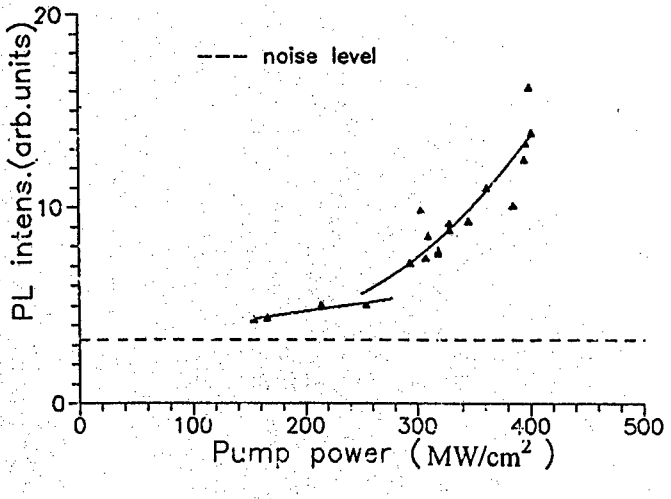

Fig.2. The dependence of the porous inP intensity of luminescence upon the pumping intensity.

This research was made possible in part by Grant 96-2-17339 of the Russian Foundation for Fundamental Research and Grant of the Russian Ministry of Science progran. 'Physics of Solid Nanostructures".

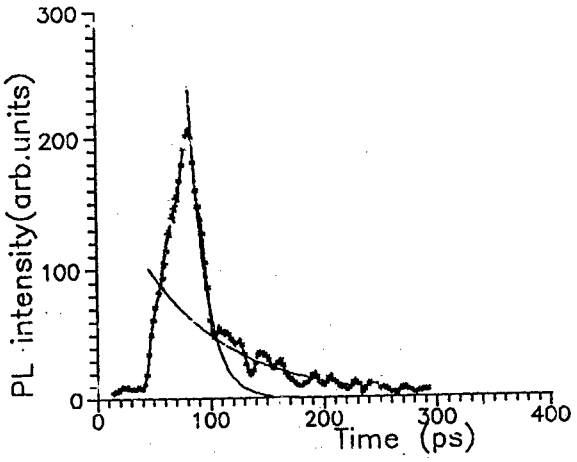

Fig.4. Time resolved intensity of porous InP luminescence at the middle level of excitation.

[1] O.I. Micic, J.S. Sprague, Z. Lu, A.J. Nozik, Appl.Phys.Lett. 68, 3150 (1996)
[2] H. Benisty, C.M. Solomeyor-Torres, C. Weisbuch, Phys.Rev. B44,10945 (1991)

Nonlinear Optical Properties of Semiconductor Quantum Wires.

V.Dneprovskii and E.Zhukov

Moscow St. University, Dept. of Physics, 119899 Moscow, Russia;

Fax:7-095-9393731; E-mail: dnepr@scond.phys.msu.su

Picosecond pump and probe laser saturation spectroscopy method [1] has been applied to investigate the physical processes leading to strong dynamic optical nonlinearities of semiconductor quantum wires (QWRs).

In QWRs different nonlinear processes may compete and coexist: the dynamic Burstein-Moss saturation effect of one-dimensional energy bands, renormalization of the energy gaps at high density of the excited carriers; bleaching and broadening of the exciton absorption line due to the phase space filling and screening of excitons; quantum-confined Stark effect of excitons, etc.

We have used the samples containing GaAs and CdSe QWRs. Molten semiconductor material was injected and crystallized in the hollow cylindrical 6 nm diameter cchannels of crysotile-asbestos [2]. A sample is a regular close packed structure of parallel crysotile-asbestos 30-nm-diameter nanotubes filled with ultrathin crystalline semiconductor wires . The diameter of the wires is comparable with the de Broglie wavelength of the electron. The size of the samples and the concentration of QWRs enable the spectra of both linear and nonlinear absorption to be measured.

Bleaching bands have been observed in the differential transmission (DT) spectra of GaAs QWRs (Fig.1) [3].

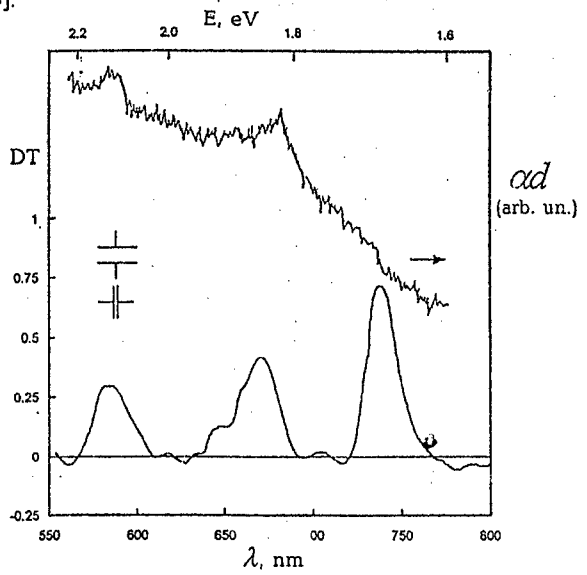

Fig.1.The linear absorption and differential transmission (zero delay between the pumping and probing pulses) of GaAs QWRs crystalliz d in crysotile asbestos nanotubes.

The low energy band (1.67 eV) has been registered only for some parts of the samples (the exciting and probing beams could be scanned along the suface of the samples). The energy positions of these bands coincide with corresponding "hills" and "shoulder" in the linear absorption (LA) spectra. The induced bleaching bands 1.85 eV (Fig.2.a) and 2.15 eV disappear over 50 ps. The relaxation time of the lower energy 1.67 eV band is shorter and could not be measured because of the insufficient time resolution of our system

It may be shown [1,2] that for GaAs QWRs of 3 nm radius the bleaching bands 1.85 eV and 2.15 eV correspond to the saturation of the transitions between the heavy hole one-dimensional band and the lowest conduction subband and to the split off by spin orbit coupling valence subband and the lowest conduction subband. As can be seen in Fig.2.a the 1.85 eV bleaching band of DT spectrum broadens - the low energy side shifts to the longer wavelength part at higher excitation. The values of the energy shifts depend upon the delay between the pumping and probing pulses and attain maximum at zero delay (at the highest plasma density).

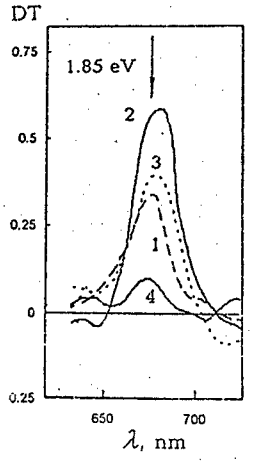

Fig.2.a. The differential transmission spectra of GaAs QWRs (1.85 eV bleaching band) at different delays between the pumping and probing pulses: (-13 ps) -1, 0 ps -2, 20 ps -3, 50 ps -4.

One may attribute these energy shifts to the band gap renormalization that arises at high density of the optically excited nonequilibrium carriers. The observed relative energy shifts may be compared (Fig.2.b) with the values of GaAs QWRs band gap shrincage obtained by S. Benner and H. Haug [5]. They have culculated the band gap shrincage of GaAs QWRs in the presence of high density e' ctron-hole plasma (Fig.1 in [5]). The band gap renormalization is shown (Fig.2.b - full line) as a function of the plasma density. The comparison of the values of obtained relative energy shifts with the theoreti al curve allows to conclude that the maximum band gap shrincage in our case is about 33-40 meV

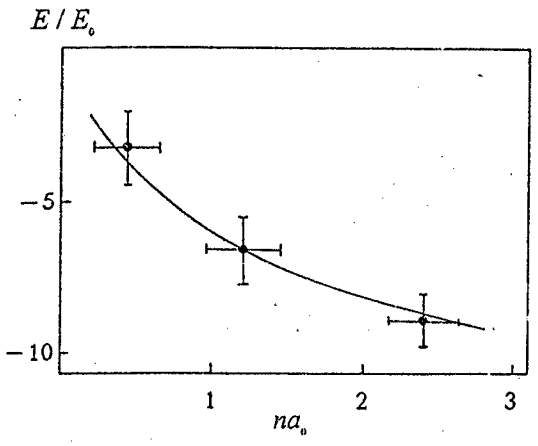

Fig.2.b. The energy shift of GaAs QWRs nonlinear absorption 1.85 eV band at different levels of excitation and the culculated [5] dependence of GaAs one-diomensional energy gap shrinkage (E_0 and a_0 are the exciton binding energy and Bohr radius of bulk GaAs).

The registered bleaching band 1.67 eV in the low energy part of the DT spectra (Fig.1) may be attributed to the "saturation" of excitons in GaAs QWRs (phase-space filling effect). The presence of high density electron-hole plasma causes a bleaching of excitonic resonance - reduces the effective electron-hole attraction by screening and phase-space filling. Space-phase filling is more efficient in QWRs than Coulomb screening [4,5]. The space-phase filling effect arises because an exciton consists of an electron and a hole, each of which obeys the Pauli exclusion principle. Hence only those electron-hole states may be used for the exciton creation that are not yet occupied by free carriers. The screening effect leads to the spatial rearrangement of the electrons and holes which is strongly restricted in QWRs.

The energy position of the "excitonic" bleaching band allows to estimate the binding energy of exciton of GaAs 3 nm radius QWRs in crysotile asbestos matrix: 130-160 meV. The increase of the excitonic binding energy may be explained not only by quantum confinement but also by the "dielectric confinement" [6]. The image potentials that arise due to the difference in the dielectric constants of semiconductor QWR and dielectric matrix become essential. They result in the marked increase of the electron-hole attraction. The binding energies of excitons in the cylindrical QWRs have been culculated in [6] as a function of the wire's radius and dielectric constants of semiconductor and surrounding dielectric. For GaAs QWRs in dielectric matrix with dielectric constant $\varepsilon \cong 2.3$ the culculated binding energy of exciton is about 130-140 meV. The measured value of the exciton binding energy of GaAs QWRs in crysotile asbestos nanotubes is in good agreement with that culculated.

As it is pointed above the 'excitonic" 1.67 eV bleaching band has been observed only for some parts of the excited samples. It may be explained by nonuniform filling of crysotile asbestos nanotubes with crystallized GaAs . Only some parts of the samples contain nanowires whose length considerably exceeds the Bohr radius of exciton.

For CdSe QWRs in crysotile asbestos nanotubes the LA and DT spectra are shown in Fig 3

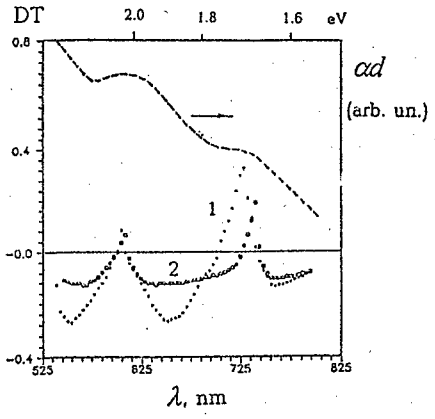

Fig.3. The linear absorption and differential transmission (at zero and 7 ps delay between the pumping and probing pulses) of CdSe QWRs crystallized in crysotile asbestos nanotubes.

The energy position of the "hills" of LA spectrum and the bands of DT spectrum (1.7 eV and 2.05 eV) allow us to attribute them to the linear and nonlinear absorption of excitons (with binding energy about 200 meV) in 3 nm radius cylindrical CdSe QWRs (1.7 eV) and to the linear and nonlinear (state filling) absorption at the frequency of the optical transition heavy holes of one dimensional energy band - the first subband of electrons (2.05 eV).

The blue shift of the "excitonic" 1,7 eV band of the DT spectrum and the increase of absorption in its vicinity in the case of higher density of the excited plasma (compare the DT spectra in Fig.3 obtained with different optical delays between the pumping and probing pulses) may be explained following [5]) by the joint action of the electric field and high density electron-hole plasma. The electric field probably arises due to carriers localized in the lateral barrier region that contain imperfections and impurities [5]. For the large lateral electric field the Stark effect dominates and the exciton absorption peak shifts red. For increasing high density of a thermal electron-hole plasma and with applied electric field the Hartry term (the reduction of the electron-hole interaction) shifts the excitonic absorption peak to higher energies due to the violation of charge neutrality [5].

This research was made possible in part by Grant 96-2-17339 of the Russian Foundation for Fundamental Research and Grant of the Russian Ministry of Science program "Physics of Solid Nanostructures".

[1] V.S. Dneprovskii, V.I. Klimov, D.K. Okorokov, Yu.V. Vandyshev, Solid State Commun. 81, 227 (1992)
[2] V.V. Poborchii, M.S. Ivanova, I.A. Salamatina, Superlattices and Microstr. 16,133 (1994)
[3] V.Dneprovskii,N.Gushina,O.Pavlov, V.Poborchii, I.Salamatina, E.Zhukov,Phys.Lett.A204, 59 (1995)
[4] S.Benner and H.Haug, Europhys. Lett.16,579 (1991)
[5] S Benner and H Haug, Phys. Rev. B47, 15750 (1993-I)
[6] E.A. Muliarov, S.G. Tihodeev, JETP 111 (1), (1997)

SIZE-DEPENDENCE OF THE CRYSTAL STRUCTURE OF CdSSe NANOCRYSTALLITES EMBEDDED IN GLASS

P.V.Giugno, I .Vasanelli and R.Cingolani
Dipartimento di Scienza dei Materiali - Universita di Lecce
Via Arnesano, I-73100 Lecce - Italy

A. Continenza
Dipartimento di Fisica – Universita dell'Aquila
Via Vetoio, Loc. Coppito, 1-67010 L'Aquila - Italy

V.G.Baru, A.Chernushich, V. Jitov and V.Luzanov
Institute of Radioengineering and Electronics,
Russian Academy of Sciences,
Vvedensky sq.1, Fryazino, 141120, Russia

We report the observation of a size-induced transition (from Zincblende phase to Wurtzite) occurring in CdSSe nanocrystallites (quantum dots) of radius 4 - 5 nm. This problem for the II-VI semiconductor crystallites was discussed in [1-4].

The investigated CdS_xSe_{1-x} quantum dots were grown in a matrix of multicomponent oxide borosilicate glass by controlled heat treatment in the range 600-710 C [5]. The stoichiometric parameter x~0.23 was determined by the resonant Raman-scattering measurements at 77K. The average nanocrystallites radius of samples varied from 1.5 to 6 nm. The quantum dot size and the size dispersion determined by the temperature and duration of the thermal annealing were obtained by transmission electron microscopy (TEM). TEM observations were made by a JEM 2010 electron microscope working at 200 kV. The bright field images and related size histograms obtained from the samples A (witn a heat treatment at 650 C for 1 hour) and B (with a heat treatment at 710 C for 1 hour) are shown in Fig.1. Information on the crystallographic phase of nanocrystallites has been obtained by the small area electron diffraction (SAD) observations. SAD measurements were performed by selecting the suitable spot size, convergence angle and condenser aperture in order to obtain the diffraction patterns from chosen areas of about 100 nm in diameter with a beam approximately parallel (the convergence angle was of about 5×10^{-5} rad).

The quantitative analysis of the ring sequences obtained from the typical SAD patterns is summarised in Tables I,II . It indicates that the smallest quantum dots have ZB structure whereas larger dots have W structure. The transition from the ZB phase to the W phase occurs at the radius 4 - 5 nm. Consistently, the sample B exhibits a mixed SAD patterns which include both the ZB and W rings (see Table II).

Notice that the samples A and B were produced at the different annealing temperature . In order to elucidate the influence of the temperature on the structure of produced CdSSe nanocrystallites x-ray diffraction measurements were performed at the samples with the same annealing temperature and the different duration of a thermal treatment. X-ray diffraction measurements were performed over a range of 2Θ from 40 to 52^0 using an automated step-scanned diffractometer DRON-3. Because of the small fraction of microcrystallites in the glass, only the samples with a big mean quantum dot radius (when almost all semiconductor

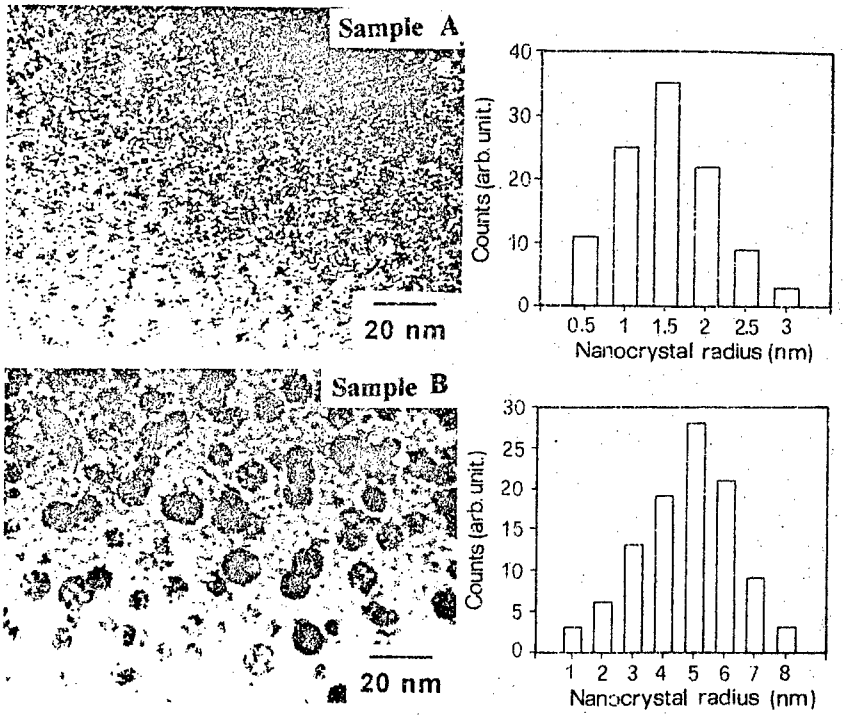

Figure 1. Bright field images and related size histograms of the samples A (with a heat treatment at 650 C for 1 hour) and B (with a heat treatment at 710 C for 1 hour) .

Table I. Identification of the diffraction rings obtained from the sample A. The "ring labels" correspond to the number of the rings of SAD patterns. R_N/R_1 is the ratio between the radius of the N-th diffraction ring and the radius of the first ring. The R_N/R_1 sequence is consistent with the d_1/d_N ratios calculated for a Zincblende crystal. Since $\lambda \cdot L = R \cdot d$ we have: $R_N/R_1 = d_1/d_N$ (λ is the electron wavelength, L is the camera length, d is the distance between relevant crystal planes). The Miller indices of the identified reflections are reported on the last column of the table.

Politype	Ring label	R_N/R_1	d_1/d_N	Miller indices (hkl)
Zincblende Structure	1	1.0	1.0	(111)
	2	1.15	1.16	(200)
	3	1.64	1.63	(220)
	4	1.93	1.92	(311)
	5	2.02	2.0	(222)
	6	2.31	2.31	(400)
	7	2.54	2.52	(331)
	8	2.82	2.83	(422)

Table II. Identification of the diffraction rings obtained from the sample B. Two sets of rings have been identified on the diffraction pattern: one set (1-5) of the weak patterns comes from the ZB structural modification, and the other (a-f) of the strong patterns from the W structural modification. In the later case the sequence of R_N/R_1 ratios agrees well with the d_1/d_N sequence calculated for a $CdS_{0.23}Se_{0.77}$ Wurtzite crystal with c/a=1.63 in cur case (a, c the lattice constants of the Wurtzite cell). The Miller indices of the identified reflections are reported on the last column of the table.

Politype	Ring label	R_N/R_1	d_1/d_N	Miller indices (hkl)
Wurtzite Structure	a	1.00	1.00	(10.0)
	b	1.74	1.73	(11.0)
	c	2.02	2.0	(20.0)
	d	2.66	2.65	(21.0)
	e	3.00	3.00	(30.0)
	f	3.48	3.46	(22.0)

(continuation of the Table II)

Zincblende structure	1	1.00	1.00	(111)
	2	1.63	1.63	(220)
	3	1.91	1.92	(311)
	4	2.81	2.83	(422)
	5	3.26	3.27	(440)

material is incorporated in the crystallites) give a measurable signal. Three relatively diffuse peaks are observed on a sloping background of diffraction of glass in the case of the sample C with a heat treatment at 650 C for 110 hours . These peaks are identified as reflections from the (11.0), (10.3), and (20.0) planes of the hexagonal W structure. The mean nanocrystallites radius of sample C exceeded 5 nm. Hence, the samples A and C produced at the same annealing temperature T=650 C but with the different annealing time (sample A- 1 hour, sample C- 110 hours) have revealed the different crystal structure (sample A - ZB, sample C - W). These and other X-ray diffraction data confirmed a prevailing size dependence of the crystallite structure.

It has been found that the ultra small CdSSe cluster are nucleated and developed in the cubic ZB phase by annealing of the investigated glass. As the radius of quantum dot exceeds approximately 4 - 5 nm the phase transition from ZB to W structure occurs.

The observed experimental results may be interpreted qualitatively in terms of the surface energy associated with the broken bonds, defects and stress at the interface nanocrystallite-glass. The quantum confinement effects could play an important role at this case. The surface energy of the small crystallites with ZB structure is less than one in the case of the W crystallites, thus ZB phase is a peculiar property of the ultra small dots. With increasing of the nanocrystallite size the relative contribution of the surface energy in the total cluster energy decreases and a consequent transition occurs from the ZB structure to the bulk W structural modification.

References

[1] Y.Wang and N.Herron, Phys. Rev., B 42 (1990) 7253.
[2] A.I. Ekimov, I.A.Kudryavtsev, M.G.Ivanov and Al.L.Efros, J.Lumin., 46 (1990) 83.
[3] S.G.Kosnikov, A.A.Lipovskii, N.V.Nikonorov, A.A.Sitnikova, and M.V.Kharchenko, Fiz. Tekn. Polupr. (Russian), 29 (1995) 1473.
[4] R. Rossetti, S.Nakahara, and L.E.Brus, J. Chem. Phys., 79 (1983) 1086.
[5] V.A.Jitov, B.S.Shchamkhalova, Yu.Ya.Tkach, and Yu.L.Kopylov, Phys Low-Dim. Struct.,2/3 (1995) 79.

MACROSCOPIC ELECTRIC PROPERTIES OF POLYDIACETHYLENE NANOSTRUCTURES

E. G. Guk, M. E. Levinstein, V. A. Marikhin, L. P. Myasnikova, S. L. Runyantsev
Ioffe Physico-technical Institute Russian Academy of Science
194021, Polytehknicheskaya 26, St Petersburg, Russia

The conductivity of any conductive polymer has its origin in transport of a free carrier (soliton or bipolaron) along a conjugated sequences in polymer molecules. These sequences can be considered as a quasi-one-dimensional wires. The length of such a "wire" is equal to the length of conjugation and reaches 1.5-15 nm (10-100 C=C bonds) in "good" conducting polymers.
In accordance with the present view, the effective carrier mobility along a conjugated sequence is sufficiently high (see, for instance [1]). The realisation of macroscopic conductivity requires, however, not only transferring carriers along a conjugated length but, also, their transport from one to another quantum wire inside of one and the same fibril as well as between the fibrils. These processes are complicated and far of being fully understandable.

Nevertheless, a lot of different devices are already designed on the basis of conducting polymers including field transistors, transistors with a permeable base, bipolar transistors, light emitting diodes and a set of other devices analogous to the semiconductor ones (see, for instance, [2,3]).

Recently, in a paper [4] a new approach to the doping of polydiacethylene (the only class of conjugated polymer capable to solid state polymerisation) has been proposed. The effectiveness of the proposed approach has been demonstrated for polymer single crystals of polydiacetyhylene poly(1,1,6,6-tetraphenilhexadyindiamin), briefly, PDA THD. Earlier, even the principal possibility of doping PDA THD has not been obvious.

Besides of the well known problems with PDA doping caused by its high crystallinity and dense packing of macromolecules in crystals, PDA THD is characterized by large geometrical sizes of the side groups, which hinders the transport of carriers between the quantum wires. Therefore, one could hardly expect the macroscopic conductivity in PDA THD even when its doping is effective.

In the paper [4] not only principal possibility of PDA THD doping was proved but a record high value of conductivity for PDA ($3 \cdot 10^{-2}$ S/cm) has been reached.
In the present paper the electrical and noise properties of doped PDA THD are investigated for the first time. (An undoped crystals were synthesised in St.Petersburg State University.)

SAMPLES.

The original needle-like single crystals of PDA THD with the length (L) of 1-3÷5 mm and 0.3÷0.5 mm in diameter (d) have been exposed to twofold disintegration in an electrical mill. This treatment resulted in significant reduction of both the crystal length (down to 30÷50 μm) and their diameter (down to 3÷5μm). PDA tablets for investigations have been produced by the compression and have been doped in iodine vapour at 70^0 C over 48 hours

RESULTS AND DISCUSSION

Stability of conductivity. The highest d.c. conductivity demonstrated by as-doped samples has been better than $5 \cdot 10^{-3}$ S/cm. The value of d.c.conductivity first reduces with time and thereupon stabilised in the course of time off. The relation of a stable conductivity σ_0 to the maximum value of conductivity σ_m has a significant dispersion from one sample to another one and depends on conditions of their preparation. This relation is equal of about 0,2 for the best samples, the characteristic time of stabilisation being tens of hours.

When a non-optimum doping regime is realised, a fall in conductivity with time was observed during weeks and sometimes even during a month. The relation σ_0/σ_m may be equal $< 10^{-4}$.

Current-voltage characteristics. I-V characteristics reveal a marked superlinearity at d.c. bias U>1 V (Fig.1). This effect is, most likely, attributed to selfheating of the samples by passing current. Indeed, on the one hand, σ increases with temperature, on the other hand, I-V characteristics are linear at pulse testing up to U ~ 100 V, which corresponds to the electrical field $E = U/L = 10^4$ V/cm (see an inset in Fig.1).

It is worthy to note that I-V characteristics of those samples in which the resistance grows with time by 3÷4 orders of magnitude, demonstrate the deviation from ohmic behaviour on direct current at practically invariant U values (though the current passing through the samples change with time upon the same U by 3÷4 orders of magnitude).

This allows to suggest a percolation conductivity in doped PDA THD samples.

Upon increasing resistance the number of the conducting ways reduces. The current density across the remained chains of skeleton of an infinite cluster is practically constant.

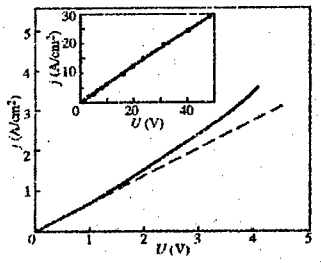

Fig.1.
dc current-voltage characteristic of PDA-THD. 300 K.
The insert represents the pulse current-voltage characteristic. Pulse duration τ=200 ns. Repetition frequency f=10 Hz.

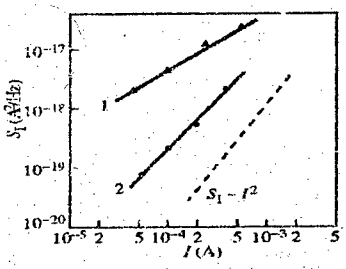

Fig.2
The dependence of the relative resistance of the sample on the uniaxial pressure.
1.Resistance has been measured along pressure (R | | P).
2.Resistance has been measured across pressure (R⊥P)

The resistance-pressure dependence. A well pronounced anisotropy of conductivity has been revealed when measuring conductivity of the samples under pressure. A curve 1 (FIg.2) corresponds to the resistance-pressure dependence R(P) measured along of applied pressure. One can see that at once resistance decreases with pressure increasing up to P < 0,5 kBar and then monotonically increases with further pressure increasing, resistance growth being irreversible. One may suggest that the latter is associated with gradual

destroying of conductivity in a direction of applied pressure. At the same time, the conductivity measured in perpendicular direction increases with pressure increasing and at P = 4 Kbar stabilises reaching the value greater than the initial one by a factor of 5. Any destruction has not been observed in this direction. The preliminary WAXS study reveals a plane texture in the samples exposed to uniaxial pressure.

Recently it was found [4] that in spite of perfect external geometrical shape,the needle-like PDA THD crystals have not a homogeneous internal structure typical of true single crystals. They consists of densely packed microfibrils, 30÷50 nm in diameter. One can assume that the external pressure hinders hopping conductivity between neighbouring microfibrils, not significantly changing the coherent transport of the charge carriers along "quantum wires" on a conjugated length.

Low frequency resistance fluctuations. The low frequency noise was measured over the frequency range from 20 Hz up to 5 kHz, in the temperature range from 200 up to 300 K and in the pressure range from 0,2 up to 1 kBar. In the whole ranges of above mentioned parameters the frequency dependence of the noise spectral density S appeared to be proportional to 1/f (flicker noise). Fig.3. represents the dependence of S versus current I for two samples of PDA THD at f=80 Hz. The spectral noise density 1/f for amorphous and polycrystalline materials is usually characterised by the generalised Hooge equation:

$$S_I(f)=\alpha I^{(2-\beta)}/Nf$$

where α is the Hooge constant which depends on temperature and frequency analysis, N is the total number of the charge carriers in a sample.

As far as we know, the dependence $S\sim I^2$ ($\beta=0$) typical of "classical" metals and semiconductors never has been observed for conducting polymers. It is seen in Fig.3 that the values β for PDA THD are in a range $0 < \beta < 1$.

In the temperature range from 200 up to 300 K S_I weakly depends on temperature.

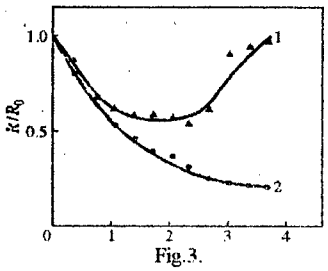

Fig.3.
The dependence of current spectral density versus current I for two samples PDA THD at 300 K, f=80 Hz. Dashed line shows the slope $S_I \sim I^2$.

The value of the Hooge constant α can be estimated from the data for conductivity and mobility (or concentration) of charge carriers in polymers. Taking values of mobility μ = 5 cm^2/Vs [6] , measuring resistance R and knowing the thickness of a sample one can calculate the amount of charge carriers: $N = L^2/q\mu R \approx 1.2\cdot10^{10}$. The estimations of α value gives $\alpha \sim 10\div20$.

This is a quite reasonable value for such a disordered material as PDA THD.

Summery

The first investigation of electric properties of PDA THD evidences a percolation character of conductivity in doped polydiacethylene THD. Uniaxial pressure P>2 kBar results in destruction of percolation system and loss of conductivity in the direction perpendicular to the long axis of PDA THD single crystals. The conductivity along single crystal axis (along microfibrils) does not decrease therewith even at the pressure P ≥ 4 kBar. A study of low frequency fluctuations of resistance also indicates a percolation type of conductivity. Noise level is characterised by the Hooge constant α equal to about 20.
This research is supported by Russian Foundation of Basic Investigation (grant N 96-03-32462-a).

References

1. Handbook of conducting polymers. ed by T.A. Skotheim, N.Y.-Basel: Marcel Dekker (1986). 1417 p.
2. R.Bruschi, F. Cacialli, A.Nannini, and B.Neri, J. Appl. Phys., 76, 6, 3640 (1994)
3. A.Dodabalapur, H.E.Katz, L.Torsi, and R.C.Haddon. J.Appl.Phys.Lett. 68, 8, 1108, (1996)
4. V.A. Marikhin, E.G.Guk, L.P.Myasnikova. Physics of the Slid Sate, in print.
5. B.I. Shklovskii, A.L.Efros. Electron Poperties of Semiconductors. Nauka. M. (1979), 416 p.
6. D.Moses, and A.J.Heeger. J.Phys.Condens.Matter 1, 8, 7395 (1989)

Dielectric Effect on Exciton Dynamics in Silicon Quantum Wires

P.K.Kashkarov, E.A.Konstantinova, A.V.Pavlikov, V.Yu.Timoshenko

Faculty of Physics, M.V.Lomonosov Moscow State University, 119899 Moscow, Russia

It is well known that porous silicon (PS) formed in an electrochemical process consists of silicon wires with diameter of several nanometers [1]. According to theoretical predictions [2,3] stable excitons can exist in PS even at room temperature because of high binding energies of E_{exc}. A visible photoluminescence (PL) in this material is associated by many researches with radiative annihilation of the excitons [3,4]. However an experimental observation and investigation of the excitonic states is rather complicated due to a singularity of density of states for one dimensional objects [2] and a dispersion of the wires dimensions in the PS structure [1,3]. At the same time it is known that the excitonic states in semiconductor nanostructures are very sensitive to dielectric properties of an ambient. In particular, the value of E_{exc} increases in semiconductor quantum wires if the dielectric function of the ambient ε is less than that of the wire material [4].

In the present work kinetics of PL and free carrier IR absorption under pulse photoexcitation of PS kept in a vacuum or dielectric ambients have been investigated. The explanation of the data obtained is based on a model that suggests the existence of photoexcited electrons and holes both in bound and free states. The relation between these components depends on the dielectric properties of the silicon quantum wires surroundings.

The samples of PS formed in the electrochemical reaction of an anodization of single crystal silicon wafers of p-type in a HF acid solution [1] were used. According to electron microscopy and Raman scattering data the samples consisted of silicon wires and clusters with cross-section of 2-5 nm. An IR spectra measurement showed that surface of nanostructures was mainly covered by hydrogen. Under steady state excitation the samples displayed a visible PL but the quantum efficiency of the PL was less than several percent, that indicated the dominant role of the nonradiative recombination.

The kinetics of the PL and IR absorption by the free nonequilibrium carriers (FNC) were measured using N_2 pulse laser (337 nm, 10 ns) as the excitation source. The PL was registered with a nanosecond time resolution in a wave length range of 350-850 nm. FNC IR absorption was observed with a microsecond time resolution as a variation of transmission of a probe He-Ne laser beam (3.39 μm). The beams of the N_2 and He-Ne lasers were focused on the same point on the PS surface. The signals of PL and FNC IR absorption were measured "*in situ*" for the samples kept in the vacuum (~10^{-4} Pa) or in saturated vapours of organic substances. Benzol, acetone, ethanol and methanol were used (dielectric constants 2.3, 21, 24, 33 correspondingly). A condensation of the above vapours in the sample pores was registered as a sharp increase of a probing light reflection from the PS surface.

Preliminary experiments showed that optical characteristics of PS changed reversibly in cycles of vapour admission - pumping. It enabled us to suggest that the organic molecules did not form strong chemical bonds with the surface atoms of the silicon skeleton but only changed the dielectric properties of the nanostructures surroundings.

The PL kinetics for PS in the vacuum were found to be well described by a monoexponentional law for all wave lengths of the PL spectrum (fig.1). A PL relaxation time τ_{PL} decreased for large. energies of the emitted quanta. This feature is well explained in the frames of the model of the exciton radiative annihilation in silicon wires. According to the calculations the probability of the emission increases for excitons with higher E_{exc} (located in wires with the lower cross-sections) [2].

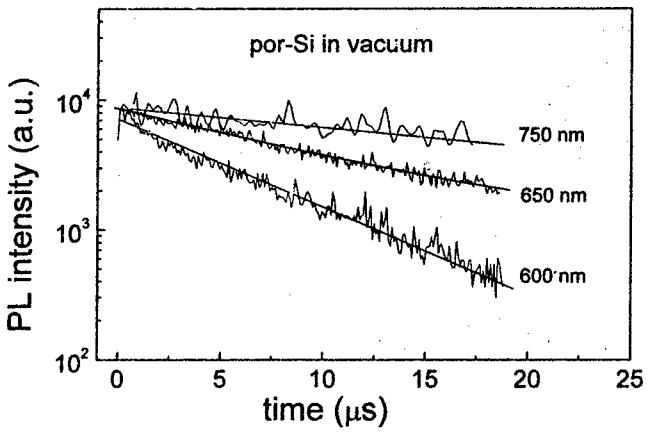

Fig.1. PL decays of porous silicon kept in a vacuum for different PL wavelengths.

The experiments showed that the significant influence of the organic vapours on PS optical parameters took place at the pressures corresponding to the beginning of the condensation in pores. The PL kinetics in this case were also monoexponential. The diminution of both the PL intensity and τ_{PL} was found after filling the pores with dielectrics characterized by $\varepsilon > \varepsilon_{Si}$ (fig.2). At the same time the FNC concentration increased. The last evidences that the concentration of nonradiative recombination centers located mostly on the nanostructures surfaces did not rise. This indirectly supports the above suggestion of the absence of the chemical interaction between dielectric molecules and atoms on the pores surface.

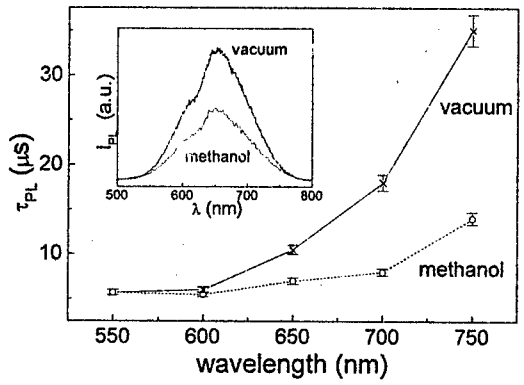

Fig.2. PL lifetime of porous silicon vs PL wavelength. Insert shows spectra of PL amplitude.

The results obtained can be explained on the base of the following model. The photoexcited charge carriers form dynamically connected subsystems of excitons and free electrons and holes. Radiative recombination takes place through annihilation of the excitons with a characteristic time τ_r. Nonradiative recombination of the free carriers occurs on surface defects with an average time constant τ_{nr}. Let us write a system of kinetic equations for concentrations of excitons (N) and FNC (n):

$$dN/dt = Cn - AN - N/\tau_r ,$$
$$dn/dt = g - Cn + AN - n/\tau_{nr} , \qquad (1)$$

where C is the probability of carriers binding in the exciton, A is the probability of exciton thermal dissociation, g is the rate of electron-hole pairs generation. According to [2,3] we neglected in (1) the contribution of exciton effects in the light absorption.

The solution of the equation (1) after the excitation is off ($g=0$) we will find taking into account the experimentally found monoexponentional law of the PL relaxation (fig.1). Therefore we insert the functions $N(t)$ and $n(t)$ in the equations (1) in the following form:

$N=N_0 exp(-t/\tau_{PL})$, $n=n_0 exp(-t/\tau_{PL})$, that results

$$\tau_{PL} = \frac{1 + N_o/n_o}{\tau_{nr}^{-1} + \tau_r^{-1} \cdot N_o/n_o} \qquad (2)$$

The effects observed in our experiments are apparently caused by a weakening of electron-hole bond in the exciton due to the dielectric effect. The diminution of the PL intensity and τ_{PL} was maximal for the ambients with larger value of ε (ethanol and methanol). The decrease of E_{exc} leads to an enhancement of the probability of the exciton thermal dissociation and hence the N_0/n_0 relation lowers at given temperature. It explains the observed PL intensity quenching in the dielectric ambients.

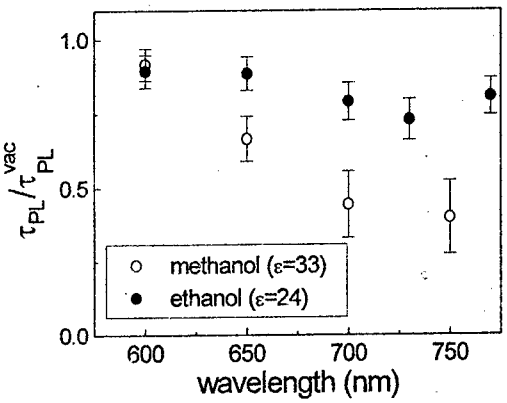

Fig.3. PL lifetime (normalized on one in vacuum) of porous silicon kept in dielectric ambients vs PL wavelength.

The analysis of (2) enables one to understand even less obvious effect of the τ_{PL} diminution. Really after simple transformation it follows from (2) that in case of $\tau_r^{-1}>\tau_{nr}^{-1}$ the PL relaxation time will increase with the decrease of N_0/n_0. If the nonradiative recombination is dominant ($\tau_r^{-1}<\tau_{nr}^{-1}$) at the dielectric dissociation of excitons (diminution of N_0/n_0) the PL relaxation time will decrease. Obviously this case is realized in our experiments with ethanol and especially methanol (fig.3). Note that because the probability of radiative recombination lowers for nanostructures of larger size (lower PL quanta energies) the effect of the τ_{PL} diminution is more significant for them.

References.

[1] R.L. Smith, S.D. Collins, J. Appl. Phys. **71**, R1 (1992).
[2] G.D.Sanders, Y.-C. Chang. Phys.Rev.B, **45**, 9202 (1992).
[3] G.C.John, V.A.Singh. Phys. Rep., **263**, 93 (1995).
[4] V.S.Babichenko, L.V.Keldysh, A.P.Silin. Fiz. Tverd. Tela, **22**, 1238 (1980).

Dynamics and Radiation of a charged particle moving in a carbon nanotube

V. V. KLIMOV* AND V. S. LETOKHOV
Institute of Spectroscopy, Russian Academy of Sciences, Troitsk, Moscow Region, 142092, Russia
**P. N. Lebedev Physical Institute, Russian Academy of Sciences, 53 Leninsky Prospect, Moscow, 117294, Russia*

Considerable advances have been made in recent years in the synthesis of the so-called carbon nanotubes – important objects for use in nanotechnologies [1]. These wonderful objects, a mere nanometer in diameter, may have quite a macroscopic length of up to a few centimeters. Being hollow, nanotubes seem to be natural candidates for transporting both neutral and charged particles in various nanodevices. On the other hand, charged particles propagating in nanotubes interact with their walls and can thus generate a coherent electromagnetic radiation which can be of individual interest. The radiation due to charged particles channeling in crystals has now been well studied [2]. Such a radiation has a whole range of properties making it of practical use. The aim of the present paper is to investigate the electromagnetic effects taking place in the course of propagation of charged particles in single-layer nanotubes. To our view, the most important pecularities of nanotubes to be studied are due to their large radius R (compared with that of channels in ordinary crystals).

Channeling near the cylindrical surface of the nanotube is possible for negatively charged particles. This motion has no analogues in crystall channeling and will be reported elsewhere. In the case of positively charged particles, the situation is more advantageous for their propagation inside the nanotube, because a particle coming close to the surface of the nanotube is acted upon by a repulsive force due to the incomplete screening of the positively charged atomic nuclei. In other words, the motion of positron is like to axial channeling of electrons in crystalls.The main difference is due high azimuthal symmetry of positron-nanotube interaction potential

The main type of interaction is the Coulomb interaction between the particle and the charge of a nucleus, partially screened by the electron shell of the atom [3].

Insofar as the nanotube radius R and the characteristic parameters of the particle trajectory inside the nanotube are large enough in comparison with the interatomic distance, the exact potential can be averaged over the periodic coordinates (z, φ) with the result that the expression for the interaction potential becomes axially symmetric:

$$\overline{U}(\rho)=\frac{Z_1 Z_2 e^2 4N}{3a}\ln\left(\frac{R^2+\rho^2+3a^{*2}+\sqrt{\left(R^2+\rho^2+3a^{*2}\right)^2-(2\rho R)^2}}{\left|R^2-\rho^2\right|+R^2+\rho^2}\right) \quad (1)$$

where a=1.42Å and $a^*=\frac{\hbar^2}{2me^2}\left(\frac{3\pi}{4\left(\sqrt{Z_1}+\sqrt{Z_2}\right)}\right)^{2/3}$ - screening radius [2].

Fig.1 shows the effective potential well for the interaction between a positron ($Z_1 = 1$) and the carbon nanotube ($Z_2 = 12$) as a function of the radial position of the particle.

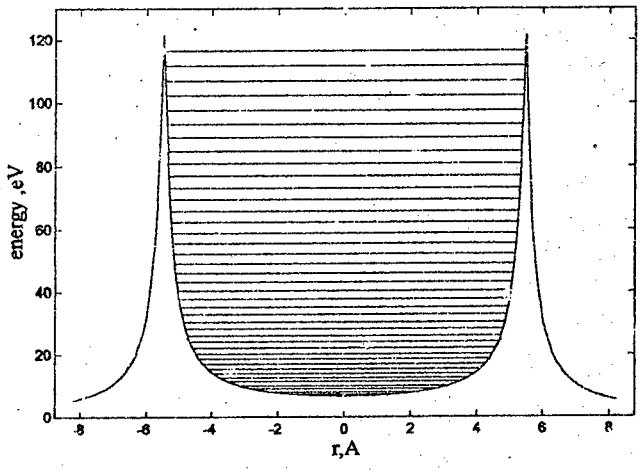

Figure 1. Positron energy well and levels(10 Mev, l = 0).

When using harmonic approximation the equation of motion in the radial direction, can easily be solved:

$$\rho = \rho_0 \cos\left(\Omega(\rho_0 = 0)t\right), \qquad \Omega^2(\rho_0 = 0) = \frac{8NZ_1Z_2e^2}{m\gamma(3a)^5}\frac{3a^{*2}}{\left(R^2 + 3a^{*2}\right)^2}. \qquad (2)$$

where ρ_0 is the radius of the point of entry of the particle into the nanotube and Ω is the radial oscillation frequency

In the case of typical nanotube 11 Å in diameter, we have:

$$\Omega \approx 2.8 \times 10^{15} / \sqrt{\gamma}\ [s^{-1}], \qquad (3)$$

which for positrons with an energy of 1 GeV gives $\Omega/2\pi = 10^{13}$ Hz. For the spatial oscillation period $\Lambda = V_z 2\pi/\Omega$, we have accordingly $\Lambda = 30$ μm i.e., a positron will execute some 33 radial oscillations while traversing a nanotube with length L=1 mm.

The radiation power of the particle has the following form:

$$P = \rho_0^2 \frac{64e^6N^2Z_1^2Z_2^2}{c^3m^2(3a)^{10}}\frac{3a^{*4}}{\left(R^2 + 3a^{*2}\right)^4}\gamma^2, \qquad (4)$$

In the case of typical nanotube with N=14 (11Å diameter), the expression for the loss per unit length will be as follows:

$$I = P/c \approx \rho_0^2 \gamma^2 / (3a)^2 10^{-14} \left[\text{erg/cm}\right]. \quad (5)$$

One can see from expression (5) that the loss per unit length rises in a quadratic fashion as the energy and entry-point radius of the positron are increased.

For positrons with an energy of $E_z = 1$ GeV, $\gamma = 2000$, $\rho_0 \approx 4.3$Å we have $I = 4\times10^{-8}$ erg/cm = 25 keV/cm. In that case, the transverse oscillation energy and velocity (with due regard for the relativistic increase in mass) are $E_\rho \approx 10$ eV and $V_\rho \approx 4.2\times10^6$ cm/s, so that the maximum angle of deviation of the particle from the nanotube axis, with which channeling takes place (the Lindhard angle) is around 10^{-4} rad. Correspondingly, if the incoming beam of positrons has a divergence of the same order of magnitude, the overwhelming proportion of the particles will be captured by the nanotube and will effectively emit radiation.

Radiation at the maximum frequency ω_{Max} is emitted forward, i.e., at $\theta = 0$. :

$$\omega_{Max}(\rho_0 = 0, \theta = 0) = \frac{\Omega}{(1-\beta_z)} \approx \frac{4e}{(3a)^2}\frac{a^*}{\left(R^2 + 3a^{*2}\right)}\sqrt{\frac{2NZ_1Z_2}{ma}}\gamma^{3/2}, \quad (6)$$

In the case of typical nanotube 11 Å in diameter, we get instead of (6):

$$\omega_{Max}(\rho_0 = 0) \approx 5.6\cdot10^{15}\gamma^{3/2} \quad [\text{s}^{-1}]. \quad (7)$$

For positrons with an energy of $E_z = 1$ GeV, the energy of the maximum-frequency quanta can easily be found from (7) to be $\hbar\omega_{Max} \approx 0.33$ MeV, i.e., hard X-quanta are emitted. Note that the maximum frequency of the quanta emitted by positrons (with the same energy) channeling in ordinary crystals is much higher than that given by (7). This is due to the smaller distances between the crystal planes and hence greater electrostatic forces acting upon the positrons and resulting in their higher oscillation frequencies.

The radiation linewidth of single positron is mainly governed by the number of oscillations n the particle executes while passing through the nanotube. For single positron with an energy of $E_z = 1$ GeV propagating in a 1 mm long nanotube ($n = 33$), the linewidth of the quanta emitted forward can easily be found to be $\hbar\Delta\omega \approx 0.01$ MeV.

Up to now we considered the approximation which is valid for single particle moving near nanotube axis. However it is difficult to provide the positron motion near axis. In fact it is some probability distribution of particle entry radius. As a result the particles with different oscillation amplitudes will have different oscillation frequencies and radiation characteristics. To find frequency distribution of total radiation intensity, i.e. inhomogeneous line breadth, one should average the radiation intensity of all particles over distribution of oscillation amplitudes, that is over nanotube cross-section.

The total intensity distribution over frequencies is shown in Fig.2. Inspection of Fig.2 reveals that the positrons with large amplitudes give inhomogeneous line breadth which is essential in comparison with the case of near axis propagation. It is interesting to note that the breadth is mainly due to dependence of oscillation frequency on amplitude. So the relative line breadth is similar for different longitudinal energies and nanotube lengths.

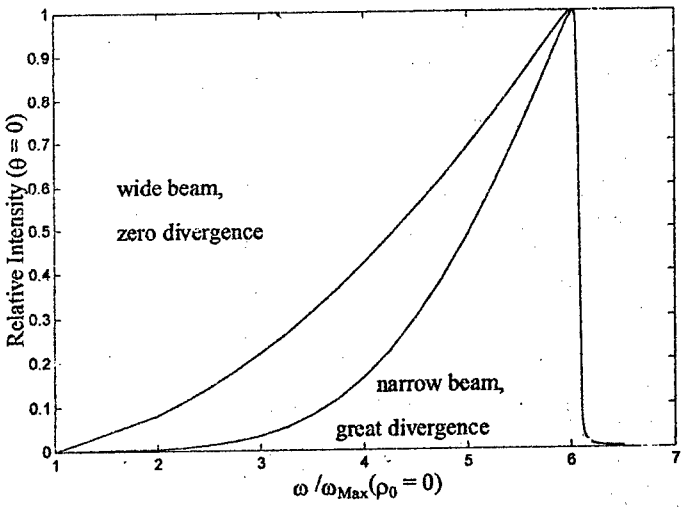

Figure 2. Total radiation intensity as a function of frequency (1 Gev, forward direction).

Thus, considered in this work is the radiation emitted by a positively charged particle propagating inside a carbon nanotube and interacting without delay with the screened charges of the nanotube nuclei. Classical equations are shown to be capable of describing the dynamics of the particle quite well. Analytical expressions are obtained for the total radiation power and the relationship between the radiation frequency and the entry angle of the particle. It is shown that the channeling of a positron beam with a divergence of the order of 10^{-4} is possible at a positron energy around 1 GeV. In that case, in the region of small entry angles there occurs the emission of hard X-quanta with an energy around 0.33-2 MeV.

References

1. R.E. Smalley. *From Balls to Tubes to Ropes: New Materials from Carbon*, Presentation, American Institute of Chemical Engineers, South Texas Section, January Meeting in Houston, 1966; T.W. Ebbesen, Phys.Today, June 1996, 26.
2. M.A. Kumakhov, F.F.Komarov. *Radiation of Charged Particles in Solids*. University Press, Minsk, 1985.
3. J. Lindhard. Mat. Fys. Medd. Dan. Vid. Selsk., **34**, No.14 (1965).

HOLE SPECTRUM IN CdTe QUANTUM DOTS

A.A.Lipovskii, E.V.Kolobkova and V.D.Petrikov[1]
St.-Petersburg State Technical University, [1]A.F.Ioffe Physico-Technical Institute
Polytechnicheskaja 29, St.-Petersburg, 195251 Russia

Introduction

First experimental studies of semiconductor quantum dots (SQD) have been performed with ensembles of **CdS-CdSe** with wide size distribution. The results were successfully described within the frames of effective mass approximation for parabolic shape of valence and conductivity bands. Later new materials containing SQD ensembles with essentially narrower size dispersion were formed. Wide application of photoluminescence excitation spectroscopy (PLE) instead of optical absorption spectroscopy and conventional luminescence spectroscopy for studies of the new SQD doped materials allowed to get new experimental results on quantum confinement of charge carriers in semiconductor quantum dots. These results influenced development of theory of quantum confinement, and influence of holes' behavior in SQD with complicated valence band on system of optical transitions in **II-VI** SQD have been analyzed. Recent studies have shown that spin-orbit subband of valence band in quantum dots of **II-VI** semiconductors influences positions of quantum confined levels both for small values of spin-orbit splitting (Δ_{SO}=0.07 eV, **CdS**) [1] and for large splittings (Δ_{SO}=0.42 eV, **CdSe**) [2,3]. It was supposed in papers [4,5] that this influence is also essential in case of **CdTe** (Δ_{SO}=0.93 eV) QD. This research is aimed to study the problem.

Experimental

Conventional optical absorption spectroscopy was applied to study **CdTe** QD formed in a novel P_2O5-Na_2O-ZnO-AlF_3-Ga_2O_3 glass matrix. The phosphate glass matrix was used as it earlier allowed us to form SQD with narrow size distribution [6]. Growth of **CdTe** QD occurred in the matrix doped with **CdTe** under heat treatment at 340-420°C during several minutes. Optical absorption spectra for several samples are presented in Fig. 1. Influence of quantum confinement - blue shift of optical absorption edge and formation of separate transitions is evident. Further annealing and growth of SQD lead to formation of bulk **CdTe** absorption edge E_g=1.50 eV (T=300K). Positions of optical transitions were determined as positions of minima of second derivatives in energy-absorption plot. Data published by Esch et al. [7] for narrowly distributed **CdTe** QD for one size of QD and by Oliveira et al. [8] for widely distributed SQD (luminescence excitation spectroscopy was used) for QD in range 3.5-5 nm are also used in this work. Results of all experiments were recalculated for room temperature.

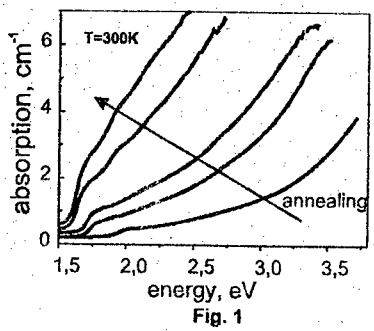

Fig. 1

Theory

Quantum size effect on conduction band can be described within the frames of single band (1B) theory and effective mass approximation [9]. We used theory described by Ekimov et al. in 1993

[2] for conduction band. The theory accounts influencing of conduction band by valence band and its nonparabolicity. More complicated description of valence band comparatively to 1B model accounts mixing of levels from 2 subbands - subbands of light and heavy holes - so called 2B model [10]. However this model failed to describe known experimental results since complicated structure of optical absorption and luminescence excitation spectra can not be described without accounting of mixing of confined levels of light and heavy holes in valence band and interaction of the levels with levels in splitted spin-orbit band. That is why a new 3 band (3B) model was developed, and a general description of the mixing for **II-VI** SQD was presented by Grigorjan et al. [1] and Ekimov et al. [2]. Most complete comparison of 3B model with experiment was performed by Norris et al. [3] for **CdSe** QD. Also 2B model [10] was extended to 3B situation by Richard et al. [4]. They modeled QD of several **II-VI** and **III-VII** semiconductors. Comparison of theory and experiments [2,3] proves that for large value of spin-orbit splitting (Δ_{SO}=0.42 eV for **CdSe**) influence of splitted spin-orbit band must not be neglected. The same was supposed by Richard et al [4] and Lefebvre et al. [5] relatively to **CdTe** since Δ_{SO}=0.93 eV is extremely high for this semiconductor. Our calculations made to try this approach for valence levels of **CdTe** SQD show that model of Richard et al. [4] gives the same results as general solution [2]. We used 3B model [2] to calculate complete set of hole levels and optical transitions in **CdTe.**

Discussion

Observed and/or calculated optical absorption bands were treated differently by different research groups, and in Table 1 we listed these interpretations for the first 5 optical absorption bands. We tried to change different notations used in papers [4,7,8] to notations after Ekimov et al. [2] when it was possible: n**QF**, **F** -total momentum of the state, **Q=S,P,D,F,...** is the minimal orbital momentum included in the hole wave function, n -principal quantum number of the state.

Table 1

absorption band	Esch, 1990 [7] r=3.6nm	Oliveira, 1995 [8] r=3.5-5nm	Richard, 1996 [4] r=2.8 nm (theory)	This work, 1997 r=3 nm
a	S_A-S_e	$1S_{3/2}$-$1S_e$	$1S_{3/2}$-$1S_e$	$1S_{3/2}$-$1S_e$
b	S_B-S_e	$2S_{3/2}$-$1S_e$	$2S_{3/2}$-$1S_e$	$2S_{3/2}$-$1S_e$
c	P_A-P_e	$1P_{3/2}$-$1P_e$	$1P_{3/2}$-$1P_e$	$1P_{3/2}$-$1P_e$
d	D_A-D_e	$2P_{3/2}$-$1P_e$	$1P_{5/2}$-$1P_e$	$1S_{1/2}$-$1S_e$
f	F_A-F_e	$1SO_{1/2}$-$1S_e$	$1P_{1/2}$-$1P_e$	$2,3S_{3/2}$-$1S_e$

When explaining experimental results presented in [7] mixing of hole levels of subbands of heavy holes (A), light hole (B) and spin-orbit subband (C) was ignored, and levels in the subbands were treated as independent ones - 1B model. However positions of optical transitions were not calculated. Later Oliveira et al. [8] used 2B model to describe data obtained for QD of different dimensions laying in range r=3.5-5nm. Notation of transitions in the research differs with conventional ones we are not sure in our identification of them. 2B approach and fitting of model parameters for valence band led to good coincidence of the computations and experiments described in [8], while 1B model was unable to describe the experimental situation. Unfortunately wide size distribution of QD used in experiments [8] and range of the SQD dimensions (3.5-5 nm) did not allowed to observe some low-intensive optical transitions in the research. Calculations performed by Richard et al. in 1996 [4] were not compared with experimental data, however they alleged

that descriptions of optical absorption spectra with 2B and 3B models were practically the same because all experimental spectra are broaden due to size distribution of QD. It was not correct as narrowly distributed ensembles of **CdS**, **CdSe** and **CdTe** QD was formed by 1996. Moreover observations of anticrossing of levels in **CdSe** QD [3] proved necessity of 3B model. Also statement [4] that PLE technique was hardly applicable for **CdSe** and **CdTe** QD was in contradiction with published results [3,8]. Experimental positions of optical absorption bands measured in our experiments were not coincide with 1B and 2B models, and we turn to 3B modeling [2] - see column 5 in Table 1.

To model **CdTe** QD it was necessary to chose a set of parameters for the material. Values of the parameters used by different researchers are listed in Table 2.

Table 2

		Δ_{SO}, eV	ε	γ_1	γ_2	m_e	E_p, eV
1	Oliveira, 1995 [8]	1.0		6.5	2.0		17.4
2	Pankov, 1971 [11]		10.9			0.11	
3	Richard, 1996 [4]	0.927	9.3	5.23	1.89	0.096	
4	Lefebvre, 1996 [5]	0.927	9.3	5.23	2.19	0.096	
5	-""-	0.927	9.3	4.11	1.58	0.096	
6	-""-	0.927	9.3	4.7	1.69	0.096	

Here ε - dielectric permittivity, γ_1 and γ_2 - Luttinger parameters, m_e effective electron mass, E_p - energetic band parameter [2]

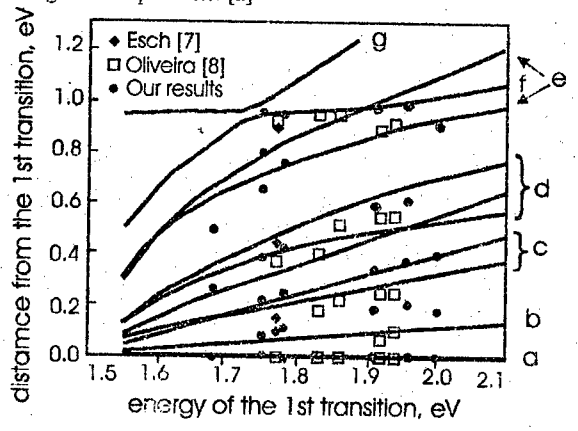

Fig.2

We compared our and other known [7,8] experimental data with calculations made for all sets of parameters from Table 2. It was found that variation of Luttinger parameters strongly influences behavior of optical transitions. The best coincidence with experimental data was obtained for sets presented in rows 3 and 6, however the set in row 3 is not refer to exact data on **CdTe** structure [5]. Rows 4 and 5 give essential difference of calculations and experimental data. We used for our calculations set of parameters from row 6 of the Table 2, results of the calculations are presented in Fig. 2 as well as experimental data. It is important that γ_1/γ_2 relation for **CdTe** essentially exceeds γ_1/γ_2 relation for **CdSe**, and this increases influence of splitted band on lower transitions in spite of higher Δ_{SO} for this material [3,5].

For chosen set of parameters the highest hole level is $1P_{3/2}$, however transition to this level from $1S_e$ state is forbidden. That is why lowest observable in optical absorption experiments transition **(a)** can be $1S_{3/2}$-$1S_e$ the same way as for other **II-VI** SQD [1,2]. Closely positioned next transition **(b)** - $2S_{3/2}$-$1S_e$ - is less intensive and it is similar with the same transition in **CdSe** [2]. The next absorption band **(c)** is due to intensive $1P_{3/2}$-$1P_e$ transition and to the next $3S_{3/2}$-$1S_e$ transition that is weaker. The next intensive wide absorption band **(d)** is due to transitions both to $1S_e$ level ($1S_{1/2}$-$1S_e$) and to $1P_e$ level ($2P_{3/2}$-$1P_e$ and $1P_{1/2}$-$1P_e$) superposed in 0.1 eV width range. **(a)**, **(b)**, **(c)** and **(d)** groups of optical transitions are laying far from split-off band even for small QD. Behavior of the transitions is quasilinear, and it can be accurately described within approximation of 2B theory [8]. However behavior of the next optical absorption band **(e)** is not linear - see Fig. 2, The absorption band is due to $2S_{1/2}$-$1S_e$ and $2P_{1/2}$-$1P_e$ transitions. For small QD these levels lie in the region of split-off band, and calculation shows that $2S_{1/2}$-$1S_e$, $3S_{1/2}$-$1S_e$ transitions are pushing away in this region Neither previous experimental studies nor 2B model describe this e absorption band. The last observable absorption band **(f)** is due to $3S_{1/2}$-$1S_e$ transition. It is necessary to note that anticrossing of the whole system of $nS_{1/2}$-$1S_e$ levels - see **(e)** and **(f)** and **(g)** bands - results with positioning of a level belonging to the system close to Δ_{SO} value for all sizes of QD. When observed this can be treated as a transition from spin-orbit subband with low quantum confinement effect. That is why transitions from different closely positioned levels are treated as transition from spin-orbit subband by 2B theory.

Conclusion

Studies of optical spectra of synthesed **CdTe** QD with narrow size distribution allow us to observe up to 6-7 quantum transitions at room temperature. To describe experimental results we had to use 3B model since in spite of relatively large value of Δ_{SO}~1 eV for **CdTe,** mixing of levels from upper subbands with spin-orbit subband strongly influenced behavior of the hole levels. Comparison of our experimental data and literary data [8] with 3B theoretical model shows that choice of the model parameters strongly influences treating of optical transitions in the SQD.

Finally complicated structure of optical transitions in **CdTe** QD was described and interpreted, and necessity to account mixing of QD levels from 3 valence subband for large spin-orbit splitting was confirmed with the experiments. We suppose observation of anticrossing of optical transitions in **CdTe** QD is possible. Further experimental studies will allow to find more exact values of parameters to be used in 3B modeling of **CdTe** QD structures.

References

1. G.B.Grigoryan, E.M.Kazaryan, Al.L.Efros, T.V.Yazeva. Sov. Phys. Solid State, **32**, 1031 (1990).
2. A.I.Ekimov, F.Hache, M.C.Schanne-Klein, et al. J. Opt. Soc. Amer. B, **10**, 100 (1993).
3. D.J.Norris, M.G.Bawendi. Phys. Rev. B, **53**, 16338 (1996).
4. T.Richard, P.Lefebvre, H.Mathiue, J.Allegre. Phys. Rev. B, **53**, 7287 (1996).
5. P.Lefebvre, T.Richard, H.Mathiue, J.Allegre. Solid State Commun., **98**, 303 (1996).
6. A.A.Lipovskii, E.V.Kolobkova, V.D.Petrikov. Proc. SPIE, **2967**, 30 (1996).
7. V.Esch, B.Fluegel, G.Khitrova, et.al. Phys. Rev. B, **42**, **12**, 4750 (1990).
8. C.R.M. de Oliveira, A.M. de Paula, et al. Appl. Phys. Lett., **66**, 439 (1995).
9. Al.A.Efros, A.L.Efros. Sov.Phys.-Semicond., **16**, 772, (1982).
10. P.C.Sercel, K.J.Vahala. Phys. Rev. B, **42**, 3690 (1990).
11. J.I.Pankove. Optical Processes in Semiconductors, Prentice-Hall, N. J., 1971.

OPTICAL TRANSITIONS IN PbSe QUANTUM DOTS

A.A.Lipovskii, E.V.Kolobkova and V.D.Petrikov[1]
St.-Petersburg State Technical University, [1]A.F.Ioffe Physico-Technical Institute
Polytechnicheskaja 29, St.-Petersburg, 195251 Russia

Most of optical research of quantum confinement phenomena were performed with II-VI semiconductor quantum dots (SQD). However synthesis of IV-VI SQD has recently been demonstrated [1,2]. Widths of forbidden gap for the semiconductors correspond to infra-red range of optical transitions between confined states of charge carriers. Contrary to theory of quantum confinement for direct band semiconductors [3], theoretical description of the phenomenon accounting anisotropy and non-parabolicity of the band has been designed just recently [4]. This research is aimed to compare positions of optical transitions in synthesed **PbSe** QD [2] with results of our computations performed in accordance with model [4].

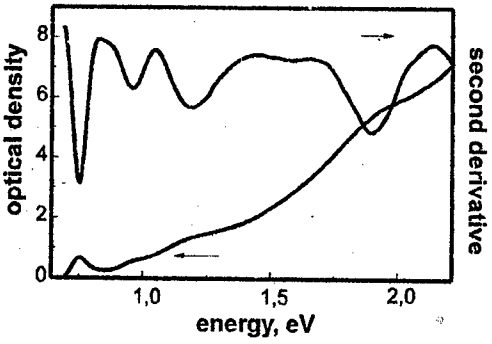

Fig. 2

We used optical absorption spectroscopy to study **PbSe** QD formed in a P_2O_5-Na_2O-ZnO-AlF_3-Ga_2O_3 glass matrix. The phosphate glass matrix was used as it earlier allowed us to form **CdS**, **Cd-S-Se**, **CdSe** and **CdTe** SQD with narrow size distribution [5]. Growth of crystalline grains occurred under heat treatment (360-410°C) of the glass samples doped with **PbSe**. Duration of the annealing was in range of several minutes. X-ray studies allowed us to identify grains formed in the glass matrix as **PbSe** QD. TEM measurements (courtesy of Dr. Frank Wise from Cornell University) showed that the SQD have perfect spherical shape at least for SQD exceeded 10 nm. Optical absorption spectra of differently annealed glass samples with **PbSe** SQD were measured in spectral range 400-1800 nm. Sets of optical absorption peaks corresponded to different quantum transitions were clearly observed in the spectra measured at room temperature, and positions of the peaks were deduced with 2nd derivative technique -- see Fig. 1, where a typical measured absorption spectrum for **PbSe** QD and second derivative of the spectra are presented

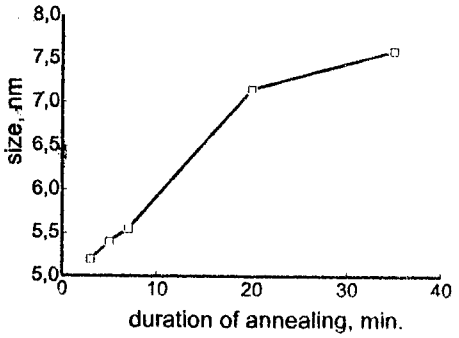

Fig. 2

Size of the SQD and position of the first optical absorption peak depend on duration of thermal processing aimed to grow QD. In Fig. 2 dependence of size of the PbSe QD (recovered from the position of the first absorption peak according to existing model [4]) versus time of annealing is presented. To describe process of growth of QD it is necessary to check if SQD size **D** dependence of time **t** can be described as $D \sim t^{1/2}$ (independent growth of nuclei) or $D \sim t^{1/3}$ (coalescence stage of growth) law [6]. Analysis of the experimental data presented in Fig. 2 showed that most probably we have situation that is intermediate between these two cases.

To compare positions of optical transitions with theoretical predictions we plotted energy distances between several lowest (permitted - solid, forbidden - dashed) optical transitions and the first optical transition versus position of the first transition - Fig. 3. The theoretical curves are linear in spite of the fact that effective mass approximation is not applicable to the system under consideration. In the same plot we marked points corresponding to measured positions of optical transitions for PbSe QD of different size. We can conclude that a set of experimental transitions corresponds to predicted positions, and that there is one more set laying very close to position of the first forbidden transition. Possibly to explain this it is necessary to check if Coulomb interaction permits the transition and to calculate matrix elements describing efficiencies of optical transitions. This is a subject of our future research.

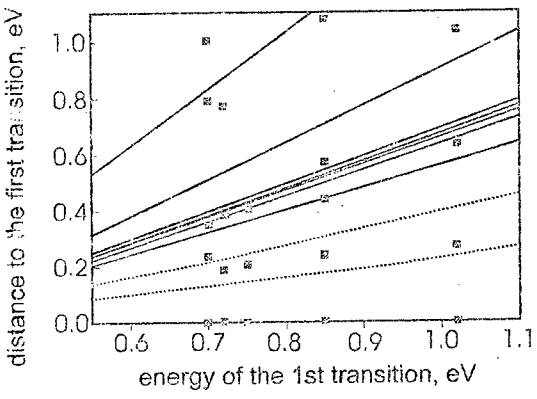

Fig. 3

Finally, studies of optical absorption spectra of synthesed PbSe QD with narrow size distribution allow us to observe several quantum transitions at room temperature. Comparison of our experimental data and positions of optical transitions calculated with existing model for IV-VI SQD [4] shows that the model adequately describes the SQD, and forbidden optical transitions have to be accounted.

References

1 N.F.Borelli, D.W.Smith, J. Non-Cryst. Solids, **180**, 25 (1994).
2 A.A.Lipovskii, E.V.Kolobkova, V.D.Petrikov, Electronics Letters, **33**, 101 (1997).
3 Al.A.Efros, A.L.Efros, Sov. Phys.-Semicond., **16**, 772, (1982)
4 I.Kang, F.W.Wise, J. Opt. Soc. Amer. B, to be published
5 A.A.Lipovskii, E.V.Kolobkova, V.D.Petrikov, Proc. SPIE, **2967**, 30 (1996).
6 S.A.Gurevich, A.I.Ekimov, I.A.Kudriavtsev, et al, Semiconductors **28**, 486 (1994)

SIZE QUANTIZATION OF EXCITON IN QUASI - ZERO - DIMENSIONAL SEMICONDUCTOR STRUCTURES

S.I.Pokutnyi, I.P.Guk, G.V.Semenova

State Maritime University, Nikolaev, 327025, Ukraine

1. Consider a simple model: a neutral semiconductor microcrystals (SMs) of the radius a with the dielectric function ε_2 surrounded by a medium with ε_1. In the bulk of such SM an electron e and a hole h with the effective masses m_e and m_h, respectively, are moving (r_e and r_h are the distances of the electron and the hole from the SM center); the dielectric functions of the SM and the matrix differ appreciably ($\varepsilon_2 \gg \varepsilon_1$). It is assumed that the bands of electrons and holes are of parabolic shape. The characteristic dimensions of the problem are the quantities: a, a_e, a_h where $a_e = \varepsilon_2 \hbar^2 / m_e e^2$, $a_h = \varepsilon_2 \hbar^2 / m_h e^2$, are the Bohr radii of the electron and the hole, respectively, in a semiconductor with ε_2 (e is the electron charge).

In the model under study within the scope of the above approximations, the Hamiltonian of the exciton is [1,2]

$$H = -\frac{\hbar^2}{2}\frac{\Delta_e}{m_e} - \frac{\hbar^2}{2}\frac{\Delta_h}{m_h} + E_g + V_{hh'}(r_h, a) + V_{eh}(r_e, r_h) + V_{ee'}(r_e, a) + V_{eh'}(r_e, r_h, a) + V_{he'}(r_e, r_h, a) \quad (1)$$

where the first two terms determine the kinetic energy of an electron and a hole, V_{eh} is the Coulomb interaction of an elctron with a hole; $V_{ee'}$ and $V_{hh'}$ is the interaction with the selfimage of an electron and a hole, respectively, $V_{eh'}$ and $V_{he'}$ are interactions with "allen" images [2,3].

2. We investigate the energy spectrum of an exciton in a small SM in the case when the size of the SM is restricted by the condition

$$a_0 < a_h \ll a \leq a_e , \quad (2)$$

at whose fulfilment polarization interaction plays an important role in the potential energy of the Hamiltonian (1). The inequality (2) also permits consideration of the electron and hole motion in the effec-

tive mass approximation. Under conditions (2) adiabatic approximation ($m_e \ll m_h$) can be used: in this case the kinetic energy of an electron is assumed to be the greatest quantity and the last four terms in (2) are considered together with the nonadiabaticity operator by the perturbation theory on the functions of the deep infinite spherical well. Then, taking into account only the first order of the perturbation theory one can easily obtain the spectrum of an exciton $E^{n_h, l_h, m_h}_{n_e, l_e, m_e}$ in the state (n_e, l_e, m_e; n_h, l_h, m_h) (here n_e, l_e, m_e are the main, orbital and magnetic quantum numbers of an electron; n_h, l_h, m_h are the main, orbital and magnetic quantum numbers of the hole) as follows [4,5]:

$$E^{t_h}_{n_e,0,0}(S) = E_g + \frac{\pi^2 n_e^2}{S^2}\cdot\frac{m_h}{m_e} + S^{-1}\left[Z_{n_e,0} + P_{n_e,0}\,\frac{\varepsilon_2}{\varepsilon_1}\right] + w\left[t_h + \frac{3}{2}\right], \quad (3)$$

where $Z_{n_e,0} = 2\int_0^1 dx_e \sin^2(\pi n_e x_e)(1-x_e^2)^{-1}$, and $P_{n_e,0} = 2Ci(2\pi n_e) - 2\ln(2\pi n_e) - 2\gamma + (\varepsilon_2/\varepsilon_1) - 1$, $\gamma = 0.577$ is the Eiler constant, $Ci(y)$ is the integral cosine, and $w(n_e, S)$ is the frequency of the hole oscillator vibrations

$$w(n_e, S) = 2(1 + (2/3)\pi^2 n_e^2)^{1/2} S^{-3/2}, \quad (4)$$

Here and below the energy is measured in $Ry_h = \hbar^2/2m_h a_h^2$ units and nondimensional values of the length $x_e = r_e/a$ and $S = a/a_h$ are used.

3. In the experimental works [6,7] interband absorption spectra of CdS SMs ($\varepsilon_2 = 9.3$) of the size from 1 to 10 nm dispersed in a transparent dielectric matric of silicate glass were investigated ($m_e = 0.2m_0$ and $m_h = 5m_0$; i.e. $m_e \ll m_h$). In [7] in the region of transitions to the lower level of dimensional quantization of the electron ($n_e = 1$) a structure was found which consisted of an equidistant series of levels. The above structure is caused by quantization of the hole energy spectrum in the adiabatic potential of the electron. In [7] by incorporating into the formula (4) SM dispersion by the radii a, an expression was obtained which determined the distance between the equidistant series in the spectrum of the hole [2,8]:

$$\bar{w}(n_e, \bar{S}) = 2.232(1 + (2/3)\pi^2 n_e^2)^{1/2} \bar{S}^{-3/2}. \quad (5)$$

where $\bar{a}$ is the average SM radius ($\bar{S} = \bar{a} / a_h$). From comparison of the formula (5) (at $n_e = 1$) with the experimental dependence of the splitting magnitude on the SM size $\bar{a}$ obtained in [7] it follows that for the region of SM radii $\bar{a} \leq 30$ Å the splitting magnitude $\bar{w}(\bar{S})$ (5) is in good agreement with the experimental data [7] and differs from the latter only slightly (≤ 4 %) [2,8].

In [9] brightness peaks were observed which are due to transitions between the size quantization levels of an exciton in the transmission spectrum of CdSe SMs (ε_2=9.4) of size a = 5 nm dispersed in a transparent dielectric matrix of silicate glass.

At decreasing radius a of a CdSe SM down to the size comparable with the exciton radius $a \sim a_{ex}$= 45.5 Å the positions of the valence band and of the conduction band as well as the dispersion laws for electrons and holes in such SM should, apparantly, change drastically. It is natural to suppose that the effective mass of an exciton $\mu = m_e m_h / (m_e + m_h)$ will also differ from such effective mass of an exciton in an unlimited CdSe SM. As a hole in CdSe is heavy (m_h / m_0=2.5 and m_e / m_0 = =0.13, i.e. $m_h \gg m_e$) we assume that its mass m_h remains unchanged, i. e. it is the same as in unlimited CdSe. Only the effective mass of an electron m (and with it also the effective mass of an exciton μ) will change and it will depend on both the SM size a and the position of the energy level of the exciton ($n_e, l_e; t_h$), i.e. $m_e = m_e(a; n_e, l_e; t_h)$ (or $\mu = \mu(a; n_e, l_e; t_h)$).

Comparing the numerical values of the exciton energy (3) in the state (n_e=1, l_e=0; t_h=0) and (n_e=2, l_e=0; t_h=0) with the experimental positions of absorptions peaks [9] $E^0_{1,\bar{0}}$ 1.913 eV and $E^0_{2,0}$=2.2047 eV we obtain for the electron (exciton) effective mass: $m_e(a$=50 Å; 1, 0; 0)= =0.195m_0 (μ=0.181m_0) and $m_e(a$=50Å; 2, 0; 0)=0.152m_0 (μ=0.144 m_0)

As the exciton level is being pushed out of the potential well, whose role for charge carriers is played by a SM, the numericalvalue of the exciton effective mass μ will approach that of the exciton

effective mass in an infinite CdSe, i.e. μ_0=0.124m_0. The latter statement is confirmed by the numerical values of exciton effective masses obtained here: $\mu(1,0;0)$=0.181m_0 and $\mu(2,0;0)$=0.144m_0. Moreover, for the fixed energy level of an exciton $E^{t_h}_{n_e,l_e,m_e}(a)$ at increasing SM radius a, so that $a \gg a_{ex}$, the value of the exciton effective mass $\mu = \mu(a, n_e, l_e, m_e; t_h)$ will also tend to the bulk value of the exciton effective mass μ_0.

We investigated the exciton energy spectrum (3) in the ground state (n_e=1, l_e=0; t_h=0) in a small SM in the region of SM sizes $a \gg a_{ex}$=2.5nm under the experimental condition of Ref.[6]. We found the numerical values of the exciton energy $E^0_{1,0,0}(S)$ in the ground state (n_e=1, l_e=0; t_h=0) in a small SM of sizes $a \geq a_{ex}$. Furthermore, comparing the obtained spectrum of exciton (3) and Refs.[10- 12] with experimental positions of the absorption peaks in a small SM [6,7] we determined the effective masses of the electron $m_e(a)$ and exciton $\mu(a)$ in a small SM as functions of SM sizes a. From the rezults follows that with growing SM radius $a \geq a_{ex}$ the effective mass of the exciton $\mu(a)$ (the electron $m_e(a)$) decreases and at a equal to the critical SM size a_c= 4.3 nm approaches the value of the exciton effective mass μ_0 (electron m^0_e) in an unlimited CdS crystal.

References

1. N.A.Efremov, S.I.Pobutnyi, Sov.Phys.- Sol.Stat.32,1637,(1990).
2. S.I.Pobutnyi , Sov.Phys.- Sol.Stat.27,48,(1985).
3. S.I.Pobutnyi , Sov.Phys.- Semicond. 25, 628, (1991).
4. S.I.Pobutnyi , Sov.Phys.- Sol.Stat. 34,2386, (1992).
5. S.I.Pobutnyi , Phys.Stat.Sol. (b). 173, 607, (1992).
6. A.Ekimov, A.Onushchenko, Sov. Phys.- JETP Lett.40, 337, (1984).
7. A.Ekimov,A.Onushchenko,Al.Efros,Sov.Phys.-JETP Lett.43,292,(1986).
8. S.I.Pobutnyi, Phys.Lett.A. 168,433, (1992).
9. Yu.Vandishev,V.Dneprovskii,Sov.Phys.- JETP Lett. 53, 301, (1991).
10. S.I.Pobutnyi, Phys.Lett.A. 203,388, (1995).
11. S.I.Pobutnyi, Sol.Stat.Phys. 38,512, (1996).
12. S.I.Pobutnyi, Sol.Stat.Phys. 38,2667, (1996).

Photoluminescence in Opal-Based Photonic Crystals Doped with Semiconductor

S.G. Romanov#*, A.V. Fokin#, V.I.Alperovich#, V.Y.Butko#, R.M. De La Rue*

#A.F. Ioffe Physical Technical Institute, St.Petersburg, 194021, Russia
*Department of Electronics and Electrical Engineering, University of Glasgow, Glasgow G12 8QQ, UK

The effect of the photonic band gap (PBG) in photonic crystals introduces a novel physics in a description of interaction between the solid structure and light within this structure. Total control upon the propagated light is possible only in a 3-dimensional (3D) photonic crystal where all modes are similarly coupled with a solid structure. In this case engineering of the spectrum of light is approached via changing PBG. A prototype of 3D photonic crystal with the option in a visible light is a precious opal [1]. Opal consists of identical silica balls with diameters D, which are closely packed and formed *fcc* lattice. Since empty voids are situated in between touched balls, the dielectric properties are changed periodically along any optical path through such a lattice [2]. To be comparable with the wavelengths of a visible light D should be in the range 200÷400nm. The light scattered from an opal is peaked at the wavelength, that is roughly corresponded to the Bragg condition for scattering on the most closely packed (111) crystal planes [3]. In bare opal the contrast of the refractive indices (RIC) is provided by difference between SiO_2 (n_1=1.45) and air (n_2=1). The scattering efficiency increases with the RIC increase. However, for structures with RIC= n_1/n_2-1=0.45÷1.3 only a few experiments are available [4,5,6]. Note, that for complete PBG crystals RIC should be above 2. Infilling of opal with semiconductors seems a promising way to approach 3D PBG crystals. Evidences concerning the impact of the photonic structure on the photoluminescence (PL) in the opal-like structures were reported up to date for dye-added colloidal crystals [7] and opals infilled with dye solutions [8], i.e. materials with low refractive indices contrast RIC<0.1. Another effect in semiconductor-doped opals is changing the conditions for radiative recombination in semiconductor. When electronic and photonic gaps coincide in opal-based material one may expect a strong non-linearity in emission properties.

For 3D crystals the dispersion of stop band is easy to reveal by changing the angle of the light incidence. With RIC>0.1 the stop band becomes detectable at any angle and no unaffected light can pass through a photonic crystal. The reflectance measurement were made on 0.5mm thick opal platelets by changing the angle of light incidence with corresponding moving of detector in order to maintain equality of angles for incoming and outgoing light. The shined area was around 1 mm^2. The angle resolution of around 2° was approached by using diversion of the scattered beam along 25cm path before collecting. PL spectra of bare opal were collected at different angles of light collection, assuming that for UV excitation (λ_{ex}=351nm) no dependence occurs upon the angle of beam incidence. Angle resolution was around 4°. For opal-semiconductor nanocomposites PL spectra were collected at ~45° geometry under excitation by 457.9nm line.

In Fig.1 we compared the reflectance spectra of bare opal (RIC=0.45) collected at different angles of the light incidence and PL measured at the same angles. The observed PL is a result of radiative recombination of carriers excited to the band of defect states (typically oxygen defects) of silica comprising opal balls [5]. Opal shows 3 PL bands in the range from 1.8 to 3.3 eV

(Fig.1a), one of them is changed with the angle of observation and another two - are not. All these bands correspond to the extrema in the density of states of silica defects, this is clearly appeared on the spectrum of disordered opal where Bragg scattering is absent. Angle dependence of the PL is caused by changing the interference conditions for emitted light. This is proved by comparison with the angle dependence of the Bragg peak in reflectance spectra of the same sample (Fig.1b). By dividing the PL spectra of ordered opal on that of disordered opal we are able to resolve the Bragg feature clearly. In Fig.1c one can see how the interference-induced dip crosses 2.3÷2.7eV PL band of silica defects.

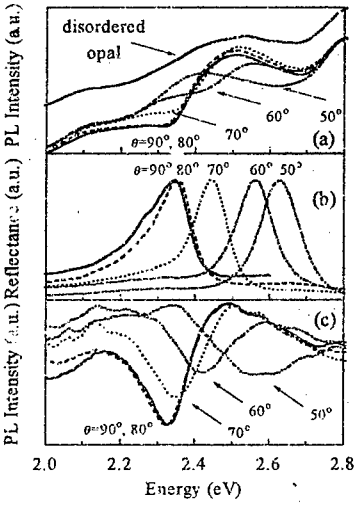

Fig.1 (a) - PL spectra at excitation by UV line (λ_{ex}=457.9nm) of Ar^+ laser and at different angles θ of detection. T=300K.
(b) - reflectance spectra for this opal at the same angles of the light incidence .
(c) - PL spectra after correction on the PL spectrum of disordered opal

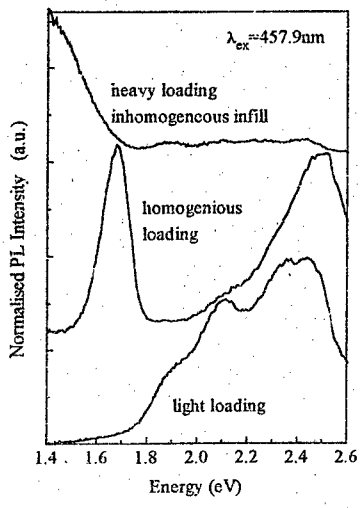

Fig.2 PL spectra of opal-CdSe at T=5K and excitation by the blue line (λ_{ex}=457.9nm) of Ar^+ laser depending on the type of void infill. Curves are shifted for clarity.

There are two observations to be emphasised: (i) redistribution of the relative PL intensity in favour of the low energy side of the dip when it moves to higher energy and (ii) red shift of dips in PL spectra comparing with corresponding reflectance peaks. The first effect is the consequence of the reduced density of photon states within photonic gap. Because of this reduction the radiative recombination is suppressed within the photonic gap. Correspondingly, the additional non-equilibrium excitations, which potentially ready for radiative transition, are build-up at energy just below the photonic gap. However, PL intensity does not directly corresponds to the density of states, it is also depends on the interplay of probability of radiative and non-

radiative processes. Within the energy range of photonic stop band the relaxation proceeds non-radiatively. Therefore, the red shift of the PL dip may be considered as the indication of postponed restoration of the radiative relaxation below the stop band.

In the case of opal-semiconductor composite one can expect a clear demonstration of coupling between the photonic and electronic energy structures. This composite is reasonably to consider as emitting and non-dissipative band-pass filtering systems integrated in one material. Any chemical routine of the semiconductor growth, that uses «ship-in-the-bottle» strategy, results in the fractional filling of the opal voids. Correspondingly, homogeneity of the infill distribution becomes the decisive point, since a volume fraction of the semiconductor in opal voids affects strongly the position and width of the stop band. Moreover, if one is looking for alignment of the stop band and electronic gap, homogeneity will define whether or not matching occurs at the same conditions throughout. Fig.2 shows how PL of opal-CdSe depends on the homogeneity and volume fraction of the CdSe component. In the case of inhomogeneous loading PL appears in form of non-structured band at energies below the electronic gap of CdSe (upper curve). For very small content of CdSe (~1% of volume fraction) in voids of opal the relaxation traffic via defect states of silica dominates (bottom curve), because of the infill-to-matrix interaction. The detailed analysis of this mechanism was given elsewhere [9]. With increased loading and homogeneously distributed infill (confirmed by electron probe microanalysis) the PL peak related to CdSe appears well separated from PL band of silica defects (middle curve).

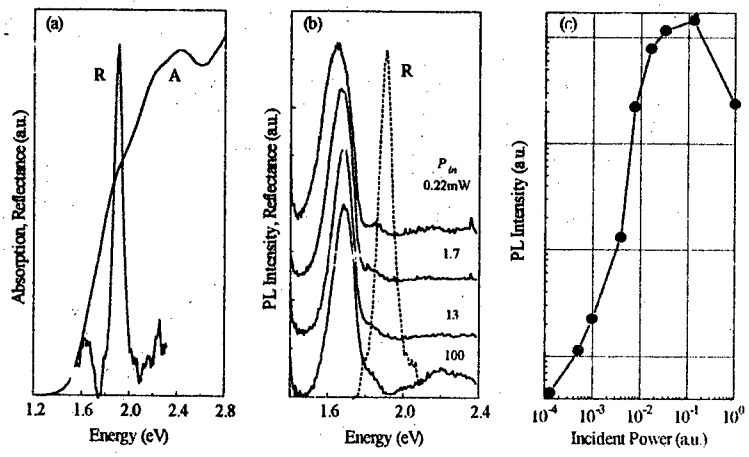

Fig.3 (a) - absorption (A) and reflection (R) spectra of opal-CdSe, the Bragg peak dominates all other contributions to the R-spectrum.
(b) - PL at T=5K and different levels of laser excitations. R-spectrum is shown by dashed line for reference.
(c) - Dependence of the PL intensity upon pumping.

In Fig.3a the electronic and photonic structures of opal-CdSe are shown in the form of absorption and reflectance spectra. Absorption edge is spread over wide energy range because of the amorphised structure of CdSe nanoparticles in opal voids, but homogeneity of CdSe infill distribution over opal voids is well enough to produce the Bragg reflectance peak, characteristics of which depends on the diameter of opal balls, volume fraction of CdSe and refractive indices contrast between silica, CdSe and air.

From Fig.3b it is seen, that PL of CdSe component is pushed out from the stop band region. Blue shift of the PL band indicates that it originates from transitions between the localised band and the valence band. Intensity of this peak increases more rapidly, than excitation power (Fig.3c). With increasing the intensity of the laser pumping this PL line becomes ~1.4 times narrower at the optimal excitation. It seems reasonably to ascribe this superlinear dependence to the formation of the non-equilibrium distribution of the density of states induced by the presence of the photonic gap. Further saturation and decrease of the PL intensity may be explained by overheating of the sample under the laser beam above the He gas flow temperature with corresponding increase of non-radiative transitions.

Concluding, we wish to stress that experiments reported here were aimed to demonstrate the impact of coupling between electronic and photonic structures on the formation of the emission properties of semiconductor integrated within photonic crystal. Obviously, the effect of such coupling will be much more pronounced if the complete photonic band gap is approached, but this requires application of more sophisticated techniques of the semiconductor deposition in opal voids, e.g. chemical vapour deposition [10].

This work was supported in part by Russian Foundation for Basic Research (grant 96-02-17963) and UK Leverhulme Trust (grant no. F/179/AK).

[1] J.V. Sanders, *Acta Cryst.* A24, 427 (1968)

V. G. Balakirev, V. N. Bogomolov, V.V.Zhuravlev, Y.A.Kumzerov, V.P.Petranovsky, S.G.Romanov, L.A.Samoilovich. *Crystallogr.Rep.* 38, 348 (1993)

[3] W.L Vos., R.Sprik, A.Blaaderen, A.Imhof,. A. Lagendijk, G.H. Wegdam, *Phys.Rev. B* 53, 16231 (1996)

[4] V. N. Astratov, V. N. Bogomolov, A. A. Kaplyanskii, A. V. Prokofiev, L. A. Samoilovich, S. M. Samoilovich and Y. A. Vlasov, *Il Nuovo Cimento*, D17, 1349, (1995)

[5] S. G. Romanov, A. V. Fokin, V. Y. Butko, V. V. Tretijakov, S. M. Samoilovich and C. M. Sotomayor Torres, *Fizika Tverdogo Tela*, 38, 3347 (1997) (in Russian) (English Translation *Phys. Solid State*, 38. (1997)

[6] R Mayoral, J.Requena, J.S.Moya, C.Lopez, A.Cintas, Hernan Miguez, F.Meseguer, L.Vazquez, M.Holgado, A.Blanco. *Advanced Materials*, 9, 257 (1997)

[7] J. Martoreli, N. M. Lawandy. *Optics Commun.* 78 169 (1990)

[8] V. N. Bogolomov, A. V. Prokofiev, S. M. Samoilovich, E. P. Petrov, A. M. Kapitonov and S. V. Gaponenko, to appear in *J Luminescence*

[9] S.G.Romanov, H.M.Yates, M.E.Pemble, J.R.Agger, M.V.Anderson, C.M.Sotomayor Torres, V.Y.Butko, Y.A.Kumzerov, *Fizika Tverdogo Tela*, 39, no.3 (1997) (*Physics Solid State*)

[10] S.G.Romanov, N.P.Johnson, H.M.Yates, M.E.Pemble, V.Y.Butko, C.M.Sotomayor Torres, *Appl.Phy.Lett.* 70, no.14 (1997)

THE ROLE OF ZERO-POINT FLUCTUATIONS IN THE NONLINEAR OPTICAL RESPONSE OF NANOSTRUCTURES

A.N. Rubtsov

Department of Physics, Moscow State University, 119899 Moscow, Russia

Optical properties of nanostructures are of significant interest, because they reveal peculiarities of the size-quantized electron motion in these structures. The second-order response of nanostructures is particularly interesting due to the surface nature of the second harmonic generation (SHG) from centrosymmetric media. The second-order susceptibility of the bulk of centrosymmetric media vanishes in the dipole approximation, therefore the SHG signal become extremely sensitive to the properties of surface and nanostructures.

The electromagnetic interaction of nanoparticle with its environment modifies both linear and nonlinear response of the particle. The presence of a substrate and neighbor particles shifts resonant peaks in the spectrum of the nanoparticle and changes value of its response.

For the theoretical description of these phenomena the semiclassical approach is commonly used, in which the response of nanoparticles is calculated using the quantum-mechanical formulae whereas the electromagnetic field is described by (classical) Maxwell equations. In this approach the interaction can be described by so-called local field factors. The local field factor L^ω for the single nanoparticle is determined by the following formula:

$$E^\omega_{loc} = L^\omega E^\omega_{ext},$$

where E^ω_{loc} is the local electric field acting on the particle at the fundamental frequency ω and E^ω_{ext} is the external field acting on the system. The linear and quadratic dipole moments of the particle are then described by the following formulae:

$$d^\omega = \chi^{(1)} L^\omega E^{ext}, \quad d^\omega = \chi^{(2)} L^\omega L^\omega E^\omega_{ext} E^\omega_{ext}.$$

Here $\chi^{(1)}$ and $\chi^{(2)}$ are linear and quadratic susceptibilities of the nanoparticle, respectively.

However this approach ignores several important factors. Particularly, it does not take into account any fluctuations in the system under consideration. It has been shown [1] that zero-point quantum fluctuations in the system affects its optical properties significantly. Namely, the linear non-resonant response of an atom in front of the dielectric surface is modified due to the Van-der-Waals interaction between the atom and surface. These effects are of the same order of magnitude as local-field corrections to the linear response. Moreover the size effect in the SHG from the $Si\text{-}SiO_2$ planar structure recently observed experimentally [2] cannot be described by semiclassical formalism but interpreted as a manifestation of zero-point fluctuations.

In the present paper we consider more general scheme of the calculation of response of nanostructures in which both nanoparticle and electromagnetic field are described quantum-mechanically. This allows us to take into account the zero-

point fluctuations. We focus our attention on the resonant response of the nanoparticle. The comparison of the obtained result with the semiclassical one shows the dramatic difference between them, in particular for the nonlinear case. Origin of this difference is discussed.

Let us consider a nanoparticle that interacts with its environment. We suppose that the environment can be taken into account by the proper renormalisation of the Green function of the electromagnetic field. In fact, this is the classical description of the environment. On the other hand, particle and electromagnetic field are treated quantum-mechanically. We will seek for a shift of the resonance of the particle response due to the interaction with an environment.

The Hamiltonian of the system under consideration is divided in the following three parts: (1) Hamiltonian of the particle H_p; (2) Hamiltonian of the electromagnetic field H_f and (3) the interaction Hamiltonian W: $H = H_p + H_f + W$. Hamiltonian H_p includes a short-range electromagnetic interaction which is responsible for the intercharge bounds in the particle. This short-range part should be excluded from H_f.

We use an approach similar to quantum-electrodynamics perturbation-theory scheme. The interaction

$$W_n = \frac{1}{2m}(2\int P_0(\mathbf{r})A_0(\mathbf{r})d^3r + \int \rho_0(\mathbf{r})A_0^2(\mathbf{r})d^3r)$$

is considered as a perturbation.

The linear and quadratic susceptibilities of the particle in the dipole approximation are given by

$$\chi^{(1)}(\omega) = \int_{-\infty}^{\infty} d\tau e^{i\omega\tau} \quad Td(t)d(t-\tau) >,$$

$$\chi^{(2)}(\omega) = \int_{-\infty}^{\infty} d\tau' \int_{-\infty}^{\infty} d\tau e^{i\omega\tau} < Td(t)d(t-\tau)d(t-\tau') >.$$

Above equations contain the dipole-moment operator $d(t)$ in the Heizenberg representation. The angular brackets denote averaging by the ground-state of the system, T is the time - ordering operator.

The response of a bare (i.e. placed in a free space) particle is described by the same formulae, but with operator $d_0(t)$ calculated for the Hamiltonian $H_p + H_f$. Hereafter subscript '0' denotes operators in the interaction representation (Heizenberg representation for Hamiltonian $H_p + H_f$).

The relation between operators in interaction and Heizenberg representations is given by the evolution operator of the system $S(t_1, t_2) = T\,\mathrm{Exp}[i\int_{t_1}^{t_2} W_0(t')dt']$. In the zero-temperature limit we obtain

$$< Td(t)d(t-\tau) > = < S >^{-1} < d_0(t)d_0(t-\tau)\,\mathrm{Exp}[i\int_{-\infty}^{\infty} W_0(t')dt'] >,$$

$$< Td(t)d(t-\tau)d(t-\tau') > = < S >^{-1} < d_0(t)d_0(t-\tau)d_0(t-\tau')\,\mathrm{Exp}[i\int_{-\infty}^{\infty} W_0(t')dt'] >, \quad |< S >| = 1.$$

The further analysis can be performed for the limit case of the frequency of the external field close to the resonance transition in the nanoparticle. This approximation allows to find out that the interaction with environment results in the shift of resonance peaks positions. These shifts are equal for linear and nonlinear cases. The resonance peak arising from the transition from level i to level j is shifted from ω_{ij} to $\omega_{ij} - g_{ii} + g_{jj}$, where

$$g_{kk} = \int_{-\infty}^{\infty} dt_n' < k|Td(t_n)d(t_n')|k > G_0(t_n - t_n'),$$

the Green function $G_0(t_n - t_n')$ is determined as follows

$$G_0(\tau) = \lim_{r' \to 0}\left\{< T\mathbf{E}_0(t,\mathbf{r})\mathbf{E}_0(t-\tau,\mathbf{r}-\mathbf{r}') > -[3\mathbf{r}'\mathbf{r}' - (r')^2]/(r')^5\right\}.$$

Last term in this formula is the short-range self-action part, which should be excluded from the interaction.

The obtained result can be interpreted as the shift of electron levels in the nanoparticle due to the Van-der-Waals interaction with the environment. The value of the shift is exactly equal to what the direct calculation of the Van-der-Waals level shift give [3].

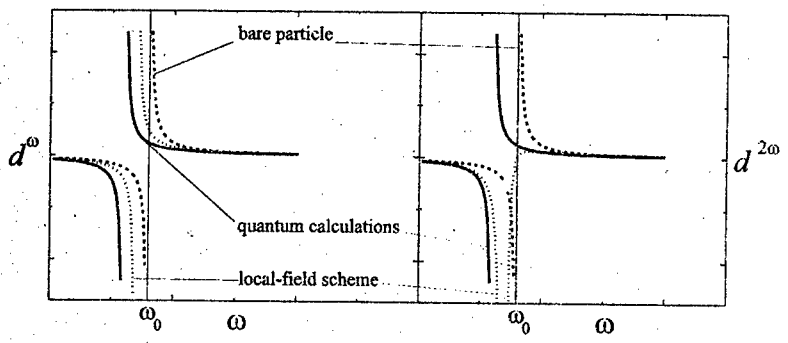

Figure 1.

Left and right panels shows the sketches of the spectral profiles of linear and quadratic response of the nanoparticle, respectively.

The following legend is used: dash curves - bare nanoparticle; dot curves - local-field calculations; solid lines - quantum calculations.

This result should be compared to the local-field factor calculations.

Let us consider the single resonance in susceptibility:

$$\chi^{(1)}(\omega) \propto \frac{1}{\omega_0 - \omega}, \omega \approx \omega_0.$$

In this case the semiclassical approach also predicts the shift in the resonance peak position due to the interaction with the substrate. However the value of the shift is different and equal to $d_i d_j G_0'(\omega_0)$, where $G_0'(\omega)$ is a Fourier transform of $G_0(t_n - t_n')$.

The semiclassical prediction for the SHG case is different. Namely, semiclassical formulae give the *second-order* pole in $d^{(2)}(\omega)$ for the particle interacting with the substrate. The corresponding curve is shown in Fig. 1. This unexpected and strange spectral behavior of the second-order response is obviously an artifact of the local-field scheme.

These discrepancies can be understood if one consider both the susceptibility of the particle and the local field as quantities with the fluctuation part:

$$\chi = \chi^{av} + \chi^{fluct};\ E_{loc} = E_{loc}^{av} + E_{loc}^{fluct}.$$

The values with superscript are averages; the values with superscript *fluct* are fluctuational parts with zero averages. Let double brackets <<>> denote the averaging over zero-points fluctuations. The local-field approach ignores the presence of this fluctuations. For example in the case of the linear response it is valid if

$$<< d >>=<< \chi E_{loc} >>=<< \chi >><< E_{loc} >>.$$

The later equality holds if $<< \chi^{fluct} E^{fluct} >>= 0$, *i.e.* if the local field and susceptibility fluctuations are independent. However it is not true, because a part of the local field results from the dipole moment of the particle itself (for example it may be a field of the image of the particle in the substrate). From this viewpoint the results of the local-field calculations are inconsistent.

Summarizing, we have presented calculations of the linear and quadratic response of a nanostructures, in which both nanoparticles and electromagnetic field are described as quantum objects We have shown that the semiclassical approach gives the result, which is qualitatively inconsistent with what more accurate quantum-electrodynamics calculations give. This is because the semiclassical scheme ignores the zero-point quantum fluctuations in the system which are actually of key importance.

Author is pleasant to acknowledge Dr. A.A.Nikulin for helpful discussions.

References:

1. *C.Girard, L.Galatry* Surf. Science **141** L338 (1984)
2. *O.A Aktsipetrov, A.A. Fedyanin, A.A. Nikulin, E.D. Mishina, A.N. Rubtsov, C.W. van Hasselt, M.A.C. Devillers, and Th. Rasing* Phys. Rev. Lett. **78** 46 (1997)
3. *J.M.Wylie, J.E.Sipe* Phys. Rev. A **32** 2030 (1985)

ELECTRON SPECTRUM IN QUANTUM SUPERLATTICE WITH AXIAL SYMMETRY.

M. Tkach, I. Pronyshyn, O. Makhanets

State University, 2 Kotsubinsky str., 274012, Chernivtsi, Ukraine

The spectra of quaziparticles (electrons, holes, excitons, phonons) in homogeneous quantum wires have been widely studied [1]. As the problem of the spectra of quaziparticles in inhomogeneous semiconductor cylindrical heterosystems with the period along radial direction is concerned, it have not been investigated at all as far as we know. Although it is interesting, because a new quantum number is arising when concerning such system. It plays a role of quazimomentum in radial direction. Due to it the heterosystem has some specific peculiarities.

Semiconductor heterosystem, which is the cylindrical quantum superlattice (CQSL) with the period in radial direction, is investigated (Fig. 1).

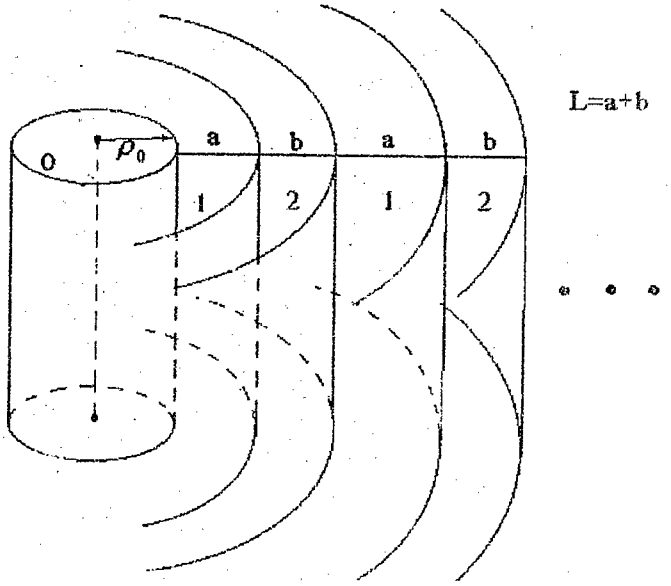

Fig. 1 Cylindrical semiconductor heterosystem with the period in radial direction.

This CQSL creates for the electron a periodic potential in the plane perpendicular to the axis of the system (the countdown is performed up from the bottom of the potential well)

$$U(\rho,\varphi)=\begin{cases} U_0; & \rho_0+pL\le\rho\le\rho_0+a+pL, \\ 0; & \rho\le\rho_0 \text{ and } \rho_0+a+pL\le\rho\le\rho_0+(\rho+1)L, \end{cases} \quad p=0,1,2,\ldots \quad (1)$$

here $L=a+b$-period of the potential, a-barrier width (material 1), b-quantum well width (material 2), ρ_0-radius of the inner crystal (material 2). The electron is characterized by the effective masses in each medium, therefore

$$\mu(\rho,\varphi)=\begin{cases} \mu_1; & \rho_0+pL\le\rho\le\rho_0+a+pL, \\ \mu_2; & \rho\le\rho_0 \text{ and } \rho_0+a+pL\le\rho\le\rho_0+(\rho+1)L, \end{cases} \quad p=0,1,2,\ldots \quad (2)$$

The Schrodinger equation in cylindrical coordinates

$$\left(-\frac{\hbar^2}{2}\vec{\nabla}\frac{1}{\mu(\rho,\varphi)}\vec{\nabla}+U(\rho,\varphi)-E\right)\psi_{n_\rho,|m|,k_z}(\rho,\varphi.z)=0 \quad (3)$$

is solved exactly. The operators $\hat{L}_z$ and $\hat{P}_z$ commutate with the Hamiltonian, so the total system of eigen functions of these operators exists

$$\psi_{n_\rho,|m|,k_z}(\rho,\varphi,z)=(2\pi\ell)^{-1/2}\exp[i(m\varphi+k_z z)]f_{n_\rho,|m|}, \quad (4)$$

where $m=0,\pm1,\ldots$-magnetic quantum number, $n_\rho=1,2,3,\ldots$-radial quantum number, k_z-electron quazimomentum in z-direction, ℓ-length of the system in z direction.

Radial wave function satisfies the periodic condition

$$f(\rho+L)=\exp(ik_\rho L)f(\rho), \quad (5)$$

where k_ρ-arbitrary real number. The solutions of the radial Schrodinger equations for the regions: 0) $\rho<\rho_0$, 1) $\rho_0\le\rho\le\rho_0+a$, 2) $\rho_0+a\le\rho\le\rho_0+L$ and 3) $\rho_0+L\le\rho\le\rho_0+L+a$, taking into account (5) can be written in the form

$$f_0(\rho)=A_0J_{|m|}(\beta\rho); \quad f_1(\rho)=A_1I_{|m|}(\alpha\rho)+B_1K_{|m|}(\alpha\rho),$$

$$f_2(\rho) = A_2 J_{|m|}(\beta\rho) + B_2 N_{|m|}(\beta\rho), \tag{6}$$

$$f_3(\rho) = \exp(ik_\rho L)\left[A_1 I^2_{|m|}(\alpha\rho) I^{-1}_{|n_\rho|}(\alpha(\rho+L)) + B_1 K^2_{|m|}(\alpha\rho) K^{-1}_{|m|}(\alpha(\rho+L))\right],$$

where $J_{|m|}(\rho)$, $N_{|m|}(\rho)$, $i_{|m|}(\rho)$, $K_{|m|}(\rho)$ -cylindrical functions and

$$\alpha = \hbar^{-1}\sqrt{2\mu_1(U_0 - E_{n_\rho,|m|})}; \qquad \beta = \hbar^{-1}\sqrt{2\mu_2 E_{n_\rho,|m|}}. \tag{7}$$

Wave functions $f_s(\rho)$ $(s = 0,1,2,3)$ and their densities of current are continuous at the interfaces of the system. These conditions determine the dispersional equation

$$\cos(k_\rho L) = F(E_{n_\rho,|m|}), \tag{8}$$

where the function $F(E_{n_\rho,|m|})$ of the energy of quazipartiele transversal movement is given as the combination of cylindrical functions and their derivatives in fixed points $\rho = \rho_0 + a$ and $\rho = \rho_0 + L$. The analysis of the equation (8) shows, that the electron energy spectrum is constructed of allowed energies (zones), as functions of quantum number k_ρ (radial quaziimpetus) and forbidden zones.

The calculations were performed for the semiconductors CdS and HgS (cubic sidecentered modification) widely used by experimentators [2]. Fig. 2 shows the dispersion law $E_{n_\rho,|m|}(k_\rho)$ for the electron with the fixed $\rho_0 = 10a_{HgS}$ and period of potential $L = 9a_{HgS} + 1a_{CdS}$ (a_{CdS}, a_{HgS} -lattices constant).

Each series with fixed $|m|$ has radial quantum number $n_\rho = 1,2,3,\ldots$ up from the lowest curve. Such system is characterized by constant potential barrier U_0, therefore there is the final number of allowed zones in the quantum well. The analysis of (8) equation shows, that when the width of potential well HgS increases and the width of barrier CdS decreases, there is only one allowed zone. It moves monotonously in the bottom well direction. Then the next allowed zones appear. The bigger is the width of the well the larger number of zones appears. The number of allowed zones essentially depends on the radius ρ_0 of inner crystal. When ρ_0 increases, the number of allowed zones is increasing and they are expanding. At $\rho_0 \approx 10 - 12a_{HgS}$ and small k_ρ for the excited states: $n_\rho = 2$, $|m| = 4,5,6,\ldots$, the forbidden zone exists. Its width is decreasing with the increase

of $|m|$. Here (at small k_ρ) space quazimomentum of the electron is equal to the quazimomentum k_z.

Considering the continuous conditions of the wave functions at the interface at $\rho = R$ we have found the binded Tamm's states with the energy localised in the forbidden zones. These energies monotonously move in the bottom well direction when L and ρ_0 increase. Their number is increasing. At $\rho_0 \to \infty$ all results of these paper are equal to the well known results [3] for the one-dimension superlattice.

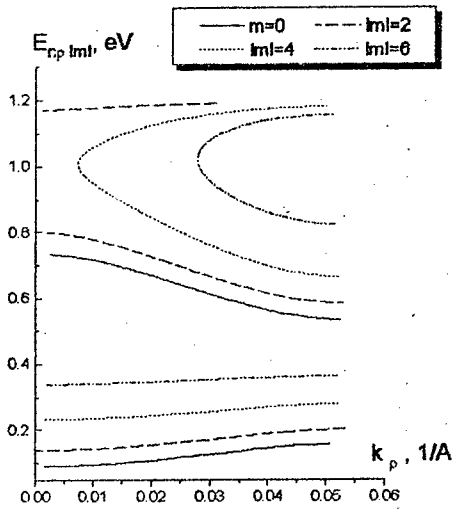

Fig. 2 Dependence of the energy of electron transversal movement on the quazimomentum at fixed $\rho_0 = 10a_{HgS}$ and $L = 9a_{HgS} + 1a_{CdS}$.

1. Hai G.Q., Peeters F.M.//Phys. Rev.B.-1993.-V.48.-N16.-p.12016-12022.

2. Schoss D., Mews A.//Phys. Rev.B.-1994.-V.49.-N24.-p.17072-17078.

3. Devison S., Levin J. Poverhnostnie (tammovskie) sostoiania. M., Mir,1978.232p.

EXCITON-PHONON INTERACTION IN SPHERICAL NANOHETEROSYSTEM CdS/HgS/H_2O.

M.Tkach, V.Holovatsky, O.Voitsekhivska, M.Mikhalyova

State University, 2 Kotsubynsky str., Chernivtsi, 274012, Ukraine

The spherical nanoheterosystem consisting of CdS core covered by HgS shell embedded into water is under research. The electron and hole spectrum for this system was found in the model of the finite rectangle potential wells and the effective mass approximation. The polarizational vectors and Hamiltonian of the confined optical and interface phonons were obtained in the framework of the dielectric continium model in Ref.[1]. Here we study the excitons electron and hole interaction with each other and with the phonons polarizational field.

The exciton basic state energy (E_{ex}) dependence on the number of monoshells (n) (or thickness) HgS at the fixed radius of CdS core ($r_0 = 4a_{CdS}$) is shown in Fig.1. From the figure one can see that though E_{ex} is decreasing when HgS thickness increases but there is a croock of the curve in the region ($2 \le n \le 4$). In order to understand the reason of its existence, one has to observe the partial terms of E_{ex}: $E_{0e,h}$ - the energy of an electron (hole), ΔE_{ex} - the exciton binding function, Δ_{ex} - the shift of the exciton energy level due to the interaction with phonons in the same figure.

As for the system under research E_{0e} and ΔE_{ex} are the monotonously decreasing functions of n then the croock is caused by the nonliniar dependence of E_{0h} and Δ_{ex} on n. The behaviour of two last values is clear from the physical considerations depicted in Fig. 2 where the density of the electron (hole) probability of presence depending on their distance from the center of the heterosystem is shown at several values of HgS monoshells (n).

From Fig.2 one can see that at $0 \le n \le 2$ the hole is mainly present in CdS and therefore its energy is determined by CdS well. At n=3,4 the hole with bigger probability transits into the deeper well HgS and consequently its energy is sharply decreasing and it causes the croocking of E_{ex} curve.

The croocking of E_{ex} curve is partly caused by the nonlinear dependence of Δ_{ex} on n. Naturally, at n=0 the HgS shell is absent (Fig.2a). Then the excitons electron and hole are located in CdS crystal on the same distance between each other. As they have the equal magnitudes of charges but the opposite signes and different effective masses,

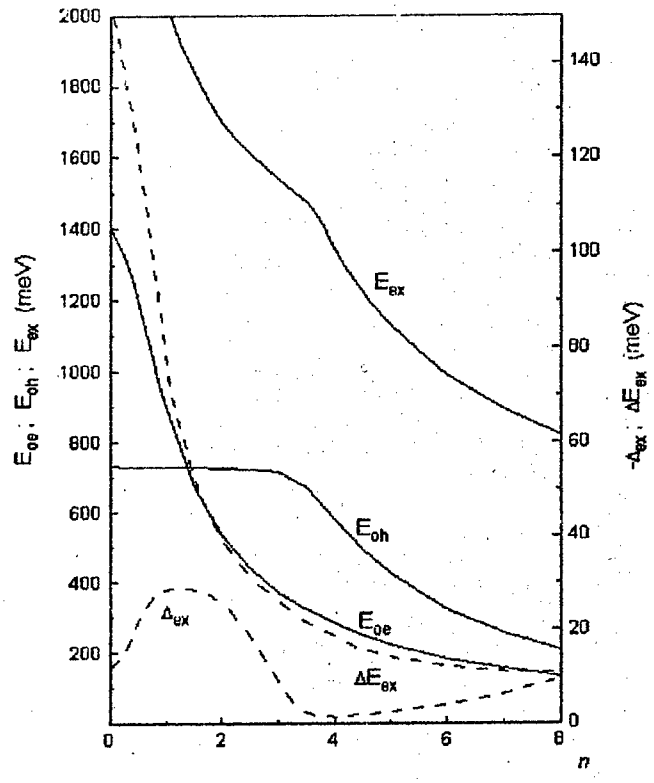

Fig.1. Exciton energy dependence(E_{ex}) on the number (n) of HgS monoshells at $r_0 = 4a_{CdS}$. The energy of an electron (E_{0e}), hole (E_{0h}), exciton (E_{ex}) - solid curves; exciton binding energy (ΔE_{ex}) and energy shift (Δ_{ex}) - dashed curves.

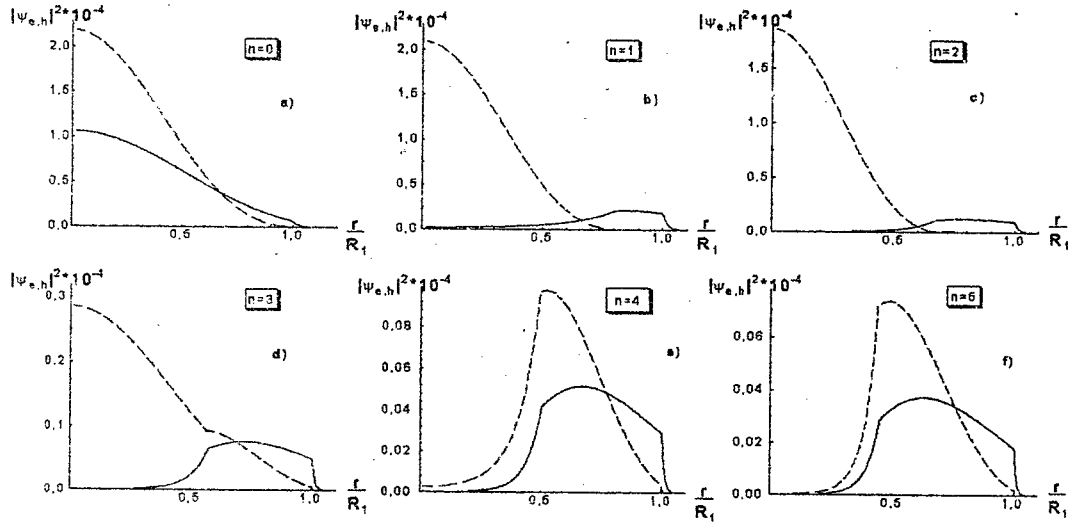

Fig. 2. Dependence of the electron (solid curves) and hole (dashed curves) density of probability on the distance of the center of theheterosystem at $r_0 = 4a_{CdS}$ and different numbers (n) of HgS monoshells.

then the interacting energy is partly compensated by the phonon field. As the result, the basic state exciton energy becomes smaller on the magnitude of the shift Δ_{ex} (n=0)< 0. When the heterosystem contains one HgS monoshell (n=1), then one can see from Fig.2b that the hole is located in CdS but the electron moves into HgS. Herein the distance between them becomes bigger, consequently the compensation of interaction energy with phonon field is smaller and that is why the energy value of exciton-phonon interaction increases. It brings to the increasing of $|\Delta_{ex}|$. At n=2 (Fig.2c) the location of electron and hole changed not very much and therefore the distance between them was not very changed and so the value $|\Delta_{ex}(n=2)|$ differs not very much from $|\Delta_{ex}(n=1)|$ (Fig.1)

At n=3 (Fig.2d) the HgS well is rather wide. There is not only electron in it but also the hole with high probability. The distance between these quasiparticles becomes smaller and so the compensation of energy increases and $|\Delta_{ex}|$ decreases (Fig.1). The addition of one more HgS monoshell n=4 (Fig.2e) causes the increasing of this well width; the maximum of electron and hole probability of presence is shifted into the middle of the well but as it is rather thin yet, this makes the distance between quasiparticle to be minimal and brings to the minimal value of $|\Delta_{ex}|$ (Fig.1).The further increasing of HgS number of monoshells (n≥5) causes the widening of the well and due to the decreasing of the influence of size quantizating effect the distance between the electron and the hole is slowly increasing (Fig.2f). This brings to the increasing of $|\Delta_{ex}|$ (Fig.1).

The calculation of E_{ex} at n>8 has not any sence because at such thickness of β-HgS, $|\Delta_{ex}|$ value becomes correlative with ΔE_{ex} and therefore it is necessary to take into account the interlevel interaction due to the phonons.

The results obtained in the developed theory can be compared with the theoretical and experimental data of Ref.[1]. The exciton energy values obtained with the accounting of exciton-phonon interaction fit the experimental data of [1] rather well. But remembering that there are only two experimentally investigated heterosystems it seems that it is necessary to research the CdS/HgS/H_2O heterosystem in wider scale of HgS thicknesses

[1] M.Tkach, V.Holovatsky, O.Voitsekhivska, M.Min'kova // International Symposium Nanostructures: Physics and Technology. - 96 – June 24-28 1996. – St.Petersburg, Russia P.315-317.

[2] Shooss J., Hews A., Eychmoller A., Weller H. // Phys. Rev. (b). 1994. V.49. №24. P.17072-17078.

ELECTRON AND HOLE SPECTRA IN ELLIPSOIDAL NANOHETEROSTRUCTURE (QUANTUM DOT)

G. Zegrya*, V. Golovach, A. Koustantinovich, M. Tkach

* A. F. Ioffe Physical Technical Institute, St. Petersburg, 194021, Russia
State University, 2 Kotsubynsky str., Chernivtsi, Ukraine

Recent experimental investigations show that the shape of the grown nanocrystals differ from the spherical one. The anysotrophy of physical characteristics (mass, dielectric constant) and conditions of nanostructure creation lead to the fact that the shape of obtained nanocrystals is more ellipsoidal than spherical. Thus, the problem of the electron (hole) spectrum and the wave functions in ellipsoidal quantum dot arises. It has no exact solution. In [1] this problem was solved only for the case of infinitely deep ellipsoidal well. The spectrum and the wave functions of the system using the approximated method and deformation of coordinates was found (at the small values of deformation)

In this paper the spectra and wave the functions of an electron (hole) in the nanoheterostructure consisting of semiconductor ellipsoidal nanocrystal embedded into a semiconductor medium are investigated. There is a finite skip of the potential energy $\left(-V_e(V_h)\right)$ at the ellipsoid well interface. The effective masses of the electron (hole) are different, in general case, in different media: $m_{e0}(m_{h0})$ – in the well; $m_{e1}(m_{h1})$ – outside of the well (in the surrounding medium). Thus, we get for the electron

$$U(\vec{r}) = \begin{cases} -V_e \text{ , inside the ellipsoid} \\ 0 \text{ , outside of the ellipsoid} \end{cases}, \; m(\vec{r}) = \begin{cases} m_{e0} \text{ , inside the ellipsoid} \\ m_{e1} \text{ , outside of the ellipsoid} \end{cases}, \quad (1)$$

$$\hat{T}(\vec{r}) = -\frac{\hbar^2}{2}\vec{\nabla}\frac{1}{m(\vec{r})}\vec{\nabla} \quad , \quad (2)$$

$$\hat{H} = \hat{T} + \hat{U} \quad (3)$$

In order to find the spectrum and the wave functions one can use Bethe's variational method. In this case the ellipsoid is approximated by a sphere with r_0 radius. It plays the role of the variational parameter. Then the exact Hamiltonian can be written as

$$\hat{H} = \hat{H}_0 + \Delta\hat{H} \quad , \quad (4)$$

where $$\hat{H}_0 = \hat{T}_s + \hat{U}_s(r) \quad (5)$$

is the Hamiltonian of the electron in the spherical quantum well with r_0 radius.

$$U_s(r) = \begin{cases} -V_e \;\; , \; r \le r_0 \\ 0 \;\; , \; r \ge r_0 \end{cases}, \quad m_s(r) = \begin{cases} m_{e0} \;\; , \; r \le r_0 \\ m_{e1} \;\; , \; r \ge r_0 \end{cases} \quad (6)$$

The excited part of the Hamiltonian is

$$\Delta H = T - T_s + U(\vec{r}) - U_s(r) \quad . \quad (7)$$

The Schrödinger equation

$$\hat{H}_0\Psi_{n\ell m}(\vec{r}) = E^0_{n\ell}\Psi_{n\ell m}(\vec{r}) \qquad (8)$$

can be solved exactly. In the energy region where the binding states exist the spectrum is defined by the solutions of the following transcendent equation

$$\left.\frac{\partial j_\ell(kr)}{\partial r}\right|_{r=r_0} = \frac{m_{e0}}{m_{e1}}\frac{j_\ell(kr_0)}{h^+_\ell(i\chi r_0)}\left.\frac{\partial h^+_\ell(i\chi r)}{\partial r}\right|_{r=r_0}, \qquad (9)$$

where $k = \frac{1}{\hbar}\sqrt{2m_{e0}(V_e - |E^0|)}$, $\chi = \frac{1}{\hbar}\sqrt{2m_{e1}|E^0|}$.

The wave functions are given as

$$\Psi_{n\ell m}(r,\theta,\varphi) = Y_{\ell m}(\theta,\varphi)A_{n\ell}\begin{cases} j_\ell(k_{n\ell}r) & , r \le r_0 \\ \dfrac{j_\ell(k_{n\ell}r_0)}{h^+_\ell(i\chi_{n\ell}r_0)}h^+_\ell(i\chi_{n\ell}r) & , r \ge r_0 \end{cases} . \qquad (10)$$

The coefficient $A_{n\ell}$ is defind by the normalization condition.Finally, in accordance with Bette's method, the spectrum of the electron (hole) is given in the form

$$E_{n\ell m} = \min_{r_0}\left[E^0_{n\ell}(r_0) + \left\langle n\ell m\middle|\Delta\hat{H}(r_0)\middle|n\ell m\right\rangle\right] \qquad (11)$$

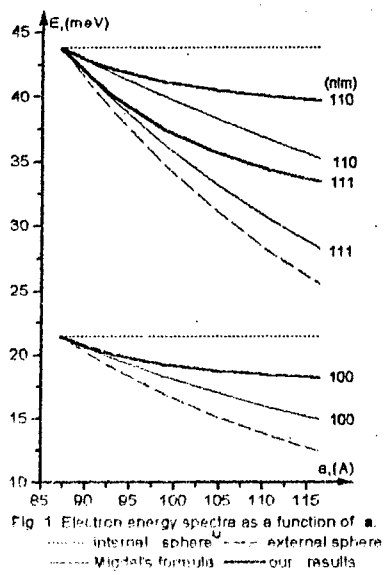

Fig. 1. Electron energy spectra as a function of **a**. ..... internal sphere - - - - external sphere ------ Migdal's formula ——— our results

Further calculations of matrix elements and minimization procedure was performed for the nanoheterostructure CdS/ZnS of cubic modification with parameters given in the Table.

We have performed the calculation of the three lower electron energy levels depending on the size of the big semiaxis a of ellipsoid in different models. The results are presented in Fig. 1. From the figure one can see that in both our approach and Migdal's method the behaviour of the energy levels is qualitativly equal: all levels are shifted to the bottom of the well when a increases (the small axis (symmetry axis) is constant $b = 15a_0 = 87.27\text{Å}$). Their energies are in the region defined by the radius of the inscribed (b) and described (a) spheres around the ellipsoid.

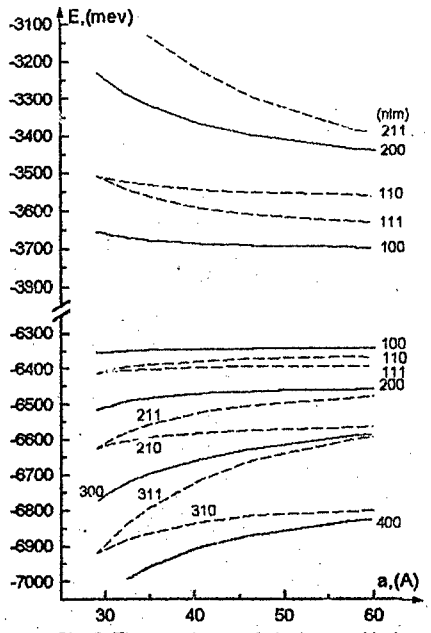

Fig. 2. The spectrums of electron and hole as a function of a (solid l=0 , dashed l=1).

The degeneration on the quantum number m is taken off in both methods. The splitting values are practically equal at the fixed a , b (not sensitive to the difference of the potential skip at the heterostructure interface) despite the fact that the Migdal's levels are always lower than our.

Figure 2 presents the electron and hole spectra depending on the value of the semiaxis a ($b = 5a_0 = 29.09\text{Å}$ -is constant).

Finally, let us note that the approach developed here can be used for the calculation of the quaziparticles spectra in different nanoheterostructures, the spatial shape of which can be approximated by a sphere.

Table

	$m_e(m_0)$	$m_h(m_0)$	$a(\text{Å})$	$\mathcal{E}_g(eV)$	$V_e(eV)$	$V_h(eV)$
CdS	0.2	0.7	5.818	2.5	-3.8	-6.3
ZnS	0.28	0.49	5.4'	3.9	-3.1	-7.0

References

[1] Migdal A. B.,Qualitative methods of Quantum Mechanics, Moscow 1975, 336.

Metal/Insulator/Semiconductor Heterostructure Quantum-Effect Devices on Si Substrate

Masahiro ASADA, Masahiro WATANABE*, and Wataru SAITOH
Department of Electrical & Electronic Engineering,
*Research Center for Quantum Effect Electronics,
Tokyo Institute of Technology
2-12-1 O-okayama, Meguro-Ku, Tokyo 152, Japan

1 Introduction

Metal/insulator ultrathin heterostructures are good candidates for high-speed electron devices, because the high carrier density of the metal and the low dielectric constant of the insulator are suitable for size reduction and high-speed operation of devices and integrated circuits[1][2]. In addition, due to a very large conduction-band discontinuity at the heterointerface, the interference of the electron wave is expected to become significant in multilayer structures, which result in high transconductance and multifunctionality of the quantum-effect devices[3][4].

We have been studying epitaxial growth of the metal/insulator heterostructure system[5] and its application to quantum-effect electron devices[6]-[9]. As the materials, $CoSi_2$ and CaF_2 have been chosen because they are nearly lattice-matched to Si with the mismatches of -1.2% and $+0.6\%$, respectively. In this paper, we describe epitaxial growth of $CoSi_2$ /CaF_2 nanometer-thick layered structures and quantum-effect devices, such as resonant tunneling transistors and quantum interference transistors. We also discuss about field-effect tunneling transistors with Si/CdF_2 /CaF_2 and its epitaxial growth, which can be extended to field-effect quantum devices on Si.

2 Epitaxial Growth of $CoSi_2$ /CaF_2 on Si

In order to create $CoSi_2$ /CaF_2 epitaxial multilayers, epitaxial growth conditions were studied separately for CaF_2 on $CoSi_2$ and $CoSi_2$ on CaF_2 [5]. In the case of $CoSi_2$ on CaF_2 , the agglomeration of Co on CaF_2 is a critical problem if we use co-deposition of Si and Co with conventional MBE technique. This problem was overcome by the following two step growth technique: First, flat four monolayers of Si were formed on CaF_2 at the substrate temperature T_s =600°C. Then, two monolayers of Co were deposited on the Si layers by the solid phase epitaxy at temperature lower than about 100°C. Since the difference of the surface energy between Co and CaF_2 , flat two molayers of $CoSi_2$ were grown on CaF_2 without the agglomeration by this technique. $CoSi_2$ layers thicker than two monolayers were obtained by repeating this process with Si growth temperature of 550°C.

In the case of CaF_2 on $CoSi_2$ /CaF_2 , T_s must be lower than about 550°C to avoid thermal deformation and agglomeration of $CoSi_2$ layers. We used the partially ionized beam epitaxy to

give external kinetic energy for migration to the evaporated particles. CaF_2 was grown on $CoSi_2$ at T_s =450°C with the acceleration voltage V_a =2kV and the ionization current I_e =400mA, at which condition the ionization ratio of the CaF_2 beam was about 2%.

3 Resonant Tunneling Transistor

We fabricated $CoSi_2$ /CaF_2 resonant tunneling transistors. The transistor is composed of a few nanometer-thick triple CaF_2 barriers and double $CoSi_2$ wells on n-Si(111). The conduction band offset at the $CoSi_2$ /CaF_2 interface is about 15eV and the Fermi level is about 13eV from the conduction band bottom of $CoSi_2$. These values were estimated from the related values of the bulk materials[7]. The emitter, base, and the collector electrodes are connected, respectively to the top $CoSi_2$ layer, one of the $CoSi_2$ quantum wells near the emitter contact layer, and the substrate. Electrons pass through the resonant levels in the two quantum wells from the emitter to collector if these levels are aligned. The condition of the alignment between the resonant levels is controlled with the collector-base voltage V_{CB}, and the amountof the electrons from the emitter is controlled with the base-emitter voltage V_{BE}. Thus, collector current I_C varies with V_{BE}, and exhibits a negative differential resistance (NDR) with respect to V_{CB} for constant V_{BE}. As a different case, if the base electrode is connected to the other quantum well near the collector, I_C exhibits an NDR with respect to V_{BE} for a constant V_{CB}, which operation is similar to the semiconductor resonant tunneling hot electron transistor (RHET) [10].

In the common-emitter configuration of the fabricated transistors, we observed NDR in I_C-V_{CE} curve, in which peak current is controlled by V_{BE}. The peal-to-valley ratio of the NDRs was 13–19 at room temperature.

4 Observation of Hot Electron Interference

As a quantum effect in metal/insulator system other than the resonant tunneling, the interference of a hot electron wave with the energy higher than the barrier height in a metal/insulator/metal structure is applicable to multifunctional electron devices[4]. The transmission coefficient of hot electron passing normally through this structure is strongly modulated by this interference. This effect is the same as that in an optical Fabry-Pérot interferometer. The interference is much larger in metal/insulator system compared to conventional semiconductor heterostructures because of the large band offset.

To observe this interference, we fabricated a quantum interference transistor structure, which is composed of a double-barrier resonant tunneling emitter, base layer, collector barrier, and a collector region on a Si substrate[9]. Hot electrons with collimated energy are emitted from the resonant tunneling emitter, and injected into the conduction band of the collector barrier in which the interference takes place. The interference can be observed as multiple NDRs in the collector current I_C as a function of V_{BE} or V_{CB}.

In the fabricated transistors, we observed multiple NDRs in I_C-V_{CB} curve at room temperature. The voltage interval between the adjacent NDRs was about 1.5V which is in reasonably agreement with theoretical calculation (about 1V) [9]. Stepwise current variation was observed in I_B-V_{CB}

curve at V_{CB}'s of the NDRs in I_C. This can be attributed to additional electrons in I_B at NDRs produced by the reflection at the collector barrier interference region.

Although room-temperature operation was obtained, the NDRs are very small due to the leak current in or around the device, and also due to the emitter parasitic resistance produced during the fabrication process. The improvement of the characteristics is possible by optimizing the device.

5 Field-Effect Quantum Device

In the view point of input impedance, circuits design, and power consumption, field-effect device is desirable also in quantum-effect devices. We proposed a very short channel tunneling field effect transistor with $CoSi_2$ /Si/CdF_2 /CaF_2 heterostrucute[11] as a basic device which can be extended to field-effect quantum devices,such as coupled waveguide devices. In device operation, current from source ($CoSi_2$) to drain ($CoSi_2$) through tunneling barrier at source (Si) – channel (CdF_2) – barrier at drain (Si) is controlled by gate electric field applied to barrier at source through gate insulator (CaF_2) and channel (CdF_2). Theoretical analysis shows that this transistor has characteristics with saturated drain current in I_D-V_{DS} curve even with the channel length of 20nm and 5nm.

To realize this transistor, growth of $CoSi_2$ /Si/CdF_2 /CaF_2 on Si is necessary. Although $CoSi_2$ /Si and CdF_2 /CaF_2 in these heterostructures have already been reported[12][13], growth of Si on CdF_2 has not yet been reported. To grow this heterostructure, we employed the two-temperature step technique; three monolayer Si was grown at low temperature (about 50°C) on CdF_2 /CaF_2 in the first step, and then, further Si layer was grown at high temperature (about 300°C) in the second step. This technique was effective in avoiding the thermal damage of CdF_2 and reaction between CdF_2 and Si. Obtained results showed a single-crystalline nature in RHEED and a flat surface image in AFM observation.

6 Conclusions

Quantum-effect devices with metal($CoSi_2$)/insulator(CaF_2) nanometer-thick heterostructures were fabricated on Si substrates, and operated at room temperature. Resonant tunneling transistors were fabricated and transistor action including negative differential resistance with the peak-to-valley ratio of about 19 was observed at roomtemperature. Quantum interference transistors utilizing electron interference in the conduction band of an insulator sandwiched between metal layers was fabricated and multiple negative differential reistance was observed at room temperature. We proposed a very short channel tunneling field effect transistor with $CoSi_2$ /Si/CdF_2 /CaF_2 heterostrucute which can be extended to field-effect quantum devices. Si layer on CdF_2 in the heterostructures of this device was grown by the two-temperature step technique.

Acknowledgement

The authors would like to acknowledge Prof.Y.Suematsu, Professor emeritus of the Tokyo Institute of Technology, for continuous encouragement. We also acknowledge Profs. K.Furuya, S.Arai, and

Assoc.Prof. Y.Miyamoto for fruitful discussions, Assoc. Prof. K.Tsutsui and Dr.A.Izumi for many useful informations and comments on CdF_2 experiment. This work was supported by a scientific grant-in-aid from the Ministry of Education, Science, Sports and Culture.

References

1. C.A.Mead, J.Appl.Phys., **32** (1961) 646
2. M.Heiblum, Solid State Electron., **24** (1981) 343
3. Y.Nakata, M.Asada, and Y.Suematsu, Electron. Lett., **22** (1986) 58
4. T.Sakaguchi, M. Watanabe, and M. Asada, IEICE Trans. **E74** (1991) 3326
5. M.Watanabe, S.Muratake, T.Suemasu, H.Fujimoto, S.Sakamori, M.Asada, and S.Arai, J. Electron. Mat., **21** (1992) 783
6. M.Watanabe, T.Suemasu, S.Muratake, and M.Asada, Appl. Phys. Lett., **62** (1993) 300
7. T.Suemasu, M.Watanabe, J.Suzuki, Y.Kohno, M.Asada, and N.Suzuki, Japan. J. Appl. Phys., **33** (1994) 57
8. T.Suemasu, Y.Kohno, W.Saitoh, M.Watanabe, and M.Asada, IEEE Trans. Electron Devices, **42** (1995) 2203
9. W.Saitoh, T.Suemasu, Y.Kohno, M.Watanabe, and M.Asada, Japan. J. Appl. Phys., **34** (1995) 4481
10. N.Yokoyama, K.Imamura, S.Muto, S.Hiyamizu, and H.Nishi, Japan. J. Appl. Phys., **24** (1985) L853
11. W.Saitoh, K.Yamazaki, M.Asada, and M.Watanabe, Japan. J. Appl. Phys., **35** (1996) L1104
12. R.T.Tung and F.Schrey, Appl.Phys.Lett., **54** (1989) 852
13. A. Izumi, K. Tsutsui, N. S. Sokolov, N. N. Faleev, S. V. Gastev, S. V. Novikov, and N. L. Yakovlev, J. Cryst. Growth **150** (1995) 1115

Lasing Oscillations in Silicon Quantum Wires

N.T.Bagraev, E.I.Chaikina, W.Gehlhoff [1], L.E.Klyachkin,I.I.Markov, and A.M.Malyarenko

A.F.Ioffe Physico-Technical Institute, St.Petersburg, 194021, Russia, E-mail: emtsev@jsc.ioffe.rssi.ru
[1]Institut für Festkörperphysik, Technische Universität Berlin,Hardenbergstr.36, D-10623 Berlin, Germany

We present the first findings of the infrared induced emission from the silicon quantum wires, which is due to the formation of a correlation gap in the DOS of degenerate hole gas. The quantum wires of this art are created by electrostatic confining potential due to impurity correlations inside ultra-shallow p^+-n junctions which are realized using controlled surface injection of self-interstitials and vacancies in the process of non-equilibrium boron diffusion.

The diffusion experiments involving boron were performed from gas phase into 350 μm thick n-type Si (100) wafers. The working and back sides of wafers were previously oxidized using the thermal oxidation process. The parameters varied in the course of the short time diffusion of boron were the oxide overlayer thickness, diffusion temperature (800°C-1100°C) and Cl levels in the gas phase. Diffusion profiles measured using SIMS technique demonstrate the depths in the range from 5 nm to 20 nm. The cyclotron resonance findings and current-voltage characteristics measured at different angles between the p n junctions plane and the bias voltage show that the p^+ diffusion profiles consist of both natural longitudinal and lateral quantum wells, the relative number of which is determined by the non-equilibrium diffusion conditions. Besides, the crystallographically dependent quantized conductance obtained at high temperature (77 K and 300 K) has revealed the quantum wires induced inside natural quantum wells by the strong electrostatic confining potential due to ordering B^+-B^- dipole centres.

Using temperature dependencies of thermal friction coefficient as well as direct and reversal CV characteristics, the C_{3v} symmetry B^+-B^- dipole centres are demonstrated to cause the formation of a correlation gap in the DOS of degenerate hole gas in the crystallographically oriented quantum wires (Fig.1). The dispersion in the energy of a correlation gap is dependent on local fluctuations in the dopant distribution along a quantum wire, which represent the places of the creation of isolated quantum dots under the gate voltage.

The generation of similar quantum wires with isolated quantum dots using external electric fields has been found to be responsible for the infrared emission in the range 1-10 μm, which is induced by the injection of non-equilibrium carriers into quantum wire systems (Fig.2). These results represent the basis toward the infrared silicon lasers in which both electrons/holes and photons are fully quantized. The dipole impurity microcavity that is a length of quantum wire (d) restricted by two isolated quantum dots is shown to produce the lasing oscillations at the wavelengths determined by a correlation gap value, which coincide with the resonance wavelength of the microcavity (λ). The microcavity dimension has been found to reveal from the period of Aharonov-Bohm-like magnetoconductance oscillations in external magnetic field directed along the quantum wire: $h/2e=\Delta B \cdot \pi d^2/4$; where $d \equiv \lambda$ (Fig.3). Besides, the magnetoconductance changes due to

the Larmor precession of holes in lateral magnetic field, which are dependent on initial spin states $|\uparrow>$ and $|\downarrow>$, demonstrate also the period (T) correlated with the resonance wavelength: $l=v\cdot T\cdot n\equiv\lambda$; where v is the spin-dependent velocity of holes (Fig.4). The threshold character of the irradiative power and dynamic spectrum narrowing found at 3591 nm, 3744 nm, 3969 nm, 4457 nm and 4881 nm as a function of the current that traverses the quantum wire with isolated quantum dots are evidence of light stimulated emission from silicon nanostructures (Figs.5 and 6).

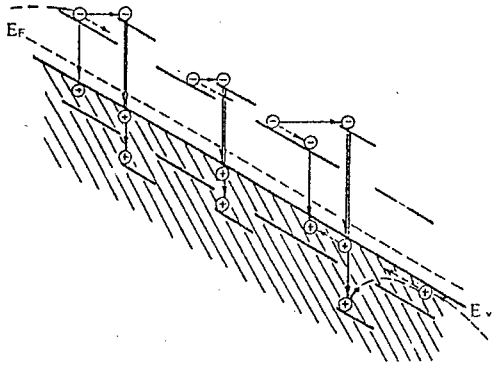

Fig.1. One-electron band scheme for a quantum wire with a correlation gap under the passage of a longitudinal current along silicon quantum wire in p^+-diffusion profile.

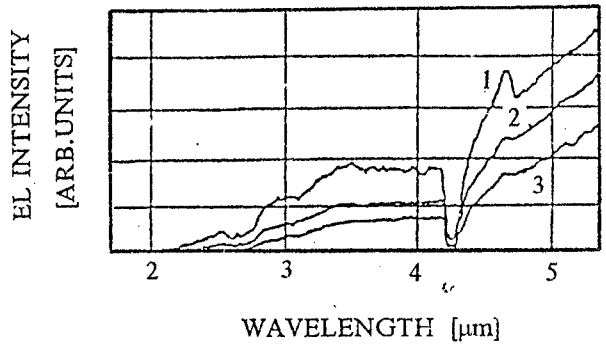

Fig.2. Spectrum of the infrared emission from the ultra-shallow silicon p^+-n junctions under the passage of a longitudinal current along silicon quantum wire in p^+- diffusion profile at 300K.The power of infrared emission at different current: 900 mW·mm^{-2}, 100 mA (curve 1); 680 mW·mm^{-2}, 50 mA (curve 2); 450 mW·mm^{-2}, 35 mA (curve 3).

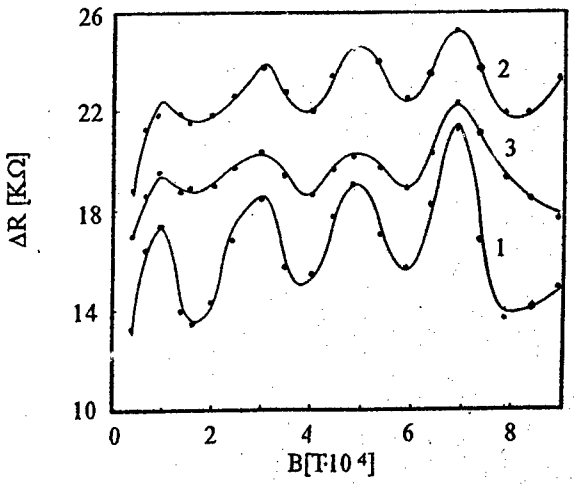

Fig.3. Aharonov-Bohm-like magnetoconductance oscillations observed in ultra-shallow silicon p^+-n junctions under reverse voltage. The periodicity of the oscillations corresponds to $\Delta\Phi=h/2e$; $h/2e=\Delta B \cdot S \rightarrow \lambda \cong d \cong (2h/\pi e \Delta B)^{1/2}$ is the wavelength of the infrared emission, which coincides with the dimension of the microcavity (d). U_{rev}: 1-0.18V; 2-0.29V; 3-0.35V.

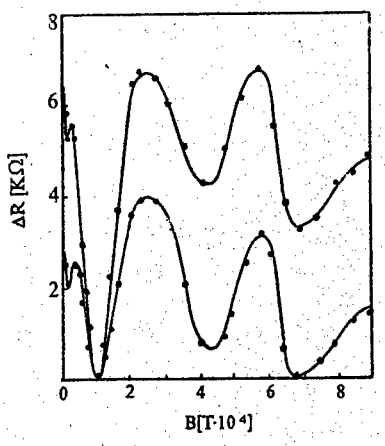

Fig.4. Larmor-like magnetoconductance oscillations induced by lateral magnetic field in a quantum wire created by reverse voltage applied to ultra-shallow silicon p^+n junctions.

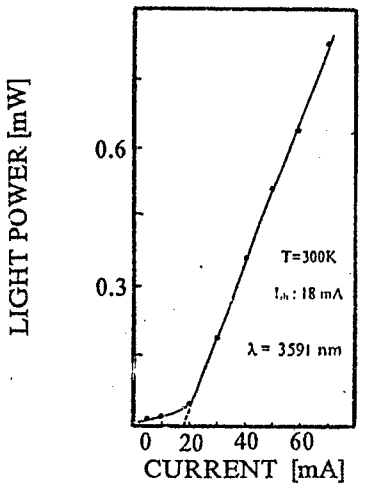

Fig.5. Dependence of the radiative power on the longitudinal current along QW silicon p^+ - diffusion profile obtained at diffusion temperature 900°C in n-type silicon (100) - wafers with thin oxide overlayer. T=300 K, λ=3591 nm. I_{th}=18 mA.

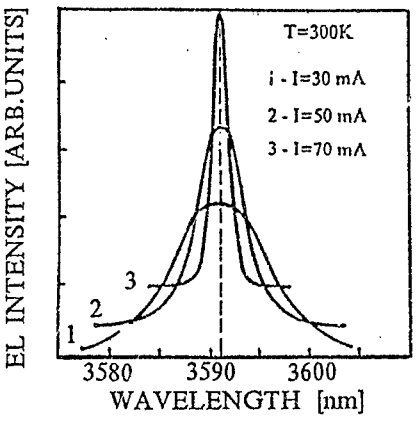

Fig.6. Electroluminescence spectra recorded at 300 K under the passage of a longitudinal current along QW silicon p^+-diffusion profile obtained at diffusion temperature 900°C in n-type silicon (100)-wafers with a thin oxide overlayer. 1-30 mA, 2-50 mA, 3-70 mA.

MULTIELEMENT PHOTODETECTOR MULTISCAN: RANDOM TELEGRAPH SIGNAL IN SINGLE-ELECTRON TUNNELING TRANSPORT

N.T.Bagraev, L.E.Klyachkin, A.M.Malyarenko, B.G.Podlaskin, N.A.Tokranova

Ioffe Physico-Technical Institute. Russian Academy of Sciences
194021, Polytekhnicheskaya 26, St.Petersburg, Russia

We present the first findings of the quantized conductance and its reproducible mesoscopic fluctuations which identify a single-electron transport in the multiscan that represents the multielement photodetector obtained using self-assembly silicon quantum wells.

The multiscan is the coordinate-sensitive photodetector intended to determine the space position of the optical signal inside the device itself by the comparison of the opposing photocurrents flowing from a resistive voltage divider and a common low-resistance signal bar through a set of the oppositely sensed pair photodiodes (Fig.1) [1]. To operate the coordinate ξ of the light spot centre, a supply voltage U is applied to the divider, whereas the signal bar is connected to a high-resistance load (Fig.1). Therefore, a potential V corresponding to the equalization of the total photocurrent in the device to zero appears on the signal bar. The coordinate feature $V \sim \frac{dU}{dx}\varsigma$ as well as its gradient $V' = -\sum_i \frac{\partial J_{ph_i}}{\partial \xi} \Big/ \sum_i \frac{\partial J_{ph_i}}{\partial V}$, that is responsible for periodic instrumental error introduced into the measurements are the most important parameters of the multiscan [1]. In order to enhance the resolution of the $V(\xi)$ and to minimize the $V'(\xi)$, it is necessary to suppress the diffusion component of the photocurrent along the multiscan area and to provide the ballistic transport of the photocarriers between the divider and the signal bar that can be achieved using quantum well systems.

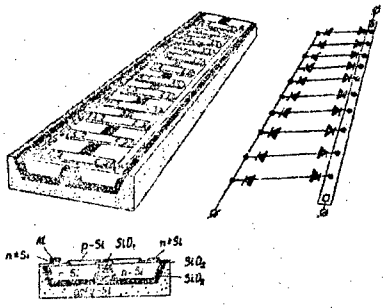

Fig.1
Topological structure and electrical equivalent scheme of the multiscane.

The goal of this work is to study the quantized conductance and its reproducible mesoscopic fluctuations as guideline in determining the optimal parameters of the multiscan performed on the basis of self-assembly silicon quantum wells.

The multiscan has been realized using controlled injection of self-interstitials and vacancies in the process of non-equilibrium boron-phosphorus diffusion [2] into n-type Si (100) monocrystalline structures insulated by the SiO_2 alloys (Fig.1). The parameters varied in the course of the short time diffusion of boron (p^+n-diodes) and phosphorus (divider and signal bar) were the oxide overlayer thickness and diffusion temperature (800°C-1100 °C). Ultra-sharp diffusion profiles measured using the SIMS technique are present in Fig.2. The cyclotron resonance findings and angular dependencies of the CV-characteristics show that both the p^+- and n^+-diffusion profiles consist of crystallographically-ordered lateral quantum wells (LaQW) (Fig.3) divided by

the high energy barriers due to self-ordering of the dopants [3]. Besides, the thermo-emf data and crystallographically dependent quantized conductance obtained at 77 K and 300 K have revealed dynamic quantum wires induced inside self-assembly quantum wells by the electrostatically ordering both the B^+- B^- and P^+- P^- dipole centres [3].

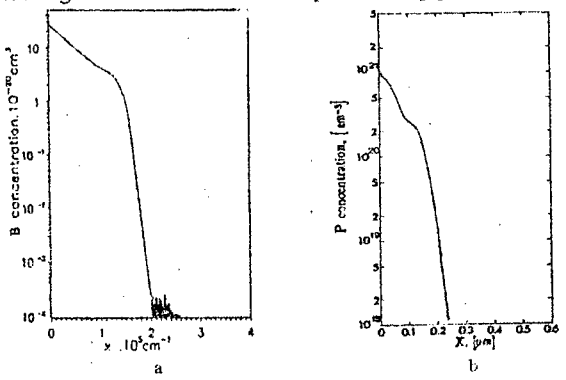

Fig.2.
SIMS data for boron (a) and phosphorus (b) diffusion profiles obtained at diffusion temperature of 800° C (a) and 1100° C (b) in n-type Si(100)

The $\sigma(V)$ dependencies obtained with studying the multiscans characterized by low dark leakage current have revealed the single step (Fig.4a), the Coulomb staircase (CS) and Coulomb blockade (CB) (Fig.5a) as well as random telegraph signal (RTS) which result from elastic back scattering and tunneling of single-electrons (SET), whereas some special features are absent in the corresponding characteristics of the ordinary multiscan (Fig.5b). Since the p^+- and n^+-diffusion profiles represent the combination of dynamic quantum wires, the conduction path is composed of very large number of parallel arrays of tunnel junctions which are able to pass or to reflect back the electrons according to the content of the dipole impurity centre's fluctuations near the LaQW edges. The elastic back scattering on such fluctuations depends for its action on the conductance step equal to $4e^2/h$ (E || [100]) or $8e^2/h$ (E || [110]), E || [111]) [3], which exhibits the influence of the conduction valleys, forming the Coulomb staircase (Fig.5a) and enhancing the conductance value (curves 2 in Figs.4a and 5a): $\sigma = g_v e^2/h$ (where $g_v = 2$ - E || [100] and $g_v = 4$ - E || [110], [111]).

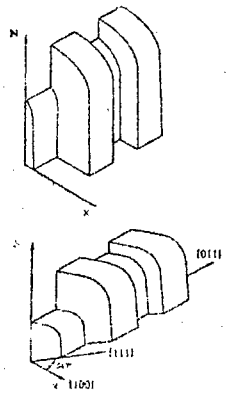

Fig.3
Self-assembly diffusion quantum wells obtained under surface injection of vacancies (QW$_V$ || [100]) and self-interstitial (QW$_I$ || [111])

The initial single step of the conductance seems to be due to a quasi-adiabatic transport of single electrons through the pair of p^+n-junctions or strong elastic back scattering directly from the p^+n junction area (Fig.4a). Random telegraph signal exhibited as reproducible mesoscopic fluctuations of the conductance (Fig.4b) results from single-electron tunneling transport through quantum dot states localized on the dipole impurity centre's fluctuations which are induced by the "gate voltage" distributed along the divider and the signal bar (Fig.1). At an applied voltage where one such quantum dot aligns with

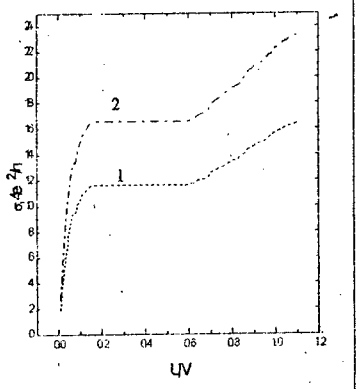

a

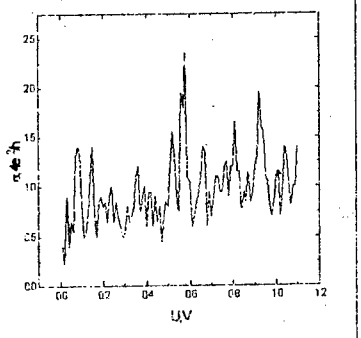

b

Fig.4.

The quantized conductance (a) and random telegraph signal (b) vs the voltage applied between divider and signal bar of the multiscan, which are dashed (a) and solid (b); (a) - 1-E | |[100], 2 - E | |[110]

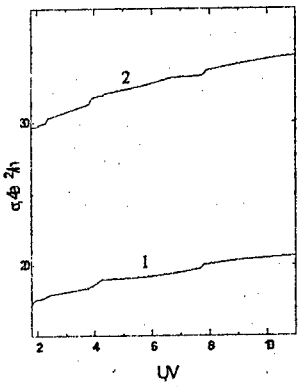

a

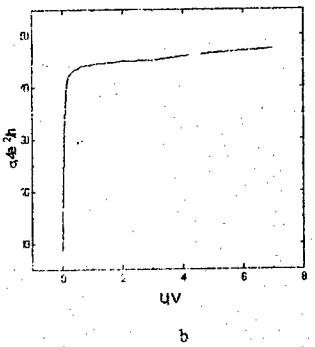

b

Fig.5.

The quantized conductance vs the voltage applied between divider and signal bar of the multiscan with low dark leakage current (a) and the ordinary multiscan (b). (a) - 1 - E | |[100], 2 - E | |[110]

the Fermi level, a new channel is opened for electron tunneling and the current through the device exhibits a $4e^2/h$ step-like increase (Fig.4b). Mesoscopic character indicates that the switching event is a quantum transport between two closely spaced tunneling channels. This conclusion has been shown to be confirmed independently by universal fluctuations of the conductance when changing the coordinate of the dark current measurements (Fig.6a). The value of these fluctuations is conserved (Fig.6b) even if the multiscan is interferior to demonstrated above because of the diffusion current component crossed some part of self-assembly quantum wells.

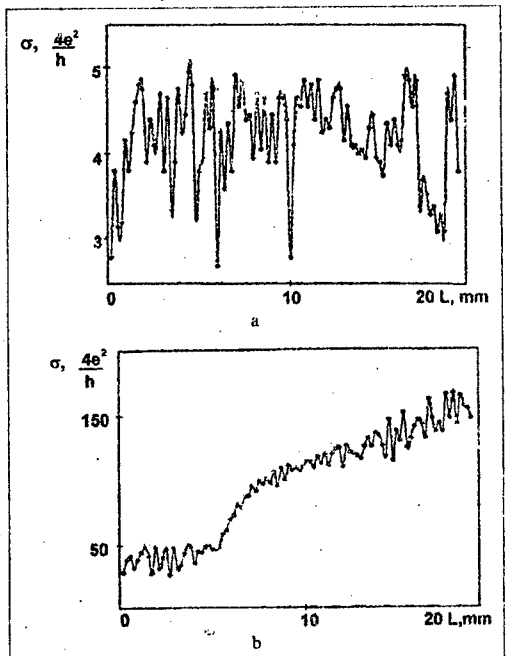

Fig.6
Dark leakage current distribution along the multiscan area.
Total current: (a) - 8.3 10^{-11}A, (b) - 1.9 10^{-9}A

Thus, the quantized conductance and single electron tunneling exhibited as its mesoscopic reproducible fluctuations have been shown to represent some criterion for the optimal characteristics of the multiscan, which are provided by using self-assembly silicon quantum wells.

References

[1].V.S.Yuferev, E.P.Romanova, B.G.Podlaskin: Sov.Phys.Tech.Phys. v.37(10), p.1033, 1992
[2].N.T.Bagraev, L.E.Klyachkin, V.L.Sukhanov: Defect and Diffusion Forum, v.103-105.p.201. 1993
[3]. N.T.Bagraev. W.Gehlhoff, L.E.Klyachkin, A.M.Malyarenko: Proc.of the 23th ICPS. Scientific World, Singapore, p.1241, 1996

SELF-ASSEMBLY QUANTUM WIRES CREATED BY IMPURITY DIPOLE ORDERING IN SILICON

N.T. Bagraev*, W. Gehlhoff**, L.E. Klyachkin*, A.M. Malyarenko*, and A. Naeser**.

*A.F. Ioffe Physico-Technical Institute, St.Petersburg, Russia.

** Institut für Festkörperphysik, Technische Universität Berlin, Hardenbergstr.36, D-10623 Berlin, Germany

We present the first findings of quantized conductance and EPR-EDEPR techniques which reveal the spin-dependent confinement and quantization phenomena in the silicon quantum wires created by electrostatically ordering self-assembly dipole boron (B^+-B^-) and phosphorus (P^+-P^-) centres. These C_{3v} symmetry dipole impurity centres are regularly arranged along the barriers of single longitudinal and lateral quantum wells (LQW and LaQW) which are naturally formed inside ultra-shallow silicon diffusion p-n junction (Fig.1).

Short-time diffusion of boron and phosphorus, respectively, was performed from gas phase into n- and p- type Si (100) wafers using controlled surface injection of self-interstitials and vacancies. By varying the parameters of the surface oxide layer and diffusion temperature (800°C-1100°C) it was possible to define the criteria leading to the ultra-shallow p-n junction (5 nm-30 nm), which were controlled using SIMS and STM techniques. The cyclotron resonance (CR) and current-voltage (CV) dependencies, which are brought about the deflection of the bias voltage from the normal to the p-n junction plane, show that the p^+- and n^+- diffusion profiles consist of LQW or LaQW generated between two-dimensional alloys that contain self-assembly boron/phosphorus centres (Fig.2). The logarithmic temperature dependence of resistivity have revealed a weak localization regime of two-dimensional hole gas (Fig.3 a), which is transformed in the quantum wire system under the voltage applied along both LQW and LaQW (Fig.3 b and Fig.2 b). A negative magnetoresistance that is evidence of a weak localization at low electric field has been also found (Fig.4). Spin-dependent antilocalization due to Dyakonov-Perel mechanism has been revealed to be in low magnetic field equal to the local magnetic field of the ^{29}Si nuclei (Fig.4). Thermo-emf and tunnelling CV measurements demonstrate that these quantum wires seem to be created by electrostatic confining potential of self-assembly dipole B^+-B^- and P^+-P^- centres (Fig.2). The crystallographically dependent quantized conductance has revealed dynamic quantum wires that are induced by the voltage applied along both LQW and LaQW and exhibited the valley's effects (Figs.5 a and b). The quantized conductance technique has also identified new near-edge resonances that appear in I(V) dependence and are due to hole scattering on single iron-related centres because of the interaction between the d-levels and minibands in quantum wires (Fig.5 c).

Spin-dependent electron/hole confinement has also made it possible to study single impurities, which are present in quantum wires, by the EPR-EDEPR method using the versions of both spin-dependent weak localization (Fig.6 a) and spin-dependent scattering (Fig.6 b). Besides signals from the iron-related centres, phosphorus and oxygen thermal donors, a new line that seems to be due to the C_{3v} symmetry B^+-B^- dipoles is found.

Finally, the quantized conductance technique is applied, for the first time, to investigate the electrically- and optically-induced nuclear polarization in a weak magnetic field as a result of the hyperfine interaction of the lattice nuclei with both spin-polarized Tomonaga-Luttinger Liquid in dipole impurity quantum wires and spin-polarized holes injected from quantum wires to the p-type silicon substrate by Aronov mechanism.

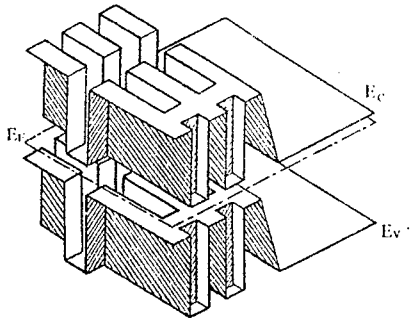

Fig1. Three dimensional diagram of the one-electron band scheme of an ultra-shallow p^+n junction which is a system of LQW and LaQW

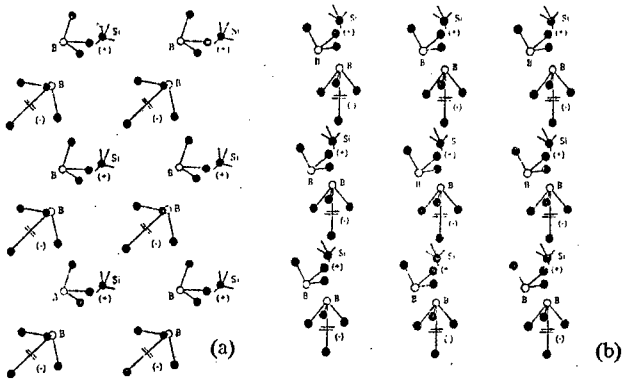

Fig.2. Model for an elastic reconstruction of a shallow acceptor, which is accompanied by the formation of C_{3v} dipole centres as a result of the negative-U reaction: $2B^0 \rightarrow B^+ + B^-$ (a - E=0; b - E||[001]).

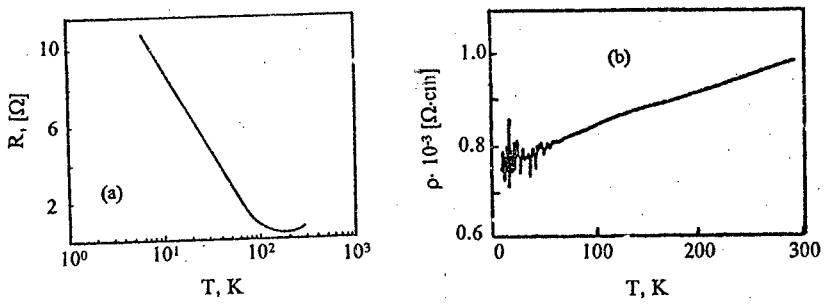

Fig.3. Temperature dependencies of the resistivity of the p^+-diffusion profile consisting of a LQW system, which was obtained at 900°C in n-type Si (100) wafer (a-low electric field; b-strong electric field).

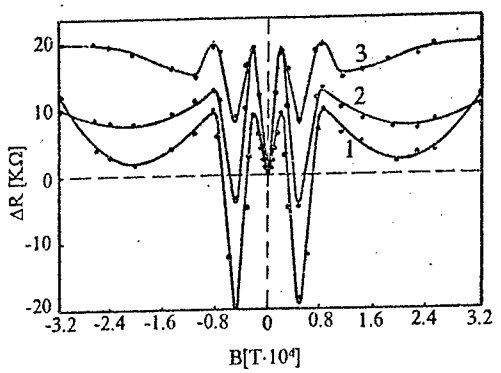

Fig.4. Variation of the resistance with magnetic field in 2D hole gas inside LaQW formed by dipole impurity ordering in ultra-shallow p^+n junction E| |[100] : 1-U=0.07V; 2- 0.13V; 3-0.22V.

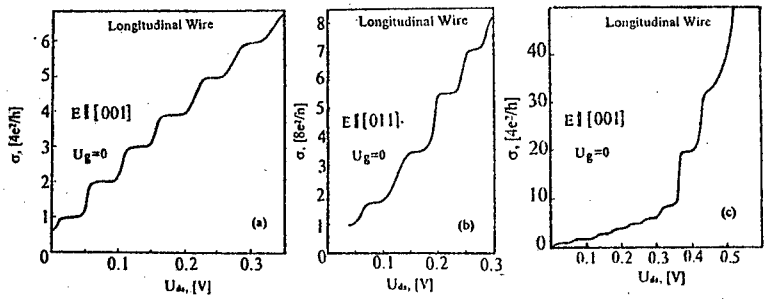

Fig.5. The quantized conductance (QC) at 77 K vs crystallographically-oriented drain-source voltage applied along the [001] (a,c) and [011] (b) crystallographic axes to the QW p^+-diffusion profile obtained at 900°C in n-type silicon (100)-wafer ($N(P)=2\cdot10^{14}cm^{-3}$) with a thin oxide overlayer.

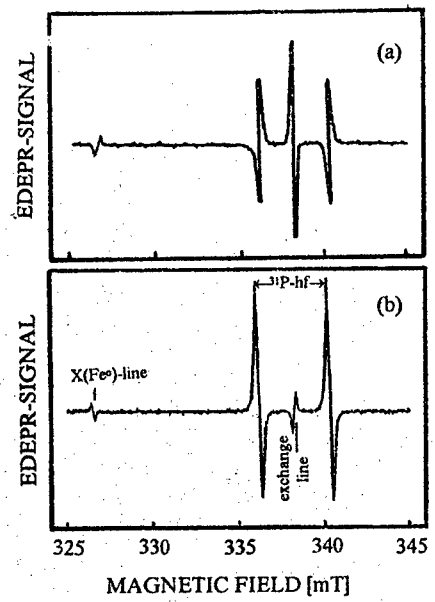

Fig.6. EDEPR signals of P-hf and exchange lines and additional X-line for QW n^+p junctions obtained at 1100°C. Magnetic field B||<111> in the plane perpendicular to the {100}-interface; T=3.8 K, microwave power 1 mW (a), 50 mW (b), ν=9.45 GHz.

Current Instabilities in the Auger Transistor

E.V.Ostroumova and A.A.Rogachev

A.F.Ioffe Physical-Technical Institute of RAS, St.-Petersburg, Russia

This paper is devoted to investigation of current instabilities in the silicon Auger transistor. For the first time we succeeded in fabricating the Auger transistor [1]. The main problem of Auger transistor is injection of high energy electrons. Another problem is to achieve a high frequency capability. Here is very important to inject high energy electrons into the collector region in which electric field is strong enough. These problems have been solved using an *Al-SiO_2- n-Si* heterostructure with tunnel transparent intermediate oxide layer [2-6]. In this case the role of the wide-gap emitter is played by a metal-oxide heterojunction.

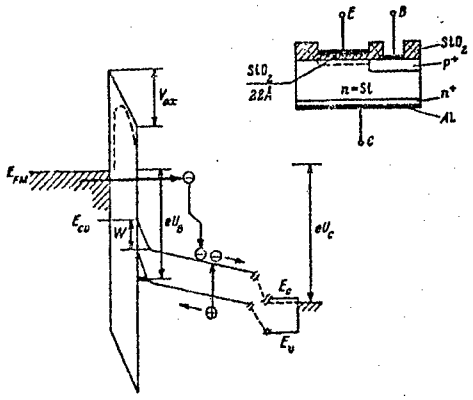

Fig 1.

Fig.1 shows the energy diagram of the Auger transistor based on the *Al-SiO_2 -n-Si* tunnel MIS-structure. In the transistor the metal is biased negatively with respect to the semiconductor. Base of the transistor is a hole charged layer induced by electric field which exists in the oxide layer. The thickness of the base is approximately equal to the width of surface selfconsistent quantum well for holes which about ~10^{-7}cm; the well depth is equal to 0.7 eV or higher [3]. In general the bigger is the voltage drop across the oxide, the higher is the energy of injected electrons.

As far as we know, virtually nothing has been published about other cases of successful use of the impact ionization process for the current amplification in transistors. The creation of electron-hole pairs by impact ioniz..tion is the fastest physical process in semiconductors, at lest known at present, which can be used for amplification and generation of electric signals. Another

semiconductor device using the Auger generation to obtain high frequency oscillations, is Read diode [7]. This device operates in a frequency range up to 10^{11} Hz or even higher. However this active device has two electric contacts, that cause considerable practical problems. The ionization and drift regions in the Auger transistor are strictly spatially separated. The energy of injected electrons is controlled by the base voltage. So the impact (Auger) ionization is governed by the base voltage, but drift of electrons depends mainly on the collector region. The electron-hole pairs are appearing in silicon layer which is about 100 Å thick. The collector voltage has very weak influence on the Auger ionization because the electric field in collector is too small. Although the presence of the base contact makes the operation a little bit slower, advantages of such a device are surely beyond any doubts.

We investigated the *S*- and *N*- type instabilities in the collector current of the Auger transistors in a circuit with a common emitter. The physical reason of instabilities is obvious. The electric current

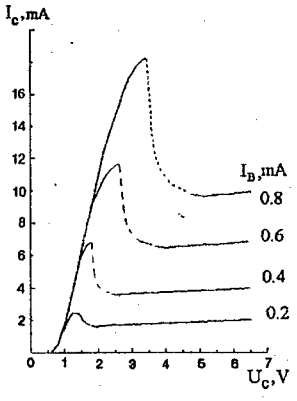

Fig.2

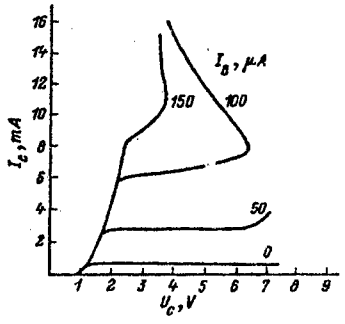

Fig.3

Fig.2,3 show the experimental common emitter output characteristics of the Auger transistor which were obtained for the *Al - SiO_2 - n-Si* structure. The thickness of the thermally grown silicon oxide layer (dry O_2), measured by means of ellipsometry, is 22 Å. Fig.2 shows the instabilities of *N*-type and Fig.3 shows the instabilities of *S*-type. The *N* -type instabilities in the Auger transistor are similar to the instabilities in the Read diode but this current instability in the Auger transistor is the fastest one.

depends not only on value of the base current , but also on *the time*. It is mainly the dissolving

time of the electron-hole clouds which are created by high energy electrons near the surface. There are two ways for the e-h cloud to be dissolved. The first is the e-h cloud is dissolved by electric field of collector. The second - dissolving of a e-h cloud by hole tunnel current to the metal. The former process leads to the *N*-type current -voltage collector characteristics (see Fig.2) and the latter one leads to S-type collector characteristics (see Fig.3).

In the previous publications [2,3] we discussed a model of a MIS Auger transistor, in which the role of the impact ionization process for the redistribution of the transistor currents was taken into account. The tunnel current of holes from silicon to the metal (a leakage) is always smaller than the electron tunnel current flowing from the metal to the conduction band of silicon, since the tunneling of holes from the silicon valence band to the metal via the oxide valence band is not likely to occur, because of the large effective mass of the holes in SiO_2: $m_h > 5$. At the same time, the tunneling of electrons from the metal to the silicon valence band via the oxide conduction band occurs over a much higher barrier than for the electrons tunneling to the silicon conduction band (Fig.1).

We also investigated the influence of surface quantum effects in a very strong electric field on the transistor operation [2-6].

The basic equation of the Auger transistor is [3]:

$$I_B + I_{Auger} - I_{ms} - I_{mv} = 0 ,$$

where I_{mc} is the electron tunnel current from the metal to the conduction band of the semiconductor; I_{ms} is the current due to the tunneling of holes from the interface surface states in the silicon forbidden gap to the metal ; I_{mv} is the current of holes which are attracted to the SiO_2 - Si interface by the oxide electric field, and tunneling to the metal through the oxide and I_B is the base current.

The *S*-type instabilities appear, when an additional hole current arising in the collector due to the impact ionization (the Auger hole current I_{Auger}) exceeds the hole current in the base circuit . Two values of the collector current correspond to one value of the base current. Every value of the base current can be in principle realized in two cases: the first at a smaller Auger current and a small base voltage, and the second at a high Auger current and a high base voltage. In the first case the collector current is small, and in the second case this current is rather high.

The calculated I–V characteristics of the Auger transistor are in a good agreement with the experimental data.

The *N*-type I-V characteristics of collector current may be explained by the following way. If a collector bias is small, electrons and holes which are the result of impact ionization (Auger) , are placed near the surface. The holes are placed in the hole selfconsistent quantum well and increase the depth of the well. It means the enhancement of transistor gain due to increase of impact ionization efficiency , which leads to increase of collector current. If we rise the collector bias, the density of electrons (and consequently of holes) near the silicon surface tends to be smaller. The impact ionization appears to be also smaller. Consequently electron current appears to be smaller too. As a result the collector characteristics became *N*-type.

In the Auger transistor there are two important time constants. First is related to charging of capacity which is formed by metal-insulator-surface of semiconductor plates. Under the current density of 10^3 A/cm^2 this time constant is equal to 10^{-10} sec. A time constant describing drift of electrons through collector is about 10^{-12} sec. Former time constant is important for S-characteristics. Latter process is important for N-characteristics. It is possible to envisage such on application of the Auger transistor .We generate pulses of 10^{-10} sec. long having frequency more then 10^{11} Hz. This is not a bad result for silicon based devices.

The work are supported by GKNT RF 213/68/4-2 , FTNS 96-1011 and RFFI 97-02-18358 grants

References

1. I.V.Grekhov, E.V.Ostroumova, A.A.Rogachev, A.F.Shulekin. Pis'ma v Zh.Tekh.Fiz., 1991, v.17, pp. 44-48. [Sov.Tech.Phys.Lett., 1991, v.17 (7), p.476].
2. E.V.Ostroumova, A.A.Rogachev. Abstr.II Intern.Symp. "Nanostructures: Physics and Technology", St.-Petersburg, Russia, 20-24 June 1994, p.209-211.
3. E.V.Ostroumova, A.A.Rogachev. Fiz.Tech.Poluprovodn. 28, 1411 (1994) [Semiconductors 28 (8), (1994)].
4. E.V.Ostroumova, A.A.Rogachev. "Microelectronics-94", Zvenigorod, Russia, 28 Nov.- 3 Dec. 1994 , Abstr., pp.367-368.
5. E.V.Ostroumova, A.A.Rogachev. 2dn Russian Conf. on Semicond. Phys., Zelenogorsk, 26 Febr.-1 March 1996, Abstr.,p 230.
6. E.V.Ostroumova, A.A.Rogachev. Proc. 26th European Solid State Device Research Conference (ESSDRC'96), p.245-248 Edit. by G.Baccarani & M.Rudan , Edition FRONTIERES, France, 1996 .
7. W.T.Read. Journ.Bell.Syst.Techn., 1958, v.37, p.401.

Carrier Transport and Mechanism of Porous Silicon Electroluminescence in Electrolytes

O. Sreseli, D. Goryachev, G. Polisski*, L. Belyakov, F. Koch*

Ioffe Physical-Technical Institute, 194021 St. Petersburg, Russia
** Technical University Munich, D-85747 Garching, Germany*

We report the polarization curves and electroluminescence (EL) of porous silicon (por-Si) - electrolyte interface. Based on these results and our previous data in [1-3], we suppose a new model of carrier transport and EL in the system of quantum-sized microcrystallites of por-Si in contact with electrolyte. The model explains the all properties of EL and helps to understand the difficulties of designing solid-state electroluminescent devices.

Por-Si layers on *n*- and *p*-type substrates were in contact with oxidizing electrolyte, acid solution of potassium or ammonium persulfate. The pulse EL is observed under cathodic current pulses with duration from 0.1 to 10 ms, amplitude from 10 to 500 mA/cm^2, and frequency ~11 Hz. The cathodic polarization curves (the current dependence on potential relative the SCE, negative to the semiconductor) were measured with voltage expansion rate 80 mV/cm^2 in the electrochemical cell with optically transparent window.

The EL spectra consist of two bands. The band with predominant intensity of EL, V-EL, has a peak at visible wavelengths whereas another EL feature, I-EL, is in near-IR range of optical spectrum [1]. The transient dependencies of both bands show a delay time between the current pulse and the rise of EL (Fig. 1). This time delay is longer for the V-EL band. The rise and fall time constants of EL are in the range from 0.1 to 10 ms and become shorter with the increase of current.

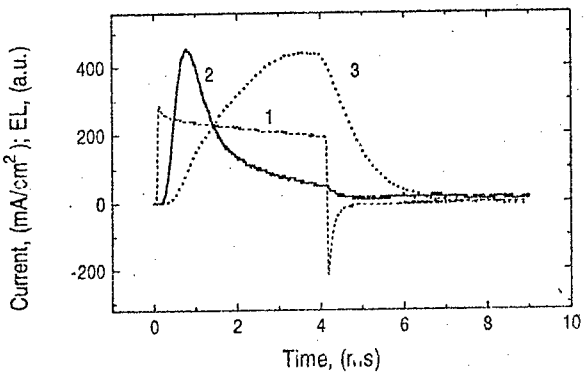

Figure 1. Current pulse (1) and EL pulses for IR (2) and visible (3) bands.

We have measured (Fig. 2) the polarization curves for the n-por-Si contacting with electrolytes of different wettability and viscosity due to addition of an organic solvent (acetone). They show a significant reduction of the resistance of the por-Si layer, being soaked in the electrolyte, with increasing wettability [2]. The data suggest that due to deep penetration of electrolyte into pores a large amount of current would rather flow through the substrate and large crystallites (bypass current) [3] than through the quantum-sized microcrystallites because of their high resistance and nearly full isolation from the substrate. The EL not only don't disappear in the process, but it appears at lower potentials as well (arrows in the Fig.2).

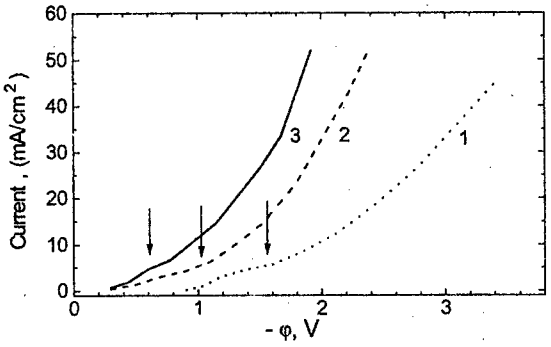

Figure 2. Polarization curves of the n-type por-Si contacting with electrolytes of different wettability. Wettability increases from (1) to (3).

The main role of the bypass current is seen to create new species injecting carriers into the semiconductor microcrystallites. As far as hole injection is concerned, the injecting species, short-living persulfate radicals, are known to be an injector. The electron injector could be atomic hydrogen. We found that the onset of EL (show by arrows) always coincide with the shoulder on polarization curves (Fig.2). This shoulder means the beginning of the second chemical reaction, the reduction of hydrogen ions (more precisely, H_3O^+ ions). Relative to porous silicon, atomic hydrogen is a strong reducing agent (his standard electrochemical potential is -2.1 V vs NHE) and so can inject electrons into the conduction band of microcrystallites. Therefore the bypass current generates simultaneously both short-living persulfate radicals (the hole injectors [4]) and atomic hydrogen (the electron injector). Both injectors can stick on the microcrystallites surface by diffusion and thereby inject electrons and holes into a microcrystallite. Their radiative recombination results in V-EL. Holes are injected in all crystallites, independent on their sizes and resistivity. The I-EL occurs as a result of hole radiative recombination with conduction electrons within the substrate and large crystallites. The delay times between current and EL pulses are due to the diffusion times of chemical species in the electrolyte.

Inter microcrystallite separation and the injection of carriers of both types from the electrolyte results in independence of the EL on the substrate conductivity and even on its type. This fact is confirmed by our observation of the EL from the interface of *p*-type por-Si /persulfate electrolyte in the same cathodic regime. We have measured polarization curves in the dark and with IR illumination (Fig.3). The current absence in the dark (curve 1) is understandable, because the semiconductor/electrolyte junction is reverse-biased in cathodic regime for p-Si.In case of IR illumination, absorbed only in the Si substrate, the photocurrent is nothing but bypass current. At curves 2 and 3 we see the same shoulder representing the reduction of hydrogen ions and onset of the V-EL (arrows) in the same region as it is in Fig.2. Saturation current of curves 2 and 3 is the photocurrent amplitude, defined by illumination intensity.

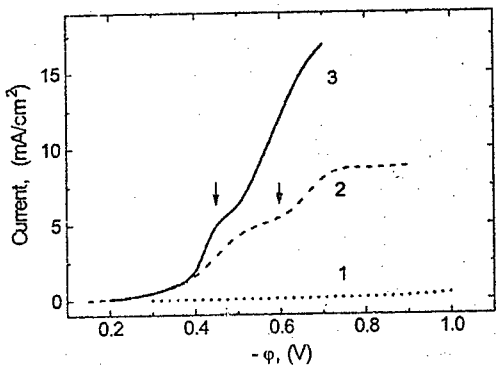

Fig.3 Cathodic polarization curves of p-type por-Si in the dark (1) and with IR illumination (2,3). IR intensity grows from (2) to (3).

To summarise we propose ionic transport of both type carriers and their bipolar injection into quantum-sized microcrystallites as a explanation of visible electroluminescence of porous silicon in oxidizing electrolytes.

The work is made at partial support of RFBR (grant N 96-02-17903) and INTAS (grant N 93-3325-ext).

[1]. O. Sreseli, V. Petrova-Koch, D. Kovalev, T. Muschik, S. Hofreiter, F. Koch. 22nd Int. Conf.on the Physics of Semiconductors. Vancouver, Canada. Ed. D.J. Lockwood, World Scientific, 3, p. 2117, (1994).
[2]. D.N. Goryachev, O.M. Sreseli, and L.V. Belyakov. Techn. Phys. Lett., **23**, 1, 35, (1997).
[3]. O.M. Sreseli, G. Polisski, D. Kovalev, D.N. Goryachev, L.V. Belyakov, F. Koch. Proc. of the 188th ECS Meeting, „Advanced Luminescent Materials", Ed. D.J. Lockwood, P.M. Fauchet, N. Koshida, and S.R.J. Brueck, **PV95-25**, 24 -29 (1995).
[4]. A. Bsiesy, F. Muller, M. Ligeon, F. Gaspard, R. Herino, R. Romestain, J. C. Vial. Phys. Rev. Lett., **71**, 637-639 (1993).

Optical Study of Silicon Nanostructure Evolution

V. Yu. Timoshenko[1], B.V.Kamenev[1] , J. Rappich[2] , Th. Dittrich[3]

[1]Faculty of Physics, M.V.Lomonosov Moscow State University, 119899 Moscow, Russia
[2]Hahn-Meitner-Institut, Abt. Photovolt., Rudower Chaussee 5, D-12489 Berlin, Germany
[3]Technische Universitat Munchen, Physik-Department E-16, D-85747 Garching, Germany

A porous silicon layer (por-Si) formed on the c-Si substrate due to electrochemical process is an example of the easy prepared silicon nanostructure. However, the mechanisms of the por-Si growth are still discussed and some models are still being proposed [1,2]. The in-situ investigation of the formation of por-Si at the initial state can help to get a deeper understanding of the processes of the nanostructure growth. Optical methods are contactless and highly sensitive. Therefore, they are the most suitable for in-situ control of nanostructure evolution (growth and modification).

In our study both a visible photoluminescence (PL) from growing silicon nanostructure and IR band-to-band PL from c-Si substrate were simultaneously investigated in situ during electrochemical process of porous silicon (por-Si) formation. Besides, the formed ultrathin (20-100 nm) por-Si layers (UPSL) on c-Si substrate were studied by an optical method of free-carrier absorption of a IR laser (3.39 μm) radiation. Nanosecond pulses of N_2 - laser (λ=337 nm) is used to excite carriers in c-Si and UPSL. The PL of c-Si and por-Si are measured at the wavelengths of 1100 nm and 600 nm respectively. The last wavelength is typical for the PL of por-Si in the red/orange region. UPSL was prepared on a p-type c-Si(100) wafer (ρ=5 Ω·cm) by anodization in 0.2 *M* NH_4F (pH 3.2). This electrolyte is well for the controlled formation of por-Si nanostructure [3]. The thickness of UPSL and its structure were controlled by field emission scanning electron microscopy (SEM).

Fig.1 shows the time dependence of the PL intensities of UPSL (open circles) and c-Si (solid circles) during the electrochemical formation of silicon nanostructure. An increase of the visible PL and a quenching of the c-Si luminescence are observed as a depth of the por-Si layer evolves from some nanometers to about 100 nm (region A on fig.1). A hydrogenation of silicon surface is found to restore the PL intensity of c-Si (region B). An anticorrelation of the PL intensities of UPSL and c-Si is observed after UPSL rinsing by water

(region C). The results demonstrate a strong redistribution of nonequilibrium carriers between silicon nanostructures and bulk material. The possible mechanism of such effect is the limitation of the out-diffusion of excess carriers from the por-Si layer into the c-Si bulk. The UV excitation light is absorbed at the top of por-Si. Therefore, the PL of c-Si is induced by carriers diffused from silicon nanostructure. Modification of the surface coverage of nanostructure changes value of the carrier transport barrier. For instance, the PL diminution of por-Si and increase of the c-Si take place after hydrogenation of UPSL (region B in fig.1).

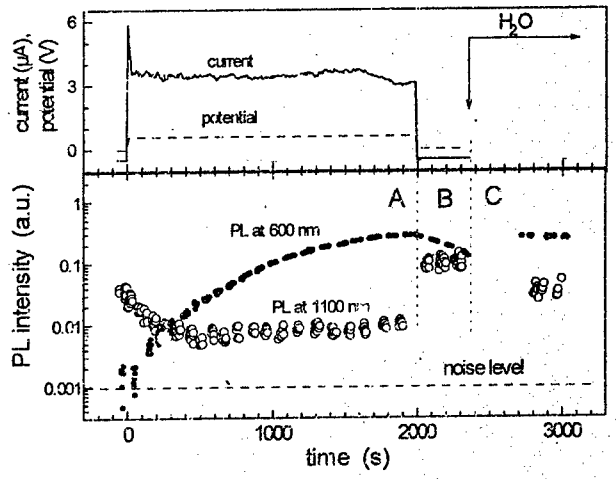

Fig.1. Dependencies of potential, current and PL of the c-Si bulk (λ=1100 nm) and por-Si nanostructure (λ=600 nm) during electrochemical growth of UPSL and its treatment.

It is found that the PL intensity of c-Si is reciprocal to the PL efficiency of silicon nanostructure after the change of ambients (water, ethanol, air). According to the free-carrier measurements the density of surface nonradiative defects (probably, silicon dangling bonds) don't change practically after the por-Si growth or filling by molecules of water or ethanol. Therefore, the different behavior of the PL of silicon nanostructure and the PL of c-Si can evidence about a specific effect

of polar ambients on the radiative recombination in nanostructure. Fig.2 shows, for example, the PL spectra of initial c-Si and UPSL in nitrogen atmosphere or in liquid water.

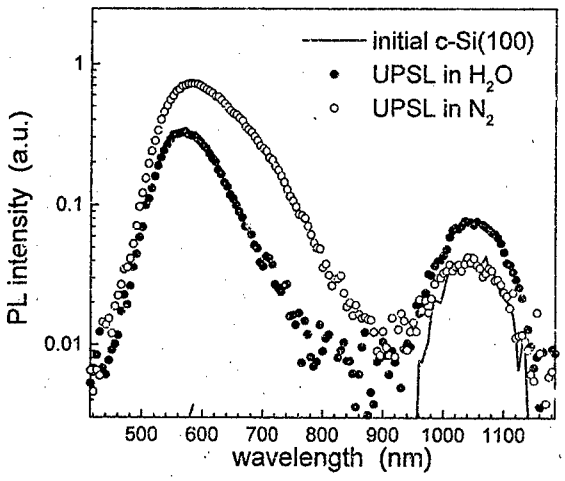

Fig.2. PL spectra of initial c-Si and UPSL in different ambients

The observed strong anticorrelation between the PL of the thin por-Si layer and the c-Si bulk can be explained as dielectric quenching of excitons in silicon nanostructure [4] and diffusion of additional free carriers into the c-Si region.

References.

1. R.L. Smith, S.D. Collins, J. Appl. Phys. **71**, R1(1992).
2. P.C. Searson, J.M. Macaulay, S.M.Prokes, J. Electr. Soc. **139**, 3373 (1992).
3. Th.Dittrich, S. Rauscher, V.Yu. Timoshenko, J. Rappich, I. Sieber, H. Flietner, H.J. Leverenz. Appl. Phys. Lett., **67**, 1134 (1995).
4. P.K. Kashkarov, E.A.Konstantinova, A.V.Pavlikov, V.Yu.Timoshenko. Phys. Low.-Dim. Struct., **1/2**, 123 (1997).

ELECTRONIC STRUCTURE OF Au-Si QUASI ONE-DIMENSIONAL SYSTEMS

V. G. Zavodinsky and I. A. Kuyanov
Institute for Automation and Control Processes
Vladivostok 690041, Russia, e-mail: zavodins@iapu2.marine.su

One-dimensional Au-Si chains have been observed on the vicinal surfaces Si(111) with different inclinations off the (111) plate [1, 2]. On another hand, Marks and Plass [3] have investigated the atomic structure of the Si(111)-(5×2)-Au surface phase. They have shown this phase has a rather complicated configuration. It consists of doubled linear Au chains pressed in the second silicon layer counting from the surface. One of the linear chains joins a zigzag silicon chain which surface bonds are saturated by Si adatoms. Another linear Au chain lies near a silicon chain with nonsaturated surface bonds.

To calculate the electronic structure of the quasi one-dimensional Au-Si systems we used the LDA method in the pseudopotential cluster version. The saturation of broken silicon bonds was executed using atoms of quasi hydrogen. To simulate the real atomic structure of the quasi one-dimensional Au domains on the Si(111) surface we used the data taken from the paper [3]. The main result is following: The electronic structure of this system has a metallic character. However, the main part of DOS at the Fermi level is made by Si atoms not by Au ones.

We have no information about the atomic structure of quasi one-dimensional domains formed by Au atoms on vicinal Si surfaces [2]. Therefore we have executed model calculations. Two cases were studied: **A**) silicon surface bonds are not saturated; **B**) all silicon bonds are saturated. A bandgap of 0.7 eV has been obtained for the **A** case. The reason is that Au *s* electrons are busy mainly on the saturation of nonsaturated silicon bonds: semiconduction properties of the silicon chain are increased, but the metallic binding between Au atoms even decreased.

In the **B** case the metallic character of the electronic structure has been obtained. Silicon bonds are saturated *ab initio* here, therefore the silicon role is to wide the "golden" wavefunctions (due to additional screening) and to improve their overlaping.

References

[1] L. Seehofer, S. Huhs, G. Falkenberg, R. L. Johnson, Surf. Sci., 329 (1995) 157.

[2] M. Jałochowski, M. Stróżak and R. Zdyb, 18th Int. Sem. Surf. Phys., Programme & Abstracts. Polanica Zdrój, Poland, 1996, p.40.

[3] L. D. Marks and R. Plass, Phys. Rev. Lett., 75 (1995) 2172.

The potential of aluminum single electron devices — A floating-gate memory and its higher temperature operation

J.S. Tsai, Y. Nakamura and C.D. Chen

NEC Fundamental Research Laboratories
34 Miyukigaoka, Tsukuba 305 Japan

We present here the recent results on the aluminum single electron device investigate of our group. Metallic single electron device usually provides a very periodic gate modulation that semiconductor single electron device most likely can not achieve. It also shows a transport characteristics that can be basically simulate and understand by a simple orthodox theory[1j. So compare to the semiconductor single electron devices, it is a more predictable technology. Moreover, aluminum tunnel junction is an established technology that provides a well controlled tunneling parameters with a large current density that required for a large transconductance. Thus the adoption of the aluminum tunnel junction as the building block of single electron device is a quite natural material choice. Combined with electron-beam-lithography delineation of the junction dimensions, aluminum single electron device technology so far has demonstrated several sophisticated functional operation[2] which no other technology can carry out.

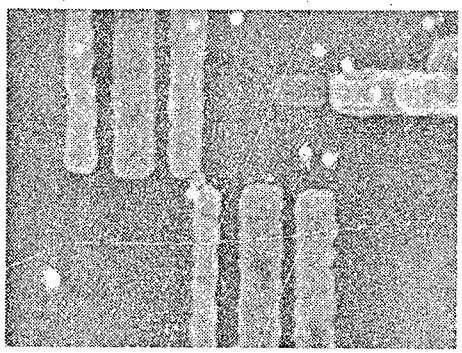

Fig 1. Aluminum SET with a 20nm island

However, the operating temperature of the aluminum single electron device have been typically limited to a deep dilution refrigerator temperature. Compared to semiconductor-based single electron device (with a same fabrication rule) that routinely

demonstrate higher temperature operation, this is not a satisfying characteristic[3]. We have demonstrated that with a good electron beam lithography and an improved angled evaporation, a 77K aluminum single electron device can be achieved. SET transistors were made with island size of 20nm, and they rea"zed an over-100K operation[4]. Figure 1 shows the SEM picture of such electrometer and its gate modulation characteristics are shown in Fig 2.

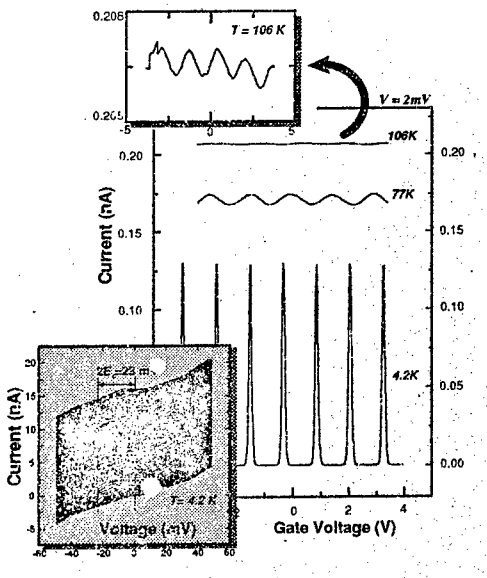

Fig 2. Gate modulation of 20nm transistor at various temperature and I-V curves taken at various gate voltages (inset).

To further demonstrate the applicability of such nitrogen-temperature aluminum single electron transistor, we created a single electron non-volatile memory cell incorporating a storage floating node, a gate electrode, a counter gate electrode, and a SET electrometer, all fabricated in aluminum[5]. Figure 3 shows the SEM picture of such memory cell.

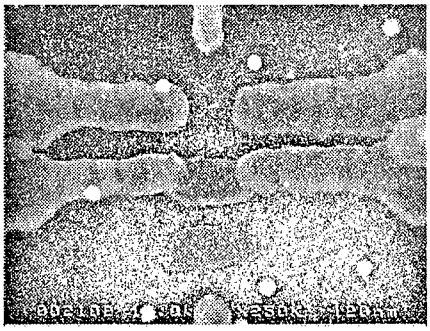

Fig. 3. A aluminum **floating-gate memory**

Electrons are injected from the gate to the floating node via Fowler-Nordheim emission. Because of the nonlinearity associated with the emission, a hysteretic characteristic appears in the relationship between the gate voltage and the electron number in the node. Thus a memory function is obtained. By employing a multi-electron operational mode, a background charge insensitive memory operation could be achieved [6]. The change in the electron number of the floating node is readout by the SET electrometer.

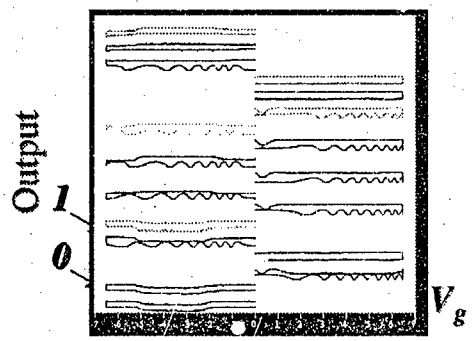

Fig. 4. Gate operation of aluminum **floating gate memory**

Figure 4 shows the electrometer output in the function of the gate voltage, and it shows a hysteretic memory function. The coupling between the node and electrometer is about

5 to 1, so each bit in Fig 4 is represented by about 40 to 50 electrons. The electrometer sensitivity limits the operation temperature of this memory, and in the present design, it is around 15K.

REFERENCES

[1] D.A. Averin, K.K. Likharev, *Mesoscopic Phenomena in Solid*, eds. B.L. Altshuler, P.A. Lee and R.A. Webb, (North-Holland, Amsterdam, 1991) Chapter 6.

[2] for example: L.J. Geerlis et al., Phys. Rev. Lett., 64, 2691, 1990; J.M. Martinis et al., 72, 904, 1994

[3] Y. Takahashi et al., Electron Lett. 31, 136, 1995

[4] Y. Nakamura, C.D. Chen, and J.S. Tsai, Jpn. J. Appl. Phys. 35, L1465, 1996

[5] C.D. Chen, Y. Nakamura, and J.S. Tsai, non published

[6] K.K. Likharev, A.N. Korotkov, Proc. of IWCE 95, to be published in VLSI Design

Fluctuations in single-electron tunneling

Alexander N. Korotkov
Nuclear Physics Institute, Moscow State University, Moscow 119899 GSP, Russia

Single-electron charging leads to the correlated tunneling of electrons in the systems of small tunnel junctions [1]. A simple and usually sufficient description of these effects is given by the "orthodox" theory [1] which treats electrons as classical particles jumping through tunnel barriers one-by-one. The rate of tunneling is determined by the corresponding energy gain, but the exact moments of tunneling events are random. This randomness leads to the intrinsic shot noise of the single-electron devices.

The simplest and probably the most important single-electron device is the Single-Electron Transistor (SET-transistor) [2] which consists of two tunnel junctions in series. The intrinsic noise limits the ultimate sensitivity of the SET-transistor making the theoretical study of the noise an important issue. One can find the first discussions of this problem in Refs. [2] and [3]. The quantitative theory of the shot noise was developed in 1991 [4,5] and was immediately applied for the calculation of the ultimate sensitivity of the SET-transistor. In the low-temperature limit the minimal detectable variation of the input charge Q_0 is given by expression

$$\min \delta Q_0 \simeq 2.7 C_\Sigma (RT\Delta f)^{1/2}, \qquad (1)$$

where T is temperature, R is the tunnel junction resistance, and Δf is the bandwidth.

To obtain Eq. (1) it is sufficient to use the Schottky formula, $S_I = 2eI$, for the approximation of the low-frequency spectral density S_I of the current I through SET-transistor. This is because the highest sensitivity is achieved in the vicinity of the Coulomb blockade threshold. The current here is carried by pairs of almost simultaneous tunneling events through two junctions of the transistor, leading to the simple Poisson process. However, the Schottky formula cannot be applied in the general case [4, 5], and the dependence of the ratio $S_I/2eI$ on the bias voltage (or gate voltage) is nontrivial. In particular, for vanishing dc bias voltage the pure thermal (Nyquist) noise is recovered. Crudely speaking, the visible features (cusps) in the dc I-V curve, which correspond to the change of the dynamics of tunneling events, necessarily have their counterparts in the $S_I/2eI$ vs. V dependence. This was recently confirmed experimentally [6] using STM-based SET-transistor. The deviation from the Schottky formula and several other particular issues of the SET-transistor noise were studied in a number of theoretical papers (see, e.g., Refs. [7-11]). Notice that in the special case when tunneling events in two junctions of SET-transistor occur in strict alternate sequence, the calculation of the current noise is formally equivalent to that in the resonant tunneling diode [12].

It may seem surprising that so far there is only one experiment [6] in which the white (thermal/shot) noise of the SET-transistor has been measured. The reason is that most experiments with SET-transistors are done at quite low frequencies (1-1000 Hz) where the contribution of 1/f noise due to fluctuating impurities dominates (the detailed study of the origin of this noise is still to be done, however, there is already some experimental progress in this direction – see, e.g., Ref. [13])

The SET-transistors operating at higher frequencies (which are necessary for a number of applications) has attracted the attention of experimentalists only recently, and we can expect that for these devices the intrinsic noise will be the major limiting factor for the charge sensitivity.

The shot noise is white for the frequency range of possible applications. The frequency dependence begins crudely from $f \sim I/e$ [4,5]; however, the spectral density does not have a peak at $f = I/e$ as in the case of an array of junctions [1]. The experimental observation of the frequency dependence is a difficult problem, but it seems to be achievable for the present-day experimental techniques.

The mathematical formalism developed in Refs. [4, 5] is suitable for the calculation of the spectral densities of currents or voltages in an arbitrary single-electron circuit (not containing Ohmic resistors). In particular, it was used [14, 15] for the calculation of the single-electron oscillations [1] in the arrays of junctions. However, the method requires the inversion of the matrix which dimension can be very large for complex circuits. In this case for the calculation of spectral densities one needs to use Monte-Carlo method which is much slower than "direct" calculations. Fortunately, there are several tricks significantly accelerating such simulations.

The "standard" method for the shot noise calculation which was used in Refs. [4, 5, 7-11, 14, 15] is based on the Fokker-Plank approach. The important features of the method are the operator-like properties of the tunneling rates in the expression for the correlation function and the existence of the separate terms which account for the high-frequency limit, $f \gg I/e$. Recently the complementary "quasi-Langevin" approach [16] (which is similar to the method developed in Ref. [17]) has been proposed. Two approaches lead to coinciding results for the "classical" shot noise which corresponds to the framework of "orthodox" theory. The advantage of the quasi-Langevin method is a natural generalization for the single-electron shot noise at "quantum" frequency range $f \sim E/\hbar$ (E is a typical energy) while these two frequency scales should be treated differently in the standard approach [14]. However, both approaches do not work in the intermediate frequency range if the frequency scales I/e and $E/\hbar$ are relatively close to each other. The correct theory in this case as well as other studies of noise beyond the "orthodox" model (there are only few of them so far—see Refs. [4, 14, 16, 18]) still present a virtually open topic.

References

[1] D. V. Averin and K. K. Likharev, in: *Mesoscopic Phenomena in Solids*, edited by B. L. Altshuler et al. (Elsevier, Amsterdam, 1991), p. 173.

[2] K. K. Likharev, IEEE Trans. Magn. **23**, 1142 (1987).

[3] M. Amman, K. Mullen, and E. Ben-Jacob, J. Appl. Phys. **65**, 339 (1989).

[4] A. N. Korotkov, D. V. Averin, K. K. Likharev, and S. A. Vasenko, *Proceedings of SQUID'91* (Berlin, 1991); in: *Single-Electron Tunneling and Mesoscopic Devices*, ed. by H. Koch and H. Lubbig (Springer-Verlag, 1992), p. 45.

[5] A. N. Korotkov, Ph. D. Thesis (Moscow State University, 1991); see also A. N. Korotkov, Phys. Rev. B **49**, 10381 (1994).

[6] H. Birk, M. J. M. de Jong, and C. Schönenberger, Phys. Rev. Lett. **75**, 1610 (1995).

[7] S. Hershfield, J. H. Davies, P. Hyldgaard, C. J. Staton, and J. W. Wilkins, Phys. Rev. B 47, 1967 (1993).

[8] L. Y. Chen, Mod. Phys. Lett. B 7, 1677 (1993).

[9] U. Hanke, Yu. M. Galperin, K. A. Chao, and N. Zou, Phys. Rev. B **48**, 17209 (1993).

[10] W. Krech and H.-O. Müller, Z. Phys. B **91**, 423 (1993).

[11] A. N. Korotkov, Appl. Phys. Lett. **69** (1996).

[12] L. Y. Chen and C. S. Ting, Phys. Rev. B **43**, 4534 (1991).

[13] A. B. Zorin, F.J. Ahlers, J. Niemeyer, T. Weimann, H. Wolf, V. A. Krupenin, and S. V. Lotkhov, Phys. Rev. B, **53**, 13682 (1996).

[14] A. N. Korotkov, D. V. Averin, and K. K. Likharev, Phys. Rev. B **49**, 1915 (1994).

[15] A. N. Korotkov, Phys. Rev. B **50**, 17674 (1994).

[16] A. N. Korotkov, to be published.

[17] Sh. M. Kogan, A. Ya. Shul'man, Zh. Eksp. Teor. Fiz. **56**, 862 (1969) [Sov. Phys. JETP].

[18] D. V. Averin, in: AIP Conf. Proc. **262** (ed. by Ari Aviram), p. 267 (1991).

Room temperature hysteresis behavior of IV-curves and memory effects in granular metal-dielectric films

S.A.Gurevich, D.A.Zakheim, V.V.Horenko, T.A.Zaraisk.ya, E.M.Tanklevskaya

A.F.Ioffe Physical-Technical Institute Russian Academy of Science
26, Polytekhnicheskaya st., 194021 St.-Petersburg, RUSSIA.

In this work we report on unusual electrical properties of amorphous SiO_2 films containing nanometer-size Cu particles. The films were fabricated by means of magnetron co-sputtering technique in Ar atmosphere Results of transmission electron microscopy, x-ray diffraction analysis and x-ray photoelectron spectroscopy show the presence of metallic particles with typical sizes of several nanometers embedded in SiO_2 matrix [1,2]. All experimental data were taken on unannealed films with Cu concentration 24 vol.%. In order to perform electrical measurements the film was deposited on Au layer used as a down contact. The top contact was designed as Cr circles 20 μm in diameter (see inset in Fig. 1).

Room temperature I-V curves of fabricated samples are shown in Fig.1. As it can be seen from the figure, the sample conductivity rapidly increases at voltages above the threshold level $U_t \approx 4V$, which corresponds to electric field in film $E_t \approx 2 \times 10^5$ *V/cm*. The other salient feature of I-V curves in Fig.1 is the hysteresis dependence of current with respect to the applied voltage. With initial voltage increase from zero to some value above the threshold U_t, the current follows branch 1 (with low differential conductivity in under-threshold region). With subsequent voltage reduction the current follows the branch 2 with higher conductivity and I-V characteristic of the sample would remain on this curve for long time if applying positive voltages lower than threshold value U_t. However, the system can be returned to the state with low differential conductivity by applying negative voltage U, $|U|>U_t$. In this case the I-V curve behaves in a similar way: first, current follows the branch 3 and when decreasing absolute value of applied voltage – branch 4. After that, if positive voltage is applied again, the I-V curve would follow branch 1.

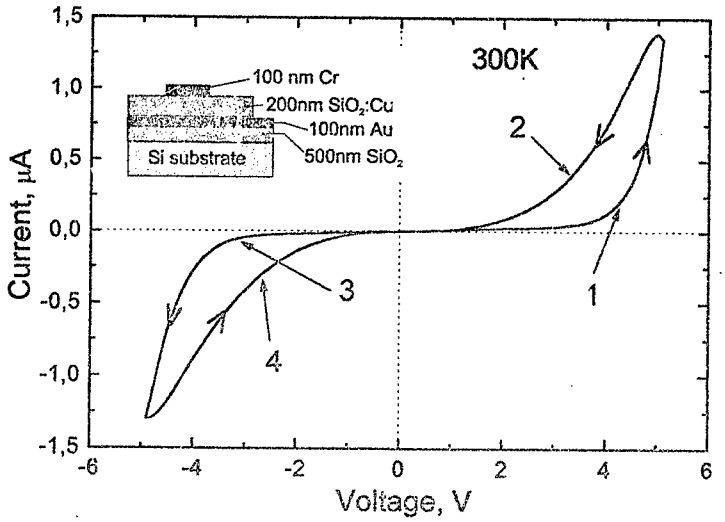

Fig.1 Hysteresis in I-V curves of composite film. Arrows indicate the original loop when voltage changes as 0→5V→ -5V→0 and so on. Inset: schematic sketch of the sample.

Thus, the investigated sample appears to be a non-volatile memory cell, in which logical states 0 and 1 correspond to low and high values of conductivity measured at some trial voltage $U_r<U_t$. The writing and erasing of information can be implemented by means of application of positive and negative voltage pulses with amplitude $|U_w|>U_t$. In our experiments the sample was switched between states with high and low differential conductivity by 10 μs pulses with amplitude *±20V* and the state was tested by 10 μs pulses with amplitude *-3.5V*. The retention time in so doing comprised several hours.

The observed electrical properties can be attributed to the process of single-electron recharging of metal granules [3]. Such a charged states having very long lifetimes can substantially affect the current flow through the film [4]. The experiments performed on the structures with different film thickness, contact layout, and type of contact metal suggest that hysteresis behavior of I-V curves is associated with thin (less than 100nm) film layer adjacent to the bottom contact where the microstructure differs from that of bulk composite material.

[1] S.A.Gurevich, T.A.Zaraiskaja et al, *Physics of the Solid State,* to be published
[2] A.V.Kolobov, H.Oyanagi et al, *J.of Surf.Analysis*, 3 (1997), to be published
[3] S.A.Gurevich, V.V.Horenko, L.Yu.Kupriyanov et al, *JETP Letters,* 64, 684 (1996)
[4] K.Yano, T.Ishii, T.Hashimoto et al, in *Dig. IEDM Washington 1993,* p. 21.2.1

Noise in metallic SET transistor with an island isolated of the substrate

V. A. Krupenin, D. E. Presnov, M. N. Savvateev

Laboratory of Cryoelectronics, Moscow State University, 119899 Moscow, Russia

H. Scherer, A. B. Zorin

Physikalisch-Technische Bundesanstalt, D-38116 Braunschweig, Germany

In the last decade, the technology of the metallic Single Electron Tunneling (SET) circuits fabrication has made great progress. Numerous and fine experiments with various SET structures, forming a new type of quantum electronic devices, were carried out. They are: detailed investigation of the SET electrometer, performance of SET pump with the accuracy 10^{-8} [1], demonstration of the memory effect in SET trap with storage time of several hours for one electron [2] and many others. These structures have been successfully demonstrated a possibility of single electrons controllable transport using. However, the experiments have also shown that the performance of SET devices depends strongly on the background charge fluctuations. At low frequencies, they substantially dominate over intrinsic fluctuations in SET devices. That is why the understanding of the background charge noise nature and the search for ways of its reducing are very important for practical realization of the SET devices. In last years first attempts to define the noise sources localization in metallic SET structures have been done[3,4]. These experiments have shown that significant part of charge noise sources could be distributed in thin dielectric layers adjacent to the central island of the transistor and in a volume of the substrate.

To continue the investigations, which could give an answer about a localization of the background charge fluctuations sources, we have fabricated and measured the SET transistor structure where the island has quite small (in area) or no contacts with the substrate. The idea is to isolate (screen) the island and exclude the input of noise sources in the substrate into total noise of the transistor. The geometry of experimental structure is depicted on Figure 1. The central island was placed on one of transistor electrodes to be screened by it from the substrate.

The experimental structures were fabricated on the Si-substrate buffered by sputtered 200 nm thick AlO_x film. First, the wafer was coated by trilayers PMMA-MAA Copolymer/Ge/PMMA with the corresponding layer thickness of 350/20/80 nm. Next, e-beam exposure was performed with the raster electron microscope. After the following wet develop process of the top PMMA the reactive-ion etching was done. In the course of the etching the pattern in PMMA is being transferred to the underlaying Ge layer. Then Ge mask was in turn used for anisotropic patterning of the copolymer layer, in-situ followed by formation of an undercut which was necessary to allow enough room on the substrate surface to accommodate Al layers shifted in respect to each other. After the mask was formed it was

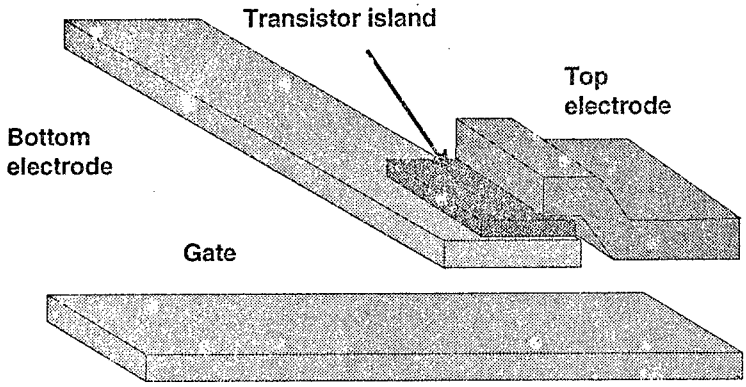

Figure 1. Topology of the transistor

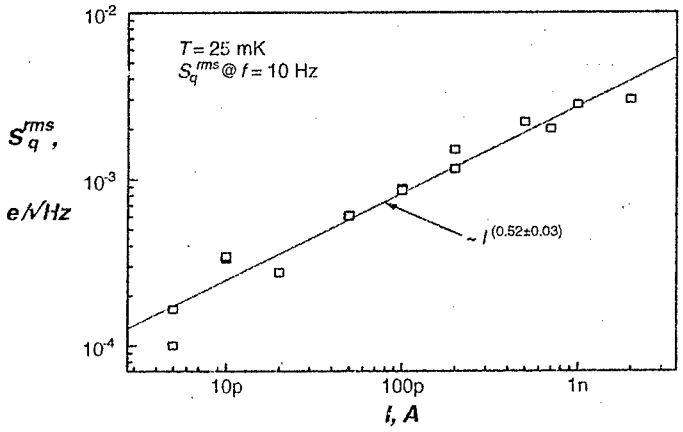

Figure 2. Noise level at 10 Hz depending on bias current

used for deposition of Al forming the strictly defined shadows on the substrate. The deposition was performed on the tilted table. There were tree successive deposition cycles *in-situ* with different angles of the table tilt. Between the depositions we oxidize previous layer of Al. Finally the sample was put in acetone bath for lift-off of all the film resting to the mask top.

We are presenting preliminary results of noise measurements in new topology SET transistor. One can see the results of noise measurements in Figure 2. The dependence noise level on bias current is very strong and is differ from the dependence for a transistor of traditional topology. It could be accounted for very small size of central island (80nmx100nmx15nm) and as a result strong hot electrons effect in this structure. However, the value of charge fluctuation level for small bias current (5 pA) is equal $1 \cdot 10^{-4}$ e/(Hz)$^{1/2}$ at 10 Hz and one can suggest that in the absence of strong hot electrons effect it could be even smaller. In order to switch off hot electrons effect we have use much smaller than 5 pA bias current or to increase a volume of the central island.

Further experiments are in progress.

The work is supported in part by the Russian Scientific Programm "Physics of Solid State Nanostructures", Russian Fund for Fundamental Research and German BMBF.

1. M.W. Keller, J.M. Martinis, A.H. Steinbach, and N.M. Zimmermann, submitted to IEEE Trans. Instrum. Meas. 6/96; M.W. Keller, J.M. Martinis, N.M. Zimmermann, and A.H. Steinbach, Appl. Phys. Lett. **69**, 1804 (1996).

2.P.D. Dresselhaus, L. Ji, S. Han, J.E. Lukens, and K.K. Likharev, Phys. Rev. Lett. **72**, 3226 (1994)

3. F.-J.Ahlers, J. Niemeyer, D. Quenter, T. Weimann, H. Wolf, A.B. Zorin, V.A. Krupenin, S.V. Lotkhov. Background charge noise in metallic single-electron tunneling systems. Phys.Rev.B, 1996, **53**, 13682-13687.

4.H. Scherer, V.A. Krupenin, S.V. Lotkhov, T. Weimann, A.B. Zorin and F.-J. Ahlers. Symp. on single-electron nanoelectronics. San-Antonio, Texas, USA (1996)].

Observation of Charge Effects on Semiconductor Surface by Low-Temperature Scanning Tunneling Spectroscopy

N.S. Maslova, S.I. Oreshkin, V.I. Panov, S.V. Savinov, A. Depuydt*, C. Van Haesendonck*

Department of Physics, Moscow State University, 119899 Moscow, Russia
**Universiteit of Leuven, Celestijnenlaan 200D, B-3001 Leuven, Belgium*

During the last few years there was plenty of low-temperature scanning tunneling microscopy (STM) and scanning tunneling spectroscopy (STS) data for oscillations of tunneling conductivity, connected with surface defects of mesoscopic and nanometer size. Often such experimental effects are ascribed to Coulomb blockade and Coulomb staircase or to resonant tunneling through localized states associated with the defect or with dimensional quantization levels [1,2,3,4]. However there is no universal answer which concrete mechanism leads to the appearance of tunneling conductivity oscillations.

In the present work [5] we report on the results of low temperature STM/STS investigations of atomic size clusters on an InAs surface. We investigated both details of the surface structure and charge effects on the surface. The most important results obtained in our experiments are: i) enormously large semiconductor band gap value (about 1.8 eV) has been observed above the flat surface region; ii) Fermi level is shifted from conduction band inside the band gap in spite of high doping ratio; iii) strong decreasing of measured band gap value occurs above the atomic cluster, but Fermi level still remains in the band gap; iiii) oscillations of tunneling conductivity near the band gap edges has been observed above the flat surface and also above the cluster, but the period of these oscillations differs.

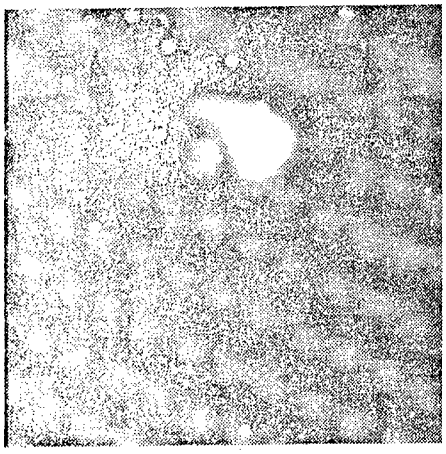

FIG. 1 STM image of a cluster on the InAs [110] surface. Scan size: 44 Å x 44 Å. Setpoint current: 100 pA. Sample voltage: -500 mV. Grey scale range: 0 to 5 Å.

We connect the observed behaviour of tunneling conductivity above the flat surface and above the cluster with charge effects caused by tip and defect induced band bending, using unique theoretical approach. In the frame of such approach the existence of localized states, finite relaxation time of unequilibrium electrons and Coulomb correlations have to be taken into account.

All the STM/STS investigations have been carried out by means of a low temperature STM with an *in situ* cleavage mechanism to obtain a clean sample surface at low temperature[6]. The samples used in the experiments are

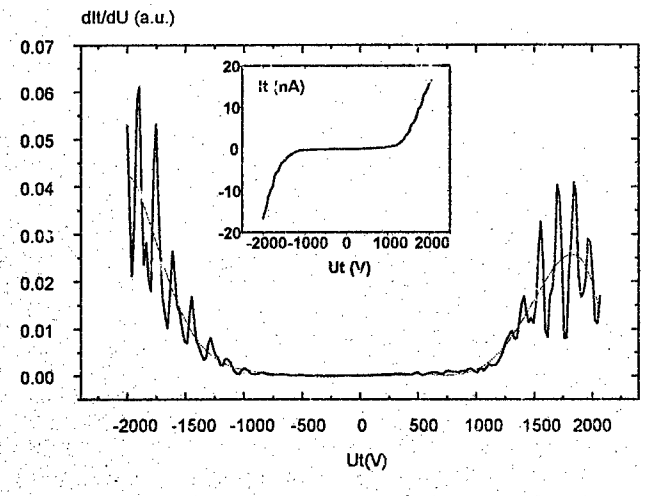

FIG. 2. The differential conductance dI/dV(V) above the atomically flat region. Best fit polynom to stress the presence of the oscillations. I(V) dependence is depicted on the insert.

highly doped ($n \sim 5*10^{17}$ cm^{-3}) n-type InAs semiconductor monocrystals which are cleaved along [110] plane in vacuum after He temperature was achieved.

STS measurements of the local density of states have been carried out above the flat InAs surface regions. A typical I(V) curve is shown on the insert of Fig.2. The presence of the wide gap ~ 1.8 eV is clearly seen on the I(V) curves. The measured surface band gap value strongly differs from its bulk value 0.43 eV at 4.2K.

Another remarkable result is the observation of the tunneling conductivity oscillations on the dI/dV(V) curves near the band gap edges (Fig. 2). The period of these oscillations is about 0.14 eV. We ascribe these oscillations to the influence of the localized states appearing due to tip induced band bending.

In our experiments we observed atomic size clusters on the atomically flat InAs surface in the topographic STM mode. On Fig.1 a cluster, consisting of 3 atoms (2 atoms are identical and the third one is different) is depicted. The lateral size of the cluster image is about 10 Å and its height is less than 5 Å. STS measurements have been made right above the cluster (Fig.3). The main feature of the dI/dV(V) curves is the decrease of the gap value to approximately 0.4 eV (bulk value), while for flat surface regions the observed gap has been about 1.8 eV (Fig.2). However, E_f remains inside the gap as for flat surface regions. At the gap edges oscillations of the tunneling conductivity versus applied bias can be seen from Fig.3. The typical period of these oscillations is about 0.09 eV. We suppose that the oscillations (different from those, observed above the flat surface) appear due to the localized states, caused by the changing of the band bending in the vicinity of the atomic cluster.

Our interpretation of the conductivity oscillations is not ascribed to Coulomb blockade or to Coulomb staircase effects. If such oscillations are caused by a Coulomb blockade due to cluster charging, the period of these oscillations can be simply estimated: If a is the cluster size, then the oscillation period is $\Delta E \propto e^2/a$. For a~5-10 Å we obtain $\Delta E \sim$ 1-0.5 eV which does not coincide with the experimental data.

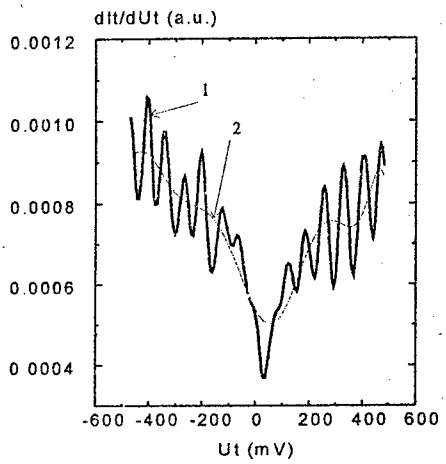

FIG. 3. (a) The differential conductance dI/dV(V) measured above the atomic size cluster shown on Fig. 3.
(b) Best fit polinom is shown to clarify the band gap width estimation.

We explain our experiments in the following way. First of all we connect the observed enormously large value of InAs band gap on the flat surface regions (~1.8 eV) with tip-induced band-bending, which depends on the polarity of the applied bias (Fig.4). Such band bending may be caused by localized charged states of the tip. For positive tip bias such states have positive charge, and for negative tip bias such states are occupied by electrons and have negative charge. The band-bending value W can be estimated as $W \propto e^2/b$, where b is the tip- sample separation. For b~ 5-10 Å, one obtains W ~ 1-0.5 eV. The experimentally observed band gap is $E_g \propto 2W + E_g$, where E_g ~ 0.43 eV, the bulk value of the band gap. So, if such band bending occurs the observed gap value of 1.8 eV coincides with our theoretical estimations.

In the presence of the atomic cluster, the band bending changes in the vicinity of the cluster (Fig.4). This can occur due to the charged localized states associated with the cluster. For positive tip bias such states are filled and have negative charge while for negative bias they have positive charge. These states partially compensate tip-induced band-bending and the observed band gap above the cluster decreases approximately to its bulk value. However E_f still remains in the band gap. This fact can be explained by asymmetric band-bending. The bending of the conduction band differs from the valence band bending, because the bending depends on the applied bias. The oscillation in the tunneling conductivity near the gap edge in the vicinity of the cluster can also be associated with localized states, formed in the quantum well, which is now changed by the presence of the atomic cluster. That is why the period of such oscillations near the cluster (0.09 eV) is smaller than the oscillation period above the flat surface region (0.14 eV). Oscillation periods in tunneling conductivity above the flat surface and above the defect differ because the quantum wells formed by band bending are not the same. So do dimensional quantization levels (DQL).

In general, tunneling conductivity oscillations can be connected not only with surface localized states but also with

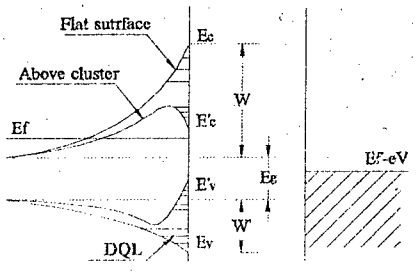

FIG. 4. Schematic energy diagram of STM tunneling junction with charge induced band bending

tip localized states. The interaction of such states with the sample surface can considerably change the initial electronic structure of the sample under investigation. In particular, additional localized states can appear in the band gap [7,8]. In this case the common model of tunneling processes drastically changes [9] and the tunneling current can be determined by these additional states for bias voltages less than the gap value, if the finite relaxation time of unequilibrium electrons is taken into account. In this case the value of the tunneling current will be determined by the relaxation rate of unequilibrium electrons, which is connected with tunneling processes, electron scattering, interaction with the substrate and thermal relaxation.

In conclusion, we have observed details of the surface structure and charge effects above the flat [110] InAs surface and above the atomic size cluster by means of STM/STS at low temperature. To explain the unusual behavior of the tunneling conductivity in the frame of unique theoretical approach, we have to take into account tip-induced band bending, the existence of localized states and the finite relaxation time of the unequilibrium electrons.

Depending on the applied bias charge effects lead to: i) enormously large band gap above the flat [110] InAs surface with Fermi level lying inside the band gap; ii) local decreasing of gap value in the presence of atomic cluster due to partially compensation of tip-induced band bending by cluster charge; iii) oscillations of tunneling conductivity near the gap edges connected with localized states appearing in quantum wells due to band bending.

References

[1] A.T. Johnson, L.P. Kouwenhoven, W. de Jong, N.C. van der Vaart, C.J.P.M. Harmans, C.T. Foxan, Phys. Rev. Lett. **69**, 1592 (1992).

[2] E.B. Foxman, P.L.McEuen, Ned S. Wingreen, Yigal Meir, P.A. Belk, N.R. Belk, M.A. Kastner, Phys. Rev. **B47**, 10020 (1993).

[3] A.E. Hanna, M.Tinkham. Phys. Rev. **B44**, 5919 (1991).

[4] D.V. Averin, A.N.Korotkov and K.K. Likharev. Phys. Rev. **B44**, 6199 (1991).

[5] N.S. Maslova, V.I. Panov, S.V. Savinov, C. Van Haesendonck, A. Depuydt, Preprint Dpt. of Physics MSU, N9, 1997 and Phys.Rev.Lett. (to be published)

[6] S.I.Oreshkin, V.I. Panov, S.V. Savinov, C. Van Haesendonck, A. Depuydt, S.I Vasil'ev, Preprint Dpt. of Physics MSU, N5, 1997 and Pribory I Technika Experim. (to be published)

[7] N.S. Maslova, Yu.N. Moiseev, V.I. Panov, S.V. Savinov, D.A. Znamensky, Sov. Phys. JETP **75**, 505 (1992).

[8] N.S. Maslova, Yu.N. Moiseev, V.I. Panov, S.V. Savinov, S.I. Vasil'ev, I.V. Yaminsky, Phys. Stat. Sol. (a) **131**, 35 (1991).

[9] P.I. Arseyev, N.S. Maslova, Sov.Phys. JETP **75**, 575 (1992).

EXPERIMENTAL INVESTIGATION OF THE INFLUENCE OF THE ELECTROMAGNETIC ENVIRONMENT ON CHARGING EFFECTS IN ULTRA-SMALL TUNNEL JUNCTIONS

Yu. A. Pashkin*, Sh. Farhangfar, J. J. Toppari, and J. P. Pekola

Department of Physics, University of Jyväskylä, P.O. Box 35, 40351 Jyväskylä, Finland

Charging effects in a single tunnel junction are affected by the external electromagnetic environment which it is attached to [1]. In the case of an ideal current source, the junction should exhibit a perfect Coulomb blockade when the tunnelling current is completely suppressed below a threshold voltage. In the opposite limit of an ideal voltage source the charging effects should vanish. In the real experiment one should consider carefully the bias circuit of the junction. When a small tunnel junction connects to its bias circuitry with a very high impedance, we expect to observe Coulomb blockade in its *IV* characteristics. A theoretical study based on the microscopic theory [1] yields, in the limit of high environment resistance R_e and at high temperature T, a similar, universal first order result for the conductance, G/G_T, (in T^{-1}) as for an array [2], independent of R_e, G_T being the asymptotic tunneling conductance. The dependence on R_e appears only in higher order corrections. At lower T the *IV* caracteristics can be calculated by numerical means. In some cases the behaviour of a single junction can also be explained with the so called "horizon" model, which is a simplified picture consistent with the microscopic theory [3].

Recently we have performed experiments with single junctions in a lithographically patterned resistive environment. The nanoscale chromium based resistors, fabricated in a single cycle with Al/AlO_x/Al tunnel junctions, were placed near the junction, with a separation distance ranging from 1-2 μm up to 200 μm. Our calculations based on the approach developed by G.-L. Ingold and Yu. V. Nazarov [1] describe the *IV* characteristics seen in the experiments reasonably well. When the separation between the junction and resistors does not exceed 10 μm the purely resistive approximation of the external circuit works well at least for $R_e \geq 1$ kΩ. However, with larger separation, one should consider the junction as to be connected to an RLC-transmission line with a termination resistor at the end.

The resistors we used were 3 or 10 μm long and had a sheet resistance of $0.3 \div 6$ kΩ/μm.

An example of a measurement in a purely resistive environment is shown in Fig. 1. The single junction with a tunnel resistance $R_T = 145$ kΩ was biased through four resistive leads having a resistance of about 60 kΩ each. At $T = 4.2$ K the conductance curve shows a dip of 6.3 % at zero bias from which the junction capacitance can be estimated (Fig. 1a). A rough estimation of the capacitance can be made using the high temperature ($k_BT >> E_c$, where k_B is the Boltzmann constant and E_c is the charging energy) dependence derived in [4,2]. This way we obtain the value for the capacitance $C = 1.17$ fF. A more accurate fit of the conductance curve using the microscopic theory gives $C = 1.13$ fF. The fitting curve with only one fitting parameter C is shown as a solid line in Fig. 1a. The same value of the junction capacitance was used to calculate the conductance curve at lower temperatures and a good agreement with the experiment has been found. Both experimental and calculated conductance curves at $T = 0.16$ K are presented in Fig. 1b. The small difference between the two curves can be attributed to the external noise and overheating of resistors at finite bias.

A collection of conductance curves corresponding to different separation between

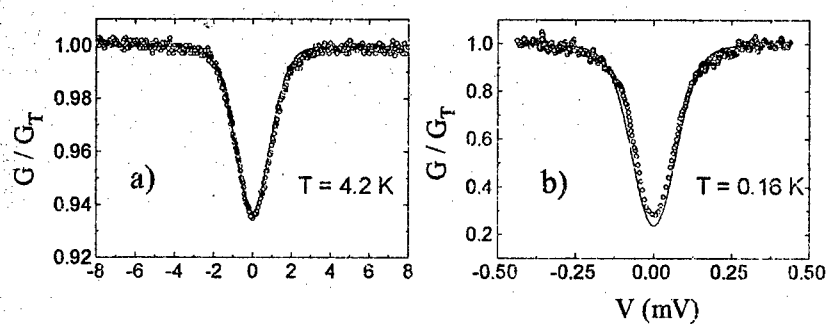

Fig. 1. Differential conductance of a single junction in a resistive environment ($R_e = 60$ kΩ) at two temperatures: $T = 4.2$ K (a) and $T = 0.16$ K (b) for the shallow and deep characteristics, respectively. The calculated curves, with $C = 1.13$ fF, are shown by the solid lines at the same temperatures. Note the difference of both the horizontal and vetical scales in a) and b), respectively.

the single junction and resistors is presented in Fig. 2. The curves drawn in thin and thick lines relate to junctions with closely connected resistors and with 100 μm separation, respectively. The qualitative difference of the latter curve from the others is rather apparent: unlike those of a short separation, it is not described by the g-function dependence [4] but it rather reaches the asymptotic conductance at a much higher bias voltage. Nevertheless, it can also be calculated fairly well using the approach developed in [1]. When the separation between the junction and resistors is large, the external circuit is assumed to be an RLC-transmission line with a terminating resistor at the end. From the calculated curve (which is not presented here) we obtaine a junction capacitance of 0.7 fF. The following parameters of the transmission line were used in the calculation: line capacitance 3 fF, line inductance 200 pH and the terminating resistor 4 kΩ. The first two of these are our estimations based on several earlier experiments and the resistance could be measured in a four wire configuration. The line resistance had very little effect at 4.2 K and it was set to zero in the calculations. The capacitances of the junctions in a resistive environment were estimated to be 1.4 fF, 0.69 fF and 0.47 fF from top to bottom, respectively. Note that the capacitance of the junction connected to the transmission line is very close to that of one of the junctions in a resistive environment (middle thin line), however the strength of the dips are about 3 times different (3.7 % and 9.4 %, respectively). This is consistent with the model we use because the transmission line contributes to the junction capacitance. This is the case even with short separation which resulted in the saturation of the depth when we tried to decrease the junction capacitance. In our experiments we could never go beyond 15 % depth which is probably determined just by the stray capacitance of the bias leads of the

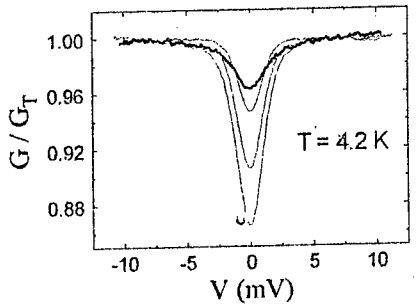

Fig. 2. Differential conductance curves of single junctions connected to RLC-transmission line (thick) and to resistive leads (thin).

order of 0.03 fF/μm. In principle, the resonances in the transmission line should be seen as steps in dI/dV curves corresponding to excited modes in the line [5]. The distance between the steps is determined by the line parameters. The necessary condition for the resonances is low damping, i.e., the total line resistance should be lower than 100 Ω. In our configuration the line resistance exceeded this and we believe this is the major reason why the resonances were not observed so far. Further experiments are under way.

The work was supported by the Academy of Finland and Jyväskylä Science Park. Yu. A. Pashkin also acknowledges support from RFBI (grant # 97-02-17056) and the Russian Program on Nanostructure Physics (grant # 1-071).

* Permanent address: P.N. Lebedev Physical Institute, Russian Academy of Sciences, 117924 Moscow, Russia.

REFERENCES

[1] G. - L. Ingold and Yu. V. Nazarov, in *Single Charge Tunneling. Coulomb Blockade Phenomena in Nanostructures*, ed. by H. Grabert and M H. Devoret (Plenum, New York, 1992), p.21.

[2] Sh. Farhangfar, K. P. Hirvi, J. P. Kauppinen, J. P. Pekola, J. J. Toppari, D. V. Averin, and A. N. Korotkov, J. Low Temp. Phys., July (1997).

[3] J. P. Kauppinen and J. P. Pekola, Phys. Rev. Lett. 77, 3889 (1996).

[4] J. P. Pekola, K. P. Hirvi, J. P. Kauppinen, and M. A. Paalanen, Phys. Rev. Lett. 73, 2903 (1994).

[5] T. Holst, D. Esteve, C. Urbina, and M. Devoret, Phys. Rev. Lett. 73, 3455 (1994).

Single-Electron Transport in a Lattice of InSb Quantum Dots

S.G. Romanov[1,2], A.V. Fokin[1], D.K. Maude[3], J.C. Portal[3,4]

[1]Ioffe Physical Technical Institute, St.Petersburg, 194021, Russia
[2]University of Glasgow, Glasgow G12 8QQ, UK
[3]High Magnetic Field Laboratory-CNRS, F38042 Grenoble, France
[4]INSA-CNRS, 31077 Toulouse, France

A variety of low-dimensional structures accommodating a small number of free electrons were designed using both metals and semiconductors [1,2] in order to fabricate single electron tunnelling (SET) devices. Periodic arrays of tunnel junctions revealed both sequential tunnelling and co-tunnelling phenomena, but these arrays were restricted to the case of several linear chains in parallel. To prepare 3D lattice of nanoparticles we have used structural confinement.

The 3D lattices of InSb grains were designed within the free volume of an opal. An opal is the close packing of nearly identical silica balls [3], in the studied samples ball diameters D were 227 and 304 nm. In *fcc* packing of balls the large $d_1=0.41D$ and small $d_2=0.23D$ voids are existed. These voids alternatively follow each other with bottle-neck constrictions of minimum $d_3=0.15D$ diameter separating them. The opals were completely impregnated with InSb. SEM shows that InSb component takes the form the lattice consisting of 8-fold co-ordinated d_1 grains alternatively connected by bridges with 4-fold co-ordinated d_2 grains and this lattice retains *fcc* structure of an opal. The SiO_2-InSb interface provides ~5eV potential wall for electrons and thus restricts the electron motion within the InSb counterpart of nanocomposite. D (diameter of the opal sphere) The geometrical modulation of InSb cross-section results in an alternating confinement potential. This potential up-shifts the ground energy level by $\Delta E = (\pi\hbar)^2 / 2m^* d_3^2 \approx 30$meV for D= 227nm. This estimation is the lower limit, since the sintering-induced squeezing of the voids and depletion of the electron population at the grain surface reduce the effective size of the cross-section. Thus d_3 constrictions induce ~$0.05D$ wide potential barriers along the current path. These barriers localise electrons in grains and leave tunnelling as the only possibility for them to complete the current path (Fig.1).

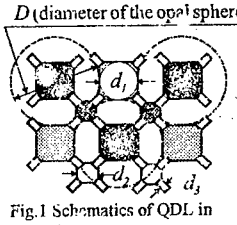

Fig.1 Schematics of QDL in (100) plane.

The electron concentration was estimated from high temperature Hall measurements as n_{300K}~10^{16}÷10^{17}cm^{-3}. Assuming a decrease in the concentration at T<1K and occupation of large grains only, the number of free electrons in each grain is Q≈10. Correspondingly, the Fermi energy in the d_2 grain is $E_F = \hbar^2 (2m^*)^{-1} \left(3\pi^2 Q/d_2^3\right)^{2/3} \approx 49$meV and λ_F≈47nm. d_2 grain may be thought of as QD since $d_2 \leq \lambda_F$. The level spacing Δ in the energy spectrum of 50nm QD is $\Delta = \rho(E_F)^{-1} = \frac{2\pi^2}{d^3}\left(\frac{2m^*}{\hbar^2}\right)^{-3/2} E_F^{-1/2} \approx 2.8\ meV$, where $\rho(E_F)$-density of states near the Fermi level. In a 3D lattice of QDs the interaction in the lattice splits the each level into a miniband and the actual level spacing becomes $\Delta << kT$ in the range 0.05÷1K. Therefore, the QD energy spectrum may be considered as a continuum.

A segment consisting of d_2 QD in between two d_1 QDs resembles the double-barrier tunnel junction. A charging energy $E_C=e^2/2C=e^2/(d_2\varepsilon_m)\approx$14meV, where C is the capacitance of 50nm dot, is required to place an extra electron in the small dot. At low-T regime QDs are coupled capacitively because of the potential barriers separating the dots. At the low bias voltage QD lattice (QDL) is similar to a lattice of chains along the field direction, since the barriers do not allow for free electron diffusion. We stress a close analogy between opal-InSb and a multiple tunnel junction (MTJ)[4,5].

The samples were shaped as 0.5mm thick plates with 6 Au-Ni-Ge contact pads deposited on the upper face and arranged as the Hall bar. The separation of the probes was around 50μm.

IVCs of the QDL look typical for tunnel junction with charging effects [6]: the current is very low below the threshold voltage V_{thr} but then increases abruptly (Fig.2a, 3). The standard Coulomb blockade implies I=0 at $V<V_{thr}$. The low-V part of observed IVC deviates from this standard, moreover, with increasing T this deviation increases. Fig.2b shows the extra current I_{ex}, which was extracted from the IVC using its high-V fit as the background. Ascribing I_{ex} to some particular resonance in the QD energy structure seems invalid because of the T-induced shift of I_{ex} maximum. At $V<V_{thr}$ the tunnelling through the whole system via a virtual intermediate state may arise due to the quantum fluctuations of the electric charge in QDs. This so-called co-tunnelling[5,7] was observed if the junction resistance is $R\geq R_Q=h/4e^2\approx$6.5kΩ. This is feasible for opal-InSb if the sample resistance is $10^5\div10^7\Omega$, potential probes are spaced by 50μm and several chains may operate in parallel.

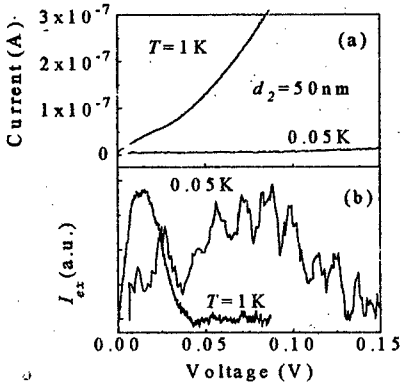

Fig.2 (a) - IVCs of QDL at T=0.05 and 1K; (b) - excess current extracted from these IVCs.

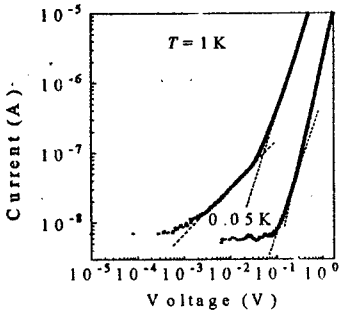

Fig.3 *Log-Log* plot of IVCs of 50nm QDL.

Elastic and inelastic types of co-tunnelling are known [2]. Elastic process results in $I\sim V$ and inelastic - $I\sim V^3$, the latter is consistent with IVC Fig.3, where $I_{ex}\sim V^m$, m=1.5÷3. From Fig.2b it is seen, that at T=1K the maximum of I_{ex} occurs at 14mV whereas for 50mK - at 75mV. Note, that the inelastic contribution is T-dependent and it is most probable if $\Delta^{-1}>>E_C^{-1}$, which is the case for QDL. Thus $I(V,T)$ let us to classify I_{ex} as the manifestation of inelastic co-tunnelling.

It seems reasonably, that not all of geometrically available current paths are really conducting at low-T due to QDL imperfections. However, owing to $10^7\div10^8$ barriers over the QDL cross-section it is always possible to find a collection of low-resistance paths. Our understanding of the transport mechanism is based on the model of the "exciton" mechanism [5].

Parallel 1D chains in QDL are coupled electrostatically. Assuming the same type of contacts throughout QDL, the inter-chain capacitance C_0 will be up to N times larger, than C. In this case the electrostatic energy of the electron and its image formed on adjacent chains is much smaller, than the energy of unpaired electron, therefore such an «exciton» is energetically favourable. The "excitons" can move along the coupled chains when $V<<V_{thr}$ for SET in the Coulomb blockade state. This is actually the movement of charge because of the separation of the electron and hole in different chains. The binding energy of "exciton" is $\varepsilon=(e^2/4C)(1-1/N)\cong e^2/4C$, if $N>>1$ [5]. We cannot resolve the true gap since $V_{thr}=e/C_0 \rightarrow 0$ for the large capacitance C_0 with regard to surrounding chains in the QDL. In the range $e/C_0<V<e/4C=\varepsilon/e$ only "exciton" transport is possible, but for $eV>\varepsilon$ the "excitons" will be destroyed and at $V>e/2C\approx 10\div 14$mV tunnelling of single electrons along the chain increasingly contributes.

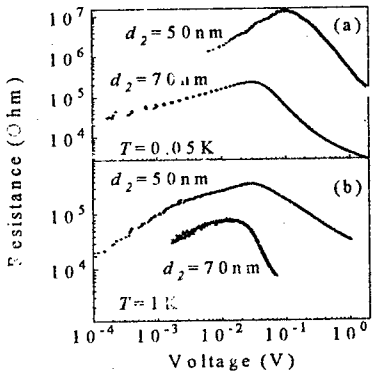

Fig.4 $R(V)$ curves for 50 and 70nm QDL at T=0.05; 1K.

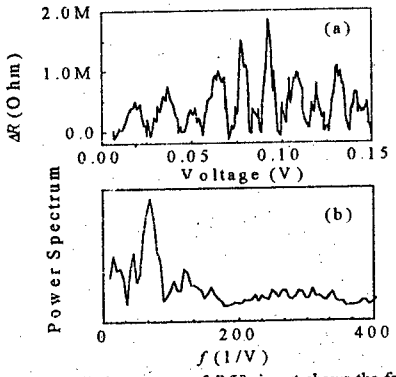

Fig.5 Oscillating pattern of $R(V)$, insert shows the fast Fourier transform of this curve.

If two coupled chains of QDs are biased with the same voltage, their "exciton" currents are strictly equal but opposite. The necessary condition for "exciton" mechanism to actually transfer charge through the array is a different V to be applied to the capacitively coupled chains of QDs. This requirement is realised in the QDL at low-T, when the inhomogeneous current distribution takes place. Particularly, if 2 neighbour chains are differently connected to the source and drain, there is a voltage difference $\Delta V=V_1-V_2\leq V$ between these chains, that is a driving force for the "excitons" to move. For the case of a two electron process the net current through 2 chains is $I=e[\gamma(U)-\gamma(-U)]$, where γ-tunnelling rate[5]. The total current through the lattice of K chains with an energy gain for this process $U=eV/N$ in the case of $\Delta V=V$ is

$$I=\frac{16\hbar C^2 K}{3\pi R^2 e^4}\times\left[\left(\frac{V}{N}\right)^3+\left(\frac{2\pi kT}{e}\right)^2\frac{V}{N}\right]$$

The $I\sim T^2$ term rises linearly with V, it is in effect in the low-V range if T not too low. I_{ex} we associate with this term since (i) the front of $I_{ex}\sim V^k$, k=0.7÷1 and (ii) the maximum of I_{ex} shifts from 15 to 70mV and I decreases sharply with T changing from 1 to 0.05K (Fig.2b). The $I\sim V^3$ term dominates at higher V, since its appearance is delayed by $1/N^2$ comparing with the linear one.

It correlates with the steeper part of the IVC, where $I \sim V^m$, m=1.5÷3, moreover, the upper lim.. is approached at 0.05K when $eV >> kT$. At 1K kT is close to $eV/N \approx 6.5\times10^{-5}$eV near the I_{ex} maximum, assuming N=200. Therefore, the denominator in (2) cannot be neglected, which results in decrease of the IVC slope. At T>1K there was no I_{ex} found.

The excess current has a remarkable effect on the resistance (Fig.4): $R(V)$ reaches a maximum with increasing voltage corresponding to the transition from "exciton" to SET transport and gradually decreases afterwards. The height of $R(V)$ peak exceeds 1 order of magnitude, which reflects the change in the transport mechanism. In Fig.4 $R(V)$ is shown for samples with d_2=52 and 70nm to demonstrate that the overall shape of $R(V)$ is not sample specific. The difference of resistance for these samples corresponds the different barrier heights. With increasing T the position of $R(V)$ maximum moves towards lower V and its magnitude decreases. The dramatic high-V drop of the resistance is inconsistent with the linear resistance regime predicted by the orthodox theory of SET [8]. This is due to the a 3D nature of QDL - with increasing V multiple co-ordination of large grains allows to increase the number of parallel circuits.

At 0.05K I_{ex} is highly modulated (Fig.2b). Correspondingly, the $R(V)$ curves demonstrate a sequence of steps. The magnitude of these modulation is ~10% of the total resistance. After subtraction the smooth background these steps are converted into a sequence of peaks separated by $\Delta V \approx$14mV (Fig.5a). The Fourier transform (Fig.5b) confirms a quasi-oscillatory behaviour. Note, that the very weak but similarly spaced features could also be seen in 1K curve of Fig.2b. The multiply-stable states of different number of electrons can be formed in a QD chain since the charging energy of the QD creates an energy barrier which blocks the entrance. Increasing $eV > E_C$ results in entering of another electron into the chain and so on. ΔV correlates well with the estimation of $E_C(d_2) \approx$14meV for this sample, therefore the addition spectrum of the QD was revealed by scanning of the source-drain voltage [2]. This is a reasonable explanation for the deep wells and high-V that was used. Besides, for QDL the surrounding chains of QDs may perform the role of gate potential with respect to one of them, thus leading to equalising the potential over the array in a self-consistent manner.

In conclusion, we have demonstrated that the conductivity of a 3D QDL in the low-T regime is dominated by a Coulomb blockade. In contrast with 1D chains of tunnel junctions the inelastic co-tunnelling plays a very important role since the inter-chain coupling leads to a large excess current. For the highly resistive arrays a staircase appears superimposed on this excess current indicating the single electron nature of the charge transfer.

This work was supported in part by Russian Foundation for Basic Research (grant 96-02-17963). SGR acknowledges the support from UK Leverhulme Trust (grant no. F/179/AK).

[1] *"The Physics of Few-Electron Nanostructures"*, eds.L.J.Greeligs, C.J.P.M.Harmans, L.P.Kouwenhoven, Elsevier Science Publ., 1993
[2] U.Meirav, E.B.Foxman, *Semicond.Sci.Technol.* **10**, 255 (1995)
[3] V. G. Balakirev, V. N. Bogomolov, V.V.Zhuravlev, Y.A.Kumzerov, V.P.Petranovsky, S.G.Romanov, L.A.Samoilovich. *Crystallogr.Rep.* **38** 348 (1993)
[4] N.S.Bahvalov, G.S.Kazacha, K.K.Likharev, S.I. Serdukova, *Sov. Phys. JETP.* **68**, 581 (1989)
[5] D.V.Averin, A.N.Korotkov, Yu.A.Nazarov, *Phys.Rev.Lett.*, 66, 2818, (1991)
[6] L.J.Greeligs, in «*Physics of Nanostructures*», eds.J.H.Davies, A.R.Long, IOP, Bristol, p.171, 1992
[7] D.V.Averin, Yu, V. Nazarov, *Phys.Rev.Lett.*, **65**, 2446 (1990)
[8] D.V.Averin, K.K.Likharev, *J.Low Temp.Phys.* **62**, 345 (1986); K.K.Likharev, A.B.Zorin, *ibid.* **59**, 347 (1985)

Correlated charge transfer and cross-tunneling in coupled nanowire junctions array

A. A. Tager[1], M. Moskovits[2], and J. M. Xu[1]
University of Toronto
[1] Department of Electrical & Computer Engineering,
10 King's College Rd., Toronto, Ontario, Canada M5S 1A4
[2] Department of Chemistry, 80 St. George St., Toronto, Ontario, Canada M5S 1A4

Single electron tunneling (SET) is one of the most promising phenomena observable in nanostructures. Of the many nano-fabrication methods, the non-lithographic approaches seem to be more attractive as well as technologically and economically more promising. An electrochemical non-lithographic nano-fabrication technique has been developed at the University of Toronto. Arrays of highly uniform, highly ordered, densely packed nanowires and dots have been fabricated using this technique and investigated. The technique is based on the creation of a template of hexagonally arranged nanopores as by anodization of Al film followed by electrochemical deposition. A wide range of tunability of wire parameters— $\sim$ 200 nm down to $\sim$ 6–8 nm in diameter and up to a few microns in length—along with a broad range of depositable materials enabled by this technique opens up many exciting opportunities for nanophysics and nanoelectronics.

These nanowire arrays, when sandwiched in-between metal/oxide layers, form 2D-arrays of either single-junction or double-junction systems which exhibit a great variety of promising device behaviors and interesting phenomena, including both periodic and anomalous conductance oscillations, as well as room temperature stair-case I–V behavior resembling the SET characteristics [1,2]. Although complete understanding of these behaviors is difficult at the present stage, progress may be made by identifying and investigating the key effects influencing the charge transfer in this new class of nano-devices.

An important feature which is common to all the nanowire devices fabricated this way is a strong electrostatic coupling between nanowires, as the wire length is normally much greater than the interwire spacing (a few wire diameters apart, typically). This capacitive coupling between galvanically isolated wires may affect different aspects of the nanowire device behavior. Although undesirable for such applications as charge storage memory, it can be exploited in other cases where inter-wire coupling is of core importance. Perhaps the most interesting consequence of such coupling is the correlated transfer of charge through nanowire arrays, when either electrical current through a particular wire or its charge depends on the state (charging) of the neighboring wires [3]. Self-organized 2D charge structures may then appear, due to Coulomb interactions between wire charges, which, among other consequences, would lead to steps in the I–V characteristics such as those observed experimentally.

We have investigated the effect of interwire coupling in one particular situation pertinent to nanostructures—the conditions of Coulomb-controlled tunneling (or SET) using Monte-Carlo simulations and analytical considerations. By analyzing a model system of two electrostatically coupled nanowires connected in parallel via nano-scale tunnel junctions, we have shown that

inter-wire coupling indeed leads to correlation between tunneling events on the neighboring wires. This results in strong anticorrelation of wire charges yielding their spontaneous polarization, when accumulation of excessive electrons on one wire is partially compensated by hole accumulation on the neighboring wire. Due to the wire charge anticorrelation, the polarization exhibits much higher noise than the total wire charge, and depends periodically on the applied voltage above the Coulomb blockade, when "lassical tunneling" is allowed. The effect influences not only the individual wire currents, but also the total electric current and can thus be observed externally.

A particularly interesting case is co-tunneling. Below the Coulomb blockade voltage, where individual single-electron tunneling is forbidden, electrical current penetrates through the Coulomb barrier via simultaneous tunneling of two electrons through the source and drain junctions [4]. Nanowire coupling opens up an additional current path via correlated charge transfer through the junctions of neighboring wires. Such a correlated cross-tunneling process leads to spontaneous polarization of the wires by creating a hole on one wire and an additional electron on another. It thus differs from standard co-tunneling, which leaves the state of the system unchanged; it is, however, allowed in the Coulomb-blockade regime if the energy of the created polarization excitation is below the Coulomb barrier, as in the case of sufficiently strong wire coupling Although the likelihood of spontaneous polarization created by these cross-tunneling processes is generally lower than that by normal SET tunneling above the Coulomb blockade, it can considerably affect the net current through the system, allowing in some cases classical single-particle tunneling to occur at voltages within the Coulomb-blockade regime, and yielding periodic current bursts as voltage is increased. The effect is greatly enhanced in the case of asymmetrical wires, with the limiting case being a double-junction system connected in parallel and coupled to a single-junction system ("defect"), where it can affect the charge and current noise characteristics of the double-junction system. In the talk, we will present the results of the Monte-Carlo simulations of correlated electronic transport, and cross-tunneling in particular, through coupled nanowires both above and below the Coulomb blockade voltage. We will emphasize the effects of inter-wire correlation of charge, and analyze possible consequences of these effects on the device behavior of the electrochemically-produced nanowire arrays.

References

[1] D. Al-Mawlawi, C. Z. Liu, and M. Moskovits, *J. Mater. Res.*, **9**, 1014 (1994);
T. Bigioni, M. Moskovits, D. Routkevitch, and J. M. Xu, *J. Phys. Chem.*, **100**, 14037 (1996);
D. Routkevich, A. A. Tager, J. Haruyama, D. Al-Mawlawi, M. Moskovits, and J. M. Xu, *IEEE Trans. Electron. Dev.*, **43**, 1646 (1996).

[2] D. Al-Mawlawi, M. Moskovits, D. Ellis, A. Williams, and J. M. Xu, in *Proc. of the Intern. Semiconductor Research Symp.*, Charlottesville, 1993, p. 311 (1993).

[3] A. A. Tager, M. Lu, J. M. Xu, and M. Moskovits, in *Extend. Abstr. of the Int. Conf. on Solid State Devices and Materials*, Osaka, p. 183 (1995);
Pys. Low-Dim. Struct., **12**, 149 (1995);
A. A. Tager, M. Moskovits, and J. M. Xu, *Phys. Rev. B*, **55**, 4530–4538, (1997).

[4] D. V. Averin, A. N. Korotkov, and Yu. V. Nazarov, *Phys. Rev. Lett.*, **66**, 2118 (1991).

Investigation of Single-Electron Effects in Nanostructures on the Base of Single Metallorganic Clusters.

A.S. Trifonov [1], V.V. Khanin [1], E.S. Soldatov [1], S.P. Gubin [2], S.A. Yakovenko [1], G.B. Khomutov [1].

[1] - Department of Physics, Moscow State University, Moscow 119899, Russia,

[2] - Institute of General and Inorganic Chemistry, Moscow 117907, Russia.

A considerable interest has been attracted to the effects of correlated single-electron tunneling [1] during the last decade. The most of experiments with lithographically fabricated structures have been done at temperatures below 1 K. To increase the operation temperature it is necessary to reduce the characteristic size d of the structure in order to decrease the typical capacitance. Operation at T=300 K requires $C < 10^{-18}$ F corresponding to $d < 3$ nm, quite a difficult task.

The technique in which the small capacitance's are easily obtained is based on scanning tunneling microscopy (STM). The simplest single-electron circuit consisting of two tunnel junctions in series can be implemented using the STM tip, small conducting particle, and the substrate. The single-electron charging survives up to room temperature for sufficiently small metal particles, [2,3] and it can be even stronger when the tunneling via single molecules or cluster molecule is studied [4,5].

Clusters and cluster molecules differ from other organic and inorganic molecules in that they contain a dense, heavy metallic core, as a rule spherical or almost spherical, surrounded by a ligand shell made up of light atoms or simple molecules [6]. The electronic structure of cluster molecules is characterized by the high density of closely spaced upper filled and lower vacant molecular states (all weakly bonding), which, on the one hand, result in numerous one-electron reversible redox transitions and, on the other, ensure sufficient stability of the molecular core to the addition or removal of an electron. We have demonstrated single-electron transistor on the base single molecule of carboran cluster using STM [7].

We assume the most clear observation of single-electron effects is possible in cluster molecules with large number of metallic atoms. In present work we report about investigation

of the tunnel system based on the cluster molecule $(C_5H_5FeS)_4$ at room temperature. This molecule is known [6] as a "reservoir of the electrons" and play an important role in the native processes of the electron transfer. The topographical measurement show that it is possible to create from such clusters (by the technique of Langmuir-Blodgett) the molecular system with both as regular monolayer lattice (Fig. 1) and single cluster molecule on the substrate (Fig. 2a). When STM tip was positioned above single cluster for the investigation of SET effects [4,7] double-junction tunnel system "STM tip - cluster molecule - substrate" was formed (Fig 2a, 2b). CVC of such system show clear SET effects with distinct Coulomb blockade region which is weakly washed out even at such high temperatureas $T = 300$ K. This property as well as very high value of Coulomb blockade region (~ 0.5 V).

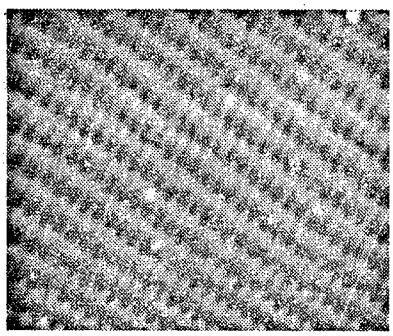

Fig. 1. STM-image of lattice of $(C_5H_5FeS)_4$ clusters. Scan size 57 Angstrom. $I_{tunnel} = 0.5$ nA, $V_{tunnel} = 150$ mV

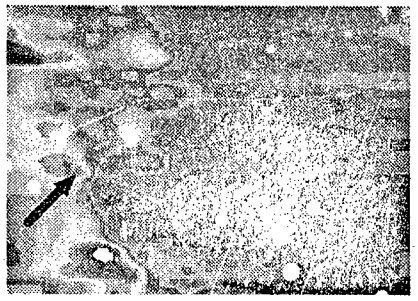

Fig. 2a STM-image of single clusters $(C_5H_5FeS)_4$. Arrow pointed on place in which CVC-characteristic was measured.

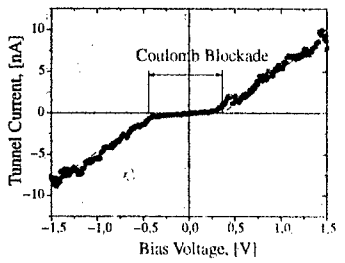

Fig. 2b. Current-Voltage characteristic at the STM-tip location above single cluster molecules.

Our experiments had shown that these cluster molecules are very prospective material for implementation of the SET effects based devices of molecular electronics at high temperature.

References

1. D.V. Averin and K.K. Likharev, in *Mesoscopic Phenomena in Solids* , edited by B.L. Altshuler, P.A. Lee, and R.A. Webb (Elsevier, Amsterdam, 1991), p. 173.
2. C. Schönenberger, H. van Houten, and H.C. Donkersloot, Europhys. Lett. **20**, 249 (1992).
3. M. Dorogi, J. Gomes, R. Osifchin, R.P. Anders, R. Reifenberger, Phys. Rev. B **52**, 9071 (1995).
4. A.A. Zubilov, S.P. Gubin, E.S. Soldatov et al., Pisma v Zh.T.Ph., **20**, 41 (1994) (Tech Phys. Lett. **20**, 195 (1994)).
5. D. Porath and O. Millo, J. Appl. Phys. **81 (5)**, 2241, (1997).
6. S.P. Gubin, *Khimiya klaserov* (Chemistry of Clusters), Moscow: Nauka, 1987.
7. E.S. Soldatov, V.V. Khanin, A.S. Trifonov, et al Pisma JETP. **64 (7)**, 510 (1996), (JETP Lett., **64 (7)**, 556, (1996)).

"Gamma-X" tunneling in GaAs/AlAs/GaAs heterosturcture

E. E. Vdovin, Yu. V. Dubrovskii, Yu. N. Khanin, N. S. Novoselov,
T. G. Andersson*, P. Omling**, S.-B. Carlsson**
Institute of Microelectronics Technology RAS, 142432, Chernogolovka, Russia
*Chalmers University of Technology, S-412 96 Gteborg. Sweden
**Lund University, S-221 00 Lund, Sweden
E-mail <dubrovsk@ipmt-hpm.ac.ru>

Tunneling from 2D accumulation layer through X-valley states in AlAs barrier was investigated in single barrier GaAs/AlAs/GaAs heterostructure with 5 nm and 3.5 nm barrier thickness.

"Gamma-X-Gamma" tunneling current arises from transfer via X-valley AlAs quantum well states derived from both conduction band minima perpendicular (Xx and Xy) and parallel (Xz) to the (100) growth direction (z). Both processes was observed on I–V tunneling dependences. In magnetic field resonant tunneling between Landau states of different effective mass determines the experimental features. Additional two small features were observed on I–V dependences at bias voltages lower then voltage when "Gamma-X" tunneling processes start to play essential role in electron transfer through the structure. These additional features are related to the resonant tunneling through zero-dimensional donors bound to X-valley states because of the residual Si barrier doping. It is shown that these two donor states are bound to different X-valley quantum well 2D ground states namely Xxy and Xz. In magnetic field main observed features can be explained by resonant tunneling between Landau levels of 2D "Gamma"-symmetry emitter and zero-dimensional donor states in barrier. Scattering of Si atoms position in the barrier in growth direction leads to the scattering of the donor energy levels in X-valley quantum well and were manifested on the experimental data as noise-like fine structure of the resonance features related to the tunneling through donor states.

PECULIARITIES OF THE WEAK LOCALIZATION OF THE 2D HOLES IN THE QUANTUM WELL ON (10$\bar{1}$0) SURFACE OF TELLURIUM

N.S. Averkiev, V.A. Berezovets,
I.I. Farbshtein, G.E. Pikus, N.I.Sablina

A.F.Ioffe Physico-Technical Institute Rus ia Academy of Sciences,
St.-Petersburg, 194021, Russia

The weak localization of 2D holes in quantum well on the (10$\bar{1}$0) crystallographic surface of tellurium crystal have been investigated experimentally [1] and theoretical [2]. The aim of this report is to compare the new experimental data and the theory.

A theory of weak localization is developed for 2D carriers with anisotropic energy spectrum when a scattering matrix element depends on the initial and final particle quasimomenta [3]. The final expression for conductivity turned out to have a standart form but the values of the diffusion coefficients and relaxation times depend on the surface orientation. It is shown that the trigonal distortion of the energy spectrum of tellurium results in spin relaxation responsible for the phase losing when the 2D layer is parallel both to the two-fold and to the trigonal axis. The results of the theory are presented in a form permitting direct comparison with anomal magnetoresistance experimental data in tellurium [2].

The experimental data are described as a function of the characteristic magnetic fields H_φ, H_ν and H_γ. H_φ is related to the inelastic scattering times, H_ν and H_γ - to the contribution of the elastic scattering times associated with intervaley and intravaley transitions correspondingly. The last of them includes a dispersion parameter γ describing the trigonal distortion of the Fermi trajectories of 2D holes and a parameter β which determining dumbbell shaped trajectories on the (10$\bar{1}$0) surface. The parameter γ found from the experimental results agrees well with the previous estimations of γ.

The study was partly supported by the Russian Basic Research Foundation (project codes 96-02-16959a and 96-02-17849) and the Programm "Physics of Solid State Nanostructures".

1.V.A.Berezovets, et al., Phys.Low-Dim.Struct.,1995, 12, pp.301-304.
2.N. S. Averkiev, G.E.Pikus . Phys. Sol.State 1997 , 39 (in press).
3.N. S. Averkiev, G.E.Pikus . Phys. Sol.State 1996 , 38 (6), pp.964-971.

Photon-induced full electron transparency of double and triple quantum-well structures

D. G. Baksheyev, D. Lenstra,† O. A. Tkachenko and V. A. Tkachenko*

Novosibirsk State University, Novosibirsk, 630090, Russia

†*Vrije Universiteit, De Boelelaan 1081 HV, Amsterdam, The Netherlands*

**Institute of Semiconductor Physics, Novosibirsk, 630090, Russia*

It was recently shown theoretically that an asymmetric double quantum-well (2QW) structure having poor electron transparency can become absolutely transparent for resonant electrons under irradiation with photon energy $\hbar\omega = E_2 - E_1$ (E_1 and E_2 the quasilevels of the different wells) [1–2]. The electrons impinging the structure in resonance with quasilevel of the nearest well, pass through the next well with absorption (or emission) of a photon. We have modeled multichannel coherent electron transmission through realistic 2QW and 3QW $GaAs/Al_xGa_{1-x}As$ structures in the presence of infrared radiation, as well as the decay of the quasienergetical electron states with respect to departure to the contacts (Figs. 1, 2). For 2QW structure in the zero limit of high-frequency (hf) field amplitude $\mathcal{E}$ the decaying states, *i.e.* the poles of scattering S-matrix on the complex plane, have equal real parts of quasienergies $E_1 = E_2 - \hbar\omega$, while corresponding widths $\Gamma_i^{(0)}$ are so that $\Gamma_2^{(0)} > \Gamma_1^{(0)}$. With increasing $\mathcal{E}$ the poles first move to each other with only imaginary parts changing. Upon a threshold amplitude $\mathcal{E}_{th}$ the vertical motion of the poles is transformed to horizontal motion with $\Gamma_1 \approx \Gamma_2 \approx (\Gamma_1^{(0)} + \Gamma_2^{(0)})/2$. From this amplitude on, the quasilevels undergo splitting similar to Rabi splitting with the difference that the latter has no threshold in hf field amplitude [$\Omega_R \propto J_1(e\mathcal{E}d/\hbar\omega)$, d the distance between the wells, Ref. 2]. In the energy dependence of transmission coefficient this behaviour is traced by the growth of *inelastic* transmission peak that reaches maximum height at some optimal amplitude $\mathcal{E}_{opt} > \mathcal{E}_{th}$ as a flat-top transparency window and then splits into the pair of peaks with decreasing height (Fig. 1).

The question arises if such photon-induced increase of transparency of a semiconductor structures can occur in *elastic* channel, without energy transfer from electromagnetic field to electrons. We have found by numerical calculation that almost impenetrable symmetric triple quantum-well (3QW) structure ($T_0 = 4\%$ without hf field) can provide high transparency ($T_0 = 80\%$) in elastic channel at $\hbar\omega = E_2 - E_1$ and $\mathcal{E} = \mathcal{E}_{opt}$. It becomes possible due to stimulated virtual transitions from quasilevel E_1 of the first well to E_2 in the second well and than to quasilevel E_1 of the third well [Figs. 2(a), 2(b)]. The trajectories of the poles of S-matrix show that with increasing $\mathcal{E}$ different-parity states 2 and 3 strongly interact and undergo anticrossing at $\mathcal{E} = \mathcal{E}_{th}$ while the first state does almost not move [Fig. 2(c)]. In the absence of hf field the transmission coefficient peak is low and have the width much less than the widths of states 1 and 2 due to their interference [Fig. 2(a)]. When the hf field moves states 1 and 2 away, this peak turns into wide window of good elastic transmission. With further increase of radiation intensity the window falls apart to the wide central peak corresponding to state 1 and two narrower side peaks corresponding to states 2 and 3.

To contrast 2QW and 3QW states, in the figures we only presented T_1 in the former and T_0 in the latter case. With account of all channels the transmission through these structures becomes full at $\mathcal{E}_{opt}$.

To give an analogy, we notice that 2QW and 3QW structures with aligned quasilevels

provide flat-top full-transparency windows in the absence of hf field when the inner barriers are made twice thicker than the outer ones (Iogansen structures [3]). In our case, however, the structures are almost opaque in the absence of hf field because levels E_1 and E_2 are not aligned, and high-transparency windows are switched on by external irradiation while the effective thickness of inner barriers is managed by its intensity.

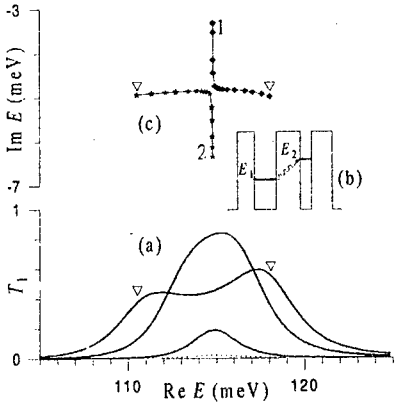

Figure 1. **(a)** Coefficient of electron transmission with photon absorption T_1 vs. energy in the vicinity of quasilevel E_1 at $\hbar\omega = E_2 - E_1 = 84$ meV. The hf field amplitudes for the low, high, and split peaks are 1.4, 5.6, and 11.2 mV/nm, respectively. Dotted line shows $T_0(E)$ in the absence of hf field. **(b)** Conduction band profile of the 2QW GaAs/$Al_{.35}Ga_{.65}$As structure: 10-13-14-7-12 monolayers from left to right. **(c)** Trajectories of the poles of scattering S-matrix in the complex quasienergy plane with amplitude of the hf field increasing from 0 to 11.2 mV/nm. Maximum approaching of the poles corresponds to $\mathcal{E}_{th} \sim 2$ mV/nm.

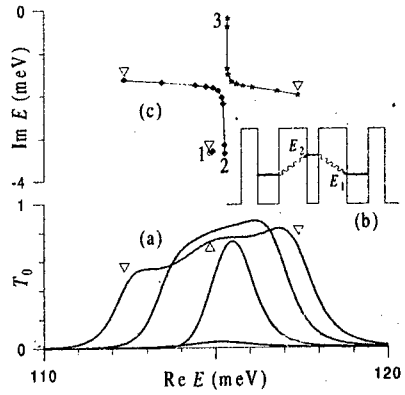

Figure 2. **(a)** Elastic transmission coefficient T_0 vs. energy in the vicinity of quasilevel E_1 at $\hbar\omega = E_2 - E_1 = 78$ meV. The hf field amplitudes for the peaks with increasing width are 0, 2.5, 5, and 7.5 mV/nm, successively. **(b)** Conduction band profile of the 3QW GaAs/$Al_{.35}Ga_{.65}$As structure: 10-13-17-7-17-13-10 monolayers from left to right. **(c)** Trajectories of the poles for the hf field amplitude increasing from 0 to 7.5 mV/nm. Maximum approaching of the poles corresponds to $\mathcal{E}_{th} \sim 2$ mV/nm.

The work was partly supported by Russian Foundation for Basic Researh, Grant No. 96-02-19060.

References

[1] M. Yu. Sumetskii and M. L. Felshtyn, Pis'ma Zh. Eksp. Teor. Fiz. **53**(1), 24 (1991).

[2] C. A. Stafford and N. S. Wingreen, Phys. Rev. Lett. **76** 1916 (1996).

[3] L. V. Iogansen, Zh. Eksp. Teor. Fiz. **47**, 270 (1964).

AC Josephson effect in a SIS tunnel junctions with localized states in the barrier

I. A. Devyatov, M. Yu. Kupriyanov
Institute of Nuclear Physics Moscow State University, Moscow, 119899 GSP, Russia

In the last few years a lot of efforts was concentrated on the problem of the current transfer across one dimensional constrictions between normal or superconducting bulk electrodes. It was shown that constriction control the current across HTS Josephson junctions with normal semiconductor interlayers [1] as well as the transport in the high-current density SIS tunnel structures. With the decrease of the junction area the contribution of constriction transport channel tends to be more and more valuable making the behavior of the Josephson structures more and more mesoscopic. The constriction itself can be both the real shot with metallic conductivity and the conductive channels via localized state in the isolator. In this paper we will restrict ourself to the last case.

Previously the ac Josephson current in the SIS junctions with localized states into the barrier was studied in the case when a large amount of LS formed the conductance channel [2],[3]. The aim of our work was to study a processes in a short constriction between two superconductors which contains a dielectric layer with localized states (LS) thus making the generalization of the developed in [4] model for the case of constriction with energy dependent transparency. The length L of the channel is assumed to be much smaller than the coherence length ξ as well as elastic and inelastic scattering lengths in the superconductors. For the sake of simplicity we will also assume that the boundaries between the banks and constriction material are transparent, the dielectric barrier has a thickness $d < L$ and locate in the constriction. This allows us to neglect scattering in the vicinity of the channel and permits to consider the electron motion in the constriction with the time-dependent Bogoiyubov-de Gennes (BdG) equations taking into account the normal electron reflections only at the barrier. In the limit $L \ll \xi$ it is possible to neglect in BdG equations all nongradient terms in the constriction region and practically reduce the problem to the analysis the processes in ScNINcS structure, which can be described directly in terms of the Andreev reflection at the two NS interfaces and normal and reflections at NI boundaries.

Following the arguments, discussed in [4] we will assume that the voltage across constriction is constant in time and that the resistance of the barrier is much smaller compare to the whole resistance of the junction.

Under the assumptions outlined above, the BdG equations for transport in the constriction can be solved in terms of the two scattering processes for electrons and holes, along the same lines as in the stationary case [4,5]. One process is Andreev reflection at the NS interfaces characterized by the reflection amplitude a as a function of the quasiparticle energy ϵ:

$$a(\epsilon) = \frac{1}{\Delta}\begin{cases} sign(\epsilon)\{|\epsilon| + \sqrt{\epsilon^2 - \Delta^2}\}^{-1}, & |\epsilon| > \Delta, \\ \epsilon - i\sqrt{\epsilon^2 - \Delta^2}, & |\epsilon| < \Delta. \end{cases} \qquad (1)$$

Another process is electron scattering in the constriction characterized by a scattering matrix:

$$S_{el} = \begin{pmatrix} r & t \\ t & r' \end{pmatrix}, \qquad r = \frac{\eta}{\delta}, \qquad r' = -\frac{\eta^*}{\delta}, \qquad t = \frac{1}{\delta}. \tag{2}$$

where $\mid t \mid^2 = D$ and $\mid r \mid^2 = R$ are the transparency and reflection coefficients correspondingly. The scattering matrix for holes is the time reverse of S_{el}, $S_h = S_{el}^*$.

We have to take into account that the energy of an electron is increased by eV each time it passes through the channel from left to right, while the hole increases its energy passing through the constriction in the opposite direction. Because of this the electron and hole wave functions are sums of the components with different energies shifted by $2eV$. For instance, the wave functions in N-regions generated by the quasiparticle incident from the left superconductor onto the channel can be written as [4]:

$$\psi_{el} = \sum_n [(a_{2n}A_n + J\delta_{n0})e^{ikx} + B_n e^{-ikx}]e^{-i(\epsilon+2neV)t}, \quad -L \le x \le -d,$$

$$\psi_h = \sum_n [A_n e^{ikx} + a_{2n}B_n e^{-ikx}]e^{-i(\epsilon+2neV)t}, \quad -L \le x \le -d. \tag{3}$$

$$\psi_{el} = \sum_n [a_{2n}C_n e^{ikx} + D_n e^{-ikx}]e^{-i(\epsilon+(2n-1)eV)t}, \quad d \le x \le L,$$

$$\psi_h = \sum_n [C_n e^{ikx} + a_{2n}D_n e^{-ikx}]e^{-i(\epsilon+(2n-1)eV)t}, \quad d \le x \le L. \tag{4}$$

Here $k = \sqrt{2m\mu}$ and ϵ are momentum (equal to the Fermi momentum since the energy gap Δ is suppose to be much smaller than the Fermi energy μ) and energy of the incident quasiparticle, $a_n \equiv a(\epsilon + neV)$, $J(\epsilon) = (1 - a(\epsilon)^2)^{1/2}$, m is effective electron mass.

The wave amplitudes in eq.(3), (4) are related by the scattering matrix (2):

$$\begin{pmatrix} B_n \\ C_n \end{pmatrix} = S_{el}(E_0', \epsilon_{el}^n) \begin{pmatrix} a_{2n}A_n + J\delta_{n0} \\ a_{2n+1}D_n \end{pmatrix}, \qquad \begin{pmatrix} A_n \\ D_{n-1} \end{pmatrix} = S_h(E_0', \epsilon_h^n) \begin{pmatrix} a_{2n}B_n \\ a_{2n-1}C_{n-1} \end{pmatrix}, \tag{5}$$

which in contrast to the situation analyzed in [4] depends on the energy of electrons $\epsilon_{el}^n = E + 2neV$, holes $\epsilon_h^n = E - 2(E + neV)$ and effective LS energy $E_0' = E_0 - \Delta E$ renormalized due to finite voltage drop on a constriction.

To find the components of the scattering matrix we will additionally assume that the dielectric barrier has a rectangular form with the height $W >> \mu$, $\mu \pm eV$ and width d and contains negative delta functional deep $-B\delta(x - z_0)$ describing the LS located at the point z_0 from the middle of the barrier [6].

Matching the electron wave functions and their derivatives at the barrier interfaces and negative delta function potential we arrived at the following expressions for parameters η and δ in (2)

$$\delta(E) = \frac{1}{\Gamma_0}\left\{\frac{2k\kappa}{k^2+\kappa^2}(E_0 - E) + i\left\{\frac{\kappa^2 - k^2}{\kappa^2 + k^2}(E_0 - E) - \frac{\kappa^2 + k^2}{2\kappa k}\gamma\right\}\right\}, \quad \Gamma_0 = 2\sqrt{D_0}(W - E),$$

$$D_0 = 16\frac{k^2\kappa^2}{(k^2+\kappa^2)^2}\exp\{-2\kappa a\}, \quad \Gamma_{1,2} = \Gamma_0 \exp\{\pm 2\kappa z_0\}, \quad E_B = E_0 + \frac{(k^2 - \kappa^2)}{2k\kappa}\gamma, \tag{6}$$

$$\eta(E) = \frac{1}{\Gamma_0}\left\{\frac{\Gamma_1 - \Gamma_2}{2} + i\left\{\frac{\kappa^2 - k^2}{\kappa^2 + k^2}\gamma - (E_0 - E)\right\}\right\}, \quad \gamma = \frac{1}{2}(\Gamma_1 + \Gamma_2).$$

Here Γ_0 is a half-width of the energy level of LS located in the middle of the barrier, D_0 is the transparency of the barrier with $B = 0$, $\kappa = \sqrt{2m(W-\mu)}$, $\Gamma_{1,2}$ are the decay rates of the electron state on LS to the right and left correspondingly, E_R is renormalized energy level of LS. From the theory of the dc supercurrent resonant tunneling [6] follows that except the coefficients $|t|^2$ and $|r|^2$ described the transport of normal electrons, for the current calculation it is necessary to have also the expressions for complex parameters

$$\delta(E)\delta^*(-E) = \frac{(E_R^2 - E^2) + \gamma^2 - 2i\gamma E}{\Gamma_0^2}, \eta(E)\eta^*(-E) = \frac{E_R^2 - E^2 + \gamma^2 - \Gamma_0^2 + iE(\Gamma_1 - \Gamma_2)/2}{\Gamma_0^2} \tag{7}$$

which is responsible for coherent scattering of quasiparticles in the direct and Andreev reflection channels.

Eliminating the wave amplitudes C_n, D_n eq. (3)-(5) we obtain the recurrence relation for the amplitudes A_n, B_n:

$$A_n = r^*(\varepsilon_h^n)a_{2n}B_n + a_{2n-1}\frac{t^*(\varepsilon_h^n)t(\varepsilon_{el}^{n-1})}{r(\varepsilon_{el}^{n-1})}\frac{B_{n-1} - a_{2n}a_{2n-1}B_nT^*(\varepsilon_{el}^{n-1}, \varepsilon_h^n)}{1 + a_{2n-1}^2T^{*-1}(\varepsilon_{el}^{n-1}, \varepsilon_h^{n-2})b(\varepsilon_{el}^{n-1}, \varepsilon_h^n)},$$

$$F_nB_{n+1} - C_nB_n + H_nB_{n-1} = -r(\varepsilon_{el}^n)J\delta_{n0}, \quad T(\varepsilon_{el}^{n-1}, \varepsilon_h^n) = \frac{t(\varepsilon_h^n)}{t(\varepsilon_{el}^{n-1})}, \quad b'(\varepsilon_{el}^n, \varepsilon_h^{n+1}) = \frac{r'(\varepsilon_h^{n+1})}{r'(\varepsilon_{el}^n)}.$$

$$F_n = \frac{a_{2n+1}a_{2n+2}t(\varepsilon_{el}^n)t^*(E_0, \varepsilon_h^{n+1})}{1 - a_{2n+1}^2b'^*(\varepsilon_{el}^n, \varepsilon_h^{n+1})}, H_n = \frac{a_{2n}a_{2n-1}b^*(\varepsilon_{el}^{n-1})t^*(\varepsilon_h^n)t(\varepsilon_{el}^{n+1})}{1 - a_{2n+1}^2b'^*(\varepsilon_{el}^{n-1}, \varepsilon_h^n)}, b(\varepsilon_{el}^{n-1}, \varepsilon_h^n) = \frac{r'(\varepsilon_h^n)}{r(\varepsilon_{el}^{n-1})}, \tag{8}$$

$$G_n = 1 - r(\varepsilon_{el}^n)r^*(\varepsilon_h^n)a_{2n}^2 - \frac{a_{2n+1}^2\, t^2(\varepsilon_{el}^n)\, r'^*(\varepsilon_h^{n+1})}{1 - a_{2n+1}^2b'^*(\varepsilon_{el}^n, \varepsilon_h^{n+1})} - \frac{a_{2n}^2a_{2n-1}^2\, r(\varepsilon_{el}^n)t^{*2}(\varepsilon_h^n)}{(1 - a_{2n+1}^2b'^*(\varepsilon_{el}^{n-1}, \varepsilon_h^n))r'(\varepsilon_{el}^{n-1})}.$$

In the Landauer approach for current calculation it is necessary to know the wave function $\psi(A_n', B_n')$ for the electrons incident on the barrier from the right side of the constriction. The symmetry relations $A_n'(E) = -A_{1-n}^*(-E - eV)$, $B_n'(E) = -(r/r^*)B_{1-n}^*(-E - eV)$ have been used in [4] is not valued here. Thus to find the wave function we have to solve the set of equations for A_n' and B_n' similar to [4]. These recurrence relations can be solved with the method developed in [7]. The amplitudes A_n, B_n and A_n', B_n' of the wave functions obtained in this way determine all Fourier components of the current $I(t)$ in the channel:

$$I(t) = \sum_k I_k e^{i2keVt/\hbar}. \tag{9}$$

Collecting contributions from the quasiparticles incident on the channel from the two superconductors, making use of the fact that at the interfaces between constriction and bulk electrodes the quasiparticle energy distribution function is the Fermi ones and take into account the form of Andreev reflection amplitude (1)) we finally arrive at:

$$I_k = \frac{e}{\pi\hbar}[eV\delta_{k0} + I_1 - I_2] \tag{10}$$

$$I_1 = \int d\epsilon\, f(\epsilon)(J_0(\epsilon)(a^*_{2k}A^*_k + a_{-2k}A_{-k}) + \sum_n (1 + a_{2n}a^*_{2(n+k)})(A_nA^*_{n+k} - B_nB^*_{n+k})),$$

$$I_2 = \int d\epsilon\, f(\epsilon+eV)(J_1(\epsilon)(a^*_{2k+1}A'^*_{k+1} + a_{1-2k}A'_{1-k}) + \sum_n (1+a_{2n-1}a^*_{2(n+k)-1})(A'_nA'^*_{n+k} - B'_nB'^*_{n+k})),$$

In the absence LS in the barrier the scattering matrixes (2), (4) are energy independent and expression (10) reduce to the result [4].

The current-voltage characteristic of the structure coincides with the first term ($k = 0$) in (10)

$$I_{dc}(V) = eV + 2\int d\epsilon\, [f(\epsilon)(J_0(\epsilon)\mathrm{Re}\{A_0a_0\} + \sum_n (1 + |a_{2n}|^2)(|A_n|^2 - |B_n|^2)] - \quad (11)$$
$$f(\epsilon + eV)(J_1(\epsilon)\mathrm{Re}\{A'_1a_1\} + \sum_n (1 + |a_{2n-1}|^2)(|A'_n|^2 - |B'_n|^2)]$$

From (10) it follows that in all current components via single LS, except well known sub-gap structure, exist additional peaks due to resonant nature of the barrier transparency. We also consider the limit of large LS concentration in the barrier. Suppose that space and energy distributions of LS uniform, for the averaged current we demonstrate that in the high-voltage region $eV >> \Delta$, the crossover from the excess current ($\Gamma_0 >> \Delta$) to current deficit ($\Gamma_0 \ll \Delta$) takes place with the decrease of the effective LS energy width Γ_0 compare to the electrode energy gap Δ. In particular we have shown that in the limit $\Gamma_0 \ll \Delta$ current deficit is relatively large $\Delta I_d \approx 0.7\{2e\Delta/\langle R_n\rangle\}$, while the excess current $\Delta I_{ex} \approx 0.05\{2e\Delta/\langle R_n\rangle\}$ considerably smaller than reported in [3]. These results provide new opportunities for interpretation the data in Josephson junctions LTS and HTS electrodes and semiconductor interlayers.

This work was supported by Russian Scientific Program Physics of Solid State Nanostractures and Russian Fond for Fundamental Research, INTAS-RFBR 95-1305.

References

[1] M. Yu. Kupriyanov, *J. Low Temp. Phys.*, **106**, 149, (1997).

[2] L. G. Aslamazov and M. V. Fistul, *Zh. Eksp. Teor. Phys.*, **83**, 1170, (1982).

[3] A. V. Tartakovski and M. V. Fistul, *Sov. Phys. JETP*, **67**, 1935, (1988).

[4] D. Averin and A. Bardas, *Phys. Rev. Lett.*, **75**, 1831, (1995).

[5] T. M. Klapwijk, G. E. Blonder, and M. Tinkham, *Physica B*, **109&110**, 1657 (1982).

[6] I. A. Devyatov and M. Yu. Kupriyanov, *Zh. Eksp. Teor. Phys.*, **112**, 1, (1997).

[7] E. N. Bratus, V. S. Shumeiko, and G. Wendin, *Phys. Rev. Lett.*, **74**, 2110, (1995).

AC response of the tunnel junctions substantiated by the junction plasmons

M.N.FEIGINOV, V.A.Volkov.
Institute of Radioengineering and Electronics, Russian Academy of Sciences,
Mokhovaya Str., 11, Moscow, 103907, Russia, E-mail: misha@mail.cplire.ru

There are several factors substantiating the high-frequency response of the tunnel devices. As a rule, as a major factor RC time is considered. But there are a peculiar low-frequency plasma excitations in the tunnel structures itself, whose influence on AC response was not studied up to date. We have shown, that the excitations appear in the skin effect regime and have substantial effect on the impedance, if the linear response is considered, and on rectification characteristics, if non-linear response is studied.

We have considered the dynamic response of the semiconductor–tunnel barrier–semiconductor and metal–tunnel barrier–semiconductor structures in the skin effect regime. The tunnel barrier could be one-barrier or two- or more barrier one. The only restriction of the applicability of our model is that the total thickness of the barrier is to be small in comparison with the skin-layer thickness in the semiconductor on the frequency of interest. That is, our approach is applicable to such diodes as resonant tunneling diodes, Shottky diodes etc. But the less the diameter of the diode, the higher the frequency where the effect appears.

We have shown that close to the barrier a specific plasma excitations—junction plasmons (JPs)—exist. JPs are characterized by the low speed of propagation along the barrier in comparison with that of the light in the material of the barrier. Or in other words, it is a low-frequency excitation, that is, for a given wavelength it oscillates with a frequency much lower than that of the light with the same wavelength. We have shown that for a typical parameters of the semiconductor tunnel structures the high-frequency response is determined by the excitation of JPs on the frequencies higher than 100 GHz.

The analytical expression for the impedance of the tunnel junction (Z_j) was derived. For simplicity, we are considering the tunnel structure of width W in one direction (x) in the plane of the barrier and infinitely large in the another one (y). The equation for the impedance per the unity of length in the y direction is the following:

$$Z_j = \frac{i}{C(\omega + i\nu_T)} \frac{qW/2}{\tan(qW/2)}, \qquad (1)$$

where C is the ordinary capacity of the tunnel junction per the unity of length in the y direction, ω is the frequency of the applied signal, $\nu_T = 4\pi G d/\varepsilon_l$ is the reciprocal $R_T C$ time ($G = 1/R_T$ is the conductivity of the tunnel junction per the unity of length in the y direction, d is the thickness of the tunnel junction, ε_l is the dielectric constant of the barrier material: it is supposed to be the same both of the barrier material and of the lattice of the semiconductor). In Eq. (1) q is the complex wavevector of the JP (with the frequency ω) propagating along the barrier and is a solution of the

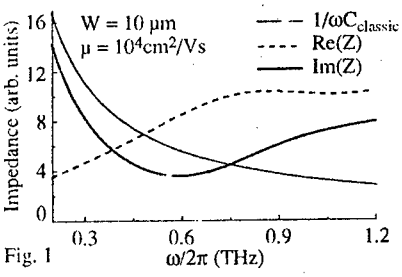

Fig. 1

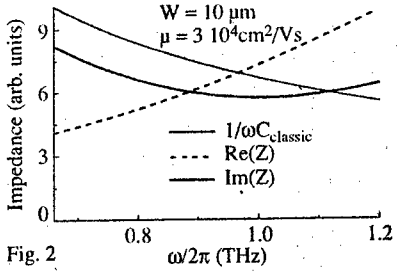

Fig. 2

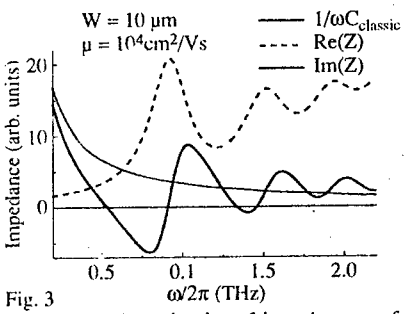

Fig. 3

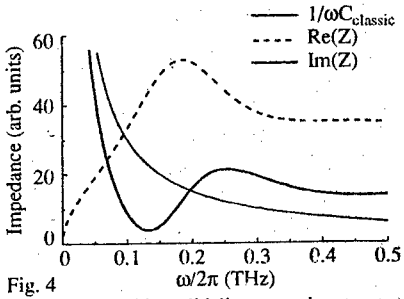

Fig. 4

Fig. 1-4 The dependencies of impedance on frequency. The thin solid lines are the structure impedances calculated for comparison in the framework of the model that does not take into account JPs excitation. Fig. 1–3 present the plots of impedance of the semiconductor–barrier–semiconductor structures with the following parameters: the lattice dielectric constants of the semiconductor and barrier are supposed to be the same for both and equal to 13.5; the electron effective mass is $m^* = 0.07m$, the electron concentration in the semiconductor is 10^{18} cm^{-3}, the thickness of the barrier is 50 nm, the diameters of the structures and the electron mobilities are shown in the figures. The frequency range in the Fig. 1–3 correspond to that where our approach is applicable and the excitation of JPs essentially changes the impedance.

Fig. 4 presents the impedance of the metal–barrier–metal structure with the following parameters: the barrier thickness is 100 nm, the lattice dielectric constants of the metal and barrier are equal to 3, the electron concentration in the metal is 6×10^{22} cm^{-3}, the electron mobility is $\mu = 50$ cm^2/Vs, the diameter of the structure is 10 cm. The structure suits to low-frequency experimental study of JP excitation.

dispersion equation

$$(\omega + i\nu)(\omega + i\nu_T)\kappa = \omega_p^2 \frac{d}{2}\left(\kappa^2 - \frac{\omega_p^2}{c^{*2}}\frac{\omega}{(\omega + i\nu)} - \frac{\omega(\omega + i\nu_T)}{c^{*2}}\right), \mathrm{Re}(\kappa) > 0, \qquad (2)$$

$$\kappa^2 = q^2 - \varepsilon_s \frac{\omega^2}{c^{*2}}, \qquad (3)$$

where ω_p is the bulk plasma frequency in the bulk of semiconductor, $\varepsilon_s = \varepsilon_l\left[1 - \omega_p^2/\omega(\omega + i\nu)\right]$ is the dielectric permittivity of the semiconductor allowing for plasma contribution, $c^*/\sqrt{\varepsilon_l}$ is the effective light velocity in the barrier, ν is the reciprocal relaxation time of the electron momentum in the semiconductor. Eq. (2) was derived in the low frequency

$$\max\left[|\nu_T|, \omega, \nu\right] << \omega_p$$

and long wavelength

$$q << 1/d$$

limits.

The dependence of the impedance is both qualitatively and quantitatively differs from that predicted by the models which do not take into account JP excitation. The plots of impedance for several typical structures are shown in Fig. 1–3. We propose a metal–barrier–metal structure that could be used for the experimental study of the JPs in the low-frequency range. The corresponding plots are shown in Fig. 4. Here, JPs determine the impedance of the structure on the frequencies higher than 50 MHz. The thin solid line in Fig. 1–4 shows the impedance of the ordinary capacitor, that is previously thought to be the impedance of the structures, if the excitation of JPs is not allowed for.

We have considered the non-linear rectification characteristics of the structures of the mentioned above types and have shown that their non-linear response in the high-frequency range is substantiated by JPs excitation. And we predict that it dramatically differs from that calculated in the frameworks of the models that do not take into account JP excitation.

So in the typical tunnel semiconductor structure with the diameter of 10 μm JPs appear on the frequency higher than 700 GHz, and in the diodes with the diameter of 5 μm they appear on the frequency higher than 200 GHz.

The work was partially supported by the National programs "Physics of Solid State Nanostructures" (project 1-094/4), "Surface Atomic Structures" (project 96-3.14), RFBR (grant 96-02-18811), INTAS-RFBR (95-0849) and CRDF (RC1-220).

Tunnel Resonance's in Structures with a Step-like Barrier.

Yu. N. Khanin, E. E. Vdovin @, Yu. V. Dubrovskii, T. G. Andersson*

Institute of Microelectronics Technology and High Purity Materials
Russian Academy of Sciences
Chernogolovka, Moscow District, 142432 Russia.
@E-mail <vdovin@ipmt-hpm.ac.ru>

*Department of Physics, Chalmers University of Technology
S-412 96 Geteborg, Sweden

Electron transport through an asymmetric AlGaAs/GaAs heterostructure with a step-like barrier is studied. Some specific features of the tunnel current are found to be related to the resonant tunnelling both through a level in a triangular quantum well induced by an external electric field over the barrier and virtual levels in a quantum pseudo-well which is restricted by a real heterobarrier on one side and a potential drop in the conductance-band edge at other side, which has transparency close to unity. Because of structure asymmetry , resonance tunneling is observed in quantum pseudo-wells of various widths, depending on the polarity of voltage bias. Calculated position of resonance's in these quantum pseudo-wells coincide well with determined ones, thus, providing evidence for the possibility to observe coherent reflection from a heavily doped region in a semiconductor (N^-/N^+ junction).

The possibility to observe effects caused by electron interference in heterostructures, owing to the persistence of phase coherence at distances of about 100 nm in GaAs [1], stimulated numerous works on the spectroscopy of states in quantum wells of various configurations.

Interference electron effects due to electron reflection from discontinuities of the conductance-band edge were observed during transport measurements. The discontinuities of the conductance-band edge can be initiated, for example, by appropriate combinations of A_3B_5 semiconductors. In structures consisting of two barriers and relatively wide quantum well (30 - 100 nm) bounded by these barriers, a number of various effects were observed, induced by electron interference. Current oscillations due to electron tunneling through quantum states in a wide quantum well were experimentally observed in [2,3]. Part of these oscillations were assumed to result from tunneling through virtual states, i.e. states above the barrier height. Virtual states can be induced by an external electric field applied to a rectangular tunnel barrier (Fowler-Nordheim oscillations [7]), which can give rise to triangular quantum pseudo-well. Apparently a real triangular quantum well can be formed in region of a tunnel barrier, by applying an external electric field to a step-like barrier. Current-voltage characteristics were calculated for these barriers, which include tunneling through levels in an electric -field -

induced quantum well [8,9]. However, no experimental studies on electron tunneling through step-like barriers have yet been reported.

Work [4] is a continuation of earlier studies. It deals with the energy spectrum of electron states in a quantum pseudo-well restricted by a real heterobarrier on one side and smooth potential drop at the conductance-band edge on the boundary of change in dopant concentration. An essential difference of the structure used in that work from those mentioned above is the absence of one heterobarrier confining the well. Its function are taken over by the smooth drop of the potential, whose reflection coefficient proved sufficient for experimental observation of electron interference. It was shown (in the work) that experimentally observed current oscillations as a function of the applied voltage result from electron tunneling through virtual states in such a quantum pseudo-well. To unambiguously determine the nature of current oscillations described in [4], the effect of the width of quantum pseudo-well should be investigated.

In this work, we study resonant tunneling of electrons in an asymmetric heterostructure with a step-like barrier. Depending on the sign of applied voltage, this structure allowed the observation of energy states corresponding to two quantum pseudo-wells of various widths (Fig. 1).

In the absence of magnetic field current oscillations were observed which depend on the voltage applied. These oscillations are connected with tunneling through quantum levels in quantum pseudo-wells positioned on the right and on the left of the main heterobarrier ($Al_{0.4}Ga_{0.6}As$). Moreover, the current-voltage characteristics exhibited a feature which can be attributed to tunneling through a state in a triangular well formed over a "small" barrier when a bias voltage is applied ($Al_{0.03}Ga_{0.97}As$).

Samples were grown by molecular-beam epitaxy on a heavily doped N^+ - GaAs substrate and had the following layer sequence : $2*10^{18}$ cm^{-3} N^+ GaAs - 50 nm thick, $2*10^{16}$ cm^{-3} N^- GaAs 50 nm thick, undoped GaAs 10 nm thick, a 5 nm thick undoped $Al_{0.4}Ga_{0.6}As$, a 30 nm thick undoped $Al_{0.03}Ga_{0.97}As$, $2*10^{16}$ cm^{-3} N^- GaAs 30 nm thick, and $3*10^{18}$ cm^{-3} N^+ GaAs 25 nm thick. Ohmic contacts were obtained by evaporating Ni-Ge-Au with subsequent annealing. A conventional procedure of chemical etching was used to fabricate a mesa-structure 100 μm in diameter.

Figure 2 shows an experimental dependence of the second derivative of the current-voltage characteristics, $d^2 I / dV_b^2$ as a function of an applied external voltage bias V_b at 4.2 K in the absence of magnetic field. The curve demonstrates a considerable oscillating component in the tunnel current. The "frequency" of these aperiodic oscillations differs substantially in the regions of positive and negative bias voltages. These oscillations are connected with resonant tunneling of electrons through the states in quantum pseudo-well formed by the main heterobarrier and smooth potential drop at the conductance -band edge in the N^- / N^+ region in the case of negative bias. At positive bias, these wells are formed by main heterobarrier and the potential break on the heterojunction $Al_{0.03}Ga_{0.97}As$ / GaAs (wall of a small barrier). Thus, electron tunneling occurs though the states in the quantum pseudo-well 60 nm wide in the first case, and 30 nm wide in the second case. The resonant positions calculated in terms of Bohr-Sommerfeld approximation according to [5] agree well with experimental data (Fig. 2).

Figure 3 presents the experimentally determined dependence of differential resistance as a function of an applied external voltage bias. In the absence of magnetic field, this curve exhibits a feature at V_b = -260 mV, which corresponds to resonance tunneling through states in a triangular well formed over the "small" barrier when a bias voltage is applied to the barrier. The position of this feature coincides with a theoretically calculated position of a level in an asymmetric triangular well, when a real potential distribution along the heterostructure is taken into account. It is seen from Fig. 3 , that the application of magnetic field perpendicular to the electric current suppresses the minimum of resistance and shifts it to higher voltages, as should be the case with tunneling through a two-dimensional state in a quantum well.

Thus, in this work we observed the dependence of the electric current oscillations on applied voltage which are associated with tunneling through pseudo-well quantum levels positioned on the right and left of the main heterobarrier ($Al_{0.4}Ga_{0.6}As$). Moreover, the I-V curves exhibited a feature which corresponds to resonance tunneling through the state in a triangular well formed over the "small" barrier when bias voltage is applied to the barrier ($Al_{0.03}Ga_{0.97}As$).

Note, in conclusion, that a good agreement between the positions of observed tunnelling oscillations and calculated values for an asymmetric single-barrier structure at both polarities of bias voltage supports the conclusion made earlier in [4] that these oscillations are manifestation of resonance tunneling through virtual states in quantum pseudo-wells. Moreover, it is due to the creation of an interference structure that coherent reflection of electrons from a heavily doped region of a semiconductor (N^+ / N^- junction) can be observed.

1. M. Heiblum, I. M. Anderson, C. M. Knoedler. Appl. Phys. Lett. **49**, 207 (1986).

2. A. F. J. Levi, R. J. Spah, J. H. English. Phys. Rev. B **36**, 9402 (1987).

3. R .C. Potter, A. A. Lakhani. Appl. Phys. Lett. **52**, 1349 (1988).

4. E.E. Vdovin, Yu. V. Dubrovskii, I. A. Larkin, Yu. N. Khanin, T.G. Andersson JETP Lett., Vol.61, 576.

5. Yu. V. Dybrovskii, Yu. N. Khanin, E.E. Vdovin, I. A. Larkin , T.G. Andersson Surfase Science 361/362 (1996), 213-216.

6. M. Helm, F .M. Peeters, P. England, J. R. Hayes, E. Colas. Phys. Rev. B **39**, 3427 (1989).

7. T.W. Hickmott Phys. Rev. B **40**. 11683 (1989).

8. P.A. Schylz, C.E.T. Goncalves da Silva Appl. Phys. Lett. **52**. 960 (1988).

9. M. Di Ventra, G. Pap, C. Coluzza and A.Baldereschi

22 nd International Conference on the Physics of Semiconductors. Vancouver. Canada. August15-19, 1994. p.1600.

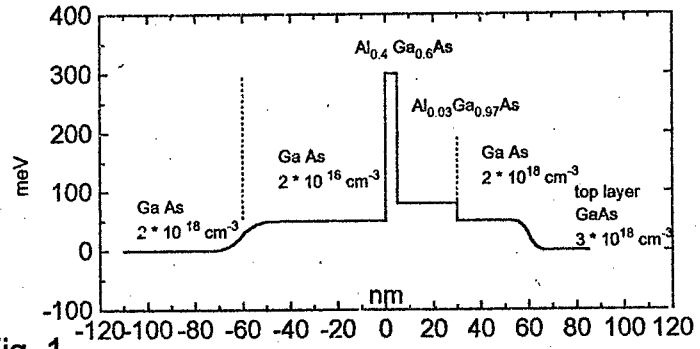

Fig. 1

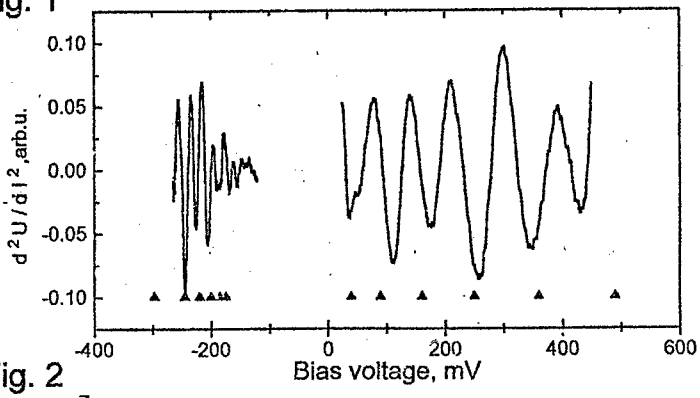

Fig. 2

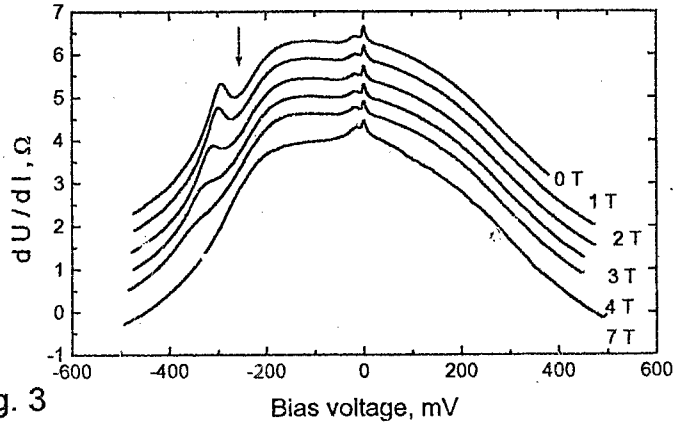

Fig. 3

Edge anomaly in tunneling of electron into p-type semiconductor

G.M.Minkov, O.E.Rut, A.V.Germanenko

Inst. of Phys. & Appl. Math., Ural University, Ekaterinburg, 620083, Russia

It is well known that for one particle tunneling the band edges in electrodes do not reveal themselves as sharp peculiarities in voltage-current characteristic at corresponding biases [1]. For example in a tunnel contact metal-insulator-p-type semiconductor with parabolic conduction band the bias dependence of the differential conductivity $(\sigma_d \equiv dj/dV)$ for tunneling in bulk states has the form

$$\sigma_d(V) \propto \left(eV - E_g - E_F\right)^{3/2},$$

where E_g, E_F are the band gap and Fermi energy respectively, and the energy is measured from the top of the valence band. This form of the σ_d-vs-V dependence takes place under the assumption that the band bending is lacking and that the tunneling transparency of the insulator has not energy and bias dependence in range of interest. In real situation these factors change the σ_d-vs-V dependence but they do not change the smoothing of the involving of the conduction band states in tunneling.

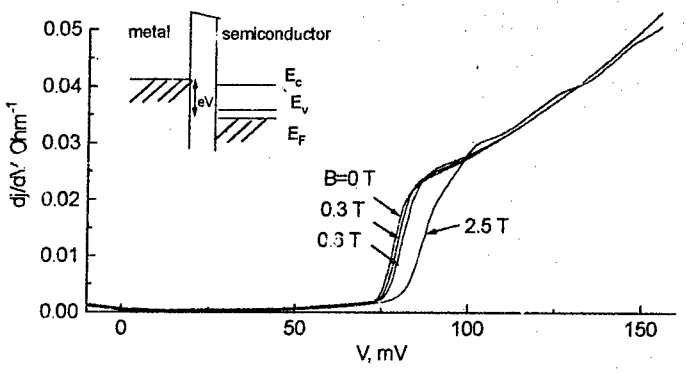

Fig.1. Bias dependences of differential conductivity taken at different magtetic fields for one of the structures investigated. Inset shows the energy diagram of tunnel structure.

The many particle effects change the σ_d-vs-V dependence. The electron-electron interaction leads to such effects as "zero-bias anomaly" in voltage-current

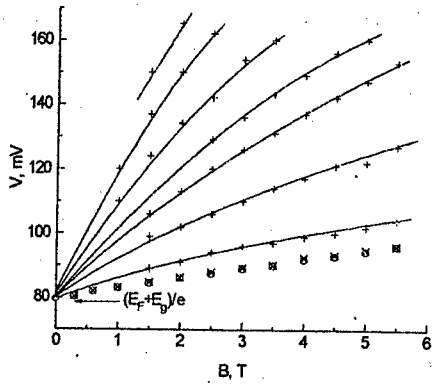

Fig.2. Positions of maxima of tunneling conductivity oscillations (+) at B||n and of the middle of step when a magnetic field direction is perpendicular (x) and parallel (o) to the normal to the contact plane.

characteristics of the various tunnel contacts [2], Coulomb blockade, etc. Specific manifestations of the many particle interaction may occur at tunneling of an electron into p-type semiconductor.

We present the experimental results of the tunneling conductivity study versus bias and magnetic field in the structures metal-insulator-heavily doped p-$Hg_{0.8}Cd_{0.2}Te$. The measurements have been performed at temperature range 1.5-40 K. Preparation of the tunnel structures has been described in [3].

The σ_d-vs-V curve for one of the structure investigated is presented in Fig.1. It is seen that at some threshold bias $V_{thr} = 30$mV the differential conductivity increases sharply. For $V > V_{thr}$ the tunneling conductivity oscillations in a magnetic field are observed (Fig.1). At fixed bias these oscillations are periodic versus reciprocal magnetic field and the oscillation periods coincide at B $\perp$n and B||n, where n is the normal to the tunnel contact plane. This fact and absence of the angle dependence of the oscillation positions in a magnetic field show that observed oscillations are due to the tunneling into Landau levels of the bulk states. Thus, the oscillation positions in (V,B) coordinates correspond to the positions of the Landau levels in the bulk (Fig.2) and their extrapolation to $B = 0$ gives the energy of the bottom of the conduction band. It is seen, that the step position eV_{thr} and the extrapolation energy coincide very closely. Thus the step in σ_d-vs-V curve corresponds to including the tunneling into bottom of the conduction band.

For analysis of experimental results the σ_d-vs-V dependence for one-particle tunneling has been calculated for metal-insulator-Kane semiconductor

structures. The calculations have been performed as for flat band so for different

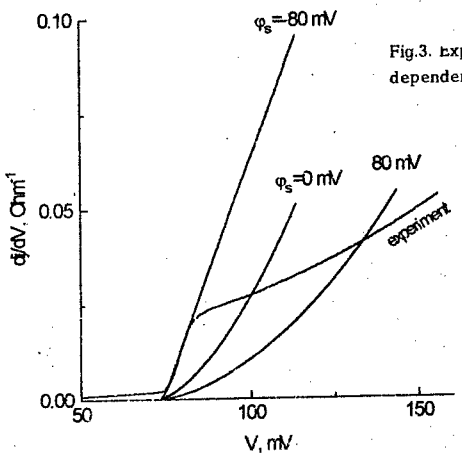

Fig.3. Experimental and theoretical bias dependences of tunneling conductivity.

values of the surface potential (φ_s). The parabolic φ(x) dependence has been assumed. This corresponds to the condition that tunneling electrons do not change the charge in space charge region significantly. The calculation results (Fig.3) show that the step-like behaviour of the σ_d-vs-V curve at bias $V = (E_g + E_F)/e$ is absent. What's more the step-like behaviour has not met with success at any changing the surface potential ($\Delta\varphi_s$) with bias at reasonable condition $\Delta\varphi_s < V$. Thus the experimental σ_d-vs-V curve is inconsistent with the calculations for one particle tunneling in framework described model.

In this report two possibilities of step-like behaviour of σ_d-vs-V dependence are discussed.

One of them is that for $eV > E_g$ an additional to tunneling of an electron into empty states of the conduction band, the tunneling into exiton-like states exists in structures based on p-type semiconductors. Naturally in heavily doped narrow gap semiconductors such states are broaden significantly and exiton structure in σ_d-vs-V curve escapes detection. In other words, electron-hole interaction in final state results in step-like σ_d-vs-V curve.

Another possibility is that tunneling into semiconductor electrons have no time to recombine with holes or to leave the region near the barrier and as a result the increasing the current at $eV > E_g$ leads to deviation of the potential in semiconductor from parabolic form (some analogue of the Coulomb blockade).

The farther investigations are necessary to clear observed experimental data.

This work was supported in part by the Russian Foundation for Basic Research (Grant No 97-02-16168) and by the Program "Physics of Solid Nanostructures".

1. Туннельные явления в твердых телах, М, "Мир", 1973.
2. B.L. Altshuler and A.G.Aronov, Solid State Commun. 30,115 (1979).
3. Г.М.Миньков; О.Э.Рут, В.А.Ларионова, А.В. Германенко, ЖЭТФ 105, 719 (1994).

Interband tunneling in RTS with type II heterojunctions

A. Zakharova
Institute of Physics and Technology, Russian Academy of Science,
Krasikov str. 25a, Moscow 117218, Russia

The interband tunneling in semiconductor heterostructures is a subject of many recent investigations (see, for example, Refs. [1]-[5]). The observation of negative differential resistance (NDR) conditioned by the interband tunneling, which provides the possibilities for device applications of interband tunneling heterostructures, is the main reason of considerable attention to this phenomenon. Especially attractive are InAs/ AlSb/GaSb resonant tunneling structures (RTS) with type II heterojunctions (see Fig. 1), which current-voltage (I-V) characteristics showed high values of peak-to-valley (P/V) current ratio at room temperature. In these structures the interband resonant tunneling through the light and heavy hole states in GaSb quantum well occurs. Previously this effect was investigated using ten-band tight-binding model [1] and three band kp model, which considers realistically the coupling among the conduction band, light and heavy hole bands [2] in terms of tunneling probability. In this paper we propose an alternative approach based on the transfer Hamiltonian method, which allows to calculate the interband tunneling probability and interband tunneling times in the framework of the envelope function approach taking into account the mixing of electron, light and heavy hole states in the case of nonzero in-plane wave vector of an incident particle. The equation for the tunnel matrix element is obtained for the interband transition into light or heavy hole states. The interband tunneling times τ corresponding to different subbands in the valence band of the GaSb quantum well of the InAs/AlSb/GaSb RTS and transmission coefficients T through single barriers are calculated using the obtained tunnel matrix element. The

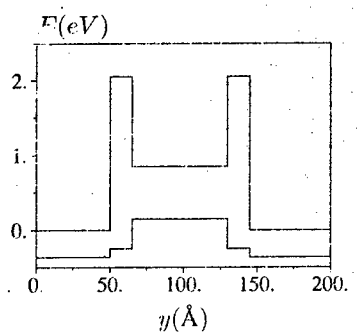

Fig. 1. Conduction and valence band diagram of InAs/AlSb/GaSb RTS.

relative role of the interband tunneling processes corresponding to the transitions into LH and HH

states is investigated. Significant dependence of τ on spin orientation of a tunneling particle is obtained. It is shown that band mixing in the case of nonzero $k_{\|}$ drastically enlarges characteristic interband tunneling times in the case of level anticrossing of 2D holes in the quantum well. The transmission coefficients in the RTS have been considered using second order perturbation theory. The peak values of T less than unity are obtained for $k_{\|} \neq 0$ in symmetrical structures due to the spin-orbit interaction. Note that previously the transfer Hamiltonian approach was applied for the description of resonant tunneling in type II heterostructures neglecting motion lateral to interfaces and mixing of electron (light hole) states with the heavy hole states [3].

We consider InAs/AlSb/GaSb RTS with type II heterojunctions, which conduction and valence band diagram under flatband conditions is shown in Fig. 1. The probability of a particle interband transition through the wide gap barrier per unit time is given by Fermi goldel rule, where the matrix element T_{rl} can be written in the following form [3]

$$T_{rl} = \int_{y>y_B} d^3r \sum_{ij} (\psi^*_{ir} \hat{H}_{ij} \psi_{jl} - \psi_{il} \hat{H}^*_{ij} \psi^*_{jr}) \tag{1}$$

In equation (1) axis y is normal to the interfaces, $y_1 < y_B < y_2$, where $y = y_{1,2}$ correspond to the barrier boundaries, ψ_{il}, ψ_{ir} are the envelope functions of the states to the left and to the right side of the barrier, $\hat{H}_{ij}$ is the Hamiltonian matrix element. After integration in equation (1) the following expression for T_{rl} is derived similarly to Ref. [3]

$$\begin{aligned} T_{rl} = \frac{iP}{\sqrt{2}} \left[\psi^*_{1r} \left(\psi_{2l} + \frac{\psi_{3l}}{\sqrt{3}} + \frac{\sqrt{2}\psi_{4l}}{\sqrt{3}} \right) + \psi_{1l} \left(\psi^*_{2r} + \frac{\psi^*_{3r}}{\sqrt{3}} + \frac{\sqrt{2}\psi^*_{4r}}{\sqrt{3}} \right) \right] + \\ (\gamma_1 + \gamma_2)(-\psi^*_{2r} \partial\psi_{2l}/\partial y + \psi_{2l} \partial\psi^*_{2r}/\partial y) - (\gamma_2 - \gamma_1)(-\psi^*_{3r} \partial\psi_{3l}/\partial y + \psi_{3l} \partial\psi^*_{3r}/\partial y) + \\ \sqrt{3}\gamma_2(-\psi^*_{2r} \partial\psi_{3l}/\partial y + \psi_{3l} \partial\psi^*_{2r}/\partial y + 2k_x \psi^*_{2r} \psi_{3l}) + \\ \sqrt{3}\gamma_2(-\psi^*_{3r} \partial\psi_{2l}/\partial y + \psi_{2l} \partial\psi^*_{3r}/\partial y - 2k_x \psi^*_{3r} \psi_{2l}) \end{aligned} \tag{2}$$

Here we have used the same basis functions as in Ref. [5], P is proportional to the interband momentum matrix element, $\gamma_{1,2}$ are the Luttinger parameters, $k_x = k_{\|}$. The value of T_{rl} should be calculated at any point y_B within the barrier layer. All normalizing lengths are supposed to be equal to unity, and the split-off energy to be equal to infinity. Due to spin-orbit interaction the transition probability through the asymmetrical single barrier of RTS depends on spin orientation of tunneling electron. Tunnel matrix element (2) corresponds to the transitions from (into) the states in the conduction band with spin $\sigma \approx 1/2$. The tunnel matrix element for transitions from (into) the states with oppposite spin orientation can be obtained from (2) by replacing k_x with $-k_x$.

The tunneling times in the structure with nonzero split-off energy depend also upon the spin of tunneling electron. In a symmetrical double barrier structure

$$\begin{aligned} \tau_l(\sigma) &= \tau_r(-\sigma), \\ \tau_r(\sigma) &= \tau_l(-\sigma), \end{aligned} \tag{3}$$

where $\tau_{l,r}$ correspond to the transitions through the left and right bariers. Using second order perturbation theory the tunneling probability in RTS in the resonance region can be written as

$$T = \frac{\hbar^2 \tau_l^{-1} \tau_r^{-1}}{(E - E_W)^2 + \hbar^2 (\tau_l^{-1} + \tau_r^{-1})^2/4} \tag{4}$$

Here E_W is the quasibound state energy with in-plane wave vector equal to the lateral wave vector of incident wave, the tunneling times are determined at the energy E_W.

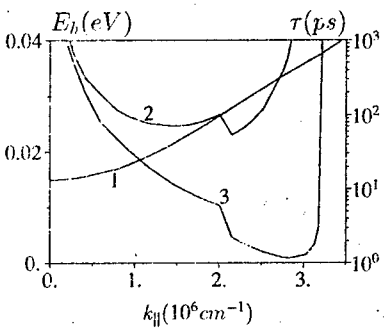

Fig. 2a

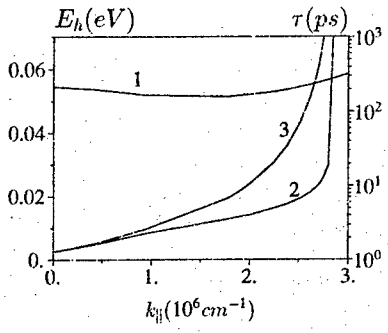

Fig. 2b

Since for $k_{\|} = k_x \neq 0$ $\tau_l \neq \tau_r$, if the split-off energy is not equal to zero, then the tunneling probability in resonance is not equal to unity even in symmetrical RTS.

The obtained tunnel matrix element was used for calculation of the transmission coefficients and tunneling times in InAs/AlSb/ GaSb RTS. The calculated dependencies of the hole quasibound state energy and interband tunneling times on in-plane wave vector for the first, second and third subbands in the 65 Å GaSb quantum well of the InAs/AlSb/GaSb RTS with 15 Å AlSb barriers are shown in Figs. 2a, 2b and 2c, respectively. In each figure curve 1 represents the quasibound state energy E_h, curve 2 (3) represents the interband tunneling time corresponding to the transition from the conduction band state with spin equal 1/2 (-1/2) in the left InAs layer into the well or the interband tunneling time corresponding to the transition from the quantum well into the conduction band state with spin equal -1/2 (1/2) in the right InAs layer. The partial escape widths, which are proportional to the corresponding reciprocal tunneling times $\tau_{l,r}^{-1}(\sigma)$, are different even in symmetrical RTS due to the dependence of the tunneling times on spin orientation, if $k_{\|} \neq 0$. Then the maxima of tunneling probability in symmetrical RTS are not equal to unity. The lowest subband in the quantum well (see Fig. 2a) corresponding to the HH1 states exhibits the greatest dependence of the tunneling time upon spin orientation. The values of $\tau(\sigma)$ are two orders in magnitude greater than the values of $\tau(-\sigma)$ for the values of in-plane wave vector of incoming wave greater than $2 \cdot 10^6$ cm^{-1}. The minima of $\tau(\pm\sigma)$ in Fig. 2a correspond to the peaks of the tunneling probability through single barrier shown in Fig. 3. The next two levels in the valence band quantum well of the InAs/ AlSb/GaSb RTS, which dispersion laws are shown in Figs. 2b, 2c, are the LH1 and HH2 states at $k_{\|} = 0$. For $k_{\|} \neq 0$ the anticrossing of these levels occurs, which is accompanied by significant mixing of the light and heavy hole states. For this reason the characteristic tunneling times corresponding to these levels are of the order of LH1 tunneling time at $k_{\|} = 0$. The total escape width, which is equal to the sum of partial escape widths $\hbar\tau_l^{-1}(\pm\sigma)$, $\hbar\tau_r^{-1}(\pm\sigma)$, for HH1 states with $k_{\|} > 2 \cdot 10^6$ cm^{-1} is of the order of characteristic LH1 escape width, while the maximum value of T through the double barrier structure corresponding to HH1 resonance is much less than those corresponding to the mixed LH1, HH2 resonances in accordance with (4).

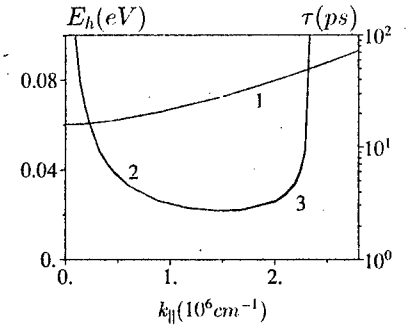

Fig. 2c.

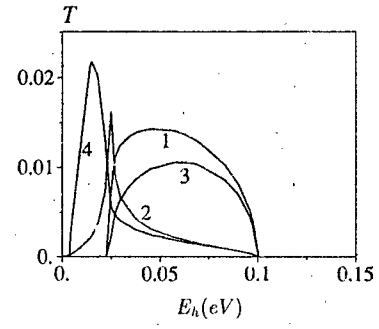

Fig. 3. Dependencies $T(E_h)$ for $k_{\|} = 2 \cdot 10^6$ cm^{-1}. Curves 1,3 correspond to final LH states and spin orientation of tunneling electron $\pm 1/2$, curves 2,4 correspond to final HH states.

This work was supported by Russian Foundation of Basic Research, Grant 97-02-16438.

References

[1] M. S. Kiledjin, J. N. Schulman, K. L. Wang, and K. V. Rousseau, Phys. Rev. B 46, 16012 (1992)

[2] M. H. Liu, Y. H. Wang, and M. P. Houng, Materials Sience and Engineering B 35, 435 (1995)

[3] A. Zakharova, and V. Gergel, Solid St. Commun. 96, 209 (1995)

[4] A. Zakharova, J. Phys.: Condens. Matter, to be published (1997)

[5] A. Zakharova, V. Ryzhii and V. Pesotzkii, Semicond. Sci. Technol. 9, 41 (1994)

Global Phase Diagram for the Quantized Hall Conductor

V.M. Pudalov

Institute for High Pressure Physics, Troitsk, Moscow District 142092, Russia

The studies of the quantum Hall effect (QHE) for a long time developed along two almost independent directions [1-3]. The first one [3,4] considers the 2D system in a pure limit, where its properties are entirely dependent on interactions between electrons. The fractional QHE is the most famous example of such a correlated electron state. Recent observation of novel features, such as composite fermions, fractional statistics, skyrmions, etc. demonstrates fruitfulness of this approach. The second approach considers the 2D system in the impure limit and studies effects of localization in magnetic field. These studies were restricted mainly to the regimes of the integer QHE. Substantial progress has been achieved by the two-parameter scaling [5], considering the conductivity as a function of two characteristic lengths determined by magnetic field and temperature. It was commonly believed that this class of phenomena may be understood in the framework of the single-particle picture. Recently, the Chern-Simons gauge theory [6] has introduced a mapping between the integer and fractional QHE regimes thus directing the way to their unified description. In this concept, the strongly correlated electrons at fractional filling $n'=1/(n^{-1}+2)$ can be mapped to the system of non-interacting electrons at the corresponding integer filling n, particularly, the composite quasiparticles at $n'= 1/2$ can be mapped to the electrons at zero magnetic field, $n= \infty$. Thus, the problem of the unified description of the interacting electrons in the presence of disorder merges with the problem of their behavior at zero magnetic field.

In the presence of a magnetic field, unitary universality class of the symmetry of the 2D system is compatible with the existence of delocalized states. A large body of experimental and theoretical studies of the quantized Hall effect confirm indeed the existence of extended states below the Fermi level. These states with nonzero Chern numbers, in high magnetic field B are centered in the corresponding Landau levels. When the energy of an extended state coincides with the Fermi energy, the electron system shows well pronounced features of the true metallic state. On the other hand, in the absence of magnetic field, the one parameter scaling theory [7] provides a clear picture of localization which is commonly accepted at the present time. In the framework of this picture there is no true metallic state in two-dimensions. In order to describe the transition between these two regimes, Khmel'nitskii [8] and Laughlin [9] suggested an elegant scenario, according to which the extended states belonging to occupied Landau levels should "float up" in energy and rise from the centre of the Landau level as

$$E_0 = \hbar\omega_c(n+1/2)\,[1+1/(\omega_c\tau)^2]. \qquad (1)$$

Here ω_c is the cyclotron frequency, and τ is the elastic collision time. In this "strong floating" scenario, the extended states are expected to leave the Fermi see one by one as $\omega_c\tau$ approaches 0, thus giving rise to the occurrence of a fully localized state. The latter picture of the QHE to insulator transition would evidently be in accord with the one-parameter scaling theory.

This prediction for a long time remained to be a challenge for experiments, and eventually, in 1990, the transitions between the QHE and insulator have been observed in experiments on high mobility Si-MOSFETs [10]. The features of this transition however appeared to be very different of the anticipated scenario. A clue to their interpretation was suggested by Kivelson, Lee and Zhang in 1993, who have introduced a Global Phase Diagram (GPD) for description of the quantized spinless particles on the plane of the two variables, magnetic field and disorder [11]. The Diagram is based upon the hypothesis of floating and using the Chern-Symons mapping. The Diagram involves three symmetry transformations (or „laws of corresponding states"), such as (i) electron-hole symmetry, (ii) symmetry with respect to addition of a fully filled Landau level, and (iii) flux-attachment symmetry. The GPD provides not a microscopic description, but a very general view on the behavior of the quantized Hall conductor. Both concepts, of the GPD and floating, suggest that the insulating state in 2D is a Hall type insulator , which should have a finite Hall resistance and diverging diagonal resistivity. A large number of experiments (e.g., [12-14]) performed at various experimental conditions and in various material systems have shown, indeed, the Hall-insulating type behavior occurring in 2D, in accord with the theoretical picture. Other predictions of the GPD, related to selection rules for the transitions between the QHE and insulator phases, to trajectories of the extended states on the „disorder-field" plane, and to floating of the extended states were found mainly to disagree with experimental data.

Selection rules for the transitions between different phases.

In the GPD picture, the transitions between different phases may occur only sequentially, when the corresponding Chern numbers are changing by $\Delta s_{xy} = \pm 1$. Each transition would thus correspond to passing of one extended state through the Fermi level. This is evidently in accord with all the experimental results (in single-layered systems) for transitions between phases within entirely the QHE regime.

The same prediction has been claimed for the transitions between the QHE ($s_{xy} \neq 0$) and insulator ($s_{xy} = 0$). The majority of the experiments studied this transition only from the lowest order QHE state ($s_{xy} = 1$): in the IQHE regime at $\nu=1$, and in the FQHE regime at $\nu=1/3$, 2/3, 4/3, 1/5. A good agreement with the GPD have been found. Transitions from QHE to insulator, driven by magnetic field (see, e.g., Refs. [14-16]), temperature [17] and disorder [18] have been found in accord with the theoretical predictions. However, these studies are not indicative of the selection rules validity. In experiments on Si-MOSFETs [10, 12], the direct transitions from $s_{xy}=2$, and 6 QHE state to insulator ($s_{xy}=0$) have been revealed, and an emerging transition from $s_{xy}=10$ to 0 has also been reported [12]. The similar direct transitions from high-order QHE states were found on different material systems: on 2D electron and hole system in GaAs-Al(Ga) As (from $\nu=2$) [15,16,19], and on 2D hole gas in a strained Ge quantum well (from $\nu=2$, and 3) [20]. While the transitions from $\nu=2$ state may somehow be explained by the spin degeneracy of the particles (which was ignored in the GPD), the higher order transitions can not be reduced to the lowest order one. Analogous experiments in the fractional QHE regime on GaAs-Al(Ga)As heterojunctions have also revealed occurrence of the direct transitions from high-order states to the insulator: $\nu=2/5$ [21,22], $\nu=2/5$ [21,23], and $\nu=2/9$ [24].

Trajectories of the extended states

The trajectories of the extended states on the „disorder-magnetic field" plane separate different phases of the 2D system characterized by different Chern numbers s_{xy}, and determine therefore topology of the Diagram. In the floating scenario, as well as in the GPD picture, the trajectories of the extended states coalesce in the singular point at zero-disorder/zero field. This corresponds to the hypothesis of their floating up in energy (1). On the experimental side, when an extended state passes through the Fermi level, a corresponding peak in the diagonal conductivity arises [17,18,25]; this effect was used as a tool to trace the trajectories of extended states. Experimental studies of floating were a matter of recent debates [17-19,25,26]. Experimentally, the electron density rather than energy is a variable, therefore the data on floating in density must be recalculated into the energy. It appears that as $\omega_c\tau$ approaches 0, the Landau bands becomes overlapping, and the Fermi energy decreases at fixed electron density. This leads to the casual floating of the extended state with respect to the Fermi energy. Despite the number of reported evidences for the floating of the lowest extended state, most of these data, to the first approximation, can be reduced to the simple effect of level broadening. In any case, there is no evidence for the „strong" or infinite floating at the lowest Landau level, while at higher Landau levels the floating would evidently contradict to the observed direct higher order transitions.

On the theoretical side, the Landau level mixing effect is considered as the microscopic driving mechanism for the extended states floating. This was studied recently by numerical simulations [27-30] and analytical calculations [31,32]. In fact, most of these studies have shown that mixing gives rise to the *Landau level- repulsion* as $\omega_c\tau$ decreases [33], this would tend to decrease rather than increase the extended states energy. The paradox has been solved in Ref. [32], where the lower Landau band energy was shown to decrease faster that the repulsion rises.

Merging of extended states, and the empirical Global Phase Diagram.

The concept of the infinite („strong") floating was introduced in order to match the predictions of the scaling theory for the absence of the extended states in 2D at zero field. Instead of the anticipated strong floating, the extended states were found to merge and remain in a finite energy range as $\omega_c\tau$ decreases [34]. These results taken on the Si-MOS structures, were recently confirmed by measurements on a strained Ge-well [20]. This is in the direct contradiction to the theoretical picture [11] and changes the topology of the GPD (as will be discussed shortly). In order to explain merging of the extended states, the attempt has been done [35] to incorporate spins in the framework of the GPD. The empirical GPD was introduced in Ref. [34]; it is based on the experimental data and is constructed by using the symmetry transformations. This empirical Diagram fits all the available data taken both in the integer and fractional QHE regimes.

The basic experimental observation we believe is of the key-importance, is that the QHE to insulator transitions occur at resolved Landau levels and in the strongly interacting system. The corresponding Coulomb interaction energy is larger than the Fermi energy by 10 times; this ratio increases with sample quality and with corresponding decrease in the critical electron density at which the transition occurs. The strong interactions were ignored in the theoretical picture of the GPD. In order to explain merging of the extended states and direct high-order transitions, it was

also suggested that the insulating state of a collective origin, like Wigner crystal, may incorporate the extended states [14]. Some features of the weak first order transition at the QHE-insulator critical boundary were found in experiments on Si-MOSFETs [36]. The topology of the empirical Diagram is different from that of the theoretical GPD, which is due to (i) merging of the extended states, and (ii) exchange interaction-enhancement of the energy splittings [34]. The empirical Diagram predicts more high-order direct transitions, the one of them, $1 \Leftrightarrow 0 \Leftrightarrow 2/3 \Leftrightarrow 0$, was recently observed [37].

Persistence of the extended states to zero magnetic field.

According to the scaling theory, there should not be extended states in the 2D system at zero magnetic field. Experimentally, the extended states were found, however, to merge at non-zero magnetic field, and to remain in a finite energy range. This suggest a puzzle, whether or not the extended states persist to zero magnetic field. Convincing evidences for existence at least some of the extended states and of the metal-insulator transition have been recently obtained by Kravchenko et al [38]. In the subsequent studies, the conductivity in high-mobility Si-MOS structures was found to display a critical behavior typical for a metal-insulator transition: conductivity scales with temperature and electric field; the scaling parameter vanishes at the critical point, and the localization length, correspondingly, diverges. By comparison with the scaling behavior of conductivity in magnetic field, the existence of the true metallic state at zero field has thus been proven [39].

This observation shows the importance of the electron-electron interactions and of the electron spin for the topology of the whole Diagram. Indeed, if the extended states do exist at zero field, they can not coalesce at the singular point of the zero disorder, and hence, must merge at a finite magnetic field. The next question becomes then of the principle importance, will all of the extended states persist to zero field? There was a theoretical suggestion [30] that the extended states are „fragile" and may be destroyed by disorder at finite $\omega_c\tau$ values. The preliminary experimental data seems do not support this suggestion.

In summary, the experimental observation of the direct transitions between the quantized Hall conductor and insulator phases has stimulated a considerable interest in the fate of delocalized electron states in 2 dimensions. The theoretical concept of the Global Phase Diagram provided a very important tool for understanding these transitions. It becomes clear that the interactions between the electrons must be incorporated into the theoretical picture of the Global Phase Diagram in order to describe the experimental data. Studies of the Global Phase diagram are intimately related to the problem of the Anderson transition at zero magnetic field, and may give a clue to its solution.

References

1. T. Chakraborty, P. Pietiläinen, The Quantum Hall effect, Springer -Verlag, (1995).

2. M. Janßen, O. Viehweger, U. Fastenrath, J. Hajdu, Introduction to the Theory of the Integer Quantum Hall Effect, VCH Verlagsgesellschaft mbH, Weinheim (1994).
3. The Quantum Hall Effect, ed. by R.E. Prange, S.M. Girvin (Springer-Verlag, 1990).
4. R.B. Laaghlin, Phys. Rev. Lett. **50**, 1395 (1983).
5. A.M.M. Pruisken, „Field Theory, Scaling and Localisation", in Ref. [3].
6. B.I. Halperin, P.A. Lee, N. Read, Phys. Rev. B 47, 7312 (1993).
7. E. Abrahams, P.W. Anderson, D.C. Licciardello, T.V. Ramakrishnan, Phys. Rev. Lett. **42**, 673 (1979).
8. D.E. Khmelnitskii, Phys. Lett. **106A**, 182 (1984).
9. R.B. Laughlin, Phys.Rev. Lett **52**, 2304 (1984).
10. M. D'Iorio, V.M. Pudalov, S.G. Semenchinsky, Phys. Lett. **150A**, 422 (1990).
11. S. Kivelson, D.-H. Lee, S.C. Zhang, Phys.Rev. B **46**, 2223 (1992).
12. V.M. Pudalov, M. D'Iorio, J.W. Campbell, Pis'ma ZhETF **57**, 592 (1993) [JETP Lett. **57**, 608 (1993)]; Surf.Sci. **305**, 107 (1994).
13. S.V. Kravchenko, J.A.A.J. Perenboom, V.M. Pudalov, Phys.Rev. B **44**, 13513 (1991).
14. V.M. Pudalov, M. D'Iorio, and J.W. Campbell, Surf. Science **305**, 107 (1994).
15. H.W. Jiang, C.E. Johnson, K.L. Wang, S.T. Hannahs, Phys.Rev.Lett. **71**, 1439 (1993)
16. T. Wang, K.P. Clark, G.F. Spencer, A.M. Mack, W.P. Kirk, Phys.Rev.Lett. **72**, 709 (1994).
17. S.V. Kravchenko, W. Mason, J.E. Furneaux, J.M. Caulfield, J. Singleton, and V.M. Pudalov, J.Phys. Condens.Matter, **7**, L41 (1995).
18. J.E. Furneaux, S.V. Kravchenko, W.E. Mason, G.E. Bowker, V.M. Pudalov, Phys. Rev. B **51**, 17227 (1995).
19. R.J. Hughes et al., J. Phys. Condens. Matter **6**, 4763 (1994).
20. S.-H. Song, D. Shahar, D.C. Tsui, Y.H. Xie, D. Monroe, Phys. Rev. Lett. **78**, 2200 (1997).
21. M.B. Santos et al, Phys. Rev. B **46**, 13639 (1992).
22. H.C. Monoharan, M. Shayegan, Phys. Rev. B **50**, 17662 (1994).
23. P.J. Rodgers et al, J. Phys. Condens. Matter, **5**, L449 (1993).
24. H.W. Jiang et al, Phys. Rev B **44**, 8107 (1991).
25. I. Glozman, C.E. Johnson, H.W.J iang, Phys.Rev.Lett. 74, 594 (1995).
26. A.A. Shashkin, G.V. Kravchenko, V.T. Dolgopolov, Pis'ma ZhETF **58**, 215 (1993) [JETP Lett. **58**, 220 (1993)].
27. V. Kagalovsky, B. Horovitz, Y. Avishai, Phys. Rev. B **52**, R17044 (1995).
28. Kun Yang, R.N. Bhatt, Phys.Rev. Lett. **76**, 1316 (1996).
29. Y.Tan, J. Phys. Condens. Matter **6**, 7941 (1994).
30. D.Z. Liu, X.C. Xie, Q. Niu, Phys.Rev. Lett. **76**, 975 (1996).
31. T.V. Shahbazyan, M.E. Raikh, Phys. Rev. Lett. **73**, 304 (1995).
32. F.D.M. Haldane, Kub Yang, Preprint Cond-mat/9606155.
33. T. Ando, J. Phys. Soc. Jpn, **53**, 3126 (1984).
34. Kravchenko, W. Mason, J. Furneaux, V.M. Pudalov, Phys.Rev. Lett. **75**, 910 (1995)
35. A.M.Tikofsky, S.A. Kivelson, Phys. Rev. B **53**, 13275 (1996).
36. V.M.Pudalov, S.-T Chui, Phys.Rev. B **49**, 14062 (1994).
37. V.M. Pudalov, in: Proc. Int.Conf.on High Magnetic Fields in Semiconductor Physics, Würzburg (1996).
38. S.V. Kravchenko, J.E. Furneaux, M. D'Iorio, V.M. Pudalov, Phys. Rev. B **49**, 8039 (1994).
39. S.V. Kravchenko, W.E. Mason, G.E. Bowker, J.E. Furneaux, V.M. Pudalov, M. D'Iorio, Phys.Rev. B **51**, 7038 (1995).

Properties of two-dimensional hole systems

S. I. Dorozhkin
Institute of Solid State Physics, Chernogolovka, Moscow district, 142432, Russia

In this lecture I present a review of our results on properties of two-dimensional hole systems (2DHS) in Si MOSFETs, Si/SiGe and GaAs/AlGaAs heterostructures. Both, general for 2DHS properties: (i) the existence of two different groups of carriers and (ii) an extreme anisotropy of the g-factor, and material specific results: (iii) occupation of the second subband and (iv) the effect of the uniaxial stress are discussed. Results on metal-insulator transitions in quantising magnetic fields together with our model capable of explaining them in terms of percolation of noninteracting carriers are also presented.

Two different groups of carriers appear in 2DHS as a result of lifting of spin degeneracy at non-zero wave vector in the absence of inversion symmetry. This feature defines many transport properties of 2DHS at low temperatures. In the intermediate range of magnetic fields, it leads to two frequencies of the Shubnikov-de Haas oscillations. At large difference between these frequencies two well resolved periods are observed which are determined by the carrier densities in the two groups. At small difference the oscillation picture shows the beating effect [1]. The former case exists usually in materials without inversion symmetry in the bulk (for example, in GaAs/AlGaAs heterostructures). The latter one was observed in Si MOSFETs where the inversion asymmetry appears as a result of the asymmetry of the potential well at the Si-SiO_2 interface. From the quantum mechanical point of view the beating effect results from interplay of the cyclotron and the Zeeman splittings slightly modified by the spin-orbit interaction [1]. The node position should be sensitive to each of these quantities, which provides a sensitive tool for measurements of the energy spectrum parameters [2]. This is demonstrated by Fig.1 where the Shubnikov-de Haas oscillations are shown for different values of an uniaxial stress applied to the Si MOSFET. The oscillations appear to be sensitive to the stress in the vicinity of the node only.

The weak dependence of the node position on the in-plane magnetic field component H_x at not very large values of H_x (Fig. 2) implies weak sensitivity of the hole energy spectrum to this component, which looks like an extreme anisotropy of the g-factor of holes. For particular case of Si MOSFETs we have shown [3] that g_z/g_x is greater than 2.5. (Here g_z and g_x are components of the g-factor tensor corresponding to magnetic field orientation perpendicular to 2DHS and along it, respectively). Such strong anisotropy can be naturally explained [3] by the fact that the lowest subband in 2DHS is produced by heavy holes with angular momentum projections $m_J = \pm 3/2$ and the in-plane magnetic field do not mix these states. Hence, this effect is general for subbands originating from the heavy holes and should, in particular, exist for ground subbands in 2DHS produced from different materials.

The existence of two groups of carriers leads to the magnetoresistance at weak magnetic fields ($\omega_c\tau \ll 1$). In the case of the small energy splitting between the groups, we observed the anomalous magnetoresistance caused by weak localization effects (Fig.3). Depending on temperature and the areal density of holes the magnetoresistance can be positive, nonmonotonic or negative. It can be well described by equations of the weak localization theory [4]. The

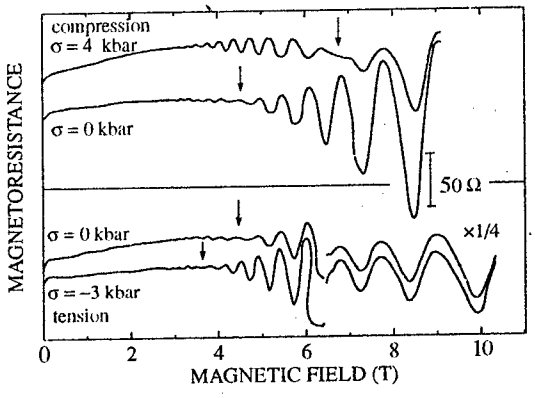

Fig 1. Shubnikov–de Haas oscillations for 2DHS in Si(110) MOSFETs in the presence of the uniaxial stress applied along [001] crystal axis. $T = 1.4$ K. Areal density of holes $n_s = 2.7 \times 10^{12}$ cm^{-2}. Positions of the node in the oscillation beating pattern are shown by arrows.

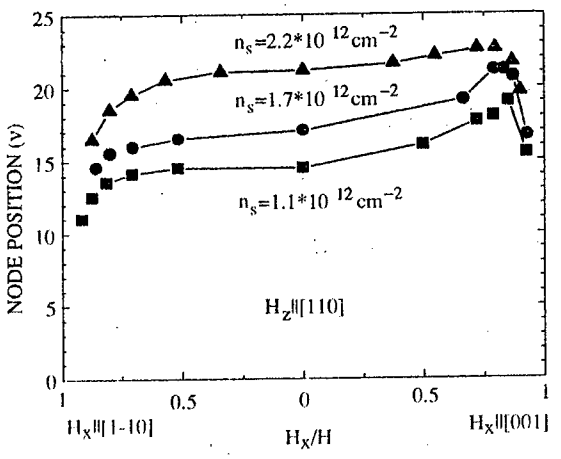

Fig 2. Filling factors ν corresponding to the nodes versus the ratio of the in-plane magnetic field component H_x to the total magnetic field H for several hole densities shown at the curves and the two orientations of H_x relative to the crystal axes.

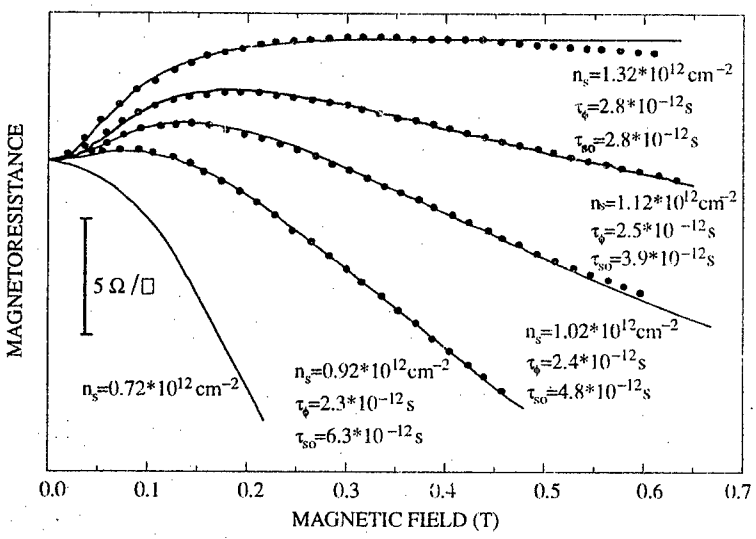

Fig 3. Anomalous magnetoresistance of 2DHS in the Si (110) MOSFET at T = 4.2 K for different areal densities of holes. The solid lines represent experimental results. Results of fitting based on the equations of the weak localization theory [4] are given by dots. Values of fitting parameters: the phase-breaking time τ_ϕ and the spin-orbit relaxation time τ_{so} are shown at the curves.

change of the magnetoresistance sign is naturally explained by the change of the relation between the phase-breaking time and the spin-orbit relaxation time. The latter is probably defined by the D'yakonov-Perel spin relaxation mechanism and depends on the energy separation between the two groups at the Fermi wave vector. In the case of a large energy splitting between the groups a rather large positive magnetoresistance appears which depends on temperature (Fig.4). We have shown [5] that the momentum exchange between the groups due to the hole-hole scattering leads to the temperature dependence of both the zero-magnetic-field resistance and the magnetoresistance. Obtained equations fit well our experimental results (Fig.4) with the temperature dependence of the frequency of the hole-hole scattering proportional to T^2.

Investigating the occupation of the second subband in the Si (110) MOSFETs we have observed several effects which imply this subband to be an excited subband of heavy holes, which contradicts the results of calculations [6]. These effects are listed below. (i) Pinning of the bottom of the second subband at the Fermi level leads to the great difference (about factor of 7) of the occupation rates for the ground and the second subband [7]. (ii) The large anisotropy of the g-factor exists also for holes in the second subband. (iii) The uniaxial stress only slightly affects the relative occupation of the subbands [8].

Quantum oscillations in dilute 2DHS in Si/SiGe heterostructures were shown to have two types of anomalous behavior [9,10]. (1) With increasing magnetic field, the normal sequence of quantum

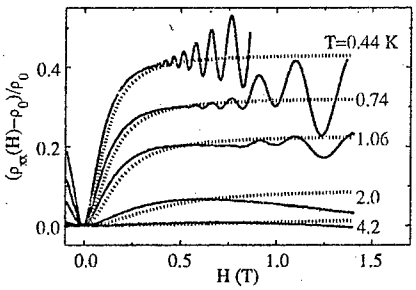

Fig 4. Magnetoresistance of 2DHS at GaAs/AlGaAs heterojunction at different temperatures. The solid lines are experimental curves, the dotted are lines are theoretical.

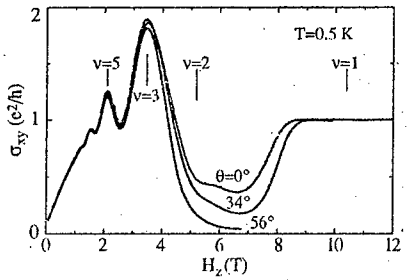

Fig 5. Hall conductivity σ_{xy} (in units of e^2/h) for sample 1 of the Si/SiGe heterostructures versus normal magnetic field H_z at different angles θ between the magnetic field and the direction normal to 2DHS. Areal density of holes $n_s = 2.5 \times 10^{11}$ cm^{-2}. $T = 0.5$ K. Values of the filling factors ν were defined from the periodicity of the Shubnikov-de Haas oscillations.

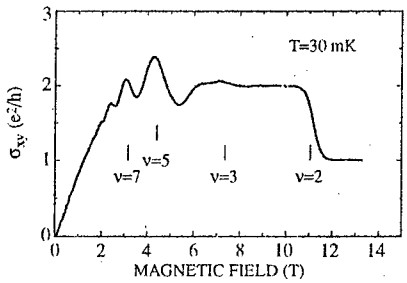

Fig 6. Hall conductivity σ_{xy} for sample 2 of the Si/SiGe heterostructures ($n_s = 5.3 \times 10^{11}$ cm^{-2}) versus magnetic field normal to the sample plane at $T = 30$ mK. The filling factors ν are defined from positions of the magnetoresistance minima at $T = 1.23$ K.

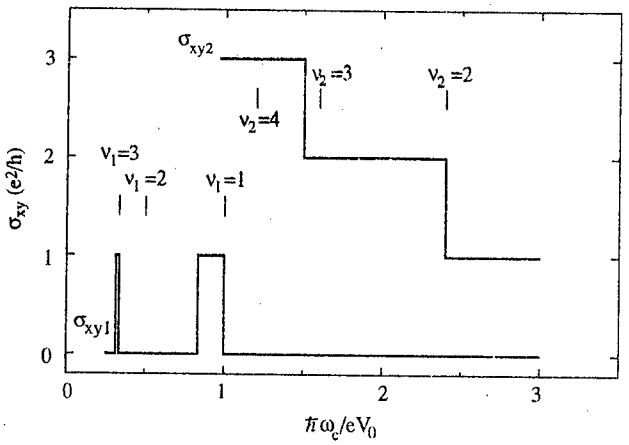

Fig 7. Hall conductivities σ_{xy}, calculated on the basis of model [11] for two areal densities of carriers corresponding to the zero-magnetic-field Fermi energies E_{f1}^0=0.5eV_0 and E_{f2}^0=2.2eV_0, versus the cyclotron energy normalized by the amplitude of the potential modulation eV_0. In the chosen potential (for details see [10]) the percolation threshold in the zero magnetic field occurs at E_f^{th}=0.5eV_0. The ratio of the Zeeman splitting to the cyclotron energy $E_z/\hbar\omega_c = 0.6$.

Hall effect states is interrupted by the appearance of the insulating state in the region of filling factor two, which in turn is replaced by the $\nu = 1$ quantum Hall effect state. Tilting the sample plane relative to the magnetic field direction increases dramatically the degree of insulating behavior (Fig.5). (2) In similar heterostructures, but ones with a higher areal density of holes, the insulating state is not observed. However the measured, almost quantised, value of the Hall conductivity turns out to be different from that expected from the Shubnikov-de Haas oscillation periodicity (Fig.6). Such effects can be naturally explained (Fig.7) by model [11] considering a two-dimensional electronic system in the presence of a long-range potential modulation with amplitude comparable to the Fermi energy. In such a system the Fermi energy oscillates as a function of the magnetic field relative to the energy of the delocalized state on a magnetic level, which leads to non-monotonic dependence of the Hall conductivity on magnetic field. In particular, in some ranges of magnetic field there are no delocalized states under the Fermi level, i.e. the system is insulating with the Hall conductivity equal to zero.

References

[1] S. I. Dorozhkin and E. B. Ol'shanetskii, *JETP Lett.* **46**, 502 (1987).

[2] S. I. Dorozhkin. *Phys. Rev. B* **41**, 3235 (1990).

[3] S. I. Dorozhkin, *Solid State Commun.* **72**, 211 (1989).

[4] S. Hikami, A. I. Larkin and Y. Nagaoka, *Progr. Theor. Phys.* **63**, 707 (1980).

[5] S. S. Murzin, S. I. Dorozhkin, G. Landwehr, and A. C. Gossard, *Proceedings of the 23rd International Conference on the Physics of Semiconductors*, p.2187. Ed. by M.Scheffler and R.Zimmermann. World Scientific, 1996.

[6] F. J. Ohkawa and Y. Uemura, *Prog. Theor. Phys. Suppl.* **57**, 164 (1975).

[7] S. I. Dorozhkin and E. B. Ol'shanetskii, *JETP Lett.* **48**, 588 (1988).

[8] S. I. Dorozhkin and G. Landwehr, *JETP Lett.* **64**, 677 (1996).

[9] S. I. Dorozhkin, C. J. Emeleus, T. Whall, and G. Landwehr, *Phys. Rev. B* **52**, R11638 (1995).

[10] S. I. Dorozhkin, C. J. Emeleus, T. Whall, G. Landwehr, and O. A. Mironov, *JETP Lett.* **62**, 534 (1995).

[11] S. I. Dorozhkin, *JETP Lett.* **60**, 595 (1994).

Acoustoelectric effects in quantum constrictions

Y. Galperin[1,2], H. Totland[2], and F. A. Maaø[3]

[1] *A. F. Ioffe Physico-Technical Institute R A S, 194021 St. Petersburg, Russia*
[2] *Fysisk institutt, University of Oslo, P. O. Box 1048 Blindern N-0316 Oslo, Norway*
[3] *Institutt for fysikk, NTNU, N-7034 Trondheim, Norway*

Recently surface acoustic waves (SAW)[1–3], as well as nonequilibrium ballistic phonons[4], have been successfully used to study quasi-one-dimensional mesoscopic systems such as quantum point contacts (QPC) and quantum wires (QW). In most cases these systems connect two reservoirs made of a two-dimensional electron gas (2DEG).

Due to the piezoelectric effect, acoustic waves induce traveling waves of electric field which propagate with the sound velocity s. Being concentrated near the surface, these waves are extremely sensitive to the electric properties of the surface's vicinity. A highly conductive 2DEG screens out the electric fields and in that way effects the sound velocity. If the electric field is not screened completely, the Joule losses in the 2DEG lead to a pronounced attenuation of the waves. In both situations acoustic waves provide a possibility of probeless measurements of the 2D conductance $G(\omega, \mathbf{q})$ as a function of the sound frequency ω and wave vector $\mathbf{q}$. The role of screening is determined by the dimensionless ratio G/s which is usually large (see e.g. Ref. 5). However, the component of G parallel to the surface can be suppressed by an external magnetic field and thus made of the same order as s. This is the case, in particular, under the conditions of the quantum Hall effect, and several beautiful and instructive experiments were conducted in that regime[6,7]. Along with coherent SAW, ballistic phonons are also used (see, e.g., Ref. 8) which can be induced either by laser beams[9] or by resistive film heaters[4].

Two groups of experiments are usually conducted. In the experiments of the first group, a *linear* response to the wave – the variations in the sound velocity and attenuation – is studied. The second group of experiments[1,2,7] is concentrated on the studies of the *nonlinear* response of the electron gas to the acoustic waves. The quantities which are investigated in these experiments are the dc electric current induced by the waves (the so-called *acoustoelectric current*), or the dc voltage induced across the sample.

The acoustic waves seem very advantageous for studies of quantum constrictions like QPC or QW. Indeed, the screening length in the 2DEG coincides with the Bohr radius, a_B. Consequently, if the dimensions of a 2D sample are much larger than a_B then the (piezoelectric) coupling to phonons is screened out, at least in the absence of a perpendicular magnetic field. However, if the width of the channel is not exceeding a_B by too much, the field penetrates the channel. As a result, it is the channel region that contributes to the interaction rather than the 2D leads where the coupling is screened out. On the other hand, the resistance of the system is also determined by the channel, and it is possible either to monitor its changes under the influence of the waves (the so-called acousto-conductance).

Recently, two experiments[1,2] on the induced acoustoelectric current in quantum constrictions revealed several interesting features. In the first paper by Shilton et al.[1] the regime of weak AE was investigated, while the second paper[2] examined the regime of a strong SAW-field. At low intensities the authors observed a very specific behavior of the AE in

a quasi-one-dimensional channel defined in a GaAs-AlGaAs heterostructure by a split-gate depletion - giant oscillations as a function of the gate voltage (see Fig. 1). In the large-amplitude regime the induced current was shown to be quantized in units of ef, with e being the electronic charge and $f = \omega/2\pi$ the wave frequency. This behavior was explained by the authors of Ref. 2 in terms of 'traveling quantum dots' with an integer number of electrons in each dot. Thus, during one period an integer number of electrons are carried from one side of the constriction to the other.

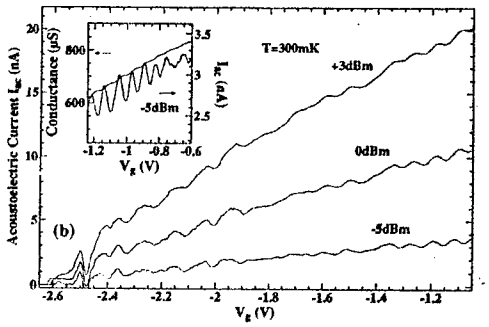

Fig. 1. Acoustoelectric current as a function of split gate voltage for different SAW power[2]). *Inset*: comparison of the conductance and acoustoelectric current.

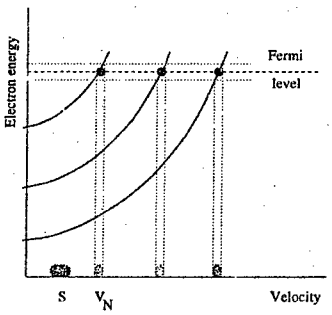

Fig. 2. To the explanation of the source of the giant oscillations in the acoustoelectric current

The low-amplitude behavior of the AE has been analyzed previously[10] on the basis of the Boltzmann equation for the electrons interacting with the traveling wave. The qualitative picture of AE is as foolows. The linear response of the electrons to the SAW with a given wave vector q is proportional the effective "interaction time" $(qv - \omega)^{-1}$, during which an electron with the velocity v moves in an almost constant field. At small v, or near the resonance ($v \approx s$) this time diverges. In this region the effect is determined either by finite length of the channel, or by electron scattering. In a homogeneous 2D system, the most important relaxation mechanism is disorder-induced scattering, and the coupling is limited by the product of the SAW wave vector times the mean free path, $q\ell$. In a point contact it can be also limited by the finite length W of the cannel. In the qualitative theory[10] the finite length was taken into account by introducing a "interaction time" $\sim W/v$. The analysis given in[10] leads to the conclusion that coupling is optimal for the electrons having their velocities in a relatively narrow range, the central velocity being close to the sound velocity s. The "resonant" region is shown in Fig. 2, its position and effective width being estimated in[10]. On the other hand, electronic states can contribute to interaction only if their energies are in a vicinity of the Fermi level. Consequently, for a given mode number n the electron velocities have to belong to a narrow interval centered around some velocity v_{NF}. One can move these intervals by changing the gate voltage. To get a non-vanishing contribution to the current one of these regions has to overlap with the region centered around s (see the Fig. 2), that is possible only for the upper level. As a result, AE experiences *giant*

oscillations as a function of the gate voltage.

The theory[10], which was able to reproduce the main features of the experimental observations, is based on a model treatment of the finite channel's length and of the role of elastic scattering. A quantum theory of AE in a uniform quantum channel was developed in Ref. 11 in an analogy to the previous treatment of equilibrium phonons[12]. The main point was to analyze the energy and momentum conservation laws which correspond to backscattering of the electrons by the traveling wave. It was shown that there is a cut-off in the electron-SAW interaction at $q = q_0 \equiv 2ms/\hbar$. At $q \leq q_0$ backscattering is forbidden, while the forward scattering cannot influence the current in a 1D system. This statement has been also expressed in a recent paper[13] where the interaction with non-equilibrium ballistic phonons was considered. At the same time, in the experiments[1,2] the interaction is clearly observed despite of the inequality $q \ll q_0$.

Our aim is to draw attention to the fact that in any realistic quantum channel, there are special regions near the leads where an acoustic wave (or non-equilibrium ballistic phonons) can cause transitions between the *propagating* states in the channel and the *reflecting* states which correspond to reflection of an electron back into the incident lead. These particular processes facilitate phonon-induced backscattering. As a result, the AE persists at $q \leq q_0$ and several new and important features of the effect appear at $q \geq q_0$. Note that the role of the processes mentioned above was emphasized in Ref. 14 in connection with photoconductance of quantum channels. However, there are important differences between the case of transverse electro-magnetic field with zero wave vector (as in the case of photoconductance) and the longitudinal wave with a finite wave vector (as in the case of the AE). Below we present a quantum theory which takes into account the above mentioned transitions and in this way explains the results obtained in realistic structures. We believe that at $q \ll q_0$ these transitions lead to the same physical effect as the introduction of a finite "relaxation length" W in the classical theory[10], while they do not have analogs in the theory for an uniform channel[11,13].

Being interested in the response of quasi-one-dimensional systems (quantum constrictions, wires, etc.) we assume that the channel's width is of the order of the Bohr radius a_B while the leads consist of a two-dimensional electron gas and have widths $\gg a_B$. On the other hand, the typical wave length $2\pi/q$ of SAW or non-equilibrium phonons is $\geq a_B$. As a result, the (piezo)electric field produced by acoustic waves is efficiently screened outside the channel. This is the reason why the response of a short channel is not completely masked by the leads. Consequently, the field is taken into account only in the region near the constriction. For simplicity here we consider the case of zero temperature and assume the quantum channel to be symmetric with respect to reflection of the longitudinal coordinate ($x \to -x$). Let the channel be elongated along the x-axis, its dimensions in the y- and z-directions being much less than q_y^{-1} and q_z^{-1}, respectively. In that case non-equilibrium phonons cannot produce transitions between the modes of transversal electron motion. Consequently, all transverse modes are subjected to the sliding potential $V(x,t) = V(x)\cos(qx - \omega t)$, since the envelope function $V(x)$ is independent of n under the assumptions made above. Here $q \equiv q_x$.

Neglecting spontaneous emission in the constriction region, we can write the dc electric current through the channel as[15,16]

$$I = \frac{2e}{h} \sum_n \int_0^\infty [T_{R,L}(E + n\hbar\omega, E) f_{\mu_L}(E) - T_{L,R}(E + n\hbar\omega, E) f_{\mu_R}(E)] \, dE . \qquad (1)$$

Here e is the electronic charge, f_μ is the Fermi distribution with the chemical potential μ, while $T_{R,L}(E + n\hbar\omega, E)$ is the sum (over the transverse modes) of transmission probabilities for particles with the energy E to be transfered from the left lead (L) to the right one (R) into the states with the final energy $E + n\hbar\omega$. $T_{L,R}(E + n\hbar\omega, E)$ denotes the reverse transition, both transitions being accompanied by absorption or (induced) emission of n phonons. Eq. (1) is actually a generalization of the Landauer formula[17].

Since we are going to study dc response in the absence of external bias, i.e. at $\mu_L = \mu_R = \mu$, the current can be expressed as

$$I(\mu) = \frac{2e}{h} \int_0^\infty \Delta T(E) f_\mu(E) \, dE, \quad \Delta T = \sum_n [T_{R,L}(E + n\hbar\omega, E) - T_{L,R}(E + n\hbar\omega, E)] . \quad (2)$$

A positive $\Delta T(E)$ means that non-equilibrium phonons enhance the L$\rightarrow$ R dc particle current.

In this work we shall study the regime of relatively small acoustic amplitudes where the perturbative approach is adequate. In particular, we restrict ourselves with the *linear in acoustic intensity* approximation where it is sufficient to consider $n = -1, 0$ and 1.

The numerical calculation of the acoustically-induced dc current based on the recursive Green function method near the continuum limit[16]. This method gives an exact solution to the scattering problem posed by the Schrödinger equation. However, the physical picture can be understood from a simplified situation which involves a constriction with smooth variations on the length scale set by the Fermi wavelength k_F^{-1}. In this case we can use an *adiabatic* and *semi-classical* analysis[18]. The essence of the *adiabatic* approximation is to assume the electronic wave function can be expressed as a product of the *transverse* part (which varies slowly as a function of the longitudinal co-ordinate x), and the *longitudinal* part which bears the main x-dependence. Consequently, the shape of the constriction manifests itself only as rather smooth x-dependence of the transverse eigen energies, $E_m(x)$, for different transverse modes. This x-dependent eigen energy, $E_m(x)$, now acts as a potential barrier for an one-dimensional scattering problem describing electron transfer in the x-direction. An important feature of the semi-classical situation is that the phonon-assisted processes are *spatially confined* to regions relatively small in comparison to the total length of the channel, W. Indeed, in complete analogy with the semi-classical theory of photoconductance[14], only in the vicinities of the points x^*, corresponding to local conservation for both momentum and energy, the phase of the integrand which enters the perturbation matrix element $\langle i|V(x,t)|f\rangle$ is a slow function if x. Consequently, only the vicinities of such points are important, and the general behavior of the induced current can be understood from the analysis of the local conservation laws. Conservation of energy and local longitudinal momentum implies that intra-band transitions can only take place only near the points x^* and between the states $k_{1,2}$ determined by the equations states

$$k_1(E) \equiv k(x^*, E) = (q_0 - q)/2 , \; k_2(E) \equiv k(x^*, E + \hbar\omega) = (q_0 + q)/2 . \qquad (3)$$

Here $k(x, E) \equiv h^{-1}\sqrt{2m[E - \mathcal{V}_m(x)]}$. Here we have taken into account that for acoustical phonons $\omega = sq$. Note that the component $\propto \exp(iqx - i\omega t)$ in $V(x,t)$ will cause a transition

from the state 1 to the state 2 (absorption), while the component $\propto \exp(i\omega t - iqx)$ will cause a transition from the state 2 to the state 1 (emission).

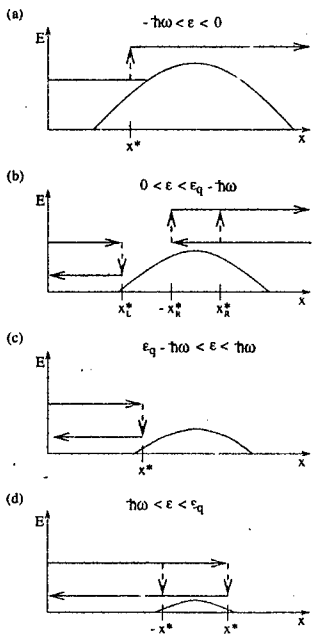

Fig. 3. Transitions between the propagating and the reflecting states due to acoustic waves.

One can observe the characteristic quantity q_0 which sets the scale for the phonon wave vector q. In a long channel with an uniform width[11,13] only the scattering between the states *propagating* in opposite directions can contribute both to the drag current and to AC. This implies that we must have $q > q_0$ in order to see any effect. However, for non-uniform wires this is no longer the case. As it follows from Fig. 3 and Eqs. (3), it is natural to analyze the cases $q < q_0$ and $q > q_0$ separately.

The case $q < q_0$ is the simplest. According to[11,13] neither current nor the change in the conductance should be induced in this case. However, the coordinate dependence of the channel width leads to a finite backscattering even at $q < q_0$. If the energy E of the initial state satisfies the condition

$$E_m(0) - \hbar\omega < E < E_m(0),$$

then a scattering from the initial *reflecting* state (incoming from the left) with the energy E to the final *propagating* (to the right) state with the energy $E + \hbar\omega$ is allowed. As a result of the absorption process described above, the initial state becomes not fully reflecting, and the total current through the channel *increases*. An emission process from the energy E to the energy $E - \hbar\omega$ will not influence the total transmission. On the other hand, when $0 < E - E_m(0) < \hbar\omega$ an emission process will *reduce* $\Delta T_{R,L}(E)$ while absorption is not important. When $E > E_m(0) + \hbar\omega$, no transitions will alter the transport properties since transitions are between the states fully transmitted in the same direction.

For the case when $q > q_0$ things are slightly more complicated since from equation (3) scattering from the acoustic field will now reverse the direction of propagation. From the conservation laws (3) one can extract the relevant energy scale, $\epsilon_q = \hbar^2(q + q_0)^2/8m$. If $\epsilon \equiv E - E_m(0) > \epsilon_q$ then no scattering is possible which fulfills conservation of both energy and local longitudinal momentum. One can discriminate between the following four energy intervals for the energy ϵ. In the first one (see Fig. 3,a), $\hbar\omega < \epsilon < 0$, there is only one point where the local conservation laws are fulfilled. The same is true for the third region, $\epsilon_q - \hbar\omega < \epsilon < \hbar\omega$, (Fig. 3,c). In the second region, $0 < \epsilon < \epsilon_q - \hbar\omega$, (Fig. 3,b), the waves incoming from both the left and the right leads will experience scattering which affects $\Delta T(E)$. It is important that there are *two* points, x_R^* and $-x_R^*$ where the conservation laws are met. The resulting state is a superposition of an incoming wave and *two* reflected waves,

the reflecting points being $\pm x_R^*$. Thus the dependence of $\Delta T_{L,R}$ vs. energy (actually, vs. the Fermi level controlled by the gate voltage) shows oscillations due to interference effects between the reflected waves. The same is true for the fourth region, $\hbar\omega < \epsilon < \epsilon_q$ (Fig. 3,d). The interference pattern calculated for $q = 50q_0, W = 2.4\mu$ by the recursive Green's function method is shown in the last figure.

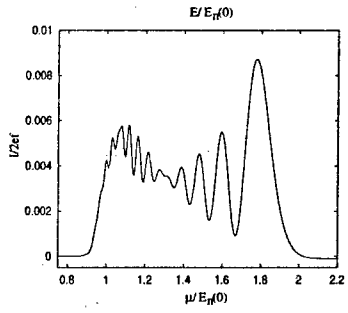

The shape of the channel is described by its x-dependent width as

$$d(x)/d_\infty = d_0/[(d_\infty - d_0)\cos^4(\pi x/W) + d_0]$$

while the envelope of acoustic field is taken as

$$V(x) = V_0[1 - \sin^8(\pi x/2W)]\,.$$

The oscillation in the current are clearly seen. However, at finite temperature, as well as in the case of non-momochromatic phonons their amplitude is decreased.

In conclusion, we have demonstrated that AE is very sensitive to the shape of the quantum wire and can be therefore effectively used for its investigation. Our numerical analysis shows that the giant oscillations of AE persist in the case $q \ll q_0$, as well as in the channels with abrupt shape. In that way the experimental results[1] are fully understood.

REFERENCES

[1] J. M. Shilton *et al.*, J. Phys.: Condens. Matter **8**, L337 (1996).
[2] J. M. Shilton *et al.*, J. Phys.: Condens. Matter **8**, L531 (1996).
[3] C. R.Nash *et al.*, Surf. Sci. **361/362**, 668 (1996).
[4] A. J. Naylor *et al.*, Surf. Sci. 361/362, 668 (1996).
[5] A. L. Efros, Yu. M. Galperin, Phys. Rev. Lett., **64**, 1959 (1990); A. Knäbchen *et al.*, preprint cond-mat/9604137.
[6] A. Wixforth *et al.*, Phys. Rev. Lett. **56**, 2104 (1986); Phys. Rev. **B40**, 7874 (1989); R. L. Willett *et al.*, Phys. Rev. Lett. **65**, 112 (1990); Phys. Rev. Lett. **71**, 3846 (1993).
[7] A. Esslinger *et al.*, Solid State Commun. **84**, 949 (1992); J. M. Shilton *et al.*, J. Phys.: Condens. Matter **7**, 7675 (1995).
[8] L. J. Challis *et al.*, Semicond. Sci. Technol. **5**, 1179 (1990); A. J. Kent, Physica B **169**, 356 (1991); D. J. McKitterick *et al.*, Phys. Rev. B **49**, 2585 (1996).
[9] H. Karl *et al.*, Phys. Rev. Lett. **61**, 2360 (1996).
[10] H. Totland, and Yu. Galperin, Phys. Rev. B **54**, 8814 (1996).
[11] V. L. Gurevich *et al.*, Phys. Rev. Lett **77**, 3881 (1996).
[12] V. L. Gurevich *et al.*, J. Phys. Cond. Matter. **6**, 8363 (1994); Phys. Rev B **51**, 5219 (1995).
[13] M. Blencowe, and A. Shik, Phys. Rev. B **54**, 13 899 (1996).
[14] A. Crincwajg *et al.*, Phys. Rev. B **52**, 12 168 (1995).
[15] Supriyo Datta, and M. P. Anantram, Phys. Rev. B **45**, 13 761 (1992).
[16] Frank A. Maaø, and L. Y.. Gorelik, Phys. Rev. B **53**, 15 885 (1996).
[17] R. Landauer, IBM J. Res. Dev **1**, 223 (1957).
[18] L. I. Glazman *et al.*, JETP Lett. **48**, 238 (1988).

SINGLE-GATED MOBILITY MODULATION TRANSISTOR

P.I. Birulin, S.P. Grishechkina, Yu.V. Kopaev, S.S. Shmelev, V.T. Trofimov, N.A. Volchkov,

P.N.Lebedev Physical Institute of RAS, Moscow 117924, Leninsky prosp.,53, Russia

We have proposed and realized field-effect transistor based on the GaAs/AlGaAs structure with double tunnel-coupled quantum wells (QW). The channel conductance modulation results from rearrangement of the electron density between two QWs that have essentially different carriers mobility. The device is effectively operated by a single gate.

Introduction. In the mobility modulation transistor (MMT) the conducting electrons are transferred on a distance about 10 nm at switching, and duration of this process can be less than 1 ps [1]. The device speed then is limited by the time of band structure deformation (i.e. time of the gate capacitance recharge) when the signal $U(F_g)$ is applied to the gate. Additional back gate [2] with opposite to $U(F_g)$ voltage applied is usually used for better control of the MMT. In this case the carriers concentration and the bulk charge in the channel do not change, and the recharging time of the front – back gates capacitance is determined by resistance of the external circuits. The paraphase gate voltages, however, are unsuitable for device applications.

Model of the structure. In this work we propose version of the MMT effectively operated by a single gate based on the Schottky barrier. We have performed numeric simulation of the device using drift-diffusion model and one-dimensional envelope method for Schrödinger equation. The conductance band edge profile, energy spectrum and electron wave functions of the quantum states in QWs, and the carriers concentration in the quantum subbands were calculated.

The model structure contains two tunnel-coupled undoped quantum wells (Fig.1). The top well (QW2) of 5 nm width is highly resistive due to low electron mobility (μ_2~100 cm^2/V·s) which is suppressed by using low temperature growth. The bottom 20 nm wide well (QW1) with μ_1~10^4 cm^2/V·s is more conductive than QW2 at any gate voltages and acts as transistor channel.

25 nm	GaAs, $N_D=1\times10^{18}$ cm^{-3}
30	$Al_{0.3}Ga_{0.7}As$, $N_D=5\times10^{17}$ cm^{-3}
10	$Al_{0.3}Ga_{0.7}As$
5	GaAs
8	$Al_{0.3}Ga_{0.7}As$
20	GaAs
4	$Al_{0.3}Ga_{0.7}As$
10	$Al_{0.3}Ga_{0.7}As$, $N_D=1\times10^{18}$ cm^{-3}
48	$Al_{0.3}Ga_{0.7}As$
Substrate	GaAs

FIG.1. Sample structure. All thicknesses are given in nanometers.

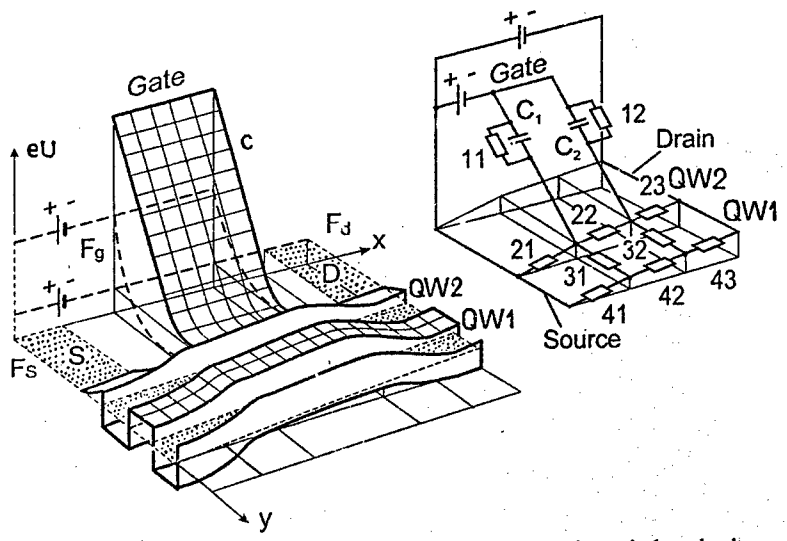

FIG.2. The simplified two-dimensional energy diagram of the MMT and its equivalent circuit.

The Si-doped parts of the top and bottom barriers supply the carriers to QWs, the bottom barrier being more doped than the top one. According to the Poisson equation the electric field changes in the region of higher bulk charge. Strong doping of the bottom barrier and usage of undoped QWs allowes to achieve deep conductance modulation. Due to the chosen doping profile it is possible to change the sheet electron concentration in QW2 from its maximum to zero keeping the sheet concentration in QW1 constant. The simplified two-dimensional energy diagram of the MMT and its equivalent circuit scheme are given in Fig. 2. QW1 and QW2 are presented by resistor circuits 41-43 and 21-23 respectively which are connected by resistors 31 and 32 (the tunnel barrier resistance). The Fermi levels position of the source (F_s), gate (F_g) and drain (F_d) as well as conductance band edge (c) are directed along the vertical axis. The Schottky barrier capacitance C1 recharges through small resistors 32 and 41 when the gate potential changes. As a result the sheet concentration n_2 decreases almoust to zero while n_1 in QW1 practically does not change (Fig. 3a). Only at $U(F_g)<-0.8$ V n_1 decreases, and the device operates as usual high electron mobility transistor (HEMT). The characteristic time of QW2 depletion is determined by expression $R \cdot C \cdot n_2/n_1$, where R is the channel resistance, in advantage to $R \cdot C$ for usual HEMT.

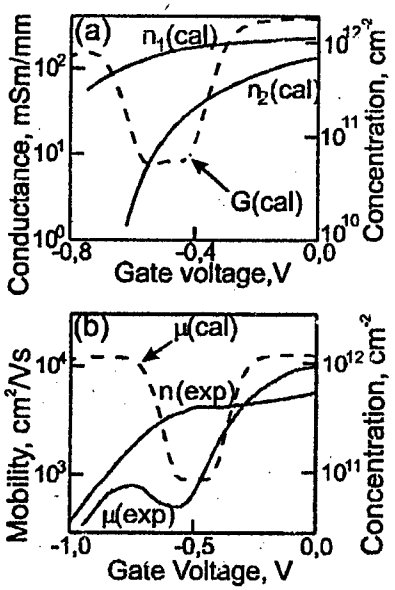

FIG.3. Calculated (cal) and experimental (exp) dependences of n_1, n_2, effective mobility and MMT transconductance G on U(Fg) at 77 K.

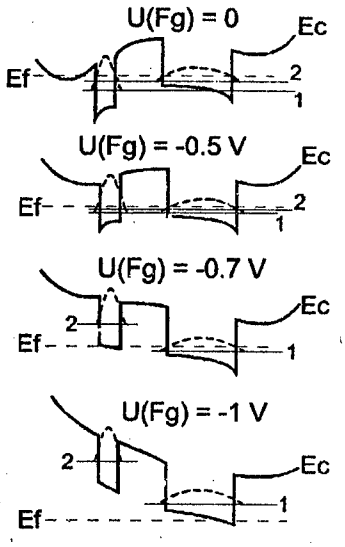

FIG.4. Energy diagram, size quantization, levels, Fermi level, and wave function for double quantum well structure at various gate voltages.

The channel conductance modulation during the depletion of QW2 is caused by abrupt mobility drop at the anticrossing of quantum levels in the tunnel-coupled quantum wells with different electron mobilities. Two lower quantum states, corresponding wave functions and Fermi level in this system at various gate voltages are shown in Fig.4. The conducting channel at any gat voltage is QW1 with a high carriers mobility. When $U(F_g)$=-0.5 V, however, the anticrossing of quantum levels occurs, and the electron wave functions in the wells delocalizes. This leads to strong increase of electron scattering on the defects in QW2. In frames of the model of the partial contributions of relaxation times the scattering probability is determined by equation:

$$\frac{1}{\tau} = \frac{1}{\tau_I} + \frac{(1 - P(QW1))}{\tau_o},$$

where τ_T is the phonon scattering time and τ_o is time for defect scattering in QW2 ($\tau_T << \tau_o$). P(QW1) is a probability for the electron to be found in QW1. Value of τ^{-1} sharply increases when P(QW1)≠1 and electrons delocalize between QW1 and QW2. At further gate voltage decrease the quantum levels moves out from the resonance and the transistor conductance again increases. The calculated dependence of conductance upon the gate voltage for the channel length taken 4 μm is shown in Fig.3a. When $U(F_g)<-0.8$ V conductance decreases due to depletion of QW1, the device being operated as usual HEMT.

Experimental results. Measured dependencies of mobility and concentration on the gate voltage at 77 K are shown in Fig.3b. The experimental structure differs from the numerically simulated one by abscence of the bottom barrier doping. This leads to lower conductance modulation than predicted due to depletion of QW1 during rearrangement of electron density in QWs. The growth of high mobility QWs with dopped bottom barrier meet certain technological problems due to Si outdiffusion in process of upper layers growth.

Conclusion. We have proposed and realized structure of mobility modulation transistor, which is effectively operated by single gate. The undoped QW with low carriers mobility is used only as the electron scattering source when the carriers wave functions are delocalized under effect of gate voltage. More than 30-fold mobility modulation ratio was obtained at 77 K while the concentration was kept practically constant.

The work was supported by RFBR and INTAS grants.

1. Sakaki H. Japan J. Appl.Phys. 21 L381 (1982)
2. Kroobe A., Kastleton J.M., Linfield E.H., Grimshaw M.P., Brown K.M., Ritchie D.A., Jones J.A.C., Pepper M. Semicond. Sci. Technol., v.9, p.1744 (1994)

THE 2DEG HEATING BY ELECTRIC FIELD OF SURFACE ACOUSTIC WAVE.

I.L.Drichko, A.M.Diakonov, V.D.Kagan,A.M.Kreshchuk
T.A.Polyanskaya,I.G.Savel'ev,I.Yu.Smirnov*, A.V.Suslov

A.F.Ioffe Physicotechnical Institute, 194021, St.Petersburg, Russia

The investigation of nonlinear effects in Bulk Piezoactive Ultrasound Waves absorption, caused by their interaction with electrons in a 3-dimensional case has shown , that the nonlinearity mechanisms depends on the state, in which electrons are. When electrons are "free" the nonlinearity mechanism is associated usually with their heating in the electric field of sound wave , and the heating character depends on the relation $\omega\tau_\epsilon$, where ω - sound frequency, τ_ϵ- the energy relaxation time [1, 2]. If electrons are localized, then the nonlinearity mechanism is determined by the type of localization (localization on single impurity or in the random potential wells). It has been shown in [3], that when electrons are localized on the single impurities a nonlinarity is determined by impurity breakdown in the electric field of sound wave, and, when the electrons appeared in conduction band, due to breakdown, their temperature began to raise because of heating in the electric field of sound wave [4].

The present work informs on the investigation of nonlinear effects associated with the interaction of delocalized 2DEG with electric field of Surface Acoustic Waves (SAW), aimed on the mechanisms of nonlinearity studying. Dependence of coefficient of SAW absorption by 2DEG on SAW intensity was observed earlier in the GaAs/AlGaAs heterostructures [5, 6] only in magnetic fields , corresponding to small filling factors, when 2DEG is localized. The authors explained this dependence by the 2DEG heating.

In the frequency range 30-210MHz we studied the magnetic field dependence of the coefficient of SAW absorption by 2DEG in GaAs/AlGaAs heterostructures on a temperature T (1.4-4.2K) in a linear regime (input power did not exceed $10^{-7}W$) and at T=1.5 K on SAW intensity. The samples used were studied earlier in [7], and had carrier density $n = 6.7 * 10^{11}cm^{-2}$ and mobility $\mu = 1.28 * 10^5 cm^{-2}/V * s$ at T=4.2 . A method of the experiments is described in [7]. The general idea of the method is that the studied structure is placed on the surface of a piezoelectric (lithium niobate), on which the SAW propagates. An alternative electric field (of the frequency equal to that of SAW), accompanying the deformation wave, penetrates into 2DEG channel producing electric currents and respectively -Joule losses.As a result of such an interaction the SAW energy is attenuated. Because the measured SAW absorption coefficient is determined by the 2DEG conductivity the electron spectrum quantizing in a magnetic field, (the SdH-oscillations), results in the SAW absorption oscillation.

Fig.1 illustrates the absorption coefficient Γ dependences on magnetic field at the temperature $T = 1.5K$ for two SAW intesities. A character of the Γ dependences on magnetic field is analyzed in [7]: maxima of the absorption are equidistant in inversed magnetic field (the splitting of the maxima in high magnetic fields is determined by the relaxation character of absorption).Dependences of Γ on temperature and SAW intensity

were derived from the experimental curves of the type of these presented on Fig.1 in magnetic fields lower than 25kOe. Fig.2 illustrates the temperature dependence of $\Delta\Gamma = \Gamma_{MAX} - \Gamma_{MIN}$,where Γ_{MAX} and Γ_{MIN} are the values of an adjacent minimum and maximum of Γ, measured in a linear regime at a frequency 150 MHz. Fig.3 presents the

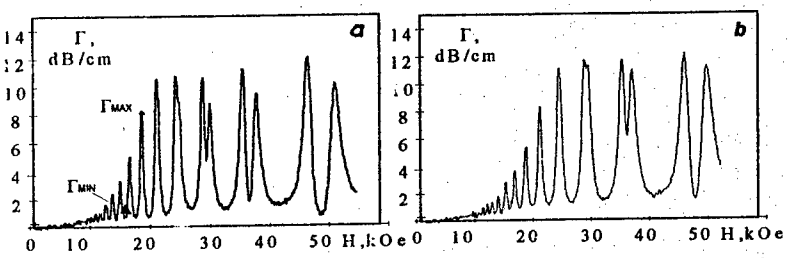

Figure 1. The absorption coefficient Γ dependences at T=1.5K at P=0.00001W (a) and at T=1.5K at P=0.0004W (b)

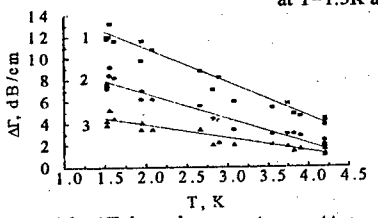

Figure 2. The $\Delta\Gamma$ dependences on temperat ture 150MHz for different magnetic fields H: 1-17.5kOe, 2 -15.5kOe, 3-14.1kOe.

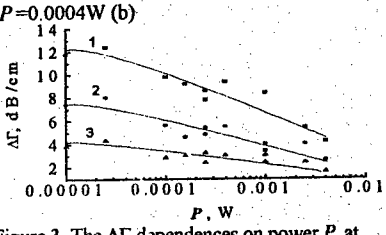

Figure 3. The $\Delta\Gamma$ dependences on power P at 150MHz for different H: 1-17.5kOe, 2-15.5kOe, 3-14.1kOe.

$\Delta\Gamma$ dependence on the output power P of the RF source of SAW at 150 MHz at T=1.5 K. It's seen from the figure,that $\Delta\Gamma$ decreases with the P increase.

It was shown in [7], that in the magnetic field region lower 25kOe, dissipative conductuvities, derived from the direct current measurements and those from SAW absorption coefficient in linear regime are equal, $\sigma_{XX}^{AC} = \sigma_{XX}^{DC}$. This fact gave us the reason to beleive the electrons to be delocalized in these magnetic fields. As was said above we shall analyze nonlinearities in this region only.

As it was shown in [8], if electrons are delocalized, than one can determine the 2DEG parameter (transport and quantum relaxation time, carriers density, mobility) from σ_{XX}^{AC} and it's dependence on a magnetic field. Therefore it's quite natural to consider the nonlinearity mechanism, which had been investigated earlier on these structures using direct current (the resistance dependence on the electric field density [9]). In this work it was shown that the dependence of resistivity on the current density can be explained by the 2DEG heating, and the energy relaxation processes are determined by a piezoacoustic electron-phonon interaction, and the impulse relaxation is due to the scattering on the ionized impurities.

For a description of the electron gas heating using temperature T_e, which differs from the lattice temperature T_0, the following condition is to be met:

$$\tau_p << \tau_{ee} << \tau_\epsilon, \qquad (1)$$

whereτ_p,τ_{ee}, τ_ϵ - the transport relaxation time, the electron-electron collisions time and energy relaxaton time respectively. The transport relaxation time can be derived from the value of mobility in the absence of magnetic field and is equal to $\tau_p = 5 * 10^{-12} s$. The electron-electron collisions time being $\tau_{ee} = 5 * 10^{-10} s$ and energy relaxaton time $\tau_\epsilon = 3.3 * 10^{-9} s$.

By analogy with [9] one can determine T_e- the temperature of 2DEG comparing the dependences of $\Delta\Gamma$ on P with its temperature dependence . Such a comparison allows one to relate the 2-dimensional electrons T_e and P.

In order to determine the energy losses Q, determing T_e, it was necessary to make the following calculations: an electric field E, in which 2D-electrons are when SAW propagates in a piezoelectric, is equal:

$$|E|^2 = K^2 \frac{32\pi}{\nu}(\epsilon_1 + \epsilon_0) b \frac{k * exp(-2ka)}{[1 + (4\pi\sigma_{xx}/\epsilon_s v) f]^2} * W, \qquad (2)$$

where K^2 -electromechanic coupling coefficient, v, k - the SAW velocity and wave vector respectively, a -the value of vacuum gap between the sample and the piezoelectric substrate, σ_{XX} -the 2DEG conductivity, ϵ_0 , ϵ_1 ,ϵ_s - the dielectric constants of vacuum, piezoelectric and the sample respectively, W -the input SAW power in the sample per the width of sound track. The functions b and f are complex functions of ϵ_0 ,ϵ_1 ,ϵ_s, v, k, a. The energy losses per one electron $Q = e\mu E^2$. Multiplying the both parts of Eq.(2) by σ_{xx}, one can obtain $Q = 4W\Gamma/n$, n-the carrier density. Fig.4 illustrates the dependence of Q on T_e for two frequencies: 30 and 150MHz. We have built dependencies $Q = f(T_e^3 - T_0^3)$, corresponding to the interaction of electrons with piezoelectric potential of acoustic phonons (PA-scattering) in a case of weak screening, for frequencies 30 and 150 MHz in different magnetic fields $Q = e\mu E^2 = A_3(T_e^3 - T_0^3)$, but because the condition of the weak screening is not fulfiled for this sample it were built the dependencies $Q = f(T_e^5 - T_0^5)$, corresponding to the case when energy relaxation happens on piezoelectric potential of acoustic phonons (PA-scattering) and the screening is strong, for the same frequencies and magnetic fields $Q = A_5(T_e^5 - T_0^5)$ [10].

The analysis, carried out by the least squares method, have shown that our experimental curves can be fitted rather well by $Q = A_5(T_e^5 - T_0^5)$. Figure 4 illustrates experimental points and theoretical dependencies $Q(T_e^5 - T_0^5)$ for frequencies 30 and 150 MHz with $A_5 = 3eV/sK^5$ and $4.1eV/sK^5$ respectively.

The results of the 2DEG heating study in high frequency electric field confirms the general conclusions of [10]. But because the $Q(T_e)$ calculations in [10] were made for a static electric field it cannot explain a different values of A_5 at different frequencies.

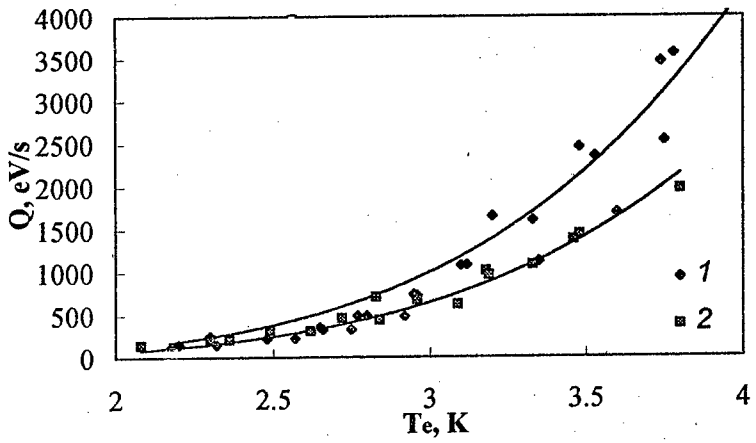

Figure 4. The dependence of Q on T_e for two frequencies (*1* -150MHz, *2* -30MHz).

This fact is associated probably with a diverse magnitude of relation $1/\omega$ and τ_ϵ for different frequencies. At 30 MHz $\omega\tau_\epsilon < 1$ (0.62), but at 150 $\omega\tau_\epsilon > 1$ (3.1). In the case of $\omega\tau_\epsilon > 1$ the heating is determined by average wave power, whereas when $\omega\tau_\epsilon < 1$ the 2DEG heating is determined by the instantaneously changing wave field. That can lead to the different heating degree at the same energy losses.

The work was supported by the RFFI N95-02-04066-a, N95-02-04042a and INTAS-1403-93-ext grants.

References

[1] Yu.M. Galperin et al. FTT, 28, 3374 (1986).
[2] I.L.Drichko.FTT,27,499,(1985)
[3] Yu.M. Galperin et al. FTT, 28, 3374 (1986).
[4] Yu.M. Galperin et al.Proc. of the SPNS.Vilnus.186, (1986).
[5] A. Wixforth et al. Phys.Rev.B, 40, 7874 (1989).
[6] A. Schenstrom et al. Sol.St.Comm., 68, 357(1988)
[7] I.L.Drichko et al. FTP, 31, 451 (1997).
[8] I.L.Drichko, I.Yu. Smirnov. FTP, 31, N9(1997)
[9] M.G.Blyumina et al. Pisma v JETP, 44, 257 (1986).
[10] V.Karpus. FTP, 22, 43 (1988).

Transition from semimetal to semiconductor in type-II p-GaInAsSb/p-InAs heterojunctions.

T.S. Lagunova, T.I, Voronina, M.P. Mikhailova, K.D.Moiseev, A.E. Rosov, Yu. P. Yakovlev.

Recently, it have been shown there is an electron channel with high carrier mobility (μ_H=50000–70000 cm²/V·s) at the interface of the type II broken gap p-GaInAsSb/p-InAs single heterojunctions with undoped quaternary layers [1]. Existence of this channel is due to spatial separation of electrons and holes and their localization in the adjacent quantum wells on the both sides of the interface.

We report here some results of detailed study of the electron channel properties and magnetotransport layer in the GaInAsSb/InAs heterojunctions in depending on acceptor doping level of the quaternary layer. Hall coefficient $R_\square$, electron conductivity and Hall mobility were measured at 77-200K under magnetic fields H=1-20kOe. An abrupt decrease in carrier mobility with increasing doping level in these heterostructures was observed, and a transition from semimetal-to-semiconductor behavior was found for the first time.

We study p-GaInAsSb/p-InAs heterojunctions with high quality interface grown by LPE. Epitaxial layers of $Ga_{0.83}In_{0.17}As_{0.22}Sb_{0.78}$ (Eg=0.63eV at T=77K) of 2μm thickness were grown on the lattice-matched p-InAs substrates (σ_{77K}=0.2 $Ohm^{-1}cm^{-1}$, $p_{77K}=10^{16}cm^{-3}$, Eg=0.40eV, T=77K) and doped by various acceptor impurities (Zn, Ge, Sn) in content from 10^{-3} up to $5\cdot10^{-2}$atom %. Band energy diagram of such structure was established before in [2] and represents a type II broken-gap alignment with a gap between GaInAsSb valence band and InAs conduction band $\Delta \approx 60 - 80$ meV. 6 contacts were made on the GaInAsSb surface of the rectangular samples by In alloy. A sign of Hall voltage indicates an electron type of conductivity in all heterostructure samples by doping of any kind of acceptors (Zn, Ge, Sn) in the wide range of doping.

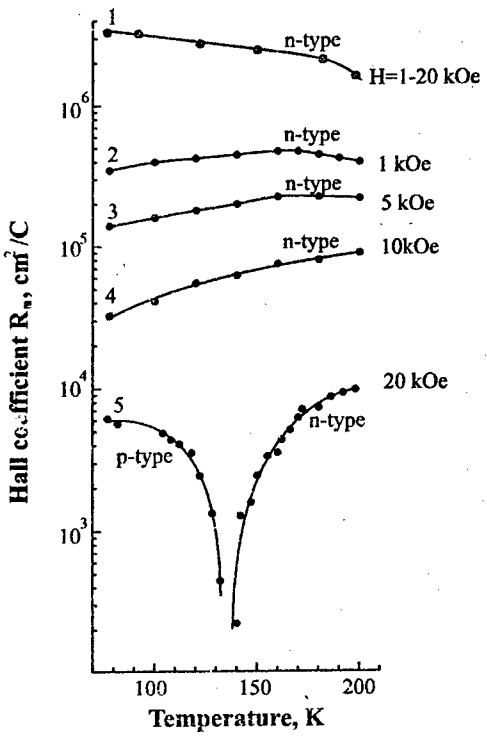

Fig. 1 Hall coefficient $R_{\square}$ temperature dependence for samples with various doping level: **1** - slight, **2-4** - moderate, **5** - the highest.

By our opinion, it is due to predominant contribution in the conductivity of electrons from the channel situated at the interface on p-InAs side. Fig. 1 represents Hall coefficient $R_{\square}$ temperature dependence for the samples with various doping level of quaternary layer (curves 1-5). As one can see, $R_{\square}(T)$ for slightly doped sample (curve 1) depends weakly on temperature and magnetic field intensity. For moderate doped samples an increase of Hall coefficient value was observed with T rising (curves 2-4). It is interesting to notice $R_{\square}(T)$ dependence changes a sign at T~130K that indicates beginning hole conductivity in a sample with the highest doping level (Fig. 2, curve 5). In such sample high mobility electrons contribute under low magnetic fields (H = 1-2 kOe), and hole contribution becomes significant only under high magnetic field (H ~ 10 - 20 kOe).

Fig. 2 represents mobility dependence versus Zn doping level at T=77K and 200K (curves 1 and 2) for p-GaInAsSb/p-InAs heterostructures. At low acceptor content (Zn<$4\cdot10^{-3}$ atomic %) high electron mobility nearly independent on T was observed in a wide temperature range (50000–

70000cm²/V·s at 4.2-200K). But drastic electron mobility drop is observed beginning in Zn content more than $4 \cdot 10^{-3}$ at.%.

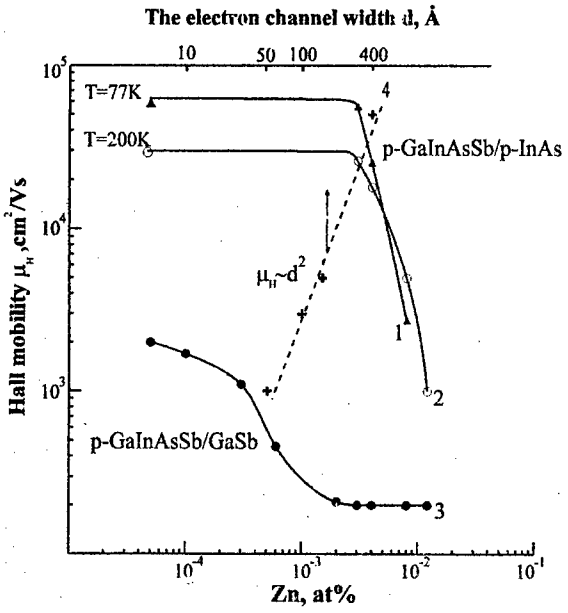

Fig.2 Hall mobility versus Zn content in p-GaInAsSb/p-InAs and p-GaInAsSb/GaSb heterostructures

These μ_H dependence versus Zn content differs significant from one for p-GaInAsSb solid solutions of the same compositions but grown on semi-isolated GaSb substrate (curve 3). It is important fact that an abrupt drop mobility for p-GaInAsSb/p-InAs heterostructures starts at the same acceptor content, while in p-GaInAsSb/GaSb structures one can observe a mobility independing of doping level due to hole degeneracy.

This result firstly demonstrates a transition from semimetal to semiconductor behavior in the type II broken gap p-GaInAsSb/p-InAs single heterostructures under study with increasing acceptor doping level. It can be due to narrowing electron quantum well at InAs side of the interface as carrier concentration increases in quaternary layer. Indeed, we obtained variation of mobility with the electron cannel width as $\mu_H \sim d^2$ (See curve 4 Fig.3). We evaluated two-dimensional electron concentration N_S and **d** in our heterostructures using two-layer model taken into account contributions in

conductivity of carrier from electron channel and from p-GaInAsSb layer, as well as inversion point of Hall coefficient (T=130K) where these contributions are equal (Fig.2,curve 5). We obtained the following **d** value for moderate doped and heavy doped quaternary layers: $N_S=10^{12}cm^{-2}$ and $8\cdot10^{12}$ cm^{-2}, **d**=50A and 100A for **p**=$2\cdot10^{18}$ cm^{-3} and $6\cdot10^{18}$ cm^{-3}, respectively. For sample with undoped quaternary layer $N_S=10^{11}cm^{-2}$, **d**=400A were obtained from Shubnikov- de Haas oscillation temperature dependence [3].

It is interest to notice that similar $\mu_H(d)$ dependence and semimetal-semiconductor transition in depending on quantum well width have been observed recently in [4] for type II broken-gap n-GaInSb/InAs superlattices. In our case the increasing doping level of quaternary layer leads to narrowing electron well near the interface. Electrons in the channel can be strongly localized in the potential wells on the interface. As a result its mobility drops, and we can see depletion of electron channel and a semimetal-semiconductor transition.

This work supported in part by Russian Basic Research Foundation grant №96-02-1784/a and Programme "Solid State Nanostructure Physics" grant 1-001.

References.

1. T.I.Voronina, T.S.Lagunova, M.P.Michailova, K.D.Moiseev, Yu.P.Yakovlev, Semiconductors, **30**, 523 (1996).
2. I.A.Andreev, M.P.Mikhailova, K.D.Moiseev, Yu.P.Yakovlev Abstract II Int. Symp. Nanostructures: Physics and Technology (St. Peterburg, Russia, 20-24 June 1994) p. 82
3. M.P.Mikhailova , T.I.Voronina, T.S.Lagunova, K.D.Moiseev, S.A.Obukov, A.E.Rosov, Yu. P.Yakovlev, Superlat. and Microstr. v.**21**, (1997)
4. C.A.Hoffman, J.R.Meyer, E.R.Yougdale, F.J.Bartoli, R.H.Miles, L.R.Ram-Mohan Sol. St. Electronics, v.**37**, p.1203 (1994)

QUANTUM CYCLOTRON RESONANCE OF 2D HOLES IN Ge LAYERS OF Ge - $Ge_{1-x}Si_x$ HETEROSTRUCTURES

L.K.Orlov, J.Leotin, F.Yang,Yu.Arapov, N.Orlova

N. Novgorod, Ekaterinburg, Russia; INSA, Toulouse, France

orlov@ipm.sci-nnov.ru

One vital trend in semiconductor physics today is a research into ways of controlling the energy spectrum of charge carriers in semiconductors. The most effective method being developed recently towards a solution of this problem involves the growth of the multilayer strained heteroepitaxial structures with nanometer - thick layers. The charge carrier spectrum in them changes due to a size - quantization effect and the action of intrinsic elastic strain in the layers. The energy characteristics of the system can also be varied by applying strong electric or magnetic fields to the structure.

In this work for periodic Ge-$Ge_{1-x}Si_x$ MQWS we investigated the influence of the above factors on a hole gas properties, using quantum cyclotron resonance (QCR) method. The quantum cyclotron resonance measurements of the hole effective mass and the quasipulse relaxation time are compared with the data obtained by the methods of classical cyclotron resonance and Shubnikov de Haas oscillations.

The Ge-$Ge_{1-x}Si_x$ heterostructures described in earlier works [1,2] were essentially partly relaxed periodic systems of alternating layers of Ge (d_1 ~18nm) and $Ge_{1-x}Si_x$ (d_2 ~30nm) with their total thickness well in excess of the critical thickness of the heterostructure. The parameters of test samples and the characteristics of hole gas in them will be listed in Table 1 below.

Table 1.

No.	d_{Ge}, nm	σ_{Ge},GPa	ΔE_{hl},meV	δ_{12},meV	E_F,meV	$m_{hh\|\|}/m_0$
1a	18.0	0.26	12	9	7	0.087
2a	16.8	0.4	21.4	10	7.5	0.082
3	25.0	0.74	38.5	5	15	0.072
4	18.0	0.6	34.0	9	1	0.070

On the Fig.1a it is shown how the hole energy spectrum in Ge layers is changed in present of uniaxial (along [111] direction) tensile deformation and due to the spatial confinment.

Our ealier investigations into the Hall mobility of holes in these heterostructures have shown that the conductivity processes along the layers' plane are connected with a charge carriers belonging to the upper split-off subband of heavy holes, which have a light longitudinal effective mass. The longitudinal component of the effctive mass of 2D charge carriers in these structures and its dependence on Fermy level position was for the first time measured in the works [3,4] using Shubnikov de Haas oscillations. This result is indicative of a strong nonparabolicity of the hole dispersion law and it is in good agreement with the classical cyclotron resonance data taken on these structures in a weak magnetic field both with and without a thermal electric field [5,6].

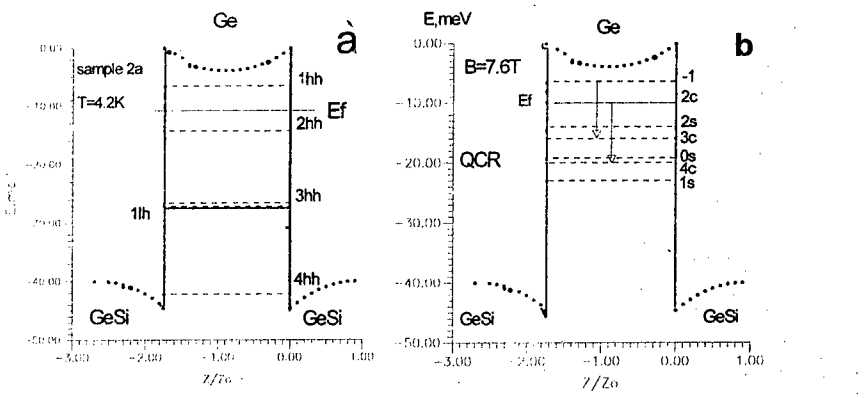

Fig.1. The position of the 2D-subbands (a) and the Landau levels and the Fermi level (b) in Ge layers of the sample 1a, calculated by the Kon-Latinger equation [4].

In this work we report the first measurements of a quantum cyclotron resonance in 2D holes in the Ge layers of the above-discussed heterostructures affected by a strong (to 10 T) quantizing magnetic field [7]. The quantum cyclotron resonance was measured using a far IR spectrometer incorporating a 40 T pulse magnet and a CO_2-laser-pumped optical resonator. The figure 2a demonstrates a typical curve of the cyclotron resonance versus magnetic field for one sample obtained at a 119 mcm frequency at T = 4,3 K. The widthlines were from 2.5 to 1.5 meV. This result correspond to holl mobility in structure about 10000 cm2/Vs and compearing itselves with data obtained other methods.

For sumples 1,2 the Fermi energy amounts to about 7 meV, and only one upper hole subband of the size-quantized HH subband appears to be filled. The LH subband in the (111) direction splits off, since the uniaxial strain and size quantization. The splitt off energy changes from 10 to 40 meV for different sumples.

In a simple band model, the hole spectrum in every size-quantization subband under a quantizing magnetic field transforms into a set of equidistant Landau levels split due to spin-orbit interaction. The resonance frequency absorption in this case is most likely to relate to transitions from the spin-orbit-split zero 0 to the 1 levels of magnetic quantization.

A considerable g-factor in Ge and strong interaction of the HH and LH subbands are providing the nonlinearly dependence of the Landau levels' position on the magnetic field, which accounts for mixing and nonequidistance of the magnetic subbands. These effects largely complicate systematization of the levels spectrum in Ge layers under a strong magnetic field. It can be seen, in particular, in the Fig1b. where the position of the magnetic sublevels and the position of the Fermi level E_f in the upper HH subband is calculated for sample 1a, using the Kon-Lattinger equation [4]. Fig.2a suggests that radiation absorption at the cyclotron resonance frequency ($\hbar\omega$ =10meV) in a 7,6 T magnetic field occurs due to hole transitions both between levels -1 and 3c and between levels 2c and 0c, 4c (Fig.1b).

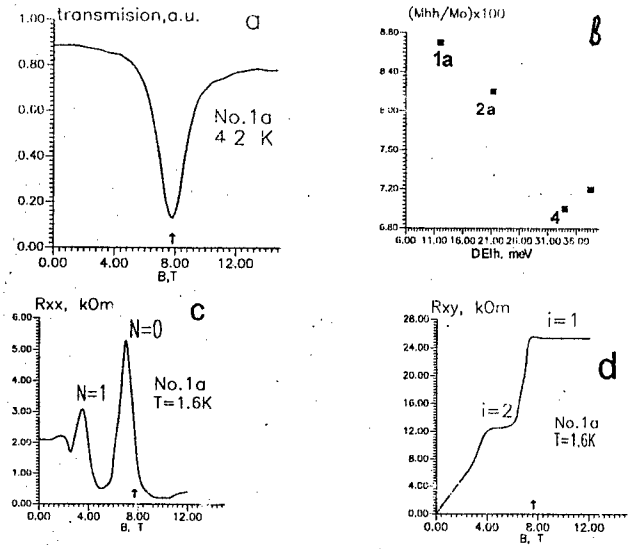

Fig.2. The quantum cyclotron resonance (a), the Shubnikov-de-Gaaz effect (c) and the Quantum Hall effect (d) versus magnetic field in sample 1a; the longitudinal effective mass of HH holes (along the Ge layers' plane) as a function of the energy of splitting of HH and LH subbands (b).

The Landau levels corresponding to the frequency of cyclotron resonance can be systematized using measurements of Shubnikov-de-Gaaz oscillations in this heterostructure. For the above sample 1a the dependences R_{xx} are given in Fig.2c. Comparing Fig. 2a and 2c we see that the cyclotron resonance occurs exactly under a magnetic field that provides for the Fermi level to intersect the second Landau level in the band. The cyclotron resonance linewidth corresponding to broadening of a Landau level is close to the width of the peak on the dependence $R_{xx}(B)$. The exact of the value of magnetic field at the cyclotron frequency to the beginning of Hall plato with filling factor i=1 on the curve $R_{xy}(B)$ implies that these are most likely to be transitions from the Fermi level coinciding with two Landau level in this case.

We made CR measurements of the effective mass of holes on samples with different values of σ_{Ge} and Δ_{Ge}. The effective cyclotron mass data and the X-ray-diffraction measurements of elastic deformation in Ge layers for the same samples are provided in Table 1. Comparing different structures (samples 1, 2,4) we see that a growing elastic stress for the same thickness of quantum wells in Ge layers causes a splitting energy of the HH and LH subbands to increase roughly from 10 to 40 meV, thus reducing the effect of the lower LH subband (mj = (1/2)) on the characteristics of holes in the upper HH subband (mj = (3/2)). In the experiment we observed a clear dependence of the value of the longitudinal component of the effective mass on deformation in Ge layers (the splitting energy of LH/HH subbands). Thus, by increasing elastic stress in Ge layers through, say, the use of $Ge_{1-x}Si_x$ layers with a high content of Si and by simultaneously

reducing the quantum well width and the concentration of a doping material we can have structures with the longitudinal effective mass of holes near its threshold value, $m_{hh} = 0.054\ m_O$, which corresponds to the mass of holes in the bulk germanium with uniaxial deformation.

Conclusion

1. The paper reports first measurements of a quantum cyclotron resonance on 2D holes in Ge layers of a strained Ge - $Ge_{1-x}Si_x$ heterostructure.

2. Comparison of the quantum cyclotron resonance data with measurements of the Shubnikov-de-Gaaz effect allowed to identify the spectrum of the levels involved in resonance transitions.

3. We provide the first experimental evidence that the longitudinal component of the effective mass of 2D holes in Ge layers depends in value on the energy of splitting of LH/HH subbands.

This work was partly supported by RFFI (grant No.96-02-19278) and INTAS (grant No.95-0615).

References.

[1] L.K.Orlov,V.Ya.Aleshkin et al. J.Appl.Phys. 79 (11), 1 June 1996.
[2] L.K.Orlov, O.A.Kuznetsov et al., Sov.Rhys.JETP, **71**, 573 (1990).
[3] Yu.A.Arapov,N.A.Gorodilov et al., Semicond., **27**, 642 (1993).
[4] Yu.A.Arapov, N.A.Gorodilov et al., JETP Lett, **59**, 245 (1994).
[7] V.I.Gavrilenko, I.N.Kozlov, A.L.Chernov et al. JETP Lett, **59**, 349 (1994).
[8] V.Ya.Aleshkin, N.A.Bekin et al., Lithuanian J. Phys., **35**, 368 (1995).
[9] L.K.Orlov,A.V.Potapov et al., Thin Solid Films, in press (1997).

Magnetic states of two-dimensional electrons near the intersection of quantum well by slipping plane

D. A. Romanov, E. B. Gorokhov, V. A. Tkachenko, and O. A. Tkachenko*

Institute of Semiconductor Physics, Novosibirsk, 630090, Russia

**Novosibirsk State University, Novosibirsk, 630090, Russia*

Insertion of crystallically perfect one-dimensional obstructions on the way of two-dimensional electrons of the buried quantum well by means of slipping planes is suggested. Positions of the (111) family slipping planes are determined by Franck-Read sources which are set in action by compressing the GaAs/AlGaAs heterostructure in a lateral direction at heating above 400°C [1,2]. The shift of the crystal lattice along the slipping planes by several monolayers result in formation of terraces on each heteroboundary, including the surface (Fig. 1). In the quantum well the adjacent terraces are separated by asymmetric oblique-shift narrowings which can reflect the electrons. Electron transparency of the systems of such obstacles has been calculated by S-matrix method [3] taking into account the excitation of additional transverse modes at the locations of narrowings. It was found that the obstacles can, with good precision, be considered as one-dimensional δ-barriers with magnitude proportional to the square of the shift height h, *i.e.* the transmission coefficient $T \approx k_y^2/(k_y^2 + G^2/4)$, where effective magnitude of the δ-barrier $G \propto h^2$.

Multiple electron reflections from such barriers should lead to 2DEG mobility anisotropy in the plane of the quantum well (x, y). Applying transverse magnetic field allows of further increased anisotropy provided that $kT/\hbar\omega_c \ll 1$, because the motion becomes finite along y-direction within magnetic length while remaining free along x-axis. The electron wave function is chosen in the form $\Psi(x, y) = \psi(y)\exp(ik_x x)$. Then $\psi(y)$ is obtained from the one-dimensional Schrödinger equation

$$-\frac{\hbar^2}{2m}\frac{\partial^2\psi}{\partial y^2} + \left[U(y) + \frac{m\omega_c^2}{2}\left(y + k_x l_B^2\right)^2\right]\psi = E\psi,$$

where $\omega_c = eB/mc$ is the cyclotron frequency, $l_B = \sqrt{c\hbar/|eB|}$ the magnetic length, and $U(y) = \sum_i G_i\delta(y - y_i)$. The energy levels E_n vs. longitudinal momentum, *i.e.* vs. position of the magnetic parabola minimum $y_B = -k_x l_B^2$, were calculated, and oscillations in $E_n(p_x)$, or $E_n(y_B)$, were found. According to perturbation theory these oscillations (magnetic valleys) are the direct exposure of total probability density at the locations of δ-barriers y_i: $E_n(p_x) - E_{n\,2\mathrm{DEG}} = \sum_i G_i|\Psi_n(y_i)|^2$. Thus, when the slipping plane spacing is much greater than magnetic length the response in $E_n(p_x)$ does not mix with those from other δ-barriers and has remarkably simple form of squared Hermitian polynom with index n (Fig. 2). So obtained deviations in dispersion law $E_n(p_x)$ from Landau levels of uniform 2DEG are proportional to the magnitude of δ-barriers and sufficiently large to be measurable.

The deviations should exhibit in asymmetric broadening of cyclotron resonance line towards lower photon energy. Moreover, increased density of states at the extrema of $E_n(p_x)$ should lead to the magnetoresistance oscillations vs. magnetic field additional to SdH-oscillations [4]. By comparing magnetooptical and magnetotransport measurements with AFM images of the surface, *i.e.* with the values of shift-narrowings in the quantum well, one could verify our suggestion about the possibility of making and using one-dimensional δ-barriers in uniform 2DEG.

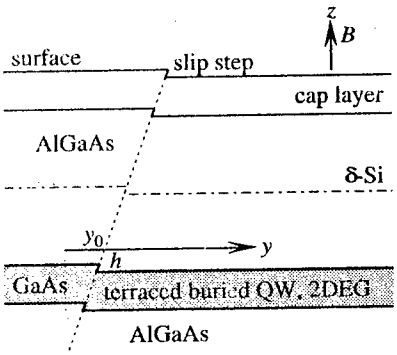

Figure 1. Schematic view: shift of the material of a heterostructure along (111) slip plane.

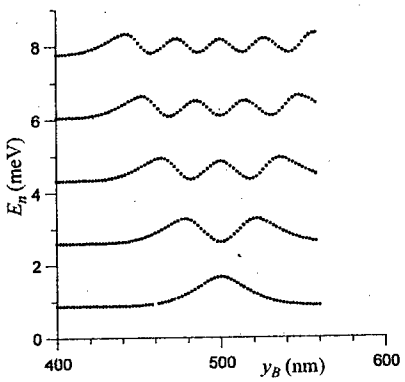

Figure 2. Dispersion law response to the single slip plane located at y_0. Magnetic field $B = 1$ T, the thickness of GaAs quantum well 10.2 nm, slip step height $h = 2.83$ nm.

Authors thank Z. D. Kvon, A. G. Pogosov and S. A. Studenikin for discussions and acknowledge partial support from Russian Foundation for Basic Research, Grant No. 96-02-19371a.

References

[1] Earlier the Franck-Read mechanism of slip step formation at the surface of Ge films was experimentally studied by Trukhanov E. M., Gorokhov E. B., Stenin S. I., Phys. Stat. Sol. (a) **32**, 435–442 (1976).

[2] Guasch C., Voillot F., Goiran M., Peyrade J. P., Bedel E., Fontaine C., Atmani H., and Rocher A., Solid State Electronics, Vol. **37**, 567 (1994).

[3] Takagaki Y., Ferry D. K., J. Phys.: Condens. Matter **4**, 10421 (1992).

[4] Romanov D. A., Studenikin S. A., Tkachenko V. A., and Tkachenko O. A., Current-carrying states engineering by nonmonotonic potential profile, in *Abstracts of ISCS-23*, St. Petesburg, Russia, 1996; in *Compound Semiconductors-96* (IOP, 1997).

OPTICAL-BEAM-INDUCED CURRENTS IN MODULATION DOPED HETEROSTRUCTURES

V.A.Sablikov[1] and S.V.Polyakov

Institute of Radio Engineering and Electronics, Russian Academy of Sciences, Vvedensky sq. 1, Fryazino, Moscow district, 141120, Russia

Effect of optical beam illumination on modulation doped heterostructures is investigated using 2D mathematical model we have developed to study in detail the spatial distribution of light-induced charge carrier concentrations and electric field. The lateral transfer of the light-induced charge carriers (both electrons and holes) along the heterostructure plane is investigated including the dynamic regime. A qualitatively new result is in finding of light-induced vortex current which appear in the buffer layer without any external circuit. This current may be high enough to affect the photoreflectance response.

This investigation is motivated by the current interest to optical excitation effects in heterostructures which may be used for contactless characterization. An urgent problem is in finding such effects which may allow one to determine kinetic characteristics of charge carriers (the mobility, the recombination characteristics). One of possibility is in using local optical generation of charge carriers and local optical probing of the photo-induced charge carriers at some distance from the exciting beam. In this case the measured optical response is determined by the charge carrier transport and hence provides information about the transport characteristics.

The scheme of the structure under the investigation and its energy diagram perturbed due to the action of the light beam is shown in Fig.1.[2]

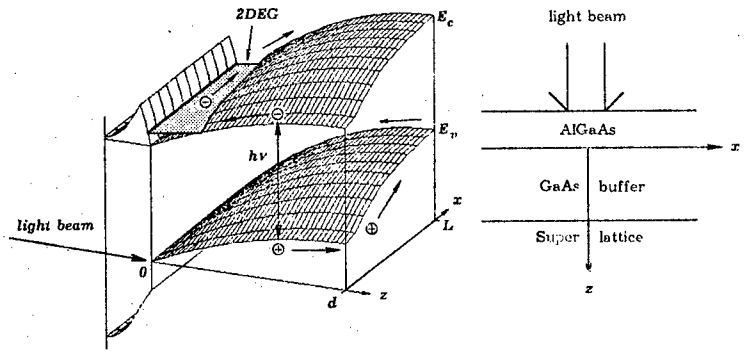

Fig. 1. Energy diagram of AlGaAs/GaAs heterostructure illuminated by the light beam and the arrangement of the beam and heterostructure layers.

[1]E-mail: vas199@ire216.msk.su

[2]Throughout the paper the right half of the heterostructure is only shown.

Electrons and holes generated by the light beam are separated by the built-in electric to the opposite surfaces of the buffer layer. The electrons run to the quantum well with 2D electron gas while the holes go to the opposite surface of the buffer layer where they are stopped by the superlattice buffer layer. Having been spatially separated the electrons and the holes are transferred along the heterostructure plane over extremely large distance. This is the lateral transfer effect [1, 2] which can be as large as several millimeters even at room temperature.

The 2D mathematical model (over $x - z$ plane) was developed with the aim to simulate the spatial distribution of the charge carrier concentration and electric field which is necessary to interpret the photoreflectance response measured locally. In the model, the total electron system of the heterostructure was divided into two subsystems: the buffer layer bulk and the 2D electron gas. In the bulk the charge carrier transport was described within the frame of conventional drift-diffusion approach. The 2D electrons was supposed to be located at the lowest quantum level. They move along the quantum well due to drift and diffusion. These two subsystems are coupled with one another via:

(i) the electron transitions through the conduction band and the recombination transitions to the valence band;

(ii) Poisson's equation for the whole system;

(iii) the electron current continuity condition at the boundary surface.

The calculations were carried out with using conventional parameters of AlGaAs/GaAs heterostructures. The thermal equilibrium density of 2DEG was obtained by self-consistent procedure for various positive charge σ located in the highly doped AlGaAs. σ was varied from 10^{10} to 10^{12} cm^{-2}, the active buffer layer thickness d was 0.35 μm, the light beam radius was 1 μm, the light intensity was in the range $I = 10^{-4}$-10^{-1} W/cm^2.

The basic results are as follows:

1. The main perturbation caused by the light beam occurs in the hole concentration and the electric field. The electric potential view is illustrated by Fig. 1. The stationary distribution of the hole concentration p is shown in Fig. 2. The lateral transfer is determined by both the hole diffusion and the self-induced drift of the holes.

2. The characteristic length of the lateral transfer is estimated as

$$l = \sqrt{\beta D_p \tau},$$

where τ is effective life time of spatially separated electrons and holes,

$$\tau = \frac{p_T d \exp\frac{eV_0}{k_B T}}{S_2 n^* + p_T (B n^* d + B_s n_s + S_1)},$$

V_0 is the built-in potential difference across the buffer layer, n^* is the equilibrium electron concentration at the boundary between the buffer bulk and 2DEG, p_T is the Shockley-Reed factor of the surface traps, S_1 and S_2 are the surface recombination velocity at the front and back edges of the GaAs buffer, respectively, B and B_s are interband recombination coefficients in the bulk and at the front surface.

3. The lateral transfer length is dependent on the 2D electron density n_s due to two factors which determine the effective lifetime: 2D electron density directly and the barrier height V_0. The first of one gives rise to the decrease of l with n_s. The second factor leads to the increase of l with V_0, however its dependence on n_s is ambiguous.

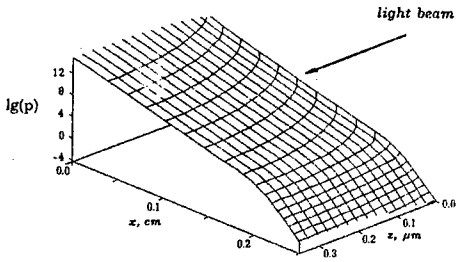

Fig. 2. Two-dimensional distribution of the light-induced hole concentration. $I = 10^{-2}$W/cm^2, $n_s = 9 \cdot 10^{11}$ cm^{-2}, T=300 K, the surface recombination was neglected.

4. The exciting light beam generates a vortex electric current whose lines are closed inside the buffer layer. The current lines are shown in Fig. 3. The origin of the vortex current is seen from Fig. 1. In the illuminated region of the sample, the electrons and the holes generated by the light move in the opposite directions giving rise to an electric current directed along the z-axis. Due to the lateral transfer of light-induced charge carriers, the light-induced voltage across the buffer layer extends over large distance from the light beam. This voltage generates the current which is directed along the photovoltage, i.e. opposite to the z-axis. The vortex current magnitude may be estimated as $j = eP/h\nu$, P being the light beam power.

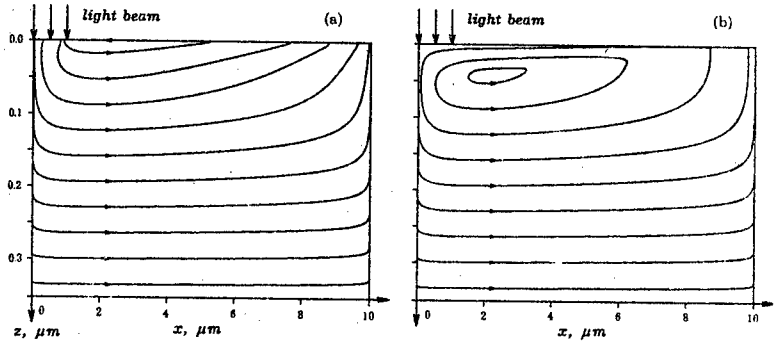

Fig. 3. Lines of the light-induced current for: (a) $n_s = 9 \cdot 10^{11}$ cm^{-2} and (b) $n_s = 5 \cdot 10^{11}$ cm^{-2}, $I = 10^{-2}$ W/cm^2, T=300 K. The lateral size of the structure was chosen to be 20 μm

This current generates a thermal effect, namely, it produces a heating in the illuminated region and a cooling in the periphery. In its magnitude the thermal effect of the vortex current may be essential to affect the photoreflectance response.

This work is supported by the Russian Program 'Physics of solid state nano-structures' (grant No 97-1054) and Russian Foundation for Basic Research (grants No 96-01-00979, 97-02-17999).

References

[1] M.Sydor, J.R.Engholm, M.O.Manasreh, K.R.Evans, C.E.Stutz, W.C.Mitchel, Phys. Rev. **B, 45**, 13796-98 (1992)

[2] V.A.Sablikov, S.V.Polyakov, O.A.Ryabushkin, *Fizika i tekhnika poluprovodnikov*, **31**, No 4 (1997)

Microwave driven dynamic barriers in uniform 2DEG as electron beam splitters and interferometers

O. A. Tkachenko, D. G. Baksheyev, M. B. Wojtsekhowski, and V. A. Tkachenko*

Novosibirsk State University, Novosibirsk, 630090, Russia

**Institute of Semiconductor Physics, Novosibirsk, 630090, Russia*

Studying photon-assisted electron transport is usually limited to quantum structures in which stationary obstacles are placed on the way of electrons. Nevertheless, in the case of zero stationary potential the interaction of a free electron with a sub-micrometer region of a non-uniform hf field $V(x)\cos\omega t$ was shown to lead to the strong modulation of transmission coefficient as a result of resonant interference between different channels of the quasienergetical wave function [1]. These effects occur around the threshold $E = \hbar^2 k_x^2/2m^* = \hbar\omega$. Besides, the hf field profile should be sharp enough: the smoothing of the edges of the hf steps or hf barriers should not exceed $\sqrt{\hbar/(m^*\omega)} \geqslant 37.5$ nm for $m^* = .067\ m_e$ and $\hbar\omega \leqslant 1$ meV. Such severe requirements can be satisfied by an inclined impingement of ballistic electrons of energy 3–4 meV on dynamic barriers in the two-dimensional electron gas of a $GaAs/Al_{0.3}Ga_{0.7}As$ heterostructure (Fig. 1).

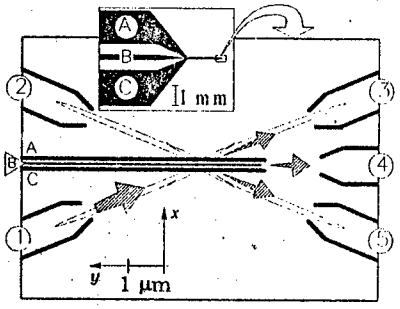

Figure 1. Suggested scheme of experiment. Solid lines denote the surface gates that make static and dynamic modulation of potential. The hf barrier across the base is created by means of the strip gates A, B, and C. Gate B is driven with the hf voltage from the antenna (shown on the top) exposed to 120 GHz microwave irradiation ($\hbar\omega =$ 0.5 meV, without irradiation these gates make no obstacle for the electrons). Ballistic electron flows from injector (1) to collector (3–5) contacts are shown by arrows. The arrow directed to (4) shows both transmitted and reflected particles which lost the transverse motion energy due to emission of $\hbar\omega$. Besides, the hf barrier generates the flows of the particles having energy $E_f + \hbar\omega$ from the 2DEG, and it is also detected by collectors 2, 3, and 5 (indicated by dashed line directivity diagram).

In this report we discuss possible manifestations of these photon-induced phenomena in 2DEG structures. While a sharp hf step can serve a semi-transparent mirror at $E = \hbar\omega$, a rectangular dynamic barrier $V\Theta(x)\Theta(d-x)\cos\omega t$ with the amplitude $V \ll \hbar\omega$ can either transmit or elastically fully reflect the particles depending on the value $k_x d$ (Fig. 2). Thus, the hf barrier acts as an interferometer though modulation period is equal to the electron wavelength in contrast to half-wave length in the Fabry-Pérot type interferometers. For several equally spaced dynamic barriers [each of width $d \approx \lambda_x/4$, the spacing $\approx \lambda_x/2$, Fig. 3(c)] the windows of almost full inelastic electron reflection with photon emission can occur at $(E - \hbar\omega)/E \ll 1$ [Fig. 3(a)], and quasitrapping of electrons to the 'levels' with small negative energies $E_i = E - \hbar\omega_i$ induced by the hf field is possible at $\hbar\omega > E$ [dips I, II in Fig. 3(a)]. The latter type resonances are characterized by strong localization of the particles in the hf field region(curves I, II, Fig. 3(b), and resemble the capture-escape resonances in the photon-assisted electron scattering on a heterostructure quantum well [2]

or a nonuniform constriction [3]. Experimental confirmation of these theoretical predictions may give a new understanding of electron-photon interaction in quantum structures.

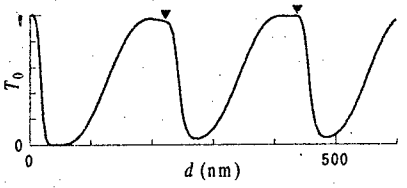

Figure 2. The coefficients of elastic transmission, T_0, versus the thickness of rectangular hf barrier d at $E = \hbar\omega = 0.5$ meV ($\lambda_x \approx 213$ nm) and $V/\hbar\omega \approx 0.2$. The triangles denote values $d = m\lambda_x$.

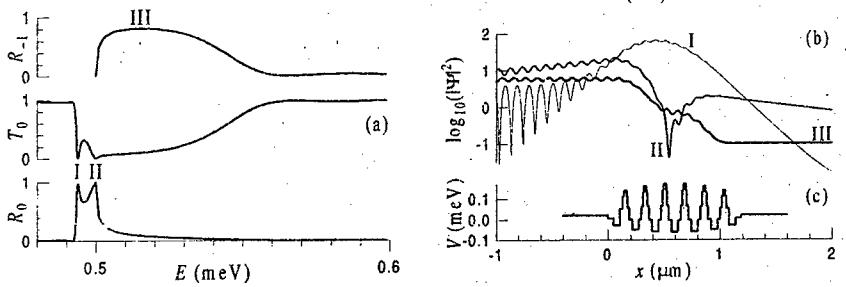

Figure 3. **(a)** Calculated elastic transmission T_0, reflection R_0, and inelastic reflection R_{-1} coefficients versus the energy of incident electrons E at photon energy $\hbar\omega = 0.5$ meV. **(b)** The time-averaged probability density for energies marked I, II, and III in **(a)**. Curves I and II resemble wave functions of the bound states in a well. Exponential decrease of curve III into the hf region is analogous to evanescent waves in a crystal at Bragg reflection. The amplitude $V(x)$ of the hf potential is shown in **(c)**.

We thank Z. D. Kvon and M. V. Budantsev for discussions and acknowledge partial support by Russian Foundation for Basic Research, Grant No. 96-02-19555a.

References

[1] O. A. Tkachenko, V. A. Tkachenko, and D. G. Baksheyev, Phys. Rev. B **53**, 4672 (1996); Phys. Rev. B **54**, 13452 (1996); Phys. Low-Dim. Structures **10/11**, 241–247 (1995).

[2] R. A. Sacks and A. Szoke, Phys. Rev. A **40**, 5614 (1989).

[3] L. Y. Gorelik *et al.*, Phys. Rev. Lett. **73**, 2260 (1994).

PECULIARITIES OF THE QUANTUM MAGNETOTRANSPORT IN A WIDE POTENTIAL WELL $Ge_{1-x}Si_x$/ p-Ge / $Ge_{1-x}Si_x$

M.V.Yakunin, Yu.G.Arapov, G.I.Harus, V.N.Neverov, N.G.Shelushinina
Institute of Metal Physics RAS, Ekaterinburg, GSP-170, 620219, RUSSIA

O.A.Kuznetsov
Scientific-Research Physicotechnical Institute, Nizhnii Novgorod State University, RUSSIA

In this work we try to trace out what new properties acquire a two-dimensional hole system in a quantum Hall state when the thickness of the layer is consecutively increased so that the system transforms into a quasi two-dimensional one. For this purpose we investigated longitudinal ρ_{xx} and the Hall ρ_{xy} magnetoresistances in a set of CVD grown multilayer samples with a following structure: substrate Ge(111) / buffer Ge ~ 1.8μ / buffer $Ge_{1-y}Si_y$ 0÷1.6μ / N×(Ge/$Ge_{1-x}Si_x$:B), $y \approx 0.07$, $x = 0.07 \div 0.10$. Thickness' of the Ge and GeSi layers in a multilayer region were approximately equal and varied from sample to sample in a range of 100 ÷ 300 Å. The GeSi layers were doped with boron in the central part with undoped spacers of ~1/4 the total layer thickness left on theirs both sides. Some sample characteristics are summarized in the table. The Fermi energy and the strain-split gap δ were deduced from the period and temperature damping of the weak field oscillations [1].

Sample	Number of periods, N	μ, $cm^2/V \cdot s$	p_s^{QHE}, $10^{11} cm^{-2}$	Well width d, Å	$\frac{S_H}{S_L}$	E_F-E_1, meV	δ, meV	$(2/3\pi)pd^2$	$\frac{E_F-E_1}{E_2-E_1}$
1006-1	90	14000	4.9	125	2.2	8.0	20	0.17	0.3
1124b3	27	10000	2.8	200	2.3	7.0	8	0.23	0.7
1123a6	15	14000	3.4	200(235)	3.1	7.7	10	0.30	0.8
1003-2	90	15000	4.8	220	3.4	7.2	21	0.49	0.9

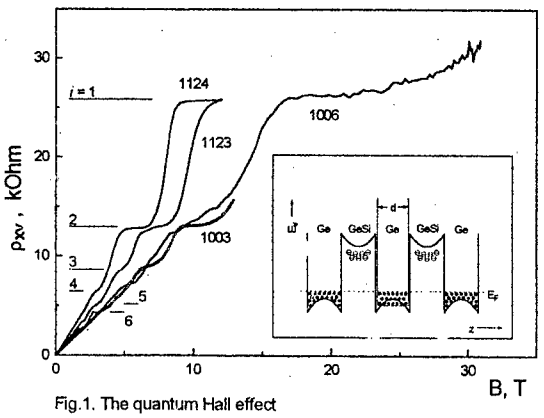

Fig.1. The quantum Hall effect

Quantum Hall plateaus concomitant with the ρ_{xx} minima were observed distinctly at T ≤ 4K. Important is that for all of our samples the plateau in the highest fields, as obtained by the multiplication of the measured Hall resistivity by the number of Ge layers N, corresponds to the fundamental value 25.8 kOhm = h/e^2 (fig.1). It means that (i) all the layers participate in the current transfer

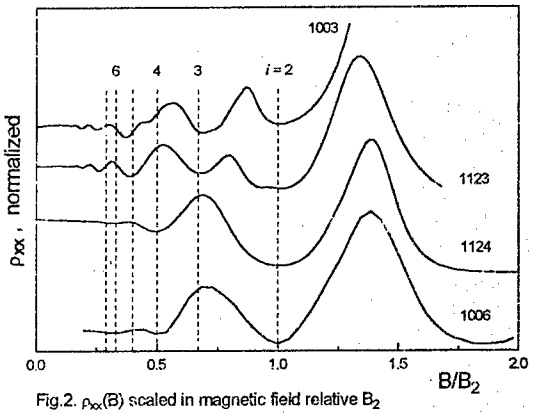

Fig.2. $\rho_{xx}(B)$ scaled in magnetic field relative B_2

equivalently and (ii) the free holes do not collect into two separate 2D sheets at the opposite interfaces even for the widest wells investigated. Our estimations for the samples in the table, based on a simple quasiclassical approach, indicate that the well bottom bending indeed does not exceed the Fermi level.

ρ_{xx} minima have different periods in inverse field 1/B for high and low fields. In the high fields, when all the levels are separated by mobility gaps, minima positions are only predetermined by the 2D-gas density p_s: $i \cdot eB_i/h = p_s$, i = 1,2,3..., and they do not depend on any details of the band structure. Contrary, in the low fields the observed minima reflect the minima in the envelope of the total density of states for unresolved levels and the observed periods may depend on the relative level positions. In the simplest case of a single spin-split-level fan chart with a spin splitting smaller than a cyclotron one the ratio of periods in the high and low fields is equal to two: $S_H/S_L = 2$, $S_{H,L} \equiv \Delta M / \Delta(1/B)$, M — the through successive numbers of the ρ_{xx} minima. This ratio value reflects the merging of levels in coupies and indicates that the numbering in low fields would be done more correctly with a step of 2, not 1. The value of $S_H/S_L = 2$ was observed in a number of experiments on 2D electron and hole gases in a sufficiently narrow well. But higher values of this ratio were found for wells wider than ~200 Å. It was interpreted as an interference with some additional subband. In such a case the low field period is connected with this additional subband and may be arbitrary higher than twice the high field period. In a 2D electron gas the additional subband is

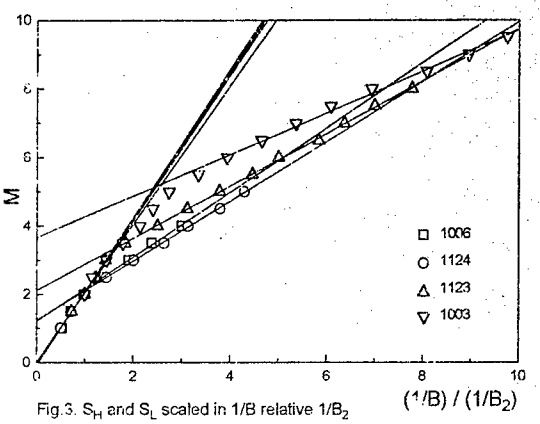

Fig.3. S_H and S_L scaled in 1/B relative $1/B_2$

unambiguously the second confinement subband. But for a 2D hole gas there is one more possibility — the splitting of the heavy hole band due to an inversion asymmetry. Just this interpretation prevailed so far [2] with an assumption that the manifestation of asymmetry increases in a wide well due to increased bottom bending.

Simultaneous observation of the quantum Hall effect (QHE) makes the analysis of the ρ_{xx} oscillations more unambiguous and transparent. The filling factors obtained from the heights of ρ_{xy} plateaus now may be used as the numbers of ρ_{xx} minima in a high field region. Such minima numbers bear a physical sense that makes it possible to compare unambiguously identical minima for different samples. Rescaling the magnetic field relative a certain minima position (e.g. $i = 2$) for each of the samples, we can remove the differences in the 2D gas densities and only compare the structure (i.e. existence or absence and relative amplitudes of oscillations) of the ρ_{xx} curves. For our samples these curves differ radically for the narrow and wide Ge layers (fig.2). The same is for the slopes $S_{H,L}$ (fig.3): in relative 1/B scales the slopes in high field S_H are almost equal for all the samples while the slopes in low fields S_L are different for the samples with narrow and wide wells. The ratio $S_H/S_L \approx 2$ for the narrowest wells but it increases appreciably for the wider wells indicating the inclusion of an additional band into magnetotransport. The samples in the table are arranged in strings according to the values of this ratio. Since our QHE data do not reveal any influence of the quantum well asymmetry and the Fermi level is higher than the bottom bending, we will try to compare the experimental data with the population of the second heavy hole confinement subband estimated for a rectangular well. For the simplest parabolic band, symmetric in all 3 dimensions: $(E_F - E_1) / (E_2 - E_1) = (\pi\hbar^2 p_s/m) / (3\pi^2\hbar^2/2md^2) = (2/3\pi)p_s d^2$. But, considering a complicated shape of the hole subbands due to both the confinement [3] and the uniaxial stress and a substantial difference of the in-plane mass from the bulk one, more correct estimations would be achieved for the independently evaluated E_F; as is done in the table for the values from the work [1]: $E_F = E_F^{[1]}$. The values of $p_s d^2$ and $(E_F^{[1]} - E_1) / (E_2 - E_1)$ increase in the same order as S_H/S_L. The value of S_H/S_L increases abruptly for the transition from the sample 1124 to 1123 implying the beginning of the population of the second subband. This corresponds to the increase of the value $(2/3\pi)p_s d^2$ from 0.23 to 0.30 and of the value $(E_F^{[1]} - E_1) / (E_2 - E_1)$ from 0.7 to 0.8. The values for the second criterion are closer to 1 indicating its higher reliability.

The high field $\rho_{xy}(B)$ data are similar for all of our samples in that they contain plateaus with $i = 1$ and 2. But below the plateau with $i = 2$ the structure of these curves differs significantly. For two of the samples 1006 and 1124 the plateau with $i = 4$ comes next on the low field side after the plateau with $i = 2$ and the other even numbered plateaus dominate. For the other two samples 1123 and 1003 the next after plateau $i = 2$ comes the plateau with $i = 3$, plateau with $i = 4$ is missed and the odd numbered plateaus dominate. These features are still more pronounced in the $\rho_{xx}(B)$ curves (fig.2). To explain this we calculated the Ge valence band energy spectra for quantisation by both a magnetic field and a confinement. The model of the rectangular infinitely deep well was used [4]. An example of these calculations for the sample 1123 is presented in fig.4. The behavior of the Fermi level corresponds to the infinitely sharp Landau levels and constant total hole density.

As follows from the calculations, in a sample 1006 the Fermi level does not reach the second confinement level and the levels are grouped in couples similar to the Landau level picture for a conduction band with a small spin splitting. That's why the even numbered peculiarities dominate. In a sample 1124 the Fermi level approaches the second subband and moves within it in small intervals of magnetic fields, but it does not lead to any essential changes.

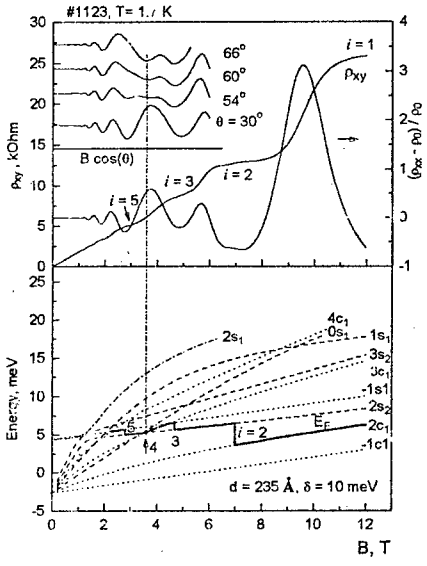

Fig.4. Comparison with calculations

The situation changes radically in samples 1123 and 1003 when the Fermi level moves within the second subband level in a considerable part of fields (fig.4). In these samples this additional level is imbedded in between the ground subband Landau levels number two and number three (the through ascending numbers are meant) and divide a single step for $i = 2$ in the Fermi level motion between these two levels into two steps with $i = 2$ and $i = 3$. That's how the peculiarity $i = 3$ arises in the experimental data. Another consequence of the imbedding an additional level is that the step number 4 no longer corresponds to a transition at the distance of about the cyclotron energy between the orbitally splitted spin-couples of the ground subband but to a transition either onto this additional level or, if the imbedded level is lower than the Fermi level, to a transition within the spin splitted couples. In the later case the numbers of peculiarities (the filling factors) are merely shifted one unit higher since the additional level arose below the Fermi level. For both cases the energy distance may be much smaller than the cyclotron energy and the amplitude of the peculiarity with $i = 4$ may become vanishingly small, as is for the sample 1123. So the crucial role of the second confinement level position relative the Fermi level is evident. On the other hand, its position is very sensitive to the width and the shape of a quantum well that must be reflected in a high sensitivity of the structure of experimental curves to diverse changes in the system. Indeed in the sample 1003 with parameters not much different from that of the sample 1123 a small peculiarity with $i = 4$ was found. In the insert on the fig.4 shown is the evolution of magnetoresistivity of the sample 1123 with a tilting of magnetic field from a normal to the sample plane. Evident is that the tilting introduces some changes into the Landau level picture that revive the peculiarity with $i = 4$, initially absent.

The work is supported in part by RFBR, Grant № 95-02-04891, and by the program «Physics of Solid State Nanostructures», Grant № 1-065/3.

[1] Yu.G.Arapov et. al., Fiz. Tech. Poluprov. 27, 1165 (1993)
[2] Y.Ive, E.E.Mendez, W.I.Wang, L.Esaki. Phys. Rev. B, 33, 5754 (1986).
[3] M.I.Diyakonov, A.V.Hayetski. JETP, 82, 1584 (1982).
[4] A.V.Germanenko et. al., Adv. Mater. Opt. Electron. 2, 57 (1993); Yu.G.Arapov et. al., Pisma JETP, 59, 247 (1994)

Real space transfer and population inversion in delta selectively doped MQW structures

V. Aleshkin, A. Andronov, A. Antonov, N. Bekin, V. Gavrilenko, A. Muravjev, S. Pavlov,
D. Revin V. Shastin, E. Linkova,I. Malkina, E. Uskova, B. Zvonkov
Institute for Physics of Microstructures RAS;
Physical-Technical Institute of NNSU
Nizhny Novgorod 603600 GSP-105 Russia; andron@ipm.sci-nnov.ru

Existing intraband semiconductor lasers—i.e. p-Ge hot hole FIR lasers [1] and quantum cascade lasers [2] have their own drawbacks.

Hot hole lasers are working in the broad region in FIR (30–120 cm^{-1}); but they are helium cooled pulsed devices (though works to get cw p-Ge lasers are under way [3]). Quantum cascade lasers are IR sources which stop operate at wavelengths longer than around 10 μm. So there is a great need to find out a mechanism which can provide lasing in wide IR region and to develop a simple semiconductor lasers which could fill frequency band from far to mid IR regions.

In the process of investigation of high electric field lateral transport and real space transfer in selectively doped p-type InGaAs- GaAs we came across seems a universal population inversion mechanism which could serve this goal. It is based on lower heating by lateral electric field of the high level (states) and could be used in quite broad type of the MQW systems

Though real space transfer (RST)—spatial redistribution of carriers in a MWQ system (from well to barriers or in the reverse direction or redistribution between nearby wells) by lateral electric field E—is studied for almost two decades (for a review see [5]) to the authors knowledge till works of the present authors [6,7] nobody has discussed so far a possibility of population inversion and a prospect for stimulated FIR and mid IR (MIR) emission under the RST (though the inversion seems is a natural consequence of the RST); also so far none has observed the appropriate spontaneous emission under the RST.

And in the present report our recent results on the consideration of a possibility of population inversion and stimulated IR emission under RST are given and results of the detailed investigations of current-voltage and spontaneous FIR and MIR emissions-voltage characteristics of hot holes in p-type selectively δ-doped InGaAs-GaAs MQW systems under RST. Also data on the hot hole photoluminescence and results on observation of absorption of the FIR radiation in the MQW structures under RST by using intracavity spectroscopy basing on p-Ge laser (which seems gives a prove for FIR radiation amplification in the "shallow" sample studied) are given.

Acknowledgment

The research described in this publication was made possible by Grants 1-064/3, 1-074/4 from Russian Scientific Programs "Physics of Solid State Nanostructures", 3.17 from Russian Scientific Programs "Physics of Microwaves", 96-02-19275 from Russian Basic Research Foundation and Grant 94-842 from INTAS.

References

[1] Optical and Quantum Electronics, v.23, N 2, Special issue "FIR semiconductor lasers", 1991.

[2] J.Faist, F.Capasso, D.L.Sivko, et al., Science, vol 264, 553-556, 1994.

[3] E.Brudermann, A.M.Linhart et al., Appl. Phys. Lett., 68, 3075 (1996).

[4] Z.S.Gribnikov, K.Hess, S.Kozinovsky. J. Appl. Phys. v.77, N.4, pp.1337-1385, 1995.

[5] B.F.Levine, J. Appl. Phys. 71, R1 (1993).

[6] V Aleshkin, A Andronov, A Antonov, N Bekin, V Gavrilenko, D Revin, E Linkova, I Malkina, E Uskova, B Zvonkov Pis'ma v Zh. Eksp. Teor. Fiz., 64, 478-482, 1996.

[7] V Aleshkin, A Andronov, A Antonov, N Bekin, V Gavrilenko, A.Muravjev,

[8] Pavlov, D Revin, E Linkova, I Malkina, E Uskova, B Zvonkov (to be published in Proceedings of Inter. Symposium on Compound Semiconductors 23, St. Petersburg 1996)

Infrared spectroscopy of intraband transitions in self-organized InAs/GaAs quantum dots

S. Sauvage, P. Boucaud, F. H. Julien, J.-M. Gérard†, J.-Y. Marzin‡
Institut d'Electronique Fondamentale, URA CNRS 22
Bat. 220, Université, Paris-Sud, 91405 Orsay, France
e-mail : phill@ief.u-psud.fr
† France Telecom, CNET Bagneux, 196 Av H. Ravera 92200 Bagneux, France
‡L2M-CNRS Bagneux, 196 Av H. Ravera, BP 107, 92225 Bagneux, France

Mid-infrared spectroscopy is an appropriate tool to investigate intraband properties of quantum dots since it provides a direct measurement of confinement energies of both electrons and holes. Unlike quantum wells, intraband absorption in these 0D confined systems also appears promising regarding strong in-plane polarization absorption and could give rise to a new generation of normal incident infrared photo detectors. In addition phonon bottleneck effects originating from the reduction of dimensionality could lead to non-radiative scattering times between intraband levels much longer than in the case of quantum wells. This situation would be beneficial for achieving population inversion in the far-infrared.

In this work, we have investigated the mid-infrared absorption between confined levels of undoped InAs/GaAs quantum dots obtained by self-organized growth. The infrared absorption is measured by a sensitive photo-induced infrared spectroscopic technique. Quantum dots with different sizes are investigated as a function of temperature, interband pump photon energy, intensity and infrared polarization. We show that in the presently investigated 90–250 meV energy range, the quantum dots exhibit intraband absorption between confined levels polarized along the growth axis as for usual conduction intersubband transitions in quantum wells. Based on their energy position and their temperature dependence, the infrared resonances are attributed either to intraband transitions between confined holes or to bound-to-continuum transitions of electrons, which respectively shift to high energy and low energy as the dot size is decreased (figure 1).

Due to the strong inhomogeneity of the dot sizes, the broadening of the conduction band transition is found very large ($\approx$ 100 meV full width at half maximum) while the broadening of intraband absorption between confined levels in the valence band is found around 15 meV. We show that intraband absorption is observed for either selective excitation of the dots or excitation via absorption in the wetting layer or in the GaAs layers. From the saturation of the infrared absorption a dipole length $\approx$ 0.5 nm has been measured for the $x000 > \rightarrow x001 >$ hole transition (figure 2). These features are found in agreement with effective-mass calculations which account for the geometry and strain distribution in the dots as reported by Grundmann *et al.*, (Phys. Rev. B 52, 11969 (1995)).

Finally we will show that the assignment of the observed intraband transitions is further confirmed by separate measurements on n-doped quantum dots.

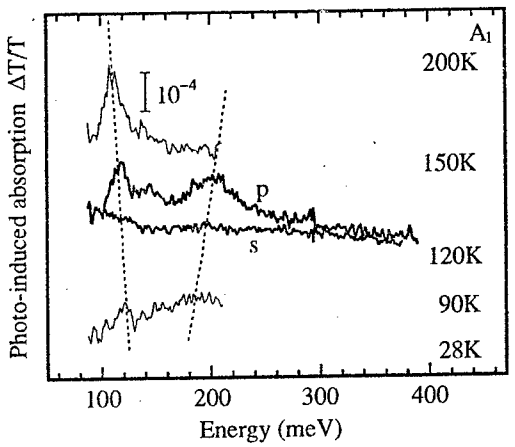

Fig 1. Mid-infrared photo-induced absorption of a InAs/GaAs QD sample with large dots (4K PL at 1.150 eV) as a function of the temperature. The pump energy is 1.504 eV, its intensity 40 mW. All curves correspon to a polarization perpendicular to the layer plane (p). The in-plane polarized absorption (s) is shown at 120 K. The resonance around 120 MeV is the $|000\rangle \rightarrow |001\rangle$ hole transition. The broad peak around 200 MeV is the electron bound to continuum transition. The observed shift as the temperature is increased are due to the depopulation of small dots in the distribution. The curves have been offset for clarity.

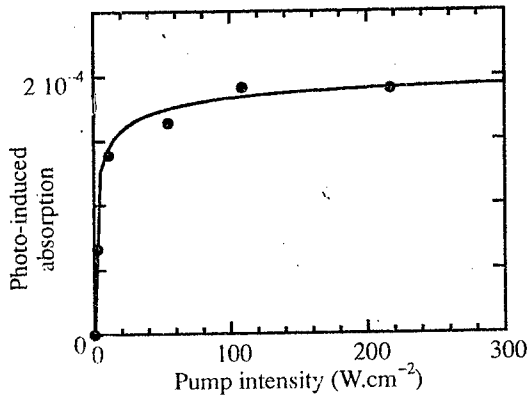

Fig 2. Saturation of the quantum dot infrared absorption due to filling of the $|000\rangle$ hole ground state.

Quantum fountain intersubband stimulated emission in GaAs/AlGaAs quantum wells

O. Gauthier-Lafaye, S. Sauvage, P. Boucaud, and F.H. Julien
Institut d'Electronique Fondamentale, URA CNRS 22
Bat. 220, Université Paris-Sud, 91405 Orsay, France

The possibility of intersubband emission has been theoretically investigated as early as 1971 by Karazinov and Suris [1]. In 1994, electrical pumping of InGaAs/AlInAs quantum wells was demonstrated to lead to stimulated intersubband emission, giving birth to a new class of unipolar semiconductor lasers, the so-called quantum cascade (QC) lasers [2]. Optical pumping has also been proposed to achieve stimulated emission between excited subbands of a three-bound-state coupled quantum well structure in the mid-infrared spectral range, i.e. for intersubband energies larger than the optical phonon energy [3]. By carefully engineering the LO-phonon scattering rates between subbands through a proper choice of the quantum well composition and layer thicknesses, it was shown that the conditions for population inversion could be fulfilled in a so-called Quantum Fountain source. However, although large stimulated gains have been predicted [3–5], only observations of intersubband spontaneous emissions at $\lambda \approx 14-15\,\mu$m have been reported until recently [6–8].

In this paper, we report on the observation of optical gain associated with the intersubband stimulated emission in optically pumped GaAs/AlGaAs coupled quantum wells [9]. The three-level quantum well structure, shown in Figure 1, is designed to present faster non-radiative relaxation of electrons between the first excited subband and the ground subband than between the two excited subbands. The stimulated emission measurements have been carried out using the picosecond two-color free-electron laser facility in Orsay [10]. Optical pumping at $\lambda \approx 9.2\,\mu$m is used to bleach the absorption between the ground subband and the second excited subband resulting in population inversion between the two excited subbands which can be probed by the second color of the free-electron laser. For increasing the interaction length, the samples are designed as infrared waveguides containing the active quantum wells. The stimulated gain at liquid nitrogen temperature is analyzed using pump-probe measurements versus the waveguide length and the probe wavelength. The emission occurs at $\lambda \approx 12.5\,\mu$m which is to our knowledge the largest wavelength reported so far for an intersubband stimulated emission. Indeed, in contrast to electrically pumped inverted systems such as QC lasers, the optically pumped emitters do not require metallic contacts or heavily doped contact and injectors layers. Free-carrier and plasmon losses can be reduced which is beneficial for long-wavelength operation.

The infrared waveguide sample was grown by molecular beam epitaxy on a GaAs substrate n-doped at 2×10^{18} cm^{-3}. In growth order, the various layers are a 5 μm thick $Al_{0.9}Ga_{0.1}As$ cladding layer, a 2.5 μm thick GaAs core layer, the multi-quantum well layer and a 2.9 μm thick GaAs core layer. The multi-quantum well layer consists of 30 periods of coupled quantum wells with 7.7 nm and 4.7 nm thick GaAs wells separated by a 1.1 nm thick $Al_{0.3}Ga_{0.7}As$ coupling barrier. The 21 nm thick $Al_{0.2}Ga_{0.7}As$ barrier separating each period is modulation doped at 5 nm from the wide well in order to achieve a bidimensional carrier concentration of 3×10^{11} cm^{-2} in the wells which corresponds to a Fermi energy 9.2 meV above the ground subband at 77 K. Energy

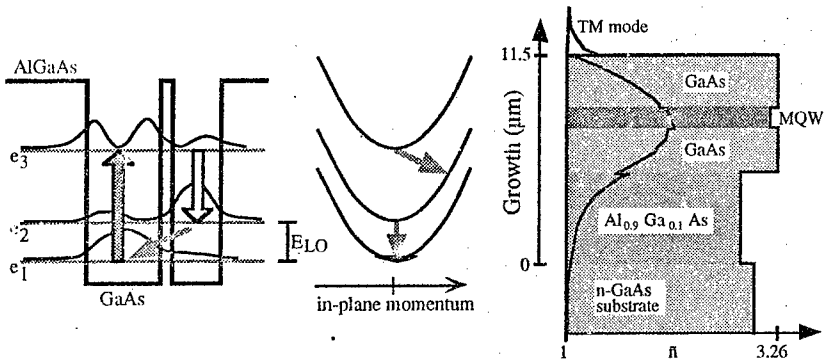

Fig 1. (left) Conduction band profile of the coupled quantum well structure for Quantum Fountain emission and in-plane dispersion diagram. The grey arrows show the dominant relaxation pathes via LO-phonon emission, (right) The infrared waveguide sample.

calculations based on the nominal growth parameters show that the coupled quantum well structure exhibit three electron bound states and that the energy of the e_1-e_2, e_1-e_3 and e_2-e_3 transitions is respectively 45 meV, 131 meV and 86 meV, in close agreement with measurements. The e_2 subband lies 36 meV above the Fermi energy which insures both negligible thermal population of the e_2 subband at 77 K and fast relaxation of electrons to the ground subband ($t_{21} \approx 0.7$ ps) through LO-phonon emission with small momemtum transfer. On the other hand, the intersubband non-radiative relaxation between the e_3 and e_2 subbands is expected to be longer ($t_{32} \approx 1.5$ ps) since the momemtum transfer is much larger

Pump-probe experiments were carried at the free-electron laser facility in Orsay (CLIO). This picosecond infrared laser can emit simultaneously at two wavelengths which can be independently tuned. The laser delivers macropulses of $\approx 10\ \mu$s duration which consist of picosecond micropulses.

Typical peak powers ≈ 10 MW can be obtained. The first color of the laser is set at 9.2 μm in order to bleach the $e_1 \rightarrow e_3$ absorption while the second color probes the transmission of the waveguide sample at the $e_3 \rightarrow e_2$ resonance wavelength (12.5 μm). The sample is cooled at 77 K. The pump intensity on the sample input facet is estimated around 30 MW.cm^{-2}. The probe transmission versus the time delay between pump and probe is presented in figure 2 (left). The transmission has been normalized to 1 at large delays. As seen, the transmission increases when both the pump and probe beams are synchroneously incident on the sample, as a result of the stimulated amplification in the sample. The net gain is of the order of 1.5 for a sample length of 0.7 mm and increases to 3.5 for a 2 mm long sample.

As shown in Figure 2 (right), the gain spectrum shows a resonance at 12.5 μm which corresponds to the stimulated emission at the $e_3 \rightarrow e_2$ intersubband resonance wavelength. The modal gain of the sample is $\approx 6\,\mathrm{cm}^{-1}$. Accounting for the overlap cross-section of the TM mode in the active layer, the stimulated intersubband gain in the quantum wells is deduced to be of the order of 80 cm^{-1}.

Lasing action could not be achieved in these free-electron laser experiments because the pulse duration was much shorter than both the excited state lifetime and the photon round-trip time

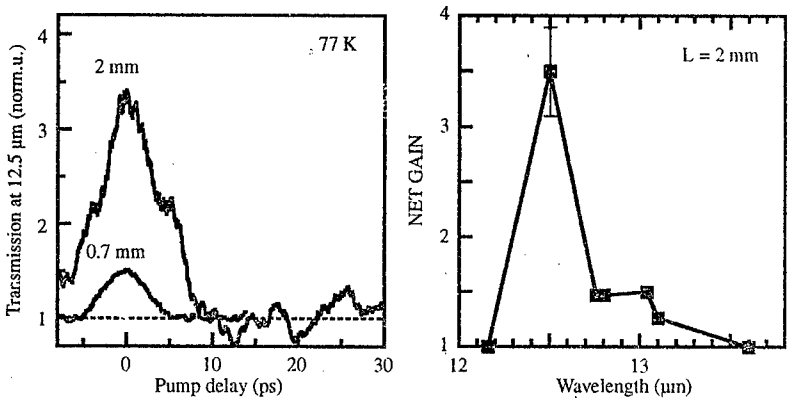

Fig 2. (left) Waveguide transmission at 12.5 μm versus the delay between pump and probe for two waveguide lengths. The pump is set in resonance with the e_1-e_3 transition. The transmission increase at zero delay is the result of intersubband stimulated amplification, (right) Gain spectrum of a 2 mm long sample.

between the cleaved facets of the sample. The stimulated gain although quite large can be further optimized by using a better design of the structure, namely by increasing the oscillator strength of both pump and emission transitions.

By doing this, amplification factors in excess of 50 for a 2 mm long waveguide have been recently achieved. The modal gain in these optimized samples is of the order of 20 cm^{-1} which is more than sufficient for achieving lasing action under optical pumping by a CO_2 laser.

References

[1] R.F. Kazarinov and R.A. Suris, *Sov. Phys. Semicond.* **5**, 707 (1971).

[2] J. Faist, F. Capasso, D. Sivco, C. Sirtori, A.L. Hutchinson, S.N.G. Chu and A.Y. Cho, *Science* **264**, 553 (1994).

[3] F.H. Julien, A. Sa'ar, J. Wang, and J.-P. Leburton, *Electron. Lett.* **31**, 838 (1995).

[4] J. Wang, J.-P. Leburton, F.H. Julien, and A. Sa'ar, *IEEE Photonics Technol. Lett.* **8**, 1001 (1996).

[5] J. Wang, J.-P. Leburton, Z. Moussa, F. H. Julien, and A. Sa'ar, *J. Appl. Phys.* **80**, 1970 (1996).

[6] Z. Moussa, P. Boucaud, F.H. Julien, Y. Lavon, A. Sa'ar, V. Berger, J. Nagle, and N. Coron, *Electron. Lett.* **31**, 912 (1995).

[7] Y. Lavon, A. Sa'ar, Z. Moussa, F.H. Julien, and R. Planel, *Appl. Phys. Lett.* **67**, 1984 (1995).

[8] F.H. Julien, Z. Moussa, P. Boucaud, Y. Lavon, A. Sa'ar, J. Wang, J.-P. Leburton, V. Berger, J. Nagle, and R. Planel, *Superlattices and Microstruct.* **19**, 69 (1996).

[9] O. Gauthier-Lafaye, S. Sauvage, P. Boucaud, F.H. Julien, R. Prazeres, F. Glotin, J.-M. Ortega, V. Thierry-Mieg, R. Planel, J.-P. Leburton, V. Berger, *Appl. Phys. Lett.* **70**, (16 June 1997).

[10] D. A. Jarozynski, R. Prazeres, F. Glotin, and J.-M. Ortega, *Phys. Rev. Lett.* **72**, 2387 (1994).

Author Index

Ahlers F.J. 47
Aktsipetrov O.A. 221, 380
Albrecht M. 122
Aleshkin V.Ya. 137, 141, 224
Alferov Zh.I. 195, 202, 206
Aliev G.N. 38, 210
Alperovich V.I. 421
Amand T. 62, 106
Andersson T.G. 497, 508
Andreani L.C. 31, 43
Andreev A.D. 168, 172
Andreev A.Yu. 310
Andronov A.A. 141, 565
Arapov Yu. 549
Arapov Yu.G. 7, 561
Aristov V.V. 345
Armitage A. 43
Aronzon B.A. 11
Asada M. 440
Asryan L.V. 176
Astakhov G. 42
Astratov V.N. 43
Averkiev N.S. 498
Babushkina N.A. 7
Bagraev N.T. 444, 448, 452
Baidakova M.B. 288
Baidakova M.V. 227, 383
Bakaushin D.A. 11
Baksheyev D.G. 159, 499, 559
Balandin A. 144
Bandyopadhyay S. 144
Banshchikov A.G. 288
Baranov P.G. 47
Barrau J. 62, 106
Baru V.G. 395
Bazhenov N.L. 152
Bekin N.A. 137
Belitsky V.I. 95
Belyakov L. 460
Belyantsev A.M. 148
Berezovets V.A. 152, 498
Berger J.D. 64
Bergman J.P. 54
Bert N.A. 233, 292, 320, 341, 361
Bimberg D. 195, 202, 296
Birulin P.I. 537
Blagnov P.A. 316
Blinov E. 287
Boltaev A.P. 231
Borevich V. 305
Boronin S.G. 24, 25, 26
Boucaud P. 567, 569
Brounkov P.N. 233, 236
Brousseau M. 62, 106
Bugge F. 263
Bukharaev A.A. 240, 242
Butenko Yu.V. 339
Butko V.Y. 421
Cantarero A. 95
Carlsson N. 354
Carlsson S.-B. 282, 497
Chaikina E.I. 444
Chaldyshev V.V. 233, 252, 292, 320
Chekalin S.V. 352
Chen C.D. 467
Cheng T.S. 73
Chernigovsky A.V. 233
Chernjaev A.V. 152
Chernoutsan K. 387
Chernushich A. 395

Chumakov N.K. 11
Cingolani R. 395
Cirlin G.E. 296
Continenza A. 395
Danilov S.N. 164
Daniltsev V.M. 224, 267
Davydov V.Yu. 244
De La Rue R.M. 421
Delimova L. 305
Demidov V.N. 296
Deppert K. 282
Depuydt A. 480
Deryagin A.G. 180
Devyatov I.A. 501
Diakonov A.M. 541
Dittrich Th. 463
Dmitriev A.P. 15
Dneprovskii V. 387, 391
Dobryakov A.L. 89
Donetsky D.V. 164
Dorozhkin S.I. 525
Drichko I.L. 541
Dubonos S.V. 24, 26, 248, 345
Dubrovskii Yu.V. 497, 508
Eaves L. 236
Egorov A.Yu 195
Egorov A.Yu. 183, 202, 236, 259, 274, 300, 341
Emel'yanov V.I. 304
Eremtchenko M.D. 256
Erofeeva I.V. 137
Evtikhiev V.P. 219, 278
Faleev N.N. 252, 278
Farbshtein I.I. 498
Farhangfar Sh. 484
Fazlitdinov V.M. 89
Fedirko V.A. 256
Fedyanin A.A. 221
Feiginov M.N. 505
Filatov D.O. 99
Firsov D.A. 161, 164
Fisher F. 81
Fisher T.A. 43
Fleischer V.G. 287
Fokin A.V. 421, 488
Forchel A. 354, GP.01i
Foxon C.T. 73
Gabriel Th. 357
Gaevski M.E. 361
Gaifullin B.N. 345
Galbraith I. 83
Galiev V.I. 118
Galperin Yu.M. 531
Gan'shina E.A. 380
Gaponova D.M. 141
Gardona M. 95
Gauthier-Lafaye O. 569
Gavrilenko V.I. 137, 141
Gehlhoff W. 444, 452
Geim A.K. 248
Georgievski A.M. 183
Gérard J.-M. 567
German E.P. 130
Germanenko A.V. 114, 512
Gibbs H.M. 64
Giugno P.V. 395
Glinskii G.F. 51
Goldys E.M. 118
Golovach V. 437
Golub L.E. 54, 161
Golubok A.O. 296
Goncharuk I.N. 244
Gordeev N.Yu. 183, 202
Gordina N.A. 259

Gornyi I.V. 15
Gorokhov E.B. 553
Gorshunov A. 77
Goryachev D. 460
Goupalov S.V. 58
Grekhov I. 305
Grinev V.I. 77
Grishechkina S.P. 537
Gubin S.P. 494
Guk E.G. 399
Guk I.P. 417
Gun'ko N.A. 187
Gurevich S.A. 474
Gurtovoi V.L. 22
Gushin S.V. 380
Gutakovsky A.K. 339
Harris J.S., Jr. 314
Hartmann E. 357
Harus G.I. 7, 561
Helm M. 137
Hofstaetter A. 47
Holovatsky V. 433
Horenko V.V. 474
Huhtinen H. 287
Hvam J.M. 77
Ichida M. 219
Ignatenkov A.N. 7
Ihn T. 236
Il'inskaya N.D. 210
Ipatova I.P. 102, 306
Ivanov-Omskii V.I. 152, 383
Ivanov A.I. 352
Ivanov S. 206
Ivanov S.V. 54, 210
Ivchenko E.L. 54, 58
Jantsch W. 99
Jitov V. 395
Julien F.H. 567, 569
Junno T. 282
Kachorovskii V.Yu. 15
Kagan V.D. 541
Kalevich V.K. 106
Kaliteevski M.A. 43, 64, 191
Kalugin N.G. 310
Kamenev B.V. 463
Kan H. 87
Karavanskii V. 387
Karczewski G. 42, 68
Karpovich I.A. 99
Kashkarov P.K. 403
Kavokin A.V. 31, 43, 58, 64
Kavokin K.V. 106
Kerkel K. 354
Khalfin V.B. 187
Khanin V.V. 494
Khanin Yu.N. 497, 508
Khavryutchenko 351
Khitrova G. 64
Khomutov G.B. 221, 494
Khrykin O.I. 224, 256, 267
Khvostikov V.P. 316
Kim J. 87
Kiselev A.A. 54
Kitaev Yu.E. 110, 244
Klimov V.V. 407
Klyachkin L.E. 444, 448, 452
Koch F. 460
Kochegarov Yu.V. 164
Kochereshko V. 42, 68, 81
Kokhanovskii S.I. 69
Kokorev M.F. 259
Kolobkova E.V. 411, 415
Kolomiichuk V.N. 339
Komarov S.A. 314

Kompanets V.O. 352
Konnikov S.G. 233, 236
Konstantinova E.A. 403
Konstantinovich A. 437
Kop'ev P.S. 183, 195, 202, 206, 210, 300, 341
Kopaev Yu.V. 537
Kopchatov V.I. 183
Korneeva N.P. 296
Korotkov A.N. 471
Korovin L.I. 95
Kosogov A.O. 320
Kossut J. 68
Kotelnikov E.Yu. 278
Kovalenko S.A. 89
Kovsh A.R. 183, 195, 202, 236, 274, 300, 341
Kozyrev A.B. 148
Krasil'nik Z.F. 137, 310
Kravchenko K.O. 51
Kreshchuk A.M. 541
Krivolapchuk V.V. 73
Kruglov A N. 118
Krupenin V.A. 477
Kryganovskii A.K. 219
Kuchinskii V.I. 180
Kudryashov I.V. 278
Kukovitskii E.F. 242
Kuksenkov D.V. 180
Kunitsyn A.E. 252
Kupriyanov M.Yu. 501
Kuyanov I.A. 466
Kuzminkov A.G. 259
Kuznetsov O.A. 137, 561
Kuznetsov V.L. 339
Kuznetsov V.P. 310
Lagunova T.S. 545
Lahderanta E. 287
Laiho R. 287
Landwehr G. 42, 68, 81
Lang I.G. 95
Larionova V.A. 114
Le Jeune P. 62, 106
Lebedev A.O. 244
Lebedev A.V. 210
Ledentsov N.N. 195, 202, 296, 274, 374
Lenstra D. 499
Leotin J. 549
Lepneva A.A. 155
Lerinman N.K. 7
Letokhov V.S. 407
Levinstein M.E. 399
Liniichuk I. 305
Lipovskii A.A. 411, 415
Lisin D.V. 352
Litvinenko K. 77
Litz Th. 81
Loiko N.N. 231
Lott J.A. 195
Lourtioz J.M. 199
Lozovik Yu.E. 37, 89, 352
Lugagne-Delpon E. 199
Luk'yanova N.V. 38
Lunev A.V. 202, 361
Luzanov V. 395
Lyngnes O. 64
Lyssenko V.G. 77
Lyublinsky A. 305
Maao F.A. 531
Magnusson M.H. 282
Main P.C. 236
Makhanets O. 429
Maleev N.A. 259

Malkina I.G. 141
Malm J.-O. 282
Malyarenko A.M. 444, 448, 452
Malyshkin V.G. 306
Maradudin A.A. 306
Marie X. 62, 106
Marikhin V.A. 399
Markov I.I. 444
Marzin J.Y. 567
Masalov S.A. 296
Maslov A.Yu. 102
Maslova N.S. 480
Matveets Yu.A. 89, 352
Maude D.K. 488
Maximov I. 354
Maximov M.V. 195, 202, 236, 274, 341
Mazurenko D.A. 73
McKillop J.S. 191
Meilikhov E.Z. 11
Melnik M.A. 263
Merkulova S.P. 352
Meyer B.K. 47
Mikhailova M.P. 152, 545
Mikhalyova M. 433
Minkov G.M. 512
Mintairov A.M. 316
Mirgorodskii A.P. 244
Misuryaev T.V. 380
Moiseev K.D. 152, 545
Moiseev Yu.N. 221
Moldavskaya M.D. 137
Monemar B. 54
Moroz E.M. 339
Moskalenko E.S. 73
Moskovits M. 492
Moumanis K. 69
Murel A.V. 224, 267
Murzina T.V. 221, 380
Musikhin Yu.G. 320
Myasnikova L.P. 399
Naeser A. 452
Nakamura A. 219
Nakamura Y. 467
Neverov V.N. 7, 561
Nikitina E.A. 351
Nikonorov V. 137
Novoselov N.S. 497
Nurgazizov N.I. 240, 242
Oda S. 281
Odintsov A.A. 368
Omling P. 354, 497
Oreshkin S.I. 480
Orlov L.K. 327, 549
Orlova N. 549
Ossau W. 42, 68, 81
Ostroumova E.V. 456
Oudar J.L. 199
Ovchinnikov D.V. 242
Paillard M. 62
Panfilov A.G. 110
Panin I.M. 304
Panov V.I. 480
Panzarini G. 31, 43
Parfeniev R.V. 152
Pashkin Yu.A. 484
Paturi P. 287
Pavlikov A.V. 403
Pavlov S.T. 95
Pedersen K. 221, 380
Pekola J.P. 484
Petrashov V.T. EPSP.02i*
Petrikov V.D. 411, 415
Petrov V.A. 324

Petrov V.N. 296
Pierz K. 47
Pikhtin A.N. 263
Pikus G.E. 498
Platonov A.V. 42, 81
Podlaskin B.G. 448
Pokutnyi S.I. 417
Poletaev N.K. 73
Polisski G. 460
Polkovnikov A.S. 218
Polupanov A.F. 118
Polyakov N.K. 296
Polyakov S.V. 555
Polyanskaya T.A. 541
Ponomarev A.I. 7
Ponomareva N.P. 296
Portal J.C. 488
Portnoi E.L. 191
Portnoi M.E. 83
Potapov A.V. 327, 331
Pozina G.R. 54
Preobrazhenskii V.V. 233, 252, 292, 320
Presnov D.E. 477
Presnov V.I. 259
Prilutsky D.V. 278
Prinz V.Ya. 339
Prokophiev A.A. 316
Pronyshyn I. 429
Proshina O.V. 102
Pudalov V.M. 520
Putyato M.A. 233, 252, 292, 320
Radojkovic P. 357
Ramvall P. 354
Rappich J. 463
Rasing Th. 221
Rebane Y.T. 122
Revin D.G. 141
Robart D. 106
Roberts J.S. 43
Rogachev A.A. 126, 456
Romanov D.A. 553
Romanov N.G. 47
Romanov S.G. 421, 488
Romstad F. 62
Rotkin V.V. 335
Rotkina L.G. 361
Rosov A.E. 545
Rubtsov A.N. 425
Rubtsova R.A. 310
Rumyantsev S.L. 399
Rut O.E. 512
Ryabushkin O.A. 270
Ryl'kov V.V. 11
Rzaev M.M. 231
Sabirzyanova L.D. 7
Sablikov V.A. 18, 555
Sablina N.I. 498
Saito K. 288
Saitoh W. 440
Sakharov A.V. 202
Samuelson L. 282, 354
Sankin V.I. 155
Sasin M.E. 69
Sauvage S. 567, 569
Savel'ev I.G. 541
Savinov S.V. 480
Savvateev M.N. 477
Scharmann A. 47
Scherer H. 477
Schnorr C. 47
Schwartzkopff M. 357
Sedova I. 206
Seifert W. 354

Seigo Taruch 368
Seisyan R.P. 69, 38
Seleznev V.A. 339
Semchinova O.K. 244
Semenova G.V. 417
Semyagin B.R. 233, 252, 292, 320
Shaligina O. 387
Shalygin V.A. 161, 164
Shapoval S.Yu. 22
Sharaya A.B. 339
Shashkin V.I. 224, 256, 267
Shchamkhalova B.S. 18
Shchukin V.A. 306
Sheka E.F. 351
Shekhovtsov S.G. 118
Shelushinina N.G. 7, 561
Shen A. 199
Shernyakov Yu.M. 202
Shmelev S.S. 537
Shreter Y.G. 122
Shubina T.V. 54, 206, 210
Siklitsky V.I. 227, 383
Sirotkin V.V. 22
Sitnikova A.A. 383
Skolnick M.S. 43
Smirnov A.N. 244
Smirnov I.Yu. 541
Smirnov M.B. 244
Smirnov V.A. 152
Smirnov V.P. 110
Sobolev M.M. 274
Sokolov N.S. 288
Sokolova Z.N. 187
Sokolovskii G.S. 180, 191
Soldatov E.S. 494
Solomon G.S. 314
Solomonov A.V. 263
Sorokin S.V. 206, 210
Sorokina S.V. 316
Soshnikov I.P. 361
Sosnin I.A. 24
Sreseli O. 460
Stelmakh N. 199
Stepanov Yu.P. 287
Stepikhova M.V. 99, 310
Stoddart S.T. 236
Subashiev A.V. 130
Suris R.A. 176
Suslov A.V. 541
Suturin S.M. 288
Suvorova A.A. 233, 236, 292, 383, 341
Svensson C. 282
Svintsov A.A. 345
Svizhenko A. 144
Tager A.A. 492
Takayanagi H. 1
Takhtamirov E.E. 134
Tanaka M. 288
Tanklevskaya E.M. 474
Tansley T.L. 118
Temkin H. 180
Timofeev V.B. 27
Timoshenko V.Yu. 403, 463
Tishin A.M. 221
Titkov A.N. 219
Titkov I.E. 164, 161
Tkach M. 429, 433, 437
Tkachenko O.A. 159, 499, 553, 559
Tkachenko V.A. 159, 499, 553, 559
Tkatchman M.G. 206, 210
Tokranov V.E. 219, 278
Tokranova N.A. 448
Tokura Y. 368

Tolmatchev A.V. 383
Toppari J.J. 484
Toropov A.A. 54, 206, 210
Totland H. 531
Towe E. 161, 164
Tret'yakov V.V. 252
Trifonov A.S. 494
Trofimov V.T. 537
Tronc P. 110
Tsai J.S. 467
Tsaregorodtsev A.M. 244
Tsatsul'nikov A.F. 202, 236, 341
Tulupenko V.N. 164
Uskova E.A. 141
Ustinov V.M. 183, 195, 202, 259, 274, 300, 341
Valyev V.V. 22
Van Haesendonck C. 480
Vasanelli L. 395
Vdovin E.E. 497, 508
Vedeneev A.S. 11
Vinogradov E.A. 89
Vladimirova M.R. 31, 43, 64
Vlasenko L. 287
Vlasov A.S. 316
Voitsekhivska O. 433
Volchkov N.A. 537
Volkov V.A. 134, 505
Volovik B.V. 341
Von Foerster W. 47
Vorob'ev A.B. 339
Vorobjev L.E. 161, 164
Voronina T.I. 545
Vul' A.Ya. 227
Waag A. 81
Wallis R.F. 306
Wang D. 365
Wang K.L. 365
Wang Q. 354
Watanabe M. 440
Werner P. 320
Whittaker D.M. 43
Willander M. 54
Wojtowicz T. 42, 68
Wojtsekhowski M.B. 159, 559
Xu J.M. 492
Yakovenko S.A. 494
Yakovlev D.R 42, 68, 81
Yakovlev Yu.P. 152, 545
Yakunin M.V. 137, 561
Yamamoto Y. 87
Yang F. 549
Yastrebov S.G. 383
Zaitsev S.I. 345
Zaitsev S.V. 183, 202
Zakharchenya B.P. 106, 288
Zakharova A. 516
Zakheim D.A. 474
Zaraiskaya T.A. 474
Zavodinsky V.G. 466
Zegrya G.G. 164, 168, 172, 187, 214, 218, 437
Zehnder U. 81
Zhao Zhen 202
Zhilyaev I.N. 24, 26, 25
Zhmodikov A.L. 73
Zhukov A.E. 183, 195, 202, 236, 259, 274, 300, 341
Zhukov E. 387, 391
Zibik E.A. 161
Zorin A.B. 477
Zubkov V.I. 263
Zvonkov B.N. 141

Notes

Отпечатано с готового оригинал-макета ФТИ в типографии ПИЯФ РАН

188350, г. Гатчина, Орлова роща

Зак. 218 тир. 250, уч.-изд. л. 25; 4.06.1997 г.